HYSTERESIS CHARACTERIZATION AND CONTROL OF ELECTRORHEOLOGICAL AND MAGNETORHEOLOGICAL MATERIALS

EDITED BY: Xian-Xu Bai, Ramin Sedaghati, Janusz Goldasz and Shuaishuai Sun
PUBLISHED IN: Frontiers in Materials

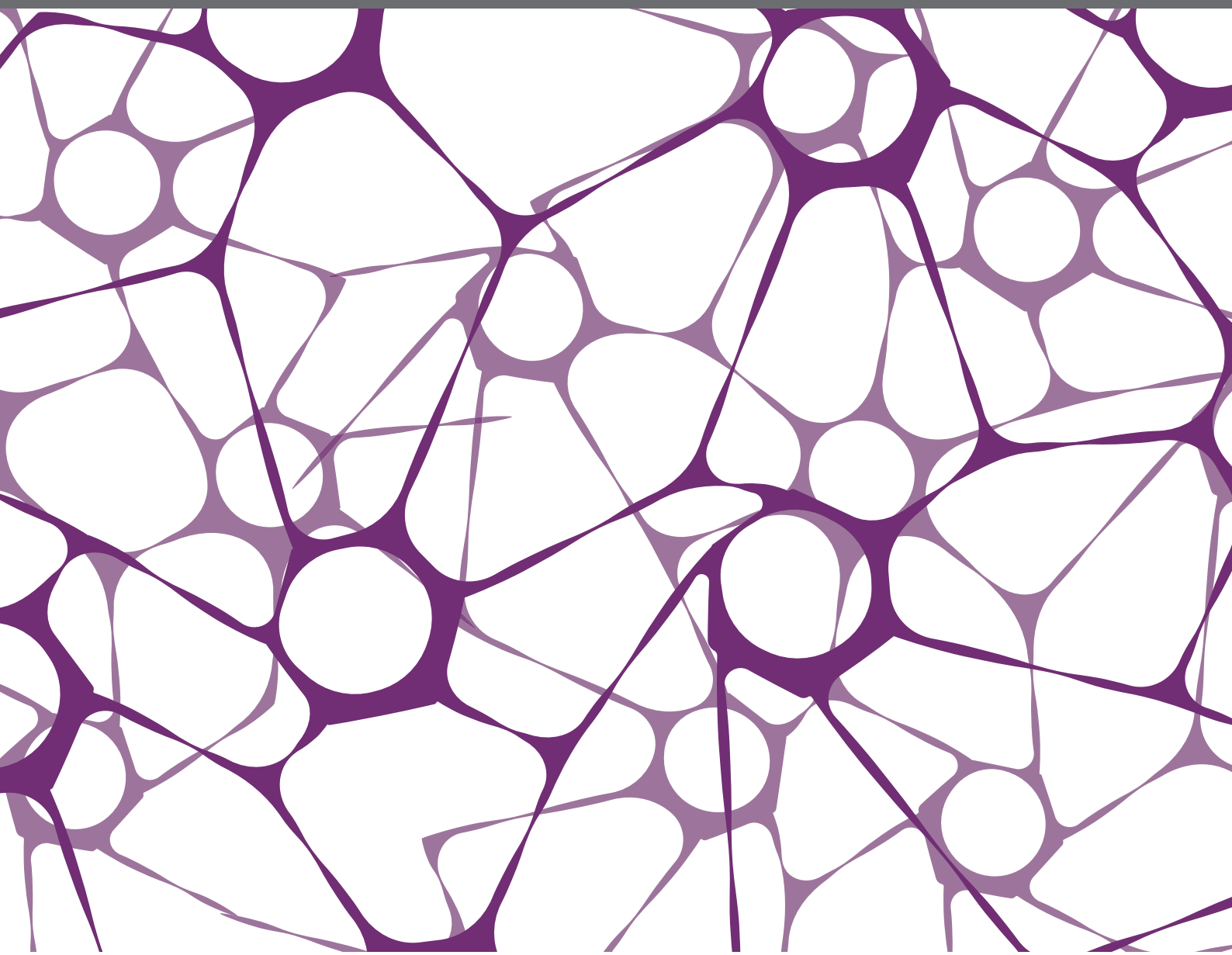

frontiers Research Topics

frontiers

ISSN 1664-8714
ISBN 978-2-88971-323-3
DOI 10.3389/978-2-88971-323-3

About Frontiers

Frontiers is more than just an open-access publisher of scholarly articles: it is a pioneering approach to the world of academia, radically improving the way scholarly research is managed. The grand vision of Frontiers is a world where all people have an equal opportunity to seek, share and generate knowledge. Frontiers provides immediate and permanent online open access to all its publications, but this alone is not enough to realize our grand goals.

Frontiers Journal Series

The Frontiers Journal Series is a multi-tier and interdisciplinary set of open-access, online journals, promising a paradigm shift from the current review, selection and dissemination processes in academic publishing. All Frontiers journals are driven by researchers for researchers; therefore, they constitute a service to the scholarly community. At the same time, the Frontiers Journal Series operates on a revolutionary invention, the tiered publishing system, initially addressing specific communities of scholars, and gradually climbing up to broader public understanding, thus serving the interests of the lay society, too.

Dedication to Quality

Each Frontiers article is a landmark of the highest quality, thanks to genuinely collaborative interactions between authors and review editors, who include some of the world's best academicians. Research must be certified by peers before entering a stream of knowledge that may eventually reach the public - and shape society; therefore, Frontiers only applies the most rigorous and unbiased reviews.
Frontiers revolutionizes research publishing by freely delivering the most outstanding research, evaluated with no bias from both the academic and social point of view. By applying the most advanced information technologies, Frontiers is catapulting scholarly publishing into a new generation.

What are Frontiers Research Topics?

Frontiers Research Topics are very popular trademarks of the Frontiers Journals Series: they are collections of at least ten articles, all centered on a particular subject. With their unique mix of varied contributions from Original Research to Review Articles, Frontiers Research Topics unify the most influential researchers, the latest key findings and historical advances in a hot research area! Find out more on how to host your own Frontiers Research Topic or contribute to one as an author by contacting the Frontiers Editorial Office: frontiersin.org/about/contact

HYSTERESIS CHARACTERIZATION AND CONTROL OF ELECTRORHEOLOGICAL AND MAGNETORHEOLOGICAL MATERIALS

Topic Editors:
Xian-Xu Bai, Hefei University of Technology, China
Ramin Sedaghati, Concordia University, Canada
Janusz Goldasz, Cracow University of Technology, Poland
Shuaishuai Sun, University of Science and Technology of China, China

Citation: Bai, X.-X., Sedaghati, R., Goldasz, J., Sun, S., eds. (2021). Hysteresis Characterization and Control of Electrorheological and Magnetorheological Materials. Lausanne: Frontiers Media SA. doi: 10.3389/978-2-88971-323-3

Table of Contents

frontiers in Materials

EDITORIAL
published: 16 July 2021
doi: 10.3389/fmats.2021.732353

Editorial: Hysteresis Characterization and Control of Electrorheological and Magnetorheological Materials

Xian-Xu Frank Bai[1]*, *Ramin Sedaghati*[2], *Janusz Goldasz*[3] and *Shuaishuai Sun*[4]

[1]Laboratory for Adaptive Structures and Intelligent Systems (LASIS), Department of Vehicle Engineering, Hefei University of Technology, Hefei, China, [2]Department of Mechanical and Industrial Engineering, Concordia University, Montreal, QC, Canada, [3]Faculty of Electrical and Computer Engineering, Cracow University of Technology, Kraków, Poland, [4]Department of Precision Machinery and Instrumentation, University of Science and Technology of China, Hefei, China

Keywords: hysteresis, magnetorhelogical, electrorheological, smart material, inverse problem, vibration control

Editorial on the Research Topic

Hysteresis Characterization and Control of Electrorheological and Magnetorheological Materials

INTRODUCTION

Smart materials, specific referring to electrorheological/magnetorheological (MR) fluids and elastomers, are providing incomparable prospect of the "old" applications, such as vehicular/seat suspensions with vibration/shock mitigation control, engine mount, brake and torque transmission systems, anti-earthquake structures for civil buildings, medical rehabilitation actuators, robotic end effectors, active vales/actuators. However, from academic and industrial viewpoints, hysteresis properties of the materials and the structures are the core of the obstacle of "optimal" applications.

Different with many other well-established smart materials and structures journals such as Smart Materials and Structures and Journal of Intelligent Material Systems and Structures, the primary objective of this Special Issue in Frontiers in Materials is to provide an open-access forum for researchers and practitioners to exchange their latest achievements and to identify critical issues and challenges for future investigation on the hysteresis-based design, modelling, optimization and control dynamic systems. This special issue has accepted 13 high-quality papers after rigorous interactive peer-review processes, the contents of which are summarized as follows.

HYSTERESIS IN MATERIALS

Sokolovski et al. enhanced the MR effect with the shear-thickening (ST) property. The viscosity of ST fluids when subjected to sudden impacts increases dramatically which may provide a viable alternative to typical MR suspensions in certain applications. The authors measured properties of MRST materials with different iron concentrations, thus demonstrating behaviours of the material, i.e., from a material with a weak MR effect and a strong ST property to the one with a strong MR effect and less pronounced ST behaviour. The authors classified the MRST fluid behaviour into three regimes for designing application-oriented materials.

In another study involving MRST fluids Yu et al. demonstrated the performance of an MR damper using such material for seismic applications. Moreover, the damper includes a fail-safe circuit (in the form of a permanent magnet) for bi-directional control. The authors presented a working principle of the damper, show their finite-element calculations of the magnetic field

OPEN ACCESS

Edited and reviewed by:
Weijia Wen,
Hong Kong University of Science and Technology, China

***Correspondence:**
Xian-Xu Frank Bai
bai@hfut.edu.cn

Specialty section:
This article was submitted to Smart Materials, a section of the journal Frontiers in Materials

Received: *28 June 2021*
Accepted: *05 July 2021*
Published: *16 July 2021*

Citation:
Bai X-XF, Sedaghati R, Goldasz J and Sun S (2021) Editorial: Hysteresis Characterization and Control of Electrorheological and Magnetorheological Materials. Front. Mater. 8:732353. doi: 10.3389/fmats.2021.732353

distribution in the MR valve, and then highlighted the experimental results of the damper subjected to various excitation inputs. It is shown that the device has the ability to be controlled by magnetic field, and reveal the ST behaviour at the same time.

In the work by Zhang et al., the dynamic mechanical properties of MR elastomers under cyclic loadings and periodic magnetic field were investigated and analyzed, including the influences of matrix, particle distribution, magnetic field on the dynamic mechanical hysteresis. They found that all the mechanical pressure, shear strain, as well as periodic magnetic field would cause a hysteresis in the dynamic mechanical properties of the MR elastomer, and the hysteresis tends to be saturated after cycles.

HYSTERESIS IN DEVICES

Lozoya-Santos et al. presented a general modeling approach for MR shock absorbers using the characteristic diagrams, i.e., force-displacement, force-velocity, and force-acceleration loops. One certain pattern of seven can be obtained for model design after analyzing the diagrams at different frequencies of interest. The experimentally validated new general modeling approach with simply mathematical expression could provide decent performance with 2–10% errors.

Gołdasz et al. thoroughly investigated the hysteretic behavior of MR dampers. Different with the existing models for combined hysteretic behavior of MR actuators by observing the relationships between the output and the inputs. They presented and explained that the two hysteretic mechanisms - mechanical/hydraulic and magnetic are the distinct terms, and they should be split in the modeling process. Both the Duhem model and the derived Maxwell type model were used in the work for illustration purposes. Based on the approach they proposed, each hysteresis mechanism can be studied independently, and then essential understanding of the hysteretic behavior of MR devices can be obtained.

Guo et al. investigated the nonlinear behavior of MR damper with emphasis on the coupled inertial-viscous-frictional-elastic transients of the two-dimensional (2D) axisymmetric flow of the compressible Herschel-Bulkley fluid. The viscoplasticity and compressibility of MR fluid are, respectively, modeled by the modified Herschel–Bulkley model and the Tait equation. Significant conclusions were: coupled transients of an MR damper are frequency dependent, and the weak compressibility of MR fluid mainly happens in the chamber rather than in the working gap and is crucial to accurately predict and understand the dynamic performances of MR dampers. It is of help in research on general MR devices design and modeling.

In the work by Li et al., they attempted to reduce or eliminate the effect of the magnetic hysteresis of the MR damper using Jiles-Atherton (J-A) model and a magnetic hysteresis compensation control method was proposed. Magnetic induction intensity was obtained via an embedded Hall sensor in MR fluid damper. The proposed hysteresis compensation method with a PID controller can eliminate the effect of hysteresis under both low frequency and high frequency inputs. The output damping force of the MR impact buffer system indicated that the buffer performance has been improved by employing the magnetic hysteresis compensation control method.

Zhong et al. combined a MR damper and a MR inerter according to the design concept of "functional integration", and realized an integrated shock absorber with both tunable inertance and damping. A new integrated inerter-spring-damper with both adjustable inertance and damping characteristics when applied with coil currents was further proposed. Mechanical output characteristics of the integrated inerter-spring-damper were analyzed, and the integrated inerter-spring-damper-based 1/4 vehicle suspension provided an improved vibration mitigation performance.

HYSTERESIS IN SYSTEMS

In the applications of seat suspensions/isolation systems, Zhu et al. and Liu et al. studied a cab seat suspension with a MR fluid damper- and a MR elastomer-based semi-active seat suspension isolator, respectively. In order to address the core problem of the nonlinear hysteresis, Zhu et al. presented a unified-format model expression for both Bingham and Bouc-Wen models, while Liu et al. used the adaptive neural network. Experimental results of the two semi-active systems show the superiority of the controlled systems.

Specifically, for the system controller of another application of MR semi-active seat suspension, Liu et al. proposed a new controller - particle swarm optimization (PSO)-improved fruit fly optimization algorithm (IFOA)-based PID. By incorporating PSO and IFOA into the PID-parameter searching processing, a globally optimal PID-parameter set can be found. Both numerical and experimental studies were conducted to evaluate the vibration isolation performance of the new controller. The results validated that the PSO-IFOA method can optimize the PID parameters for controlling the semi-active seat suspension and outperforms the other controllers.

For the application of vehicle suspensions, in the work by Vivas-Lopez et al., multi-body dynamic analysis considering the mechanical components–nonlinear MR damper and the joints of a McPherson suspension was conducted. The stress concentration analysis was also given for the semi-active suspension performance evaluation. It provided very helpful results that the semi-active suspension will not only improve the vibration attenuation, but also decrease the stress concentrations in the suspension elements.

Dong et al. proposed a new variable stiffness and damping vibration absorber using MR technology for torsional vibration application - powertrain systems. Detailed model of the system input excitation from the powertrain system as well as the human-simulated intelligent controller for the new MR semi-active system are provided. With consideration of the nonlinear hysteresis of the components, reasonable results were provided in the work. The proposed concept of the smart device would be helpful for engineering applications.

Finally, we know that the selected topics and papers are not a comprehensive representation of the area of this special issue. Nonetheless, they represent the rich and many-faceted knowledge that we have the pleasure of sharing with the readers. We would like to express appreciation to the authors for their excellent contributions, to the reviewers for the quality check of the special

section, and to the Frontiers in Materials Editors and the Editorial office staff for their great support.

AUTHOR CONTRIBUTIONS

X-XB: Writing - original draft, review, and editing RS: Writing - original draft, review, and editing JG: Writing - original draft, review, and editing SS: Writing - original draft, review, and editing.

Conflict of Interest: The authors declare that the research was conducted in the absence of any commercial or financial relationships that could be construed as a potential conflict of interest.

frontiers in Materials

ORIGINAL RESEARCH
published: 15 November 2019
doi: 10.3389/fmats.2019.00269

Optimizing Vibration Attenuation Performance of a Magnetorheological Damper-Based Semi-active Seat Suspension Using Artificial Intelligence

Xinhua Liu[1], Ningning Wang[1], Kun Wang[1], Hui Huang[2], Zhixiong Li[3,4], Thompson Sarkodie-Gyan[5] and Weihua Li[4]*

[1] School of Mechanical and Electrical Engineering, China University of Mining & Technology, Xuzhou, China, [2] Key Laboratory of Fluid Power and Intelligent Electro-Hydraulic Control (Fuzhou University), Fujian Province University, Fuzhou, China, [3] Department of Marine Engineering, Ocean University of China, Tsingdao, China, [4] School of Mechanical, Materials, Mechatronic and Biomedical Engineering, University of Wollongong, Wollongong, NSW, Australia, [5] Department of Electrical and Computer Engineering, College of Engineering, University of Texas, El Paso, TX, United States

OPEN ACCESS

Edited by:
Shuaishuai Sun, Tohoku University, Japan

Reviewed by:
Yang Yu, University of Technology Sydney, Australia
Yancheng Li, University of Technology Sydney, Australia

***Correspondence:**
Zhixiong Li
zhixiong_li@uow.edu.au

Specialty section:
This article was submitted to Smart Materials, a section of the journal Frontiers in Materials

Received: *01 August 2019*
Accepted: *16 October 2019*
Published: *15 November 2019*

Citation:
Liu X, Wang N, Wang K, Huang H, Li Z, Sarkodie-Gyan T and Li W (2019) Optimizing Vibration Attenuation Performance of a Magnetorheological Damper-Based Semi-active Seat Suspension Using Artificial Intelligence. Front. Mater. 6:269. doi: 10.3389/fmats.2019.00269

This paper aims to improve control performance for a magnetorheological damper (MRD)-based semi-active seat suspension system. The vibration of the suspension is isolated by controlling the stiffness of the MRD using a proportion integration differentiation (PID) controller. A new intelligent method for optimizing the PID parameters is proposed in this work. This new method appropriately incorporates particle swarm optimization (PSO) into the PID-parameter searching processing of an improved fruit fly optimization algorithm (IFOA). Thus, the PSO-IFOA method possesses better optimization ability than IFOA and is able to find a globally optimal PID-parameter set. The performance of the PID controller optimized by the proposed PSO-IFOA for attenuating the vibration of the MRD suspension was evaluated using a numerical model and an experimental platform. The results of both simulation and experimental analysis demonstrate that the proposed PSO-IFOA is able to optimize the PID parameters for controlling the MRD semi-active seat suspension. The control performance of the PSO-IFOA-based PID is superior to that of individual PSO-, FOA-, or IFOA-based methods.

Keywords: magnetorheological damper, semi-active seat suspension, vibration control, artificial intelligence, PID controller

INTRODUCTION

Engineers often work in a high vibration environment, which seriously affects their health (Maikala and Bhambhani, 2013). Seat suspension is widely used as a buffer unit to solve the hostile vibration problem. Compared to other existing seat suspension systems, semi-active seat suspension based on a magnetorheological damper (MRD) has the advantages of a simple structure, low power consumption, strong damping force-adjustment capability, and fast response speed. Moreover, the natural frequency and damping characteristics of the semi-active seat suspension can be adjusted according to the excitation frequency, which can improve damping performance. However, it is difficult to obtain the proper natural frequency and damping performance in the absence of an

effective control strategy. For this reason, achieving high performance control for semi-active seat suspension systems has become an essential research topic in recent years.

Proportion integration differentiation (PID) controllers have been widely used in industrial contexts because of their advantageous characteristics of having a simple structure, strong robustness, high cost-benefit ratio, and high reliability (Kuntanapreeda, 2016; Zamani et al., 2017; Pan et al., 2018). PID controllers have found application in process control (Mukherjee and Ghoshal, 2007), flight control (Savran et al., 2006), motor driving control (Hernandez-Guzman and Carrillo-Serrano, 2011), and instrumentation (Feng et al., 2014). The most important factor that affects the performance of a PID controller is the determination of the PID parameters (Ang et al., 2005; Ramezanian et al., 2013). Because of the strong non-linearity and time delay that is in the nature of an engineered system such as a semi-active seat suspension system (Zhou et al., 2011; Lu et al., 2015), it is necessary to optimize the parameters of the PID controller. The fruit fly optimization algorithm (FOA) (Shi et al., 2015), which has been developed according to the foraging behavior of fruit flies, is able to address the problem of PID parameter optimization (Wang and Liu, 2014; Han et al., 2016; Wang et al., 2016). However, due to the fixed flight distance and blind search direction in individual fruit flies, the optimization performance of the FOA is not always satisfactory due to the fact that some individual fruit flies cannot escape from a local optimum (Pan et al., 2014). Particle swarm optimization (PSO), which is based on the feeding behavior of flocks, is another method for optimizing the PID parameters (Meissner et al., 2006). However, it is easy to fall into a local optimum, and a particle cannot jump out of its own cycle (Srivastava and Agarwal, 2010). The improved fruit fly optimization algorithm (IFOA) is an optimization of the FOA with increased global search capability for optimizing the PID parameters. However, its control accuracy is still not ideal (Liu et al., 2017). To solve this problem, this paper develops a new method based on particle swarm optimization and the improved fruit fly optimization algorithm (PSO-IFOA) to optimize the PID parameters for the vibration control of semi-active seat suspension and shows that it possesses better dynamic response characteristics and control accuracy compared with FOA, PSO, and IFOA. The control performance of the PID controller optimized by PSO-IFOA is evaluated using simulations and experimental tests.

The rest of this paper is organized as follows. In section Literature Review, a literature review is performed. In section Proposed Method, the basic theories of PID parameter optimization and FOA are presented, the PSO-IFOA is proposed. In section Vibration Control Performance, Simulation and experimental tests are carried out to evaluate the PSO-IFOA method. Conclusions and future work are summarized in section Conclusions and Future Work.

LITERATURE REVIEW

The most recent publications relevant to this paper have mainly been concerned with two research streams: PID parameter optimization and FOA. In this section, we try to summarize the relevant literature.

PID Parameter Optimization

The parameter adjustment of a traditional PID mainly relies on working experience. In Xu (2015), the leapfrog algorithm was used to improve the global search capability of the FOA and optimize the PID parameters, and the relevant experimental results indicated that the performance of the PID controller had been optimized significantly. Fuzzy logic, genetic algorithms, and neural networks were used to tune the PID parameters, and the results indicated that a controller with a combination of these algorithms was better than the conventional controller (Alkamachi and Erçelebi, 2017; Eduardo et al., 2018; Eltag et al., 2019). Vijayakumar and Manigandan (2016) proposed an ant colony optimization algorithm to optimize the genetic algorithm and PID parameters and found through experimental study that a non-linear PID-based on the enhanced genetic algorithm was more suitable for servo control and supervisory operation. Liu et al. (2018) proposed a parameter adjustment approach for PIDs based on iterative learning control. The relevant simulation and experimental results indicated that the proposed approach could intelligently adjust the PID parameters of an atomic force microscope. Bhambhani and Shah (2016) adjusted the parameters of a PID controller by a novel optimization approach called queue intelligence, and it proved to present a better response than the genetic algorithm. Mei and Luo (2017) proposed a parameter optimization approach for PID controllers based on improved coevolution and found that this approach had better convergence speed, adaptability, and precision and wider application prospects.

Fruit Fly Optimization Algorithm

In recent years, many researchers have started to focus on the FOA. In Yu et al. (2015), an IFOA was proposed to identify the parameters for an improved LuGre friction model used in the modeling for MRD. The IFOA was shown to be able to enhance the convergence rate of the algorithm and to avoid local optima. Yu et al. (2014, 2016) used an IFOA based on a self-adaptive step update strategy (SSFFOA) to characterize a magnetorheological elastomer (MRE) base isolator, and an enhanced PSO was used to identify the model parameters for the MRE base isolator. Meanwhile, the superiority and feasibility of the proposed algorithms were verified. Ahmet et al. (2017) proposed an improved version of FOA and showed through experiment that the improved version of FOA was more equal and fairer in terms of screening the solution space. Xu et al. (2016) proposed an IFOA and illustrated its effectiveness and superiority through a comprehensive comparison among five typical algorithms. Han et al. (2017) developed a novel FOA with trend search and coevolution and showed experimentally that the novel FOA had higher robustness. Lei et al. (2016) proposed a novel fruit fly optimization clustering algorithm to identify dynamic protein complexes by combining FOA and gene expression profiles. Zheng and Wang (2016) proposed a knowledge-guided FOA

to deal with the dual resource-constrained flexible job-shop scheduling problem and experimentally verified the effectiveness of the proposed algorithm.

Discussion

Many PID parameter optimization approaches have been proposed in the above literature and have been applied in recent decades, but these also have some shortcomings. Firstly, PID controllers designed by different intelligent algorithms have diverse control effects on the same system. Secondly, conventional PID controllers have a worse control effect than PID controllers designed with an intelligent algorithm. Thirdly, due to the large non-linearily and hysteresis of semi-active seat suspension, it is necessary to design a control system with a faster response, more accurate control, and less overshoot to address these problems. Lastly, FOA has great advantages in terms of iteration rate and encoding efficiency but still has the potential to fall into a local optimum.

Therefore, a PSO-IFOA is proposed to adjust the parameters for the PID controller of an MRD-based semi-active seat suspension. The velocity formula of PSO is utilized to redefine the flight distance and direction of IFOA to reduce the possibility of blind search of individual fruit flies. The convergence precision of IFOA can be enhanced, and local optima can be avoided. Both a simulation model and an experimental system of the MRD-based semi-active seat suspension are established to evaluate the effectiveness and correctness of the proposed PSO-IFOA-PID method.

PROPOSED METHOD

Proposed PSO-IFOA Method

FOA is a global intelligent optimization algorithm that is established by simulating the foraging behavior of the fruit fly. The FOA can be implemented via the following steps (Liu et al., 2017).

Step 1: Determine the population amount (PA), the maximum iteration number (IN_{max}), flying distance range (FR), group location range (LR), and initial location (X_{-axis}, Y_{-axis}) of the fruit fly population.

Step 2: Calculate the random flight direction and distance to search for the food of the individual fruit fly.

$$\begin{cases} X_i = X\_axis + 2FR \times \ Rand_i - FR \\ Y_i = Y\_axis + 2FR \times \ Rand_i - FR \end{cases} \tag{1}$$

Step 3: Calculate the distance between the individual fruit fly and the origin, and then calculate the flavor concentration parameter, which is the reciprocal of the distance.

$$\text{Distance}: \ Dist_i \ = \ \sqrt{{X_i}^2 + {Y_i}^2}, \tag{2}$$

$$\text{Concentrationparameter}: \ S_i \ = \ 1/Dist_i. \tag{3}$$

Step 4: Substitute S_i into the fitness function, calculate the value of the flavor concentration function $Smell_i$, and find the best flavor concentration in the fruit fly population. In this paper, the minimum value is taken as the best flavor concentration.

$$Smell_i = Function(S_i), \tag{4}$$

$$[bestSmell, bestindex] = \min(Smell). \tag{5}$$

Step 5: Obtain the best flavor value and the coordinates of (X_{-axis}, Y_{-axis}).

$$Smellbest = bestSmell, \tag{6}$$

$$\begin{cases} X\_axis = X(bsetindex) \\ Y\_axis = Y(bsetindex) \end{cases} \tag{7}$$

Step 6: When the smell concentration reaches the preset precision value or the iteration number reaches the maximal IN_{max}, the search stops. Otherwise, repeat Steps 2–5.

Because the flight distance of an individual fruit fly in FOA is within a fixed interval and the search direction is blind, the probability of individual fruit fly falls into a local optimum greatly increases. In order to enhance the capacity of global and local search, the FR should be optimized.

The position of particles in PSO is affected by the current speed, memory, and optimal location of the population. The search direction of an individual fruit fly could be guided by PSO. The velocity equation of PSO can be used to replace the random flight distance of FOA to improve the search capability; this is described as follows:

$$\begin{cases} X_i = X\_axis + (wV_{xi} + c_{x1}r_1(X\_axis - X_i) \\ \qquad\qquad +c_{x2}r_2(X_{best} - X_i)) \\ Y_i = Y\_axis + (wV_{yi} + c_{y1}r_1(Y\_axis - Y_i) \\ \qquad\qquad +c_{y2}r_2(Y_{best} - Y_i)) \end{cases}, \tag{8}$$

where w is the inertia weight and c_{x1}, c_{x2}, c_{y1}, and c_{y2} are the learning factors; the random constants r_1 and r_2 are within [0, 1]; V_{xi} and V_{yi} are the flying speed of an individual fruit fly along the X and Y directions. The increase of the inertia weight can enhance the global search capability but decrease the local search capability and vice versa. Therefore, in order to achieve a good trade-off between global and local search capabilities, the inertia weight w should maintain a large value in the early stage of operation and a small value in the later stage of operation. In this paper, the normal distribution formula is used as the prototype, and the difference x between the individual's position and the global optimum position is used as an independent variable to update the inertia weight w, as follows:

$$x \ = \ k_1(smell(i) - smellbest), \tag{9}$$

$$f(x) \ = \ \frac{k_2}{\sqrt{2\pi}} e^{(-\frac{x^2}{2})}, \tag{10}$$

$$w \ = \ k_3 e^{(-f(x))} + k_4, \tag{11}$$

where $k_1 = 100$, $k_2 = 16$, $k_3 = 1$, $k_4 = 0.2$, k_1, k_2, and k_3 are used to control the change rate of the inertial weight and the upper limit of the control parameters, and k_4 is used to control the upper and lower limits of the inertia weight. In this method, when the gap between the individual and the global optimum

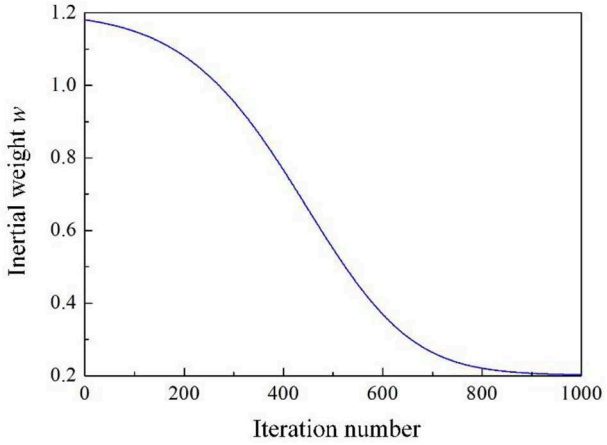

FIGURE 1 | The change rule of inertia weight with iteration number.

positions is large, the calculated inertia weight is large, which increases the individual's global search capability. Meanwhile, when the gap between the individual and the global optimum positions is small, the calculated inertia weight is small, which can accelerate toward the optimal point. **Figure 1** shows the change rule of inertia weight with iteration number in the calculation, which indicates that the inertia weight maintains a large value in the early stage of operation and a small value in the later stage of operation and that the parameter values of k_1-k_4 can meet our requirements in the calculation. The flowchart of the proposed PSO-IFOA is illustrated in **Figure 2**.

Feasibility Verification of Search Capability of PSO-IFOA

In order to verify the search capability of the PSO-IFOA, four tests were conducted using four popular functions (i.e., Ackely, Rastrigin, Schewell, and Matyas) (Xu et al., 2016). The convergence trend and optimization precision of the tests were compared using FOA, PSO, IFOA, and PSO-IFOA. **Table 1** shows the optimal solutions of the four test functions. The initialization conditions were the same for the four algorithms; that is, the population quantity was 30, and the iteration number was 100. **Figure 3** shows the convergence curves of the test functions.

As can be seen in **Table 1**, the smallest optimal solution of the four test functions is produced by the proposed PSO-IFOA method. **Figure 3** shows that the proposed PSO-IFOA has a fast convergence speed and a higher convergence precision than the other three methods.

Feasibility Verification of PSO-IFOA for Optimizing PID Parameters

The feasibility of PSO-IFOA for optimizing PID parameters was investigated using a numerical model of a semi-active seat suspension system. Modeling of the semi-active seat suspension system mainly included two aspects, which were human body dynamics modeling and seat dynamics modeling. The research

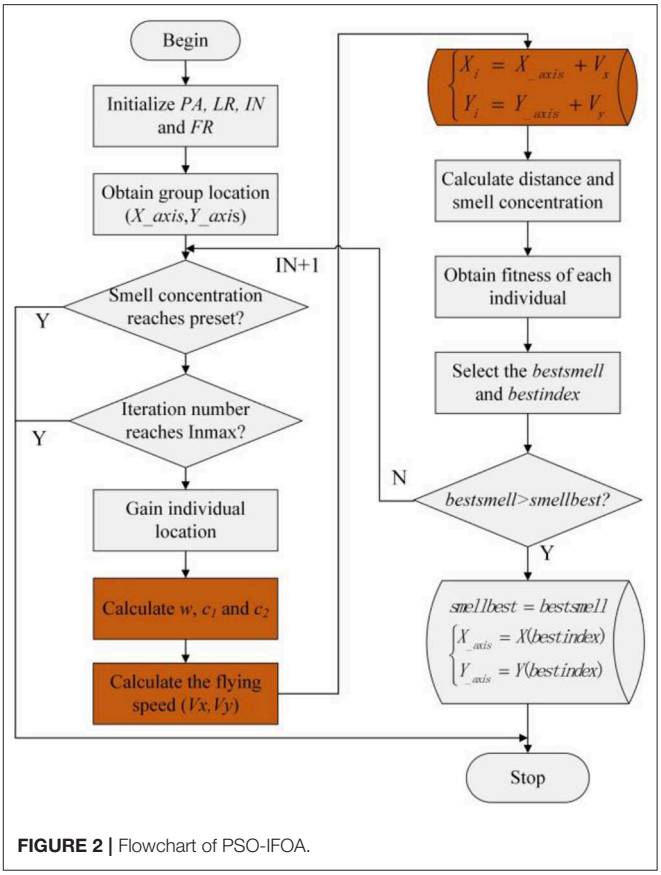

FIGURE 2 | Flowchart of PSO-IFOA.

TABLE 1 | The optimal solution of the four test functions.

Algorithm	Ackely	Rastrigin	Schewell	Matyas
FOA	0.0421	0.0357	−0.00175	3.54e-06
PSO	6.68e-08	0.0368	−0.000782	7.44e-13
IFOA	0.00241	0.00112	−0.0000741	9.80e-09
PSO-IFOA	2.22e-15	7.11e-15	−1.70e-20	8.06e-21

in this paper is mainly concerned with the vibration absorption performance of semi-active seat suspension, which is the vibration attenuation transmitted from a cab to a human body. In this situation, the human body can be considered to a mass block without considering its internal vibration characteristics. In the actual seat suspension, the cushion also possesses vibration damping performance due to its characteristics of stiffness and damping. Therefore, the vibration damping characteristics of the cushion should be considered in establishing the semi-active seat suspension model. A shear suspension structure was adopted in this research due to its good lubrication at the turning structure, and the friction resistance at the rotating structure was then ignored. In order to simplify the calculation process, a 2-DOF semi-active seat suspension model was established. The human body was simplified as a mass block with equivalent mass of m_1, the cushion was simplified as a spring and a damper, with a massless elastic coefficient and a damping coefficient of k_1 and

c_1, respectively. The suspension was regarded as a subsystem with equivalent mass of m_2, equivalent stiffness of k_2, and variable damping coefficient of c_2. The kinematics equation was established according to the 2-DOF semi-active seat suspension model, as shown in Equation (12).

$$\begin{cases} m_1\ddot{x}_1 + c_1(\dot{x}_1 - \dot{x}_2) + k_1(x_1 - x_2) = 0 \\ m_2\ddot{x}_2 - c_1(\dot{x}_1 - \dot{x}_2) - k_1(x_1 - x_2) - c_2(\dot{u} - \dot{x}_2) \\ \quad -k_2(u - x_2) = 0 \end{cases} \tag{12}$$

where u is the vibration excitation transmitted from the cab to the seat suspension, x_2 is the displacement response of the top plate of the seat suspension, and x_1 is the displacement response of the human body; $\dot{x}_1$ and $\ddot{x}_1$ are the first and second derivatives of x_1, $\dot{x}_2$, and $\ddot{x}_2$ are the first and second derivatives of x_2, and $\dot{u}$ is the first derivative of u. In this study, $k_1 = 19{,}496$ N/m, $k_2 = 150{,}261$ N/m, $c_1 = 2{,}165$ Ns/m, $c_2 = 1{,}600$ Ns/m, $m_1 = 18$ kg, $m_2 = 70$ kg.

The kinematic Equation (12) was transformed in Laplace transform, and the transfer function of human displacement

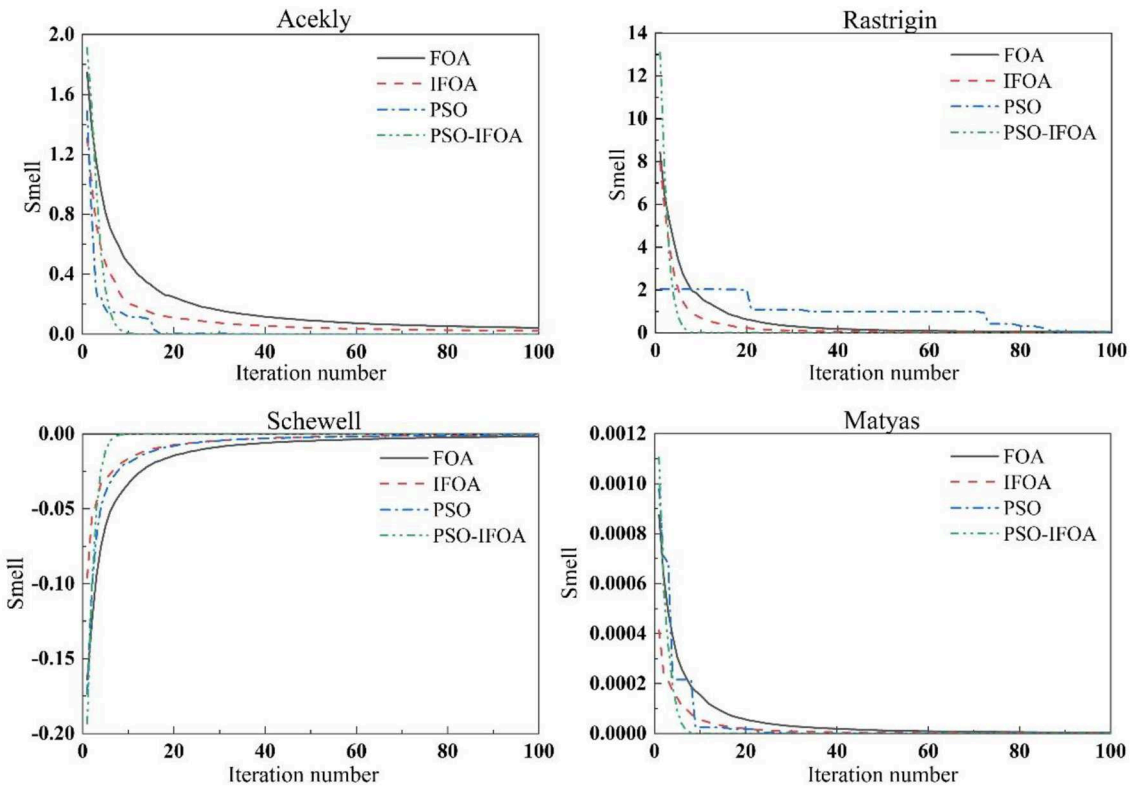

FIGURE 3 | Convergence curves of the test functions.

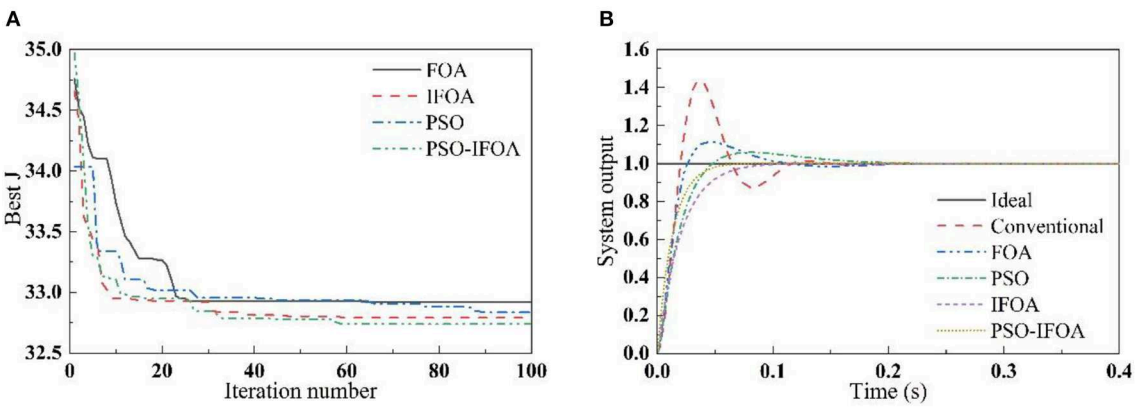

FIGURE 4 | (A) Convergence curves of Best *J* and **(B) s**tep response curves of the controllers.

response x_1 and vibration excitation u could be obtained as follows:

$$G(s) = \frac{x_1}{u} = \frac{(c_1 s + k_1)(c_2 s + k_2)}{(m_1 s^2 + c_1 s + k_1)(m_2 s^2 + c_1 s + c_2 s + k_1 + k_2) - (c_1 s + k_1)^2}. \quad (13)$$

The parameters of the PSO-IFOA, IFOA, PSO, and FOA were set as: $PA = 50$, $IN_{max} = 100$, $(X_{-axis}, Y_{-axis}) \in (0, 5)$, $FR = 0.5$, $\omega_1 = 0.999$, $\omega_2 = 0.001$, $\omega_3 = 2.0$, and $\omega_4 = 100$.

TABLE 2 | Control performance evaluation indicators of the controllers.

Controller type*	Conventional	FOA	PSO	IFOA	PSO-IFOA
σ/%	42.33	14.65	7.95	0	0
t_s/s	0.113	0.094	0.098	0.078	0.052
t_r/s	0.028	0.032	0.046	0.091	0.062

*σ is the overshoot, and t_s is the adjustment time.

In the simulation, a step command signal was input into the control system. The simulation time was 0.4 s. The convergence curves of the comprehensive performance index function J for the different control methods are shown in **Figure 4A**, and the step response curves of each controller are shown in **Figure 4B**. **Table 2** provides the control performance evaluation indicators. It can be seen in **Figure 4A** that the convergence speed and precision of the PSO-IFOA controller are superior to those of the FOA, PSO, and IFOA controllers. This is because the proposed PSO-IFOA method possesses a stronger global search capability than the others. One can observe in **Figure 4B** and **Table 2** that the PSO-IFOA-optimized PID controller produces the best overshoot and adjustment time of the four methods. The proposed PSO-IFOA PID controller outperforms the other three methods in terms of dynamic characteristics.

VIBRATION CONTROL PERFORMANCE

Simulation Results

In order to evaluate the effectiveness of the PSO-IFOA-optimized PID controller, an MRD-based semi-active seat suspension

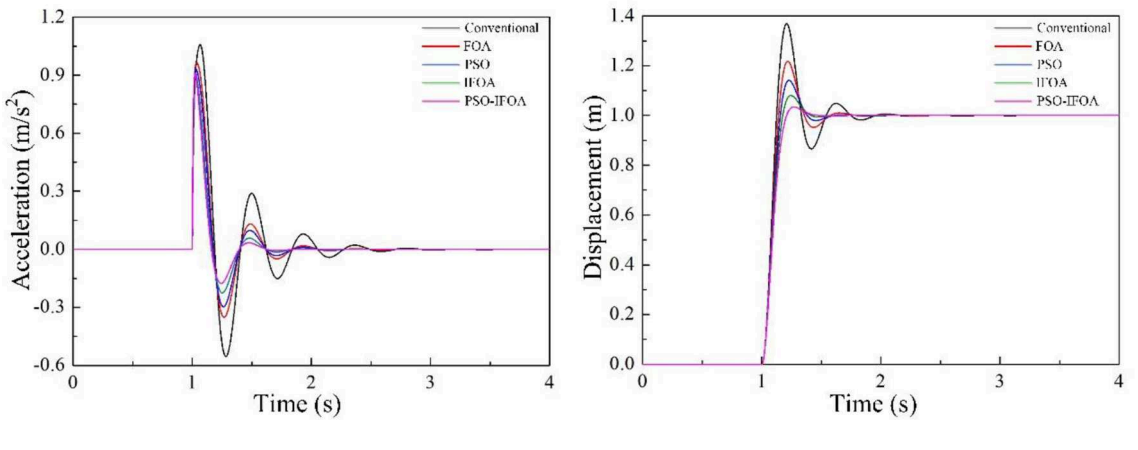

FIGURE 5 | Acceleration and displacement responses under collision vibration.

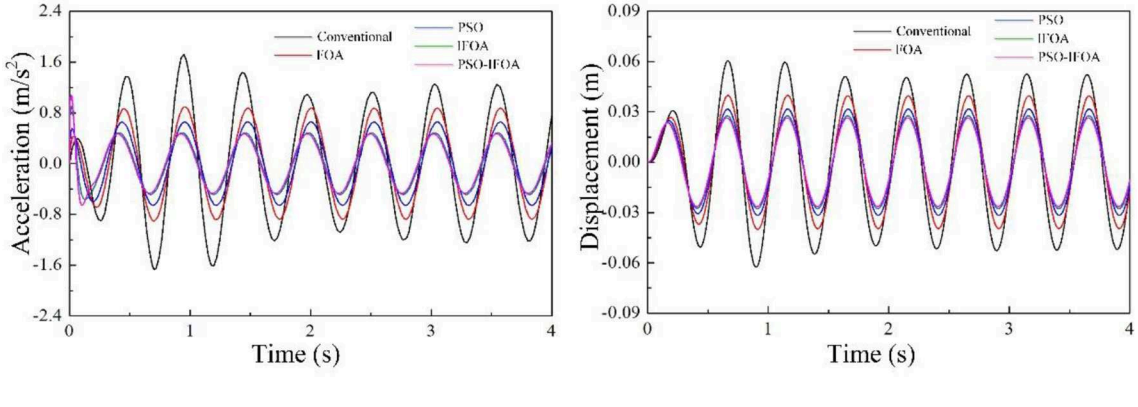

FIGURE 6 | Acceleration and displacement responses under harmonic vibration.

system was established using Matlab/Simulink. The MRD damping effect was considered in this model. The displacement and acceleration responses of the human body were measured under different excitations such as collision and harmonic and random vibrations that were imposed on the seat model. The vibration control performances of the FOA-PID, PSO-PID, IFOA-PID, and PSO-IFOA-PID methods are shown in **Figures 5–7**. The root-mean-square (RMS), peak-to-peak (PTP), and vibration-dose-value (VDV) of the acceleration response were adopted as the criteria with which to evaluate the random vibration effect.

The displacement and acceleration responses of the human body in the condition of collision vibration are shown in **Figure 5**. As can be seen in the figure, compared to the other three controllers, the peak values of human acceleration at the first four waves were smallest with the proposed PSO-IFOA method, the overshoot of the proposed method was, respectively, reduced by 16.29, 6.04, 2.35, and 0.43%, and the stabilizing time was, respectively, decreased by 35.6, 20.6%, 12.99, and 2.5% compared to the other methods.

The displacement and acceleration responses of the human body in the condition of harmonic vibration are shown in **Figure 6**. As can be seen in the figure, compared to the other three controllers, the proposed PSO-IFOA method has the smallest peak values of human acceleration at the first four waves, and its overshoot was, respectively, reduced by 71.2, 47.6, 28.7, and 3.7% compared to the other methods.

Figure 7 depicts the displacement and acceleration responses of the human body in the condition of random vibration. As can be seen in the figures, compared to the other three controllers, the displacement and acceleration amplitudes are smallest with the proposed PSO-IFOA method. Thus, the damping effect of the MRD can be better controlled by the proposed method.

Table 3 compares the RMS, PTP, and VDV of the acceleration amplitude using different controllers. One can note that the proposed PSO-IFOA-PID controller decreased the RMS values by 60.26, 46.25, 33.06, and 9.17%, respectively, when compared with the other four methods; the PTP was, respectively, decreased by 43.74, 36.85, 28.95, and 13.06%, and the VDV was, respectively, reduced by 39.93, 29.87, 17.37, and 7.08%. As a result, the control performance of the proposed method is superior to those of the other methods in the simulations.

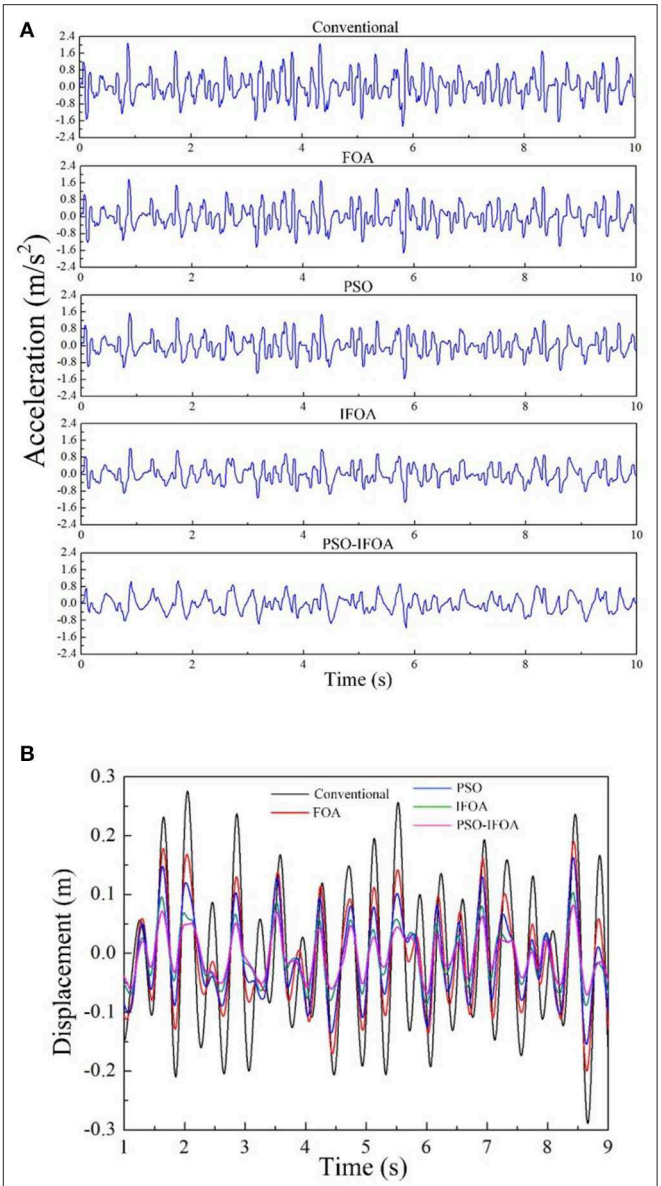

FIGURE 7 | (A) Acceleration responses under random vibration, and **(B)** displacement responses under random vibration.

TABLE 3 | Acceleration response characteristics under random vibration.

	Conventional	FOA	PSO	IFOA	PSO-IFOA
RMS (m/s^2)	0.4112	0.3057	0.2441	0.1799	0.1634
PTP (mm)	3.9362	3.5095	3.1193	2.5494	2.2162
VDV ($m/s^{1.75}$)	1.5356	1.3156	1.1165	0.9928	0.9225

Experiments

Introduction to MRD

The design principle of MRD is that the curing degree of magnetorheological fluid (MRF) is controlled in real time by changing the magnetic field intensity at the damping channel so as to achieve the purpose of controllable damping force. The structure of the MRD is shown in **Figure 8**. When uneven road excitation occurs, relative motion will appear in the vehicle body and seats, which results in variation in displacement on either side of the MRD. The MRD will then be stretched or compressed, and the MRF will be pushed from one working space to another. In this process, the friction between the MRF and the pore wall and the internal friction between liquid molecules cause the generation of damping force, which causes the vibration energy of the whole suspension system to be converted into thermal energy and consumed to achieve the aim of reducing vibration.

In order to make the design of MRD more reasonable, the key sizes of the MRD are optimized by the genetic multi-objective optimization algorithm, which possesses better accuracy in achieving multi-objective optimization. The implementation

of the optimization processes can be achieved through the following steps.

Step 1: Define the damping force equation and the adjustable multiple calculation model of the MRD, which is as follows:

$$F_v = F_\eta + F_\tau = \frac{12\eta L {A_p}^2 v}{\pi D h^3} + \frac{3LA_p\tau}{h}, \tag{14}$$

$$\beta_v = \frac{F_\tau}{F_\eta} = \frac{\pi D\tau h^2}{4\eta A_p v}, \tag{15}$$

where F_η is the non-adjustable viscous damping force, F_τ is the adjusted coulomb damping force, η, τ, and v are the dynamic viscosity, shear yield stress, and flow velocity of MRF, respectively. L, A_p, D, and h indicate the effective length, effective area of the inner ring, inner diameter, and clearance thickness of the damped channel, respectively.

Step 2: Establish the mathematical model of the optimized objective function, which as follows:

$$G(x) = m\frac{F_v}{F_{vmax}} + n\frac{\beta_v}{\beta_{vmax}}, \tag{16}$$

where m and n are the weighting coefficients, and the sum of m and n is 1.

Step 3: Set the optimization variables and the corresponding value range. These are shown in Equations (17) and (18).

$$X = \left[L,\ h, D, d\right]^T, \tag{17}$$

$$\begin{cases} 0.01\ m \le L \le 0.04\ m \\ 0.0005\ m \le h \le 0.003\ m \\ 0.025\ m \le D \le 0.045\ m \\ 0.015\ m \le d \le 0.025\ m \end{cases}. \tag{18}$$

where d is the diameter of a coil. In this study, the optimized parameters were set as $L = 0.026$ m, $h = 0.001$ m, $D = 0.03$ m, and $d = 0.022$ m and the turns of coil as $N = 240$. A photograph of the physical MRD developed is shown in **Figure 9**.

The MRF for this experiment is MRF-250, purchased from Zhang Dongnan intelligent materials studio. It is comprised of soft magnetic carbonyl iron particles (average diameter: 8 μm, density: 7.86 g/cm^3; Beijing DK Nano Technology Co., Ltd.), dimethyl silicone oil (viscosity: 100 cSt at 25°C, density: 0.965 g/cm^3; Shin-Etsu, Japan), sodium dodecylbenzenesulfonate, oleic acid (purity 90%), graphite, and diatomite powder. The zero-field viscosity, saturation yield stress, and working temperature of MRF-250 are 242.5 mPa•s, 55.25 kPa, and −40 to 150°C, respectively.

Introduction of the Experimental System

Vibration experiments were performed on the semi-active seat suspension with MRD to evaluate the actual control performance of the proposed control method. The experimental system consists of a 6-DOF vibration table (model 6ZYD,

FIGURE 9 | Photograph of the developed MRD.

TABLE 4 | Main technical indicators of the TMS320F28335 development board.

Master processor	TMS320F28335, dominant frequency: 150 KHz
SRAM	34 K × 16 bits in chip, 0 waiting; 512 K × 16 bits out of chip, 15 ns.
FLASH	256 K × 16 bits in chip, 36 ns; 512 K × 16 bits out of chip, 70 ns.
ROM	BOOT ROM 8 K×16 bits in chip; OPT ROM 1 K × 16 bits out of chip, 15 ns.
A/D	2 × 8 channels in chip; resolution: 12 bits; switching rate: 80 ns.
HOST USB2.0	One channel; full speed.
CAN bus	One channel; maximum transmission rate: 1 Mbps.

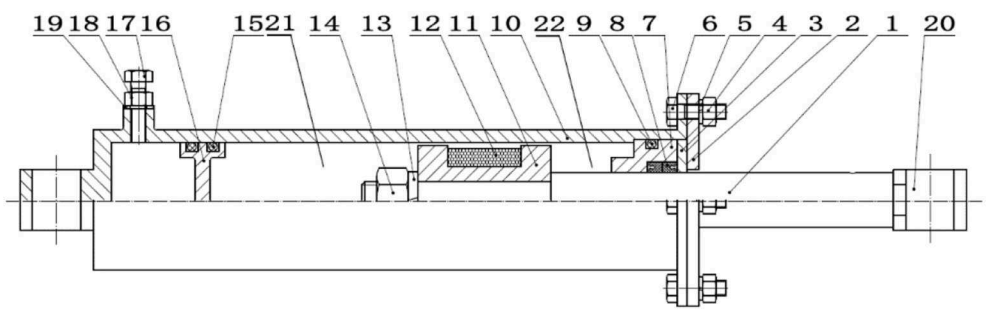

FIGURE 8 | Structural diagram of MRD. One to twenty-two are the piston rod, end cover, pressing plate, nut-M5, washer, screw-M5, guide holder, seal ring, O-ring (41.2 × 3.55A), cylinder block, piston, coil, spring washer, nut-M12, O-ring (38.7 × 3.55G), floating piston, screw-M5, nut-M5, sealing washer, joint, working space 1, and working space 2, respectively.

rated load: 500 kg, frequency: 50 Hz, maximum displacement and acceleration: ±400 mm and 50 m/s^2), a semi-active seat suspension with MRD, two acceleration sensors (model CT1005L, sensitivity: 50 mv/g, frequency range: 0.5–800 Hz, measuring range: 0–100 g, maximum impedance and linearity: 100 Ω and 1%), a constant current adapter (model CT5204, maximum frequency, output amplitude, accuracy, and noise: 0.31 KHz, 10 VP, 1.5%, and 1 mVrms), a data acquisition card (model PCI8735, measuring range: 0–10 V, accuracy: 0.0001, non-linearity: ±1 LSB, sampling rate: 500 KHz), a programmable current source (model DP811A, voltage range: 0–40 V, current range: 0–5 A, maximum response speed: 50 μs, resolution: 1/0.5 mV), and a digital signal processor (model TMS320F28335). The main performance parameters of the digital signal processor are shown in **Table 4**. An **Figure S1** has been provided as a Supplementary Material to describe the experimental system.

The 6-DOF vibration table consists of a foundation platform, a top platform, and six hydraulic cylinders, which can realize shock vibration, simple harmonic vibration, random vibration,

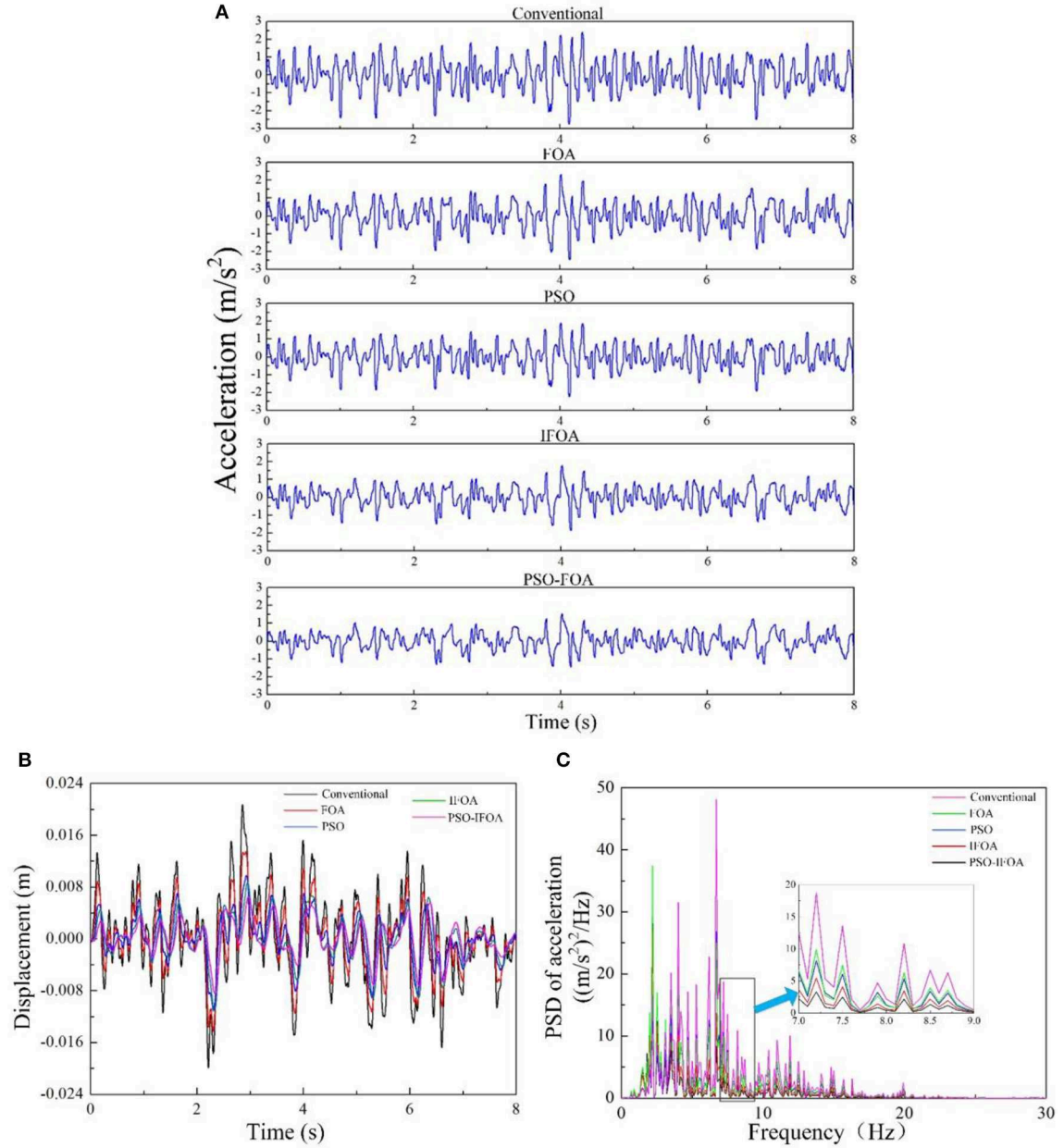

FIGURE 10 | (A) Acceleration responses under random vibration, **(B)** displacement responses under random vibration, and **(C)** human vibration magnitude under random vibration.

and path spectrum reappearance. One acceleration sensor is used to measure the acceleration response of the human body, and another acceleration sensor is used to measure the excitation acceleration of the seat suspension. The constant current adapter is used to provide appropriate working voltage for the acceleration sensors, meanwhile, which can amplify the signal detected by the sensors and de-noise the measured signal. The data acquisition card is used to collect data and transmit the collected data to the controller and computer. The digital signal processor is the core of the whole control system and is employed as the controller for the semi-active seat suspension with MRD. Semi-active seat suspension with MRD is a kind of suspension system that uses MRF as a damping medium and is designed by using the rheological effect of MRF. The damping force of the suspension can be adjusted in real time according to the vibration state of the automobile cab. Compared to other suspension systems, semi-active seat suspension with MRD possesses the strengths of a simple structure, controllable performance, fast response, strong adaptability, and continuously adjustable damping force.

Experimental Results

Figures 10A,B present the acceleration and displacement responses of the semi-active seat suspension with MRD under random vibration by using the control methods of traditional PID, FOA-PID, PSO-PID, IFOA-PID, and PSO-IFOA-PID. **Figure 10C** presents the power spectral densities (PSD) of the acceleration response under random vibration by using the same control methods. The RMS, VDV, and VDV values for the acceleration response are presented in **Table 5**. **Figure 10A** indicates that the lowest acceleration amplitude is generated under the PSO-IPOA-PID control method during the entire time history. **Figure 10B** indicates that the maximum displacements under the control methods of traditional PID, FOA-PID, PSO-PID, IFOA-PID, and PSO-IFOA-PID are 0.0343, 0.0294, 0.0258, 0.0231, and 0.0197 m, respectively; thus, the maximum displacement in the PSO-IFOA-PID is significantly lower than with the other methods. **Figures 10A,B** prove that the best damping effect is achieved by using the PSO-IFOA-PID control method. **Figure 10C** indicates that the largest peak value of the PSD of acceleration appears at 6.7 Hz under the PSO-IPOA-PID control method, which is lower than with the other methods. This result proves that the PSO-IFOA-PID can effectively reduce the PSD of acceleration response. **Table 5** shows that, compared to the control methods of traditional PID, FOA-PID, PSO-PID, and IFOA-PID, the RMS of the acceleration response in PSO-IFOA-PID is, respectively, decreased by 65.58, 52.93, 43.27, and 20.63%, the PTP of the acceleration response is, respectively, decreased by 47.53, 38.34, 33.67, and 18.3%, the VDV of the acceleration response is, respectively, decreased by 42.65, 32.88, 26.65, and 12.36%. **Table 5** also indicates that only under the PSO-IFOA-PID control method can the damping effect meet the ISO2361-1 comfort evaluation standard (RMS $\leq$ 0.315 m/s^2). The experiments verify the effectiveness and superiority of the purposed PSO-IFOA-PID control method.

TABLE 5 | Evaluation indices of the acceleration response.

	Conventional	FOA	PSO	IFOA	PSO-IFOA
RMS (m/s^2)	0.7475	0.5474	0.4536	0.3242	0.2573
PTP (mm)	6.0759	5.1708	4.8066	3.9023	3.1881
VDV (m/s$^{1.75}$)	1.1574	0.9888	0.9048	0.7573	0.6637

CONCLUSIONS AND FUTURE WORK

This paper proposed a PSO-IFOA-PID control method to improve the control performance for an MRD based semi-active seat suspension system. In order to verify the feasibility and superiority of the PSO-IFOA-PID, the search and control parameter optimization ability of traditional PID, FOA-PID, PSO-PID, IFOA-PID, and PSO-IFOA-PID were compared. The results indicated that the PSO-IFOA-PID had better optimization accuracy, faster convergence speed, and higher convergence precision in solving four test functions. Meanwhile, the PSO-IFOA-PID exhibited the advantages of adjusting the control parameters with better convergence speed and precision, and a shorter adjustment time, without overshoot, and having better steady and dynamic response characteristics. Furthermore, example simulations and experiments using the traditional PID, FOA-PID, PSO-PID, IFOA-PID, and PSO-IFOA-PID were carried out, and the results of both the simulations and experiments indicated that PSO-IFOA-PID control was the most ideal method.

In future work, new intelligent algorithms should be researched to achieve better response characteristics for the control performance of the semi-active controller of MRD seat suspension. Moreover, the temperature of MRD rises when it has been working for a long time, which will increase the internal pressure of the cylinder and result in the leakage of MRF. This adversely affects the damping characteristics of MRD, so further study is needed on how to improve the damping characteristics by controlling the temperature, and relevant experiments will also need to be carried out.

DATA AVAILABILITY STATEMENT

The datasets generated for this study are available on request to the corresponding author.

AUTHOR CONTRIBUTIONS

NW, XL, and KW: conceptualization, methodology, and formal analysis. NW, KW, ZL, and HH: software. WL, NW, and TS-G: validation. NW, WL, and HH: investigation. XL and ZL: resource and data curation. NW and KW: writing–original draft preparation and visualization. HH, TS-G, and WL: writing–review and editing. XL: supervision and project administration.

FUNDING

This research was funded by the National Science Foundation of China (No. 51975568), National Natural Science Foundation of Jiangsu Province (No. BK20191341), Key Laboratory of Fluid Power and Intelligent Electro-Hydraulic Control (Fuzhou University), Taishan Scholar (tsqn201812025), and Priority Academic Program Development of Jiangsu Higher Education Institutions (PAPD) and Australia ARC DECRA (No. DE190100931).

ACKNOWLEDGMENTS

The authors would like to thank the reviewers for their contributions to this paper.

SUPPLEMENTARY MATERIAL

The Supplementary Material for this article can be found online at: https://www.frontiersin.org/articles/10.3389/fmats.2019.00269/full#supplementary-material

Figure S1 | Experimental system.

REFERENCES

Ahmet, B., Hazim, I., and Ismail, B. (2017). An improvement in fruit fly optimization algorithm by using sign parameters[J]. *Soft Comput*. 22, 1–17. doi: 10.1007/s00500-017-2733-1

Alkamachi, A., and Erçelebi, E. (2017). Modelling and genetic algorithm based-PID control of h-shaped racing quadcopter. *Arab. J. Sci. Eng*. 42, 1–10. doi: 10.1007/s13369-017-2433-2

Ang, K. H., Chong, G., and Li, Y. (2005). PID control system analysis, design, and technology. *IEEE Trans. Contr. Syst. Technol*. 13, 559–576. doi: 10.1109/TCST.2005.847331

Bhambhani, A., and Shah, P. (2016). "PID parameter optimization using cohort intelligence technique for D.C motor control system," in *2016 International Conference on Automatic Control and Dynamic Optimization Techniques (ICACDOT 2016)* (Pune). doi: 10.1109/ICACDOT.2016.7877629

Eduardo, F. O., Rossomando, F. G., and Soria, C. M. (2018). Self-tuning of a neuro-adaptive PID controller for a SCARA robot based on neural network. *IEEE Lat. Am. Trans*. 16, 1364–1374. doi: 10.1109/TLA.2018.8408429

Eltag, K., Aslamx, M. S., and Ullah, R. (2019). Dynamic stability enhancement using fuzzy PID control technology for power system. *Int. J. Control Autom. Syst*. 17, 234–242. doi: 10.1007/s12555-018-0109-7

Feng, G. D., Liu, M., and Wang, G. L. (2014). Genetic algorithm based optimal placement of PIR sensors for human motion localization. *Optim. Eng*. 15, 643–656. doi: 10.1007/s11081-012-9209-z

Han, X. M., Liu, Q. M., and Wang, H. Z. (2017). Novel fruit fly optimization algorithm with trend search and co-evolution. *Knowl. Based Syst*. 11, 16–27. doi: 10.1016/j.knosys.2017.11.001

Han, Y. Y., Gong, D. W., Li, J. Q., and Zhang, Y. (2016). Solving the blocking flow shop scheduling problem with makespan using a modified fruit fly optimisation algorithm. *Int. J. Prod. Res*. 54, 6782–6797. doi: 10.1080/00207543.2016.1177671

Hernandez-Guzman, V. M., and Carrillo-Serrano, R. V. (2011). Global PID position control of PM stepper motors and PM synchronous motors. *Int. J. Control* 84, 1807–1816. doi: 10.1080/00207179.2011.626457

Kuntanapreeda, S. (2016). Adaptive control of fractional-order unified chaotic systems using a passivity-based control approach. *Nonlinear Dyn*. 84, 2505–2515. doi: 10.1007/s11071-016-2661-0

Lei, X. J., Ding, Y. L., and Fujita, H. (2016). Identification of dynamic protein complexes based on fruit fly optimization algorithm. *Knowl. Based Syst*. 105, 270–277. doi: 10.1016/j.knosys.2016.05.019

Liu, H., Li, Y. Z., Zhang, Y., Chen, Y., Song, Z., Wang, Z., et al. (2018). Intelligent tuning method of PID parameters based on iterative learning control for atomic force microscopy. *Micron* 104, 26–37. doi: 10.1016/j.micron.2017.09.009

Liu, X. H., Shi, Y., and Xu, J. (2017). Parameters tuning approach for proportion integration differentiation controller of magnetorheological fluids brake based on improved fruit fly optimization algorithm. *Symmetry* 9, 109–121. doi: 10.3390/sym9070109

Lu, Y. Z., Yan, D. P., Zhang, J. Y., and Levy, D. (2015). A variant with a time varying PID controller of particle swarm optimizers. *Inform. Sci.* 297, 21–49. doi: 10.1016/j.ins.2014.11.017

Maikala, R. V., and Bhambhani, Y. N. (2013). Estimating reduced oxygenation levels in the erector spinae lumbar muscle region during seated whole-body vibration. *Int. J. Ind. Ergonom*. 43, 121–128. doi: 10.1016/j.ergon.2012.11.006

Mei, L., and Luo, J. (2017). PID Parameters optimization with improved cooperative coevolution algorithm. *Comput. Tech. Dev*. 27, 37–42. doi: 10.3969/j.issn.1673-629X.2017.08.008

Meissner, M., Schmuker, M., and Schneider, G. (2006). Optimized particle swarm optimization (OPSO) and its application to artificial neural network training. *BMC Bioinformatics* 7:125. doi: 10.1186/1471-2105-7-125

Mukherjee, V., and Ghoshal, S. P. (2007). Intelligent particle swarm optimized fuzzy PID controller for AVR system. *Electr. Pow. Syst. Res*. 77, 1689–1698. doi: 10.1016/j.epsr.2006.12.004

Pan, Q. K., Sang, H. Y., Duan, J. H., and Gao, L. (2014). An improved fruit fly optimization algorithm for continuous function optimization problems. *Knowl. Based Syst*. 62, 69–83. doi: 10.1016/j.knosys.2014.02.021

Pan, W., Lyu, M. Y., Hwang, K. S., Ju, M. Y., and Shi, H. B. (2018). A neuro-fuzzy visual servoing controller for an articulated manipulator. *IEEE Access*. 99, 3346–3357. doi: 10.1109/ACCESS.2017.2787738

Ramezanian, H., Balochian, S., and Zare, A. (2013). Design of optimal fractional-order PID controllers using particle swarm optimization algorithm for automatic voltage regulator (AVR) system. *J. Control Autom. Electr. Syst*. 24, 601–611. doi: 10.1007/s40313-013-0057-7

Savran, A., Tasaltin, R., and Becerikli, Y. (2006). Intelligent adaptive nonlinear flight control for a high performance aircraft with neural networks. *ISA Trans*. 45, 225–247. doi: 10.1016/S0019-0578(07)60192-X

Shi, H. S., San, Y., and Zhu, Y. (2015). An improved fruit fly optimization algorithm and its application. *Expert Syst. Appl*. 42, 4310–4323. doi: 10.1016/j.eswa.2015.01.048

Srivastava, S., and Agarwal, B. N. P. (2010). Inversion of the amplitude of the two-dimensional analytic signal of the magnetic anomaly by the particle swarm optimization technique. *Geophys. J. Int*. 182, 652–662. doi: 10.1111/j.1365-246X.2010.04631.x

Vijayakumar, K., and Manigandan, T. (2016). Nonlinear PID controller parameter optimization using enhanced genetic algorithm for nonlinear control system. *Control Eng. Appl. Inf*. 18, 3–10.

Wang, L., Liu, R., and Liu, S. (2016). An effective and efficient fruit fly optimization algorithm with level probability policy and its applications. *Knowl. Based Syst*. 97, 158–174. doi: 10.1016/j.knosys.2016.01.006

Wang, W. C., and Liu, X. G. (2014). Melt index prediction by least squares support vector machines with an adaptive mutation fruit fly optimization algorithm. *Chemometr. Intell. Lab*. 141, 79–87. doi: 10.1016/j.chemolab.2014.12.007

Xu, C. (2015). An improved fruit fly optimization algorithm and its application of PID parameters tuning. *J. Inf. Comput. Sci*. 12, 3647–3654. doi: 10.12733/jics20105957

Xu, J., Wang, Z. B., Tan, C., and Si, L. (2016). Adaptive wavelet threshold denoising method for machinery sound based on improved fruit fly optimization algorithm. *Appl. Sci*. 6, 199–208. doi: 10.3390/app6070199

Yu, Y., Li, Y. C., and Li, J. C. (2014). Parameter identification of a novel strain stiffening model for magnetorheological elastomer base isolator utilizing enhanced particle swarm optimization. *J. Intel. Mat. Syst. Str*. 26, 2446–2462. doi: 10.1177/1045389X14556166

Yu, Y., Li, Y. C., and Li, J. C. (2015). Parameter identification and sensitivity analysis of an improved LuGre friction model for magnetorheological elastomer base isolator. *Meccanica* 50, 2691–2707. doi: 10.1007/s11012-015-0179-z

Yu, Y., Li, Y. C., Li, J. C., and Gu, X. Y. (2016). Self-adaptive step fruit fly algorithm optimized support vector regression model for dynamic response prediction of magnetorheological elastomer base isolator. *Neurocomputing* 211, 41–52. doi: 10.1016/j.neucom.2016.02.074

Zamani, A. A., Tavakoli, S., and Etedali, S. (2017). Fractional order PID control design for semi-active control of smart base-isolated structures: a multi-objective cuckoo search approach. *ISA Trans.* 67, 222–232. doi: 10.1016/j.isatra.2017.01.012

Zheng, X. L., and Wang, L. (2016). A knowledge-guided fruit fly optimization algorithm for dual resource constrained flexible job-shop scheduling problem. *Int. J. Prod. Res.* 54, 1–13. doi: 10.1080/00207543.2016.1170226

Zhou, D. W., Gao, X., Liu, G. H., Mei, C. L., Jiang, D., and Liu, Y. (2011). Randomization in particle swarm optimization for global search ability. *Expert Syst. Appl.* 38, 15356–15364. doi: 10.1016/j.eswa.2011.06.029

Conflict of Interest: The authors declare that the research was conducted in the absence of any commercial or financial relationships that could be construed as a potential conflict of interest.

frontiers in Materials

ORIGINAL RESEARCH
published: 20 November 2019
doi: 10.3389/fmats.2019.00292

Dynamic Mechanical Hysteresis of Magnetorheological Elastomers Subjected to the Cyclic Loading and Periodic Magnetic Field

Yunfei Zhang[1,2], *Fengzhou Fang*[2]*, *Wen Huang*[1], *Yuchuan Chen*[1], *Song Qi*[3] *and Miao Yu*[3]*

[1] *Institute of Machinery Manufacturing Technology, China Academy of Engineering Physics, Mianyang, China,* [2] *State Key Laboratory of Precision Measuring Technology and Instruments, Centre of Micro/Nano Manufacturing Technology (MNMT), Tianjin University, Tianjin, China,* [3] *Key Lab for Optoelectronic Technology and Systems, Ministry of Education, College of Optoelectronic Engineering, Chongqing University, Chongqing, China*

Magnetorheological elastomer (MRE) is one of the most promising smart materials with excellent magnetic-control mechanical properties. This work focuses on the study of the dynamic mechanical properties of MRE under cyclic loadings and periodic magnetic field. The influences of matrix, particle distribution, magnetic field on the dynamic mechanical hysteresis are systematically investigated. It is found that all the normal force, magnetic fields and shear strain would cause a hysteresis in the dynamic mechanical responses of MRE. The continuous cycle tests reveal the hysteresis tended to be saturated after several initial cycles. The hysteresis of MRE under the constant magnetic field can be attributed to the rearrangement of particles, which causes a hardening effect of MRE under the continuous dynamic tests. The periodic magnetic field causes a hysteresis in the dynamic modulus which could be attributed to the irreversible movement of the particles. Among them, the polymer matrix of MRE plays an important role in the dynamic mechanical hysteresis, which suggests more stable molecular chain structures in the matrix reducing the magnitude of hysteresis and improving its stability. Besides, the saturation of the mechanical hysteresis had also been studied, and then relevant physical mechanism was proposed for the qualitative explanation.

Keywords: magnetorheological elastomer, cyclic loading, periodic magnetic field, mechanical hysteresis, viscoelasticity

OPEN ACCESS

Edited by:
Xian-Xu Bai,
Hefei University of Technology, China

Reviewed by:
Yang Yu,
University of Technology Sydney, Australia
Xiang Ben Ju,
Chongqing University of Technology, China

***Correspondence:**
Fengzhou Fang
fzfang@tju.edu.cn
Miao Yu
yumiao@cqu.edu.cn

Specialty section:
This article was submitted to Smart Materials, a section of the journal Frontiers in Materials

Received: *22 August 2019*
Accepted: *01 November 2019*
Published: *20 November 2019*

Citation:
Zhang Y, Fang F, Huang W, Chen Y, Qi S and Yu M (2019) Dynamic Mechanical Hysteresis of Magnetorheological Elastomers Subjected to the Cyclic Loading and Periodic Magnetic Field. Front. Mater. 6:292. doi: 10.3389/fmats.2019.00292

INTRODUCTION

The fiber-rubber composites exhibit an appreciable change in their mechanical response resulting from the previous maximum loading. This mechanical hysteresis, also known as Mullins effect, has been recognized in polymer science and engineering (Ogden and Roxburgh, 1999; Hanson et al., 2005; Qi and Boyce, 2005; Webber et al., 2007). The stress-strain curve demonstrates a marked hysteretic response during the loading-unloading cycle, in which the stress under unloading is significantly less than that under loading at the same strain (Dorfmann and Ogden, 2005). The magnitude of the hysteresis can be represented by the area between the tension and relaxation curves. Plenty of explanations and phenomenological models were reported for Mullins effect, and these were mainly based on the concepts of slippage and disentanglement of polymer molecules,

bond rupture between particle fillers and polymer matrix, and breakdown of particle aggregation (Diani et al., 2009). Apart from the Mullins effect, the mechanical properties of fiber-rubber composites under the cyclic loading can be used to evaluate the stability of materials, which is a crucial performance index for the engineering application. Consequently, improving the stability of polymer composites is an urgent requirement, and the mechanism study of mechanical hysteresis has continuously been a research focus (Merabia et al., 2008; Drozdov, 2009; Machado et al., 2012; Chai et al., 2013).

Magnetorheological elastomer (MRE) belongs to the group of smart materials, which is stimulated to change its mechanical behavior by an external magnetic field. The MRE consists of micronized magnetic particles dispersed in a nonmagnetic elastic matrix, such as polyurethane (PU), natural rubber and silicone rubber (Gong et al., 2005; Stepanov et al., 2007; Li and Nakano, 2013; Wang et al., 2014; Jung et al., 2016; Qi et al., 2018b). As an intelligent engineering material, the MRE exhibits excellent magnetic-control properties as well as potentials for applications in the fields of noise reduction, vibration attenuation, smart sensing, electromagnetic shielding, etc. (Kashima et al., 2012; Hoang et al., 2013; Xing et al., 2015, 2016; Fu et al., 2016; Wang et al., 2016; Yu M. et al., 2016; Qi et al., 2018a). For the magnetorheological (MR) materials, the magnetic particles are inclined toward columns paralleled to the magnetic orientation. When the magnetic field is removed, the magnetic particle cannot return to its original position immediately. It will cause the hysteresis in the viscoelastic properties of MR materials, especially in the viscous matrix rather than in the elastic matrix. The hysteresis behaviors of devices based on MR materials have attracted the attention of many researchers (An and Kwon, 2003; Dominguez et al., 2004; Yu Y. et al., 2016; Chen et al., 2018; Xian-Xu et al., 2019). For the MRE, Gundermann et al. have investigated the motion of particles in MREs by X-ray micro-computed tomography (X-μCT) (Gundermann and Odenbach, 2014). They found that the process of particle motion was not reversible. It reveals the possibility of mechanical hysteresis behavior caused by the magnetic field in the MRE, which have been ignored in most literatures. However, in the area of polymer science and engineering, relevant researches on the dynamic mechanical behavior of MRE under the repeated cyclic loading or periodic magnetic field are comparatively rare.

The MR effect computed by the ratio of the magnetic-induced modulus to the initial modulus is the most considerable evaluation index of MREs. Generally, in order to improve the MR effect, the researchers enhanced the magnetic-induced modulus by increasing the concentration of magnetic particles, interface modification, incorporating additive, etc. (Li and Sun, 2011; Qiao et al., 2012; Yang et al., 2013; Aziz et al., 2016). The other defective method is decreasing the initial modulus by adding vast plasticizer or reducing the crosslinking density of MRE, which weakens the mechanical strength of MRE. These viscous matrices are able to make the mechanical hysteresis more serious in the MRE. As an engineering material, the MRE has to suffer different cyclical loadings and magnetic fields when under variable application conditions. The cyclic loadings and the variable magnetic field will change the mechanical performance of MRE, which leads the instability of the MRE-based device. Therefore, it is necessary to study the mechanism of the mechanical hysteresis, and improve the stability of MRE for the engineering application.

Previously, An et al. (2012) found a stress hardening phenomenon for the MR gel in the presence of stable magnetic field under the cyclic loading. They also deduced this phenomenon, which was opposite to the Mullins effect of the conventional particle-filled polymer composite, was caused by the rearrangement of particles under the external magnetic field. Xu et al. (2016) have also proposed a magneto-induced hardening mechanism to explain the transition from stress softening to stress hardening under cyclic loadings. For the elastomer reinforced by the magnetic particles, the hysteresis in the dynamic mechanical responses was first reported in the elastomer that contains hard magnetic particles, in which the magnetic remanence of hard magnetic particles was the priority consideration (Stepanov et al., 2012; Kramarenko et al., 2015; Yu et al., 2015c). Sorokin et al. (2015) have studied the hysteresis in dynamic modulus, loss factor and normal forces with regard to the MRE. The influences of particle size and composition have been studied, and they also discussed the possible mechanism for the mechanical hysteresis. In addition, Sorokin et al. (2014) further studied the Payne effect in the MRE using synthetically cycling measurements; the Payne effect increased significantly in the presence of an external magnetic field and varied with the cyclic loading, which reached saturation after several cycles. Thus, far, the study on the mechanical hysteresis of MRE is not enough, and the deeper investigation about the saturation of the mechanical hysteresis is eagerly needed.

PU has better degradation stability than natural rubber and superior mechanical stability than silicone rubber (Wei et al., 2010), and it has been widely used to be the matrix of the MRE (Wu et al., 2010, 2012; Ge et al., 2015). In this paper, two kinds of MRE based on the PU matrix and PU/epoxy (EP) interpenetrating network (IPN) matrix were prepared, respectively. The material properties and the details of the process and principle of preparation could be obtained in our previous work (Yu et al., 2015a,b). Several cycling tests have been carried out to study the most critical influences on the mechanical hysteresis of MRE, including the matrix, particle distribution, magnetic field. The saturation of the mechanical hysteresis has also been studied, and then relevant physical mechanism is proposed to explain it qualitatively. This work turns out that the material properties of MRE should be characterized by the repeating test rather than merely single test. More effective evaluation tests of MRE are of benefit to the potential applications. In particular, the discussion on the influences of matrix will provide guidance for improvement of material preparation.

EXPERIMENT

Materials

The soft magnetic carbonyl iron powder (CIP) (Type: CN; size distribution: 1–8 μm) was provided by BASF in Germany. PU matrix (Castor oil purchased from Sinopharm Chemical

TABLE 1 | Detailed formation of MRE samples with different proportions of EP.

Sample	Matrix (20 wt%)		Plasticizer (10 wt%)	CIP (70 wt%)
	PU (%)	EP (%)		
ani-PU	20 wt	0	10 wt	70 wt
ani-IPN	15 wt	5 wt	10 wt	70 wt
iso-IPN	15 wt	5 wt	10 wt	70 wt

Reagent Co., Ltd., China; MDI (MDI: 4,4-∼50%, 2,4-∼50%) purchased from Yantai Wanhua Polyurethanes Co., Ltd., China), Stannous octoate (Sinopharm Chemical Reagent Co. Ltd., China) was used as catalyst in the process of PU preparation. EP based on diglycidyl ether of bisphenol-A was purchased from Baling Petrochemical Co., Ltd., Hunan, China. The 2,4,6-Tri(dimethylaminomethyl)phenol (DMP-30) acting as the curing agent of EP was acquired from Wuhan Hongda Co., Ltd., China. The Di-butyl phthalate (DBP) used as a plasticizer was bought from Tianjin Bodi Chemical Holding Co., Ltd., China.

MRE Preparation

In order to study the influence of the matrix and particle distribution on the hysteresis properties, we prepared different kinds of MRE samples. The isotropic samples and anisotropic samples were fabricated in the absence and presence of magnetic field, respectively. The PU and IPN denote that the MRE samples were based on PU matrix and PU/EP IPN matrix, respectively. The detailed compositions of MRE samples are listed in **Table 1**. Here the prefix of "ani" and "iso" denote the isotropic and anisotropic sample, respectively. Details about the process and principle of reaction of PU/EP IPN and PU can be obtained from our previous works (Yu et al., 2015a; Yang et al., 2016). The incorporation of EP would improve the crosslink degree of PU, and the interpenetration and entanglement of molecular chains in the PU/EP IPN would improve the structural stability of the polymer. Therefore, it should be noticed that the PU-MRE has higher viscous component, and the IPN-MRE has higher elastic component.

Characterization

The morphologies of the particles in the MRE samples were characterized via scanning electron microscopy (SEM; MIRA3 TESCAN). The microphotographs of MRE samples were taken for the fractured surface, on which the gold powder was coated prior to testing.

The cycling tests of MRE samples were implemented under shear oscillation mode using an advanced commercial rheometer (Model: MCR301, Anton Paar). A parallel-plate rotor and magnetron device were installed in the rheometer. The testing magnetic field of magnetron devices was generated by an electromagnet. The magnetic flux density could be changed from 0 to ∼1.2 T by varying the drive current in the coil of the electromagnet with a range of 0–5 A. The details about this rheometer could be obtained from our previous work (Yu et al., 2013). In this study, the samples were prepared in disc forms with 20 mm in diameter and 2 mm in thickness. During the testing process, the samples were secured between the lower stationary plate and the upper movable plate that was connected to a forced torsional oscillator.

RESULTS AND DISCUSSION

This work focuses on the influences of mechanical pressure, magnetic fields and shear strain on the dynamic mechanical hysteresis of MRE. Initially, the normal force cycling tests in the absence and presence of magnetic field were carried out to study the influences of the mechanical pressure. Then the MRE samples were tested under a triangular (periodic increase and decrease) magnetic field, and the hysteresis in the dynamic modulus caused by the magnetic field has been studied. Finally, the analysis of the amplitude cycle tests at different magnetic field strengths is presented.

Normal Force Cycling Tests

Compressive stress is a common loading when the MRE-based device is working. In order to study the mechanical hysteresis behavior of MRE under changing compressive stress, we tested the dynamic modulus of MRE under a cyclic normal force in the range of 5–30 N. The strain amplitude of 0.1%, pre-compression force of 5 N and test frequency of 5 Hz were selected for these tests. Measurements were carried out in several consecutive stages. Initially, the dynamic mechanical properties were measured under an increasing normal force actuated from 5 to 30 N. After reaching the maximum value, the normal force was linearly reduced from 30 to 5 N. These tests were conducted in the absence and presence of magnetic field to study the influence of magnetic field, and the number of cycles was set 5 for each test.

Figure 1 illustrates the dependence of dynamic modulus of iso-IPN, ani-IPN, and ani-PU samples on the cycling normal force, respectively. The color change of curves indicates the process of the cyclic tests. As can be seen, the dynamic modulus of all samples increases with the increasing normal force. This phenomenon also has been reported by Feng et al. (2015). It is attributed to the enhancement of the particle–particle and particle–matrix interactions with the high normal force. After the normal force declined linearly, an apparent hysteresis has been observed in all curves, while the modulus tends to saturate after several cycles. It indicated that the possibility of the balance between destruction and reformation of the particle structures which caused by the coupling effect of the cyclic mechanical loading and magnetic field. It also can be seen that the storage modulus increases with the increasing test cycle. It means that the compressive loading in the initial cycle produces a hardening effect of the MRE sample. The hardening effect is more obvious when the samples under the magnetic field. Similar to the MR gel and MR plastomer, this hardening effect in the magnetic field can be attributed to the rearrangement of CIPs (An et al., 2012; Xu et al., 2016). The qualitative comparative analyses of the hysteresis were carried out in the following section.

The magnitude of the hysteresis can be represented by the area between the ascending and descending curves. From the qualitative compare we can deduce that the hysteresis is more obvious in the presence of magnetic field than in the absence

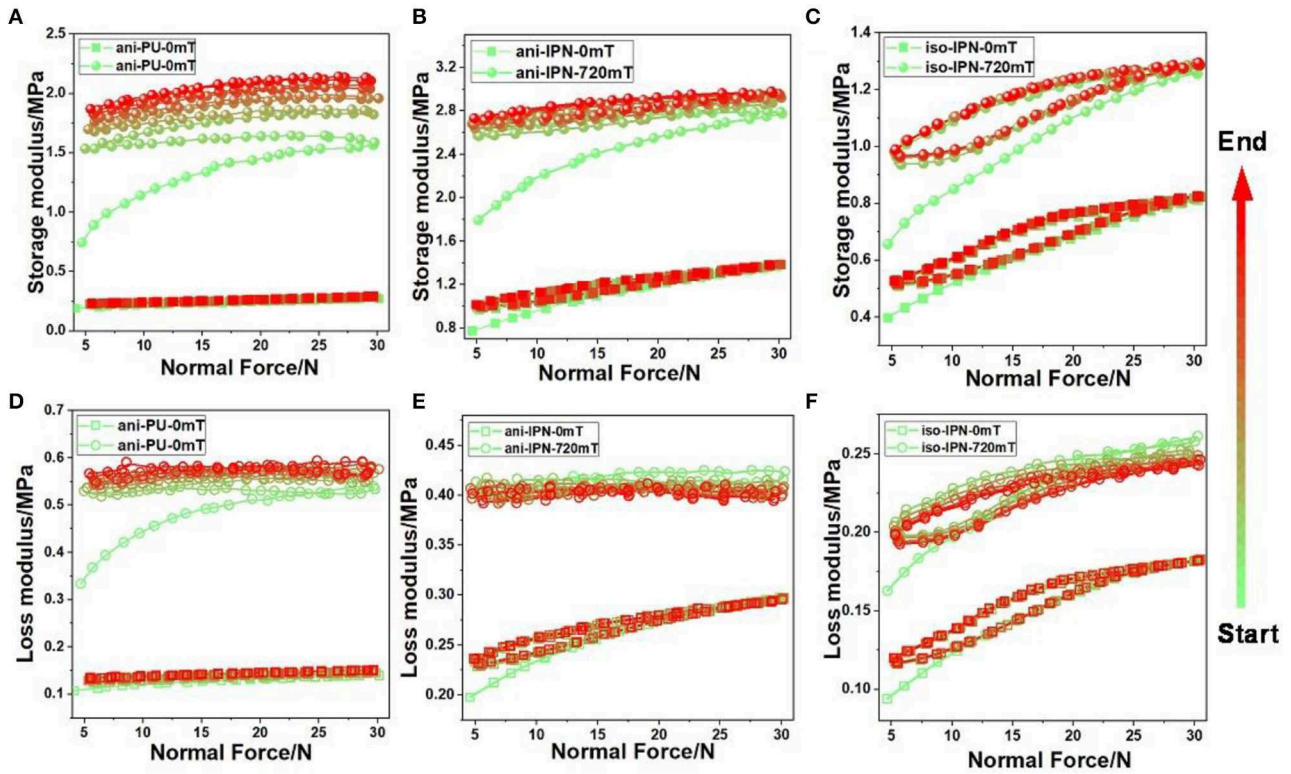

FIGURE 1 | The influence of the normal force on the dynamic viscoelastic properties of MRE samples. Dependence of storage modulus of ani-PU sample **(A)**, ani-IPN sample **(B),** and iso-IPN sample **(C)** on the normal force in the absence and presence of magnetic field. Dependence of loss modulus of ani-PU sample **(D)**, ani-IPN sample **(E)**, and iso-IPN sample **(F)** on the normal force in the absence and presence of magnetic field. The color scale indicates the progress of the cycle tests.

of magnetic field. The hysteresis of PU sample also greater than that of IPN sample, which indicated that the matrix played an important role in the destruction and reformation of the particle structures. To obtain a better understanding the influence of matrix, particle distribution and magnetic field on the hysteretic property, here we defined

$$\lambda = (G_n - G_1)/G_1 \quad (1)$$

where G_n is the maximum value of dynamic modulus in the nth cyclic curve, and the G_1 is the maximum value of dynamic modulus in the initial cyclic curve. The parameter λ can commendably reflect the changes of dynamic modulus of MRE in the cycles, as **Figure 2** shows. As can be seen the parameter λ of PU sample is significantly larger than that of IPN sample. In addition, the saturation of IPN sample is more apparent than that of PU sample, which indicates that the interpenetration and entanglement of molecular chains in IPN matrix would improve the stability of MRE. Comparing the curves in the absence and presence of magnetic field, we can deduce that the magnetic force between the magnetized CIPs intensifies the motion of CIPs when the MRE suffers compressive loading. The movement of CIPs and the enhancement of interaction forces between the CIPs and matrix are going to cause a larger hysteresis. Another phenomenon is that the parameter λ of ani-IPN is greater than that of iso-IPN, which can be attributed to the difference of the particle distribution. As can be seen from **Figures 3a,b**, it is observed that the CI particles are uniformly dispersed in the isotropic sample while they exhibited patterned chain-like structure in the anisotropic sample. The deformation and reagglomeration of the chain structure paralleled to the normal force will be enhanced by the compressive loading. In addition, the parameter λ of curves with magnetic field is greater than that of curves without magnetic field. It indicates that the magnetic field also causes a decrease in the stability of MRE when the MRE suffers the compressive loading. Since the magnetic field can enlarge the movement of particles in the process of reagglomeration, another phenomenon that the parameter λ of IPN samples has a slightly decrease in the presence of magnetic field can be seen in the **Figure 2B**. The decrease of the loss modulus can be attributed to the saturation of particle movement in the IPN matrix. It's contrary to the IPN sample, the loss modulus of PU sample increases with the cycle number because of the weaker restriction of the PU matrix. It revealed that the particle movement in PU sample is not saturated in these five cyclic tests.

Magnetic Field Cycling Test

The linear increasing magnetic field has been carried out by many researchers to study the MR effect of MR materials (Xu

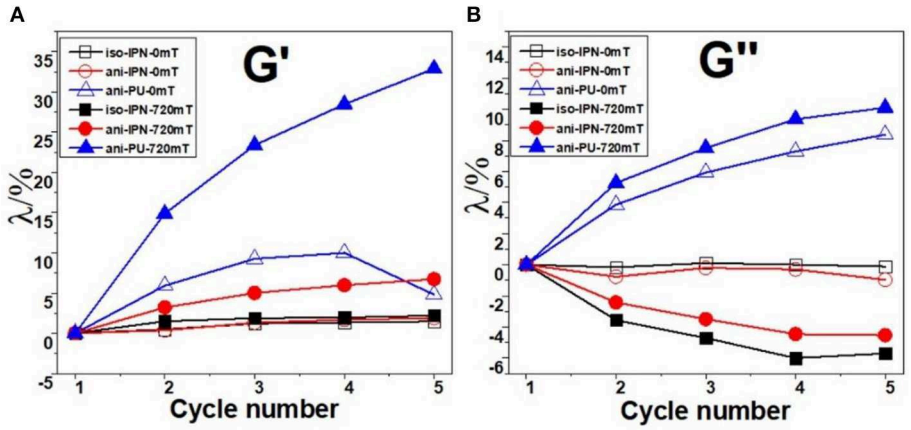

FIGURE 2 | Dependence of the parameter λ (**A**: storage modulus *G'*; **B**: loss modulus *G''*). on cycle number for the samples under the ascending and descending normal force (The hollow symbol and solid symbol indicated the tests under 0 and 720 mT, respectively).

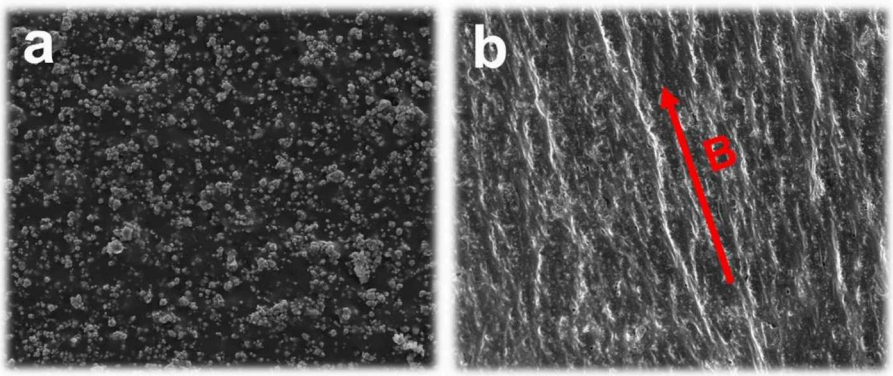

FIGURE 3 | SEM images of iso-IPN **(a)** and ani-IPN **(b)**. The red arrow indicates the direction of the pre-structure magnetic field.

et al., 2011; Bica, 2012). In order to study the magneto-induced mechanical hysteresis of MRE under the triangular magnetic field, we tested the dynamic modulus of MRE under a cyclic triangular magnetic field in the range of 0–1,100 mT. The strain amplitude of 0.1%, pre-compression force of 5 N and test frequency of 10 Hz were selected for this test. Measurements were carried out in several consecutive stages. The dynamic mechanical properties were initially measured under the magnetic field increased from 0 to 1,100 mT. After reaching the maximum value, the magnetic field was linearly decreased from 1,100 to 0 mT, and the number of cycle also was 5 for each test.

Figure 4 shows the dynamic modulus as a function of the triangular magnetic field. The color change of curves indicates the direction of the cyclic test process. It can be seen that the dynamic modulus of all samples increases with the increasing magnetic field strength and decreases with the decreasing magnetic field strength. An apparent magneto-induced mechanical hysteresis has also been observed in these curves. As can be seen the descending curves are above the ascending curves, the similar phenomenon in MRE and electrorheological elastomer (ERE) has been reported by Sorokin and Niu, respectively (Niu et al., 2015; Sorokin et al., 2015). Mainly it is because the particles and the particle chains do not immediately revert to their original positions under the cyclical magnetic fields. Previously, Shen et al. (2004) proposed a mathematical model to estimate the magneto-induced storage modulus. According to their study, the magneto-induced modulus of MRE is determined by

$$G = \frac{9\phi Cm^2\left(4-\gamma^2\right)}{8r_0^3\pi^2a^3\mu_0\mu_1\left(1+\gamma^2\right)^{7/2}} \tag{2}$$

where ϕ is the volume fraction of CIPs, a is the diameter of CIPs, μ_0 denotes the vacuum permeability, μ_1 is the permeability of MREs, r_0 is the initial spacing between two adjacent dipoles, γ is the shear strain, and m is the magnetic dipole moment. It can be deduced by Equation (2), due to the space between the magnetized particles r_0 in the descent stage is smaller than that in ascent stage, the larger magneto-induced modulus G causes a larger storage modulus in descent stage. It should be emphasized that the hysteresis of IPN samples tends to saturation after the initial cycle, and the storage modulus returns to its initial value

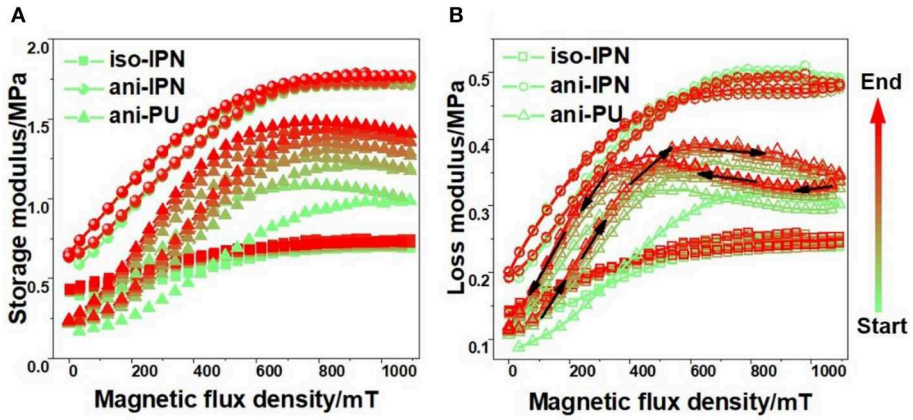

FIGURE 4 | Dynamic modulus (**A**: storage modulus; **B**: loss modulus) as a function of the triangular magnetic field. The change of loss modulus is denoted by the direction of the black arrow in **(B)**.

on the elimination of magnetic field in later cycles. Due to the weaker restriction of PU matrix, the PU sample needs more cycles to achieve the saturation. In the engineering applications of MRE, due to the variable magnetic field and changing loads upon the MRE-based device, the material properties of MRE in the saturated region can make the device more effective.

Unlike the curve shape of storage modulus, **Figure 4B** shows the loss modulus of descending curves is greater than that of ascending curves under the low magnetic field strength, but the contrary is under the high magnetic field strength. Since the loss modulus is based on the energy dissipation which is proportional to the relative movement of particles (Yang et al., 2012), this phenomenon can be explained by the state of particle motion. There is a critical magnetic field strength to keep the balance between magnetic interactions (between the magnetized particles) and elastic interactions (between the particles and matrix), and the critical magnetic field strength can be reflected by the intersection of loss modulus curves. **Scheme 1** shows the advance and return movement of CIPs under the ascending and descending magnetic fields, and the cycle has been divided into ascent stage (stage A and stage B) and descent stage (stage C and stage D). Among them, the advance movement was caused by magnetic interactions at the ascent stage, and return movement was caused by elastic interactions at the descent stage. The energy dissipation of MRE mainly depended on the friction between the CIP and matrix (Li and Gong, 2008), and it could be expressed with the following equation (Yu et al., 2013):

$$\mathrm{ED} \propto F_r S \tag{3}$$

where F_r is the interfacial friction force between the CIP and the matrix; this force is decided with the magnetic flux density and elastic interactions. In addition, S represents the displacement of interfacial slipping between the CIP and the matrix. As can be seen from the **Scheme 1**, with the increase of distance between the particles and its initial positions, the particles become closer and the polymer molecular chain stretched longer. As a consequence, the F_r of MRE in stage B and stage C is greater than that of in stage A and stage D. When the magnetic field strength is lower than this critical value, the elastic interaction is dominated. The relative movement of CIPs has been restricted in the ascent stage (stage A) and accelerated in the descent stage (stage D). Correspondingly, when the magnetic field strength is higher than this critical value, the magnetic interaction is dominated. The relative movement of particles has been accelerated in the ascent stage (stage B) and restricted in the descent stage (stage C). Therefore, the displacement of interfacial slipping S in stage D is greater than that of in stage A, and S in stage B is greater than that of stage C. It leads to the descending curves of loss modulus is greater than that of ascending curves under the low magnetic field strength, and the contrary is under the high magnetic field strength. In addition, as can be seen from **Figure 6B**, the critical magnetic field of ani-PU is smaller than that of ani-IPN, which can be attributed to the weaker elastic interactions in the PU matrix.

Correspondingly, the parameter λ calculated from Equation (1) has been plotted to study the stability of the magneto-induced mechanical hysteresis. **Figure 5** shows the dependence of the parameter λ on the cycle number under the triangular magnetic field. Similarly, the parameter λ of PU sample is also significantly larger than that of IPN sample. This phenomenon occurred mainly because the displacement of interfacial slipping between the CIP and the matrix in PU sample is greater than that in IPN sample. The interpenetration and entanglement of molecular chains in IPN matrix would improve the elastic interactions, which can accelerate the particles revert to their original positions. In addition, the parameter λ of the iso-IPN is greater than that of the ani-IPN. It is mainly because the particles have formed the chain structure in the anisotropic sample, while the particles are distributed randomly in the isotropic sample, as shown in **Figure 5**. As the particles tend to form a columnar paralleled to the magnetic field, the movement of the particle in the isotropic sample is greater than that in the anisotropic sample, which causes a greater variation of the parameter λ.

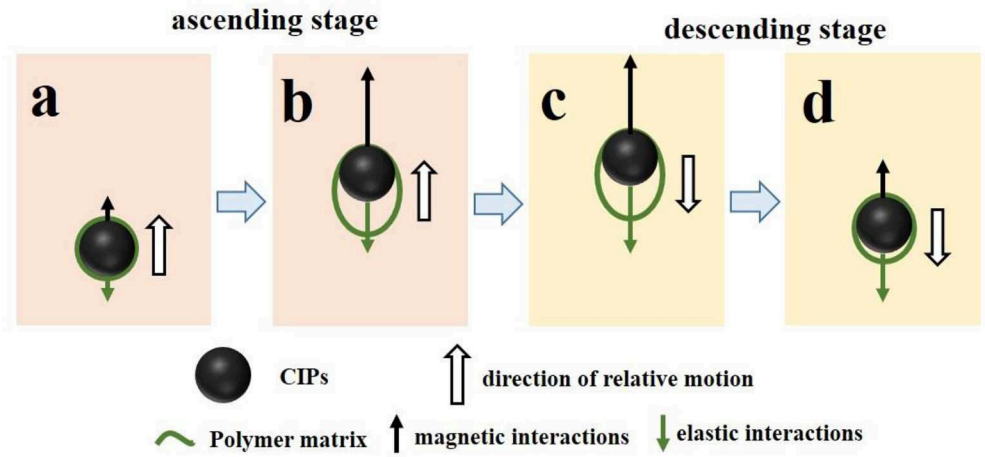

SCHEME 1 | The schematic of the movement of CIP under the ascending and descending magnetic field. **(a)** ascending stage with a smaller relative displacement; **(b)** ascending stage with a larger relative displacement; **(c)** descending stage with a larger relative displacement; **(d)** descending stage with a smaller relative displacement.

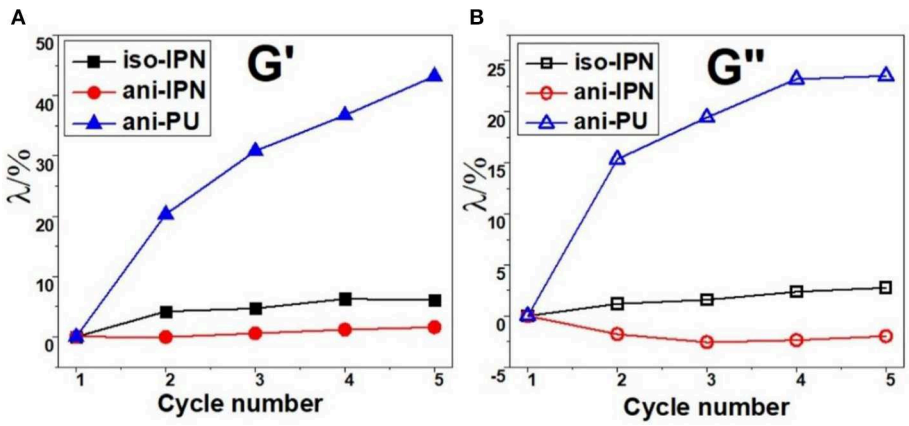

FIGURE 5 | Dependence of the parameter λ (**A**: storage modulus; **B**: loss modulus) on cycle number for the samples under the triangular magnetic field.

Amplitude Cycling Tests

Decreasing in storage modulus G′ with the increasing strain amplitude, termed as Payne effect (Payne, 1962, 1967), has been recognized in polymer science and engineering (Meera et al., 2009; Papon et al., 2012; Ponnamma et al., 2013; Gan et al., 2016). The Payne effect of MRE has been studied by many researches, but the mechanical hysteresis caused by the shear strain has been rarely studied (Sorokin et al., 2014, 2015). In order to study the mechanical hysteresis of MRE under the ascending and descending strain, we tested the Payne effect of MRE under the cyclical amplitude in the absence and presence of magnetic field. The strain amplitude ranges of 0.01–20%, pre-compression forces of 10 N and test frequency of 5 Hz were selected for this test. Measurements were also carried out in several consecutive stages. The dynamic mechanical properties were initially measured under the changing strain that increased from 0.01 to 20%. After reaching the maximum value, the amplitude of strain was decreased from 20 to 0.01%. Five consecutive cycles were held for each sample in the absence and presence of magnetic field.

Figure 6 shows that the dynamic modulus as the functions of strain amplitude for iso-IPN, ani-IPN, and ani-PU samples is measured in the absence and presence of magnetic field, respectively. It can be seen that all samples demonstrate the Payne effect: the storage modulus decreases with the increasing strain (Payne, 1962, 1967). The loss modulus increased with the increasing strain initially, and then decreased with the increasing strain when it reaches its maximum. An apparent hysteresis has been observed in all curves, and the MRE samples show a strain hardening effect. The hysteresis is more obvious in the presence of magnetic field than in the absence of magnetic field, and the hysteresis of PU sample also greater than that of IPN sample. It can be seen that the modulus increased with the increasing test cycle, and the modulus tends to saturation after the several cycles. A significant change can be observed within the first cycle while only minor changes in

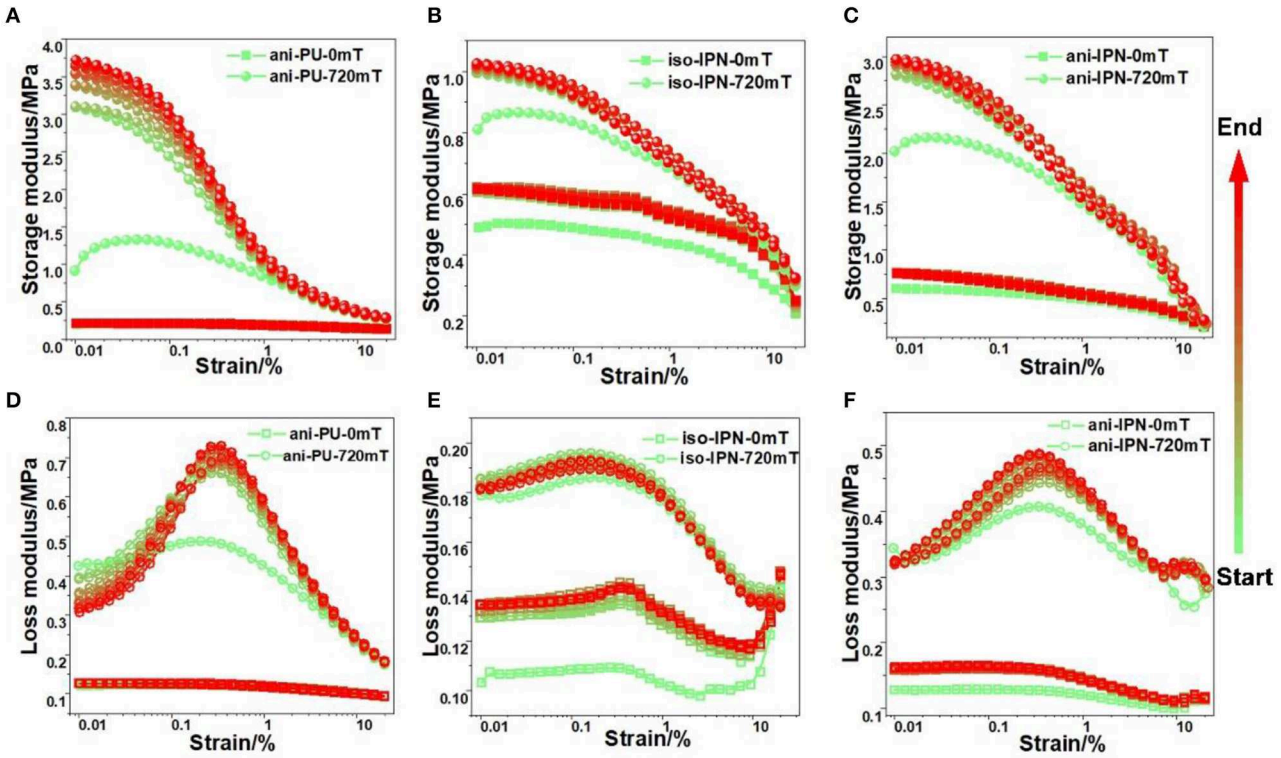

FIGURE 6 | The influence of the shear strain on the dynamic viscoelastic properties of MRE samples. Dependence of storage modulus of ani-PU sample **(A)**, ani-IPN sample **(B)**, and iso-IPN sample **(C)** on the shear strain in the absence and presence of magnetic field. Dependence of loss modulus of ani-PU sample **(D)**, ani-IPN sample **(E)**, and iso-IPN sample **(F)** on the shear strain in the absence and presence of magnetic field. The color scale indicates the progress of the cycle tests.

the following cycles, which also has been reported by Sorokin et al. (2014, 2015). In particular, under the magnetic field, the Payne effect becomes much more pronounced, particularly for the anisotropic MRE samples. The quantitative comparison of Payne effect among these samples is discussed later using a phenomenological model.

There have been many explanations and phenomenological models are well reported for Payne effect, and they are mainly based on the concepts of change in the microstructure of the composites. Kraus model is based on the concepts of change in particle–particle interactions, and the strain hardening effect of MRE under the cycling strain tests is mainly caused by the particle reagglomeration. Therefore, for the better understanding of the hysteresis of Payne effect of MRE, Kraus model is adopted to determine the influence mechanism of Payne effect. The Kraus model is the first phenomenological model to represent and explicate the Payne effect, which provides the relations for the dynamic modulus and strain amplitude in Equation (3) (Kraus, 1984),

$$\frac{G'_{\gamma} - G'_{\infty}}{G'_0 - G'_{\infty}} = \frac{1}{1 + (\gamma/\gamma_c)^{2m}} \tag{4}$$

where G'_{∞} is the value of storage modulus at very large strain; G'_0 is equal to the value of storage modulus at very small strain; where γ_c and m are the fitting parameters, and γ_c is the critical strain when G'_{γ} reaches the half value of $G'_0 - G'_{\infty}$; m is the shear strain sensitivity of the mechanism of particle-particle contact breakage and defines the shape of the G'_{γ} curve (Qu et al., 2014). To obtain a better understanding of the influence of matrix, particle distribution and magnetic field on the Payne effect, we fitted the G'_{γ} curves with the increasing strain amplitude. The obtained values of G'_0, G'_{∞}, γ_c, and m for all samples are shown in **Tables 2–5**, respectively. It can be seen that the Kruas model can be used to describe the Payne effect of MRE samples felicitously, as shown in **Figure 7**. For clarity, only the first curves of the samples are presented. The dependences of the fitting parameters on the cycle number are shown in **Figures 8**, **9**. It can be seen from the **Figure 8** that both G'_0 and G'_{∞} slightly increase with the cycle number in the absence of magnetic field. It attributes to that the matrix becomes stiffer for the subsequent measurement (Sorokin et al., 2015). On the other hand, the G'_0 and G'_{∞} increase evidently after the first cycle and then tend to be saturated. The application of magnetic field and increasing strain amplitude helps magnetic particles to rearrange. The particles become closer to form stronger chains structures under the magnetic field. The enhancement of MR effect is caused by the increase of G'_0 and G'_{∞} in the subsequent cycles. In addition, the G'_0 and G'_{∞} of the sample in the presence of magnetic field are both larger than that in the absence of magnetic field. The increscent modulus is also caused by the magneto-induced modulus.

TABLE 2 | G'_0 (MPa) of the samples in the different cycles.

Sample-magnetic field	Cycle				
	1st	2nd	3rd	4th	5th
iso-IPN-0mT	0.49	0.59	0.6	0.6	0.6
iso-IPN-720mT	0.85	1.01	1.02	1.03	1.04
ani-IPN-0mT	0.59	0.75	0.77	0.75	0.76
ani-IPN-720mT	2.1	2.87	2.99	3.05	3.03
ani-PU-0mT	0.199	0.22	0.215	0.218	0.219
ani-PU-720mT	1.25	3.2	3.5	3.66	3.77

TABLE 3 | G'_∞ (MPa) of the samples in the different cycles.

Sample-magnetic field	Cycle				
	1st	2nd	3rd	4th	5th
iso-IPN-0mT	0.2	0.22	0.24	0.245	0.245
iso-IPN-720mT	0.29	0.31	0.32	0.33	0.325
ani-IPN-0mT	0.199	0.215	0.22	0.22	0.218
ani-IPN-720mT	0.21	0.237	0.266	0.266	0.267
ani-PU-0mT	0.143	0.143	0.144	0.144	0.144
ani-PU-720mT	0.268	0.28	0.285	0.288	0.29

TABLE 4 | Fitting parameter γ_c (%) of the samples in the different cycles.

Sample-magnetic field	Cycle				
	1st	2nd	3rd	4th	5th
iso-IPN-0mT	8.9	8.76	7.98	7.78	6.05
iso-IPN-720mT	2.64	1.92	1.7	1.62	1.54
ani-IPN-0mT	3.52	2.5	2.42	2.35	2.2
ani-IPN-720mT	2.18	1.4	1.14	1.06	1.03
ani-PU-0mT	4.84	3.19	3.08	2.77	2.69
ani-PU-720mT	1.43	0.375	0.35	0.35	0.35

Figure 9 shows the cycle number dependence of the critical strain γ_c and fitting parameter m. Similarly, the critical strain γ_c and fitting parameter m decrease after the first cycle and then tend to be saturated in the subsequent cycles.

The decrease of critical strain γ_c indicates that the particle networks can be destroyed easily after the first destruction. It also can be seen that the critical strain γ_c of samples in the absence of magnetic field is larger than that in the presence of magnetic field. The interaction force between the magnetized CIPs would enhance the strength of particle networks, which leads the decrease of γ_c. But the magneto-induced Payne effect caused by the breakdown of the magnetic particle network is more obvious. The decrease of γ_c caused by magneto-induced Payne effect is larger than the increase of γ_c caused by enhanced interaction force, thus the γ_c is smaller under the magnetic field. The fitting parameter m is related to the particle agglomerate structure (Heinrich and Kluppel, 2002). The decrease of m after the first cycle indicates the destruction of particle networks in high strain reduces the particle aggregates in the MRE. Besides, the m of the sample in the absence of magnetic field is larger than that in the presence of magnetic field. It's mainly because the particles tend to form a columnar paralleled to the direction of the magnetic field when imposes on the MRE. Some particles can overcome the restriction of matrix and begin to slip relatively to the elastomer matrix. Thus, the movement of particles leads to the increase in particle aggregates.

TABLE 5 | Fitting parameter m (a.u) of the samples in the different cycles.

Sample-magnetic field	Cycle				
	1st	2nd	3rd	4th	5th
iso-IPN-0mT	0.58	0.53	0.53	0.52	0.518
iso-IPN-720mT	0.44	0.37	0.37	0.37	0.36
ani-IPN-0mT	0.496	0.37	0.36	0.35	0.365
ani-IPN-720mT	0.46	0.36	0.35	0.34	0.36
ani-PU-0mT	0.7	0.57	0.58	0.56	0.56
ani-PU-720mT	0.57	0.5	0.51	0.52	0.52

CONCLUSIONS

The dynamic mechanical hysteresis of MRE under the cyclic loading and periodic magnetic field is studied in this paper. The experimental results show that all the mechanical pressure, shear strain and periodic magnetic field would cause a hysteresis in the dynamic mechanical properties of MRE, and the hysteresis tends to be saturated after several cycles. The conclusions can be drawn as follows:

(1) The hysteresis in the dynamic mechanical properties of MRE is caused by the coupling effect of the cyclic mechanical loading and magnetic field. The saturation of the hysteresis indicates that there is a balance between destruction and reformation of the particle structures. In addition, the magnetic field can cause an obvious hardening effect of MRE under the mechanical pressure and high shear strain.

(2) The hysteresis of PU sample is greater than that of IPN sample, which indicates that the viscidity and elasticity of the matrix play important roles in the destruction and reformation of the particle structure. A stable molecular chain structure in the matrix would reduce the magnitude of the mechanical hysteresis and improve the stability of the hysteresis in the saturation stage.

(3) A significant increase of the storage modulus can be observed within the first cycle in each test, which means that the first dynamic oscillatory shear tests would destroy the unstable structure, making the matrix become stiffer.

(4) The periodic triangular magnetic field also caused the hysteresis in the dynamic modulus which can be attributed to the irreversible movement of the particles. The test result of loss modulus can be explained by the relative movement of CIPs. For the influence of the particle distribution, the hysteresis of the isotropic sample is greater than that of anisotropic sample in the presence of magnetic field, which can be attributed to the optimization of particle structure in the magnetic field.

This work turns out that the material properties of MRE should be characterized by the repeating tests rather than merely single

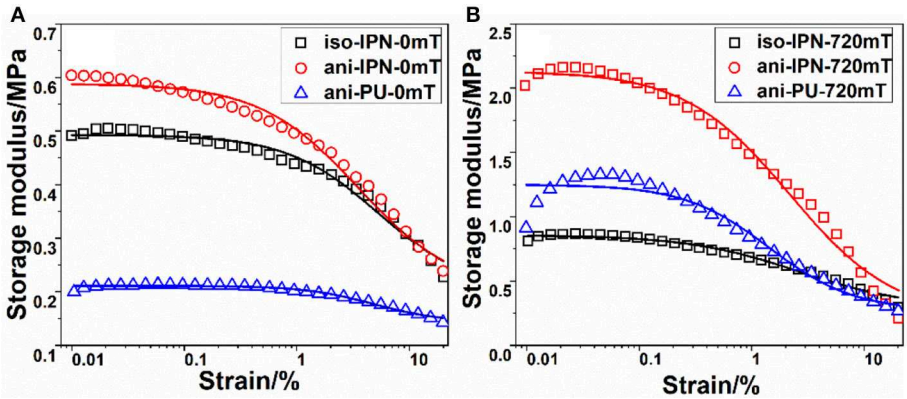

FIGURE 7 | Fitting of the first G'_{γ} curve with the increasing strain amplitude obtained in the absence **(A)** and presence **(B)** of magnetic field. (Symbols are experimental date, and solid lines are the fitting curves).

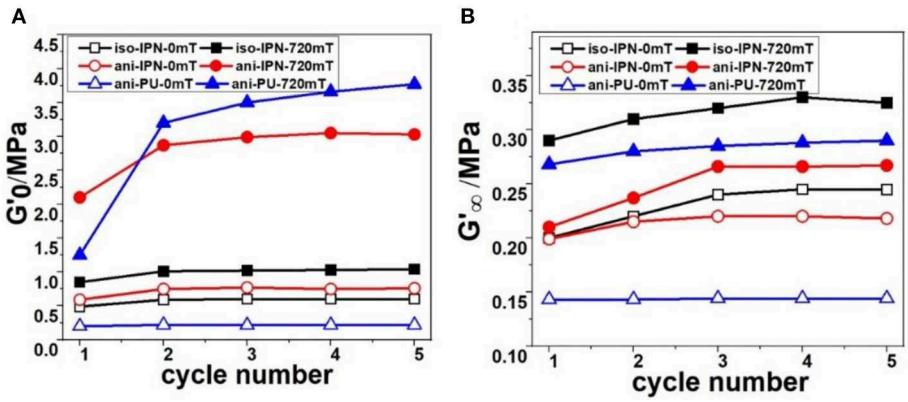

FIGURE 8 | Cycle number dependence of the G'_0 **(A)** and G'_{∞} **(B)**. The hollow symbol and solid symbol indicated the tests under 0 and 720 mT, respectively.

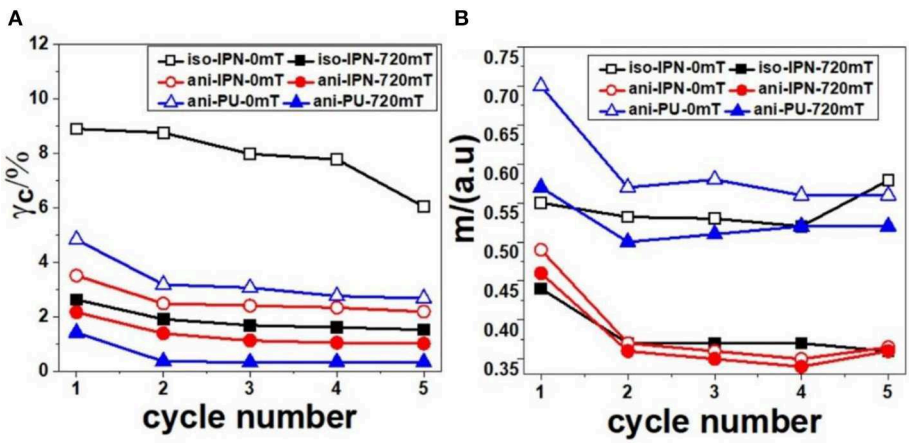

FIGURE 9 | Cycle number dependence of the critical strain γ_c **(A)** and fitting parameter m **(B)**. The hollow symbol and solid symbol indicated the tests under 0 and 720 mT, respectively.

test. More effective evaluation tests of MRE are of benefit to the potential applications. The hysteresis caused by mechanical loading and magnetic field is an intrinsic property of MRE and should be taken into account in future studies. In future work, we should not only explore the material preparation methods that reduce the hysteresis characteristics of MRE, but also carry out in-depth mechanism modeling research. The results achieved are important for fundamental understanding of material behavior

of MRE, which would provide a guidance for the improvement of material preparation and the development of MRE devices.

DATA AVAILABILITY STATEMENT

The datasets generated for this study are available on request to the corresponding author.

AUTHOR CONTRIBUTIONS

YZ, FF, and MY proposed and designed the research. YZ and SQ performed all experiments. The experimental data were analyzed by YZ, WH, and YC. All authors wrote the paper and participated in discussions.

FUNDING

This research was supported by the Science Challenge Project (No. TZ2016006-0504-01), High-end CNC Machine Tools and Basic Manufacturing Equipment Major National Science and Technology Project, China (2017ZX04022001), and National Key Research and Development Program of China (Grant No. 2017YFA0701200). Funding Support by Laboratory of Precision Manufacturing Technology, CAEP, China.

REFERENCES

An, H. N., Picken, S. J., and Mendes, E. (2012). Direct observation of particle rearrangement during cyclic stress hardening of magnetorheological gels. *Soft Matter* 8, 11995–12001. doi: 10.1039/c2sm26587g

An, J., and Kwon, D.-S. (2003). Modeling of a magnetorheological actuator including magnetic hysteresis. *J. Intell. Mater. Syst. Struct.* 14, 541–550. doi: 10.1177/1045389X03036506

Aziz, S. A. A., Mazlan, S. A., Ismail, N. I. N., Ubaidillah, U., Choi, S. B., Khairi, M. H. A., et al. (2016). Effects of multiwall carbon nanotubes on viscoelastic properties of magnetorheological elastomers. *Smart Mater. Struct.* 25:077001. doi: 10.1088/0964-1726/25/7/077001

Bica, I. (2012). The influence of the magnetic field on the elastic properties of anisotropic magnetorheological elastomers. *J. Ind. Eng. Chem.* 18, 1666–1669. doi: 10.1016/j.jiec.2012.03.006

Chai, A. B., Verron, E., Andriyana, A., and Johan, M. R. (2013). Mullins effect in swollen rubber: experimental investigation and constitutive modelling. *Polym. Test* 32, 748–759. doi: 10.1016/j.polymertesting.2013.03.006

Chen, P., Bai, X. X., Qian, L. J., and Choi, S. B. (2018). An approach for hysteresis modeling based on shape function and memory mechanism. *IEEE/ASME Trans. Mechatronics* 23, 1270–1278. doi: 10.1109/TMECH.2018.2833459

Diani, J., Fayolle, B., and Gilormini, P. (2009). A review on the Mullins effect. *Eur. Polym. J.* 45, 601–612. doi: 10.1016/j.eurpolymj.2008.11.017

Dominguez, A., Sedaghati, R., and Stiharu, I. (2004). Modelling the hysteresis phenomenon of magnetorheological dampers. *Smart Mater. Struct.* 13:1351. doi: 10.1088/0964-1726/13/6/008

Dorfmann, A., and Ogden, R. W. (2005). A constitutive model for the Mullins effect with permanent set in a particle-reinforced rubber. *Int. J. Solids Struct.* 42, 4909–4910. doi: 10.1016/j.ijsolstr.2004.12.001

Drozdov, A. D. (2009). Mullins' effect in semicrystalline polymers. *Int. J. Solids Struct.* 46, 3336–3345. doi: 10.1016/j.ijsolstr.2009.05.001

Feng, J. B., Xuan, S. H., Liu, T. X., Ge, L., Yan, L. X., Zhou, H., et al. (2015). The prestress-dependent mechanical response of magnetorheological elastomers. *Smart Mater. Struct.* 24:085032. doi: 10.1088/0964-1726/24/8/085032

Fu, J., Li, P. D., Wang, Y., Liao, G. Y., and Yu, M. (2016). Model-free fuzzy control of a magnetorheological elastomer vibration isolation system: analysis and experimental evaluation. *Smart Mater. Struct.* 25:035030. doi: 10.1088/0964-1726/25/3/035030

Gan, S. C., Wu, Z. L., Xu, H. L., Song, Y. H., and Zheng, Q. (2016). Viscoelastic behaviors of carbon black gel extracted from highly filled natural rubber compounds: insights into the Payne effect. *Macromolecules* 49, 1454–1463. doi: 10.1021/acs.macromol.5b02701

Ge, L., Xuan, S. H., Liao, G. J., Yin, T. T., and Gong, X. L. (2015). Stretchable polyurethane sponge reinforced magnetorheological material with enhanced mechanical properties. *Smart Mater. Struct.* 24:037001. doi: 10.1088/0964-1726/24/3/037001

Gong, X. L., Zhang, X. Z., and Zhang, P. Q. (2005). Fabrication and characterization of isotropic magnetorheological elastomers. *Polym. Test* 24, 669–676. doi: 10.1016/j.polymertesting.2005.03.015

Gundermann, T., and Odenbach, S. (2014). Investigation of the motion of particles in magnetorheological elastomers by X-mu CT. *Smart Mater. Struct.* 23:105013. doi: 10.1088/0964-1726/23/10/105013

Hanson, D. E., Hawley, M., Houlton, R., Chitanvis, K., Rae, P., Orler, E. B., et al. (2005). Stress softening experiments in silica-filled polydimethylsiloxane provide insight into a mechanism for the Mullins effect. *Polymer* 46, 10989–10995. doi: 10.1016/j.polymer.2005.09.039

Heinrich, G., and Kluppel, M. (2002). Recent advances in the theory of filler networking in elastomers. *Filled Elastomers Drug Deliv. Syst.* 160, 1–44. doi: 10.1007/3-540-45362-8_1

Hoang, N., Zhang, N., Li, W. H., and Du, H. (2013). Development of a torsional dynamic absorber using a magnetorheological elastomer for vibration reduction of a powertrain test rig. *J. Intell. Mater. Syst. Struct.* 24, 2036–2044. doi: 10.1177/1045389X13489361

Jung, H. S., Kwon, S. H., Choi, H. J., Jung, J. H., and Kim, Y. G. (2016). Magnetic carbonyl iron/natural rubber composite elastomer and its magnetorheology. *Compos. Struct.* 136, 106–112. doi: 10.1016/j.compstruct.2015.10.008

Kashima, S., Miyasaka, F., and Hirata, K. (2012). Novel soft actuator using magnetorheological elastomer. *IEEE Trans. Magn.* 48, 1649–1652. doi: 10.1109/TMAG.2011.2173669

Kramarenko, E. Y., Chertovich, A. V., Stepanov, G. V., Semisalova, A. S., Makarova, L. A., Perov, N. S., et al. (2015). Magnetic and viscoelastic response of elastomers with hard magnetic filler. *Smart Mater. Struct.* 24:035002. doi: 10.1088/0964-1726/24/3/035002

Kraus, G. (1984). Mechanical losses in carbon-black-filled rubbers. *Appl. Polym. Symp.* 39, 75–92.

Li, J. F., and Gong, X. L. (2008). Dynamic damping property of magnetorheological elastomer. *J. Cent. South Univ. Technol.* 15, 261–265. doi: 10.1007/s11771-008-0359-2

Li, R., and Sun, L. Z. (2011). Dynamic mechanical behavior of magnetorheological nanocomposites filled with carbon nanotubes. *Appl. Phys. Lett.* 99:131912. doi: 10.1063/1.3645627

Li, W. H., and Nakano, M. (2013). Fabrication and characterization of PDMS based magnetorheological elastomers. *Smart Mater. Struct.* 22:055035. doi: 10.1088/0964-1726/22/5/055035

Machado, G., Chagnon, G., and Favier, D. (2012). Induced anisotropy by the Mullins effect in filled silicone rubber. *Mech. Mater.* 50, 70–80. doi: 10.1016/j.mechmat.2012.03.006

Meera, A. P., Said, S., Grohens, Y., and Thomas, S. (2009). Nonlinear viscoelastic behavior of silica-filled natural rubber nanocomposites. *J. Phys. Chem. C* 113, 17997–18002. doi: 10.1021/jp9020118

Merabia, S., Sotta, P., and Long, D. R. (2008). A microscopic model for the reinforcement and the nonlinear behavior of filled elastomers and thermoplastic elastomers (Payne and Mullins effects). *Macromolecules* 41, 8252–8266. doi: 10.1021/ma8014728

Niu, C. G., Dong, X. F., and Qi, M. (2015). Enhanced electrorheological properties of elastomers containing TiO_2/urea core-shell particles. *ACS Appl. Mater. Interfaces* 7, 24855–24863. doi: 10.1021/acsami.5b08127

Ogden, R. W., and Roxburgh, D. G. (1999). A pseudo-elastic model for the Mullins effect in filled rubber. *Proc. R. Soc.*

A Math. Phys. Eng. Sci. 455, 2861–2877. doi: 10.1098/rspa.1999.0431

Papon, A., Merabia, S., Guy, L., Lequeux, F., Montes, H., Sotta, P., et al. (2012). Unique nonlinear behavior of nano-filled elastomers: from the onset of strain softening to large amplitude shear deformations. *Macromolecules* 45, 2891–2904. doi: 10.1021/ma202278e

Payne, A. R. (1962). The dynamic properties of carbon black-loaded natural rubber vulcanizates. Part I. *J. Appl. Polym. Sci.* 6, 57–64. doi: 10.1002/app.1962.070061906

Payne, A. R. (1967). Dynamic properties of PBNA-natural rubber vulcanizates. *J. Appl. Polym. Sci* 11, 383–388. doi: 10.1002/app.1967.070110306

Ponnamma, D., Sadasivuni, K. K., Strankowski, M., Moldenaers, P., Thomas, S., and Grohens, Y. (2013). Interrelated shape memory and Payne effect in polyurethane/graphene oxide nanocomposites. *RSC Adv.* 3, 16068–16079. doi: 10.1039/c3ra41395k

Qi, H. J., and Boyce, M. C. (2005). Stress-strain behavior of thermoplastic polyurethanes. *Mech. Mater.* 37, 817–839. doi: 10.1016/j.mechmat.2004.08.001

Qi, S., Guo, H. Y., Chen, J., Fu, J., Hu, C. G., Yu, M., et al. (2018a). Magnetorheological elastomers enabled high-sensitive self-powered tribo-sensor for magnetic field detection. *Nanoscale* 10, 4745–4752. doi: 10.1039/C7NR09129J

Qi, S., Yu, M., Fu, J., Zhu, M., Xie, Y. P., and Li, W. (2018b). An EPDM/MVQ polymer blend based magnetorheological elastomer with good thermostability and mechanical performance. *Soft Matter.* 14, 8521–8528. doi: 10.1039/C8SM01712C

Qiao, X. Y., Lu, X. S., Li, W. H., Chen, J., Gong, X. L., Yang, T., et al. (2012). Microstructure and magnetorheological properties of the thermoplastic magnetorheological elastomer composites containing modified carbonyl iron particles and poly(styrene-b-ethylene-ethylenepropylene-b-styrene) matrix. *Smart Mater. Struct.* 21:115028. doi: 10.1088/0964-1726/21/11/115028

Qu, L. L., Wang, L. J., Xie, X. M., Yu, G. Z., and Bu, S. H. (2014). Contribution of silica-rubber interactions on the viscoelastic behaviors of modified solution polymerized styrene butadiene rubbers (M-S-SBRs) filled with silica. *RSC Adv.* 4, 64354–64363. doi: 10.1039/C4RA09492A

Shen, Y., Golnaraghi, M. F., and Heppler, G. R. (2004). Experimental research and modeling of magnetorheological elastomers. *J. Intell. Mater. Syst. Struct.* 15, 27–35. doi: 10.1177/1045389X04039264

Sorokin, V. V., Ecker, E., Stepanov, G. V., Shamonin, M., Monkman, G. J., Kramarenko, E. Y., et al. (2014). Experimental study of the magnetic field enhanced Payne effect in magnetorheological elastomers. *Soft Matter.* 10, 8765–8776. doi: 10.1039/C4SM01738B

Sorokin, V. V., Stepanov, G. V., Shamonin, M., Monkman, G. J., Khokhlov, A. R., and Kramarenko, E. Y. (2015). Hysteresis of the viscoelastic properties and the normal force in magnetically and mechanically soft magnetoactive elastomers: effects of filler composition. strain amplitude and magnetic field. *Polymer* 76, 191–202. doi: 10.1016/j.polymer.2015.08.040

Stepanov, G. V., Abramchuk, S. S., Grishin, D. A., Nikitin, L. V., Kramarenko, E. Y., and Khokhlov, A. R. (2007). Effect of a homogeneous magnetic field on the viscoelastic behavior of magnetic elastomers. *Polymer* 48, 488–495. doi: 10.1016/j.polymer.2006.11.044

Stepanov, G. V., Chertovich, A. V., and Kramarenko, E. Y. (2012). Magnetorheological and deformation properties of magnetically controlled elastomers with hard magnetic filler. *J. Magn. Magn. Mater.* 324, 3448–3451. doi: 10.1016/j.jmmm.2012.02.062

Wang, Y., Gong, X. L., Yang, J., and Xuan, S. H. (2014). Improving the dynamic properties of MRE under cyclic loading by incorporating silicon carbide nanoparticles. *Ind. Eng. Chem. Res.* 53, 3065–3072. doi: 10.1021/ie402395e

Wang, Y., Xuan, S. H., Dong, B., Xu, F., and Gong, X. L. (2016). Stimuli dependent impedance of conductive magnetorheological elastomers. *Smart Mater. Struct.* 25:025003. doi: 10.1088/0964-1726/25/2/025003

Webber, R. E., Creton, C., Brown, H. R., and Gong, J. P. (2007). Large strain hysteresis and mullins effect of tough double-network hydrogels. *Macromolecules* 40, 2919–2927. doi: 10.1021/ma062924y

Wei, B., Gong, X. L., and Jiang, W. Q. (2010). Influence of polyurethane properties on mechanical performances of magnetorheological elastomers. *J. Appl. Polym. Sci.* 116, 771–778. doi: 10.1002/app.31474

Wu, J. K., Gong, X. L., Fan, Y. C., and Xia, H. S. (2010). Anisotropic polyurethane magnetorheological elastomer prepared through *in situ* polycondensation under a magnetic field. *Smart Mater. Struct.* 19:105007. doi: 10.1088/0964-1726/19/10/105007

Wu, J. K., Gong, X. L., Fan, Y. C., and Xia, H. S. (2012). Improving the magnetorheological properties of polyurethane magnetorheological elastomer through plasticization. *J. Appl. Polym. Sci.* 123, 2476–2484. doi: 10.1002/app.34808

Xian-Xu, B., Fei-Long, C., and Peng, C. (2019). Resistor-capacitor (RC) operator-based hysteresis model for magnetorheological (MR) dampers. *Mech. Syst. Signal. Process.* 117C, 157–169. doi: 10.1016/j.ymssp.2018.07.050

Xing, Z. W., Yu, M., Fu, J., Wang, Y., and Zhao, L. J. (2015). A laminated magnetorheological elastomer bearing prototype for seismic mitigation of bridge superstructures. *J. Intell. Mater. Syst. Struct.* 26, 1818–1825. doi: 10.1177/1045389X15577654

Xing, Z. W., Yu, M., Sun, S. S., Fu, J., and Li, W. H. (2016). A hybrid magnetorheological elastomer-fluid (MRE-F) isolation mount: development and experimental validation. *Smart Mater. Struct.* 25:015026. doi: 10.1088/0964-1726/25/1/015026

Xu, Y. G., Gong, X. L., Xuan, S. H., Zhang, W., and Fan, Y. C. (2011). A high-performance magnetorheological material: preparation, characterization and magnetic-mechanic coupling properties. *Soft Matter* 7, 5246–5254. doi: 10.1039/c1sm05301a

Xu, Y. G., Liao, G. J., Zhang, C. Y., Wan, Q., and Liu, T. X. (2016). The transition from stress softening to stress hardening under cyclic loading induced by magnetic field for magneto-sensitive polymer gels. *Appl. Phys. Lett.* 108:161902. doi: 10.1063/1.4947131

Yang, J., Gong, X. L., Deng, H. X., Qin, L. J., and Xuan, S. H. (2012). Investigation on the mechanism of damping behavior of magnetorheological elastomers. *Smart Mater. Struct.* 21:125015. doi: 10.1088/0964-1726/21/12/125015

Yang, J., Gong, X. L., Zong, L. H., Peng, C., and Xuan, S. H. (2013). Silicon carbide-strengthened magnetorheological elastomer: preparation and mechanical property. *Polym. Eng. Sci.* 53, 2615–2623. doi: 10.1002/pen.23529

Yang, P. G., Yu, M., and Fu, J. (2016). Ni-coated multi-walled carbon nanotubes enhanced the magnetorheological performance of magnetorheological gel. *J. Nanopart. Res.* 18:61. doi: 10.1007/s11051-016-3370-9

Yu, M., Fu, J., Ju, B. X., Zheng, X., and Choi, S. B. (2013). Influence of x-ray radiation on the properties of magnetorheological elastomers. *Smart Mater. Struct.* 22:125010. doi: 10.1088/0964-1726/22/12/125010

Yu, M., Qi, S., Fu, J., Yang, P. A., and Zhu, M. (2015a). Preparation and characterization of a novel magnetorheological elastomer based on polyurethane/epoxy resin IPNs matrix. *Smart Mater. Struct.* 24:045009. doi: 10.1088/0964-1726/24/4/045009

Yu, M., Qi, S., Fu, J., and Zhu, M. (2015c). A high-damping magnetorheological elastomer with bi-directional magnetic-control modulus for potential application in seismology. *Appl. Phys. Lett.* 107:111901. doi: 10.1063/1.4931127

Yu, M., Yang, P., Fu, J., Liu, S., Qi, S. (2016). Study on the characteristics of magneto-sensitive electromagnetic wave-absorbing properties of magnetorheological elastomers. *Smart Mater. Struct.* 25:085046. doi: 10.1088/0964-1726/25/8/085046

Yu, M., Zhu, M., Fu, J., Yang, P. A., and Qi, S. (2015b). A dimorphic magnetorheological elastomer incorporated with Fe nano-flakes modified carbonyl iron particles: preparation and characterization. *Smart Mater. Struct.* 24:115021. doi: 10.1088/0964-1726/24/11/115021

Yu, Y., Li, Y., Li, J., and Gu, X. (2016). A hysteresis model for dynamic behaviour of magnetorheological elastomer base isolator. *Smart Mater. Struct.* 25:055029. doi: 10.1088/0964-1726/25/5/055029

Conflict of Interest: The authors declare that the research was conducted in the absence of any commercial or financial relationships that could be construed as a potential conflict of interest.

frontiers in Materials

ORIGINAL RESEARCH
published: 22 November 2019
doi: 10.3389/fmats.2019.00293

A Two-Dimensional Axisymmetric Finite Element Analysis of Coupled Inertial-Viscous-Frictional-Elastic Transients in Magnetorheological Dampers Using the Compressible Herschel-Bulkley Fluid Model

Pengfei Guo[1]*, *Jing Xie*[1], *Xufeng Dong*[2] and *Yonghu Huang*[3]

[1] School of Civil Engineering, Xi'an University of Architecture and Technology, Xi'an, China, [2] School of Materials Science and Engineering, Dalian University of Technology, Dalian, China, [3] School of Civil Engineering and Architecture, East China Jiaotong University, Nanchang, China

OPEN ACCESS

Edited by:
Xian-Xu Bai,
Hefei University of Technology, China

Reviewed by:
Jianqiang Yu,
Chongqing University, China
Hung Quoc Nguyen,
Vietnamese-German University, Vietnam

***Correspondence:**
Pengfei Guo
pengfeiguo@xauat.edu.cn

Specialty section:
This article was submitted to Smart Materials, a section of the journal Frontiers in Materials

Received: *09 August 2019*
Accepted: *01 November 2019*
Published: *22 November 2019*

Citation:
Guo P, Xie J, Dong X and Huang Y (2019) A Two-Dimensional Axisymmetric Finite Element Analysis of Coupled Inertial-Viscous-Frictional-Elastic Transients in Magnetorheological Dampers Using the Compressible Herschel-Bulkley Fluid Model. Front. Mater. 6:293. doi: 10.3389/fmats.2019.00293

It has been challenging to accurately predict the unique characteristics of magnetorheological (MR) dampers, due to their inherent non-linear nature. Multidimensional flow simulation has received increasing attentions because it serves as a general methodology for modeling arbitrary MR devices. However, the compressibility of MR fluid which greatly affects the hysteretic behavior of an MR damper is neglected in previous multidimensional flow studies. This paper presents a two-dimensional (2D) axisymmetric flow of the compressible Herschel-Bulkley fluid in MR dampers. We simulated the fully coupled inertial-viscous-frictional-elastic transients in MR dampers under low-, medium-, and high frequency excitations. An arbitrary Lagrangian-Eulerian kinematical description is adopted, with the piston movements represented by the moving boundaries. The viscoplasticity and compressibility of MR fluid are, respectively, modeled by the modified Herschel–Bulkley model and the Tait equation. The streamline-upwind Petrov–Galerkin finite element method is used to solve the model equations including the conservation laws and mesh motion equation. We tested the performances of an MR damper under different electric currents and different frequency displacement excitations, and the model predictions agree well with the experimental data. Results showed that the coupled transients of an MR damper are frequency dependent. The weak compressibility of MR fluid, which mainly happens in the chamber rather than in the working gap, is crucial for accurate predictions. A damper's transition from the pre-yield to the post-yield is essentially a step-response of a second order mass-spring-viscous system, and we give such step-response a detailed explanation in terms of mass flow rate.

Keywords: magnetorheological fluid damper, coupled transients, high frequency, finite element analysis, weak compressibility

INTRODUCTION

Magnetorheological (MR) fluids are suspensions that exhibit a rapid, reversible and tunable transition from a free-flowing state to a semi-solid state upon the application of an external magnetic field (Carlson et al., 1996; Jolly et al., 1999). MR dampers, which utilize the advantages of MR fluids, are semi-active control devices that are capable of generating a magnitude of force sufficient for large-scale applications, while requiring only a battery for power (Alghamdi et al., 2014). Accurate prediction of the unique characteristics of MR dampers has been one of the challenging aspects for developing and utilizing these devices due to their inherent non-linear nature. Lumped parameter models have been the main tool for modeling of MR dampers because of their simplicity. They are comprehensively reviewed in works (Sahin et al., 2010; Wang and Liao, 2011), and more recent works can be found in Yu et al. (2017) and (Chen et al., 2018).

Compared to the lumped parameter modeling, the multidimensional flow analysis in MR dampers is not only more accurate, but also serves as a general methodology of modeling of MR devices with arbitrary geometries. For example, a 2D computational fluid dynamics (CFD) model was constructed by Sahin et al. (2013) for an MR valve having complex flow region. The CFD model showed apparent advantages of better agreements with the experimental data than the lumped parameter model.

Over the past few years, CFD modeling of MR/ER devices is receiving more and more research interests. Ursescu (2005) simulated the ER flow in a channel with a prescribed inlet flow velocity and the free outlet. The model was validated by comparing with the experimental data, and was used to optimize the configuration of the electrodes to improve the ER-effect. With the piston movements described by a deformed mesh, Case et al. (2016) developed a multiphysics finite element model for a small scale MR damper. The model was concluded to be suitable for the prediction of oscillatory MR fluid behavior and thus for further development and optimization of the semi-active dampers. A similar work was conducted by Sternberg et al. (2014) in which a 3D magneto-static analysis was coupled with the flow analysis. Zheng et al. (2015) established a more sophisticated multiphysics model which considered the magnetic, temperature and flow fields together. Zhou and Bai (2014) conducted a 3D numerical FEM flow analysis for MRF seal technology in a circular cooler. Both of the three-dimensional numerical simulation and experimental results demonstrated that the air leakage of a circular cooler was solvable effectively with the magnetorheological fluid seal method. Gołdasz and Sapinski (2015) studied a squeeze mode MR damper with a CFD model, and the well-known fact was confirmed that the compressive loads increase with the decreasing gap height.

More recently, using finite volume method on a two dimensional moving grid, Syrakos et al. (2016) successfully captured the hysteretic behavior of a damper caused by the inertia of fluid under high frequency loadings. In a later theoretical study of a fluid damper, they (Syrakos et al., 2018) extended the numerical model by including the effects of shear-thinning and viscoelasticity. Guo and Xie (2019) developed a 2D incompressible viscoelastic fluid CFD model which was validated by the experimental data in a literature.

So far, the previous studies on multidimensional flow analysis in MR dampers were restricted to incompressible flows. However, as indicated by lumped parameter models, the weak compressibility of MR fluids is responsible for the hysteretic behavior of MR dampers. Thus, a compressible fluid multidimensional flow analysis (which has not been reported in previous studies to our best knowledge) will be conducted in this study.

PROBLEM DEFINITION AND GOVERNING EQUATIONS

Problem Definition

The layout of a typical single-coil double-ended magnetorheological (MR) fluid damper is shown in **Figures 1A,B**. The main structural parameters of an MR damper include the radius of piston (R_p), the radius of piston shaft (R_r), the working gap width (g), the effective length of the piston (L), and the stroke of the damper (s_0).

The piston reciprocates inside the house cylinder filled with MR fluid. Then the MR fluid is forced to flow from one chamber to the other, through the annular gap between the cylinder and the piston. Since the structure is axisymmetric, the fluid flow in an MR damper can often be reasonably assumed to be axisymmetric too. A small electromagnet coil wound around the piston generates a magnetic field in the working gap (in the r direction) which is perpendicular to the fluid flow (mainly in the z direction). The magnetic field causes iron particles in the MR fluid to form linear chains parallel to the field. This phenomenon solidifies the suspended iron particles and restricts the fluid movement. Consequently, the yield strength which can be adjusted by controlling input currents is developed within the fluid. The aim of a mechanical model is to predict the damping force under various input currents and piston movements.

Governing Equations for Viscous Fluid in ALE Form

The governing equations for viscous fluids can be expressed in either total ALE form (both time derivatives and spatial derivatives are in the referential configuration) or updated ALE form (only time derivatives are kept in the referential form). The latter is more convenient for the finite element implementation.

The mass and momentum conservations in the updated ALE form can be derived as (Bazilevs et al., 2013; Belytschko et al., 2013)

$$\left.\frac{\partial \rho}{\partial t}\right|_{\chi} + \mathbf{c}\cdot\nabla\rho + \rho\nabla\cdot\mathbf{v} = 0 \tag{1}$$

$$\rho\left.\frac{\partial \mathbf{v}}{\partial t}\right|_{\chi} + \rho\mathbf{c}\cdot\nabla\mathbf{v} = \nabla\cdot\boldsymbol{\sigma} + \rho\mathbf{g} \tag{2}$$

where ρ is the fluid density, the total stress tensor is $\boldsymbol{\sigma} = -p\mathbf{I} + \eta\mathbf{D} - \frac{2}{3}\eta(\nabla\cdot\mathbf{v})\mathbf{I}$, p is the pressure, $\mathbf{D} = \nabla\mathbf{v} + (\nabla\mathbf{v})^T$ is the strain rate tensor, η is the viscosity of fluids, the convective velocity is

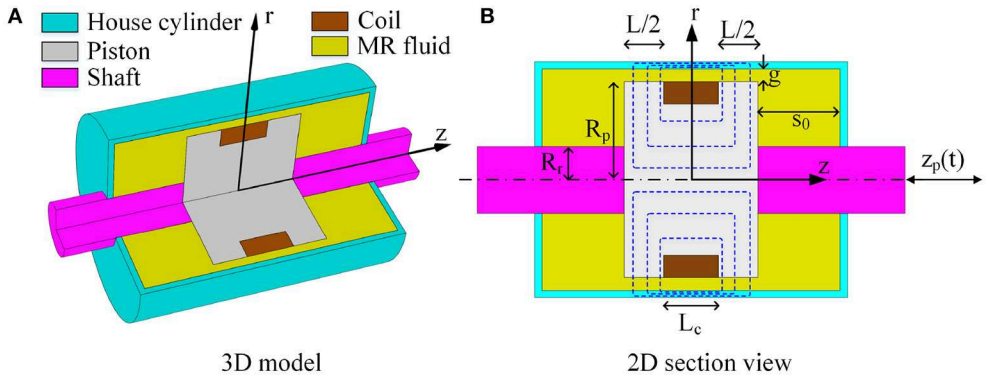

FIGURE 1 | Layout of the MR damper. **(A)** Main components. **(B)** Main design parameters.

defined by $\mathbf{c} = \mathbf{v} - \hat{\mathbf{v}}$. $\frac{\partial}{\partial t}\big|_{\chi}$ is the ALE time derivative, that is, the partial derivative with respect to time (t) when holding the ALE coordinate (χ) fixed. As mentioned above, an axisymmetric flow is assumed in an MR damper, and the spatial coordinates ($\mathbf{x}$) are denoted by (r, θ, z), and the ALE coordinate (χ) by ($\hat{r}$, $\hat{\theta}$, $\hat{z}$) throughout this study.

Since the structure is, the fluid flow in an MR damper can often be reasonably assumed to be axisymmetric too.

Constitutive Equation: Weakly Compressible Bingham Fluid

Viscoplasticity

The ability of MR fluids to reversibly change from free-flowing linear viscous fluids to semi-solid can be described by the Bingham constitutive equation in which the stress tensor is related to the velocity field by

$$\begin{cases} \mathbf{D} = 0 & |\boldsymbol{\tau}| \le \boldsymbol{\tau}_y, \ \text{pre} - \text{yield zone} \\ \boldsymbol{\tau} = \boldsymbol{\tau}_y + \eta_p \mathbf{D} & |\boldsymbol{\tau}| > \boldsymbol{\tau}_y, \ \text{post} - \text{yield zone} \end{cases} \tag{3}$$

where, $|\mathbf{D}| = \left(\frac{1}{2}\mathbf{D}{:}\mathbf{D}\right)^{1/2}$ is the magnitude of the strain rate tensor. $|\boldsymbol{\tau}|$ is the magnitude of deviatoric stress tensor $\boldsymbol{\tau}$. The post-yield viscosity η_p is assumed to be a constant, and $\boldsymbol{\tau}_y$ is the shear yield strength dependent on magnetic field intensity. However, it is difficult to identify, in advance, the pre- and post- yield zones in order to apply Equation (3) to the different zones. A popular approach to overcoming this difficulty is to approximate Equation (3) by a regularized equation which is applicable throughout the material without branches. Several such regularized equations were proposed (Frigaard and Nouar, 2005), and here we adopt the one proposed by Papanastasiou (1987), as in previous studies (Syrakos et al., 2016). It is formulated as follows:

$$\boldsymbol{\tau} = \left[\frac{\boldsymbol{\tau}_y}{|\mathbf{D}|}\left(1 - e^{-m|\mathbf{D}|}\right) + \eta_p\right]\mathbf{D} = \eta_{MR}\mathbf{D} \tag{4}$$

where m is a parameter controlling the quality of the approximation. Increasing this parameter makes Equation (4) better approximate (3), but also makes the equations stiffer and harder to solve, so a compromise has to be made. η_{MR} is the effective viscosity of MR fluid.

For better controllability, we construct the following flexible viscoplastic model in this study. Compared to the modified Bingham model (4), details such as the "stiction" phenomenon and the shear thinning/thickening effect are added.

$$\boldsymbol{\tau} = \frac{\tanh\left(k_{\mathrm{pre}}|\mathbf{D}|\right)\left(\boldsymbol{\tau}_{\mathrm{pre}} + \boldsymbol{\tau}_{\mathrm{pos}}\right)}{|\mathbf{D}|}\mathbf{D} = \eta_{\mathrm{MR}}\mathbf{D} \tag{5}$$

where $\boldsymbol{\tau}_{\mathrm{pre}} = \frac{1-\tanh\left[k_{\mathrm{pos}}\left(|\mathrm{D}|^2 - w^2\right)\right]}{2}\left(\boldsymbol{\tau}_{\mathrm{ys}} - \boldsymbol{\tau}_{\mathrm{yd}}\right)$, $\boldsymbol{\tau}_{\mathrm{pos}} = \boldsymbol{\tau}_{\mathrm{yd}} + k_{\mathrm{HB}}|\mathrm{D}|^{1/m_{\mathrm{HB}}}$, k_{pre}, k_{pos} and w are the dimensionless parameters controlling the pre-yield viscosity, post-yield viscosity and the "stiction" strain range width. $\boldsymbol{\tau}_{\mathrm{ys}}$ (Pa) and $\boldsymbol{\tau}_{\mathrm{yd}}$ (Pa) are the static (or critical) and dynamic yield stress strengths of MR fluids which are analogous to static and dynamic frictions in tribology. k_{HB} (Pa· s) and m are fluid parameters of the well-known Herschel-Bulkley model. A typical curve of the above model in one dimension is presented in **Figure S1**.

Weak Compressibility

A closure condition in the form of equation of state (EOS) has to be provided to complete the problem we want to solve. For compressible liquids, the Tait equation of state is widely used in many applications and hence employed in this study. It relates the pressure to the fluid density by (Koukouvinis et al., 2017)

$$p = B\left[\left(\frac{\rho}{\rho_0}\right)^n - 1\right] + p_0 \tag{6}$$

where B is the bulk modulus, ρ_0 is the reference density, p_0 is the reference pressure, and n is an exponent adjusting the stiffness of the fluid. Alternatively, the density can be expressed in terms of the pressure as

$$\rho = \left(1 + \frac{p - p_0}{B}\right)^{1/n}\rho_0 \tag{7}$$

Spatial Domains and Boundary Conditions

As shown in **Figure 2**, the whole spatial domain (Ω) is composed of the chamber domain (Ω_{C1},Ω_{C2}) and the working

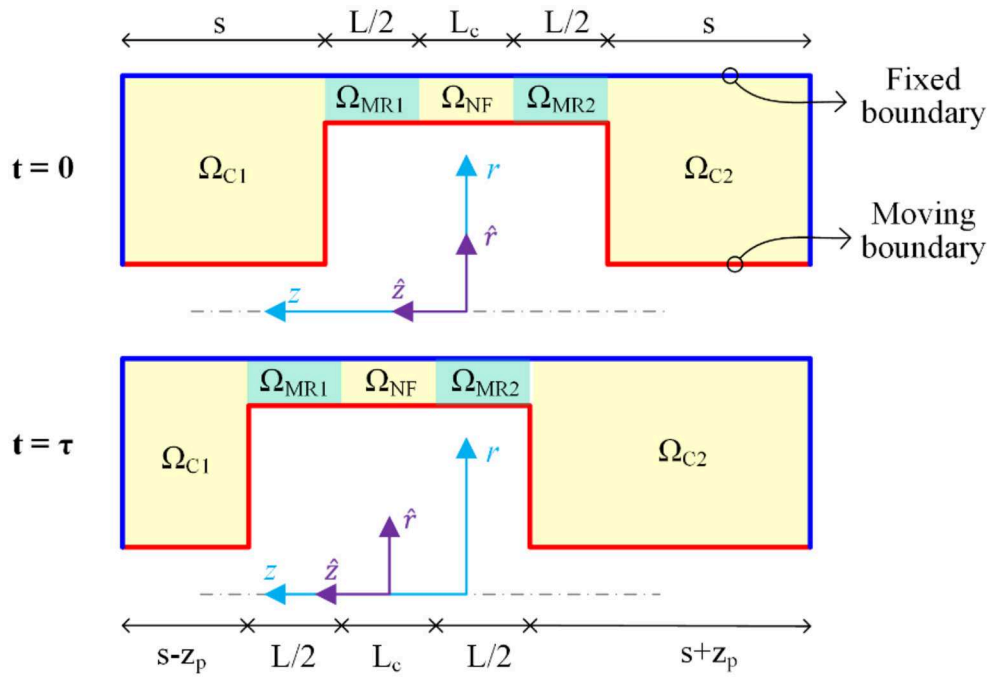

FIGURE 2 | Fluid domains and boundary condition.

gap domain (Ω_g) so that $\Omega = \Omega_{C1} \bigcup \Omega_g \bigcup \Omega_{C2}$, and $\Omega_{C1} \bigcap \Omega_g \bigcap \Omega_{C2} = \varnothing$.

The gap domain is further divided into the subdomain right above the electromagnetic coil where no magnetic flux passes through (Ω_{NF}) and the subdomains themselves being parts of the magnetic circuit (Ω_{MR1} and Ω_{MR2}). That is $\Omega_g = \Omega_{MR1} \bigcup \Omega_{NF} \bigcup \Omega_{MR2}$ and $\Omega_{MR1} \bigcap \Omega_{NF} \bigcap \Omega_{MR2} = \varnothing$.

The fluids in domains Ω_{C1}, Ω_{C2}, and Ω_{NF} are not exposed to the magnetic field, so they freely flow like the Newtonian fluid with constant viscosity η_p, while the fluids domains Ω_{MR1} and Ω_{MR2} behave like the Bingham fluid with a magnetic field dependent viscosity. Thus, these two types of fluids are distinguished from each other by their viscosities (η):

$$\eta = \begin{cases} \eta_p\,(r,z) & (r,z) \in \Omega_{C1}\ or\ \Omega_{C2}\ or\ \Omega_{NF} \\ \eta_{MR}\,(r,z) & (r,z) \in \Omega_{MR1}\ \text{or}\ \Omega_{MR2} \end{cases} \tag{8}$$

The fluid velocities at the inner wall of the house cylinder are set to zeros, and the fluid velocities at the surface of the piston are set to the piston velocity, as shown in **Figure 2**. Initially, the piston is located midway along the cylinder and the MR fluid is at rest.

Mesh Updating Equation

The fluid domain varies with time due to the piston movement. Mesh updating is necessary to track the moving boundaries as well as to avoid the severe distortions of elements. For simplicity, the mesh points are allowed to move only in the axial direction when taking account of the physical domain changes. The mesh motion on the gap domain is simply a rigid translation along the axial direction, i.e.,

$$z\left(\hat{z},t\right) = \hat{z} + z_p,\ \hat{z} \in \Omega_g \tag{9}$$

where $z_p = z_0 \sin\left(2\pi f t\right)$ is the piston displacement, z_0 is the amplitude, f is the excitation frequency.

A linear interpolation strategy is used to describe the motions of mesh nodes in the chambers, such that the displacements at the left and right piston ends ($\hat{z}_{L1} = -\left(L + L_c\right)/2$ and $\hat{z}_{R1} = \left(L + L_c\right)/2$ in **Figure 2**) is equal to the piston velocity and the displacements at the left and right fixed cylinder ends ($\hat{z}_{L0} = -\left(L + L_c + 2s\right)/2$, $\hat{z}_{R0} = \left(L + L_c + 2s\right)/2$ in **Figure 2**) are zeros. The mesh motions for the left (Ω_{C1}) and right chambers (Ω_{C2}) are

$$z\left(\hat{z},t\right) = \begin{cases} \left(\hat{z} + z_0 \sin\left(2\pi f t\right)\right) \frac{\hat{z}-\hat{z}_{L0}}{\hat{z}_{L1}-\hat{z}_{L0}} & \hat{z} \in \Omega_{C1} \\ \left(\hat{z} + z_0 \sin\left(2\pi f t\right)\right) \frac{\hat{z}-\hat{z}_{R0}}{\hat{z}_{R1}-\hat{z}_{R0}} & \hat{z} \in \Omega_{C2} \end{cases} \tag{10.a}$$

The mesh nodes are fixed in the radial direction, that is, their spatial positions of are kept unchanged

$$r\left(\hat{r},t\right) = \hat{r}, \hat{r} \in \Omega_{C1} \cup \Omega_{C2} \tag{11}$$

FINITE ELEMENT FORMULATIONS

Weak Forms

In order to apply the finite element method (FEM) to the problem, all of the above differential equations should be transformed into equivalent weak forms. This transformation can be formulated in different manners. Here, the Galerkin

method is applied to the continuity equation, while the consistent streamline upwind Petrov-Galerkin (SUPG) formulation is used for the momentum equation (Huerta and Liu, 1988). Triangular elements of continuous linear velocity and pressure are used for the spatial discretization of the integral equations.

The weak form of the continuity equation is obtained by multiplying the strong form (1) by the pressure test function δp and integrating over the current spatial domain (Ω):

$$\int_{\Omega} \delta p \left(\left. \frac{\partial \rho}{\partial t} \right|_{\chi} + \mathbf{c} \cdot \nabla \rho + \rho \nabla \cdot \mathbf{v} \right) d\Omega = 0 \tag{12}$$

Another equivalent weak form of continuity, which is expressed in terms of pressure, can be obtained by using Equation (7). Firstly, a straightforward differentiation gives the relationship between the material time derivatives of fluid density and pressure as

$$\dot{\rho} = \frac{\rho_0}{\beta} \dot{p} \tag{13}$$

where $\beta = Bn \left(1 + \frac{p - p_0}{B}\right)^{1-1/n}$.

Then making use of Equations (7, 13), the mass Equation (1) is rewritten as

$$\dot{p} + \beta \left(1 + \frac{p - p_0}{B}\right)^{1/n} \nabla \cdot \mathbf{v} = 0 \tag{14}$$

If $n = 1$, the above equation is reduced to the simpler form

$$\dot{p} + \left(B + p - p_0\right) \nabla \cdot \mathbf{v} = 0 \tag{15}$$

Furthermore, if only a perturbation of the incompressible state is of interest (i.e., the cases for which $\left|p - p_0\right| / B \ll 1$), the above equation is simplified to the more familiar form (Phelan et al., 1989)

$$\dot{p} + B \nabla \cdot \mathbf{v} = 0 \tag{16}$$

Finally, an alternative weak form of the continuity equation is obtained as

$$\int_{\Omega} \delta p \left[\left. \frac{\partial p}{\partial t} \right|_{\chi} + \mathbf{c} \cdot \nabla p + \beta \left(1 + \frac{p - p_0}{B}\right)^{1/n} \nabla \cdot \mathbf{v} \right] d\Omega = 0 \tag{17}$$

This equation will be used in the following development of finite element implementation.

In the SUPG method, the velocity test function, $\delta \tilde{\mathbf{v}}$, is the sum of two terms, i.e., $\delta \tilde{\mathbf{v}} = \delta \mathbf{v} + \delta \mathbf{v}^{\mathrm{pg}}$. The first term, $\delta \mathbf{v}$, is continuous within the elements and across their boundaries and the second term, $\delta \mathbf{v}^{\mathrm{pg}}$, is the discontinuous streamline contribution. Moreover, $\delta \mathbf{v}^{\mathrm{pg}}$ is given by (Belytschko et al., 2013)

$$\delta \mathbf{v}^{\mathrm{pg}} = \boldsymbol{\tau}_m \mathbf{c} \cdot \nabla \delta \mathbf{v} \tag{18}$$

where the stabilization parameter $\boldsymbol{\tau}_m$ is chosen to be (Tezduyar et al., 1992)

$$\boldsymbol{\tau}_m = \left[\left(\frac{2}{\Delta t}\right)^2 + \left(\frac{2\left|\mathbf{v}^h\right|}{h}\right)^2 + \left(\frac{4\upsilon}{h^2}\right)^2 \right]^{-1/2} \tag{19}$$

where t is the time-step size, $\left|\mathbf{v}^h\right| = \sqrt{\left(v_r^h\right)^2 + \left(v_z^h\right)^2}$ is the velocity norm, h is the element length and $\upsilon = \frac{\eta}{\rho}$ is the kinematic viscosity.

Multiplying Equation (2) by the velocity test function $\delta \tilde{\mathbf{v}}$ and then integrating over the current spatial domain yields the weak form of the momentum equation:

$$\begin{aligned} &\int_{\Omega} \delta \mathbf{v} \cdot \left(\rho \left. \frac{\partial \mathbf{v}}{\partial t} \right|_{\chi} + \rho \mathbf{c} \cdot \nabla \mathbf{v} - \nabla \cdot \boldsymbol{\sigma} \right) d\Omega \\ &+ \int_{\Omega} \delta \mathbf{v}^{\mathrm{pg}} \cdot \left(\rho \left. \frac{\partial \mathbf{v}}{\partial t} \right|_{\chi} + \rho \mathbf{c} \cdot \nabla \mathbf{v} - \nabla \cdot \boldsymbol{\sigma} \right) d\Omega = \mathbf{0} \end{aligned} \tag{20}$$

where $\delta \mathbf{v}$ vanishes on essential boundaries (where the flow velocity is imposed). The first term of the above equation is the standard Galerkin terms while the last term serves as a stabilization term.

Matrix Equations

The continuous element shape functions for the velocity and pressure at node "I" are, respectively, N_I, N_I^p.

Continuity Equation

The pressure and its test function are, respectively, approximated by

$$p = p_J(t) N_J^p \tag{21}$$

$$\delta p = \delta p_I(t) N_I^p \tag{22}$$

Then the spatial discretization of the weak form of the continuity equation, Equation (13), gives

$$\mathbf{M}^p \left. \frac{\partial \mathbf{p}}{\partial t} \right|_{\chi} + \mathbf{L}^p \mathbf{p} + \mathbf{G} \mathbf{v} = 0 \tag{23}$$

where the nodal pressure vector is

$$\mathbf{p} = \left[p_J\right] \tag{24}$$

and its ALE time derivative is

$$\left. \frac{\partial \mathbf{p}}{\partial t} \right|_{\chi} = \left[\left. \frac{\partial p_J}{\partial t} \right|_{\chi} \right] \tag{25}$$

the flow velocity vector is

$$\mathbf{v} = \left[v_{ij}\right] \tag{26}$$

the mass matrix is

$$\mathbf{M}^p = \sum_e \left[\int_{\Omega^e} N_I^p N_J^p d\Omega \right] \tag{27}$$

the matrix $\mathbf{L}^p$ is

$$\mathbf{L}^p = \sum_e \left[\int_{\Omega^e} N_I^p c_i N_{J,i}^p d\Omega \right] \tag{28}$$

the matrix $\mathbf{G}$ is

$$\mathbf{G} = \sum_e \left[\int_{\Omega^e} N_I^p \beta \left(1 + \frac{p - p_0}{B} \right)^{\frac{1}{n}} N_{J,i} d\Omega \right] \tag{29}$$

In the above notations used in the formulations of matrix equations, lowercase subscripts are used for components, and uppercase subscripts for nodal values. Square brackets denote matrix notation of tensors. The sum over elements is interpreted as the assembling of the element contributions.

Momentum Equation

The velocity is approximated by

$$v_i = v_{iJ} N_J \tag{30}$$

The velocity test function is discretized as

$$\delta \tilde{v}_i = \delta v_i + \delta v_i^{PG} \tag{31}$$

where $\delta v_i = \delta v_{iI} N_I$ and $\delta v_i^{PG} = \boldsymbol{\tau} c_j \delta v_{iI} N_{I,j}$, and it is equivalent to

$$\delta \tilde{v}_i = \delta v_{iI} \tilde{N}_I \tag{32}$$

where $\tilde{N}_I = N_I + \boldsymbol{\tau}\ c_j N_{I,j}$.

Substituting discretizations of velocity and its test function (Equations 30–32) into the weak form of momentum equation (Equation 20) yields

$$(\mathbf{M}+\mathbf{M}_{\text{stab}}) \left. \frac{\partial \mathbf{v}}{\partial t} \right|_{\chi} + (\mathbf{L}+\mathbf{L}_{\text{stab}})\, \mathbf{v} + \left(\mathbf{f}^{\text{int}}+\mathbf{f}_{\text{stab}}^{\text{int}}\right) = \left(\mathbf{f}^{\text{ext}}+\mathbf{f}_{\text{stab}}^{\text{ext}}\right) \tag{33}$$

where the material velocity vector is $\mathbf{v}$ and its ALE time derivative is

$$\left. \frac{\partial \mathbf{v}}{\partial t} \right|_{\chi} = \left[\left. \frac{\partial v_{iJ}}{\partial t} \right|_{\chi} \right] \tag{34}$$

the mass matrices are

$$\mathbf{M} = \sum_e \left[\int_{\Omega^e} \rho N_{I,j} N_J d\Omega \right] \tag{35}$$

$$\mathbf{M}_{\text{stab}} = \sum_e \left[\int_{\Omega^e} \rho \boldsymbol{\tau} c_j N_{I,j} N_J d\Omega \right] \tag{36}$$

the viscosity matrices are

$$\mathbf{L} = \sum_e \left[\int_{\Omega^e} N_I \rho c_j N_{J,j} d\Omega \right] \tag{37}$$

$$\mathbf{L}^{\text{stab}} = \sum_e \left[\int_{\Omega^e} \rho \boldsymbol{\tau} c_j N_{I,j} c_k N_{J,k} d\Omega \right] \tag{38}$$

the internal force matrices are

$$\mathbf{f}^{\text{int}} = -\sum_e \left[\int_{\Omega^e} N_I \boldsymbol{\sigma}_{ji,j} d\Omega \right] \tag{39}$$

$$\mathbf{f}_{\text{stab}}^{\text{int}} = -\sum_e \left[\int_{\Omega^e} \boldsymbol{\tau} c_j N_{I,j} \boldsymbol{\sigma}_{ki,k} d\Omega \right] \tag{40}$$

the external force matrices are

$$\mathbf{f}^{\text{ext}} = \sum_e \left[\int_{\Omega^e} N_I \rho b_i d\Omega \right] \tag{41}$$

$$\mathbf{f}_{\text{stab}}^{\text{ext}} = \sum_e \left[\int_{\Omega^e} \boldsymbol{\tau} c_j N_{I,j} \rho b_i d\Omega \right] \tag{42}$$

Finally, the velocity and pressure fields are obtained by numerically solving these non-linear ordinary differential equations. Then the damping force of the MR damper, F_L, can be calculated by integrating the total stress along the moving piston boundary in **Figure 2**

$$F_L = \int_{R_r}^{R_p} \boldsymbol{\sigma} \cdot \hat{\mathbf{n}}_z d\hat{\Gamma} \tag{43}$$

where $d\hat{\Gamma}$ is the differential line element of the piston surface with the outward unit normal vector $\hat{\mathbf{n}}_z$ in the z-direction. In addition to the force that fluid acts on the piston, the measured forces include the inertial force of the piston, so the final damping force should be calculated as

$$F = F_L + F_m \tag{44}$$

where the inertial force is $F_m = m_p a_p$, m_p is the total mass of the piston and connectors, a_p is the acceleration of the piston.

Implementations of Weak Form PDEs in a General FEM Program

The above SUPG based FEM model was implemented in the general-purpose FEM program software Comsol Multiphysics (Version, 5.0a) which provides an efficient computational platform to solve various types of PDEs (COMSOL Inc., 2014). Three weak-form PDE modules were used, respectively, for the continuity equation (variable: pressure), momentum equation (variables: flow velocities), and the constitutive equation (variables: viscous stress). Heavy use was made of Comsol's scalar expressions (for example, expressions for the total stress components) in order to keep the whole model organized. The built-in for element length allows the stabilization terms to be implemented easily.

TABLE 1 | Main design parameters of MR damper and material properties of MR fluid.

Structural parameter	Value
Gap width (g)	1.5 mm
Piston radius (R_p)	38.5 mm
Effective length (L)	54 mm
Stroke (s_0)	58 mm
Number of coils	1
Piston (& connector) mass (m_p)	6 kg
Shaft radius (R_r)	15 mm
Winding length (L_c)	50 mm
Density of MR fluid (ρ_0)	1,500 kg/m^3
Yield strength of MR fluid (input current, 0.5 A) (τ_{ys})	6,500 Pa
Viscosity of magnetically activated MR fluid (k_{HB})	12 Pa·s
Viscosity of inactivated MR fluid (η_p)	0.22 Pa·s
Modulus of MR fluid (B)	3×10^8 Pa
Shear thinning/thickening index (m_{HB})	1.7
Pre-yield viscosity controlling parameter (k_{pre})	5×10^{-2}
Post-yield viscosity controlling parameter (k_{pos})	5×10^{-6}
Stiction strain range (w)	10

Owing to the strong nonlinearity of the problem, small time steps and tight absolute solver tolerances (10^{-5} for the flow velocities, 10^{-3} for the pressure and viscous stresses) were adopted. The implicit the backward differentiation formula (BDF) solver with the second order of accuracy was used to discretize model PDEs in time. The resulted system of nonlinear algebraic equations was solved using the Newton-Raphson algorithm. We then took advantage of the efficient built-in direct solver "MUMPS" solver (MUltifrontal Massively Parallel Sparse direct Solver) to solve the system of linear equations. The calculation of the damping force in Equation (43) was implemented in Comsol as a boundary coupling operator.

PARAMETRIC STUDY ON INERTIAL-VISCOUS-FRICTIONAL-ELASTIC TRANSIENTS

In this section, we take an overall picture of the coupled inertial-viscous-frictional-elastic transients, by conducting a parametric analysis for an MR damper which will be experimentally study later. The structural parameters of this damper and the material properties of the MR fluid are shown in **Table 1**. The damper will be excited by a medium-frequency sinusoidal displacement (8 mm, 10 Hz), and the low- and high- frequency loading cases will be included in later sections. For each parametric analysis, only one dominant parameter is changed by three levels while keeping the other parameters fixed.

The inertial effect becomes more significant with larger fluid densities. When increasing the fluid density, larger fluctuations in the damping force appear when the damper enters the post-yield zone, as shown in **Figure 3**. Meanwhile, the displacement-force loop in **Figure 3A** rotates clockwise. It is reasonable to expect that under a frequency excitation frequency these inertia related effects will be further enhanced, and this will be seen in later sections.

When increasing the viscosity (k_{HB}), the damping force increases apparently and the shape of the displacement-force loop becomes more elliptic, as shown in **Figure 4**.

Figure 5 shows the "frictional" effect which is perhaps the most salient feature of MR dampers. The damping force is strongly in proportion to the shear yield strength of MR fluids which can be continuously adjusted by controlling the input currents.

The elastic effect due to the compressibility of MR fluids, which has been neglected in most previous computational fluid studies on MR dampers, however, has a great impact on the performance of an MR damper.

Because of the compressibility of MR fluid, the damping force cannot change instantly but gradually varies when the piston reversing its direction as shown in **Figure 6A**, and this leads to an obvious velocity-force hysteresis loop in the pre-yield region as shown in **Figure 6B**.

EXPERIMENT

After having a basic overview of coupled inertial-viscous-frictional-elastic transients in MR dampers, an experimental study will be performed to validate the FEM model. The performance of an MR damper (Zhixing S & T Ltd., Jiangsu, China) was tested on a hydraulic universal testing machine, with the experimental test setup shown in **Figure 7**. The main design parameters of the damper were listed in **Table 1**, and the material properties of MR fluids are also shown in **Table 1**.

A DC current source was used to apply electric currents to the damper. The damping forces were tested under the low-, medium and high- frequency sinusoidal displacement excitations: 40 mm/2 Hz, 8 mm/10 Hz, 5 mm/20 Hz. To ensure that the dissipation heating is not too high, the temperatures at typical positions was measured by thermocouples connected to a data acquisition system.

For confirming the applied input currents, a digital multimeter was used to monitor in real time the input currents. It was found that the temperature nearly remained unchanged due to the short testing time, and that the DC current source output was accurate. Supplied by the manufacture (Zhixing S & T Ltd., Jiangsu, China), the shear yield strength at typical input currents of 0.5 and 1 A are, respectively, 6,500 and 13,000 Pa. According to previous work by Guo et al. (2014), the equivalent shear yield strength without input current can be calculated from the frictional force (483 N) as 17,000 Pa.

MESH SENSITIVITY EXAMINATION

Before validating the FEM model by using the experimental data, it is necessary to study the effect of mesh dependency of the model results. Three refinement levels, i.e., coarse,

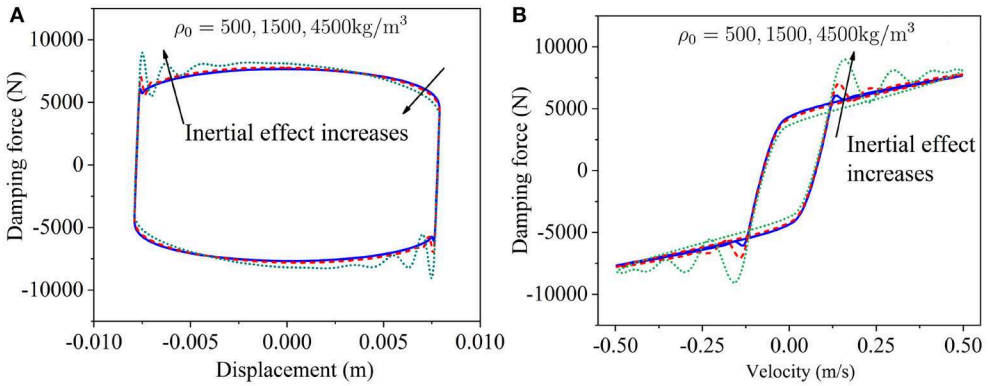

FIGURE 3 | The inertial effect in MR dampers. **(A)** Displacement-force loop. **(B)** Velocity-force loop.

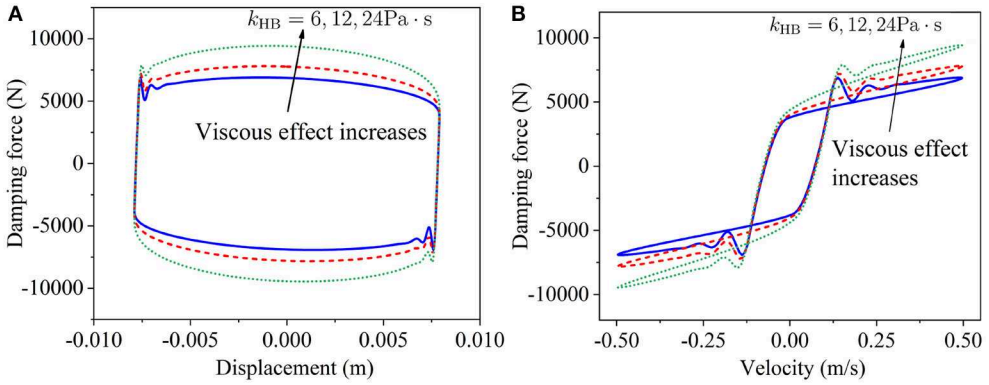

FIGURE 4 | The viscous effect in MR dampers. **(A)** Displacement-force loop. **(B)** Velocity-force loop.

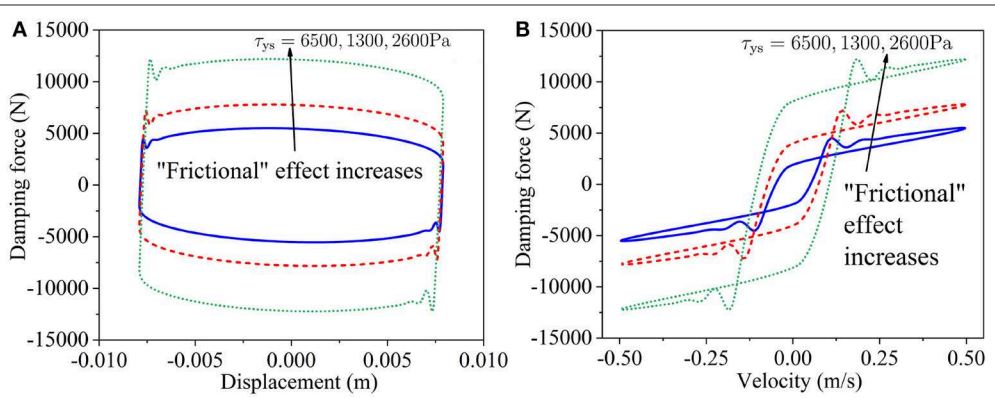

FIGURE 5 | The "frictional" effect in MR dampers. **(A)** Displacement-force loop. **(B)** Velocity-force loop.

normal, and fine meshes with 5,473, 13,075, and 26,734 degrees of freedom (DOFs), respectively (**Figure S2**), were used to simulate the performance of the MR damper under the medium-frequency sinusoidal displacement excitation. As shown in **Figure S3**, the difference between the model results is negligible (in terms of either displacement-force or velocity-force loop), and we will choose the normal mesh in the following validation of the model. It is worth pointing out that about 2 days were used to solve the model with the fine mesh on a personal computer (i7 CPU, 8G RAM), while

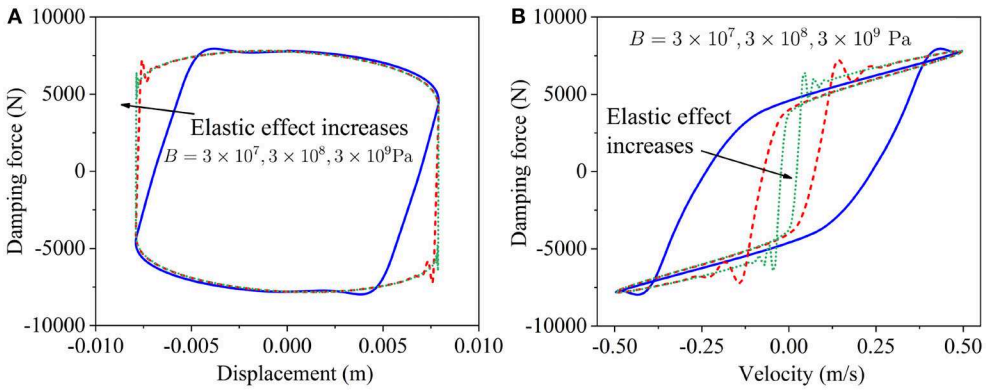

FIGURE 6 | Elastic effect in MR dampers. **(A)** Displacement-force loop. **(B)** Velocity-force loop.

the models with the coarse and normal meshes only took several hours.

VALIDATION OF THE FEM MODEL

The performance of the tested MR damper in previous section is simulated in this section. As shown in **Figures 8–10**, the overall agreement is good between the model predictions and the experimental data.

The hysteretic behavior of MR dampers, either in terms of the force-displacement or the force-velocity, is frequency dependent. With increasing excitation frequency, the force-displacement loop rotates because of the larger inertial effect. The damping force oscillates more violently under the high frequency excitation. With increasing excitation frequency, the force-velocity loop in the pre-yield grows fatter and the loop in the post-yield is no longer ignorable. It is interesting to note that force oscillation is observed when the MR damper switches from the pre-yield region to the post-yield region, and it is very similar to the classical step response for a mas-spring-damper second order system. Although similar results were achieved in the previous studies on lumped parameter modeling of MR dampers (Nguyen and Choi, 2009; Gołdasz and Sapinski, 2013), few attempts have been made to explain such step-response-like force variation. Detailed explanation well be made later in this study in terms of mass the flow rates.

The discrepancy between the experimental and calculated results, which becomes more apparent under high frequency-excitations, is still not clear and worth further studying in future works. However, we believe that a more realistic modeling the compressibility of MR fluid should enhance the accuracy of the FEM model.

DISCUSSION AND FUTURE WORKS

Flow Field Within Damper

The FEM model makes it possible to have a clear picture of the flow of MR fluid in an MR damper. As shown in **Figure 11**, the flow velocity magnitude during one complete high-frequency excitation cycle is presented at typical time instants (0, $T/4$, $2T/4$, $3T/4$, T; $T = 0.05s$ is the excitation period).

The high-speed flow of MR fluid mainly happens in the working gap as expected. The mean velocities throughout the gap [including both unenergized zone (Ω_{NF}) and the energized zones (Ω_{MR1} and Ω_{MR2})] should be roughly equal, in order to satisfy continuity. However, in the energized section, due to the yield stress, the velocity profile is more plug-like, i.e., flatter and this can be seen clearly in **Figure S4**.

The velocity profile in the unenergized sections is more pointed. Therefore, in the unenergized section, the maximum velocity is higher, but in the energized sections the velocity is closer to the piston velocity. The overall flow rates should be roughly equal in both energized and unenergized sections. When the piston reversing its direction (t =T/4, 3T/4), a large vortex is observed near the gap end, and the fluid elsewhere moves slowly in the chamber.

Mass Flow Rate

The mass flow rate in the working gap directly determines the damping force of an MR damper. In the following, let's examine the mass flow rates under different frequency loadings. The normalized flow rates at three key locations as shown in **Figure 12**, i.e., the left piston end (Q_P), the left (Q_L) and right (Q_R) working gap ends, are computed using boundary integral operators and then compared in **Figure 13A**.

Near the maximum displacement, the flow rates at the left and right piston ends (Q_L and right Q_R) are negligibly different (as shown in **Figures 13B,C**), but they are apparently distinguishable from the flow rate at the piston end (Q_P). This implies that the compression of MR fluid mainly happens in the chambers rather than in the working gap.

As in the history of damping force (**Figures 11–13**), the similar step-response like oscillations are also observed in the mass flow rate as shown in **Figure 13A**. To reveal such oscillations, let's take a close view on the process when the piston changing its direction (yellow highlight zone in **Figure 13A**). For

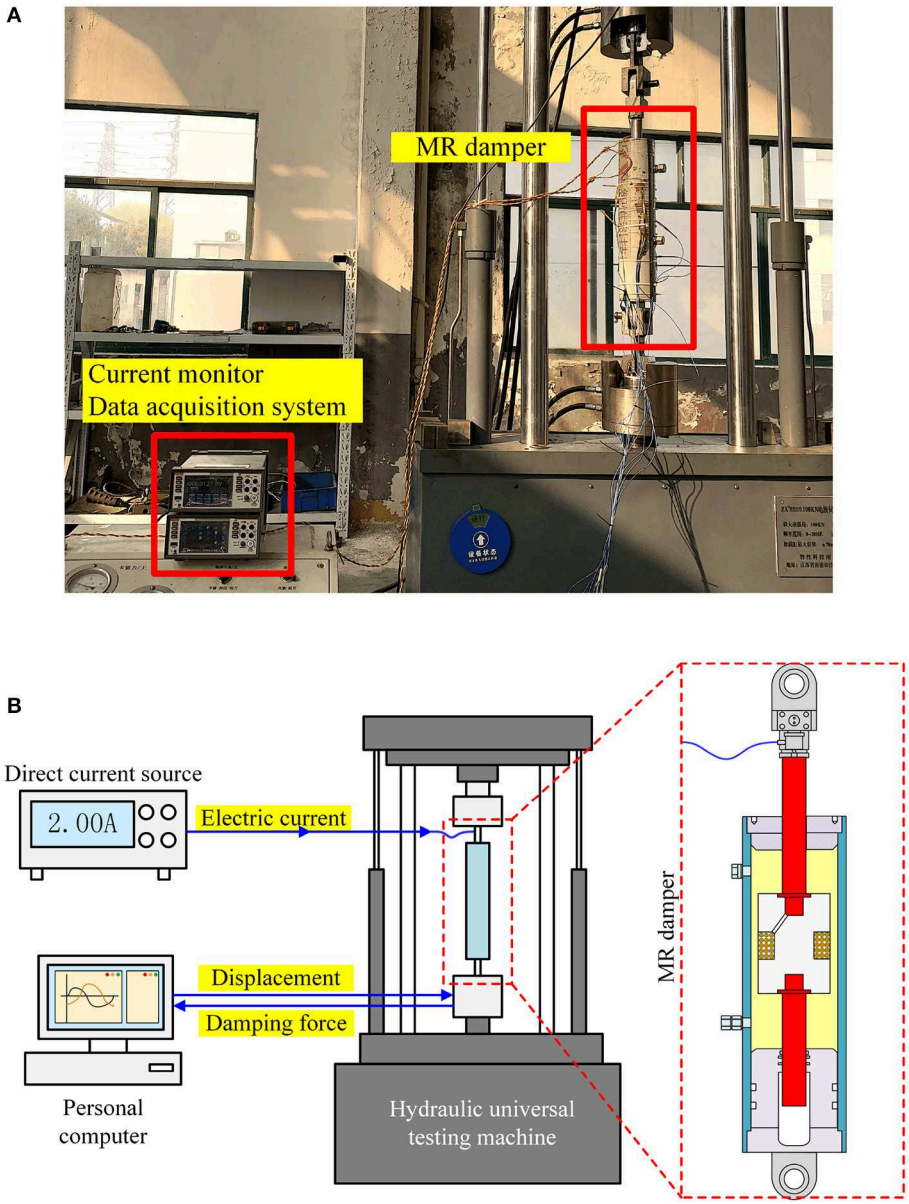

FIGURE 7 | Experimental setup. **(A)** Picture of the experimental setup. **(B)** Schematic diagram of experiment.

simplicity, we will focus the fluids in the pressurized chamber and the working gap. Several key points ($P_1 \sim P_4$) in **Figure 13B**) split this process into different periods as below.

(1) $P_1 \sim P_2$ period: In this period, the MR damper works in the pre-yield zone. After changing its direction (at P_1 moment), the piston moves slowly and the fluid in the working gap is almost locked due to the large pre-yield viscosity (or the friction effect). Meanwhile, the fluid in the pressurized chamber is constantly being compressed and the pressure inside increases with the piston movement. This process continues up to P_2 moment when the accumulated pressure in the chamber become large enough to balance the friction force in the working gap. The nonzero flow rate in this (pre-yield) period is because we have used in our FEM model a very large but finite pre-yield viscosity instead of an infinitely large one as in the ideal Herschel-Bulkley model, and the fluid can flow very slowly even in the pre-yield zone.

(2) P_2-P_3 period: After P_2 moment, the damper enters the post-yield zone. Because the post-yield viscosity is several orders lower than the pre-yield viscosity, the fluid in the working gap finally can move much more freely from now on. Under the thrust of the large chamber pressure accumulated in the $P_1 \sim P_2$ period, the fluid in the working gap suddenly

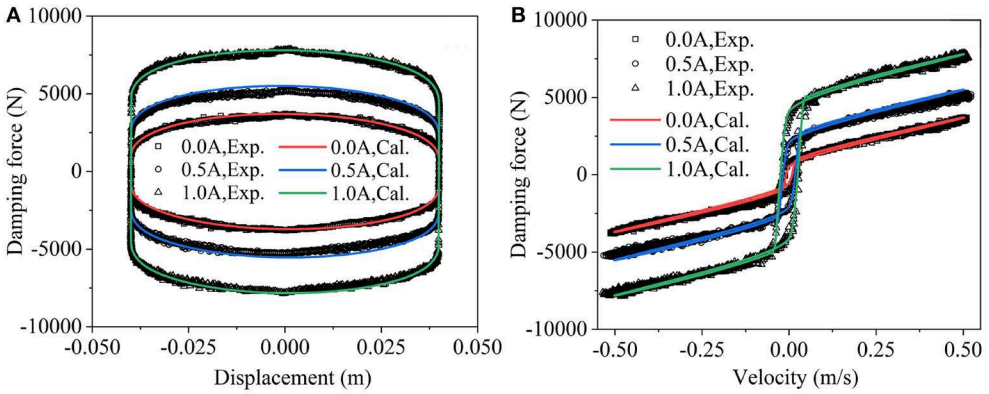

FIGURE 8 | Performance of MR damper under low-frequency excitations (40 mm/^{2} Hz, symbols: experimental data; lines: FEM predictions). **(A)** Displacement-force loop. **(B)** Velocity-force loop.

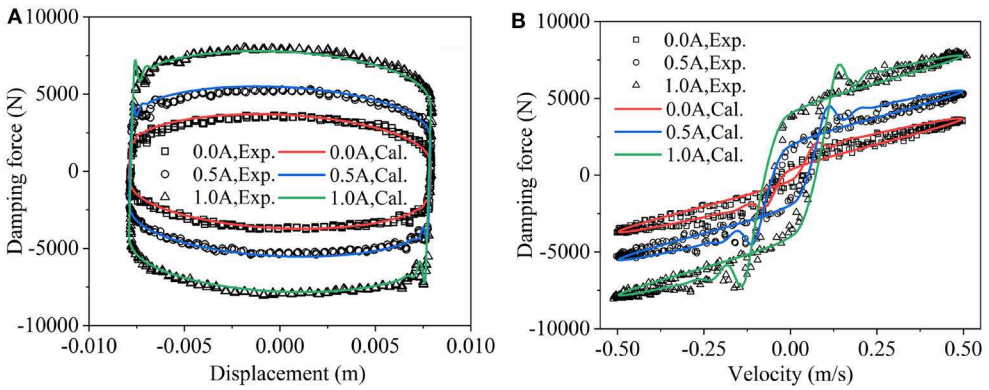

FIGURE 9 | Performance of MR damper under medium-frequency excitations (8 mm/10 Hz, symbols: experimental data; lines: FEM predictions). **(A)** Displacement-force loop. **(B)** Velocity-force loop.

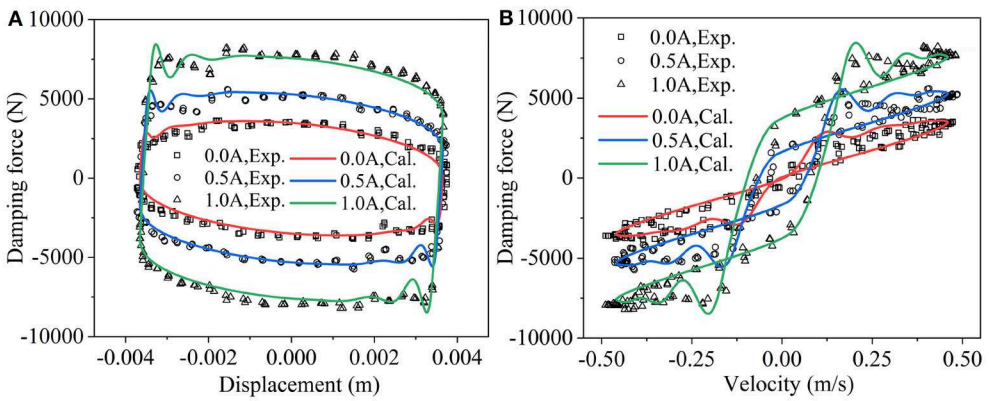

FIGURE 10 | Performance of MR damper under high-frequency excitations (4 mm/20 Hz, symbols: experimental data; lines: FEM predictions). **(A)** Displacement-force loop. **(B)** Velocity-force loop.

flows "freely" at a large acceleration. At this time instant, the inertial effect becomes dominant, as evidenced by the peak in the flow rate (Point P_3 in **Figure 13B**) or the overshoot in the damping force.

(3) P_3-P_4 period: Much like the case of a small extending instantly applied to a pre-compressed spring, when the fluid in the chamber suddenly starts to flow outward, the pressure inside drops slightly, and the

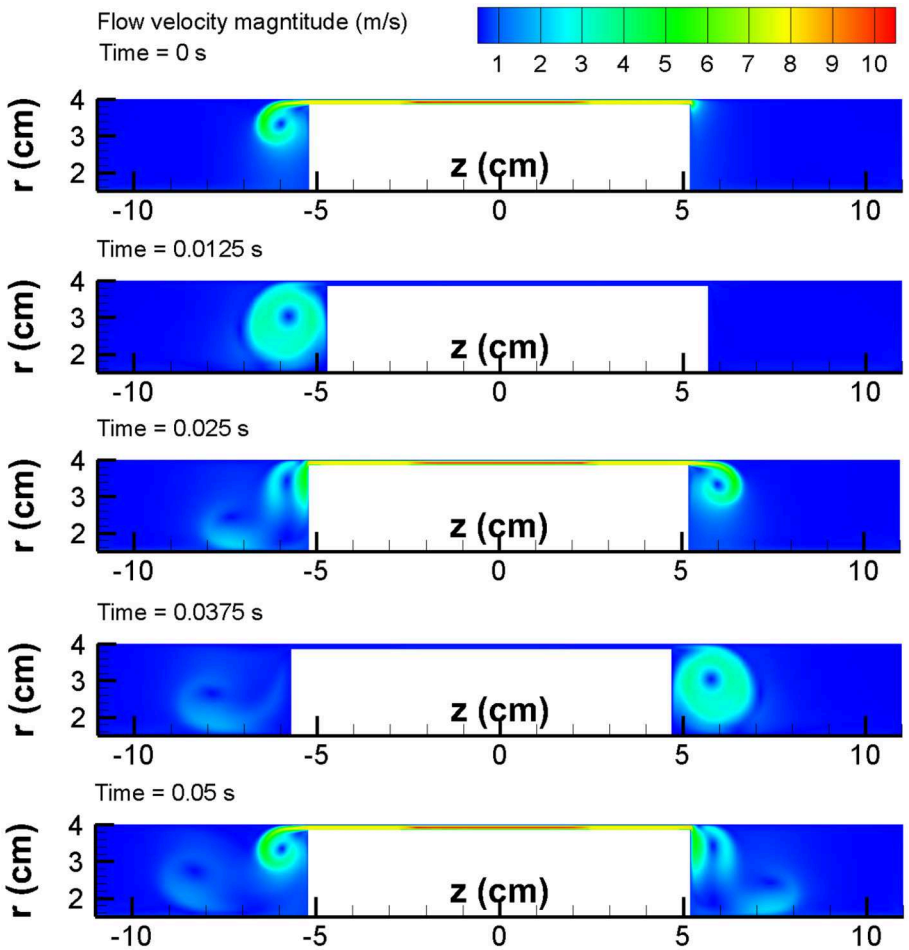

FIGURE 11 | Snapshots of the flow field (Sinusoidal displacement excitation: 8 mm/10 Hz, 0.5 A).

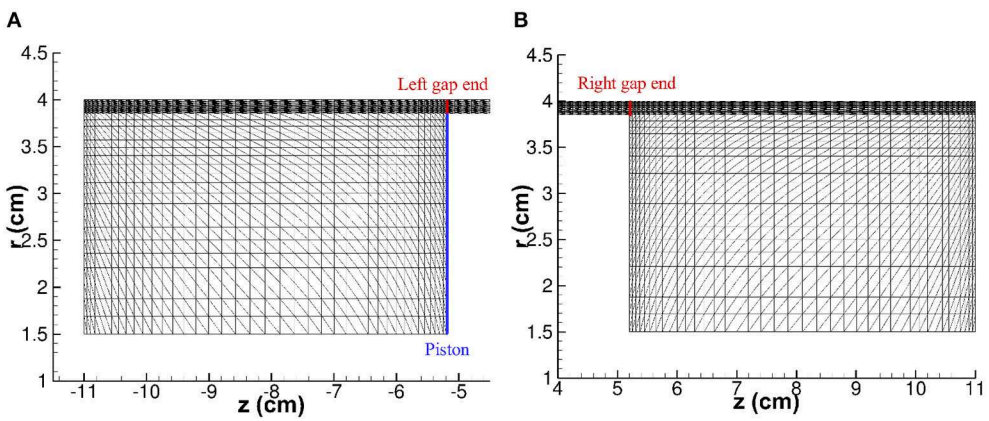

FIGURE 12 | Key locations [left piston end (Q_P), left (Q_L), and right (Q_R) gap ends] where mass flow rates will be calculated and compared. **(A)** Left piston end and left gap end. **(B)** Right gap end.

flow rate in the working gap as well as the damping force decreases accordingly. Consequently, a small undershoot (P4 in figure) appears for the first time in the post-yield zone.

(4) From P_4 to the next piston reversing moment: After the damper enters the post-yield zone, it becomes hard for the piston to squeeze the chamber fluid as it does in the pre-yield zone. Conceptually, just like it is difficult

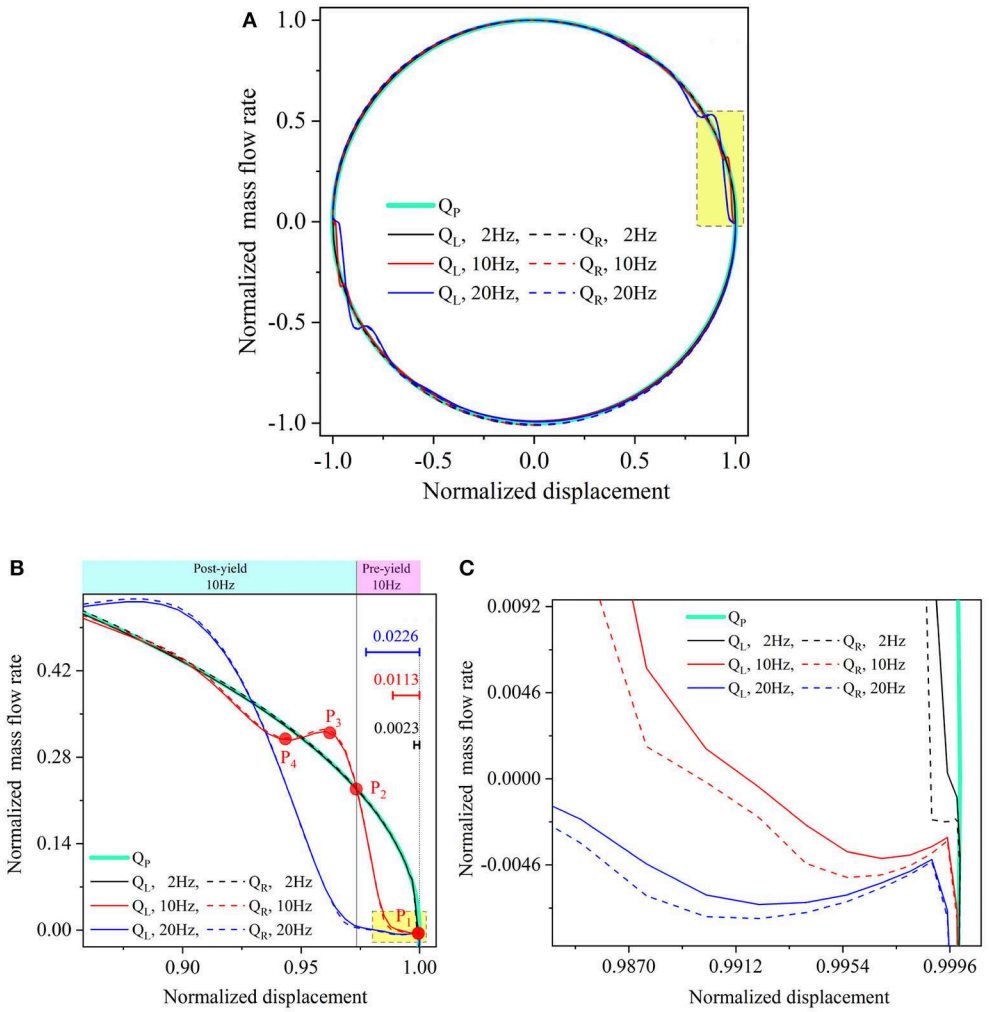

FIGURE 13 | Normalized mass flow rate against normalized piston displacement (0.5 A). **(A)** Normalized displacement-mass flow rate loop. **(B)** Details on yellow highlight zone in **(A,C)**. Details on yellow highlight zone in **(B)**.

to compress a spring at an end when the other end can move. The increase in the damping force mainly is contributed by the increase in the piston velocity which leads to an increasing viscous damping force (due to the viscous effect).

If we look very closely at the mass flow rates at the two ends of the working gap, we can find small difference between them as shown in **Figure 13C**). Such difference results from the compressibility of MR fluid in the working gap, and it is expected to become larger with the increasing volume of the gap.

Keeping in our mind the above picture of transition of MR fluid from the pre-yield to the post-yield zone, we can actually give a reasonable estimation on the amount of the fluid compression during the pre-yield period. According to the simple Bingham fluid model, the chamber pressure (p_y) at the yield moment (P_2 in **Figure 13B**) can be approximated by

$$p_y = 2\,\tau_y \frac{L}{g} \tag{45}$$

Under this pressure, the piston displacement variation (or the fluid compression along the axial direction of the damper), Δz, can then be calculated from

$$p_y = B\frac{dV}{V} = B\frac{\Delta z\, A}{(s_0 - \Delta z)\ A} = B\frac{\Delta z}{s_0 - \Delta z} \tag{46}$$

Where the distance of the piston away from its maximum displacement position $\Delta z = z_0 \sin\left(2\pi f t\right) - z_0 \sin\left(2\pi f \frac{T}{4}\right), \frac{T}{4} < t < \frac{T}{2}$. The meanings and values of other variables in equations (45) and (46) can be found in **Table 1**.

The normalized compression $\left(\frac{\Delta z}{z_0}\right)$ obtained using the Equations (45, 46) are presented in **Figure 13B**, and they can be used as reasonable approximations of the total fluid compression accumulated in the pre-yield zone. Moreover, the piston velocity at the yield point can also be estimated by using Equations (45, 46), and they indeed offer a good estimation on the width of the pre-yield zone (about twice the piston velocity at the yield

point), as shown in **Figure 14**. In other words, the frictional effect and the elastic effect of MR fluid together dominate the pre-yield hysteretic behavior of MR dampers. If a small pre-yield loop is desired, the chamber volume should be as small as possible and a MR damper should work under a low input excitation current.

Compared to the previous CFD modeling studies of MR dampers, the main contribution of this study includes two aspects: (a) the compressibility of MR fluids, which has been neglected in previous studies, is proven to be essential for accurate predictions of hysteretic behavior of MR dampers; (b) the mechanism behind the step-response-like force oscillation of an MR damper, which has been rarely reported in previous researches, is explained in detail in this study.

It is interesting to note that the hysteretic behavior of an MR damper can be described either by an incompressible viscoelastic fluid as shown in recent studies or by a compressible viscoplastic fluid as demonstrated in this work. Thus, the combination of these two constitutive models, that is, a compressible viscous-elastic-plastic fluid model, is believed to predict the hysteretic behavior of MR dampers more accurately, and this will be investigated in our future works.

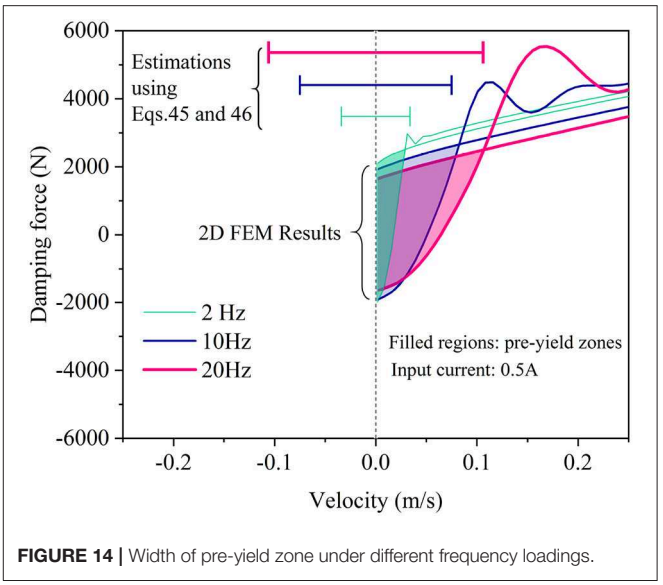

FIGURE 14 | Width of pre-yield zone under different frequency loadings.

CONCLUSION

In this paper, the coupled inertial-viscous-frictional-elastic transients in MR dampers was investigated using finite element simulation and experimental validation under low-, medium-, and high- frequency sinusoidal displacement excitations and different input electric currents. The main concluding points are as follows:

(1) Representing the piston movements by the moving boundaries, the ALE form of the conservation laws offers a natural way to describe the fluid flow in MR dampers. The flow problem in MR dampers can be effectively solved by the SUPG based FEM method and the solution exhibits little mesh-size sensitivity.

(2) The weak compressibility of MR fluids is crucial to accurately predict and understand the dynamic performances of MR dampers. It should not be ignored, as in most previous studies on modeling of MR devices. The compression of fluids mainly happens in the pressurized chamber instead of the working gap, and it can be reasonably estimated on the basis of the shear yield strength and bulk modulus of MR fluid.

(3) The mechanical model of MR dampers is essentially a second order mass-spring-viscous (friction) model. The widely used Bouc-Wen model is intrinsically deficient for accurate predictions, because it is only a first order system. In the second order system of MR dampers, the fluid density reflects the inertial effect, as indicated by the fatness of the hysteretic loop in the post-yield zone. The post-yield viscosity controls the proportion between the damping force and the piston velocity in the post-yield zone. The shear yield strength gives rise to the fictional effect and governs the magnitude of damping force in the post-yield zone. The compressibility of fluids, playing the role of a spring, is responsible for both the hysteretic loop in the pre-yield zone and the force fluctuations in the poste yield zone.

(4) The ratio of shear yield strength to the bulk modulus (τ_y/B) determines the boundary between the pre- and post-yield zones. When a MR damper crosses this boundary, a step response is observed as in a second order mass-spring-viscous system model, and it can be explained in terms of mass flow rate.

(5) The hysteretic behavior of MR dampers shows a strong dependence on the excitation frequency. With the same maximum piston velocity, both pre-yield and post-yield hysteric loops grow apparently fatter with increasing sinusoidal excitation frequency. Moreover, the damping force oscillation becomes more violent under higher frequency excitations and it becomes significant under low input currents.

To the best of our knowledge, this is the first compressible fluid based 2D flow simulation and experimental validation of coupled inertial-viscous-frictional-elastic transients in MR dampers, and it can be a valuable aid in research on general MR devices.

DATA AVAILABILITY STATEMENT

The datasets generated for this study are available on request to the corresponding author.

AUTHOR CONTRIBUTIONS

PG fully controls and performs the FEM modeling, and scientific writings. JX designs experiments and data processing. YH performs the parameter modeling of MR damper

under random displacement excitation. XD guides the whole logic of this study, from modeling to experiments and to writing.

FUNDING

This research was supported by National Natural Science Foundation of China (No. 51308450), Research Foundation of Xi'an University of Architecture and Technology (No. RC1368), National Key R&D Program of China (2018YFC0705603), and Jiangxi Province Science Foundation for Youths (No. 20171BAB216041).

SUPPLEMENTARY MATERIAL

The Supplementary Material for this article can be found online at: https://www.frontiersin.org/articles/10.3389/fmats.2019.00293/full#supplementary-material

REFERENCES

Alghamdi, A. A., Lostado, R., and Olabi, A.-G. (2014). "Magneto-rheological fluid technology," in *Modern Mechanical Engineering*, ed D. J. Paulo (Berlin; Heidelberg: Springer), 43–62. doi: 10.1007/978-3-642-45176-8_3

Bazilevs, Y., Takizawa, K., and Tezduyar, T. E. (2013). *Computational Fluid-Structure Interaction: Methods and Applications*. John Wiley & Sons. doi: 10.1002/9781118483565

Belytschko, T., Liu, W. K., Moran, B., and Elkhodary, K. (2013). *Nonlinear Finite Elements for Continua and Structures*. John Wiley & Sons.

Carlson, J. D., Catanzarite, D., and St. Clair, K. (1996). Commercial magneto-rheological fluid devices. *Int. J. Mod. Phys. B* 10, 2857–2865. doi: 10.1142/S0217979296001306

Case, D., Taheri, B., and Richer, E. (2016). Multiphysics modeling of magnetorheological dampers. *Int. J. Multiphys*. 7, 61–76. doi: 10.1260/1750-9548.7.1.61

Chen, P., Bai, X.-X., Qian, L.-J., and Choi, S. B. (2018). An approach for hysteresis modeling based on shape function and memory mechanism. *IEEE/ASME Trans. Mech*. 23, 1270–1278. doi: 10.1109/TMECH.2018.2833459

COMSOL Inc. (2014). *Comsol Multiphysics User's Manual Ver. 5.0a*.

Frigaard, I., and Nouar, C. (2005). On the usage of viscosity regularisation methods for visco-plastic fluid flow computation. *J. Nonnewton. Fluid Mech.* 127, 1–26. doi: 10.1016/j.jnnfm.2005.01.003

Gołdasz, J., and Sapinski, B. (2013). Verification of magnetorheological shock absorber models with various piston configurations. *J. Intell. Mater. Syst. Struct.* 24, 1846–1864. doi: 10.1177/1045389X13479684

Gołdasz, J., and Sapinski, B. (2015). Application of CFD to modeling of squeeze mode magnetorheological dampers. *Acta Mech. Autom.* 9, 129–134. doi: 10.1515/ama-2015-0021

Guo, P., Guan, X., and Ou, J. (2014). Physical modeling and design method of the hysteretic behavior of magnetorheological dampers. *J. Intell. Mater. Syst. Struct.* 25, 680–696. doi: 10.1177/1045389X13500576

Guo, P., and Xie, J. (2019). Two-dimensional CFD modeling of hysteresis behavior of MR dampers. *Shock Vib*. 2019:9383047. doi: 10.1155/2019/9383047

Huerta, A., and Liu, W. K. (1988). Viscous flow with large free surface motion. *Comput. Methods Appl. Mech. Eng.* 69, 277–324. doi: 10.1016/0045-7825(88)90044-8

Jolly, M. R., Bender, J. W., and Carlson, J. D. (1999). Properties and applications of commercial magnetorheological fluids. *J. Intell. Mater. Syst. Struct.* 10, 5–13. doi: 10.1177/1045389X9901000102

Koukouvinis, P., Mitroglou, N., Gavaises, M., and Lorenzi, M. (2017). Quantitative predictions of cavitation presence and erosion-prone locations in a high-pressure cavitation test rig. *J. Fluid Mech.* 819, 21–57. doi: 10.1017/jfm.2017.156

Nguyen, Q.-H., and Choi, S.-B. (2009). A new approach for dynamic modeling of an electrorheological damper using a lumped parameter method. *Smart Mater. Struct*. 18:115020. doi: 10.1088/0964-1726/18/11/115020

Papanastasiou, T. C. (1987). Flows of materials with yield. *J. Rheol.* 31, 385–404. doi: 10.1122/1.549926

Phelan, F. Jr., Malone, M., and Winter, H. (1989). A purely hyperbolic model for unsteady viscoelastic flow. *J. Nonnewton. Fluid Mech.* 32, 197–224. doi: 10.1016/0377-0257(89)85036-0

Sahin, H., Wang, X., and Gordaninejad, F. (2013). Magneto-rheological fluid flow through complex valve geometries. *Int. J. Vehicle Des.* 63, 241–255. doi: 10.1504/IJVD.2013.056154

Sahin, I., Engin, T., and Çeşmeci, S. (2010). Comparison of some existing parametric models for magnetorheological fluid dampers. *Smart Mater. Struct*. 19:035012. doi: 10.1088/0964-1726/19/3/035012

Sternberg, A., Zemp, R., and De La Llera, J. C. (2014). Multiphysics behavior of a magneto-rheological damper and experimental validation. *Eng. Struct*. 69, 194–205. doi: 10.1016/j.engstruct.2014.03.016

Syrakos, A., Dimakopoulos, Y., Georgiou, G. C., and Tsamopoulos, J. (2016). Viscoplastic flow in an extrusion damper. *J. Nonnewton. Fluid Mech.* 232, 102–124. doi: 10.1016/j.jnnfm.2016.02.011

Syrakos, A., Dimakopoulos, Y., and Tsamopoulos, J. (2018). Theoretical study of the flow in a fluid damper containing high viscosity silicone oil: Effects of shear-thinning and viscoelasticity. *Phys. Fluids* 30:030708. doi: 10.1063/1.5011755

Tezduyar, T. E., Mittal, S., Ray, S. E., and Shih, R. (1992). Incompressible flow computations with stabilized bilinear and linear equal-order-interpolation velocity-pressure elements. *Comput. Methods Appl. Mech. Eng.* 95, 221–242. doi: 10.1016/0045-7825(92)90141-6

Ursescu, A. (2005). *Channel Flow of Electrorheological Fluids Under an Inhomogeneous Electric Field*. Berlin: Technische Universität.

Wang, D., and Liao, W. H. (2011). Magnetorheological fluid dampers: a review of parametric modelling. *Smart Mater. Struct*. 20:023001. doi: 10.1088/0964-1726/20/2/023001

Yu, J., Dong, X., and Zhang, Z. (2017). A novel model of magnetorheological damper with hysteresis division. *Smart Mater. Struct*. 26:105042. doi: 10.1088/1361-665X/aa87d6

Zheng, J., Yancheng, L., Zhaochun, L., and Jiong, W. (2015). Transient multi-physics analysis of a magnetorheological shock absorber with the inverse Jiles–Atherton hysteresis model. *Smart Mater. Struct*. 24:105024. doi: 10.1088/0964-1726/24/10/105024

Zhou, H., and Bai, M. (2014). Three-dimensional numerical simulation of magnetorheological fluid seal technology applied on circular cooler and its experimental validation. *Mech. Adv. Mater. Struct*. 21, 329–340. doi: 10.1080/15376494.2013.815832

Conflict of Interest: The authors declare that the research was conducted in the absence of any commercial or financial relationships that could be construed as a potential conflict of interest.

frontiers in Materials

ORIGINAL RESEARCH
published: 05 December 2019
doi: 10.3389/fmats.2019.00299

Magnetic Hysteresis Compensation Control of a Magnetorheological Damper

Zhaochun Li, Yao Gong, Sihao Li and Wanjun Wang*

College of Mechanical and Electronic Engineering, Nanjing Forestry University, Nanjing, China

The hysteresis non-linearity of a magnetorheological (MR) fluid damper is one of the main reasons to restrict it to be widely used in shock buffering fields. This research aims to reduce or eliminate the effect of the magnetic hysteresis of the MR damper. A magnetic hysteresis compensation control method is proposed and verified in this paper. Jiles-Atherton (J-A) model is employed to descript the hysteresis non-linearity between the adjustable damping force and the actual magnetic induction intensity in the effective damping channel of the MR fluid damper. The simulation of the magnetic compensation control system is performed to evaluate the effectiveness of the proposed method and the employed model. In order to obtain the actual magnetic induction intensity, a MR fluid damper embedded in a Hall sensor is designed and manufactured. The experimental study is carried out to verify the proposed PID control of hysteresis compensation method. Both the simulation results and the experimental results show the MR fluid damper employed proposed hysteresis compensation method with PID control can almost completely eliminate the effect of hysteresis under both low frequency and high frequency input. The experimental results indicate the hysteresis control system of MR fluid damper is of good dynamic performance which make it suitable for the shock buffering system. At last, a simulation model of the MR-damper-based impact buffer system with hysteresis compensation control is established to verify the buffer effect of the system. The output damping force of the MR impact buffer system indicates the buffer performance has been improved by employing the magnetic hysteresis compensation control method.

Keywords: MR fluid damper, hysteresis non-linearity, compensation control, shock buffering system, PID control

OPEN ACCESS

Edited by:
Xian-Xu Bai,
Hefei University of Technology, China

Reviewed by:
Donghong Ning,
University of Wollongong, Australia
Jianbo Yin,
Northwestern Polytechnical University, China

****Correspondence:***
Zhaochun Li
lzc.hn@163.com

Specialty section:
This article was submitted to Smart Materials, a section of the journal Frontiers in Materials

Received: *27 July 2019*
Accepted: *08 November 2019*
Published: *05 December 2019*

Citation:
Li Z, Gong Y, Li S and Wang W (2019) Magnetic Hysteresis Compensation Control of a Magnetorheological Damper. Front. Mater. 6:299. doi: 10.3389/fmats.2019.00299

INTRODUCTION

Magnetorheological (MR) damper is a new semi-active control device with magnetorheological fluid as working medium. It changes the shear yield stress of magnetorheological fluid by changing the current applied to the inner coil, thus changing its output damping force (Carlson, 2002). Magnetorheological damper has the advantages of simple structure, large damping force, wide adjustable range, low energy consumption, fast response speed, and wide dynamic range. Extensive research has been carried out in the field of vibration control of buildings, bridges, automobiles and machinery, and preliminary applications have been obtained (Dyke et al., 1998; Choi et al., 2000; Sahasrabudhe and Nagarajaiah, 2005). At present, most of the applications of MR dampers are in the field of low-speed and low-frequency random loadings. In recent years, the application of

MR dampers in the field of impact loadings under high-speed conditions has also begun to attract attentions (Goncalves et al., 2006; Wereley et al., 2011; Bai et al., 2018; Shou et al., 2018; Li et al., 2019). MR shock buffers have good application prospects in the fields of aviation, aerospace, weapons, vehicles, and ships. However, the hysteretic non-linearity of MR damper limits its further application and development, especially in the field of shock buffering. In the impact buffer system, because of the short impact time, MR dampers are required to have fast and accurate response characteristics. The hysteresis of a MR damper will affect the prediction and control accuracy of the damping force, and also cause time delay to the system. Unlike the low-speed shock absorption process, the shock buffering process usually lasts only for a short period of time from several 100 ms to several seconds. The hysteresis characteristics of MR dampers seriously affect the performance of the buffer control.

Because of the soft magnetic properties of iron particles and their fluidity in fluids, the hysteresis of magnetorheological fluids is very small or non-existent and the magnetization curve of MRF is almost linear (Jolly et al., 1998). The hysteretic non-linearity of MR fluid dampers mainly comes from two aspects (Seong et al., 2009; Li et al., 2019). One is from the non-linearity between damping force and velocity. It is caused by frictional force and fluid compressibility in the damper and the non-linear rheological properties of MR fluid such as yield stress and shear thinning. The other one is the hysteresis non-linearity between the adjustable damping force and the control current of the MR damper caused by the magnetic hysteresis characteristic. It is the hysteresis non-linearity between magnetic induction intensity and magnetic field intensity due to the magnetization characteristics of ferromagnetic materials in the internal structure of MR damper. The output adjustable damping force of the MR damper is controlled by the control current applied on the coils. While the magnetic field intensity is directly generated by the control current and the output adjustable damping force is a function of the magnetic induction intensity. Therefore, the hysteresis non-linearity between the magnetic induction intensity and the magnetic field intensity in the MR damper shows the hysteresis non-linearity between the adjustable damping force and the control current.

The hysteretic non-linearity between the damping force and velocity of MR dampers can be described and eliminated by establishing a hysteretic dynamic model. In order to describe the hysteretic non-linearity of MR dampers, a lot of research work has been done on the dynamic modeling of MR dampers. On the basis of theoretical and experimental analysis, many hysteretic models, such as non-linear hysteretic double-viscous model, Bouc-Wen model, phenomenal model, polynomial model, and S-type hysteretic model etc. have been proposed (Wang and Gordaninejad, 2007; Wang and Liao, 2011). Fuzzy theory, neural network, and other intelligent theory are utilized to establish hysteretic model of MR damper (Xia, 2003). Compared with the commonly used simple models, such as Bingham model and Herschel-Bulkley model, the above hysteretic dynamic models have improved the fitting accuracy in varying degrees. However, these existing hysteretic non-linear models are all aimed at the hysteretic characteristics between damping force and velocity. The hysteretic non-linearity between adjustable damping force and control current are not considered in the models. Unlike the low-speed vibration reduction process, the shock buffering process usually lasts only for a short period of time from several 100 ms to several seconds. The hysteretic non-linearity caused by the transient change of control current seriously affects the performance of buffer control.

Hysteresis modeling of ferromagnetic materials has been extensively studied. Many different models have been proposed. All of these models can be roughly divided into two categories: operator-based model and differential equation-based model. Preisach model is the most general operator-based model proposed by Preisach. It is a hysteresis model based on magnetization mechanism (Preisach, 1935). It assumes that hysteresis can be modeled as the sum of a weighted hysteresis operator. However, it requires a weight function constructed from experimental data (Joseph, 2001). A large number of data points and repeatability of system behavior have a direct impact on the accuracy of the model. Prandtl-Ishlinskii model is another operator-based model, which assumes that hysteresis can be described by the superposition of hysteresis operators with single threshold and density functions similar to Preisach model (Wang et al., 2010). The advantage of this model is that the computation time is less. However, Prandtl-Ishlinskii model presents asymmetric hysteresis loops and saturated output. Hodgdon model assumes the mapping relationship between magnetic induction and magnetic field intensity. It is described by differential equations based on physical insight into the magnetization process (Coleman and Hodgdon, 1986; Hodgdon, 1988). Jiles-Atherton (J-A) hysteresis model is based on domain wall theory of ferromagnetic materials. According to the domain wall motion mechanism, the hysteresis loop between the magnetization intensity and the external magnetic field is obtained by deducing two differential equations of the irreversible magnetization component and the reversible magnetization component. J-A is a model based on first-order differential equation (Jiles and Atherton, 1986). Because of its stable algorithm, simple calculation, and clear physical meaning, it has been attracted attentions.

Few studies have proposed complete solutions to both the two kinds of hysteretic non-linearity of MR dampers. Choi et al. used Preisach model to build magnetic hysteresis compensator for MR dampers used in vehicle vibration reduction and tried to eliminate the effect of hysteresis non-linearity (Seong et al., 2009). More attentions have been paid on the hysteresis characteristics of MR clutch or brake as follows. Mechanical models including hysteresis characteristics have been established by theoretical analysis method (An and Kwon, 2003). A hysteresis non-linear model considering both hydrodynamics and magnetic hysteresis characteristics was established (Jedryczka et al., 2009). Magnetic hysteresis was reduced by feedback of the magnetic induction intensity (Erol et al., 2012). The results show that these methods for eliminating hysteresis effect of MR actuators can reduce hysteresis non-linearity and zero input torque to a large extent.

In order to eliminate the influence of hysteresis non-linearity on the performance of MR dampers, especially to improve the performance of MR dampers in impact buffer system.

This research aims at the magnetic hysteresis non-linearity of MR dampers. A magnetic hysteresis compensation control method is proposed. A Hall sensor is embedded in the effective damping channel position of the MR damper. Then, the magnetic induction intensity measured by the Hall sensor is fed back to a PID controller. The control current is output and applied to the electromagnetic coils of the MR damper. The hysteresis compensation effects of hysteresis compensation control method under both low frequency input signal and high frequency input signal are verified by simulation and experiment, respectively. At the end of this paper, a simulation model of the MR impact buffer system is established to verify the effect of the proposed hysteresis compensation method.

THEORY OF MAGNETIC HYSTERESIS MODEL OF MR DAMPER

Because the internal structure of MR damper contains of ferromagnetic materials, the hysteresis non-linearity between magnetic induction intensity B and magnetic field intensity H is caused by its magnetization characteristics. Magnetorheological damper controls the output of adjustable damping force by changing the input of control current I, and the magnetic field intensity is directly generated by the control current, so the output adjustable damping force F_τ is a function of magnetic induction intensity. Therefore, the hysteresis non-linearity between B and H is shown as the hysteresis non-linearity between F_τ and I in a MR damper.

J-A hysteresis model is a typical differential equation-based model. It is based on domain wall theory of ferromagnetic materials. The total magnetization M consists of irreversible magnetization component M_{irr} and reversible magnetization component M_{rev} shown as:

$$M = M_{irr} + M_{rev} \tag{1}$$

Assuming that the direction of the external magnetic field H is the same as that of magnetization M, the effective magnetic field H_e can be expressed as:

$$H_e = H + \alpha M \tag{2}$$

where α is the coefficient of the molecular field. According to Weiss's molecular field theory, α can be expressed as $\alpha = \frac{\theta}{C}$, where θ is the paramagnetic Curie temperature and C is the Curie constant.

The differential of total magnetization to magnetic field intensity can be expressed as:

$$\frac{dM}{dH} = (1-c)\frac{(M_{an} - M_{irr})}{k\delta - \alpha\,(Man - Mirr)} + c\frac{dMan}{dH}, \tag{3}$$

where c is a reversible magnetization coefficient. M_{an} is hysteresis-free magnetization. k is the constraint parameter. It is multiplied by vacuum permeability μ_0 as hysteresis loss parameter K. K represents the change of energy loss in each element during magnetization, which is proportional to the number of pinning points and energy. δ is a parameter indicating the direction of magnetic field change. When $dH/dt > 0$, $\delta = 1$. When $dH/dt < 0$, $\delta = -1$.

The hysteresis-free magnetization M_{an} in Equation (3) is described by an improved Langevin function shown as:

$$M_{an} = M_s\left[\coth\left(\frac{H_e}{a}\right) - \frac{a}{H_e}\right], \tag{4}$$

where M_s is the saturation magnetization. It depends on the material's own characteristics and temperature. a is the shape parameter of hysteresis-free magnetization curve.

As shown in Equation (3), the differential equation of J-A model describes the relationship between magnetization M and magnetic field H. In a MR damper system, the magnetic induction intensity is measured by a Hall sensor embedded in the MR damper. Hence, the differential equation shown as Equation (3) can be transformed into the differential relationship of B-H. As,

$$B = \mu_0(H + M), \tag{5}$$

the magnetic field intensity can be obtained from the following equation:

$$H = \frac{NI}{L_e}. \tag{6}$$

Where H is the intensity of magnetic field. N is the turn number of excitation coil. I is the excitation current. L_e is the effective length of magnetic circuit.

In order to facilitate the modeling and simulation of hysteresis J-A model, Equation (3) is transformed into a time-dependent differential equation. The two sides of Equation (3) are multiplied

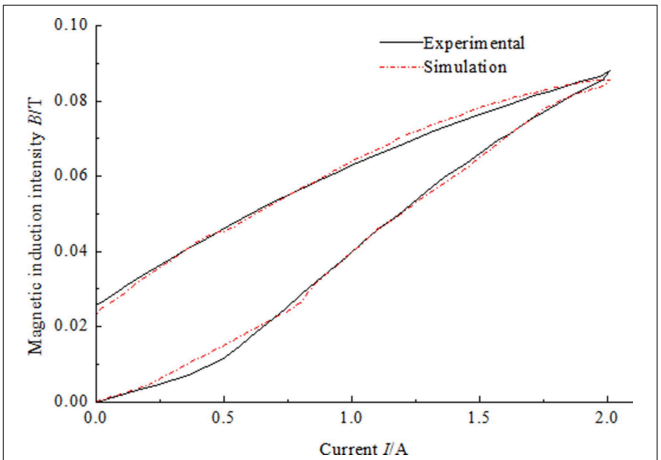

FIGURE 1 | Measured magnetic hysteresis curve and the fitting curve generated by Jiles-Atherton model ($M_s = 1.24 \times 10^6$, $a = 2.68\times10^4$, $\alpha = 1.47\times10^{-4}$, c = 0.54, $k = 5.69\times10^3$).

by dH/dt simultaneously so that Equation (3) is transformed into a differential of time, as shown in the following equation:

$$\frac{dM}{dt} = (1-c)\frac{(Man - Mirr)}{k\delta - \alpha\,(Man - Mirr)}\frac{dH}{dt} + c\frac{dMan}{dt}. \quad (7)$$

By using simulation software MATLAB/SIMULINK, the J-A model represented by Equation (7) can be dynamically modeled, simulated, and analyzed. In combination with Equations (5–7) is transformed into a set of differential equations with current as input and magnetic induction intensity as output. Given five parameters M_s, a, α, c, k of J-A hysteresis model, the hysteresis loop between excitation current and magnetic induction intensity can be obtained, as shown in **Figure S1**.

During the operation of the MR damper, the direction of current applied to coils of the MR damper usually keeps same. Therefore, the hysteresis non-linearity of the MR damper is tested only in the first quadrant and fitted by J-A model as shown in **Figure 1** (Li and Gong, 2019).

HYSTERESIS COMPENSATION CONTROL METHODS

In order to reduce or eliminate the obvious hysteresis non-linearity between the control current of the MR damper and the magnetic flux intensity in the effective damping channel, a control method of hysteresis compensation is proposed in this paper. First of all a relationship of the theoretical optimal adjustable damping force $F_\tau(t)$ and the desired magnetic flux density $B_d(t)$ was derived by calculation (Erol et al., 2012). As shown in **Figure 2**, the error $e(t)$ between the theoretical magnetic flux density $B_d(t)$ and the measured magnetic flux density $B_m(t)$ is derived. Then the error is as the input of the PID (Proportional-Integral-Derivative) controller. The PID controller outputs the control current to the coils of the MR damper or J-A model.

PID control is a traditional control strategy which is easy to realize and widely used in the industry automatic control system.

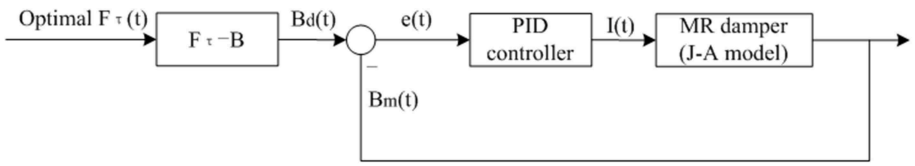

FIGURE 2 | Schematic of PID control of the magnetic compensation control for a MR damper.

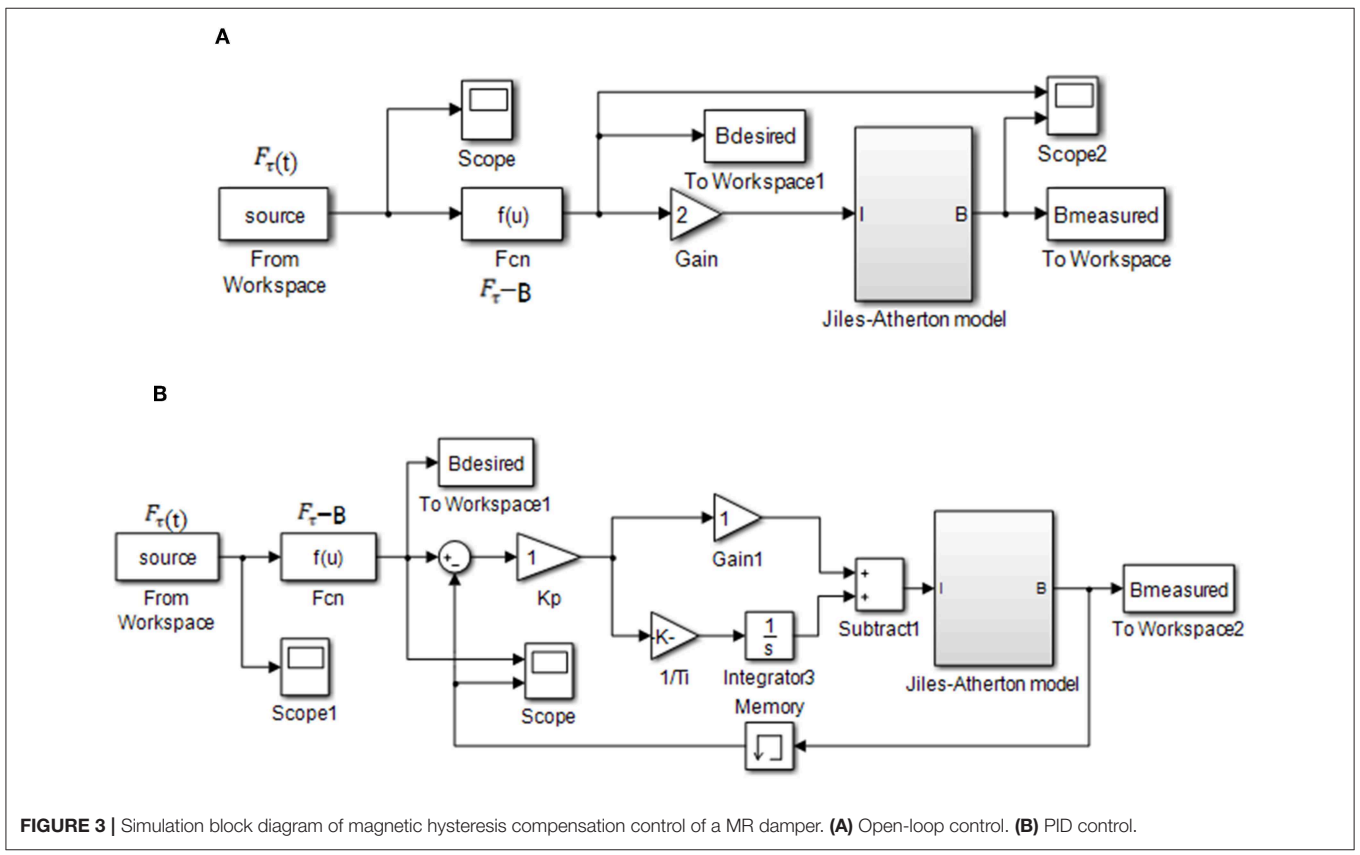

FIGURE 3 | Simulation block diagram of magnetic hysteresis compensation control of a MR damper. **(A)** Open-loop control. **(B)** PID control.

In a control system, Equation (8) indicates the relationship of the output signal $u(t)$ and the error signal $e(t)$:

$$u(t) = K_p e(t) + K_I \int e(t) + K_D \frac{de(t)}{dt}. \quad (8)$$

Where, K_P is the proportional coefficient, K_I is the integral coefficient and K_D is the derivative coefficient. For PID controller, $u(t)$ is the controlled value. Defining T_I as integral time constant and T_D as derivative time constant. The relationships of time constants and coefficients can be expressed as follows:

$$K_I = \frac{K_P}{T_I} \quad (9)$$

and

$$K_D = K_P^* T_D. \quad (10)$$

The proportional element in PID controller represents the speed of the control system. The larger the K_P the faster the response

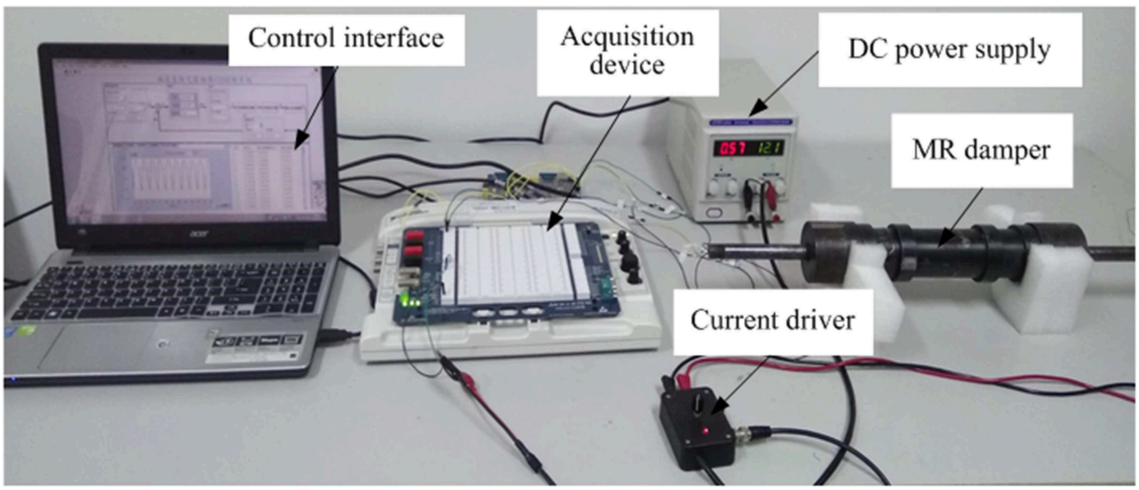

FIGURE 4 | Experimental setup of the magnetic hysteresis compensation control for the MR damper.

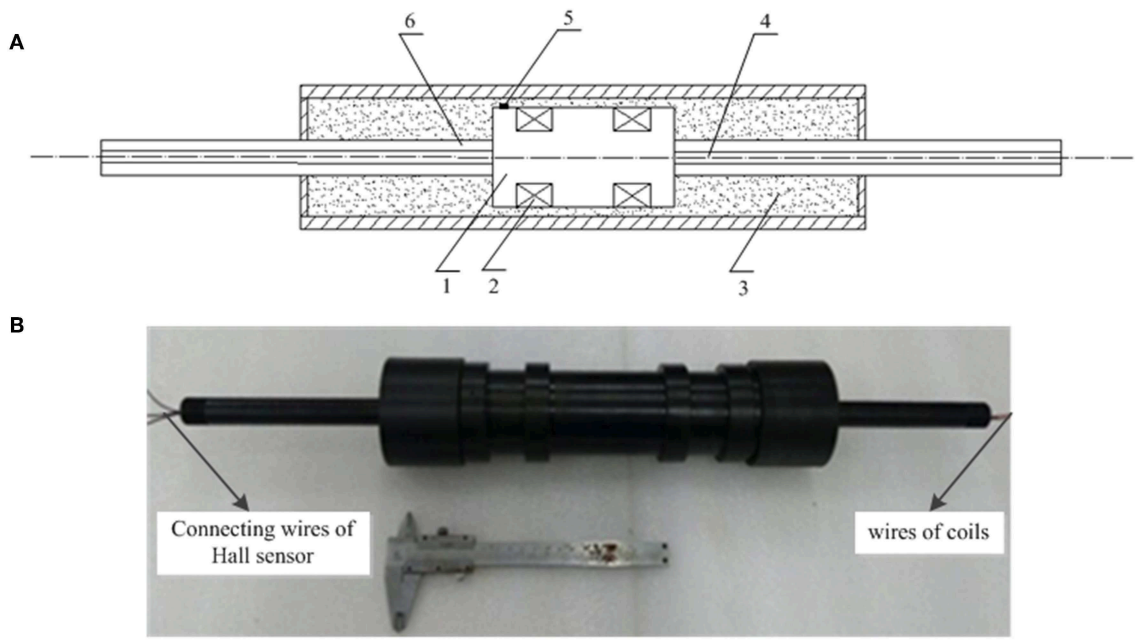

FIGURE 5 | MR damper with embedded in Hall sensor. **(A)** Schematic of the MR damper (1) piston, (2) coil, (3) MR fluid, (4) fairlead hole, (5) Hall sensor, and (6) piston rod. **(B)** Picture of the MR damper.

speed of the system is and the higher the adjustment precision is, but it may cause overshoot and oscillation. On the contrary, the system response is slow. The integral element represents the accuracy of the control system. The integral term is introduced to make up for the defect that proportional control cannot eliminate steady-state error. When the error is integrated, the integral effect will increase with the increase of time and the output of the controller will be increased so that the steady-state error will be further reduced to zero. If the integral time constant T_I is small, it means that the integral effect is strong, and vice versa, the weaker. However, if the integral coefficient K_I is too large, the dynamic performance of the system will deteriorate and the overshoot and oscillation will occur. Hence, the stability of the system will be reduced. The differentiation of errors reflects the rate of variation of errors, that is, the trend of system errors. Because the phase angle of the differential element is ahead, when the error becomes larger, the differential of the error is greater than zero. And when the error decreases, the differential of the error is less than zero. So the differential control can produce the effect of early correction. When the error increases or decreases, the differential control will change the trend and reduce the error ahead of time so that the response speed of the system will be accelerated and the adjustment time will be reduced. So the differential control makes the system has good dynamic performance. But differential control needs to be used properly, otherwise the system will oscillate. In order to avoid oscillation, the value of differential coefficient K_D is usually small (Li and Wang, 2012). The proportion coefficient, integral coefficient, and differential coefficient affect the control effect together. Reasonable adjustment of three parameters of K_p, K_I, and K_D is the key of the effectiveness of PID controller.

The J-A model of the magnetic hysteresis non-linearity of the MR damper above is utilized here to establish a control model in Simulink. The simulation model of the magnetic hysteresis control of a MR damper is shown in **Figure 3**. **Figure 3A** is the open-loop control system that means there is no magnetic flux density signal feedback. **Figure 3B** is the PID control system that means the magnetic flux density signal feedback and the PID controller works. In the feedback system, the module of Memory is employed to solve the problem of algebraic loop which will reduce the simulation speed or even reduce the accuracy of the simulation results or result in error results. As the constant δ in the Equation (3), the differential equation of the J-A model, is a symbol function which is inconvenient for derivation. Hence, the derivate module is not used in the magnetic hysteresis compensation control system.

EXPERIMENTAL SETUP

The experimental setup of the magnetic hysteresis compensation control for the MR damper is mainly composed of a MR damper embedded in Hall sensor, acquisition device, current driver, DC power supply, test interface as shown in **Figure 4**.

ELVIS (National Instruments Corporation) suite is adopted as the hardware of data acquisition device. ELVIS is an educational laboratory virtual instrumentation suite as well as a common used high performance data acquisition card. The maximum sampling frequency of ELVIS is 1 MS/s and the resolution of analog input is 16 bit. The resolution of analog output is 16 bit as well. The function of analog + output is to output the control voltage to the current driver which is controlled by voltage of 0–5 V. The current driver (Lord, RD-3003-03) output current of 0–2 A according to the analog output of ELVIS. The control interface software is programmed by LabVIEW as shown in **Figure S2**. As the experiments with open-loop control is used to compare with the experiments with PID control, the relative software interfaces are designed and programmed, respectively.

The MR damper embedded in a Hall sensor is designed specially for research of the magnetic hysteresis control as shown in **Figure 5**. As we can see from **Figure 5A**, the Hall sensor (Allegro, A1304) is pasted in the cylinder surface of the piston.

A1304 linear Hall-effect sensor IC outputs analog signal which is convenient for data acquisition. It provides a miniature and low profile surface mount package as shown in **Figure S3**. A small plane is filed on the cylinder surface of the piston in order to mount the sensor. The branded face of the sensor IC is pasted firmly on the plane of the piston utilizing adhesive. As can be seen, the height of the IC is 1 mm so that it can be mounted on the piston which moves within the small gap of 2 mm. Hence, the miniature and low profile of the sensor IC is in favor of its mount. The footprints of Hall sensor and their connecting cables are covered with sheaths to insulation. The Hall sensor and the two coils of the MR damper are sealed by epoxy resin. The MR damper consists of a mono-tube and a two-ended piston with two stage coils. Because both the wire of the coils and the connecting wire of the sensor IC are needed to lead out of the MR damper, the double-ended piston is suitable for the MR damper embedded Hall sensor. The two-ended piston rods are hollow. The wires of the coils is leaded out from one end of the piston rod and the conducting wires connected to the footprints of the Hall-sensor IC is leaded out from the other end of the piston rod as shown in **Figure 5B**.

For the MR damper in this paper is designed and manufactured specially for verify the magnetic hysteresis compensation control method, both the dimension and the damping force is designed small. The structural dimensions of the MR damper are shown in **Table 1**.

SIMULATION AND EXPERIMENTAL RESULTS

Simulation Results

The adjustable damping force F_τ is a non-linear but single-valued function of magnetic induction intensity B. For comparison,

TABLE 1 | Structural dimensions of the MR damper.

Inside diameter of the cylinder, D_1 (mm)	39
Diameter of the piston, D_2 (mm)	35
Diameter of the piston rod, d (mm)	18
Gap length of the magnetic field, L_0 (mm)	32
Gap length of the flow, L (mm)	80

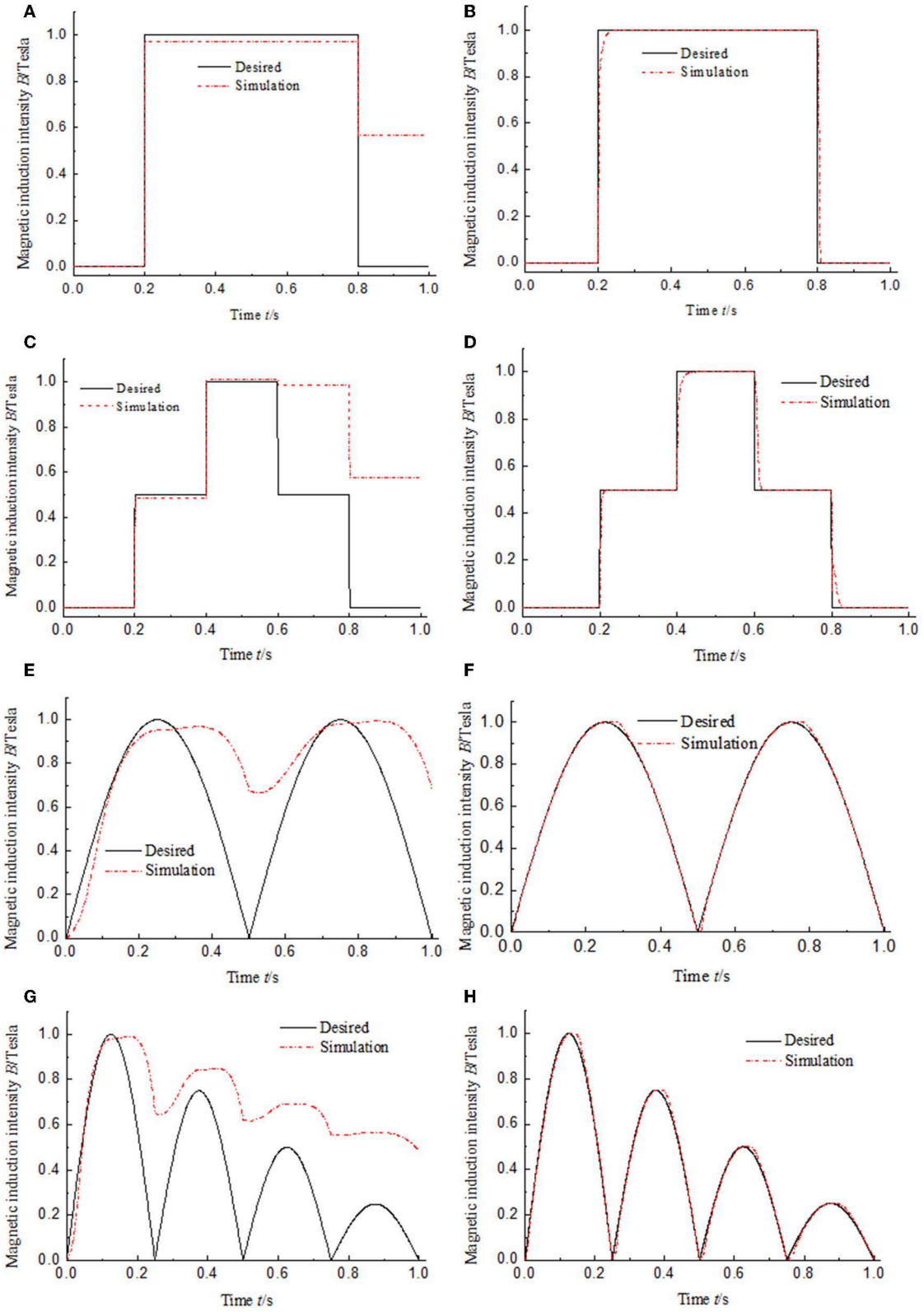

FIGURE 6 | Simulation results of magnetic hysteresis control of the MR damper under the low frequency input signals. **(A)** Open-loop control under window function input signal. **(B)** PID control under window function input signal. **(C)** Open-loop control under multistep function input signal. **(D)** PID control under multistep function input signal. **(E)** Open-loop control under semi-sinusoidal function input signal. **(F)** PID control under semi-sinusoidal function input signal. **(G)** Open-loop control under semi-sinusoidal functions with variable amplitude input signal. **(H)** PID control under semi-sinusoidal functions with variable amplitude input signal.

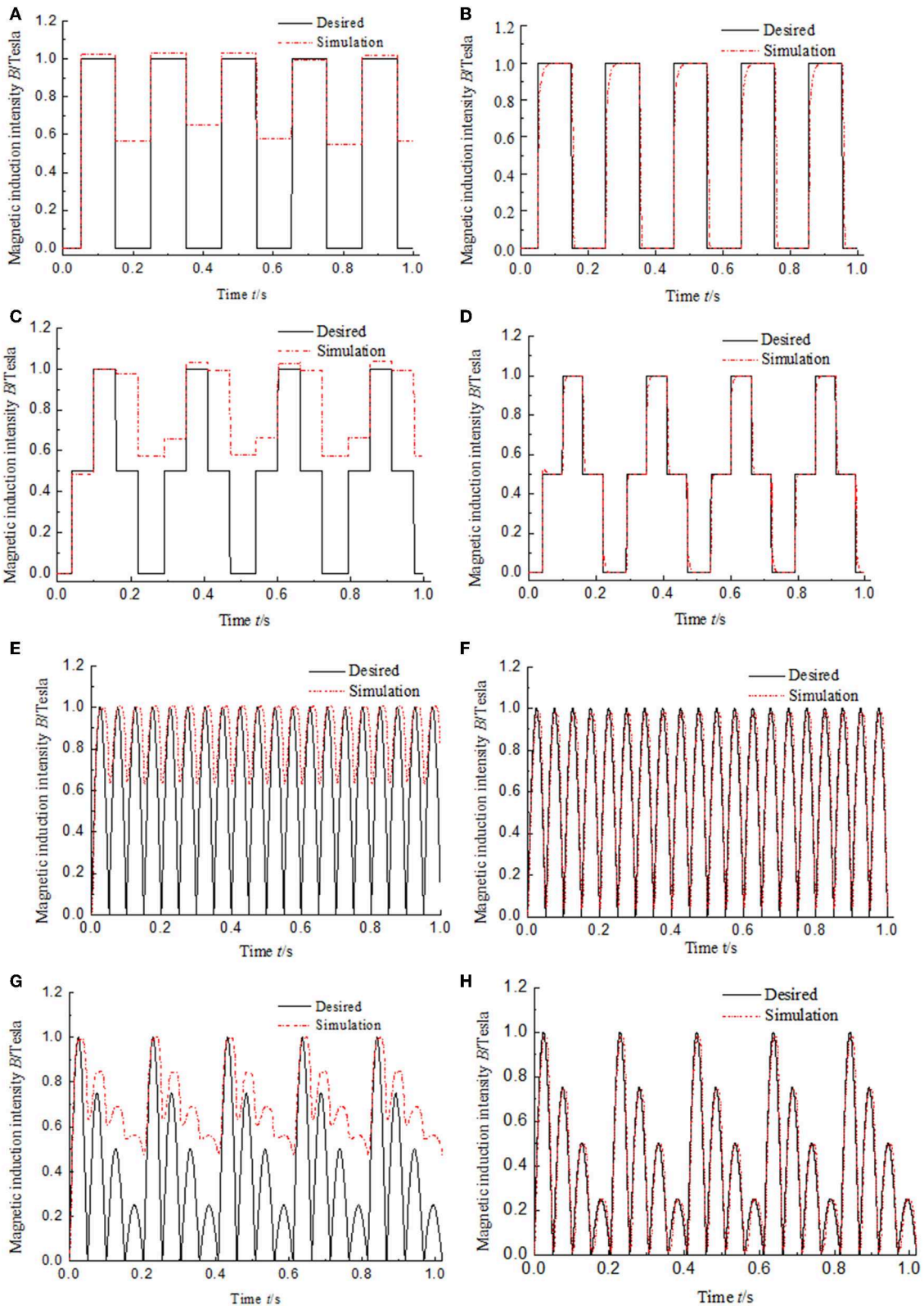

FIGURE 7 | Simulation results of magnetic hysteresis control of the MR damper under the high frequency input signals. **(A)** Open-loop control under window function input signal. **(B)** PID control under window function input signal. **(C)** Open-loop control under multistep function input signal. **(D)** PID control under multistep function input signal. **(E)** Open-loop control under semi-sinusoidal function input signal. **(F)** PID control under semi-sinusoidal function input signal. **(G)** Open-loop control under semi-sinusoidal functions with variable amplitude input signal. **(H)** PID control under semi-sinusoidal functions with variable amplitude input signal.

the desired magnetic induction intensity instead of optimal adjustable damping force in **Figure 2** is given as several typical signals of window function, multistep function, semi-sinusoidal function, and semi-sinusoidal functions with variable amplitude. The maximum amplitude of every simulation signal is set as 1 Tesla so that the relative magnetic hysteresis shows obviously in the curve. The simulation results of magnetic hysteresis compensation control of the MR damper are shown in **Figure 6**. The results in **Figures 6A,C,E,G** indicate that the magnetic induction intensity output by the MR damper cannot track the desired magnetic induction intensity after the signal start to decline in the open-loop control system. It is the reason that J-A magnetic hysteresis model established in the MR damper as shown in **Figure 3**. The results in **Figures 6B,D,F,H** show that the output signals of magnetic induction intensity can always track the changes of the input signals in the PID control system when $K_P = 0.5$ and $K_I = 400$. That means the PID control with appropriate coefficients can eliminate the effect of the magnetic hysteresis. The dynamic performance of the PID control system of MR damper is also obviously shown in **Figures 6B,C**. There is no overshoot in the dynamic process that partly leads to fast track of the output. The rising time is around 40 ms and the falling time is around 20 ms. The rising time and falling time in the simulation system are partly caused by the Memory module as shown in **Figure 3** which leads to delay of the output. Moreover, the differential coefficient is zero. That means that there is no differential element in the PID control system. However, differential element can improve dynamic performance of the PID control system.

As we know, the duration of the impact loading of the buffering system is short and always <0.1 s (Li and Wang, 2012). To verify whether the method of hysteresis compensation control can work well in a buffering system, four kinds of high frequency input signal is used for simulation. The simulation results are shown in **Figure 7**. **Figures 7B,D,F,H** show the PID control results of hysteresis compensation of MR damper under four kinds of high frequency input signals. The frequency of semi-sinusoidal signal is 200 Hz that means the time of one period is 0.05 s as shown in **Figure 7F**. Under the condition of high frequency input signal, the compensation effect of the PID control of hysteresis compensation is not different from that under the condition of low frequency input signal. The

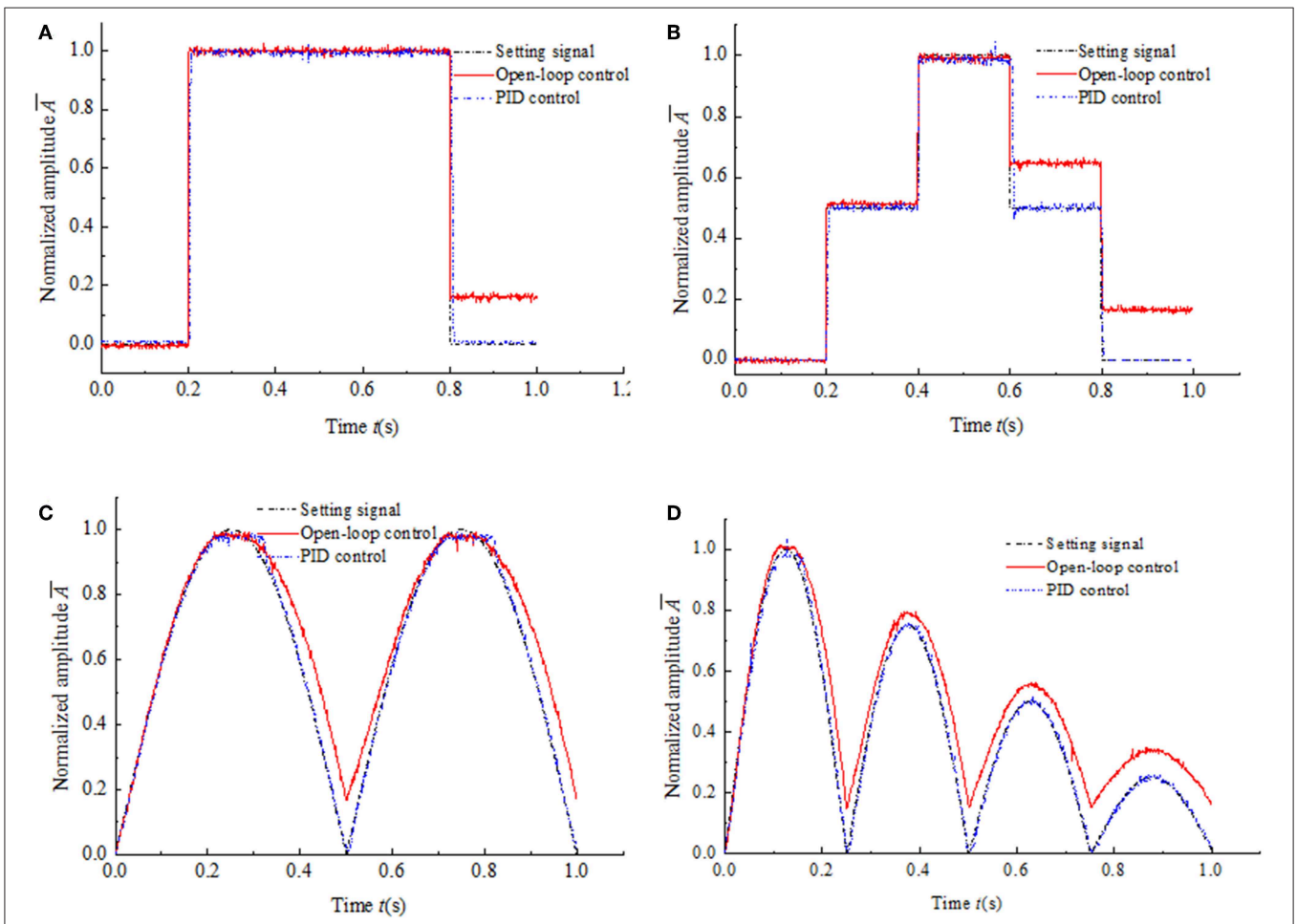

FIGURE 8 | Experimental results of magnetic hysteresis control of the MR damper under the low frequency input signals. **(A)** Window function input signal. **(B)** Multistep function input signal. **(C)** Semi-sinusoidal function input signal. **(D)** Semi-sinusoidal functions with variable amplitude input signal.

values of hysteresis are close to 0. That shows that the hysteresis compensation control method proposed in this paper is suitable for shock buffering system with short working period, and will be beneficial to improve the control accuracy of MR damper in shock buffering system. Under the condition of high frequency signal, the dynamic performance is also affected by Memory simulation module and lack of differential element as shown in **Figure 7B**. The rising response time is about 40 ms as same as that under low frequency input signal.

Experimental Results

The experimental results of magnetic hysteresis compensation control of the MR damper under four kinds of low frequency and high frequency input signals are shown in **Figures 8**, **9**, respectively. The frequency of every kind of input signal is as same as that in the simulation system for comparison. In the experimental system, the input signal is the control current generated by the current deriver as shown in **Figure 4**. The experimental results shown in **Figures 8**, **9** indicate that the hysteresis under the PID control is almost completely compensated under both low frequency and high frequency input signals. Compared with the simulation results, the dynamic performances of the experimental results have been significantly improved. The response time is much shorter than that in simulation. The maximum response time is around 15 ms. The reason is that the experimental system does not include the Memory simulation module. It also reveals that the response time of the simulation system is mainly caused by the delay of the simulation module.

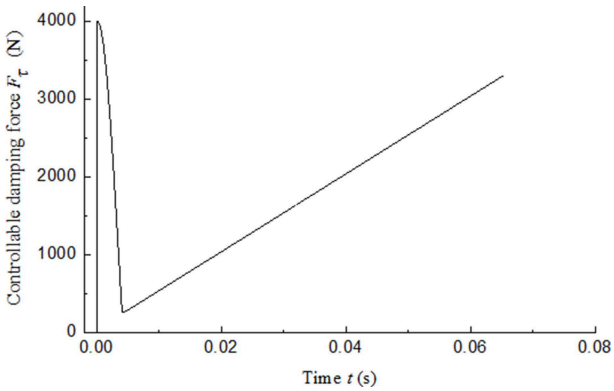

FIGURE 10 | Ideal controllable damping force.

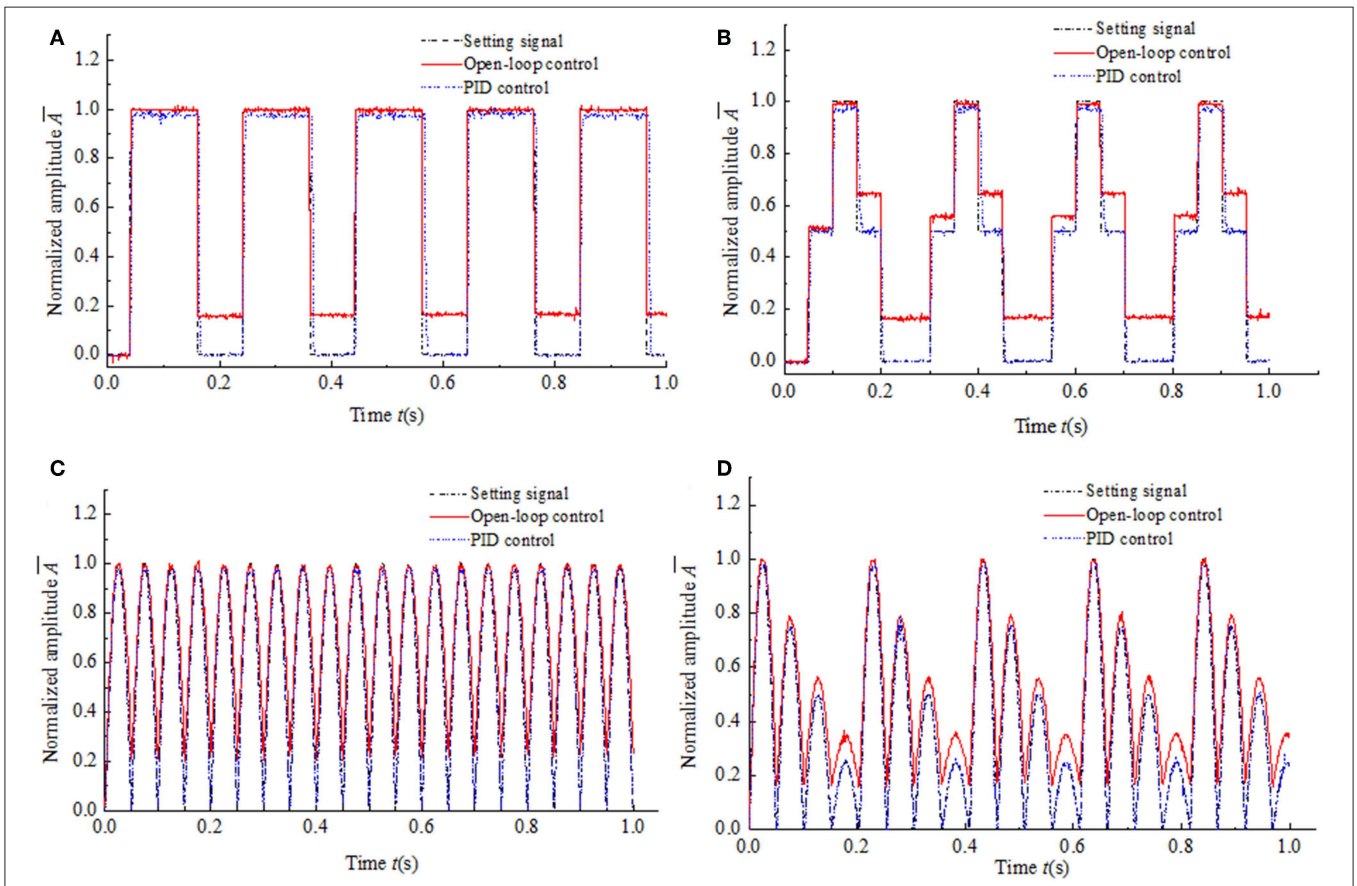

FIGURE 9 | Experimental results of magnetic hysteresis control of the MR damper under the high frequency input signals. **(A)** Window function input signal. **(B)** Multistep function input signal. **(C)** Semi-sinusoidal function input signal. **(D)** Semi-sinusoidal functions with variable amplitude input signal.

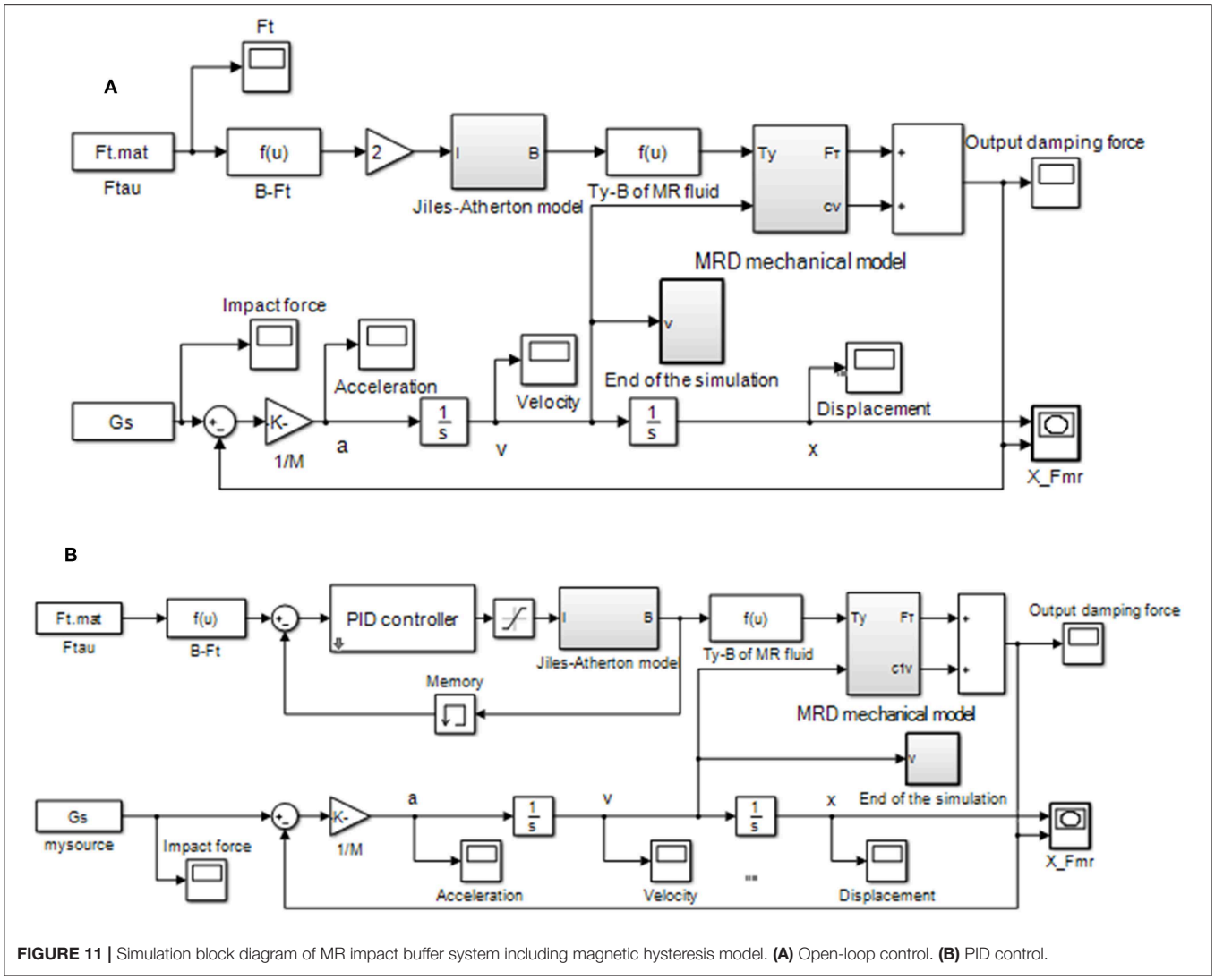

FIGURE 11 | Simulation block diagram of MR impact buffer system including magnetic hysteresis model. **(A)** Open-loop control. **(B)** PID control.

The LabVIEW software generates the four kinds of typical signals as the setting values of the control system, respectively. Then the setting values convert to the analog voltage from the digital value by the DAQ device. Taking the analog voltage signals as the input of the experimental hysteresis compensation control system, the unit of the input signals is Volts and the voltage range is 0–5 V. The output signal of the experimental system is the output voltage of the Hall sensor. The voltage range of the Hall sensor is 0–3.3 V. Hence, the normalized amplitudes of the input and the output are plot in **Figures 8**, **9** for comparison.

SIMULATION VERIFICATION OF HYSTERESIS COMPENSATION CONTROL IN MR IMPACT BUFFER SYSTEM

Ideal Impact Buffer

A typical MR impact buffer system can be descripted as a MR damper and a mass as shown in **Figure S4**. The MR damper outputs damping force F_{mr} which consists of uncontrollable part F_{μ} and controllable part F_{τ}. F_{μ} is related to the velocity of the piston of the MR damper. While F_{τ} is related to the magnetic flux density of the effective damping channel.

According to Newton's second law, the motion equation of the system can be descripted as

$$F_{pt} - F_{mr} = m\ddot{x}, \tag{11}$$

where F_{pt} is the impact force loaded on the mass. m is the mass of the object subjected to the impact loading. x is the displacement of the mass.

The ideal impact buffer effect is obtained when the damping force equals to constant (Li and Wang, 2012) as shown

$$F_{mr\_i} = F_{\tau} + c_1\dot{x} = constant, \tag{12}$$

where F_{mr_i} is the ideal damping force and c_1 is the coefficient determined by the dimension of the MR damper.

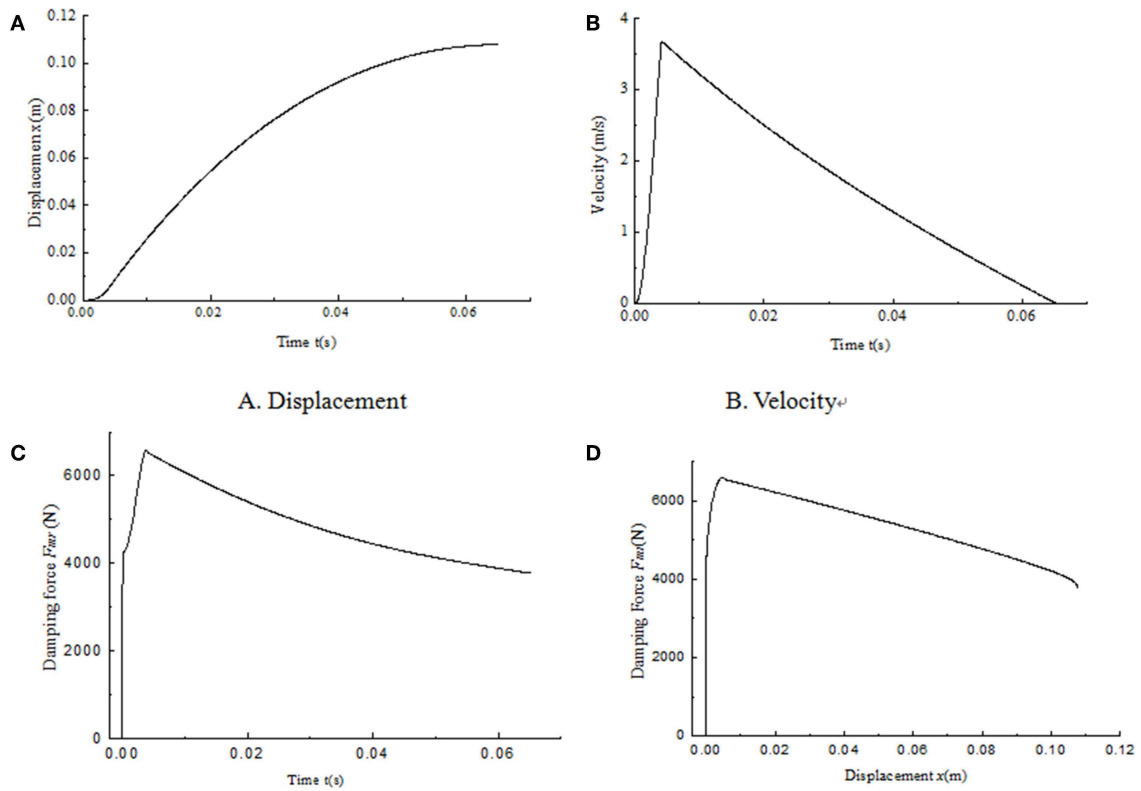

FIGURE 12 | Simulation results of the MR impact buffer system under open-loop control. **(A)** Displacement. **(B)** Velocity. **(C)** Damping force. **(D)** Damping force vs. displacement.

According to the impact loading in the gun recoil system (Li and Wang, 2012), the impact force as shown in **Figure S5** is given to verify the effect of the hysteresis compensation control.

Combine Equations (11) and (12), the ideal displacement $x(t)$ and the ideal velocity $\dot{x}(t)$ can be obtained by solving the second order differential equation. Assuming the ideal damping force F_{mr_i} equals to 4,000 N, the ideal controllable damping force F_τ can also be obtained as shown in **Figure 10**. The impact buffer motion starts when the impact force loaded in the mass and the motion ends when the velocity of the mass changes to 0. As we can see, the calculated ideal controllable damping force F_τ changes within 0.07 s. That means the control current needs to be changed quickly. Fast change of the current leads to the obvious decrease in performance of the system caused by the magnetic hysteresis. Hence, the magnetic hysteresis of the MR damper in the impact buffer system will inevitably reduce the buffer effect.

Simulation of the MR Impact Buffer System

The model of the MR-damper-based impact buffer system is established and the simulation block diagrams of MR impact buffer system including magnetic hysteresis model are shown in **Figure 11**. The mechanical model and the magnetic hysteresis model of the MR damper are both included in the simulation system. Although the ideal damping force is as a condition of the calculation for Equation (11), the actual output damping force of the MR damper is not constant for the existence of the magnetic hysteresis. **Figure 11A** shows open-loop control and **Figure 11B** shows PID control. In **Figure 11B**, the magnetic flux density of the MR damper is fed back for obtaining the error of the ideal magnetic flux density and the actual magnetic flux density as the input of the PID controller.

RESULTS

The simulation results of the MR impact buffer system under open-loop control and PID control are obtained as shown in **Figures 12**, **13**, respectively. For the impact buffer system, the relationship of the actual damping force and time or the relationship of the actual damping force and displacement of the mass is used to evaluate the buffer performance. The closer the curve is to the constant, the better the buffer performance will be. **Figures 12C,D** indicates that the peak damping force is much larger than the ideal value 4,000 N and is not keep constant in the whole buffer process under open-loop control. **Figures 13C,D** shows that a peak damping force still exists at the very beginning buffer process under PID control. While the value of the peak damping force under PID control is much less than that under open-loop control.

For comparison, the curves of the damping force and the displacement under two control methods are shown together as shown in **Figure 14**. As we can see, the damping force under PID

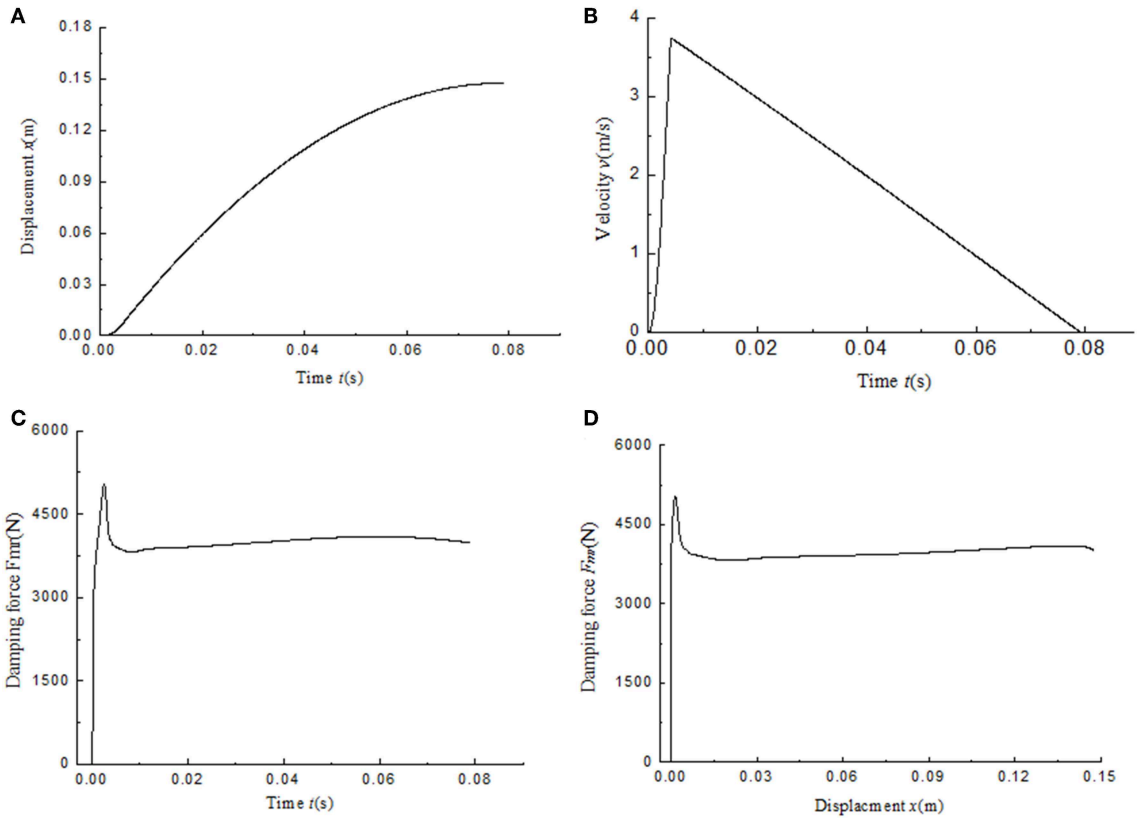

FIGURE 13 | Simulation results of the MR impact buffer system under PID control. **(A)** Displacement. **(B)** Velocity. **(C)** Damping force. **(D)** damping force vs. displacement.

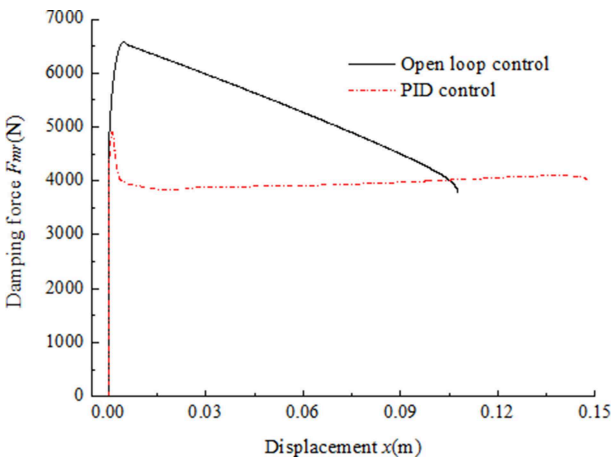

FIGURE 14 | Comparison of impact buffer effect under two different control methods.

control is similar to constant mostly except for the part at the very beginning of the buffer process. The damping force under open-loop control can't keep constant during the whole buffer process. The results indicate the magnetic hysteresis of the MR damper decreases the buffer performance and the PID control based on magnetic flux density feedback can greatly compensate the effect of the hysteresis.

SUMMARY

In this research, the magnetic hysteresis compensation control method for MR damper was investigated. Jiles-Atherton model was employed to descript the magnetic hysteresis non-linearity of the MR damper. A MR damper embedded in a Hall sensor was designed and manufactured for verify the effective of the magnetic hysteresis compensation control method proposed in this paper. A PID controller is employed in the hysteresis compensation system to adjust the performance of the magnetic induction intensity feedback system. The numerical simulation proved the feasibilities of the PID control of the magnetic hysteresis compensation system of the MR damper under both low frequency input and high frequency input. The experimental setup was established by integrating the MR damper embedded in a Hall sensor and the measurement, control device, and software interface. The experimental results show that the measured magnetic induction intensity can track the input signal well under any of the four kinds of setting signals both with low frequency and high frequency by PID control. This means that the effect of magnetic hysteresis

was nearly completely eliminated by PID controller. At the same time, the dynamic performance of the experimental magnetic hysteresis system is good with no overshoot and fast response speed. In order to verify the effect of the proposed hysteresis compensation control method in the MR impact buffer system, a simulation model of the MR-damper-based impact buffer system is established. The results show that the impact buffer system with PID control obtains the better buffer performance than that with open-loop control. It means the proposed hysteresis compensation method in this paper is suitable for the shock buffering system with a MR damper to improve the buffering performance of the system subject to impact loadings.

DATA AVAILABILITY STATEMENT

The datasets generated for this study are available on request to the corresponding author.

AUTHOR CONTRIBUTIONS

ZL proposed the magnetic hysteresis compensation method, designed the MR damper embedded in a Hall sensor, and conducted the experiments. YG carried out the simulation of the hysteresis compensation control of the MR damper and conducted the experiments. SL processed and analyzed the experimental data. WW designed the MR damper embedded a Hall sensor and tested the basic performance of the MR damper.

FUNDING

This work was supported by National Natural Science Foundation of China (NSFC) grant funded by the Chinese Government (No. 51305207) and Natural Science Foundation of Jiangsu Provincial College (Grand Nos. 13KJB460010 and 17KJB413002).

SUPPLEMENTARY MATERIAL

The Supplementary Material for this article can be found online at: https://www.frontiersin.org/articles/10.3389/fmats.2019.00299/full#supplementary-material

Figure S1 | Magnetic hysteresis curve plotted by Jiles-Atherton model ($M_s = 1.25 \times 106$, $a = 1{,}100$, $\alpha = 0.0017$, c = 0.5, $k = 400$).

Figure S2 | Software interface of magnetic hysteresis compensation control of MR damper utilizing LabVIEW. **(A)** Open-loop control. **(B)** PID control.

Figure S3 | Schematic of Hall sensor (Allegro, A1304). **(A)** Top view. **(B)** Side view.

Figure S4 | The MR impact buffer system.

Figure S5 | Impact force loaded on the impact buffer system.

REFERENCES

An, J., and Kwon, D. S. (2003). Modeling of a magnetorheological actuator including magnetic hysteresis. *J. Intell. Mater. Syst. Struct.* 14, 541–550. doi: 10.1177/104538903036506

Bai, X. X., Shen, S., Wereley, N. M., and Wang, D. H. (2018). Controllability of magnetorheological shock absorber: I. Insights, modeling and simulation. *Smart Mater. Struct.* 28:015022. doi: 10.1088/1361-665X/aaf072

Carlson, J. D. (2002). What makes a good MR fluid? *J. Intell. Mater. Syst. Struct.* 13, 431–435. doi: 10.1106/104538902028221

Choi, S. B., Nam, M. H., and Lee, B. K. (2000). Vibration control of a MR seat damper for commercial vehicles. *J. Intell. Mater. Syst. Struct.* 11, 936–944. doi: 10.1106/AERG-3QKV-31V8-F250

Coleman, B. D., and Hodgdon, M. L. (1986). A constitutive relation for rate-independent hysteresis in ferromagnetically soft materials. *Int. J. Eng. Sci.* 24, 897–919. doi: 10.1016/0020-7225(86)90023-6

Dyke, S. J., Spencer B. F. Jr., Sain, M. K., and Carlson, J. D. (1998). An experimental study of MR dampers for seismic protection. *Smart Mater. Struct.* 7, 693–703. doi: 10.1088/0964-1726/7/5/012

Erol, O., Gonenc, B., Senkal, D., Alkan, S., and Gurocak, H. (2012). Magnetic induction control with embedded sensor for elimination of hysteresis in magnetorheological brakes. *J. Intell. Mater. Syst. Struct.* 23, 427–440. doi: 10.1177/1045389X11435432

Goncalves, F. D., Ahmadian, M., and Carlson, J. D. (2006). Investigating the magnetorheological effect at high flow velocities. *Smart Mater. Struct.* 15, 75–85. doi: 10.1088/0964-1726/15/1/036

Hodgdon, M. L. (1988). Applications of a theory of ferromagnetic hysteresis. *IEEE Trans. Magn.* 24, 218–221. doi: 10.1109/20.43893

Jedryczka, C., Sujka, P., and Szelag, W. (2009). The influence of magnetic hysteresis on magnetorheological fluid clutch operation. *COMPEL Int. J. Comput. Math. Electr. Electr. Eng.* 28, 711–721. doi: 10.1108/03321640910940963

Jiles, D. C., and Atherton, D. L. (1986). Theory of ferromagnetic hysteresis. *J. Magn. Magn. Mater.* 61, 48–60. doi: 10.1016/0304-8853(86)90066-1

Jolly, M. R., Bender, J. W., and Carlson, J. D. (1998). "Properties and applications of commercial magnetorheological fluids," in *SPIE 5th Annual International Symposium on Smart Structures and Materials* (San Diego, CA).

Joseph, D. S. (2001). *Parameter Identification for the Preisach Model of Hysteresis* (Doctoral dissertation). Blacksburg, VA: Virginia Tech.

Li, Z., and Gong, Y. (2019). Research on ferromagnetic hysteresis of a magnetorheological fluid damper. *Front. Mater.* 6:111. doi: 10.3389/fmats.2019.00111

Li, Z., Gong, Y., and Wang, J. (2019). Optimal control with fuzzy compensation for a magnetorheological fluid damper employed in a gun recoil system. *J. Intell. Mater. Syst. Struct.* 30, 677–688. doi: 10.1177/1045389X17754258

Li, Z. C., and Wang, J. (2012). A gun recoil system employing a magnetorheological fluid damper. *Smart Mater. Struct.* 21:105003. doi: 10.1088/0964-1726/21/10/105003

Preisach, F. (1935). Über die magnetische nachwirkung. *Zeitschr. Phys.* 94, 277–302. doi: 10.1007/BF01349418

Sahasrabudhe, S. S., and Nagarajaiah, S. (2005). Semi-active control of sliding isolated bridges using MR dampers: an experimental and numerical study. *Earthquake Eng. Struct. Dyn.* 34, 965–983. doi: 10.1002/eqe.464

Seong, M. S., Choi, S. B., and Han, Y. M. (2009). Damping force control of a vehicle MR damper using a Preisach hysteretic compensator. *Smart Mater. Struct.* 18:074008. doi: 10.1088/0964-1726/18/7/074008

Shou, M., Liao, C., Zhang, H., Li, Z., and Xie, L. (2018). Modeling and testing of magnetorheological energy absorbers considering inertia effect with non-averaged acceleration under impact conditions. *Smart Mater. Struct.* 27:115028. doi: 10.1088/1361-665X/aae6a0

Wang, D. H., and Liao, W. H. (2011). Magnetorheological fluid dampers: a review of parametric modelling. *Smart Mater. Struct.* 20:023001. doi: 10.1088/0964-1726/20/2/023001

Wang, K., Zhang, Y., and Jones, R. W. (2010). "Modelling of hysteresis in smart actuators using the generalised Prandtl-Ishlinskii operator," In *ICCAS 2010* (Gyeonggi-do: IEEE), 261–266.

Wang, X., and Gordaninejad, F. (2007). Flow analysis and modeling of field-controllable, electro-and magneto-rheological fluid dampers. *J. Appl. Mech.* 74, 13–22. doi: 10.1115/1.2166649

Wereley, N. M., Choi, Y. T., and Singh, H. J. (2011). Adaptive energy absorbers for drop-induced shock mitigation. *J. Intell. Mater. Syst. Struct.* 22, 515–519. doi: 10.1177/1045389X10393767

Xia, P. Q. (2003). An inverse model of MR damper using optimal neural network and system identification. *J. Sound Vib.* 266, 1009–1023. doi: 10.1016/S0022-460X(02)01408-6

Conflict of Interest: The authors declare that the research was conducted in the absence of any commercial or financial relationships that could be construed as a potential conflict of interest.

frontiers in Materials

ORIGINAL RESEARCH
published: 22 May 2020
doi: 10.3389/fmats.2020.00121

Magneto-Rheological Variable Stiffness and Damping Torsional Vibration Control of Powertrain System

Xiaomin Dong, Wenfeng Li, Jianqiang Yu, Chengwang Pan, Jun Xi, Yaqin Zhou and Xuhong Wang*

State Key Laboratory of Mechanic Transmission, Chongqing University, Chongqing, China

A novel magneto-rheological variable stiffness and damping torsional vibration absorber (MR-VSDTVB) is proposed, fabricated and tested. According to the test data, the control model of MR-VSDTVB is established. Meanwhile, the analysis of the multi-degree-of-freedom model of the powertrain system provides the key frequency and the rotating velocity of the torsional vibration control of the powertrain system and further determines the installation position and structural parameters of MR-VSDTVB. Besides, a human-simulated intelligent controller (HSIC) is developed and numerical simulation of the powertrain system with MR-VSDTVB is carried out. Ultimately, the results verify the effectiveness of the powertrain system with MR-VSDTVB and the semi-active HSIC algorithm on the torsional vibration control.

Keywords: MR-VSDTVB, powertrain system, semi-active, HSIC, control model

OPEN ACCESS

Edited by:
Xian-Xu Bai,
Hefei University of Technology, China

Reviewed by:
Mei Shu Chen,
Fuzhou University, China
Benyuan Fu,
Chongqing University of Technology, China

****Correspondence:***
Xiaomin Dong
xmdong@cqu.edu.cn

Specialty section:
This article was submitted to Smart Materials, a section of the journal Frontiers in Materials

Received: *29 August 2019*
Accepted: *16 April 2020*
Published: *22 May 2020*

Citation:
Dong X, Li W, Yu J, Pan C, Xi J, Zhou Y and Wang X (2020) Magneto-Rheological Variable Stiffness and Damping Torsional Vibration Control of Powertrain System. Front. Mater. 7:121. doi: 10.3389/fmats.2020.00121

INTRODUCTION

With the gradual improvement of people's ride comfort requirements, the research of vehicle noise, vibration, and harshness (NVH) characteristics has become a hot spot. Many factors would affect the NVH performance of vehicles, among which the torsional vibration of the powertrain system is absolutely critical (Qing-Hua et al., 2015). The power of the vehicle is generated periodically in every second rotation of crankshaft for each cylinder creating dynamic forces on the crankshaft. The torque generated by the engine is the main reason for the torsional vibration of the automobile power system (Ye, 2012). As the torsional vibration energy of powertrain system is transmitted to the vehicle body, the vehicle will produce vibration and noise, which will ultimately affect the ride comfort.

In addition to improving and optimizing the control system of electronic fuel injection (EFI) engines, the most common method of suppressing torsional vibration is to install a torsional vibration absorber in the powertrain system. The common installation positions of the torsional vibration absorbers in the powertrain system are the engine output shaft or the specific inertia disks directly. The first type of effective torsional vibration absorber includes the dual mass flywheel (DMF), the centrifugal pendulum vibration absorber (CPVA) and the DMF with CPVA, etc. (Johann et al., 2014). The second type of torsional vibration absorber is the dynamic vibration

absorber, which is attached to the primary system. Dynamic vibration absorbers have attracted the attention of many scholars because they do not need to change the powertrain system significantly. Besides, Dynamic vibration absorbers can also effectively improve the torsional vibration response of the powertrain system in a large frequency range.

In recent years, with the emergence of various new intelligent materials, the research on semi-active dynamic vibration absorber is also prevailing. The semi-active dynamic vibration absorber can vary its inherent frequency to follow the external excitation frequency, which needs very little energy input. The frequency of dynamic vibration absorber can be changed by means of variable stiffness or variable inertia. Furthermore, the semi-active variable stiffness torsional vibration absorber becomes the most common type on account of its ease of control and simplicity of structure (Xu, 2010; Zhang, 2015). Davis et al. (1997) proposed a piezoelectric semi-active torsional vibration absorber, which controlled the stiffness of piezoelectric ceramics by changing the electric field and ultimately achieved semi-active control of the natural frequency of the absorber. Williams et al. (2002) used shape memory alloys as a variable stiffness core component and proposed a novel semi-active variable stiffness vibration absorber. Because the stiffness of the material varied with the working temperature, the working temperature could be changed by turning the power on or off. The variable stiffness characteristic of the magneto-rheological elastomer (MRE) under the external magnetic field made it applicable to the frequency-tunable absorber. A series of torsional vibration absorbers with simple structure and superior performances have been designed (Deng and Gong, 2007; Hoang, 2011; Fu et al., 2016; Qian et al., 2017; Wang and Jing, 2018; Yu et al., 2018). Nagaya et al. (1999) designed a MRE absorber and proposed a system with the MRE absorber, and then a relevant controller of the system with the MRE absorber was proposed by setting the torsional vibration amplitude of the system as the input signal and the minimum torsional vibration amplitude of the system response as the control objective. Through numerical simulation, Zhang and Li (2009) proved that the semi-active vibration absorber had a good damping effect by utilizing a real-time control strategy. Gao et al. (2018) realized the torsional vibration control of the system in a wide range of excitation frequency by configuring the MRE absorber groups in the system and using the input excitation frequency as the input signal. Huang et al. (2019), Sun et al. (2016) and Harris et al. (2017) applied MR fluid to the design of the variable stiffness and damping devices, and proved their effectiveness through prototype test.

At present, there are few studies on the application of magneto-rheological fluid in variable stiffness devices, especially torsional variable stiffness devices, and the research on variable stiffness devices mainly focuses on theoretical analysis and physical realization, which often ignores the practical limitations of the prototype, such as the range of variable stiffness values and other nonlinearities in an actual implementation.

This paper focuses on the application of MR fluid in a magneto-rheological variable stiffness and damping torsional vibration absorber (MR-VSDTVB), which is designed, fabricated and tested to demonstrate the output characteristics of MR-VSDTVB. Then, the research on the powertrain system with MR-VSDTVB is carried out. Variable stiffness and variable damping control strategy and its control performance will be investigated. The organization of this study is as follows. In Section 2, the vibration characteristics of a powertrain system are analyzed. The discussion on MR-VSDTVB is shown in Section 3. The human-simulated intelligent control (HSIC) algorithm of the powertrain system with MR-VSDTVB is investigated in Section 4. Section 5 reveals the simulation results and discussion. Conclusions are drawn in section 6.

VIBRATION CHARACTERISTICS OF THE POWERTRAIN SYSTEM

The automobile powertrain system is a typical multi-degree-of-freedom system. A front-mounted rear drive car powertrain system, which was proposed by Kang et al. (2014), etc. is adopted here. Based on the principle that the kinetic energy and potential energy of the system remain unchanged before and after simplification, the equivalent model is composed by simplifying the powertrain system as the inelastic inertia disks and the massless inertial axes, as shown in **Figure 1**. The corresponding relationship between the components of the powertrain system and the parameters in **Figure 1** is detailed in nomenclature to ensure the readability of the paper, which is not listed separately here. The red block in **Figure 1** is the proposed torsional vibration absorber with variable stiffness and variable damping.

Based on the equivalent model, the dynamic equation of the powertrain system can be obtained as shown in Equation (1). When $K_d = 0$ and $C_d = 0$, the equation is the differential equation of the currently common automobile powertrain system.

$$J\left\{\ddot{\theta}\right\} + K\{\theta\} + K_g\left\{\theta_g\right\} = \{T\} \tag{1}$$

$$J = \begin{pmatrix} J_1 \\ J_2 \\ J_3 \\ \vdots \\ J_{17} \end{pmatrix}, \{\theta\} = \begin{pmatrix} \theta_1 \\ \theta_2 \\ \theta_3 \\ \vdots \\ \theta_{17} \end{pmatrix}, K_g = \begin{pmatrix} 0 & 0 \\ \vdots & \vdots \\ C_d & K_d \\ \vdots & \vdots \\ 0 & 0 \end{pmatrix} \begin{matrix} \} 11 \\ \} 5 \end{matrix},$$

$$\left\{\theta_g\right\} = \begin{pmatrix} \dot{\theta}_{12} - \dot{\theta}_d \\ \theta_{12} - \theta_d \end{pmatrix}, T = \begin{pmatrix} 0 \\ T_{total} \\ T_{total} \\ T_{total} \\ T_{total} \\ 0 \\ \vdots \\ 0 \\ T_f \\ 0 \\ T_f \end{pmatrix}_{17\times 1}$$

$$
\mathrm{K}=\begin{pmatrix}
K_1 & -K_1 & 0 & 0 & 0 & 0 & 0 & 0 & 0 & 0 & 0 & 0 & 0 & 0 & 0 & 0 & 0\\
-K_1 & K_1+K_2 & -K_2 & 0 & 0 & 0 & 0 & 0 & 0 & 0 & 0 & 0 & 0 & 0 & 0 & 0 & 0\\
0 & -K_2 & K_2+K_3 & -K_2 & 0 & 0 & 0 & 0 & 0 & 0 & 0 & 0 & 0 & 0 & 0 & 0 & 0\\
0 & 0 & -K_3 & K_3+K_4 & -K_4 & 0 & 0 & 0 & 0 & 0 & 0 & 0 & 0 & 0 & 0 & 0 & 0\\
0 & 0 & 0 & -K_4 & K_4+K_5 & -K_5 & 0 & 0 & 0 & 0 & 0 & 0 & 0 & 0 & 0 & 0 & 0\\
0 & 0 & 0 & 0 & -K_5 & K_5+K_6 & -K_6 & 0 & 0 & 0 & 0 & 0 & 0 & 0 & 0 & 0 & 0\\
0 & 0 & 0 & 0 & 0 & -K_6 & K_6+K_7 & -K_7 & 0 & 0 & 0 & 0 & 0 & 0 & 0 & 0 & 0\\
0 & 0 & 0 & 0 & 0 & 0 & -K_7 & K_7+K_8 & -K_8 & 0 & 0 & 0 & 0 & 0 & 0 & 0 & 0\\
0 & 0 & 0 & 0 & 0 & 0 & 0 & -K_8 & K_8+K_9 & -K_9 & 0 & 0 & 0 & 0 & 0 & 0 & 0\\
0 & 0 & 0 & 0 & 0 & 0 & 0 & 0 & -K_9 & K_9+K_{10} & -K_{10} & 0 & 0 & 0 & 0 & 0 & 0\\
0 & 0 & 0 & 0 & 0 & 0 & 0 & 0 & 0 & -K_{10} & K_{10}+K_{11} & -K_{11} & 0 & 0 & 0 & 0 & 0\\
0 & 0 & 0 & 0 & 0 & 0 & 0 & 0 & 0 & 0 & -K_{11} & K_{11}+K_{12} & -K_{12} & 0 & 0 & 0 & 0\\
0 & 0 & 0 & 0 & 0 & 0 & 0 & 0 & 0 & 0 & 0 & -K_{12} & K_{12}+K_{13}+K_{15} & -K_{13} & 0 & -K_{15} & 0\\
0 & 0 & 0 & 0 & 0 & 0 & 0 & 0 & 0 & 0 & 0 & 0 & -K_{13} & K_{13}+K_{14} & -K_{14} & 0 & 0\\
0 & 0 & 0 & 0 & 0 & 0 & 0 & 0 & 0 & 0 & 0 & 0 & 0 & -K_{14} & K_{14} & 0 & 0\\
0 & 0 & 0 & 0 & 0 & 0 & 0 & 0 & 0 & 0 & 0 & 0 & -K_{15} & 0 & 0 & K_{15}+K_{16} & -K_{16}\\
0 & 0 & 0 & 0 & 0 & 0 & 0 & 0 & 0 & 0 & 0 & 0 & 0 & 0 & 0 & -K_{16} & K_{16}
\end{pmatrix}
$$

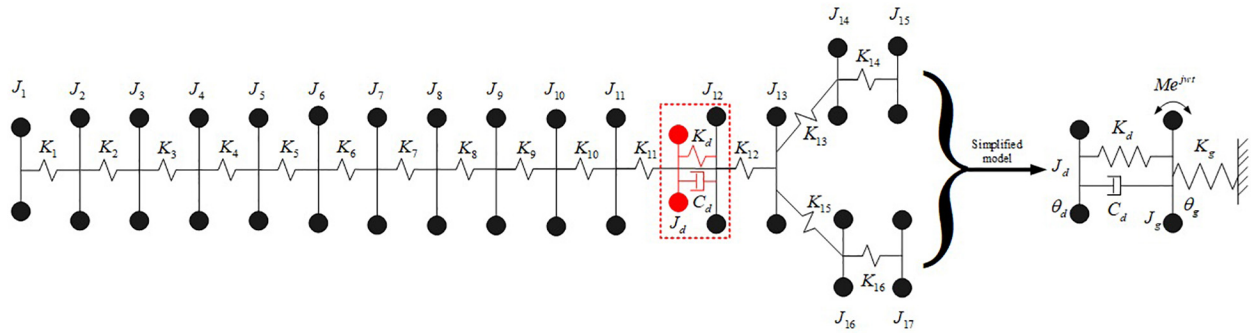

FIGURE 1 | System equivalent model with torsional vibration absorber.

The periodic fluctuating torque of the engine is the main excitation source of the powertrain system, including the torque T_g produced by the cylinder gas pressure and the inertial torque T_i of the rotating parts. The formulas of the output torque T_{total} of the engine are as follows (Robert, 2007).

$$T_g = \left(P_A A_g\right) R \sin\left(\omega t\right)\left[1+\frac{R}{l}\cos\left(\omega t\right)\right] \tag{2}$$

$$T_i = \frac{1}{2} m_B R^2 \omega^2 \left[\frac{R}{2l}\sin\left(\omega t\right) - \sin\left(2\omega t\right) - \frac{3R}{2l}\sin\left(3\omega t\right)\right] \tag{3}$$

$$T_{total} = T_g + T_i \tag{4}$$

The equivalent damping torque of the powertrain system is formulated as follows.

$$T_f = \left(F_w + F_r\right) r_{wheel}/i_0 \tag{5}$$

$$F_w = \frac{C_D A V^2}{21.15} \tag{6}$$

$$F_r = \chi m_v g \tag{7}$$

TABLE 1 | Natural frequency value and sensitivity analysis.

Order	1th	2th	3th	4th	5th	6th
Natural frequency (Hz)	1.59	6.82	32.06	36.70	64.01	211.03
Sensitivity analysis	J_{16}	J_{15}	J_5	J_{13}	J_{12}	J_8

To solve the inherent characteristics of the powertrain system, the torsional differential equation of the un-damped free vibration of the powertrain system is obtained as follow.

$$J\left\{\ddot{\theta}\right\} + K\left\{\theta\right\} = \left\{0\right\} \tag{8}$$

The natural frequencies and sensitivity analysis of the powertrain system are obtained as shown in **Table 1**.

A four-cylinder four-stroke engine is adopted here. The second-order main harmonic is the main excitation of the engine and the main factor that causes the torsional vibration of the powertrain system. From the following formula, the frequency of the second-order main harmonic of engine excitation can be obtained.

$$f = \frac{r \cdot n_p}{60} \tag{9}$$

Here r = 2 is set. It is well known that the rotating velocity range of an automobile engine is generally between 1500 and 6000 rpm. Formula 9 and **Table 1** show that the rotating

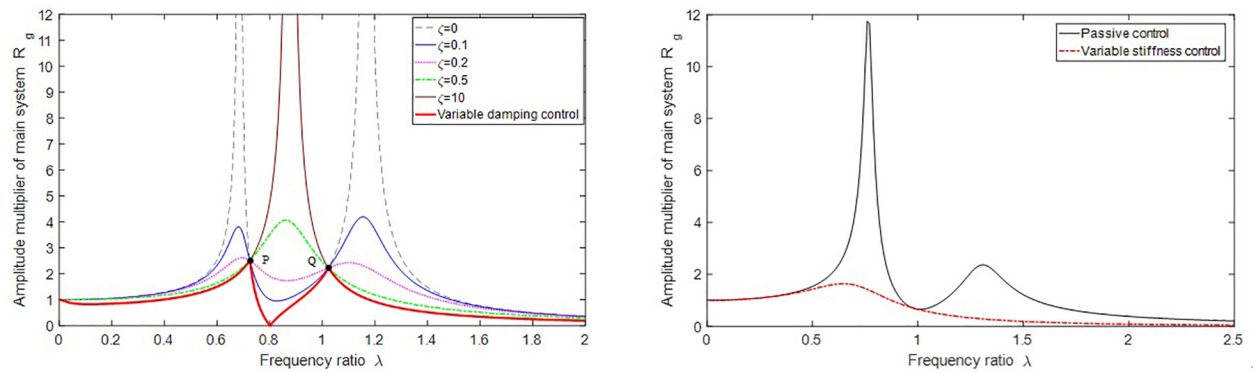

FIGURE 2 | Effect of damping and stiffness parameter control of torsional vibration absorber on the powertrain system.

velocity corresponding to the 5th order natural frequency of the powertrain system is 1920 rpm, which is within the normal working rotating velocity range of the engine. When the engine approaches this rotating velocity, resonance will occur, which will affect the ride comfort of the vehicle, and may cause fatigue damage to the system components. The emphasis of this paper is to effectively suppress the torsional vibration of the powertrain system near to the rotating velocity of 1920 rpm by installing a torsional vibration absorber.

According to the sensitivity analysis of the moment of inertia to the eigenvalues of the system, it can be seen that the moment of inertia of the J_{12} inertia disk is most sensitive to the 5th-order natural frequency of the system, which also determines the installation position of the torsional vibration absorber as shown in **Figure 1**.

To analyze the vibration reduction mechanism of the torsional vibration absorber, a two-degree-of-freedom simplified torsional vibration model is obtained as shown on the right side of **Figure 1** by taking the powertrain system as a whole. The dynamic equation of the two-degree-of-freedom torsional vibration model is as follows.

$$\begin{cases} J_g \ddot{\theta}_g + C_d(\dot{\theta}_g - \dot{\theta}_d) + K_d(\theta_g - \theta_d) + K_g\theta_g = M(t) \\ J_d \ddot{\theta}_d - C_d(\dot{\theta}_g - \dot{\theta}_d) - K_d(\theta_g - \theta_d) = 0 \end{cases} \tag{10}$$

Take the excitation torque as $M(t) = Me^{jwt}$. Assume that the solution to equation (10) is as follows.

$$\theta_g = A_g e^{i\omega t}\theta_d = A_d e^{i\omega t} \tag{11}$$

Then the amplitude of the main system can be obtained.

$$A_g = \frac{M\left(K_d - J_d\omega^2 + iC_d\omega\right)}{\left[\left(K_g - J_g\omega^2\right)\left(K_d - J_d\omega^2\right) - J_dK_d\omega^2\right] + iC_d\omega\left(K_g - J_g\omega^2 - J_d\omega^2\right)} \tag{12}$$

Here we introduce the following parameter variables.

$$\mu = \frac{J_d}{J_g}, \lambda = \frac{\omega}{\omega_g}, \gamma = \frac{\omega_d}{\omega_g}, A_{st} = \frac{M}{K_g}, \zeta = \frac{C_d}{2\sqrt{J_dK_d}}.$$

TABLE 2 | Equivalent model parameters of the powertrain system.

Number	The moment of inertia ($kg \cdot mm^2$)	Torsional stiffness (Nm/rad)
1	141	20883.49
2	5386	99891.12
3	5512	99891.12
4	5512	99891.12
5	5421	45362.60
6	85200	2109.55
7	1171	3155.81
8	551	89160.87
9	2332	5340.25
10	1592	15831.01
11	2898	28871.35
12	2722	1919.67
13	547	278.06
14	11722	331.63
15	1554162	303.06
16	11722	331.63
17	1554162	

The amplitude multiplier of the main system R_g can be expressed as.

$$R_g = \left|\frac{A_g}{A_{st}}\right| = \sqrt{\frac{\left(\gamma^2 - \lambda^2\right)^2 + (2\zeta\lambda)^2}{(2\zeta\lambda)^2\left(\lambda^2 - 1 + \mu\lambda^2\right)^2 + \left[\mu\lambda^2\gamma^2 - \left(\lambda^2 - 1\right)\left(\lambda^2 - \gamma^2\right)\right]^2}} \tag{13}$$

As a typical two-degree-of-freedom system, when the absorber's damping ratio ς is changed, the system's amplitude radio curves with different damping ratios can be obtained. When the natural frequency ratio of torsional vibration absorber to the main system $\gamma = 1$ is set, the passive control curve in the right picture of **Figure 2** can be obtained. The following results can be obtained by introducing $f = \frac{\omega}{\omega_d}$ into Equation (13).

$$R_g = \left|\frac{A_g}{A_{st}}\right| = \sqrt{\frac{\left(1 - f^2\right)^2 + \left(2\zeta\frac{f^2}{\lambda}\right)^2}{\left(2\zeta\frac{f^2}{\lambda}\right)^2\left(\lambda^2 - 1 + \mu\lambda^2\right)^2 + \left[\mu\lambda^2 - \left(\lambda^2 - 1\right)\left(f^2 - 1\right)\right]^2}} \tag{14}$$

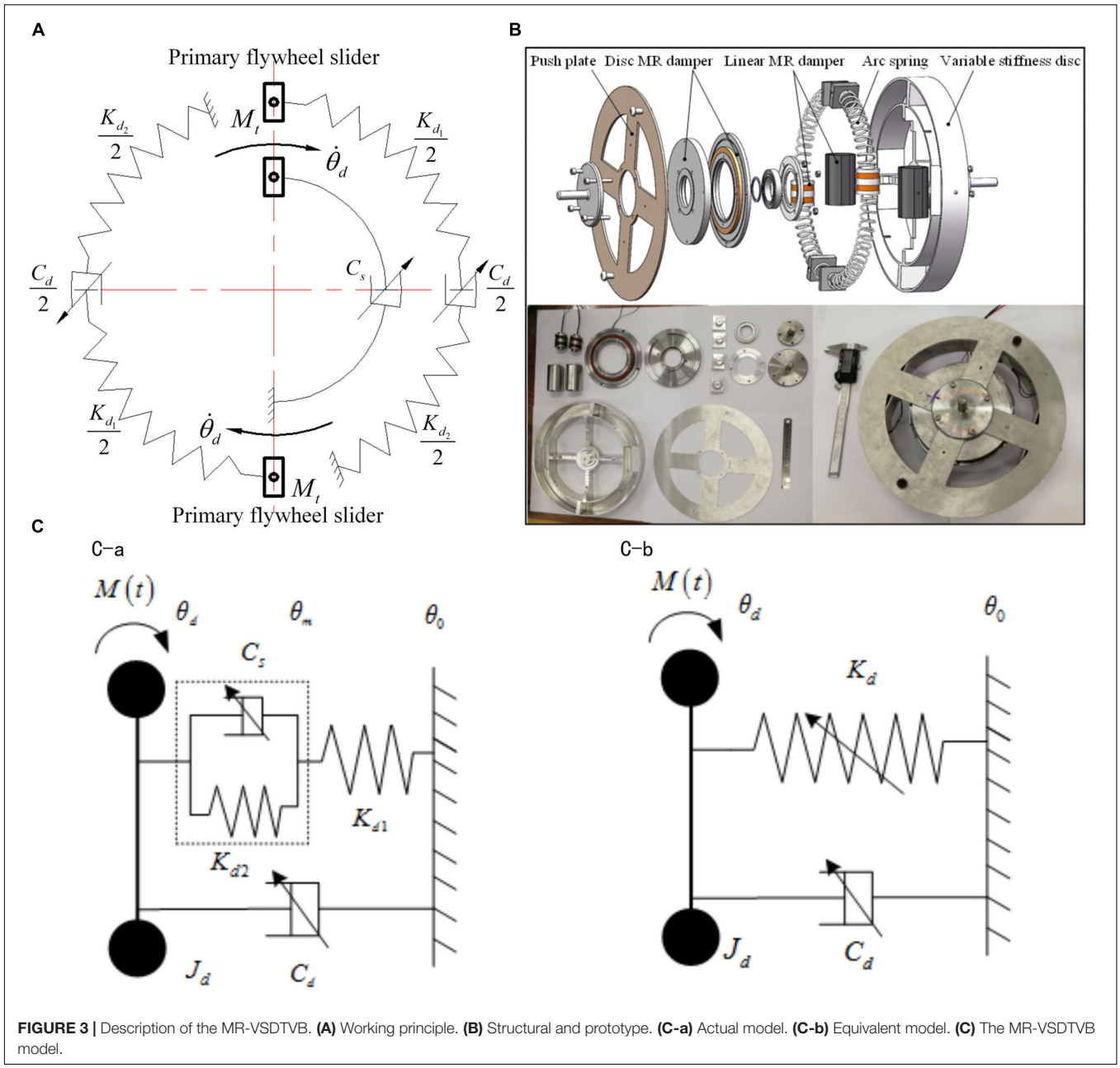

FIGURE 3 | Description of the MR-VSDTVB. **(A)** Working principle. **(B)** Structural and prototype. **(C-a)** Actual model. **(C-b)** Equivalent model. **(C)** The MR-VSDTVB model.

Where f is the ratio of the excitation frequency to the natural frequency of the torsional vibration absorber. When $f = 1$ is set, it means that the natural frequency of the torsional vibration absorber changes with the change of the excitation frequency. Hence, the variable stiffness control curve in the right picture of **Figure 2** is obtained. It can be seen that the vibration response of the main system can be effectively improved by real-time control of the damping and stiffness of the torsional vibration absorber.

Here the ratio $\mu = \frac{I_d}{I_g}$ is obtained and the equivalent model parameters of the powertrain systerm are shown in **Table 2**. The moment of inertia J_d of the torsional absorber can be selected. Since the required control frequency of the powertrain system is $f_5 = 64Hz$, the stiffness adjustment range of the MR-VSDTVB needs to cover the stiffness value corresponding to the frequency f_5.

MR VARIABLE STIFFNESS AND DAMPING VIBRATION ABSORBER

Sections 2 verifies that the variable stiffness and damping torsional vibration absorber can effectively suppress the torsional vibration of the main system within a certain frequency range, through changing the stiffness and damping values in real time. A magneto-rheological variable stiffness and damping torsional

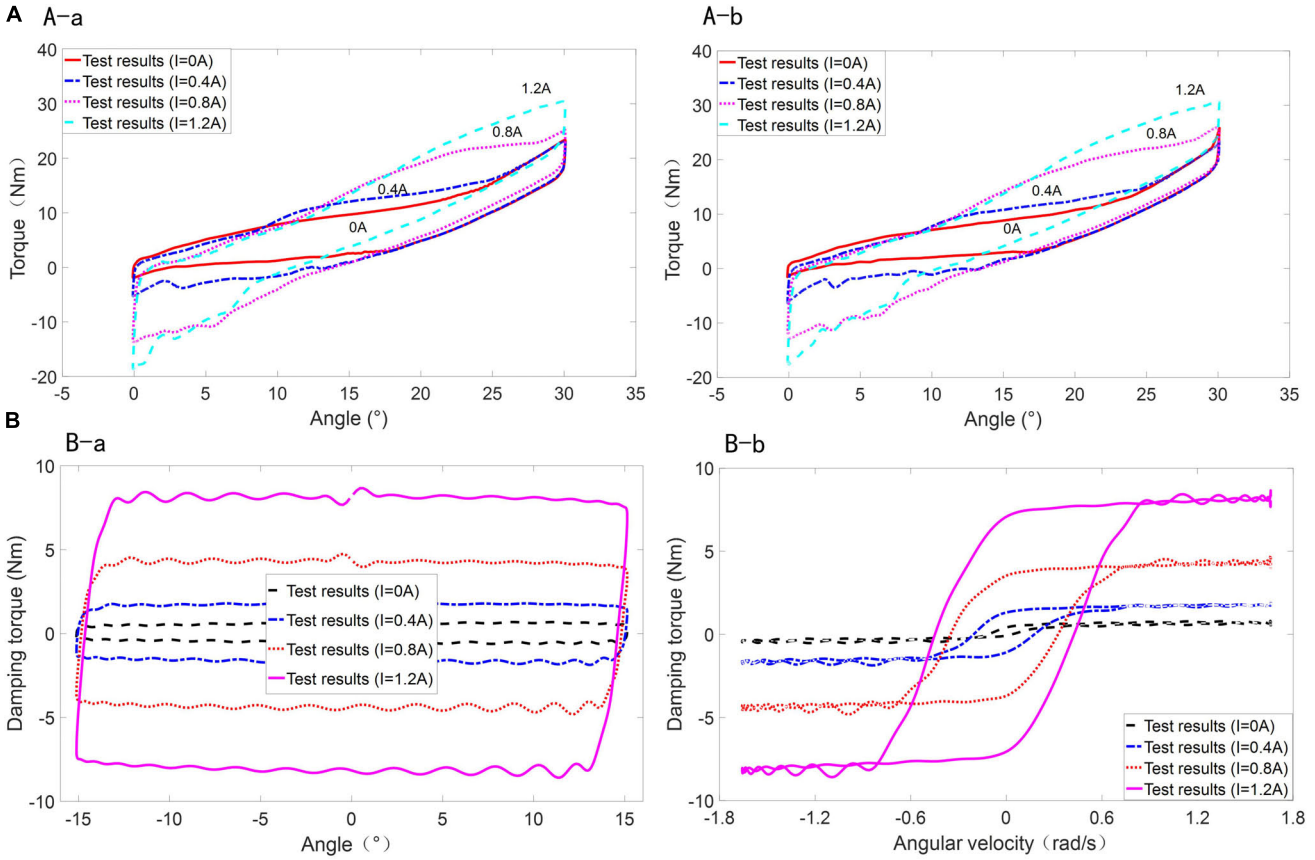

FIGURE 4 | The test curve of MR-VSDTVB under different current. **(A-a)** Rotating angle-torque (0.2 Hz). **(A-b)** Rotating angle-torque (0.6 Hz). **(A)** Variable stiffness element for MR-VSDTVB. **(B-a)** Rotating angle-torque (1.0 Hz). **(B-b)** Rotating velocity-torque (1.0 Hz). **(B)** Variable damping element for MR-VSDTVB.

vibration absorber (MR-VSDTVB) was designed and fabricated to realize the research on torsional vibration control of the powertrain system.

Structure and Working Principle of MR-VSDTVB

Figures 3A,B show that the MR-VSDTVB consists of a rotating variable damping element and a rotating variable stiffness element in parallel. The core component of the rotating variable damping element is a disk MR damper. The rotating variable stiffness element consists of two sets of variable stiffness components which are symmetrically installed in the variable stiffness disc groove. Each set of variable stiffness components involes a linear MR damper and two arc springs with different stiffness, which are placed at both ends of the damper.

When the primary flywheel and the sliders of the MR-VSDTVB rotate under the action of the external torque, the primary and secondary flywheels of the MR-VSDTVB rotate relatively to each other accordingly. In addition, the torque between them is composed of the damping torque generated by variable damping element and the stiffness generated by variable stiffness element. The semi-active adjustment of the damping torque of variable damping element can be achieved by changing the current applied to the disk MR damper. The stiffness torque generated by variable stiffness element is composed of the damping forces generated by linear MR dampers, and the spring forces generated by compression deformation of the springs K_{d2} and K_{d1}. The damping forces provided by the linear MR dampers can be adjusted by changing the currents applied to coils of the dampers, and compressive deformation of the springs K_{d2} and K_{d1} can be changed, respectively, without changing the total deformation amount. Finally, the purpose of indirectly adjusting the stiffness of variable stiffness element is achieved. The details of the MR-VSDTVB are specified in paper (Wang, 2019), which will not be described here. The MR-VSDTVB model can be obtained from the working principle and structure of the MR-VSDTVB as shown in **Figure 3C**.

Figure 3C-a shows that MR damper C_s is connected in parallel with arc spring K_{d2}, then connected in series with arc spring K_{d1} to form equivalent variable stiffness element, and finally connected in parallel with MR damper C_d to form the MR-VSDTVB. The equations of motion for the system shown in **Figure 3C-a** are as follows.

$$\begin{cases} J_d \cdot \ddot{\theta}_d + C_s \cdot (\dot{\theta}_d - \dot{\theta}_m) + K_{d2} \cdot (\theta_d - \theta_m) + C_d \cdot (\dot{\theta}_d - \dot{\theta}_0) = M(t) \\ K_{d1} \cdot (\theta_m - \theta_0) = C_s \cdot (\dot{\theta}_d - \dot{\theta}_m) + K_{d2} \cdot (\theta_d - \theta_m) \end{cases} \quad (15)$$

TABLE 3 | Parameters of the MR- VSDTVB model.

Positive rotating velocity				Negative rotating velocity			
d_0	2.38	e_0	−5.58	d_0	9.89	e_0	−17.64
g_0	−6.18	h_0	−0.22	g_0	−6.62	h_0	−0.66
d_1	−2.69	e_1	6.30	d_1	15.11	e_1	−27.41
g_1	3.14	h_1	1.98	g_1	12.46	h_1	−0.33
d_2	0.29	e_2	−0.70	d_2	−3.21	e_2	6.41
g_2	−1.37	h_2	−0.31	g_2	−3.13	h_2	0.39
d_3	3.78e-2	e_3	−7.74e-2	d_3	0.25	e_3	−0.56
g_3	0.24	h_3	3.09e-2	g_3	0.31	h_3	−0.07
d_4	−7.19e-3	e_4	1.44e-2	d_4	−9.63e-3	e_4	2.37e-2
g_4	−1.79e-2	h_4	−1.66e-3	g_4	−1.53e-2	h_4	4.9e-3
d_5	3.29e-4	e_5	−6.4e-4	d_5	1.82e-4	e_5	−5.1e-4
g_5	5.8e-4	h_5	4.43e-5	g_5	3.71-4	h_5	−1.6e-4
d_6	−4.65e-6	e_6	8.91e-6	d_6	−1.41e-6	e_6	4.55e-6
g_6	−6.82e-6	h_6	−4.39e-7	g_6	−3.62e-6	h_6	1.83e-6
b_1	1.75	b_2	−6.4	b_3	3.28	b_4	0.09
b_5	−0.29	b_6	0.15	b_7	10.23	b_8	0.65
b_9	−12.22	b_{10}	28.82	b_{11}	−2.26	b_{12}	−3.73
b_{13}	9.61	b_{14}	−3.13	f_0	0.27		

Let the excitation torsion torque $M(t) = M_0 e^{iwt}$, $\theta_0 = 0$, and it can be obtained from the upper equations.

$$\frac{\Theta_d}{M_0} = \frac{1}{\begin{array}{c}-J_d \cdot \omega^2 + K_{d1} - (K_{d1}^2 \cdot (K_{d1} + K_{d2})/(K_{d1} + K_{d2})^2 + C_s^2 \cdot \omega^2) \\ +i \cdot (C_d + (K_{d1}^2 \cdot C_s/(K_{d1} + K_{d2})^2 + C_s^2 \cdot \omega^2)) \cdot \omega\end{array}} \tag{16}$$

The corresponding transfer function of the equivalent model shown in **Figure 3C-b** is

$$\frac{\Theta_d}{M_0} = \frac{1}{-J_d \cdot \omega^2 + K_d + i \cdot C_d \cdot \omega} \tag{17}$$

Comparing Equation (17) with Equation (16), the equivalent stiffness and damping coefficients are as follows.

$$\begin{aligned} K_d &= K_{d1} - \frac{K_{d1}^2 \cdot (K_{d1} + K_{d2})}{(K_{d1} + K_{d2})^2 + C_s^2 \cdot \omega^2} \\ &= K_{d1} \cdot \left[1 - \frac{1+\eta}{(1+\eta)^2 + \left(\frac{C_s \cdot \omega}{K_{d1}}\right)^2}\right] \end{aligned} \tag{18}$$

$$C_d' = C_d + \frac{K_{d1}^2 \cdot C_s}{(K_{d1} + K_{d2})^2 + C_s^2 \cdot \omega^2} = C_d + \frac{1}{\frac{(1+\eta)^2}{C_s} + C_s \cdot \left(\frac{\omega}{K_{d1}}\right)^2} \tag{19}$$

Where $\eta = \frac{K_{d2}}{K_{d1}}$. Equations (18) and (19) indicate that equivalent stiffness K_d is only related to C_s, and C_d' is influenced by C_s and C_d. If $C_s = 0$, the n$K_d = K_{d1} \cdot K_{d2}/(K_{d1} + K_{d2})$, $C_d' = C_d$.If $C_s = \infty$, then $K_d = K_{d1}$, $C_d' = C_d$. Hence, adjusting the damping coefficient C_s can play an equivalent role in regulating the stiffness of the system. Although adjusting the damping coefficients C_s and C_d can adjust the equivalent damping C_d' of the system, the effect of damping C_d on the equivalent damping of the system is much greater than that of damping C_s. Consequently, two MR dampers C_s and C_d with controllable damping coefficients can be used to adjust the equivalent damping and stiffness of the system approximately independently.

Control Modeling of MR-VSDTVB

Considering that the variable stiffness element and variable damping element of MR-VSDTVB are arranged in parallel, the test scheme adopted here is to test the mechanical characteristics of the two elements separately. The performances of MR-VSDTVB under different excitation frequencies, different excitation angular amplitudes, and different currents were tested on the MTS test bench. The stiffness and damping mechanical properties of MR-VSDTVB were tested, respectively, and the test curves of **Figures 4A,B** are selected as representative for display.

Figure 4A shows that the torque required by MR-VSDTVB at the same rotation angle increases with the increase of current, which also indicates that the stiffness of MR-VSDTVB increases gradually.

It can be seen from **Figure 4B-a** that under the same amplitude and frequency conditions, the damping force of MR-VSDTVB also increases continuously with the increment of current, so is the envelope of the power diagram. Consequently, the energy consumption of MR-VSDTVB increases with the increase of current. From **Figure 4B-b**, it is known that the damping torque of MR-VSDTVB increases with the increment of the current at the same rotation velocity.

Figures 4A,B show that the stiffness force and damping force of MR-VSDTVB have a controllable characteristic. The semi-active control of the stiffness and damping of the MR-VSDTVB can be achieved indirectly by controlling the coil currents.

According to the characteristic analysis of the test curves of the MR-VSDTVB's variable stiffness element and variable damping element, it is found that the polynomial model is suitable for the modeling of the variable stiffness element T_d, and the hyperbolic tangent model is suitable for the modeling of the variable damping element T_c. The mathematical expressions of the hyperbolic tangent model and polynomial model are as follows.

$$T_c = c \cdot \omega + k \cdot \theta + \alpha \tanh(\beta \cdot \omega + \delta sign(\theta)) + f_0 \tag{20}$$

$$T_d = \sum_i^n a_i \omega^i \tag{21}$$

Where $c = b_1 I^2 + b_2 I + b_3$, $k = b_4 I^2 + b_5 I + b_6$, $\alpha = b_7 I + b_8$, $\beta = b_9 I^2 + b_{10} I + b_{11}$, $\delta = b_{12} I^2 + b_{13} I + b_{14}$, $a_i = d_i I^3 + e_i I^2 + g_i I + h_i$ and I is the applied current input.

By fitting the test data with the above mathematical models, the parameters of the mathematical models are obtained as shown in **Table 3**.

Equations (20) and (21) may be expressed as.

$$\left\{\begin{array}{l} \min \xi_1(I) = abs \left\{\begin{array}{l} T_c - (b_1 I^2 + b_2 I + b_3) \cdot \omega + (b_4 I^2 + b_5 I + b_6) \cdot \theta \\ +(b_7 I^2 + b_8 I + b_9) \tanh((b_{10} I + b_{11}) \cdot \omega \\ +(b_{12} I + b_{13}) sign(\theta)) + f_0 \end{array}\right\} \\ s.t.\ \ 0 \le I \le 2 \end{array}\right. \tag{22}$$

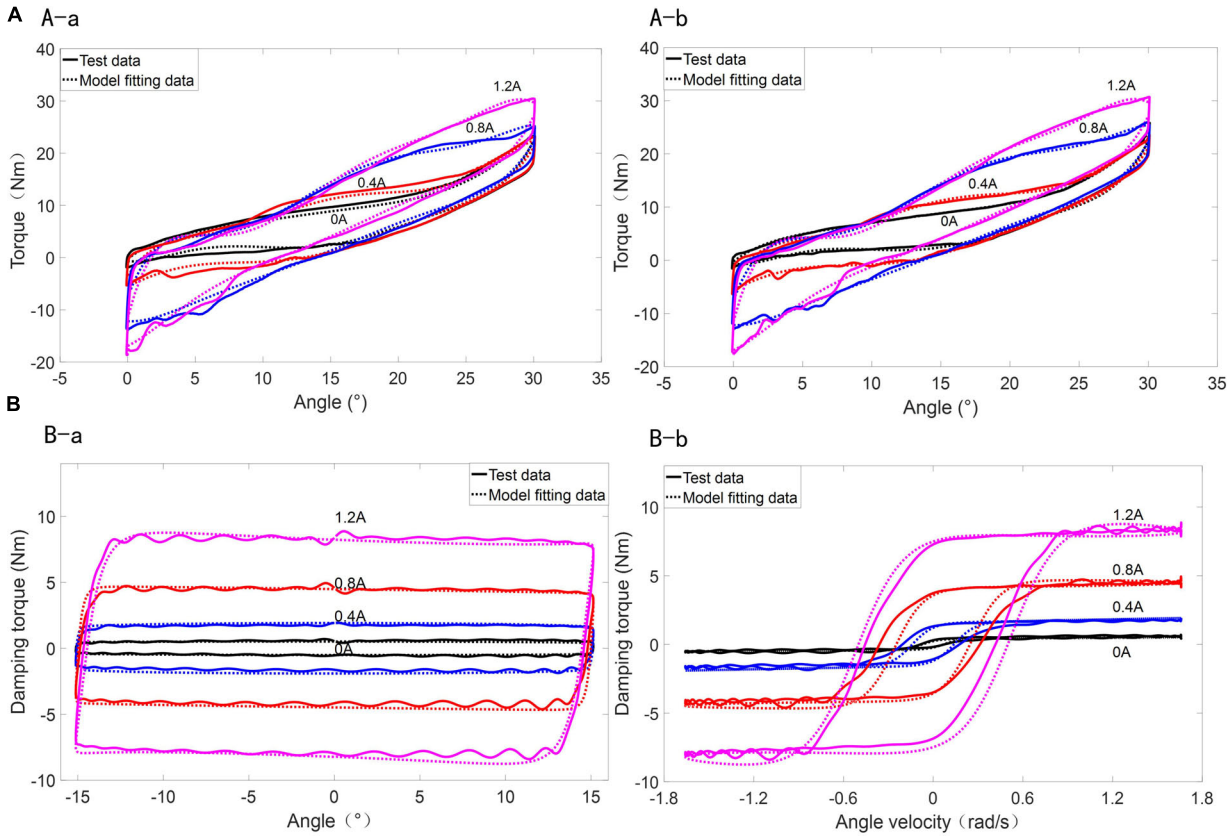

FIGURE 5 | Model Prediction of the MR-VSDTVB. **(A-a)** Rotating angle-torque (0.2 Hz). **(A-b)** Rotating angle-torque (0.6 Hz). **(A)** Model prediction of variable stiffness element for the MR-VSDTVB. **(B-a)** Rotating angle-torque (1.0 Hz). **(B-b)** Rotating velocity-torque (1.0 Hz). **(B)** Model prediction of variable damping element for the MR-VSDTVB.

$$\begin{cases} \min \xi_2(I) = abs\left\{T_d - \sum_i^n (g_i I + h_i)\omega^i\right\} \\ s.t. \quad 0 \le I \le 2 \end{cases} \tag{23}$$

For functions (22) and (23), the optimization method, such as the Golden Section method, can be used to obtain the required control currents of the variable stiffness element and the variable damping element (Aliases are the inverse models), respectively. In the actual system test, the look-up table method can be used to ensure the response speed of the real-time control.

$$I_c = \min \xi_1^{-1}(I) \tag{24}$$

$$I_d = \min \xi_2^{-1}(I) \tag{25}$$

The control currents of the variable damping element I_c and the variable stiffness element I_d are used for semi-active control of the MR-VSDTVB's damping torque and stiffness torque, respectively.

The polynomial model of the variable stiffness element and hyperbolic tangent model of the variable damping element are compared with the test data of MR-VSDTVB as shown in **Figures 5A,B**.

Figures 5A,B show that the mathematical models used here can approximate the test data well and describe the hysteresis characteristics of MR-VSDTVB under the illustrated frequency and amplitude as well as different currents. Similar results are also found at other excitation frequencies and amplitudes. **Figure 5** also shows that when the torque of the variable stiffness element of MR-VSDTVB is known at any relative angle, the corresponding stiffness can be obtained, which reveals the stiffness and the torque are both controllable and available in real time.

HUMAN-SIMULATED INTELLIGENT CONTROL (HSIC) ALGORITHM OF THE POWERTRAIN SYSTEM WITH MR-VSDTVB

The Origin of HSIC Algorithm

To effectively suppress the torsional vibration of the powertrain system, a human-simulated intelligent controller (HSIC) is designed. The original HSIC algorithm, which was first proposed by Zhou and Bai (1983) in 1983, has become a fundamental and systematic method used in resolving some general industrial

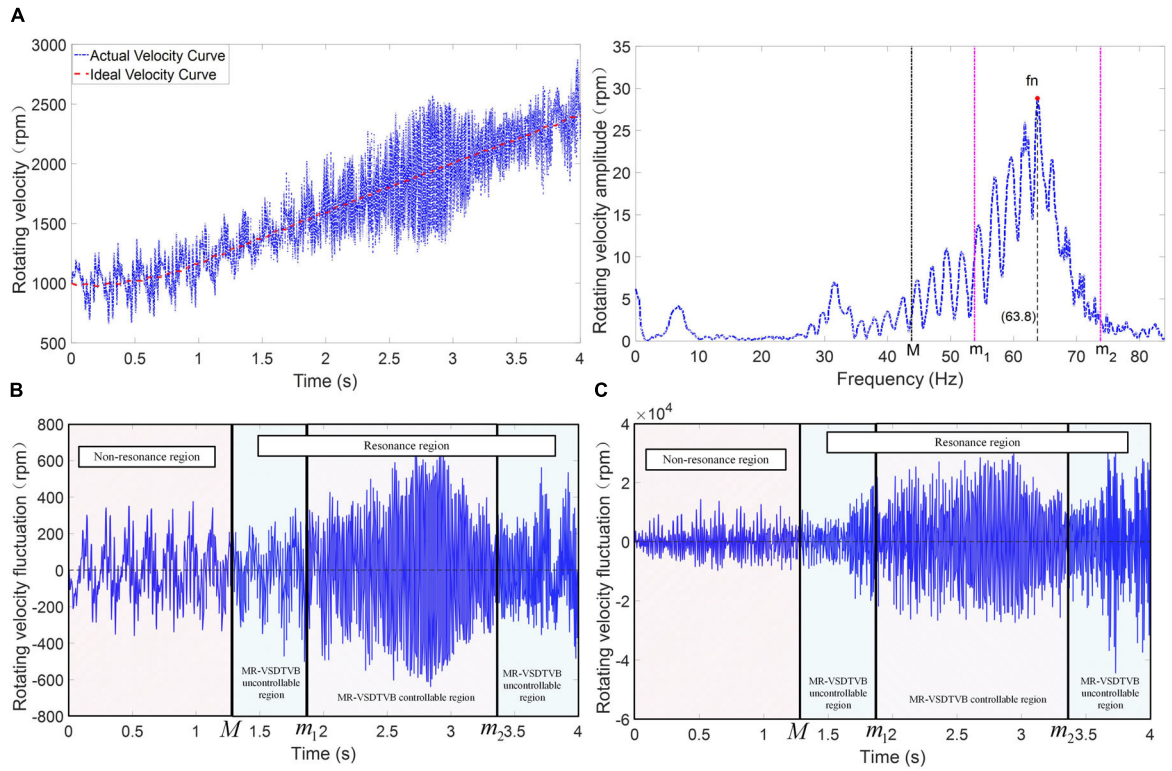

FIGURE 6 | Control input signal of the powertrain system. **(A)** Rotating velocity-time relationship and amplitude-frequency relationship. **(B)** Rotating velocity fluctuation error. **(C)** Rotating acceleration fluctuation error.

control problems for the last 30 years. In recent years, the HSIC theory has been further advanced through combing with the schema theory of modern cognitive science. After many years of research, HSIC theory based on sensory-motor intelligent schema (SMIS) has come into being (Li et al., 2004). The theory provides a more effective and systematic method in resolving some complex control problems.

Design of HSIC Controller

By setting the engine cylinder pressure in the time domain, the ideal rotating velocity of the main reducer's shaft is obtained from the design of the test plan. In the numerical simulation process, the ideal rotating velocity of the main reducer's shaft is obtained through the transmission ratio of the powertrain system. The input shaft of the main reducer actual rotating velocity-time relationship and ideal rotating velocity-time relationship are shown in **Figure 6A**. In the process of acceleration, the difference between the actual rotating velocity curve and the ideal rotating velocity curve are selected as the rotating velocity fluctuation error. The photograph on the right side of **Figure 6A** is the amplitude-frequency curve, which is obtained by Fourier transforming of the rotating velocity curve of the main reducer's input shaft.

The system excitation main frequency f_e, the rotating velocity fluctuation error and the rotating acceleration fluctuation error (error e and error derivative $\dot{e}$) of the main reducer's input shaft are selected as input signals as shown in **Figure 6**. The excitation frequency f_e is used to judge the state of the system. The resonance frequency f_n of the powertrain system, which is shown in the photograph on the right side of **Figure 6A**, is basically consistent with the 5th natural frequency of the powertrain system shown in **Table 1**. The photograph on the right side of **Figure 6A** shows that the region near the resonance frequency f_n is set as the resonance region, and the remaining region is set as non-resonant region. The second section shows that the torsional vibration of the system in the resonance region can be suppressed to a large extent by adjusting the MR-VSDTVB stiffness to make the natural frequency consistent with the excitation frequency of the powertrain system. Because the natural frequency adjustment of the MR-VSDTVB does not cover the entire resonance region in the design and test of the MR-VSDTVB, the resonance region is divided into the MR-VSDTVB controllable region and the MR-VSDTVB uncontrollable region in the actual control as shown in **Figure 6**. The controller divides the state characteristic information space of the system into the following three regions according to **Figure 6**.

$$\begin{cases} \text{Resonant and MR}-VSDTVB \text{ controllable region}: & m_1 \le f_e \le m_2 \\ \text{Resonant and MR}-VSDTVB \text{ uncontrollable region}: & -M \le f_e \le m_1 or m_2 \le f_e \le M \\ \text{Non}-\text{resonant region}: & |f_e - f_n| > M \end{cases} \tag{26}$$

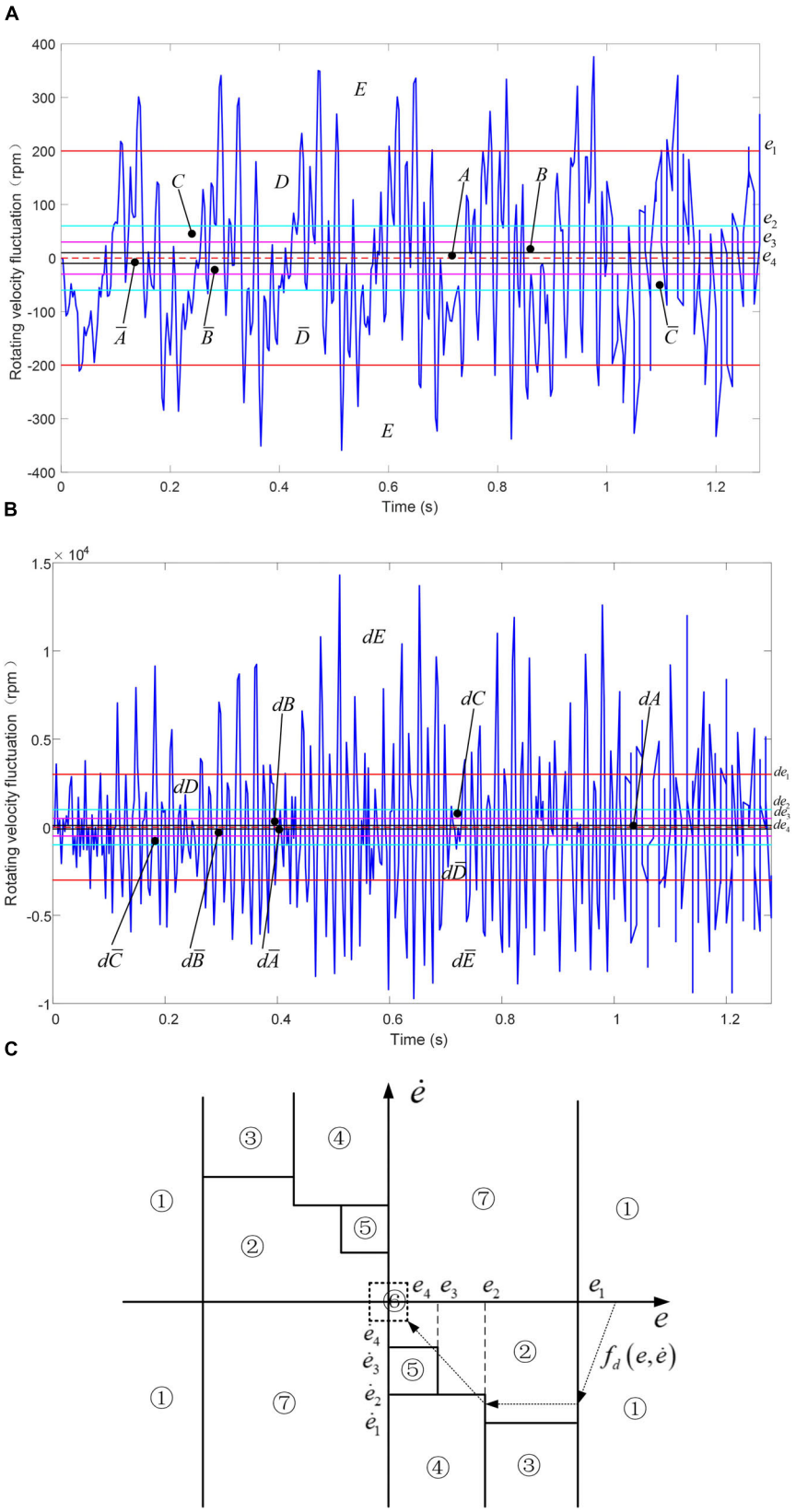

FIGURE 7 | Error Classification of HSIC. **(A)** Rotating velocity fluctuation error in non-resonant region. **(B)** Rotating acceleration fluctuation error in non-resonant region. **(C)** Feature model of HSIC.

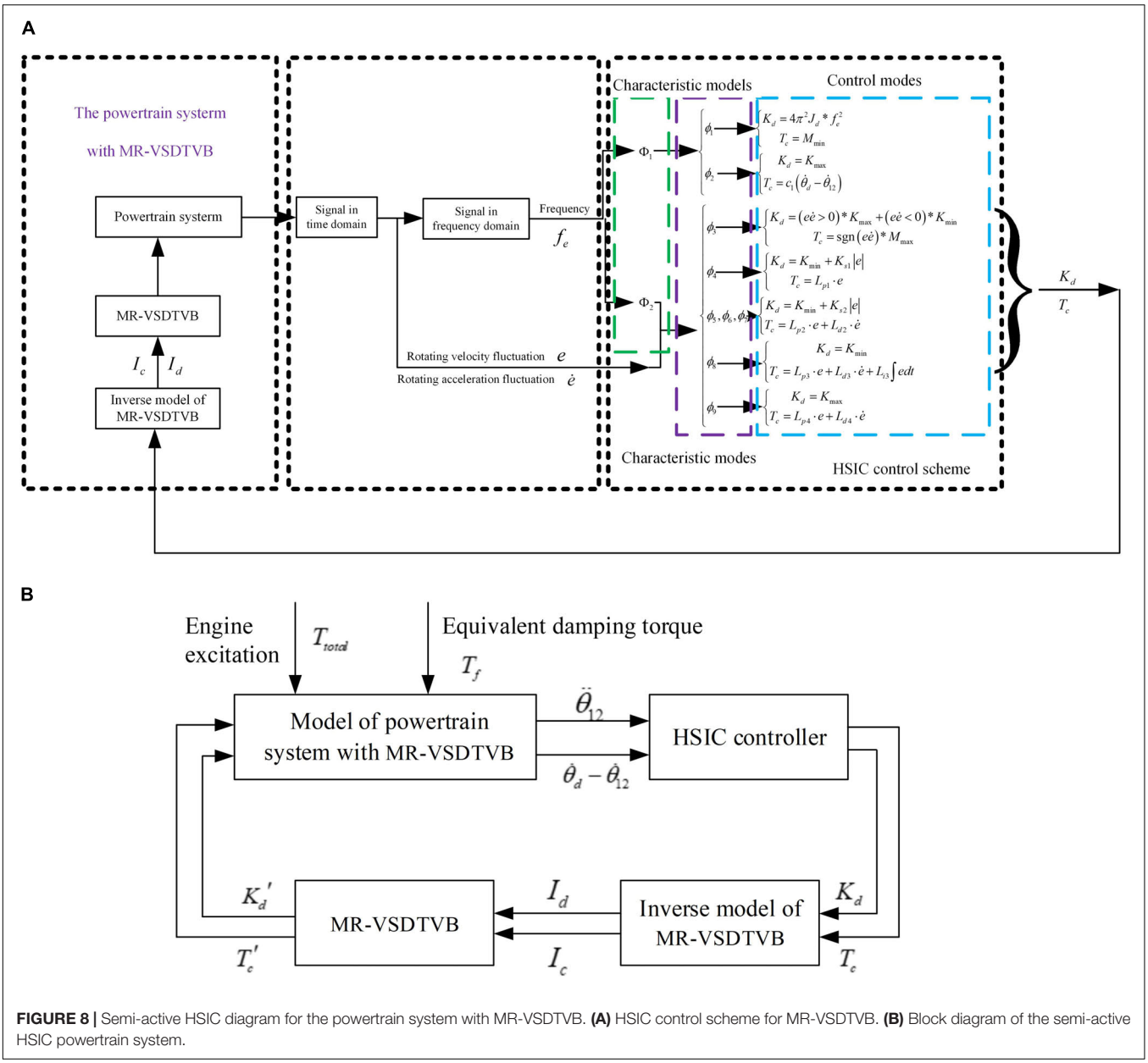

FIGURE 8 | Semi-active HSIC diagram for the powertrain system with MR-VSDTVB. **(A)** HSIC control scheme for MR-VSDTVB. **(B)** Block diagram of the semi-active HSIC powertrain system.

Where f_n represents the 5th natural frequency of the powertrain system, which is approximately 64 Hz. M denotes the range of the resonance region. M = 20 is adopted according to the description of **Figure 6**. $[m_1 m_2]$ represents the operating frequency range of MR-VSDTVB.

For the non-resonant region as shown in **Figures 7A,B**, four thresholds e_1, e_2, e_3 and e_4 are set to divide the rotating velocity fluctuation error curve into $A - \bar{A}$, $B - \bar{B}$, $C - \bar{C}$, $D - \bar{D}$, and $E - \bar{E}$ regions according to fluctuation error value. Similarly, four thresholds de_1, de_2, de_3 and de_4 are set to divide the rotating acceleration fluctuation error curve into $dA - d\bar{A}$, $dB - d\bar{B}$, $dC - d\bar{C}$, $dD - d\bar{D}$ and $dE - d\bar{E}$ regions. Different control parameters and control strategies are selected to control the torsional vibration of the system under different combinations of rotating velocity fluctuation region and rotating acceleration fluctuation region.

Feature model of HSIC in non-resonant region is shown in **Figure 7C**. The abscissa is represented by the rotating velocity fluctuation$e$, and the ordinate is represented by the rotating acceleration fluctuation$e$. **Figure 7C** shows that the whole region is transformed into seven characteristic modes, and the dotted lines indicate the desired phase trajectory f_d $(e, \dot{e})$.

The ideal objective for controlling the error trajectory is to make the rotating velocity fluctuation error and the rotating acceleration fluctuation error both reach zero, and the actual

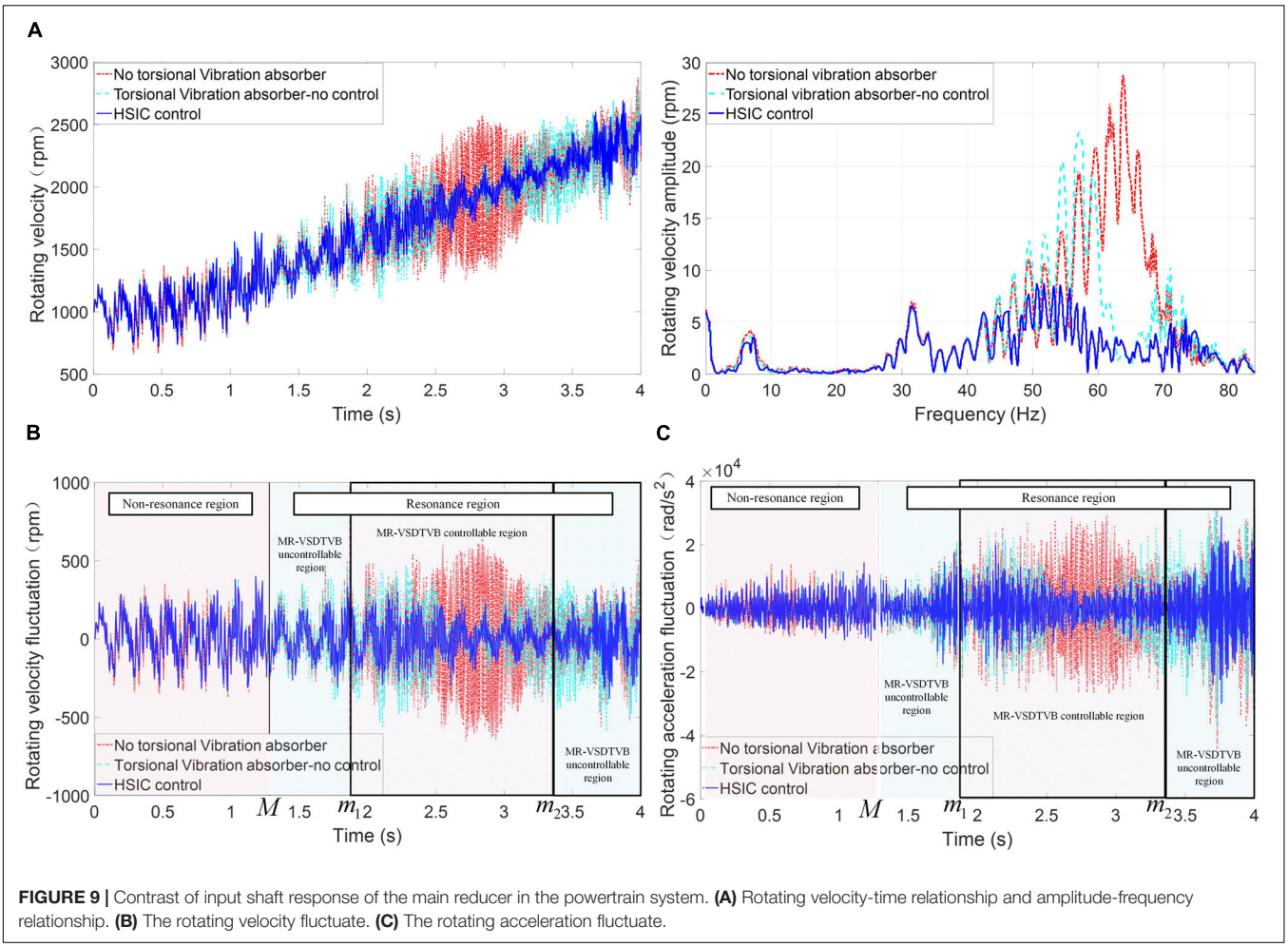

FIGURE 9 | Contrast of input shaft response of the main reducer in the powertrain system. **(A)** Rotating velocity-time relationship and amplitude-frequency relationship. **(B)** The rotating velocity fluctuate. **(C)** The rotating acceleration fluctuate.

rotating velocity follows the ideal rotating velocity of the shaft of the main reducer as shown in **Figure 6A**. When there are errors in the system response, the error trajectory is adjusted along the phase trajectory curve in **Figure 7C** from the larger error regions to the smaller error regions, and finally the desired minimum errors are expected.

Sensed Schema

A sensed schema group can be formulated by:

$$S_p =< R_s, Q, K, \otimes, \Phi >$$

The characteristic primitive set is chosen according to the states of the powertrain system, which can be expressed as follow.

$$Q_1 = \{q_1, q_2\}, Q_2 = \{q_3, q_4, q_5, q_6, q_7, q_8, q_9, q_{10}, q_{11}\}$$

in which $q_1 : |f_e - f_n| \le M, q_2 : m_1 \le f_e \le m_2, q_3 : e^* \dot{e} \le 0, q_4 : |e| \ge e_1, q_5 : |e| \ge e_2, \quad q_6 : |e| \ge e_3, \quad q_7 : |e| \ge e_4, \quad q_8 : |\dot{e}| \ge \dot{e}_4, q_9 : |\dot{e}| \ge \dot{e}_3, q_{10} : |\dot{e}| \ge \dot{e}_2, q_{11} : |\dot{e}| \ge \dot{e}_1$.

The sensed characteristic model can be written as follows, and the characteristic modes are represented by ϕ_i.

$$\Phi_1 = \begin{Bmatrix} \phi_1 \\ \phi_2 \end{Bmatrix} = K_1 \otimes Q_1^T = \begin{Bmatrix} q_2 \\ q_1 \cap \bar{q}_2 \end{Bmatrix}$$

$$\Phi_2 = \begin{Bmatrix} \phi_3 \\ \phi_4 \\ \phi_5 \\ \phi_6 \\ \phi_7 \\ \phi_8 \\ \phi_9 \end{Bmatrix} = K_2 \otimes Q_2^T = \begin{Bmatrix} q_4 \\ q_3 \cap \left(\begin{matrix} (\bar{q}_7 \cap q_8 \cap \bar{q}_9) \cup (\bar{q}_6 \cap q_7 \cap \bar{q}_9) \\ \cup (\bar{q}_5 \cap q_6 \cap \bar{q}_{10}) \cup (\bar{q}_4 \cap q_5 \cap \bar{q}_{11}) \end{matrix} \right) \\ q_3 \cap \bar{q}_4 \cap q_5 \cap q_{11} \\ q_3 \cap \bar{q}_5 \cap q_{10} \\ q_3 \cap \bar{q}_6 \cap q_9 \cap \bar{q}_{10} \\ \bar{q}_7 \cap \bar{q}_8 \\ \bar{q}_3 \cap \bar{q}_4 \end{Bmatrix}$$

Motion Schema and Association Schema

The motion schema can be described as follow.

$$S_M =< R_s, P, L, \Psi, U >$$

The associated schema can be expressed as follow.

$$\Omega = \{w_1, w_2, w_3, w_4, w_5, w_6, w_7\}$$

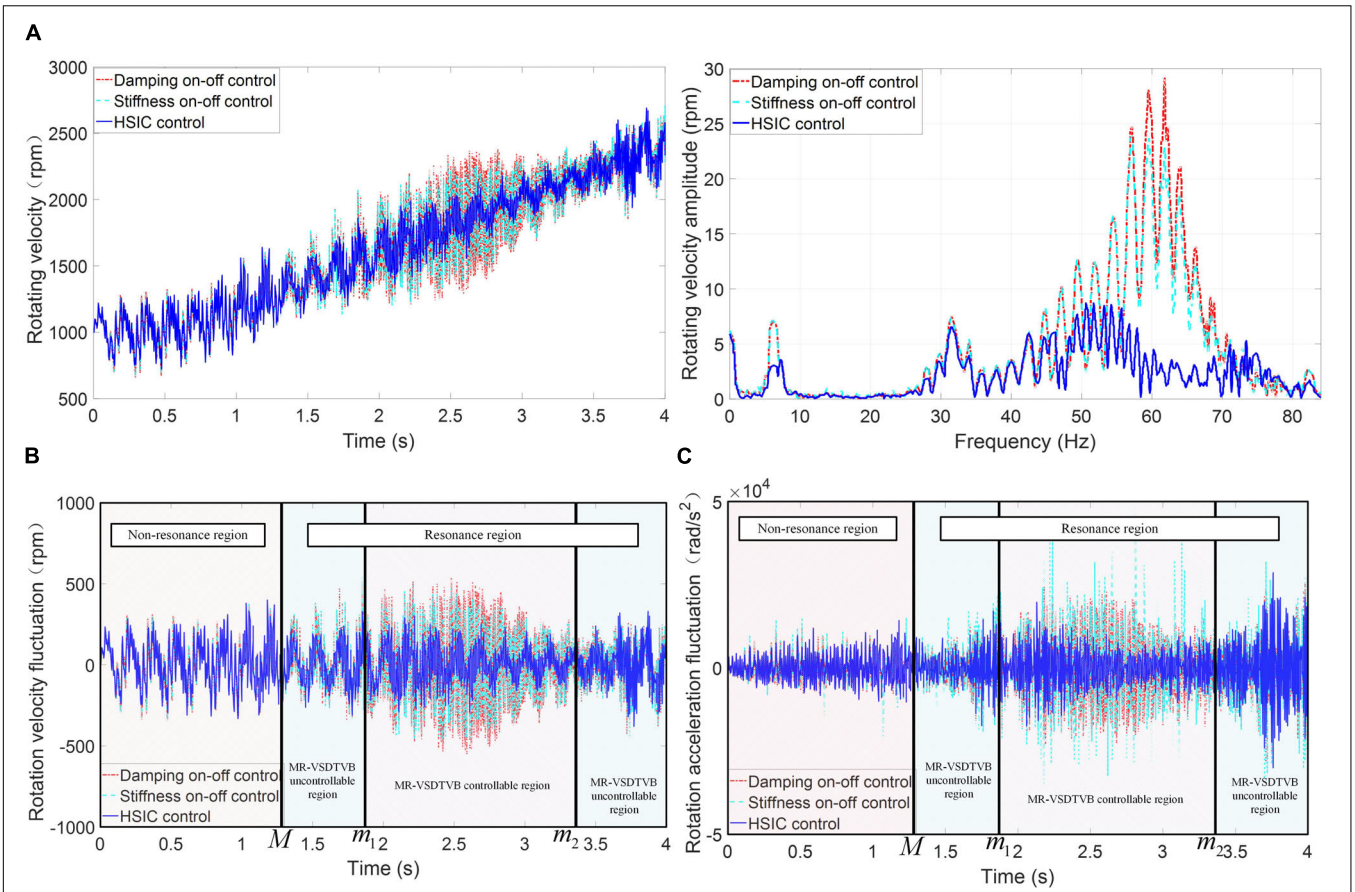

FIGURE 10 | Contrast of input shaft response of the main reducer in the powertrain system with different controls. **(A)** Rotating velocity-time relationship and amplitude-frequency relationship. **(B)** The rotating velocity fluctuate. **(C)** The rotating acceleration fluctuate.

where

$$w_1 : \phi_1 \Rightarrow \psi_1 w_2 : \phi_2 \Rightarrow \psi_2 w_3 : \phi_3 \Rightarrow \psi_3 w_4 : \phi_4 \Rightarrow \psi_4$$
$$w_5 : \phi_5 \cup \phi_6 \cup \phi_7 \Rightarrow \psi_5 w_6 : \phi_8 \Rightarrow \psi_6 w_7 : \phi_9 \Rightarrow \psi_7.$$

Figure 8A shows the operation process of the HSIC control scheme of MR-VSDTVB and the relationship between different schemes. According to the measured rotating velocity of the shaft of the main reducer, the corresponding excitation frequency f_e is obtained by Equation (9). When the excitation frequency is in the resonance region, it is necessary to further distinguish whether the excitation frequency is in the MR-VSDTVB controllable region or MR-VSDTVB uncontrollable region, and then the required MR-VSDTVB stiffness value K_d and damping torque value T_c can be obtained through corresponding control modes. When the excitation frequency f_e is in the non-resonant region, the characteristic mode of the current system response is judged by **Figure 7**, and then the required MR-VSDTVB stiffness value K_d and damping torque value T_c can be obtained according to the corresponding relationship between the characteristic modes and the control modes. Further, the control current I_c applied to the variable damping element and I_d applied to the variable stiffness element can be obtained from the inverse model Equation (19) and (20) of the MR-VSDTVB. Finally, the obtained control currents I_d and I_c are, respectively, applied to the variable stiffness element and the variable damping element of the MR-VSDTVB to realize the semi-active control of the MR-VSDTVB. **Figure 8B** shows the block diagram of the semi-active HSIC powertrain system obtained from **Figure 8A**.

Due to the limitation of the stiffness adjustment range of the MR-VSDTVB and the fact that the damping element of the MR-VSDTVB is an energy dissipating element, the control output is adjusted as follows.

$$K_d^{'} = \begin{cases} K_{\max} & K_d > K_{\max} \\ K_d & K_{\min} < K_d < K_{\max} \\ K_{\min} & K_d < K_{\min} \end{cases}$$

$$T_{MR} = \begin{cases} T_{\max} & T_c\left(\dot{\theta}_d - \dot{\theta}_{12}\right) < 0 and T_c > T_{\max} \\ T_c & T_c\left(\dot{\theta}_d - \dot{\theta}_{12}\right) < 0 and T_{\min} < T_d < T_{\max} \\ T_{\min} & Others \end{cases}$$

Where $K_d^{'}$ and T_{MR} represent the actual output stiffness value and damping torque value of the MR-VSDTVB $K_{\max}$ and $K_{\min}$ are the maximum and minimum stiffness values that the MR-VSDTVB

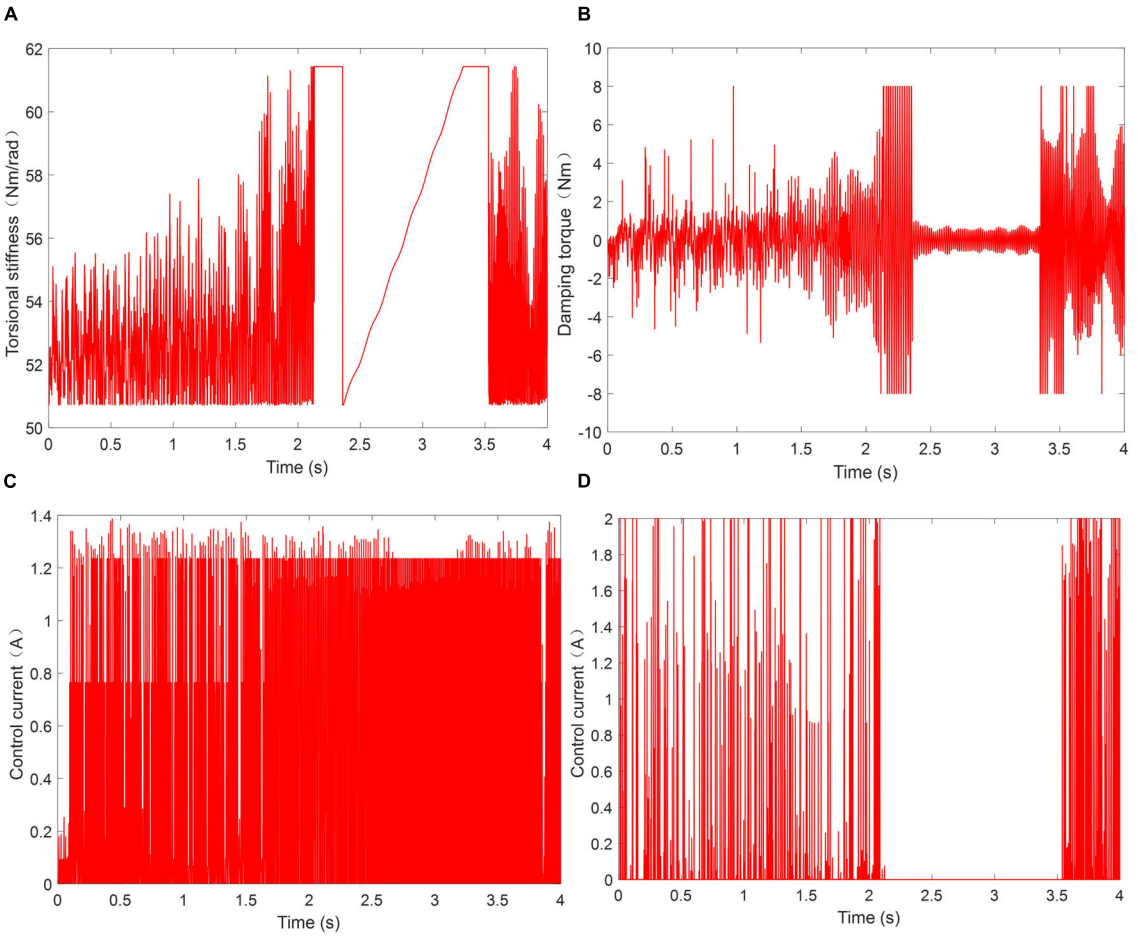

FIGURE 11 | Variation of parameters in the simulation process. **(A)** The stiffness change. **(B)** The damping torque change. **(C)** Current of variable stiffness part. **(D)** Current of variable damping part.

can provide,respectively $\dot{\theta}_d$ and $\dot{\theta}_{12}$ indicate the rotating velocity of the MR-VSDTVB and the main reducer's shaft. $T_{\max}$ and $T_{\min}$ are the maximum and minimum damping torque values that the MR-VSDTVB can provide.

SIMULATION RESULTS AND DISCUSSION

To verify the effectiveness of the proposed semi-active HSIC controller, a numerical simulation system based on MATLAB/Simulink is established.

In this paper, the torsional vibration response of the main reducer in the powertrain system is taken as the control objective, and the RMS value and the decreasing index of the torsional vibration response are taken as the criteria for evaluating the control effectiveness (Wang et al., 2015). The numerical simulation condition is the acceleration process of the automobile engine from idle condition (900 rpm) to 2500 rpm.

The torsional vibration responses of the input shaft of the main reducer in the powertrain system are compared in three cases, which are without MR-VSDTVB, MR-VSDTVB without control and MR-VSDTVB with control. **Figure 9** shows the numerical simulation results.

The simulation results show that the amplitude of the rotating velocity fluctuation and the rotating acceleration responses can be reduced by installing MR-VSDTVB on the input shaft of the main reducer, and the semi-active HSIC control of MR-VSDTVB can suppress the torsional vibration of the powertrain system to a large extent.

To further verify the control effect of HSIC, the on-off damping control and the on-off stiffness control are adopted for comparison. The expressions of the on-off damping control and the on-off stiffness control are as follows.

$$\begin{cases} c = c_{\max} \ \ if \ \ e\dot{e} \geq 0 \\ c = c_{\min} \ \ if \ \ e\dot{e} < 0 \end{cases}$$

$$\begin{cases} k = k_{\max} \, and \, c = c_{\max} \ \ if \ \ e\dot{e} \geq 0 \\ k = k_{\min} \, and \, c = c_{\min} \ \ if \ \ e\dot{e} < 0 \end{cases}$$

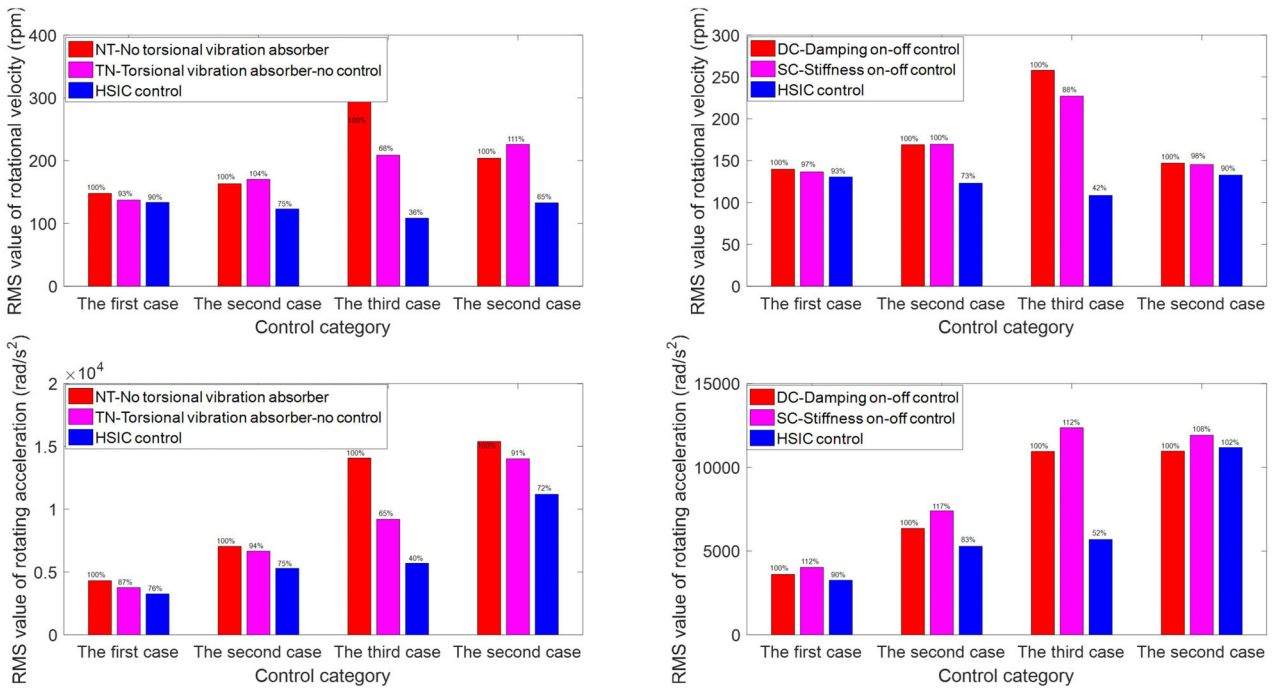

FIGURE 12 | Root mean square value of vibration response in different regions. The first case – Non-resonant region; the second case – Resonant and MR-VSDTVB uncontrollable region; The third case – Resonant and MR-VSDTVB controllable region.

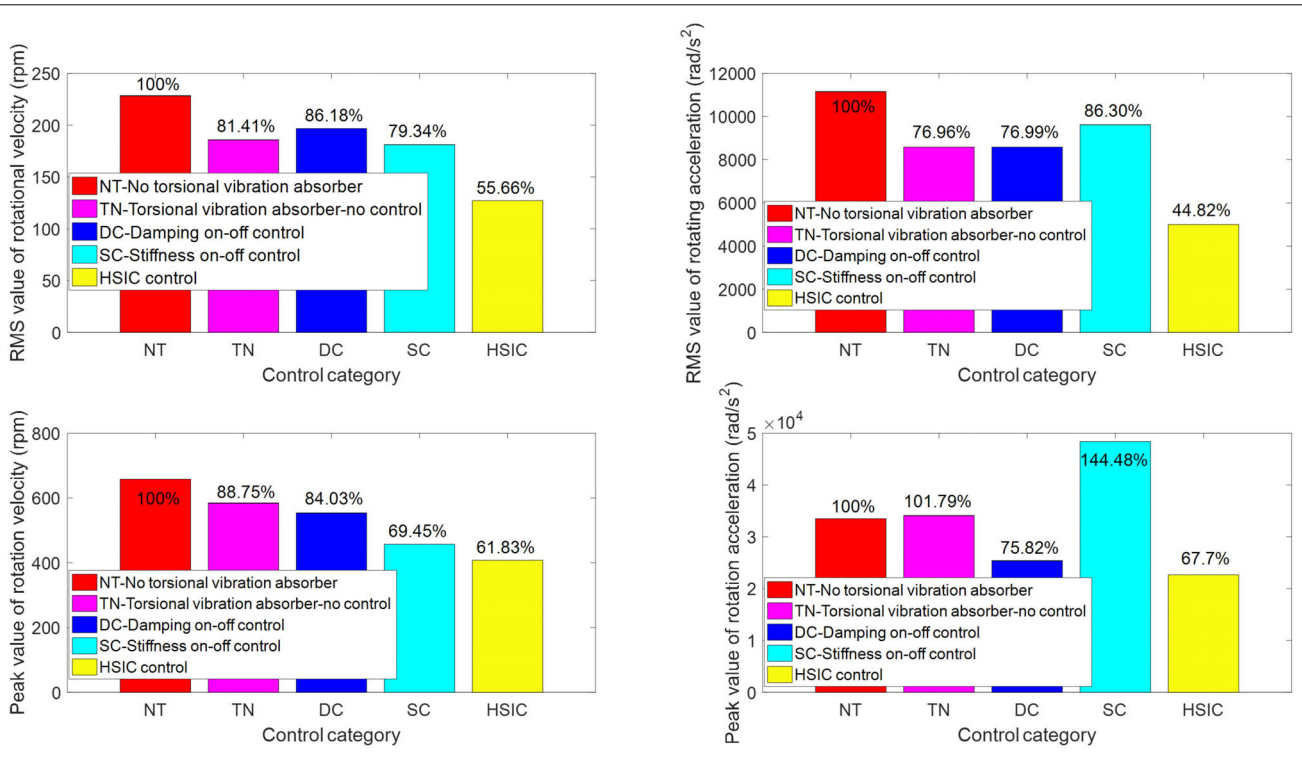

FIGURE 13 | Peak value and root mean square value of vibration response.

The output responses of the powertrain system under different controls are shown in **Figure 10**. **Figure 10** demonstrates that the torsional vibration control effect of HSIC is obviously better than the on-off damping control and the on-off stiffness-damping control, and HSIC can effectively suppress the rotating velocity fluctuation amplitude and rotating acceleration amplitude of the main reducer's input shaft, when the excitation frequency approaches the resonance frequency. The rotating acceleration curve of the on-off stiffness control contains some abrupt amplitudes, which are mainly caused by the step change of stiffness in the control process.

The stiffness change curve and damping torque change curve in the HSIC control process are shown in **Figure 11**, from which the control output under different system responses can be observed. The root mean square values of system responses under different controls in different regions are shown in **Figure 12**, respectively. **Figure 12** shows that HSIC in resonant and MR-VSDTVB controllable region has the excellent torsional vibration control effect, which is obviously better than that in MR-VSDTVB uncontrollable region and non-resonance region. It also shows that a better vibration control effect can be achieved, by adopting the variable stiffness control strategy to make the natural frequency of MR-VSDTVB consistent with the excitation frequency of the system in the resonance region (the RMS values of rotating velocity can be reduced to 36% at most.). The HSIC control in the non-resonance region can also suppress the torsional vibration of the system to a certain degree, and the RMS values of the rotating velocity and the rotating acceleration can be reduced to 90 and 74% at most, respectively.

Based on the above simulation results, the overall peak and RMS values of rotating velocity fluctuation and rotating acceleration of the main reducer's input shaft under different controls are calculated as shown in **Figure 13**. In view of the overall effect of torsional vibration suppression, the peak and RMS values of rotating acceleration can be reduced by 55.18 and 32.3%, respectively, when the HSIC control is applied to MR-VSDTVB. Even the on-off stiffness control and the on-off damping control can effectively reduce the peak and RMS values of rotating velocity to a lower level (by 20.66 and 30.55% at most, respectively).

CONCLUSION

In this study, a MR-VSDTVB and a HSIC controller are proposed to suppress the torsional vibration response of the powertrain system. The details can be concluded as follows.

(a) A MR-VSDTVB is designed, fabricated and tested. Based on the test results, the models of the variable stiffness element and variable damping element of the MR-VSDTVB are proposed.

(b) The multi-degree-of-freedom dynamic model of the powertrain system is established, and the installation position and adjustment range of MR-VSDTVB are determined by system analysis.

(c) A HSIC controller is proposed to control the MR-VSDTVB to suppress the torsional vibration response of the powertrain system.

(d) The performance of the proposed control strategy is evaluated under the acceleration process of the engine. The numerical simulation results indicate that the semi-active control of MR-VSDTVB with the HSIC controller has a better control effect than other controllers. Compared with the case without MR-VSDTVB, the RMS reduction rates of e and $\dot{e}$in the powertrain system with MR-VSDTVB are 44.34 and 55.18%, respectively. At the same time, the peak values of e and $\dot{e}$ in the powertrain system with MR-VSDTVB are reduced by 38.17 and 32.30%, respectively, compared with the case without MR-VSDTVB. The torsional vibration of the powertrain system can be suppressed in a wide frequency band by installing the MR-VSDTVB at the specified position of the powertrain system.

DATA AVAILABILITY STATEMENT

The raw data supporting the conclusions of this article will be made available by the authors, without undue reservation, to any qualified researcher.

AUTHOR CONTRIBUTIONS

XD contributed to content layout, and the conception and verification of the whole manuscript. WL was responsible for writing the manuscript and the numerical simulation. CP contributed to auxiliary parts of the simulation and data collection. JX was responsible for verifying the manuscript. XW was responsible for designing and providing technical support for the torsional vibration absorber used in the manuscript. JY contributed to the conception and discussion of the overall framework of the manuscript, and helped to determine and discuss the revision scheme for the manuscript. YZ participated in drawing some of the figures in the manuscript and the modification of the manuscript.

FUNDING

The authors disclosed receipt of the following financial support for the research, authorship, and/or publication of this article: This work was financially supported by the National Natural Science Foundation of People's Republic of China (Project No. 51675063), this research is also supported by graduate Research and Innovation Foundation of Chongqing, China (Grant No. CYB17023). These supports are gratefully acknowledged.

REFERENCES

Davis, C. L., Lesieutre, G. A., Dosch, J. J., and Davis, L. P. (1997). A tunable electrically shunted piezoceramic vibration absorber. *Proc. -Int. Soc. Opt. Eng.* 3045, 51–59.

Deng, H. X., and Gong, X. L. (2007). Adaptive tuned vibration absorber based on magnetorheological elastomer. *J. Intell. Mater. Syst. Struc.* 8, 1205–1210.

Fu, J., Li, P., Liao, G., Lai, J., and Yu, M. (2016). Development and dynamic characterization of a mixed mode magnetorheological elastomer isolator. *IEEE Trans. Mag.* 53, 1–4.

Gao, P., Xiang, C., Liu, H., and Zhou, H. (2018). Reducing variable frequency vibrations in a powertrain system with an adaptive tuned vibration absorber group. *J. Sound Vib.* 425, 82–101.

Harris, B. J., Sun, S. S., and Li, W. H. (2017). Improving stability and curving passing performance for railway vehicles with a variable stiffness MRF rubber joint. *Smart Mater. Struc.* 26, 035–055.

Hoang, N. (2011). *An Adaptive Tunable Vibration Absorber Using Magnetorheological Elastomers for Vibration Control of Vehicle Powertrains*. Sydney: University of Technology Sydney, 1–20.

Huang, H., Sun, S. S., Chen, S. M., and Li, W. H. (2019). Numerical and experimental studies on a new variable stiffness and damping magnetorheological fluid damper. *J. Intell. Mater. Syst. Struc.* 30, 1639–1652.

Johann, M. G., Hermann, P., and Karsten, S. (2014). Innovative torsional vibration reduction devices - vehicle-related design and component strength analysis. *SAE Int. J. Passeng. Cars Mech. Syst.* 7, 1392–1403.

Kang, Q., Wu, Y. D., Deng, J. H., and He, S. D. (2014). Study on the application of torsional vibration damper for the drivetrain torsional vibration of a FR car. *Manuf. Autom.* 36, 92–94.

Li, Z. S., Zhang, H., and Wen, Y. L. (2004). "Human simulated intelligent control based on sensory-motor intelligent schemas," in *Proceedings of the 5th World Congress on Intelligent Control and Automation*, Hangzhou: IEEE 3, 2423–2427.

Nagaya, K., Kurusu, A., Ikai, S., and Shitani, Y. (1999). Vibration control of a structure by using a tunable absorber and an optimal vibration absorber under autotuning control. *J. Sound Vib.* 228, 773–792.

Qian, L. J., Xin, F. L., Bai, X. X., and Wereley, N. (2017). M.State observation–based control algorithm for dynamic vibration absorbing systems featuring magnetorheological elastomers: Principle and analysis. *J. Intell. Mater. Syst. Struc.* 28, 2539–2556.

Qing-Hua, Z., Zhi-Yong, C., Wen-Ku, S., Qing-Hua, Z., and Zhi-Yong, C. (2015). Torsional vibration semi-active control of drivetrain based on magneto-rheological fluid dual mass flywheel. *Math. Probl. Eng.* 2015, 1–17.

Robert, L. (2007). *Norton. Design of machinery*. New York, NY: McGraw Hill, 521–561.

Sun, S. S., Yang, J., and Li, W. H. (2016). Development of an isolator working with magnetorheological elastomers and fluids. *Mech. Syst Signal Process.* 83, 371–384.

Wang, D., Yan, B., Wang, D. L., and Wang, Y. W. (2015). Noise control method of interior booming induced by torsional vibration of driveline system. *Noise Vib. Control.* 35, 73–76.

Wang, X. H. (2019). *Principle and Experiment of Variable Stiffness Damping of Magnetorheological Torsional Damper in Power Driveline*. Chongqing: Chongqing University, 21–49.

Wang, Y., and Jing, X. J. (2018). Nonlinear stiffness and dynamical response characteristics of an asymmetric X-shaped structure. *Mecha. Syst. Signal Process.* 125, 142–169.

Williams, K., Chiu, G., and Bernhard, R. (2002). Adaptive-passive absorbers using shape-memory alloys. *J. Sound Vib.* 249, 835–848.

Xu, Z. B. (2010). *Study on Adaptive Tuned Vibration Absorbing Technology*. Hefei: University of Science and Technology of China, 1–10.

Ye, S. C. (2012). *Passive and Semi-Active Torsional Vibration Control*. Tuscaloosa: The University of Alabama, 1–10.

Yu, J. Q., Dong, X. M., Zhang, Z. L., and Chen, P. G. (2018). A novel scissor-type magnetorheological seat suspension system with self-sustainability. *J.Intell. Mater. Sys. Struc.* 30:1045389X1775425.

Zhang, D. (2015). *Optimizing the Parameters of Dynamic Vibration Absorber and Researching on the Active Control*. Xi'an: Changan University, 1–20.

Zhang, X. Z., and Li, W. H. (2009). Adaptive tuned dynamic vibration absorbers working with MR elastomers. *Smart Struct. Syst.* 5, 517–529.

Zhou, Q. J., and Bai, J. K. (1983). "An intelligent controller of novel design," in *Proceedings of Multi-National InstruCion Conference, Part. 1*, (Shanghai: Science Technology Literature Press), 137–149.

Conflict of Interest: The authors declare that the research was conducted in the absence of any commercial or financial relationships that could be construed as a potential conflict of interest.

APPENDIX

Nomenclature

J_1 The moment of inertia at the free end of the engine, $kg \cdot mm^2$
J_2, J_3, J_4, J_5 The 1∼4 moments of inertia of cylinder crank connecting rod group on the engine,$kg \cdot mm^2$
J_6 The moment of inertia of the flywheel and the front of the clutch,$kg \cdot mm^2$
J_7 The moment of inertia of the driven disk of the clutch and the front part of the input shaft of the transmission,$kg \cdot mm^2$
J_8 The moment of inertia of the rear end of the transmission input shaft and the pair of constant meshing gears,$kg \cdot mm^2$
J_9 The moment of inertia of the main and follower gear pairs in each gear position and the front section of the output shaft,$kg \cdot mm^2$
J_{10} The moment of inertia of the rear section of the output shaft and the front section of the transmission shaft,$kg \cdot mm^2$
J_{11} The moment of inertia of the middle section of the output shaft,$kg \cdot mm^2$
J_{12} The moment of inertia of the rear section of the drive shaft and the main reducer's active components, $kg \cdot mm^2$
J_{13} The moment of inertia of the follower of the main reducer, the differential and the front half of the shaft,$kg \cdot mm^2$
J_{14}, J_{16} The moment of inertia of left axle and left wheels, right axle, and right wheels, respectively,$kg \cdot mm^2$
J_{15}, J_{17} Half of the translational mass equivalent moment of inertia of the vehicle body, respectively,$kg \cdot mm^2$
K_1, K_5 The torsional stiffness between the free end of the engine and the crankshaft, between the flywheel and the crankshaft of the engine,Nm/rad
K_2, K_3, K_4 The torsional stiffness of cylinder crank connecting rod group on the engine, respectively,Nm/rad
K_6 The torsional stiffness of the clutch,Nm/rad
K_7, K_8, K_9 The input shaft torsional stiffness, intermediate shaft torsional stiffness and output shaft torsional stiffness of transmission,Nm/rad
K_{10}, K_{11} The torsional stiffness of the front and middle segments of the transmission shaft,Nm/rad
K_{12} The torsional stiffness of the input shaft of the main reducer,Nm/rad
K_{13}, K_{15} The torsional stiffness of the left and right axes, respectively, Nm/rad
K_{14}, K_{16}The equivalent torsional stiffness of the left and right wheels, Nm/rad
P_A The single cylinder gas pressure, N/m^2;
A_g The piston area of the cylinder,m^2;
R,l The crankshaft radius and connecting rod length, m
ω The crankshaft angular velocity,rad/s
m_B The piston equivalent mass, kg
F_w The air resistance, N
F_r The rolling resistance in motion, N
r_{wheel} The wheel radius, m
i_0 The transmission ratio
C_D The air drag coefficient
A The windward area of the vehicle,m^2
V The driving speed of the vehicle, m/s
χ The rolling damping coefficient between wheel and road
m_v The vehicle mass, kg
g The gravity acceleration, m/s^2
T_g The torque produced by the cylinder gas pressure, Nm
T_i The inertial torque of the rotating parts, Nm
T_{total} The output torque of the engine, Nm
r The order of engine excitation
n_p The resonance speed of the system, rpm
R_s, Q, K,$\otimes$,Φ The input information set, the characteristic primitive set, the relation matrix, the operational symbol, and the characteristic model set, respectively
P, L, Ψ, U The control mode primitive set, the coordination relation matrix, the control mode set, and the control output, respectively
$M_{\min}, M_{\max}$ The minimum and maximum damping torque provided by MR-VSDTVB, respectively, Nm
$K_{\min}, K_{\max}$ The minimum and maximum stiffness provided by MR-VSDTVB, respectively, Nm/rad
$c_{\min}, c_{\max}$ The minimum and maximum damping coefficient provided by MR-VSDTVB, respectively,Nms/rad
K_{s1}, K_{s2} The controllable stiffness selected under different control modes respectively,Nm/rad
$L_{p1\sim p4}, L_{d2\sim p4}, L_{i3}, c_1$ The control coefficients selected under different control modes, respectively
J_g The moment of inertia of the main system,$kg \cdot mm^2$
K_g The stiffness of the main system,Nm/rad
J_d The moment of inertia of the torsional vibration absorber,$kg \cdot mm^2$
K_d The stiffness of the torsional vibration absorber,Nm/rad
C_d The damping coefficient of the torsional vibration absorber,Nms/rad
θ_g,θ_d The rotation angle of the main system and the rotation angle of the torsional vibration absorber, rad
$M(t)$ The excitation torque, Nm
μ The Inertia ratio of torsional vibration absorber to the main system
λ The frequency ratio of forced vibration
γ The natural frequency ratio of the torsional vibration absorber to the main system
A_{st} The static deformation of the main system
ζ The damping ratio
ω_g The natural frequency of the main system
ω_d The natural frequency of the torsional vibration absorb

frontiers in Materials

ORIGINAL RESEARCH
published: 26 June 2020
doi: 10.3389/fmats.2020.00171

Development and Control of Magnetorheological Elastomer-Based Semi-active Seat Suspension Isolator Using Adaptive Neural Network

Chenxiang Liu[1,2], *Masoud Hemmatian*[1]*, *Ramin Sedaghati*[1] *and Guilin Wen*[2]

[1] *Department of Mechanical, Industrial and Aerospace Engineering, Concordia University, Montreal, QC, Canada,* [2] *School of Mechanical and Electrical Engineering, Guangzhou University, Guangzhou, China*

The present study aims at the development of a magnetorheological elastomer (MRE) based semi-active seat suspension isolator and its adaptive control using a neural network (NN) control scheme. Isotropic MRE samples with 25% volume fraction of iron particles have been fabricated and then characterized under shear mode using a rotary magneto-rheometer to obtain MRE's viscoelastic properties (shear storage and loss moduli) under different levels of applied magnetic flux density. Results reveal a significant change in the storage and loss moduli with respect to the varied magnetic field. The viscoelastic properties of the MRE are then utilized to design an MRE-based seat suspension isolator in order to attenuate the transmitted vibration to the driver. For this purpose, the modeling of the seat incorporated with the MRE-based isolator is derived and subsequently, a novel NN control scheme is proposed for the semi-active control of the MRE-based isolator. The convergence and stability of the proposed control strategy have been mathematically verified using the Lyapunov method. Finally, the performance of the proposed control strategy is compared with those obtained using passive and widely used sky-hook controllers under different types of excitation including harmonic motion, road bump, and random profile. It is shown that the proposed NN controller considerably mitigates the vibration of the driver seat and outperforms the passive and skyhook controllers over the frequency range of interest.

Keywords: magnetorheological elastomer (MRE), MRE-based isolator, seat suspension, adaptive neural network control, Lyapunov method

OPEN ACCESS

Edited by:
Miao Yu,
Chongqing University, China

Reviewed by:
Xufeng Dong,
Dalian University of Technology, China
Yu Tian,
Tsinghua University, China

***Correspondence:**
Masoud Hemmatian
masoud.hemmatian@concordia.ca

Specialty section:
This article was submitted to Smart Materials, a section of the journal Frontiers in Materials

Received: *04 March 2020*
Accepted: *11 May 2020*
Published: *26 June 2020*

Citation:
Liu C, Hemmatian M, Sedaghati R and Wen G (2020) Development and Control of Magnetorheological Elastomer-Based Semi-active Seat Suspension Isolator Using Adaptive Neural Network. Front. Mater. 7:171. doi: 10.3389/fmats.2020.00171

INTRODUCTION

Long-term exposure to the low frequency and large amplitude vibrations from car seats can lead to severe adverse health effects on the drivers (Wilder et al., 1994). Seat suspension isolators play a critical role in the improvement of ride comfort and mitigation of whole-body vibration transmitted to the driver (Choi et al., 2001). Generally, the seat suspension isolator systems are categorized as passive, active, or semi-active systems (Symans and Constantinou, 1999). The seat suspension systems incorporating a passive control scheme are mainly effective for a narrow high-frequency range, which has been defined at early stages of design (Deng and Gong, 2008).

While active isolators demonstrate a considerably better performance compared to the passive systems, their practical applications are limited mainly due to their complex control hardware, high energy consumption, and potential instability (Yang et al., 2014). Considering this, the semi-active seat suspension systems, which have the fail-safe features of passive systems and adaptability of active systems, have received considerable attention (Du et al., 2011; Nguyen et al., 2015).

Semi-active isolators featuring smart magnetorheological (MR) materials can effectively utilize the adjustable viscoelastic properties to develop the required control forces. This unique adaptability feature combined with their inherent fail-safe design and low power requirements makes MR-based isolators attractive adaptive devices which can attenuate transmitted vibrations in a wide range of applications. Magnetorheological elastomers (MREs) are solid analogs of MR fluids which can provide both variable stiffness and damping under varying applied magnetic fields. This unique feature can be effectively utilized for the development of novel and practical semi-active isolators. MREs consist of micron-sized ferromagnetic particles dispersed into an elastomeric medium. Thus, they do not encounter the limitations often posed by MR fluids, such as sedimentation and leakage (Li et al., 2014). Upon application of an external magnetic field, the magnetic particles attempt to align themselves along the magnetic field line, which results in an instant change in MRE's viscoelastic properties.

While substantial efforts have been made on the development, characterization, modeling, and design of MRE-based devices (Kallio et al., 2007; Fu et al., 2016a; Nguyen et al., 2018; Dargahi et al., 2019a,b), very limited studies have focused on the design of controllers for MRE-based vibration isolation systems. The strong non-linearity of MRE-based isolation systems and the constraint of the applied magnetic density make controller design highly complicated. In this subject, an ON-OFF or sky-hook control strategy is the most widely used control strategy for the vibration attenuation of MRE-based devices, due to its robustness, simple control law design, and effectiveness in resonance alleviation (Liao et al., 2012). However, the control performance of the ON-OFF control is limited mainly due to the fact that only two control input states (ON- and OFF-state) can be performed. Fuzzy logic controller, in which the control law is designed by taking advantage of the expert knowledge, was also proposed for the MRE-based vibration isolation devices (Fu et al., 2016a; Nguyen et al., 2018; Gu et al., 2019). The merit of the fuzzy controller is that it does not require complicated mathematical modeling. However, its effectiveness relies highly on the preset fuzzy rules based on expert knowledge. The clipped-optimal and Lyapunov-based controllers were also proposed for MRE-based vibration isolation devices (Opie and Yim, 2009; Du et al., 2011; Behrooz et al., 2014). However, these controllers require accurate dynamic modeling of the system integrated with MRE-based devices, which is unavailable in most practical cases. A neural network-based inverse model has recently been proposed for the accurate modeling of MRE-based vibration isolation devices, however, the inverse model obtained from the off-line training cannot be directly utilized for a real-time controlled system (Fu et al., 2016b; Gu et al., 2017). In the last few decades, an adaptive neural network (NN) controller has been well established in active control areas (Noriega and Wang, 1998; Ge et al., 2002; He and Dong, 2018), which may be considered as a suitable candidate for the control system with a complex non-linear dynamic, owing to its excellent online approximate performance. To the best of our knowledge, adaptive NN has not yet been introduced for MRE-based devices. Moreover, very few research studies have considered the limit on stroke and static deformation, as well as the constraint of the imposed magnetic field density in MRE-based devices, which may occur in practical implementation.

The present study firstly addresses the development of an MRE-based seat suspension isolator design considering the constraints on the magnetic field density, stroke, and static deformation of the MRE. The MRE samples with 25% volume fraction of carbonyl iron particles are fabricated and then characterized using a rotary magneto-rheometer. Secondly, a novel adaptive NN control scheme is developed to mitigate the transmitted vibration of the developed MRE-based seat suspension isolator. The convergence and stability of the proposed control system are verified using the Lyapunov stability theory. Finally, the superior performance of the proposed controller over the passive control and ON-OFF control is demonstrated.

FABRICATION, CHARACTERIZATION, AND MODELING OF THE MRE

The MRE samples with 25% volume fraction of magnetic particles were fabricated in the laboratory at room temperature using silicon rubber, *Ecoflex* 0020 − *Smooth on*, as the matrix and carbonyl iron particles (CIPs), *SQ* − *grade*, acquired from BASF Corporation. The CIPs and silicone rubber were thoroughly mixed together for about 5 min with the volume ratio of 1 : 3. Subsequently, the mixture was placed in a vacuum chamber with 95 kPa pressure less than the air environment for 5 min to remove air bubbles, and then poured into a mold. The mixture was then left for 24 h at room temperature to be cured. After that, cylindrical MRE samples with a diameter of 20 mm and a thickness of 2.0 mm were fabricated.

In the present study, an advanced MRE testing system equipped with a rotary rheometer (*Discovery HR* − 3, *TA Instrument*), as shown in **Figure 1A**, was utilized to characterize the MRE samples in shear mode. **Figure 1B** shows the schematic of the rotational parallel-plate setup with the magnetorheological accessory. The MRE sample was placed between the upper and lower geometries and and 10 N axial preload was applied to assure that no slippage occurs during the test. The magnetorheology accessory is capable of generating a uniform and homogeneous magnetic flux density along the axis of the cylindrical MRE sample, which is basically perpendicular to the direction of shear motion. The hall probe sensor placed right beneath the MRE sample provides the measurement of the flux density and feedback signal for the rheometer's closed-loop controller to adjust the applied flux density in a wide range of 0.0 to 1.0 T. It should be noted that all the experimental tests were

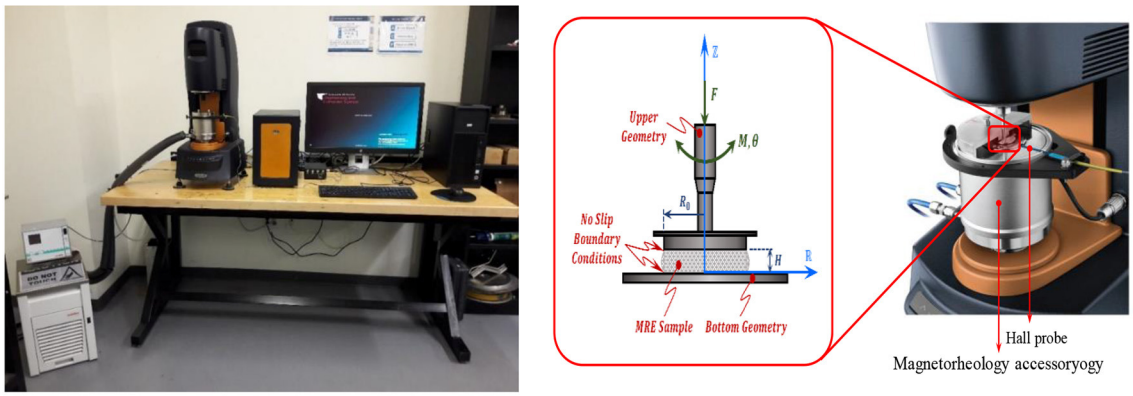

FIGURE 1 | (A) The MRE testing system and **(B)** schematic diagram of the rotational parallel-plate setup of the rotary rheometer equipped with magnetorheology accessory.

conducted at a temperature of 20 °C. The measured torque and angular displacement were processed to obtain the storage and loss moduli of the MRE.

The hysteresis loop, applied force vs. displacement, results of the MRE sample under various levels of applied magnetic flux density are presented in **Figure 2**. Area inside the hysteresis loop and its major axis represent equivalent damping and stiffness of the MRE, respectively, which as expected are increasing as the applied magnetic field increases. **Figure 3** shows the storage and loss moduli with respect to the excitation frequencies under various levels of the applied flux density and fixed shear strain of 15%. Results suggest that storage and loss moduli highly depend on the value of the applied magnetic field, while their dependency on the excitation frequency is not considerable in the frequency range of 1–10 Hz. The dependence of the storage and loss moduli with respect to the shear strain amplitude (2–30%) under the fixed excitation frequency of 2.0 Hz is presented in **Figure 4**, which clearly shows that the MRE operating under a higher shear strain has a smaller MR effect, and that storage and loss moduli decrease by increasing the strain amplitude. The effect of the applied magnetic field on the storage and loss moduli with an excitation frequency of 2 HZ and the strain amplitude of 15% and its corresponding curve fitting results are further investigated in **Figure 5**. The results clearly show that storage and loss moduli increase monotonically and considerably by increasing the applied magnetic flux density, however they are subject to saturation for magnetic flux density nearly beyond 1.0 T. This is mainly because the CIPs magnetically saturate as the applied magnetic flux density reaches 1.0 T. It is noted that storage and loss moduli vary from 62.2 (*KPa*) and 13.3 (*KPa*) at 0 T to 235.6 (*KPa*) and 69.0 (*KPa*) at 1 T, respectively, demonstrating the relative MR effect of 379 and 519% for storage and loss moduli, respectively.

Using the experimental data shown in **Figure 5**, a cubic polynomial function is derived to approximate the variation of the storage modulus with respect to the applied magnetic flux density as:

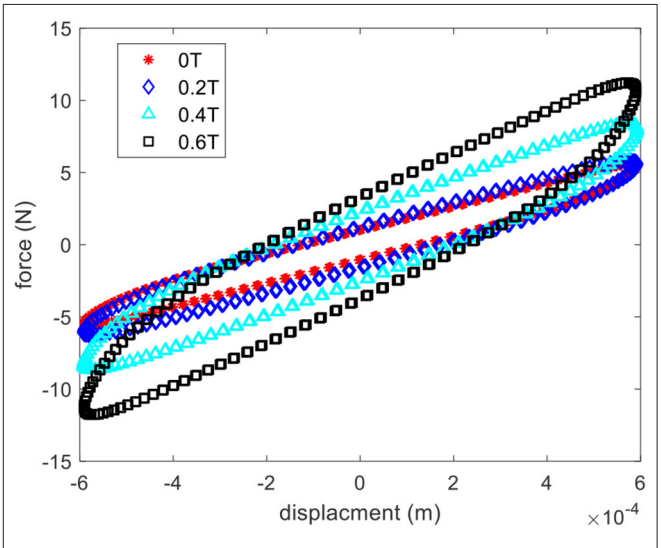

FIGURE 2 | The force with respect to displacement under different levels of applied magnetic flux density and fixed frequency of 1 Hz.

$$G^{'} = a_1 T^3 + b_1 T^2 + c_1 T + d_1 \quad (1)$$

where $G^{'}$ and T are the storage modulus in kPa and the applied magnetic flux density in T, respectively. The constant parameters $a_1 = -234.3$, $b_1 = 396.7$, $c_1 = 10.94$, and $d_1 = 63.04$ are identified using the least square method. The approximated function of the loss modulus vs. magnetic flux density is also derived by using a cubic polynomial function, which can be described as:

$$G^{''} = a_2 T^3 + b_2 T^2 + c_2 T + d_2 \quad (2)$$

where $G^{''}$ is the loss modulus in kPa. Similarly, the constant parameters $a_2 = -103.2$, $b_2 = 151.1$, $c_3 = 7.79$, and

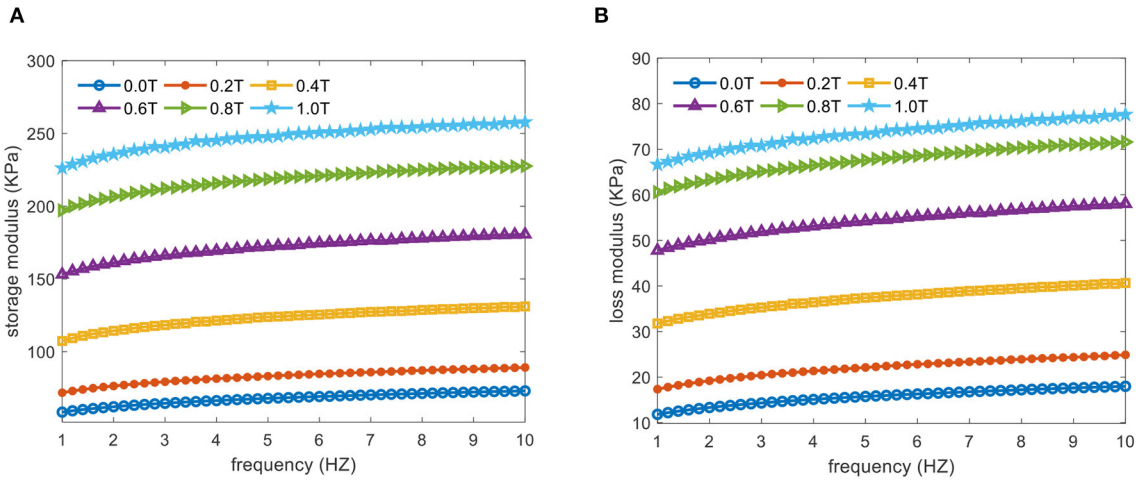

FIGURE 3 | (A) Storage and **(B)** loss moduli compared to excitation frequencies under various levels of applied magnetic flux density and fixed shear strain amplitude of 15%.

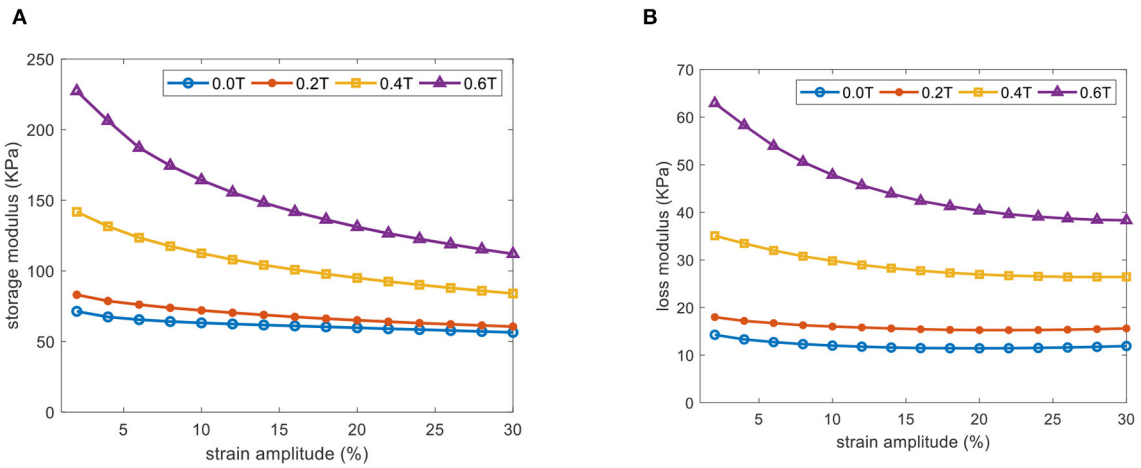

FIGURE 4 | (A) Storage and **(B)** loss moduli with respect to shear strain amplitudes under various levels of applied magnetic flux density and fixed frequency of 2 Hz.

$d_4 = 13.27$ are identified using the least square method. The results obtained using the models presented in Equations (1) and (2) are compared with those measured experimentally in **Figure 5**.

ANALYTICAL MODELING OF MRE BASED ADAPTIVE SEAT ISOLATOR

The schematic diagram of the MRE-based seat suspension isolator operating in shear mode is presented in **Figure 6A**. The proposed isolator includes two MRE layers connecting the seat frame through two permanent magnets to the core base. The applied magnetic flux density is controlled by varying the current input to the electromagnet coils and is guided through the magnetic base into the MRE layers. It is noted that the two permanent magnets are mounted next to the MRE layers in order to extend the working range of the magnetic flux density. The embedded permanent magnets also enhance the stiffness of the MRE layers in the absence of applied current to the coils, which subsequently reduces the static deformation of the MREs, due to the weight of the seat and driver. Moreover, the stoke limit design is considered for the MRE-based seat isolator to make sure MREs do not undergo very large deformation.

The schematic diagram of the driver seat equipped with the proposed MRE-based seat suspension isolator and its equivalent mechanical system are shown in **Figure 6B**, in which m, k, and c represent mass, stiffness, and damping of the elements, respectively, and the subscripts d, c, and s denote the driver, cushion, and seat frame, respectively. The equivalent stiffness and damping of the MRE-based isolator are denoted by k_{MRE} and c_{MRE}, respectively. An extra linear spring k_b is added in parallel to the MREs to reduce the static deformation of the MRE layers

due to the weight of the seat and driver. The dynamics modeling of the MRE-based seat suspension system can be described as:

$$m_s\ddot{x}_s = -c_{MRE}(\dot{x}_s - \dot{x}_b) - (k_{MRE} + k_b)(x_s - x_b) - c_c(\dot{x}_s - \dot{x}_c) - k_c(x_s - x_c) \quad (3)$$

$$m_c\ddot{x}_c = -c_c(\dot{x}_c - \dot{x}_s) - k_c(x_c - x_s) - c_d(\dot{x}_c - \dot{x}_d) - k_d(x_c - x_d) \quad (4)$$

$$m_d\ddot{x}_d = -c_d(\dot{x}_d - \dot{x}_c) - k_d(x_d - x_c) \quad (5)$$

Let us define:

$$\triangle k = k_{MRE} - k_{min} \quad (6)$$

$$\triangle c = c_{MRE} - c_{min} \quad (7)$$

where k_{min} and c_{min} are the equivalent stiffness and damping of the MRE-based isolator in absence of applied magnetic flux density, respectively. $\triangle k$, $\triangle c$ are the change in the stiffness and the damping coefficients due to the applied magnetic field. Considering the two MREs in the MRE-based isolators, the equivalent stiffness, k_{MRE}, and damping, c_{MRE}, can be described as Li et al. (2013) and Yang et al. (2014):

$$k_{MRE} = \frac{2G'A}{h} \quad (8)$$

$$c_{MRE} = \frac{2G''A}{\omega h} \quad (9)$$

where A and h are the area and thickness of the MRE operating in shear mode, respectively, and ω denotes the excitation frequency in rad/s. Substituting the Equations (1) and (2) into Equations (8) and (9), respectively, yields the equivalent stiffness and damping as a function of applied magnetic flux density as follows:

$$k_{MRE} = \frac{2A}{h}(a_1T^3 + b_1T^2 + c_1T + d_1) \quad (10)$$

$$c_{MRE} = \frac{2A}{\omega h}(a_2T^3 + b_2T^2 + c_2T + d_2) \quad (11)$$

Substituting k_{MRE} and c_{MRE} from Equations (6) and (7) into Equation (3) yields:

$$m_s\ddot{x}_s + (k_{min} + k_b)(x_s - x_b) + c_{min}(\dot{x}_s - \dot{x}_b) + c_c(\dot{x}_s - \dot{x}_c) + k_c(x_s - x_c) = f_{MRE} \quad (12)$$

where f_{MRE} is the generated actuation force induced by MREs in the presence of the applied field and is described as:

$$f_{MRE} = \triangle k(x_b - x_s) + \triangle c(\dot{x}_b - \dot{x}_s) \quad (13)$$

Using Equations (1) and (2), and knowing that $k_{min} = \frac{2A}{h}d_1$ and $c_{min} = \frac{2A}{\omega h}d_2$, f_{MRE} can be obtained as:

$$f_{MRE} = \frac{2A}{h}(a_1T^3 + b_1T^2 + c_1T)(x_b - x_s) + \frac{2A}{\omega h}(a_2T^3 + b_2T^2 + c_2T)(\dot{x}_b - \dot{x}_s) \quad (14)$$

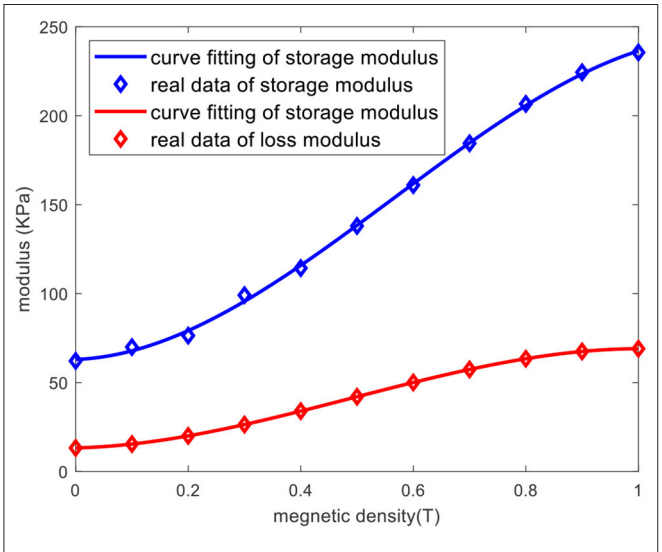

FIGURE 5 | Storage and loss moduli in the presence of varied magnetic flux density with the fixed frequency of 2 Hz and shear strain amplitude of 15% and its corresponding curve fitting results.

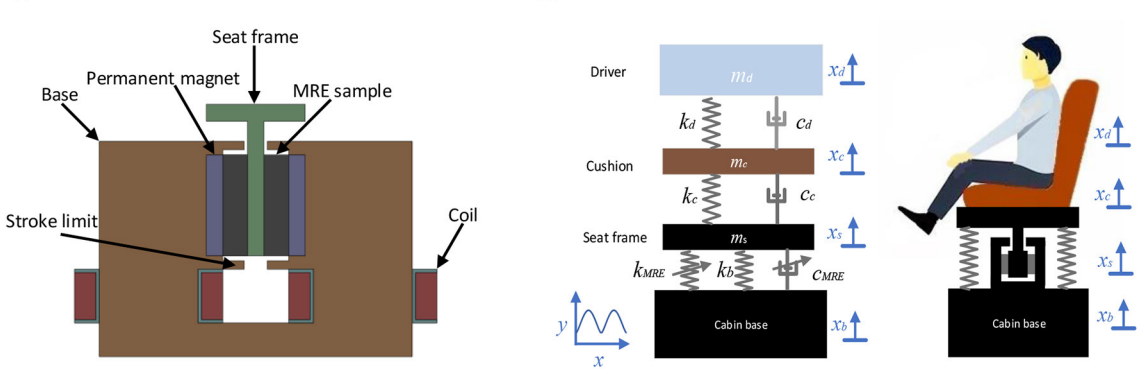

FIGURE 6 | (A) Schematic diagrams of MRE-based seat suspension isolator and **(B)** the modeling of the MRE-based seat isolation system.

It can be realized from Equation (14) that the proposed MRE-based seat suspension isolator has complex non-linear dynamics, and the actuation force of the MRE can be adjusted by the ratio of A/h and magnitude of the magnetic flux density generated at the location of the MREs. It should be noted that by increasing A/h, the bandwidth of the generated actuation force will also increase. However, increasing the A or h results in a bulkier and heavier electromagnet to generate the required uniform magnetic field in the MREs. In this study, the effective area, A, and thickness, h, of MREs are selected so that the maximum strain experienced in MREs is limited to 15% while the required magnetic flux density up to 800 mT can be achieved at the location of MREs with an applied current of maximum 3 A.

Magnetostatic analysis is also performed to further examine the capability of the proposed MRE-based isolator to supply the required magnetic flux density. For this purpose, the magnetostatic finite element (FE) model of the isolator is developed using an open-source finite element software (Meeker, 2020). **Figure 7** shows the developed FE model of the electromagnet and its dimensions. The electromagnet includes 1010 steel core and two coils each contains 1,800 turns of 18AWG copper wire capable of continuously working under 3.0 A current input. The electromagnet also includes two neodymium (N52) permanent magnets (80 × 80 × 5 mm) placed next to the MRE layers to enhance the applied magnetic field and increase the stiffness of the MREs to reduce the static deformation in the absence of applied current to the coils. It should be noted that the relative permeability of the MRE sample with 25% volume fraction of CIPs is measured as 1.4. The effective area, A, and the thickness, h, of the MREs are selected based on trial and error to respect stiffness, stroke limit, and magnetic field requirements and are found to be 64 cm^2 and 1.6 cm. The simulation results for

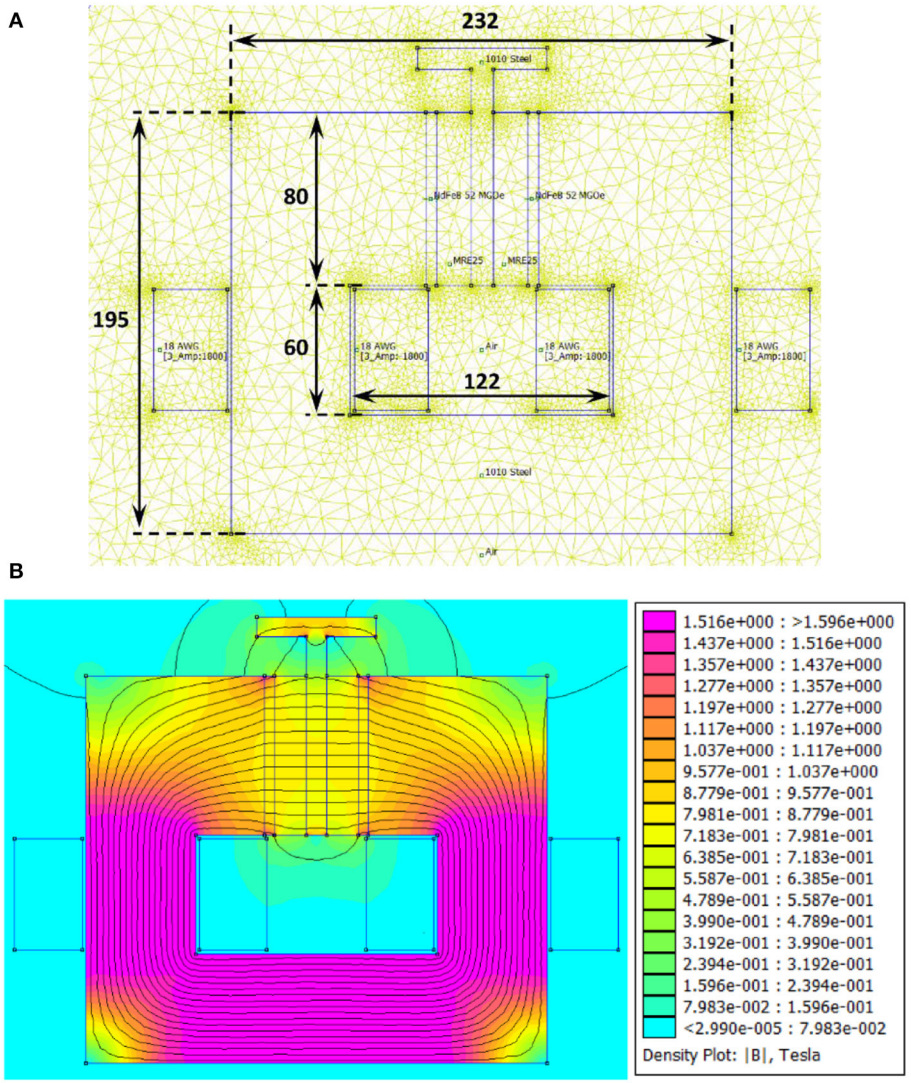

FIGURE 7 | FE magnetic analysis of the MRE-based isolator; **(A)** FE model and **(B)** results for 3 A current input to the coils.

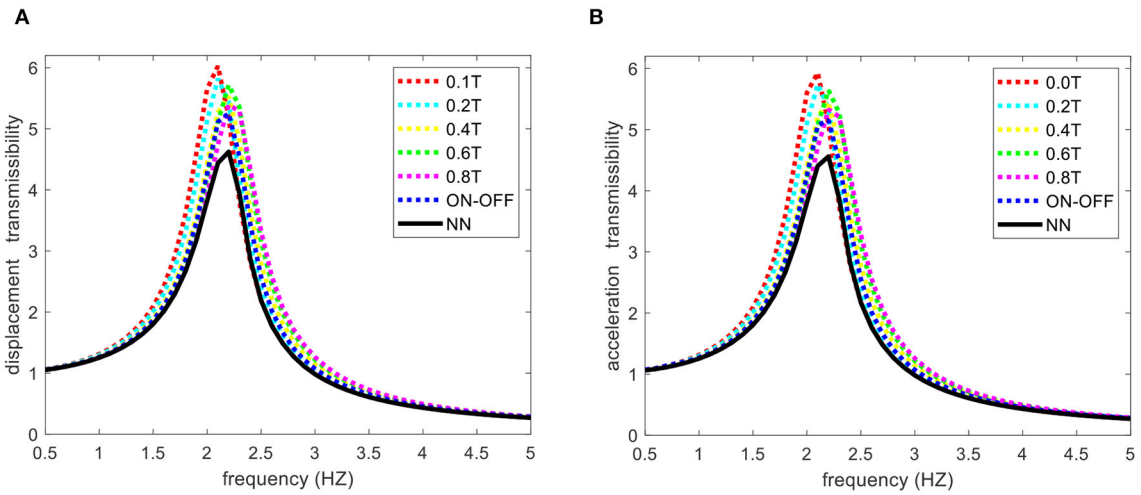

FIGURE 8 | (A) Displacement, and **(B)** acceleration transmissibility of the human body (x_d) with respect to the excitation frequencies in the presence of various controllers.

TABLE 1 | Magnetic flux density at the center of the MRE layers under different levels of applied current to the coils.

I = −2.5 A	I = −2.0 A	I = −1.0 A	I = 0.0 A	I = 1.0 A	I = 2.0 A	I = 3.0 A
B = 2 mT	B = 95 mT	B = 275 mT	B = 430 mT	B = 566 mT	B = 700 mT	B = 806 mT

the distribution of the magnetic flux density under 3.0 A current input to the coils are presented in **Figure 8B**. Results show that the isolator base core properly guides the magnetic field directly through the MRE layers perpendicular to the shear direction. The magnetic flux density at the center of the MRE layers is evaluated and presented in **Table 1** for different levels of applied current to the electromagnets. The results reveal that applying 3.0 A current to the coils provides over 800 mT magnetic flux density at the center of MRE layers, while nearly no magnetic field is applied to the MREs by applying 2.5 A negative current. Moreover, the permanent magnets are able to apply 430 mT magnetic flux density to the MRE layers in an off-state situation to prevent large deformation.

DEVELOPMENT OF THE ADAPTIVE CONTROLLER USING NEURAL NETWORK (NN)

In this section, the NN control law is developed to isolate the transmitted vibration to the seat under varying base excitations. The convergence and stability of the proposed control scheme are subsequently verified using the Lyapunov theory.

Neural Network Controller

NN controller is a powerful technique used to address complex non-linear systems under uncertainties (Ge et al., 2002). In the present study, the ideal NN controller output is described as:

$$Y(Z) = \overline{W}^T \Phi(Z) + \varepsilon \tag{15}$$

where $Y(Z)$ is the unknown dynamics function to be approximated; $W = [\overline{W}_1, \overline{W}_2, \ldots, \overline{W}_l] \subset R^l$ is the vector of ideal weights; $\Phi(Z) = [\Phi(Z)_1, \Phi(Z)_2, \ldots, \Phi(Z)_l] \subset R^l$ is vector of the basic functions; Z denotes the input variable; l is the number of the NN nodes; ε is the approximation error vector, which is bounded over the compact set, such that $|\varepsilon| \leq \bar{\varepsilon}$; and $\bar{\varepsilon}$ is a positive constant. In this study, Gaussian radial basic function $\Phi(Z)$ is considered, which can be written as:

$$\Phi(Z) = exp\left[\frac{-(Z - C_k)^2}{R_k^2}\right],\ k = 1, 2, \ldots l \tag{16}$$

where $C_k = [C_1\ C_2\ \ldots\ C_l]$ are the centers of the radial basic functions and R_k are the width of the radial basic functions. The estimated weights $\hat{W}$ can be presented as:

$$\hat{W} = \overline{W} + \tilde{W} \tag{17}$$

where $\tilde{W}$ is the error vector of the approximated weights.

NN Control Law Design and Stability Analysis

The control objective is to attenuate the transmitted vibration to the seat frame and, subsequently, to the driver. Let us choose the

NN input as:

$$s = \gamma \dot{x}_s + \beta x_s \tag{18}$$

where γ and β are positive constants. The proposed control law is designed as:

$$f_{MRE} = -\tau x_s - \vartheta \dot{x}_s + \hat{W}^T \Phi(s) \tag{19}$$

where τ and ϑ are positive constant. It is worth noting that the proposed control scheme is model-free. As the accurate dynamic of the MRE-based isolator is generally unavailable in the real application, the model-free control strategy would be beneficial for practical implementation.

The unknown function to be approximated is defined as:

$$\begin{aligned} Y &= m_s \ddot{x}_s + \left(k_{min} + k_b\right)(x_s - x_b) + c_{min}(\dot{x}_s - \dot{x}_b) + c_c(\dot{x}_s - \dot{x}_c) \\ &+ k_c(x_s - x_c) \end{aligned} \tag{20}$$

Substituting Equations (20) and (19) along with Equation (17) into Equation (12), we can obtain:

$$Y = -\tau x_s - \vartheta \dot{x}_s + \overline{W}^T \Phi(s) + \tilde{W}^T \Phi(s) \tag{21}$$

Then substituting Equation (15) into Equation (21), we may write:

$$\tau x_s = \tilde{W}^T \Phi(s) - \varepsilon - \vartheta \dot{x}_s \tag{22}$$

In the following, Lyapunov theory has been utilized to prove the convergence and stability of the proposed control scheme. The first Lyapunov function candidate may be selected as:

$$V_1 = \frac{1}{2}\varphi^{-1}\tilde{W}^T\tilde{W} \tag{23}$$

where φ is a positive constant. Taking the derivative of the first Lyapunov function yields:

$$\dot{V}_1 = \varphi^{-1}\tilde{W}^T\dot{\tilde{W}} \tag{24}$$

The updated law is proposed as:

$$\dot{\hat{W}} = -\varphi\left(x_s \Phi(s) + \sigma \hat{W}\right) \tag{25}$$

where σ is a positive constant. Substituting the proposed updated law along with Equation (17) into Equation (24), yields:

$$\dot{V}_1 = -x_s\tilde{W}^T\Phi(s) - \sigma\tilde{W}^T\hat{W} \tag{26}$$

Since $-\tilde{W}^T\hat{W} = -\tilde{W}^T\left(\overline{W} + \tilde{W}\right) = -\tilde{W}^T\overline{W} - \tilde{W}^T\tilde{W}$ and $-\tilde{W}^T\overline{W} \le \frac{1}{2}(\tilde{W}^T\tilde{W} + \overline{W}^T\overline{W})$, then we have $-\tilde{W}^T\hat{W} \le -\frac{1}{2}\tilde{W}^T\tilde{W} + \frac{1}{2}\overline{W}^T\overline{W}$. Thus, an inequality can be established as:

$$\dot{V}_1 \le -x_s\tilde{W}^T\Phi(s) - \frac{\sigma}{2}\tilde{W}^T\tilde{W} + \frac{\sigma}{2}\overline{W}^T\overline{W} \tag{27}$$

Choosing the second Lyapunov function as:

$$V_2 = \frac{1}{2}\vartheta x_s^2 \tag{28}$$

and taking its derivative:

$$\dot{V}_2 = \vartheta \dot{x}_s x_s \tag{29}$$

and then substitute Equation (22) into Equation (29) yields:

$$\dot{V}_2 = x_s\left(\tilde{W}^T\Phi(s) - \varepsilon - \tau x_s\right) \tag{30}$$

Finally, combining the above two Lyapunov functions, we can write:

$$V = V_1 + V_2 \tag{31}$$

Taking derivative of the above Lyapunov function, and considering inequality in Equations (27) and (30), it can be shown that:

$$\begin{aligned} \dot{V} \le\ & -x_s\tilde{W}^T\Phi(s) - \frac{\sigma}{2}\tilde{W}^T\tilde{W} + \frac{\sigma}{2}\overline{W}^T\overline{W} \\ & + x_s\left(\tilde{W}^T\Phi(s) - \varepsilon - \tau x_s\right) \end{aligned} \tag{32}$$

The above equation can be simplified as:

$$\begin{aligned} \dot{V} &\le -\frac{\sigma}{2}\tilde{W}^T\tilde{W} + \frac{\sigma}{2}\overline{W}^T\overline{W} - x_s\bar{\varepsilon} - \tau x_s^2 \\ &\le -\frac{\sigma}{2}\tilde{W}^T\tilde{W} + \frac{\sigma}{2}\overline{W}^T\overline{W} + \frac{1}{2}x_s^2 + \frac{1}{2}\bar{\varepsilon}^2 - \tau x_s^2 \le -\frac{\sigma}{2}\tilde{W}^T\tilde{W} \\ &\quad - \left(\tau - \frac{1}{2}\right)x_s^2 + \frac{\sigma}{2}\overline{W}^T\overline{W} + \frac{1}{2}\bar{\varepsilon}^2 \le -\rho V + \varpi \end{aligned} \tag{33}$$

where ρ and ϖ are defined as:

$$\rho = \min\left(\phi\sigma, (2\tau - 1)\vartheta^{-1}\right) \tag{34}$$

$$\varpi = \frac{\sigma}{2}\overline{W}^T\overline{W} + \frac{1}{2}\bar{\varepsilon}^2 \tag{35}$$

Choosing $\tau \ge \frac{1}{2}$ to make sure $\rho > 0$, then multiplying Equation (33) by $e^{\rho t}$, we can obtain:

$$\frac{d}{dt}\left(Ve^{\rho t}\right) \le \varpi e^{\rho t} \tag{36}$$

Integrating Equation (36), yields:

$$V \le \left(V(0) - \frac{\varpi}{\rho}\right)e^{-\rho t} + \frac{\varpi}{\rho} \le V(0) + \frac{\varpi}{\rho} \tag{37}$$

Using Equations (23), (28), and (37), we have the followings identities:

$$\frac{1}{2}\varphi^{-1}\tilde{W}^T\tilde{W} \le V(0) + \frac{\varpi}{\rho} \tag{38}$$

$$\frac{1}{2}\tau x_s^2 \le V(0) + \frac{\varpi}{\rho} \tag{39}$$

$$\Omega\tilde{W} := \left\{ \tilde{W} \in R^l \mid \left|\tilde{W}\right| \leq \sqrt{\phi\alpha} \right\} \tag{40}$$

$$\Omega x_s := \left\{ x_s \in R \mid |x_s| \leq \sqrt{\frac{\alpha}{\tau}} \right\} \tag{41}$$

$$\alpha = 2\left(V(0) + \frac{\varpi}{\rho} \right) \tag{42}$$

Hence, in the closed-loop system, $\tilde{W}$ and x_s remain in the compact set $\Omega\tilde{W}$ and Ωx_s, respectively. Considering above, the following theorem can be stated:

Theorem 1: For the governing equation given in Equations (3)–(5), with the control law and update law provided in Equations (19) and (25), respectively, and given that the initial states of the isolation system are bounded and the displacement and velocity of the isolator can be obtained accurately, it can be concluded that the isolator system using the proposed control scheme is semi-global uniformly bounded, which will eventually converge to the original position by appropriately choosing the control parameters.

Proposed Adaptive Neural Network Controller

Using the proposed control scheme and considering that the current of 3.0 A can reach to the maximum applied magnetic flux density ($T_{\max} = 806\ mT$) and the current of −2.5 A can reach to the minimum applied magnetic flux density ($T_{\min} = 2\ mT$), as provided in **Table 1**, the actuation force induced by the MREs can be described as:

$$f_{MRE} = \begin{Bmatrix} (k_{max} - k_{min})(x_b - x_s) + (c_{max} - c_{min})(\dot{x}_b - \dot{x}_s) & T_{est} > T_{max} \\ -\tau x_s - \vartheta \dot{x}_s + \hat{W}^T \Phi(s) & T_{min} < T_{est} < T_{max} \\ 0 & T_{est} < T_{min} \end{Bmatrix} \tag{43}$$

where T_{est} is obtained from Equation (14). The control parameters τ and ϑ are identified as 10 and 2, respectively, and the control parameters γ and β in Equation (18) are chosen as 4 and 1, respectively. The centers of the nodes are evenly distributed in [−0.5, 0.5] and the width of the centers R_k is fixed at 2. The initial weights are chosen as zero. The parameters φ and σ in the updated law are chosen as 2,000 and 0.1, respectively. Two hundred nodes are used for the NN approximation. Note that the provided control parameters comply with the control law design and stability analysis described in section Development of the Adaptive Controller Using Neural Network (NN), and a trial and error method is adopted to select the control parameters to achieve satisfactory control performance.

Sky-Hook Controller

In order to evaluate the effectiveness of the proposed control scheme, its performance is compared with those of the two most widely used vibration isolation control approaches, namely passive control and sky-hook control strategies. In the case of passive control, the MRE-based isolator operates in an OFF- or ON-state in which the applied magnetic flux density is set to its minimum (0.0 T) or maximum (0.8 T) values. From Equation (13), it is clear that in passive control, the stiffness and damping of the MRE-based isolator are constant and the actuation force of a passive system is zero. In sky-hook control, the actuation force is generally described as Gu et al. (2019):

$$f_{MRE} = \begin{Bmatrix} (k_{max} - k_{min})(x_b - x_s) + (c_{max} - c_{min})(\dot{x}_b - \dot{x}_s) & (\dot{x}_s - \dot{x}_b)\dot{x}_s \geq 0 \\ 0 & (\dot{x}_s - \dot{x}_b)\dot{x}_s \leq 0 \end{Bmatrix} \tag{44}$$

RESULTS AND DISCUSSIONS

The parameters of the MRE-based seat suspension system are provided in **Table S1**. The parameter values for the mass of the seat and mass, stiffness, and damping of the cushion and driver for the model shown in **Figure 6B** are obtained from Xu et al. (2018) and Choi and Han (2007). It should be noted that an additional linear spring with spring coefficient of k_b is added in parallel to the MRE isolator in order to limit the

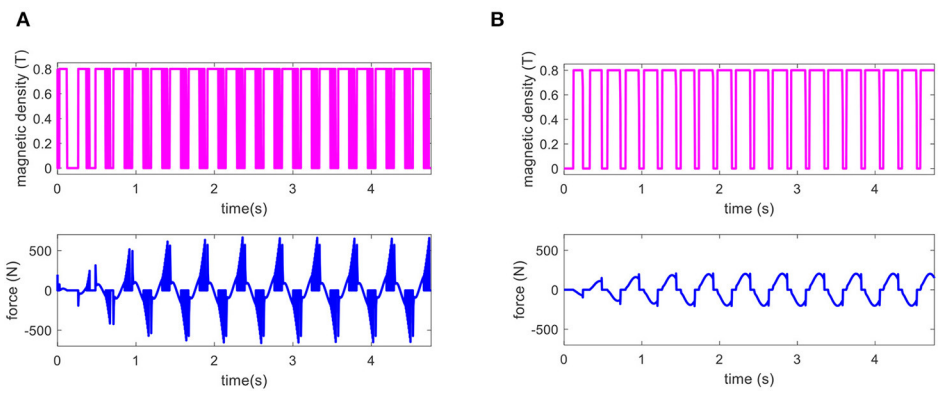

FIGURE 9 | The control input to the MRE-based isolator for harmonic excitation; **(A)** ON-OFF controller, and **(B)** adaptive NN controller.

static deformation of the MREs, and two cuboid MREs operating in shear mode with the effective area of $A = 64\ cm^2$ and the thickness of $h = 1.6$ cm are considered. In addition, a stroke amplitude limit of 5 mm, as shown in **Figure 6**, has been considered. Thus, we can write:

$$-5\ (mm) < x_s - x_b < 5\ (mm) \tag{45}$$

In the following, the effectiveness of the proposed control is demonstrated under different types of base excitations.

Harmonic Excitation

The performance of the proposed controller is investigated under harmonic excitation. The simulation is conducted in the frequency range of 0.5 to 5 Hz, which is the typical frequency range of a vehicle seat suspension system. Five cycles with a constant amplitude of 5 mm are considered for each excitation frequency. The Root-Mean-Square (RMS) values of the displacement and acceleration with respect to frequencies are shown in **Figures 8A,B**, respectively. Results clearly show the superior vibration isolation capability of the proposed adaptive NN controller over the various fixed levels of applied magnetic flux density (passive control) and On-Off sky-hook controller. The control output using On-Off and the adaptive NN controller are also provided in **Figures 9A,B**, respectively. As it can be realized, the high-speed control input switching, which may cause high energy loss in the electrical system, occurs using the On-Off control strategy. The RMS value of the displacement, acceleration, and transmissibility at the resonance frequency are provided in **Table 2**. Results clearly demonstrate the prominent vibration isolation ability of the proposed control scheme at the resonance frequency compared with passive control and On-Off control strategies.

TABLE 2 | Comparison of the performance of various control schemes under harmonic excitation, bump shock, and random excitation.

	RMS value	OFF-State (0.0 T)	ON-State (0.8 T)	ON-OFF	NN
Harmonic excitation	Displacement (cm)	2.17	1.98	1.83	1.66
	Acceleration (m/s^2)	3.60	3.84	3.28	3.06
	Transmissibility	6.13	5.63	5.17	4.67
Bump shock	Displacement (mm)	6.00	6.14	5.74	4.19
	Acceleration (m/s^2)	2.28	2.20	2.13	2.06
Random excitation	Displacement (mm)	8.7	9.4	7.6	6.3
	Acceleration (m/s^2)	1.45	1.83	1.22	1.06

Bump Shock

In this section, the performance of the adaptive NN controller on the transient response of the designed MRE-based seat suspension isolator is evaluated using the bump shock excitation described as:

$$x_b = \begin{cases} \frac{(1-cos(w_b\pi))\ h_0}{2} & \frac{6}{w_b} \le t \le \frac{8}{w_b} \\ 0 & t < \frac{6}{w_b}\ or\ t > \frac{8}{w_b} \end{cases} \tag{46}$$

where $h_0 = 0.01$ m denotes the height of the bump shock transferred to the seat and $w_b = 20$ is a constant determining the width of the bump. The displacement responses of the seat suspension system to the bump shock using OFF and ON states passive control, on-off skyhook control, and the proposed adaptive NN strategies are provided in **Figures S1A–D**, respectively. The displacement and acceleration responses of the driver's mass to the bump shock using the proposed control strategy and its comparison with passive off/on and sky-hook control strategies are shown in **Figures 10A,B**, respectively. The performance comparison results of various control schemes under the bump shock using the max peak of displacement and acceleration values are also listed in **Table 2**. Results clearly show the superior performance of the proposed adaptive NN control scheme compared with other control strategies in reducing

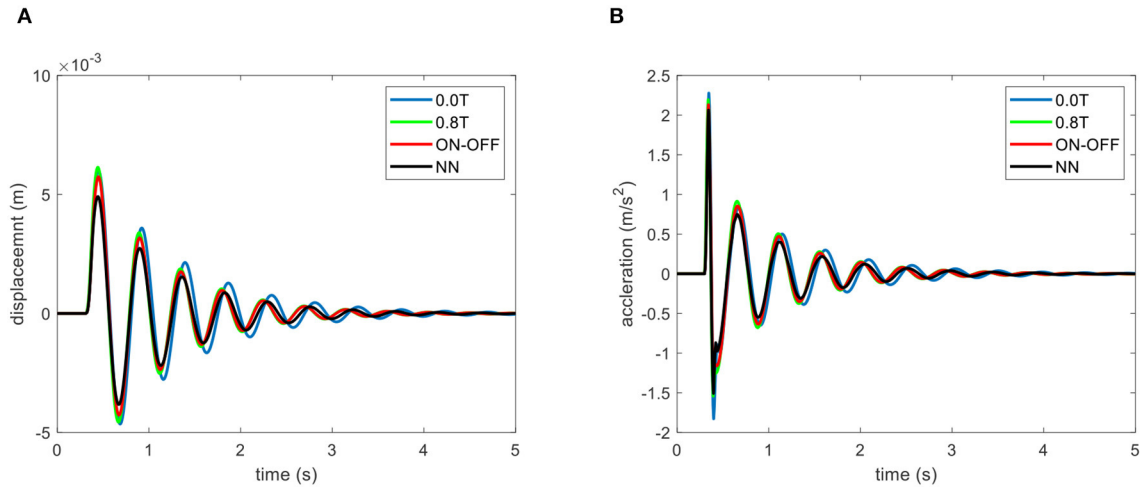

FIGURE 10 | (A) Displacement, and **(B)** acceleration of the human body (x_d) for bump shock input in the presence of various controllers.

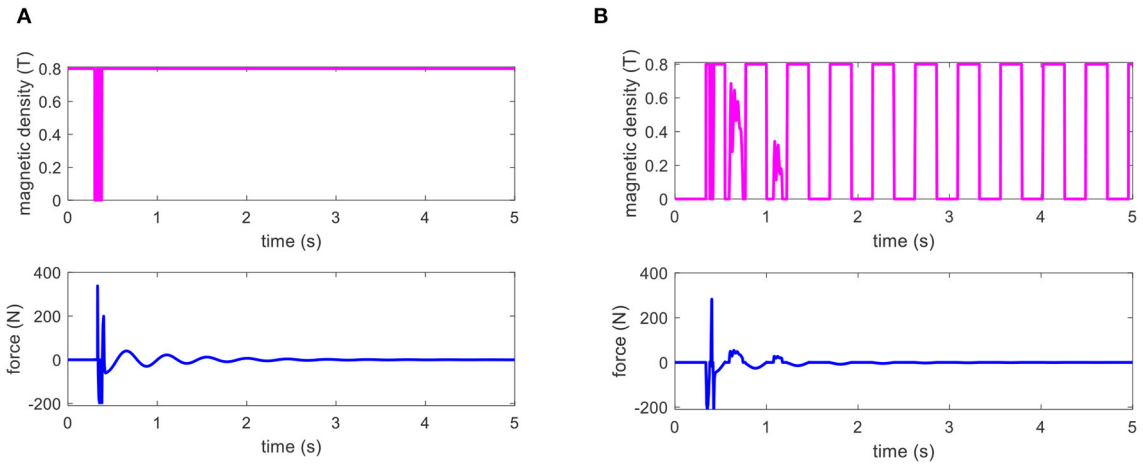

FIGURE 11 | The control input to the MRE-based isolator for bump shock; **(A)** ON-OFF controller, and **(B)** adaptive NN controller.

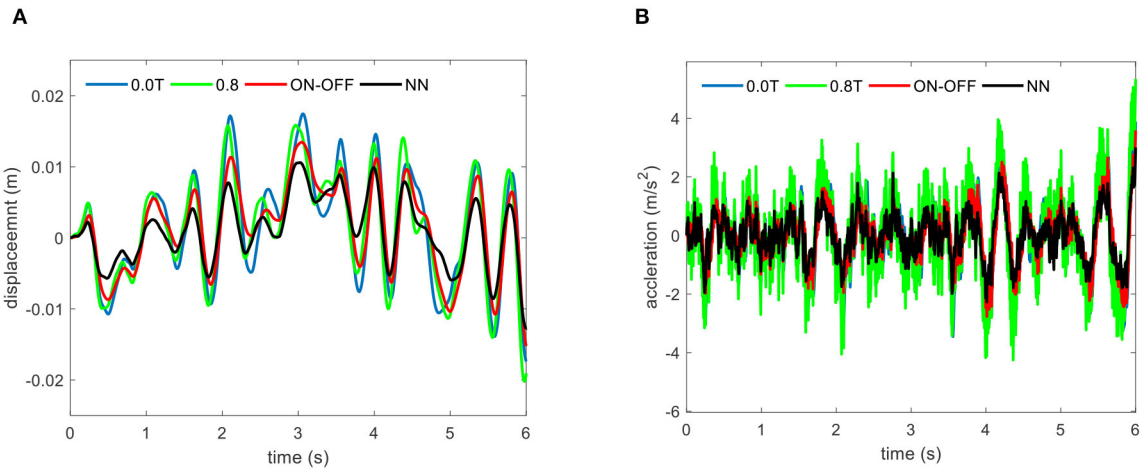

FIGURE 12 | (A) Displacement, and **(B)** acceleration of the human body (x_d) for a random excitation case in the presence of various controllers.

both displacement and acceleration. The corresponding control output of the ON-OFF control strategy and the adaptive NN controller are also presented in **Figures 11A,B**, respectively. As it can be realized from **Figure 11A**, after transient bump duration, the ON-OFF control output is basically equivalent to ON state passive control. This is because the ON-OFF control law is based on the relative velocity between the base and seat frame as well as the velocity of the seat frame. Once the base excitation approaches zero, the control output is set to its maximum value. However, as shown in **Figure 11B**, the adaptive NN control, which possesses the self-learning ability, shows a variation on the control input based on its control law and update law. Considering that the applied magnetic field to the MRE layers is limited between 0.0 to 0.8 T, the control output and, consequently, the actuation force induced by MREs in the presence of the applied field vary between the minimum and maximum values.

Random Excitation

In this case, the random excitation is provided to further investigate the control performance of various control schemes. The displacement responses of the designed seat suspension system under random excitation using OFF and ON states passive control, on-off skyhook control, and the proposed adaptive NN strategies under the random excitation are provided in **Figures S2A–D**, respectively. As it can be seen, the developed MRE-based isolator can efficiently suppress the random excitation due to the road profile, and the proposed adaptive NN controller presents better performance compared with passive and on-off control strategies. The prominent performance of the developed controller can also be further verified in **Figure 12**, in which the displacement and acceleration response of the driver mass obtained using the proposed controller compared with those of the passive OFF/ON and sky-hook control strategies. The RMS values of the displacement and

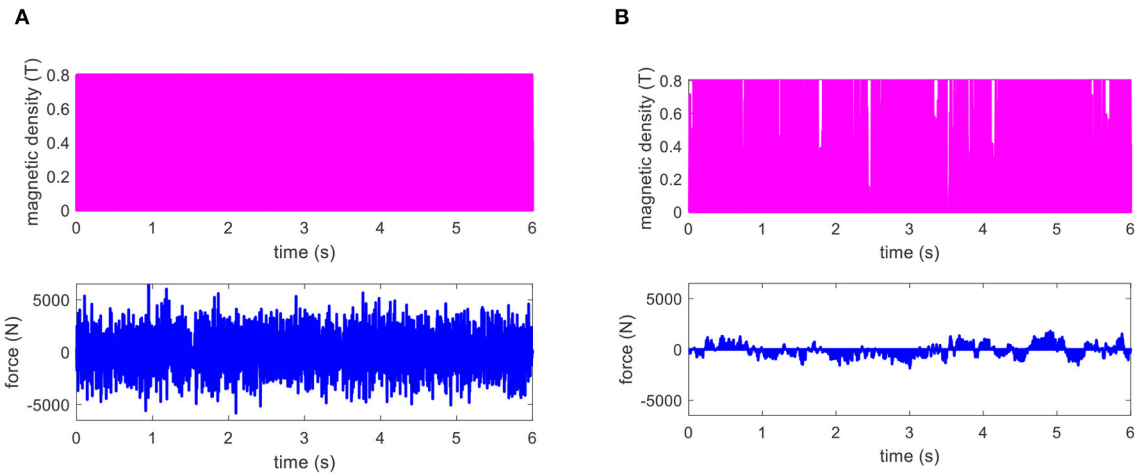

FIGURE 13 | The control input to the MRE-based isolator for random excitation; **(A)** ON-OFF controller, and **(B)** adaptive NN controller.

acceleration of the driver mass are also provided in **Table 2**. The results show that the proposed control scheme can reduce the transmitted vibration to a greater extent than passive and On-Off sky-hook controllers under the random road profile. Comparing the corresponding control outputs of the sky-hook and adaptive NN controllers in **Figure 13** also shows the effectiveness of the adaptive NN controller in reducing the required control force and, subsequently, decreasing the consumed energy.

CONCLUSION

In this study, MRE samples with 25% volume fraction of carbonyl iron particles were fabricated and then experimentally characterized to evaluate their viscoelastic properties and their variation with respect to the applied magnetic field. An MRE-based seat suspension isolator has been developed considering the constraints on the applied magnetic flux density, stroke limit, damping effect, and static deformation. Adaptive NN control was proposed for the MRE-based seat suspension isolator to alleviate unwanted vibration. The stability and convergence of the proposed control scheme were proven using the Lyapunov method. The superior control performance of the proposed control scheme has then been verified under various base excitation profiles through the comparison with passive control and On-Off control strategies. Results suggest the superior performance of the proposed adaptive NN-based control strategy.

DATA AVAILABILITY STATEMENT

The raw data supporting the conclusions of this article will be made available by the authors, without undue reservation, to any qualified researcher upon request.

AUTHOR CONTRIBUTIONS

CL, MH, RS, and GW contributed conception and design of the study. CL developed the modeling of MRE-based isolator and semi-active adaptive neural network controller. MH developed magnetic analysis, MRE fabrication, testing, and characterization. RS and GW supervised the research study. CL wrote the first draft of the manuscript. All authors contributed to manuscript revision, read, and approved the submitted version.

ACKNOWLEDGMENTS

Support from the Natural Sciences and Engineering Research Council of Canada (NSERC) and National Natural Science Foundation of China (11832009) are gratefully acknowledged.

SUPPLEMENTARY MATERIAL

The Supplementary Material for this article can be found online at: https://www.frontiersin.org/articles/10.3389/fmats.2020.00171/full#supplementary-material

REFERENCES

Behrooz, M., Wang, X., and Gordaninejad, F. (2014). Performance of a new magnetorheological elastomer isolation system. *Smart Mater. Struct.* 23: 045014. doi: 10.1088/0964-1726/23/4/045014

Choi, S. B., and Han, Y. M. (2007). Vibration control of electrorheological seat suspension with human- body model using sliding mode control. *J. Sound Vib.* 303, 391–404. doi: 10.1016/j.jsv.2007.01.027

Choi, S. B., Nam, M. H., and Lee, B. K. (2001). Vibration control of a MR seat damper for commercial vehicles. *J. Intell. Mater. Syst. Struct.* 11, 936–944. doi: 10.1177/104538900772664242

Dargahi, A., Rakheja, S., and Sedaghati, R. (2019a). Development of a field dependent Prandtl-Ishlinskii model for magnetorheological elastomers. *Mater. Des.* 166:107608. doi: 10.1016/j.matdes.2019.107608

Dargahi, A., Sedaghati, R., and Rakheja, S. (2019b). On the properties of magnetorheological elastomers in shear mode: design, fabrication and characterization. *Compos. Part B Eng.* 159, 269–283. doi: 10.1016/j.compositesb.2018.09.080

Deng, H., and Gong, X. (2008). Application of magnetorheological elastomer to vibration absorber. *Commun. Nonlinear Sci. Numer. Simul.* 13, 1938–1947. doi: 10.1016/j.cnsns.2007.03.024

Du, H., Li, W., and Zhang, N. (2011). Semi-active variable stiffness vibration control of vehicle seat suspension using an MR elastomer isolator. *Smart Mater. Struct.* 20:105003. doi: 10.1088/0964-1726/20/10/105003

Fu, J., Li, P., Wang, Y., Liao, G., and Yu, M. (2016a). Model-free fuzzy control of a magnetorheological elastomer vibration isolation system: analysis and experimental evaluation. *Smart Mater. Struct.* 25:035030. doi: 10.1088/0964-1726/25/3/035030

Fu, J., Liao, G., Yu, M., Li, P., and Lai, J. (2016b). NARX neural network modeling and robustness analysis of magnetorheological elastomer isolator. *Smart Mater. Struct.* 25:125019. doi: 10.1088/0964-1726/25/12/125019

Ge, S. S., Hang, C. C., Lee, T. H., and Zhang, T. (2002). *Stable Adaptive Neural Network Control*. Boston, MA: Springer. doi: 10.1007/978-1-4757-6577-9

Gu, X., Yu, Y., Li, J., and Li, Y. (2017). Semi-active control of magnetorheological elastomer base isolation system utilising learning-based inverse model. *J. Sound Vib.* 406, 346–362. doi: 10.1016/j.jsv.2017.06.023

Gu, X., Yu, Y., Li, Y., Li, J., Askari, M., and Samali, B. (2019). Experimental study of semi-active magnetorheological elastomer base isolation system using optimal neuro fuzzy logic control. *Mech. Syst. Signal Process.* 119, 380–398. doi: 10.1016/j.ymssp.2018.10.001

He, W., and Dong, Y. (2018). Adaptive fuzzy neural network control for a constrained robot using impedance learning. *IEEE Trans. Neural Netw. Learn. Syst.* 29, 1174–1186. doi: 10.1109/TNNLS.2017.2665581

Kallio, M., Lindroos, T., Aalto, S., Järvinen, E., Kärnä, T., and Meinander, T. (2007). Dynamic compression testing of a tunable spring element consisting of a magnetorheological elastomer. *Smart Mater. Struct.* 16, 506–514 doi: 10.1088/0964-1726/16/2/032

Li, Y., Li, J., Li, W., and Du, H. (2014). A state-of-the-art review on magnetorheological elastomer devices. *Smart Mater. Struct.* 23:123001 doi: 10.1088/0964-1726/23/12/123001

Li, Y., Li, J., Tian, T., and Li, W. (2013). A highly adjustable magnetorheological elastomer base isolator for applications of real-time adaptive control. *Smart Mater. Struct.* 22:095020. doi: 10.1088/0964-1726/22/9/095020

Liao, G. J., Gong, X. L., Xuan, S. H., Kang, C. J., and Zong, L. H. (2012). Development of a real-time tunable stiffness and damping vibration isolator based on magnetorheological elastomer. *J. Intell. Mater. Syst. Struct.* 23, 25–33. doi: 10.1177/1045389X11429853

Meeker, D. (2020). *Finite Element Method Magnetics (FEMM 4.0.1)* [Online]. Available online at: http://www.femm.info (accessed February 10, 2020).

Nguyen, S. D., Nguyen, Q. H., and Choi, S. B. (2015). A hybrid clustering based fuzzy structure for vibration control - Part 2: an application to semi-active vehicle seat-suspension system. *Mech. Syst. Signal Process.* 56, 288–301. doi: 10.1016/j.ymssp.2014.10.019

Nguyen, X. B., Komatsuzaki, T., Iwata, Y., and Asanuma, H. (2018). Modeling and semi-active fuzzy control of magnetorheological elastomer-based isolator for seismic response reduction. *Mech. Syst. Signal Process.* 101, 449–466. doi: 10.1016/j.ymssp.2017.08.040

Noriega, J. R., and Wang, H. (1998). A direct adaptive neural-network control for unknown nonlinear systems and Its application. *IEEE Trans. Neural Netw.* 9, 27–34. doi: 10.1109/72.655026

Opie, S., and Yim, W. (2009). "Design and control of a real-time variable stiffness vibration isolator," in *IEEE/ASME International Conference On Advanced Intelligent Mechatronics, AIM* (Singapore), 380–385. doi: 10.1109/AIM.2009.5229983

Symans, M. D., and Constantinou, M. C. (1999). Semi-active control systems for seismic protection of structures: a state-of-the-art review. *Eng. Struct.* 21, 469–487. doi: 10.1016/S0141-0296(97)00225-3

Wilder, D., Magnusson, M. L., Fenwick, J., and Pope, M. (1994). The effect of posture and seat suspension design on discomfort and back muscle fatigue during simulated truck driving. *Appl. Ergon.* 25, 66–76. doi: 10.1016/0003-6870(94)90067-1

Xu, L., Zou, A., Fu, J., Yu, M., and Bai, J. (2018). "Development and simulation evaluation of a magnetorheological elastomer isolator for transformer vibration control," in *Proceedings of 30th Chinese Control* and *Decision Conference CCDC* 2018 (Shenyang), 2600–2604.

Yang, J., Sun, S. S., Du, H., Li, W. H., Alici, G., and Deng, H. X. (2014). A novel magnetorheological elastomer isolator with negative changing stiffness for vibration reduction. *Smart Mater. Struct.* 23:105023. doi: 10.1088/0964-1726/23/10/105023

Conflict of Interest: The authors declare that the research was conducted in the absence of any commercial or financial relationships that could be construed as a potential conflict of interest.

frontiers in Materials

ORIGINAL RESEARCH
published: 09 July 2020
doi: 10.3389/fmats.2020.00204

Integrated Shock Absorber With Both Tunable Inertance and Damping

Wei-Min Zhong[1], An-Ding Zhu[1], Xian-Xu Frank Bai[1], Norman M. Wereley[2]* and Nong Zhang[1]*

[1] Laboratory for Adaptive Structures and Intelligent Systems (LASIS), Department of Vehicle Engineering, Hefei University of Technology, Hefei, China, [2] Smart Structures Laboratory, Department of Aerospace Engineering, University of Maryland, College Park, MD, United States

Inerter is a two-terminal mass element, and the applied force is proportional to the relative acceleration between the terminals. According to the second class of mechanical–electrical analogy, the inerter corresponds exactly to the capacitor in the electric network. Aiming at improving the limited vibration isolation performance using the constant inertance of a conventional inerter, a new semi-active inerter based on smart material, magnetorheological (MR) fluid, is proposed in this paper. Furthermore, according to the design concept of "functional integration", the MR inerter, an MR damper, and a spiral spring are integrated to realize a new integrated inerter-spring-damper (IISD) with both adjustable inertance and damping characteristics. The MR inerter consists of a ball screw, an MR clutch, MR fluid, excitation coils, an excitation shell, a flywheel, a flywheel shell, a connector, upper and lower covers, bearings, and seals. The tunable inertance is achieved by adjusting the excitation current in the excitation coils to change the operating state of the MR clutch. The MR damper and the spiral spring provide variable damping and constant stiffness, respectively. The mathematical model of the IISD is established. The adjustment principle of inertance is verified by numerical simulation, and the mechanical output characteristics of the IISD are analyzed. Besides that, the 1/4 vehicle suspension model based on the proposed IISD is built by using MATLAB/SimMechanics. The frequency response and the unit impulse response characteristics of the suspension are obtained *via* the comfort-oriented virtual experiment. The simulation results show that the suspension with the IISD has 23.0% higher performance than the conventional suspension in vehicle body acceleration, and the suspension deflection and the dynamic tire load are also improved.

Keywords: tunable inertance, magnetorheological fluid, MR inerter, ISD suspension, functional integration

OPEN ACCESS

Edited by:
Ilkwon Oh,
Korea Advanced Institute of Science and Technology, South Korea

Reviewed by:
Jung Woo Sohn,
Kumoh National Institute of Technology, South Korea
Seung-Bok Choi,
Inha University, South Korea

****Correspondence:***
Xian-Xu Frank Bai
bai@hfut.edu.cn
Norman M. Wereley
wereley@umd.edu

Specialty section:
This article was submitted to Smart Materials, a section of the journal Frontiers in Materials

Received: *08 November 2019*
Accepted: *03 June 2020*
Published: *09 July 2020*

Citation:
Zhong W-M, Zhu A-D, Bai X-XF, Wereley NM and Zhang N (2020) Integrated Shock Absorber With Both Tunable Inertance and Damping. Front. Mater. 7:204. doi: 10.3389/fmats.2020.00204

INTRODUCTION

According to the first class of mechanical–electrical analogy, the mass, spring, and damper in the mechanical network correspond to the capacitor, inductance, and resistance in the electric network, respectively. Meanwhile, Newton's Second Law states that the applied force is proportional to the absolute acceleration of mass, i.e., mechanical grounded. Therefore, the mass can only correspond to the grounded capacitor, which greatly limits the application of the method applied to

electrical circuits in a mechanical network design. In response to the above problem, in 2002, a new mass element termed "inerter" was introduced by Smith (2002) according to the second class of mechanical–electrical analogy, which completely corresponds to the capacitor in an electrical network. The inerter has two movable terminals, and the applied force is proportional to the relative acceleration between its terminals. There is no longer a "ground" limitation during the mechanical network design by using the electric method, which greatly enriches the structure and the design ideas of the mechanical network. The performance of vibration control systems based on inerter is further improved compared to the mass–spring–damper system. At the same time, the inerter has smaller volume and weight than the traditional mass element. Therefore, the inerter has received extensive attention from researchers in different fields (Smith and Wang, 2004; Papageorgiou and Smith, 2006; Chen et al., 2009; Papageorgiou et al., 2009; Brzeski et al., 2015; Matamoros-Sanchez and Goodall, 2015; Giaralis and Petrini, 2017).

The vibration isolation performance of the passive inerter is limited because of the fixed inertance. Different types of semi-active inerter have been introduced recently. Hu et al. (2016) proposed a mechanical adjustable inerter that is mainly composed of mass blocks sliding along the radial direction and a linear actuator. The linear actuator can change the radius of gyration of the mass, that is, continuous adjustment of the inertance can be achieved by changing the rotational inertia of the flywheel. The use of magnetorheological (MR) fluid to achieve an adjustable inerter has also been preliminarily studied. Tipuric et al. (2018) studied the feasibility of a spiral-tube semi-active inerter based on MR fluid. Bai et al. (2018) extended a semi-active inerter concept using MR fluid, while its feasibility has not been verified. We later proposed a tunable inerter based on MR fluid (Zhong et al., 2019); however, an additional force compensation mechanism is needed to achieve a continuous adjustment of the inertance.

Although the inertance of the existing semi-active inerters can be adjusted by different ways, there is still potential to improve the adjustment speed and extend the range of inertance. A tunable inerter with a wide adjustment range, fast response, and low energy consumption needs to be developed. In the field of semi-active control, MR fluid has exactly the above properties. At present, the intelligent actuators based on MR fluid have been thoroughly studied in many fields (Imaduddin et al., 2013; Kaluvan et al., 2015; Bai et al., 2016; Sapiński et al., 2016; Shiao et al., 2016). Nevertheless, applying the MR fluid to semi-active inerter and inerter–spring–damper (ISD) vibration isolation systems it is still preliminary. Based on the concept of "functional integration" (Bai et al., 2017), this paper proposes an adjustable inerter. The MR inerter, an MR damper, and a spiral spring are highly integrated to realize the integrated ISD (IISD) with a compact structure, quick response, and wide adjustment range. Besides that, the 1/4 vehicle suspension model with the IISD is built by using MATLAB/SimMechanics, and virtual experiment was carried out to validate the performance.

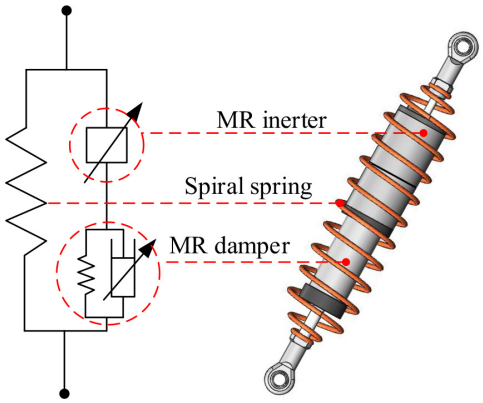

FIGURE 1 | Schematic of the integrated inerter-spring-damper.

STRUCTURAL PRINCIPLE OF THE IISD

Integrated Design

The connection between the MR inerter, MR damper, and spiral spring should be considered during the integrated design procedure. The integrated layout of the IISD is demonstrated in **Figure 1**. The spiral spring acts as a support, and the inerter in series with the damper can provide better performance than that of the parallel form (Smith and Wang, 2004). The MR inerter and the MR damper have a common terminal, and the other two terminals are connected to the ends of the spiral spring, respectively. The spring in parallel with the MR damper in **Figure 1** refers to the accumulator inside the MR damper (see **Figure 3**).

MR Inerter

The structural principle of the MR inerter is shown in **Figure 2**. The MR inerter consists of a ball screw, an MR clutch, MR fluid, excitation coils, an excitation shell, a flywheel, a flywheel shell, a connector, upper and lower covers, bearings, and seals. The inner casing of the MR clutch is connected to the nut of the ball screw. The outer casing of the MR clutch is engaged with the flywheel, and the excitation coils are winded on the excitation shell around the MR clutch. The space between the inner and the outer casings of the MR clutch is filled with MR fluid, which is working under pure shear mode. When a displacement excitation is applied to the terminals of the MR inerter, the inner casing of the MR clutch rotates with the nut of the ball screw. When there is no current in the excitation coils, the outer and the inner casing of the MR clutch are completely disconnected, and the output force of the MR inerter is independent of the flywheel. When a certain current is applied, the rotating inner casing of the MR clutch will rotate the outer casing for the effect of the MR fluid, i.e., rotate the flywheel. The nut on the ball screw receives additional torque from the flywheel due to the effect of the additional mass, and additional inertance can be provided. The complete disengagement and engagement of the MR clutch correspond to the minimal and the maximal inertance, respectively.

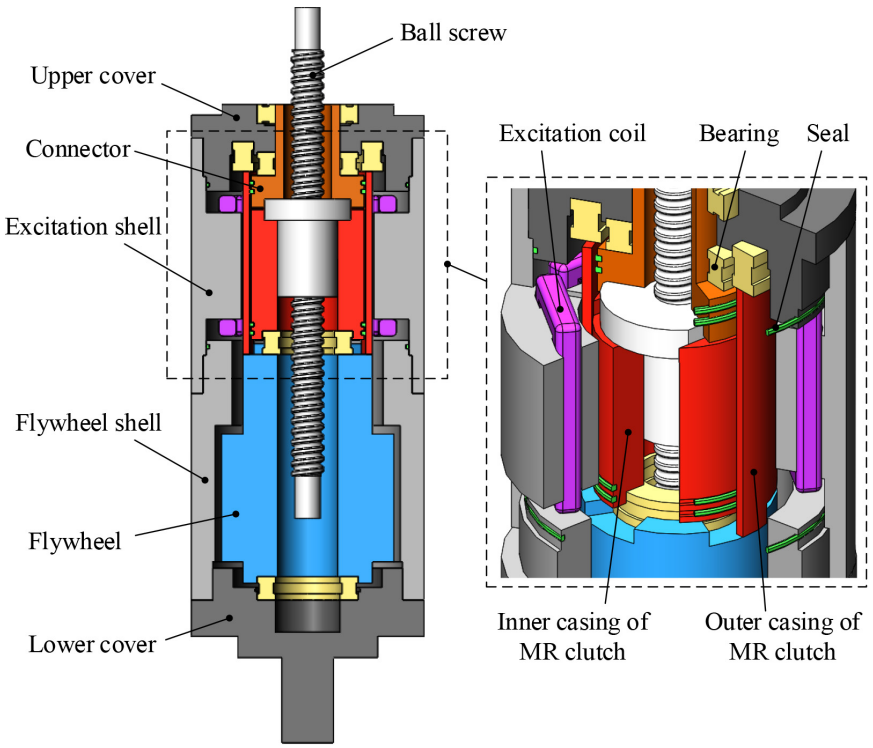

FIGURE 2 | Structural principle of the magnetorheological inerter.

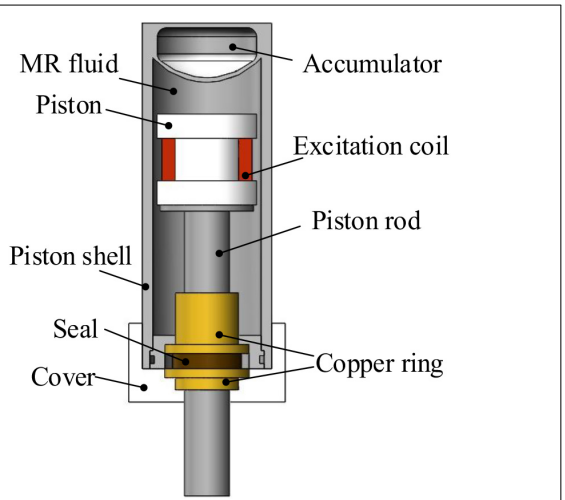

FIGURE 3 | Structural principle of the magnetorheological damper.

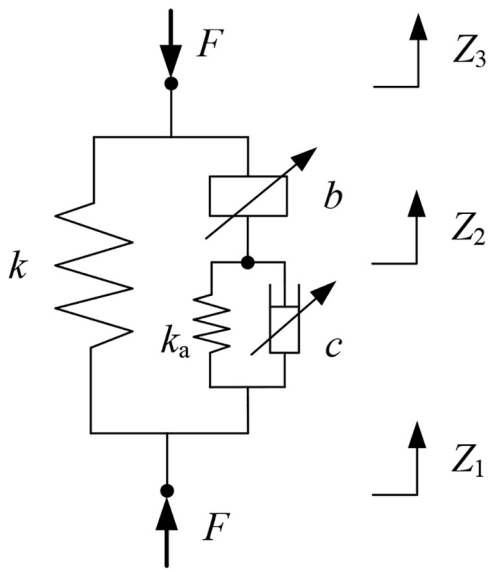

FIGURE 4 | Mechanical model of the integrated inerter-spring-damper.

MR Damper

Figure 3 demonstrates the structural principle of the MR damper. The MR damper mainly includes a piston, a piston rod, excitation coils, MR fluid, an accumulator, a piston shell, a cover, copper rings, and a seal. The viscosity of the MR fluid can be changed by adjusting the current in the excitation coils; thereby, the damping coefficient of the MR damper can be adjusted.

MATHEMATICAL MODEL OF THE IISD

As shown in **Figure 4**, the output force of the IISD is related to four factors, i.e., the spring stiffness k, the inertance b of the MR inerter, the damping coefficient c of the MR damper, and

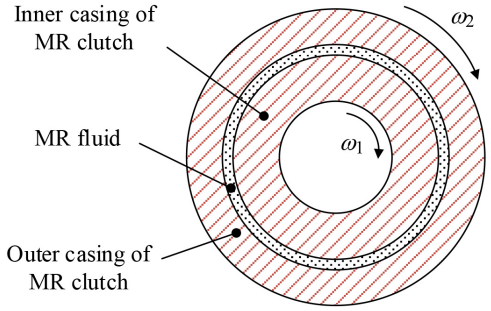

FIGURE 5 | Simplified model of the magnetorheological clutch.

the accumulator stiffness k_a. Since the MR inerter is connected in series with the MR damper, and the accumulator is connected in parallel with the MR damper, the output force of the MR inerter is equal to the sum of the output forces of the MR damper and the accumulator, and then the output force of the IISD can be expressed as:

$$\begin{aligned} F &= k(Z_1 - Z_3) + k_a(Z_1 - Z_2) + c(\dot{Z}_1 - \dot{Z}_2) \\ &= k(Z_1 - Z_3) + b(\ddot{Z}_2 - \ddot{Z}_3) \end{aligned} \tag{1}$$

where Z_1 and Z_3 are the displacement at the terminals of the spiral spring, Z_2 is the displacement at the junction of the MR damper and the MR inerter, $\dot{Z}_1$ and $\dot{Z}_2$ are the velocity at the terminals of the MR damper, and $\ddot{Z}_2$ and $\ddot{Z}_3$ are the acceleration at the terminals of the MR inerter.

The proposed MR inerter is designed based on ball-screw type and its inertance b can be expressed as (Wang and Chan, 2008):

$$b = J\left(\frac{2\pi}{p}\right)^2 \tag{2}$$

where J is the moment of inertia of the flywheel and p is the lead of the ball-screw.

According to the principle analysis of the MR inerter, the completely disengaged and engaged states of the MR clutch corresponding to the minimal and the maximal inertance, respectively, can be expressed as:

$$\begin{cases} b_{\min} = J_1\left(\frac{2\pi}{p}\right)^2 \\ b_{\max} = (J_1 + J_2)\left(\frac{2\pi}{p}\right)^2 \end{cases} \tag{3}$$

where J_1 is the moment of inertia of the inner casing of the MR clutch and J_2 is the sum of the moments of inertia of the outer casing of the MR clutch and the flywheel.

It can be seen from Eq. (3) that the minimal and the maximal inertances of the MR inerter are only dependent on the parameters of the structure itself. So, the adjustment range of the inertance is determined by the geometry of the structure. The inertance between the minimal and the maximal can be obtained by controlling the MR clutch.

Figure 5 shows a simplified model of the MR clutch. The angular velocity of the inner and the outer casings of the MR clutch is ω_1 and ω_2, respectively. Under an ideal condition (i.e., the MR clutch can be completely disengaged and engaged), the relationship between the angular velocities of the inner and the outer casings of the MR clutch corresponding to the minimal inertance is $\frac{\omega_2}{\omega_1} = 0$. The relationship of the maximal inertance refers to $\frac{\omega_2}{\omega_1} = 1$. Any intertance between the minimal and the maximal can be reached by setting the ratio of the outer casing to the inner casing angular velocity of the MR clutch between 0 and 1. Since the angular velocity of the inner casing of the MR clutch is generated by external excitation, the problem of adjusting the inertance is actually transformed into the control of the angular velocity of the outer casing.

The output force F_i of the MR inerter depends on the torque applied on the nut of the ball-screw. The torque consists of two parts, i.e., the torque generated by the inner casing of the MR clutch and the additional torque generated by the rotation of the flywheel, which can be expressed as:

$$F_i = T\left(\frac{2\pi}{p}\right) \tag{4}$$

$$T = J_1\omega_1^{'} + J_2\omega_2^{'} \tag{5}$$

where $\omega_1^{'}$ is the angular acceleration of the inner casing of the MR clutch and $\omega_2^{'}$ is the angular acceleration of the outer casing of the MR clutch, i.e., the angular acceleration of the flywheel.

Defining $\gamma = \frac{\omega_2^{'}}{\omega_1^{'}}$, then Eq. (5) can be rewritten as:

$$T = (J_1 + \gamma J_2)\omega_1^{'} \tag{6}$$

The inertance can be obtained simultaneously from Eqs (1, 4, and 6), and $\omega_1^{'} = (\ddot{Z}_2 - \ddot{Z}_3)(\frac{2\pi}{p})$:

$$b = (J_1 + \gamma J_2)\left(\frac{2\pi}{p}\right)^2 \tag{7}$$

From Eq. (7), any inertance between the minimal and the maximal can be achieved by adjusting the proportional coefficient γ .

The torque T_{MR} transmitted by the MR clutch equals to the additional torque T_e acting on the nut of the ball-screw, which consists of two parts: one is the uncontrollable torque T_η caused by the viscous force due to the different angular velocity between the inner and the outer casings of the MR clutch, and the other one is the controllable torque T_τ caused by the shear stress under the effect of the magnetic field. They can be respectively expressed as:

$$T_{MR} = T_\eta + T_\tau \tag{8a}$$

$$T_\eta = \frac{4\pi\eta L_c r_1^2 r_2^2(\omega_2 - \omega_1)}{r_2^2 - r_1^2} \tag{8b}$$

$$T_\tau = \frac{4\pi\tau_y L_c r_1^2 r_2^2 \ln(\frac{r_2}{r_1})}{r_2^2 - r_1^2} \tag{8c}$$

where η is the viscosity of the MR fluid without magnetic field, L_c is the effective length of the MR fluid in the MR clutch, r_1 and r_2

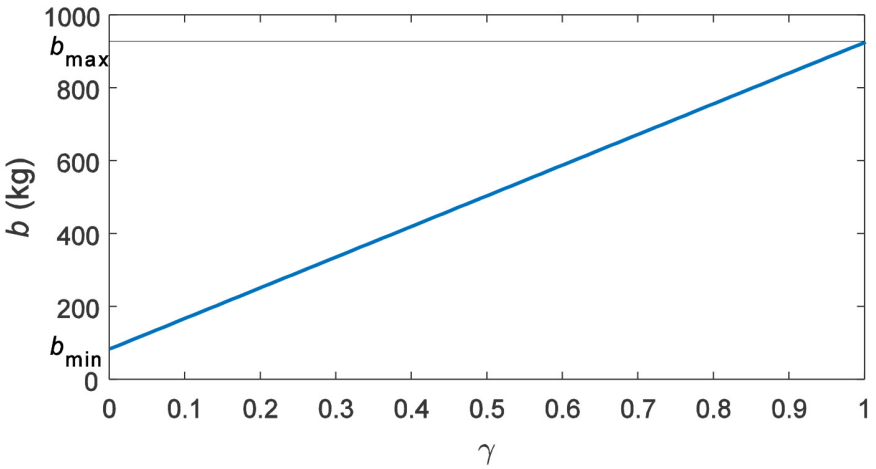

FIGURE 6 | Adjustment process of the inertance under an ideal situation.

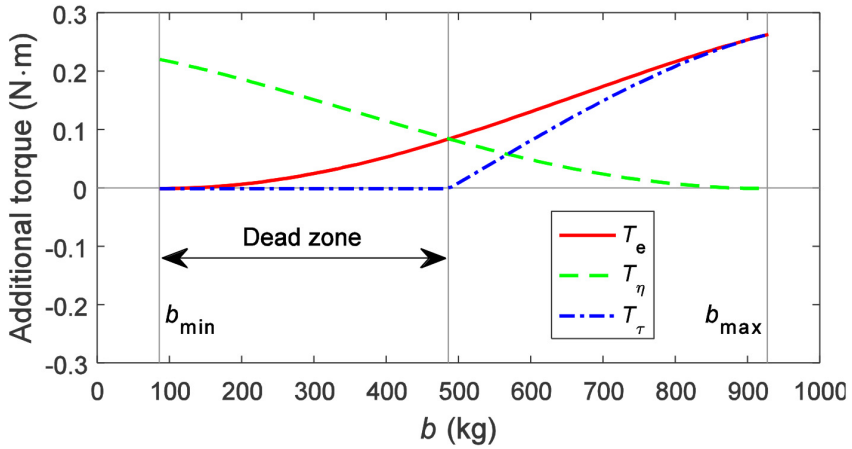

FIGURE 7 | Additional torque during the adjustment of the inertance.

are the inner and the outer radius of the annular gap filled with the MR fluid, respectively, and τ_y is the yield shear stress of the MR fluid under the effect of the magnetic field.

Replacing the T_{MR} in Eq. (8a) with the load torque T_L, the angular velocity of the outer casing of the MR clutch can be obtained:

$$\omega_2 = \omega_1 - \frac{r_2^2 - r_1^2}{4\pi\eta L_c r_1^2 r_2^2}\left[T_L - \frac{4\pi\tau_y L_c r_1^2 r_2^2 \ln(\frac{r_2}{r_1})}{r_2^2 - r_1^2}\tau_y\right] \quad (9)$$

NUMERICAL SIMULATION

Table A1 presents a list of the main structural parameters of IISD. According to the parameters in **Table A1**, under an ideal situation, the adjustment range of the inertance that can be realized by the MR inerter is shown in **Figure 6**. The minimal inertance is 86 kg and the maximal inertance is 927 kg. In the process of the change of the proportional coefficient γ from 0 to 1, the inertance experiences a proportional increase.

Although the adjustment range and change trend of inertance can be observed under an ideal situation, the actual torque of the MR clutch and whether continuous adjustment can be achieved are not known. In order to further verify the adjustment principle of the inertance, a simulation is performed by applying a certain displacement excitation to the MR inerter. The displacement excitation has an amplitude of 20 mm and a frequency of 0.5 Hz. The simulation condition is set as adjusting the inertance from the minimal to the maximal within 0.5 s to observe the changes of the expected additional torque T_e, the uncontrollable torque T_η, and the controllable torque T_τ. The simulation results are shown in **Figure 7**.

It can be seen from **Figure 7** that, as the inertance increases, the expected additional torque is continuously increased from 0 Nm to about 0.26 Nm. During the increase of the inertance, the rotational velocity of the inner and the outer casings of the MR clutch is gradually getting close until eventually synchronous;

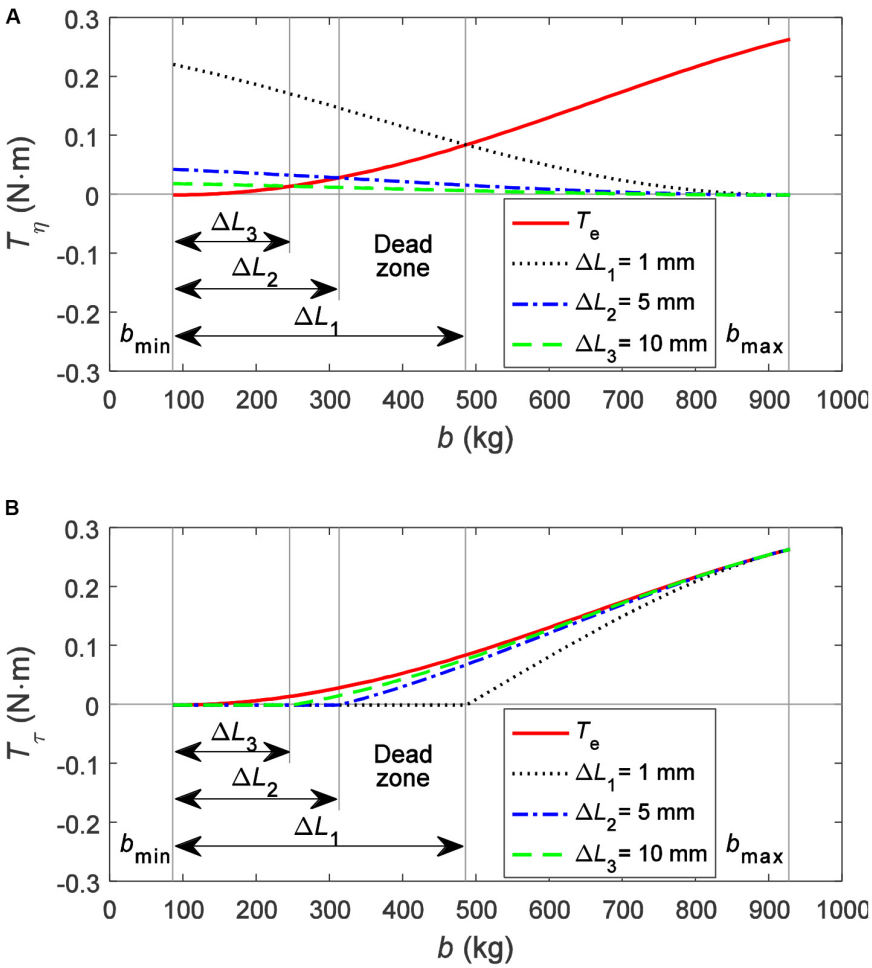

FIGURE 8 | Additional torque under different gap widths: **(A)** uncontrollable torque and **(B)** controllable torque.

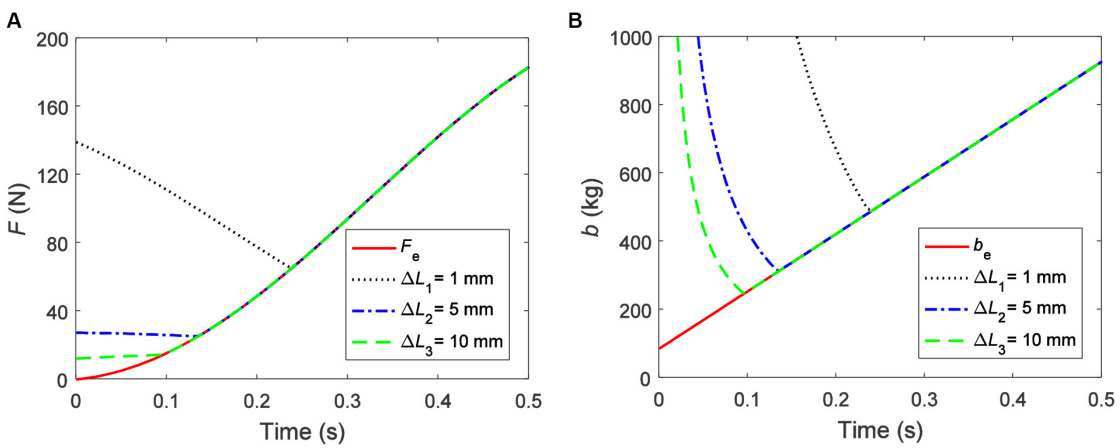

FIGURE 9 | Output characteristics of the magnetorheological inerter under different gap widths: **(A)** force and **(B)** inertance.

the uncontrollable torque T_η is gradually reduced from about 0.22 to 0 Nm. The controllable torque T_τ is 0 Nm before the inertance of 486 kg, after which it gradually fits with the expected additional torque T_e and finally increases to about 0.26 Nm. The process of adjusting the inertance is actually the process of controlling the torque generated by the MR

clutch to track the expected additional torque. Since the torque generated by the MR clutch contains uncontrollable torque, when the expected additional torque is less than the uncontrollable torque, the MR clutch can no longer provide less torque, i.e., the expected additional torque cannot be tracked. In this situation, the expected additional torque can only be replaced by the uncontrollable torque. The range of which the expected additional torque is less than the uncontrollable torque is defined as the "dead zone". Therefore, the controllable torque of 0 Nm in **Figure 7** is explained. When the expected additional torque is

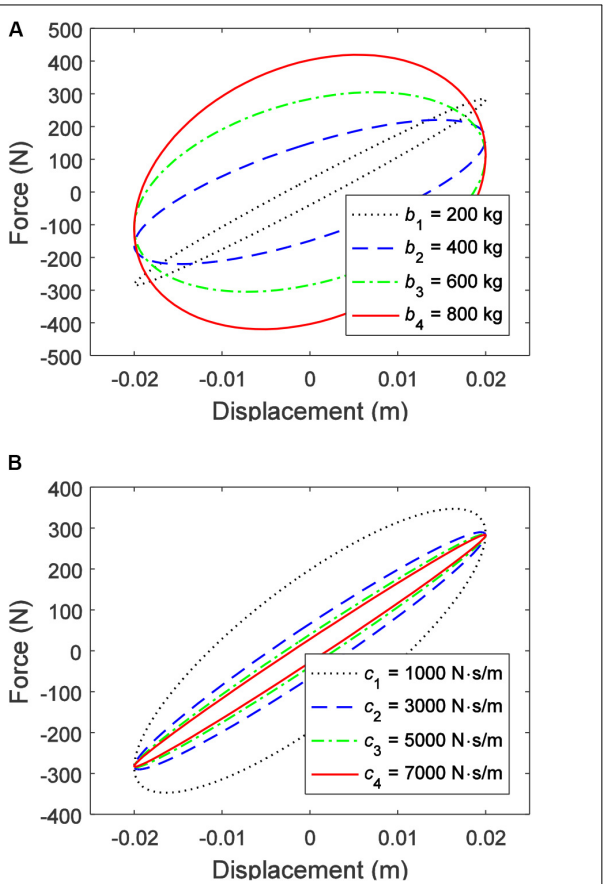

FIGURE 10 | Force–displacement characteristics of the integrated inerter-spring-damper: **(A)** different inertances and **(B)** different damping coefficients.

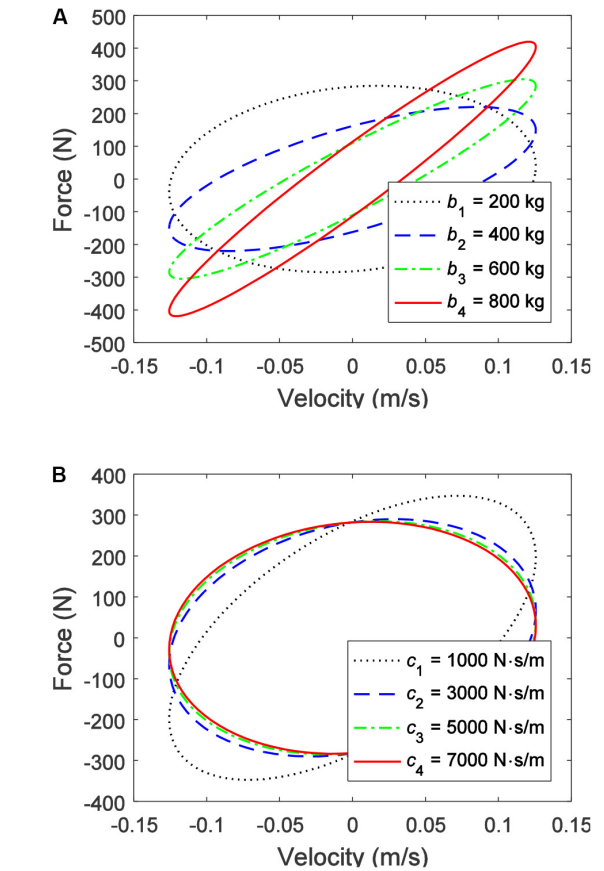

FIGURE 11 | Force–velocity characteristics of the integrated inerter-spring-damper: **(A)** different inertances and **(B)** different damping coefficients.

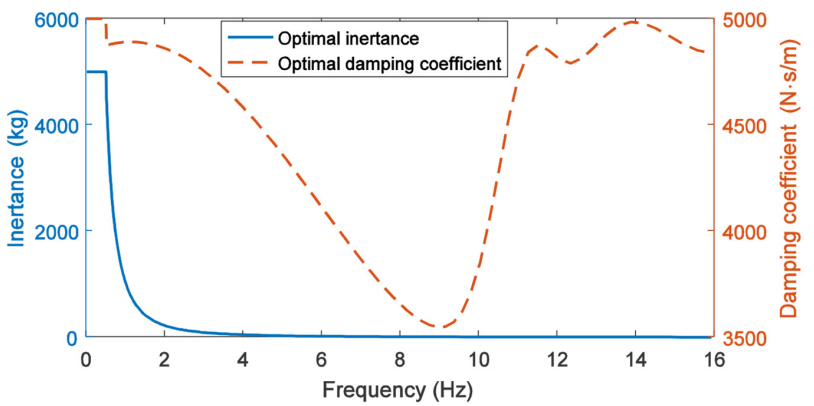

FIGURE 12 | Optimal inertance and optimal damping coefficient.

greater than the uncontrollable torque, a controllable torque will be generated to compensate for the difference between them so that the torque produced by the MR clutch can reach the expected additional torque.

The existence of the dead zone reduces the adjustment range of the inertance. Although the dead zone is unavoidable due to the existence of uncontrollable torque, its interval can be shortened. Observing Equation (8b), it can be seen that, when the gap width of the MR clutch casings $\Delta L = r_2 - r_1$ is increased, the uncontrollable torque will decrease. Therefore, the range of the dead zone can be reduced by changing the structural parameters of the MR clutch. The gap widths of the MR clutch casings are selected as $\Delta L_1 = 1$ mm, $\Delta L_2 = 5$ mm, and $\Delta L_3 = 10$ mm as simulation parameters, and the simulation results are shown in **Figure 8**.

As shown in **Figure 8A**, as the gap width increases, the uncontrollable torque decreases significantly, and the dead zone is obviously shortened. Observing **Figure 8B**, the controllable torque becomes closer to the expected additional torque throughout the adjustment range as the gap width increases. This demonstrates that the increasing gap width can effectively reduce the influence of the dead zone and improve the adjustment performance of the inertance.

Figure 9 shows the variation trends and ranges of the output force and the inertance of the MR inerter under different gap widths of the MR clutch. It can be seen from **Figure 9** that, similar to the controllable torque, the output force and the inertance are getting closer to the expected output force F_e and the expected inertance b_e, respectively, as the gap width increases.

In order to investigate the influence of different inertances and damping coefficients on the mechanical output characteristics of the IISD, sinusoidal displacement excitations, with an amplitude of 20 mm and a frequency of 1.0 Hz, are set as simulation parameters. The values of the inertance and the damping coefficient are uniformly selected from 200–800 kg and 1,000–7,000 N·s/m, respectively. The force–displacement characteristics and the force–velocity characteristics under different inertances (the damping coefficients are all 5,000 N·s/m) and damping coefficients (the inertances are all 200 kg) are shown in **Figures 10**, **11**, respectively.

As shown in **Figure 10A**, as the inertance increases, an obvious phase change of the output force of the IISD can be observed, and the value of the output force is increasing overall. In contrast, **Figure 10B** shows that different damping coefficients have less influence on the phase of the output force. Especially when the damping coefficient exceeds 5,000 N·s/m, the phase of the output force hardly changes. However, the larger the damping coefficient, the closer the ISD is to the linear device. A consistent conclusion can be obtained from the force–velocity characteristics shown in **Figures 11A,B**.

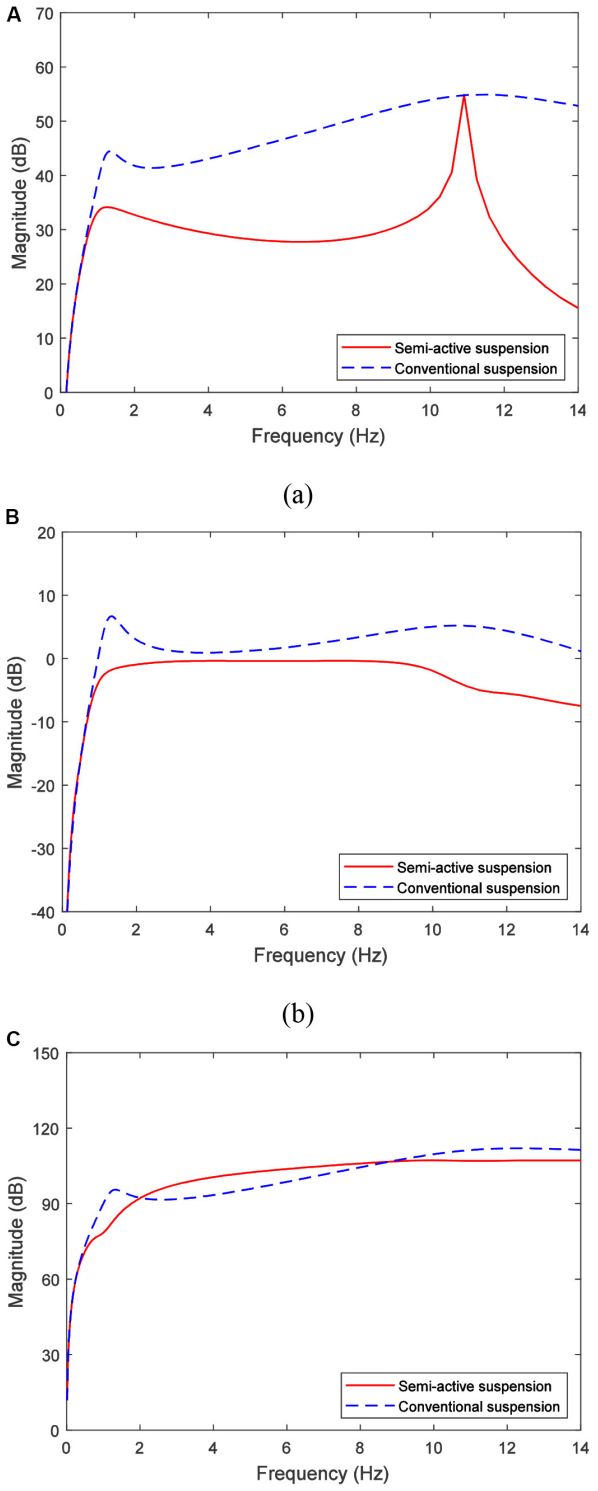

FIGURE 13 | Frequency response of the 1/4 vehicle suspension: **(A)** vehicle body acceleration, **(B)** suspension deflection, and **(C)** dynamic tire load.

VIRTUAL EXPERIMENT OF 1/4 VEHICLE SUSPENSION WITH IISD

The 1/4 vehicle suspension with the IISD is built and virtually tested by using the software MATLAB/SimMechanics. The mechanical components are assembled into a 1/4 vehicle suspension by establishing a mutual position and connection relationship between each component in

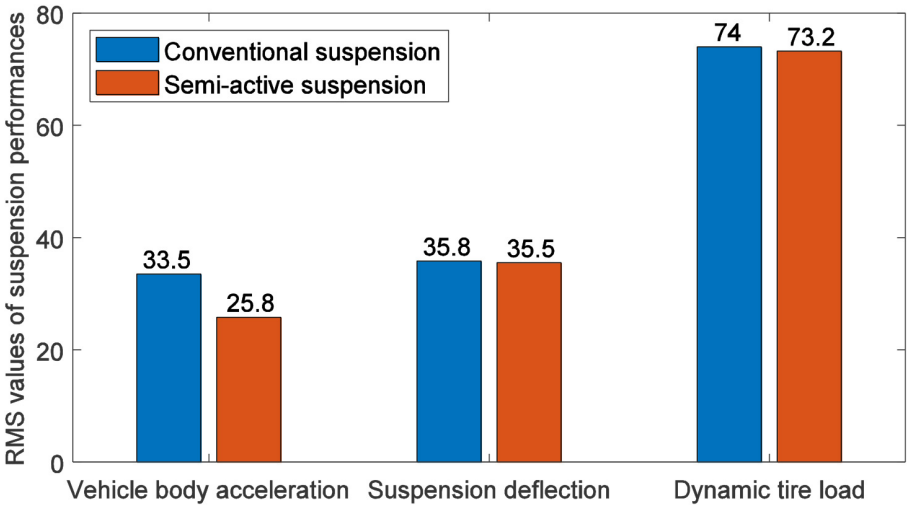

FIGURE 14 | Root mean square values of the suspension performances.

MATLAB/SimMechanics. The working status of the specific components can be detected in real time, such as displacement, velocity, acceleration, and force. The virtual experimental system is demonstrated in **Figure A1**, and the specific structural parameters are listed in **Tables A1**, **A2** in the **Appendix**.

For the performance of semi-active suspension based on both tunable inertance and damping, the key factor is the selection of inertance and damping coefficient. Here the parameter optimization of the semi-active suspension is comfort-oriented, that is to say, the optimal inertance and the optimal damping coefficient should minimize the vehicle body acceleration. Since the minimal and the maximal inertance of the MR inerter are determined by the moment of inertia of the inner casing of the MR clutch and the flywheel, respectively, the adjustment range of the inertance can be expanded by the structural design. Similarly, the structural parameters of the MR damper determine the adjustment range of the damping coefficient. In order to observe the performance of the IISD under a large range of inertance and damping coefficient as well as provide reference for the structural design of MR inerter and MR damper, the inertance is selected between 0 and 5,000 kg and the damping coefficient is limited to 0–5000 N·s/m during the parameter optimization. The excitation conditions here are sinusoidal displacement signals with different frequencies. The optimization process is carried out by the MATLAB optimization toolbox and the result is shown in **Figure 12**.

The MR inerter controller is an adjustment module for the inertance, and selects the optimal inertance based on the excitation frequency. Similarly, the MR damper controller selects the optimal damping coefficient because this study uses a numerical simulation method, that is, the optimal inertance and the damping coefficient are obtained by sinusoidal displacement excitation at different frequencies. Therefore, the MR inerter and the MR damper controller here are not complicated. The MR inerter and the MR damper controller can be regarded as the correspondence between the optimal inertance and the damping coefficient and the excitation frequency, as shown in Eqs (10, 11), respectively.

$$b_{\mathrm{opt}} = 1020 f_{\mathrm{e}}^{-2.2} \tag{10}$$

$$c_{\mathrm{opt}} = 4876\mathrm{e}^{-(f_{\mathrm{e}}-1.027)/10.51)^2} + 4805\mathrm{e}^{-(f_{\mathrm{e}}-19.53)/7.669)^2} + 1199\mathrm{e}^{-(f_{\mathrm{e}}-13.16)/2.441)^2} + 811.5\mathrm{e}^{-(f_{\mathrm{e}}-11.13)/1.011)^2} \tag{11}$$

where b_{opt}, c_{opt}, and f_{e} are optimal inertance, optimal damping coefficient, and excitation frequency, respectively.

In reality, the road excitation is unknown, and a method that identifies the frequency of excitation is needed. For the unsteady signal like road excitation, the commonly used methods include short-time Fourier transform and wavelet analysis. The performance of controllers, which outputs the optimal control parameters based on road excitation, will be tested in subsequent experimental studies.

Based on the optimal inertance and the optimal damping coefficient, the frequency response characteristics of the vehicle body acceleration, the suspension deflection, and the dynamic tire load are obtained as shown in **Figure 13**. Moreover, as likewise shown in **Figure 13A**, the vehicle body acceleration of the semi-active suspension has two peaks, which appear at 1.5 and 11 Hz, respectively. The frequency of 1.5 Hz is the first-order natural frequency of the suspension (i.e., the vehicle body resonance frequency), and the amplitude of the sprung mass at this frequency is much larger than the amplitude of the unsprung mass. The frequency of 11 Hz is the second-order natural frequency of the suspension (i.e., the tire resonance frequency). At this frequency, the amplitude of the unsprung mass is much larger than the amplitude of the sprung mass. As a result, vehicle body acceleration peaks at these two frequencies. The amplitude of the first-order natural frequency decreases significantly due to the large inertance. The amplitude of the second-order natural

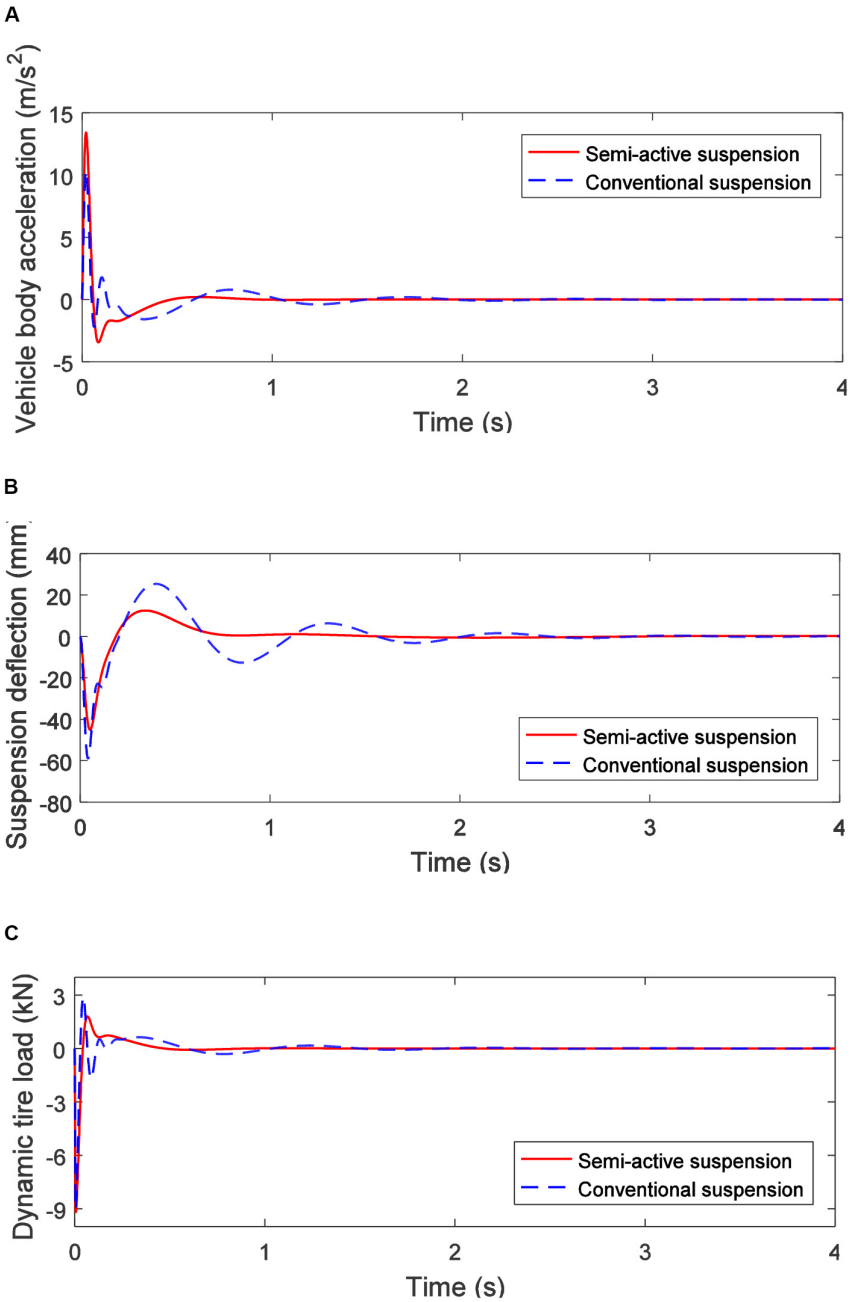

FIGURE 15 | Unit impulse response of the 1/4 vehicle suspension: **(A)** vehicle body acceleration, **(B)** suspension deflection, and **(C)** dynamic tire load.

frequency is mainly related to the suspension parameters, which can be decreased by reducing the unsprung mass. It can be observed from **Figures 13B,C** that the suspension deflection is slightly decreased in the whole range of frequency, while the dynamic tire load is slightly deteriorated during 2–8 Hz.

Figure 14 demonstrates the root mean square values for the different performances of the conventional suspension and the semi-active suspension. The simulation results show that the performance of the vehicle body acceleration of the semi-active suspension is significantly improved, which was by 23.0% compared with the conventional suspension. The performance of the suspension deflection and the dynamic tire load are slightly improved (0.8 and 1.1%, respectively), which is consistent with the comfort-oriented optimization goal.

The unit impulse responses of semi-active and conventional suspensions are shown in **Figure 15**. It can be seen from **Figure 15A** that, at the very beginning of the impulse response, the vehicle body acceleration of the semi-active suspension is slightly greater than that of the conventional suspension. This is because the impulse is an excitation generated in a very short

time, which is equivalent to a very high frequency excitation, and this requires that the inertance must be very small. Due to the mass of the inerter flywheel, the inertance cannot be reduced indefinitely, so it is slightly deteriorated in the case of extremely high frequencies (i.e., the very beginning of the impulse response). The vehicle body acceleration of the semi-active suspension quickly stabilized in the subsequent period, while the conventional suspension lasted for a while.

As shown in **Figure 15B**, the suspension deflection performance of the semi-active suspension is significantly better than that of the conventional suspension, and the amplitude and the attenuation speed are both significantly improved compared to the conventional suspension. As shown in **Figure 15C**, the dynamic tire load of the semi-active suspension is almost equivalent to that of the conventional suspension and has a slight advantage in attenuation speed.

CONCLUSION

In this paper, an adjustable inerter based on MR fluid—MR inerter, and its adjustment principle of inertance were proposed. Based on the design concept of "functional integration", the MR inerter, MR damper, and spiral spring were highly integrated to realize a new IISD with both tunable inertance and damping. The MR inerter is mainly composed of an MR clutch, a ball screw, a flywheel, excitation coils, and MR fluid. The mathematical model of the IISD was established, and the adjustment principle of the inertance was verified by numerical simulation. The mechanical output characteristics of the IISD under different inertance and damping coefficients were analyzed. Finally, a 1/4-vehicle suspension model with the IISD was established by using MATLAB/SimMechanics, and a virtual comfort-oriented experiment was carried out. The concluding remarks are summarized as follows:

1. The adjustment of inertance based on the MR fluid, which has the advantages of rapid response, low energy consumption, and wide adjustment range, i.e., the inertance can be tuned from 86 to 927 kg.
2. The functional integration concept makes the IISD realize a combination of both tunable inertance and damping coefficient with a very compact structure, which is beneficial to the application of specific limited installation cases, such as vehicle suspensions.
3. The proposed MR inerter transfers the problem of inertance adjustment to rotate velocity control by using MR clutch, which simplified the adjustment method of inertance.
4. Increasing the gap width between the MR clutch casings can effectively improve the adjustment range of the inertance.
5. The vehicle body acceleration of the semi-active suspension is reduced by 23.0% compared with the conventional suspension, and the suspension deflection and the dynamic tire load are reduced by 0.8 and 1.1%, respectively.

DATA AVAILABILITY STATEMENT

The datasets generated for this study are available on request to the corresponding author.

AUTHOR CONTRIBUTIONS

W-MZ carried out the modeling, computation and simulation work, and drafted and revised the manuscript. A-DZ investigated the technical background, and helped draft and revise the manuscript. X-XB conceived the conception, designed and coordinated the study, and revised the manuscript. NW did modeling checking, and helped draft and revise the manuscript. NZ helped revise the manuscript. All authors contributed to the article and approved the submitted version.

FUNDING

The authors wish to acknowledge the Key Research and Development Projects of Anhui Province (Grant No. 1704E1002211) for the support of this research.

REFERENCES

Bai, X. X., Jiang, P., and Qian, L. J. (2017). An integrated semi-active seat suspension for both longitudinal and vertical vibration isolation. *J. Intellig. Mater. Syst. Struct.* 28, 1036–1049. doi: 10.1177/1045389x16666179

Bai, X. X., Wereley, N. M., and Chio, Y. T. (2016). Magnetorheological energy absorber with dual concentric annular valves. *J. Intellig. Mater. Syst. Struct.* 27, 944–958. doi: 10.1177/1045389x15577659

Bai, X. X., Zhong, W. M., Zou, Q., Zhu, A. D., and Sun, J. (2018). Principle, design and validation of a power-generated magnetorheological energy absorber with velocity self-sensing capability. *Smart Mater. Struct.* 27:075041. doi: 10.1088/1361-665x/aac7ef

Brzeski, P., Pavlovskaia, E., Kapitaniak, T., and Perlikowski, P. (2015). The application of inerter in tuned mass absorber. *Int. J. Non Linear Mech.* 70, 20–29. doi: 10.1016/j.ijnonlinmec.2014.10.013

Chen, M. Z., Papageorgiou, C., Scheibe, F., Wang, F. C., and Smith, M. C. (2009). The missing mechanical circuit element. *IEEE Circ. Syst. Magaz.* 9, 10–26. doi: 10.1109/mcas.2008.931738

Giaralis, A., and Petrini, F. (2017). Wind-induced vibration mitigation in tall buildings using the tuned mass-damper-inerter. *J. Struct. Eng.* 143:04017127. doi: 10.1061/(asce)st.1943-541x.0001863

Hu, Y., Chen, M. Z., Xu, S., and Liu, Y. (2016). Semiactive inerter and its application in adaptive tuned vibration absorbers. *IEEE Trans. Control Syst. Technol.* 25, 294–300. doi: 10.1109/tcst.2016.2552460

Imaduddin, F., Mazlan, S. A., and Zamzuri, H. (2013). A design and modelling review of rotary magnetorheological damper. *Mater. Des.* 51, 575–591. doi: 10.1016/j.matdes.2013.04.042

Kaluvan, S., Thirumavalavan, V., Kim, S., and Choi, S. B. (2015). A novel magnetorheological actuator for micro-motion control: identification of actuating characteristics. *Smart Mater. Struct.* 24:105006. doi: 10.1088/0964-1726/24/10/105006

Matamoros-Sanchez, A. Z., and Goodall, R. M. (2015). Novel mechatronic solutions incorporating inerters for railway vehicle vertical secondary suspensions. *Vehicle Syst. Dyn.* 53, 113–136. doi: 10.1080/00423114.2014.983529

Papageorgiou, C., Houghton, N. E., and Smith, M. C. (2009). Experimental testing and analysis of inerter devices. *J. Dyn. Syst. Meas. Control* 131:011001.

Papageorgiou, C., and Smith, M. C. (2006). Positive real synthesis using matrix inequalities for mechanical networks: application to vehicle suspension. *IEEE Trans. Control Syst. Technol.* 14, 423–435. doi: 10.1109/tcst.2005.863663

Sapiński, B., Rosół, M., and Wêgrzynowski, M. (2016). Investigation of an energy harvesting MR damper in a vibration control system. *Smart Mater. Struct.* 25:125017. doi: 10.1088/0964-1726/25/12/125017

Shiao, Y., Ngoc, N. A., and Lai, C. H. (2016). Optimal design of a new multipole bilayer magnetorheological brake. *Smart Mater. Struct.* 25:115015. doi: 10.1088/0964-1726/25/11/115015

Smith, M. C. (2002). Synthesis of mechanical networks: the inerter. *IEEE Trans. Autom. Control* 47, 1648–1662. doi: 10.1109/tac.2002.803532

Smith, M. C., and Wang, F. C. (2004). Performance benefits in passive vehicle suspensions employing inerters. *Vehicle Syst. Dyn.* 42, 235–257. doi: 10.1080/00423110412331289871

Tipuric, M., Deastra, P., Wagg, D., and Sims, N. (2018). "Semi-active inerters using magnetorheological fluid: a feasibility study," in *Proceedings of the Active and Passive Smart Structures and Integrated Systems XII. International Society for Optics and Photonics*, Denver, CO.

Wang, F. C., and Chan, H. A. (2008). "Mechatronic suspension design and its applications to vehicle suspension control," in *Proceedings of the 2008 47th IEEE Conference on Decision and Control*, (Piscataway, NJ: IEEE), 3769–3774.

Zhong, W. M., Bai, X. X., Tang, C., and Zhu, A. D. (2019). Principle study of a semi-active inerter featuring magnetorheological effect. *Front. Mater.* 6:17. doi: 10.3389/fmats.2019.00017

Conflict of Interest: The authors declare that the research was conducted in the absence of any commercial or financial relationships that could be construed as a potential conflict of interest.

APPENDIX

According to the structural parameters of the integrated inerter-spring-damper (IISD) listed in **Table A1**, a 1/4 vehicle suspension model with the IISD is established in MATLAB/SimMechanics, as shown in **Figure A1**, and the suspension parameters are listed in **Table A2**.

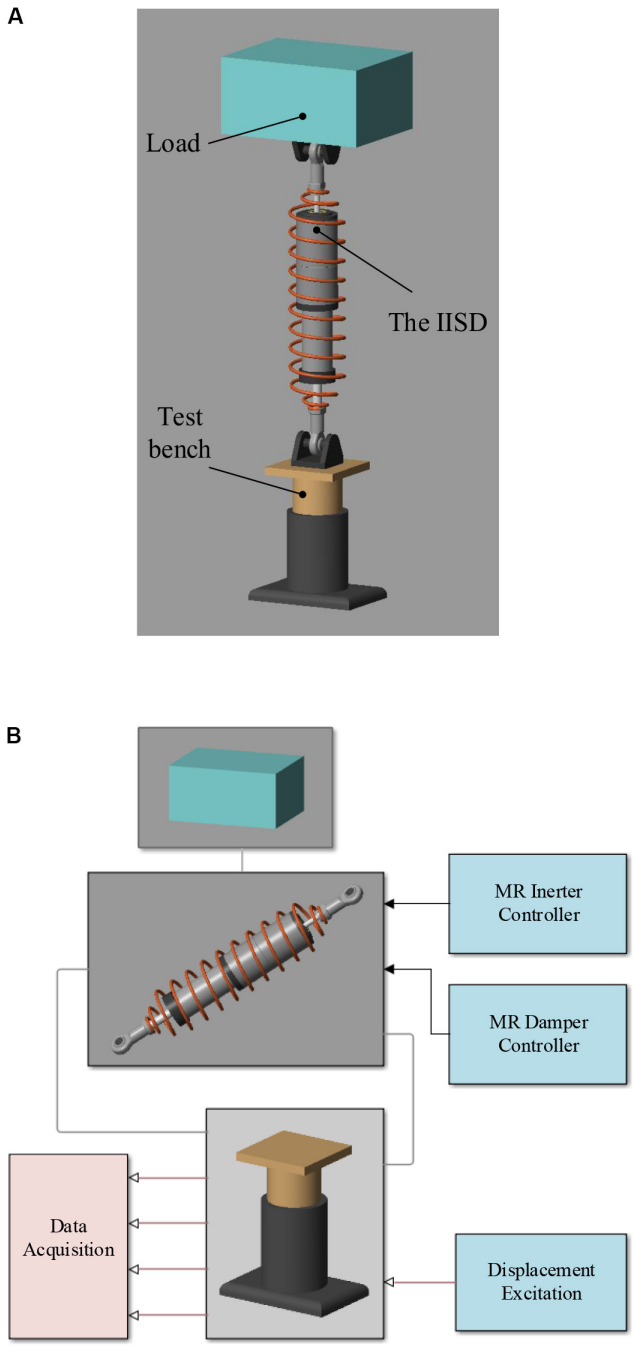

FIGURE A1 | MATLAB/SimMechanics model of the 1/4 vehicle suspension: **(A)** three-dimensional model and **(B)** Simulink model.

TABLE A1 | Structural parameters of the integrated inerter-spring-damper.

Symbol	Parameter	Value	Unit
p	Lead of the ball-screw	10	mm
M_1	Mass of the inner casing of the magnetorheological (MR) clutch	0.5	kg
M_2	Total mass of the flywheel and the outer casing of the MR clutch	3.0	kg
D_i	Outer diameter of the MR inerter	108	mm
L_i	Length of the MR inerter (equilibrium position)	315	mm
D_d	Outer diameter of the MR damper	80	mm
L_d	Length of the MR damper (equilibrium position)	300	mm
k_a	Stiffness of the accumulator	7,800	N/m
D_s	Outer diameter of the spiral spring	140	mm
k	Stiffness of the spiral spring	22,000	N/m
L	Total length of the IISD (equilibrium position)	615	mm

TABLE A2 | Simulation parameters of 1/4 vehicle suspension.

Parameter	Value	Unit
Sprung mass	400	kg
Unsprung mass	35	kg
Spring stiffness	22,000	N/m
Tire stiffness	192,000	N/m
Tunable inertance	0–5,000	kg
Tunable damping coefficient	0–5,000	N·s/m
Passive damping coefficient	7,000	N·s/m

frontiers in Materials

ORIGINAL RESEARCH
published: 06 October 2020
doi: 10.3389/fmats.2020.00236

Dual Hysteresis Model of MR Dampers

Janusz Gołdasz[1,2]*, *Bogdan Sapiński*[3], *Łukasz Jastrzębski*[3] and *Michal Kubik*[4]

[1] Faculty of Electrical and Computer Engineering, Cracow University of Technology, Kraków, Poland, [2] BWI Technical Center, BWI Group, Kraków, Poland, [3] Department of Process Control, AGH University of Science and Technology, Kraków, Poland, [4] Faculty of Mechanical Engineering, Brno University of Technology, Brno, Czechia

This study concerns the modeling of the hysteretic behavior of magnetorheological (MR) dampers. In general, hysteresis is one of key factors influencing the output of such actuators. So far, more attention has been paid to studying the combined hysteretic behavior of MR actuators by observing the relationships between the output (force/torque) and the inputs (current, velocity, and position). However, these devices feature two distinct hysteretic mechanisms: mechanical/hydraulic and magnetic. The mechanical hysteresis is of different nature than the magnetic hysteresis due to the properties of ferromagnetic materials forming the actuator's electromagnet circuit, and these should be split in the modeling process. In the present study, we separate the magnetic hysteresis from the mechanical/hydraulic one by investigating the magnetic flux vs. exciting current relationship of a commercial flow-mode MR damper subjected to sinusoidal current loading and independently of the mechanical excitations. The resulting behavior of the electromagnetic circuit is then examined using the non-linear inductor approach with hysteresis. Total hysteresis is then modeled using a non-linear inductor model in combination with a phenomenological parametric Maxwell type model of the damper.

Keywords: MR damper, hysteretic behavior, magnetic hysteresis, inductor model, hysteresis

OPEN ACCESS

Edited by:
Weihua Li,
University of Wollongong, Australia

Reviewed by:
Xianzhou Zhang,
Independent Researcher, Tomago, Australia
Luwei Zhou,
Fudan University, China

***Correspondence:**
Janusz Gołdasz
jgoldasz@pk.edu.pl

Specialty section:
This article was submitted to Smart Materials, a section of the journal Frontiers in Materials

Received: *16 April 2020*
Accepted: *29 June 2020*
Published: *06 October 2020*

Citation:
Gołdasz J, Sapiński B, Jastrzębski Ł and Kubik M (2020) Dual Hysteresis Model of MR Dampers. Front. Mater. 7:236. doi: 10.3389/fmats.2020.00236

1. INTRODUCTION

Magnetorheological (MR) fluids are well-known representatives of so-called smart materials. The material develops a yield stress when exposed to magnetic field (Rabinow, 1948), and it has been successfully used in commercial applications, i.e., semi-active vehicle dampers or powertrain mounts (Jolly et al., 1999).

Fundamentally, a typical MR flow-mode/shear-mode damper features an internal control valve in the form of an electromagnet with a fixed height planar/annular flow channel. The electromagnet's core contains a coil assembly. Supplying the electrical current to the coil results in inducing magnetic field in the flow channel, thus activating the fluid. The effect is a resistance-to-flow build-up manifested by changes in the output force or torque. The effect is reversible and fast. At the same time, various factors make the conversion process complicated (Gołdasz et al., 2018a), namely, temperature, friction, material's liability to sedimentation, non-linear magnetization characteristics of the materials of which the damper's magnetic circuit is built, magnetic hysteresis, mechanical hysteresis, current driver dynamics, control coil dynamics, non-linear relationship between the magnetic flux and the field-dependent yield stress, etc. (Kubik et al., 2017). Generally, the contributors make the control algorithm development process a challenge and the optimal control algorithm difficult or impossible to obtain. Of the above contributors,

the magnetic hysteresis is present virtually in any ferromagnetic material, though on a different scale. Although the electromagnetic circuits of MR valves are usually developed with soft magnetic alloys, the flux's hysteresis should be accounted for in engineering an MR damper-based control system. As MR dampers are by principle solenoid actuators (in which the topic has been subject to extensive research, Mayergoyz et al., 1989), the significance of hysteresis is similarly important. In latching two-position solenoids, for instance, the hysteresis and the residual magnetism affect the control circuit's capacity to maintain the solenoids at a given position. In MR dampers the hysteresis complicates controlling the output of these devices, and residual forces have a usually negative impact on the damper's output at off-state forces in particular.

In literature, magnetic hysteresis models are classified into two groups (Mazgaj, 2010). The first one includes energy-based models of which the Stoner-Wohlfart (S-W) model or Jiles-Atherton (J-A) model are the most well-known representatives (Jiles and Atherton, 1984). The other class incorporates the so-called phenomenological models of Preisach (Mayergoyz and Friedman, 1988; Mayergoyz et al., 1989), Duhem/Hodgdon-Coleman (Macki et al., 1993) or Chua (Chua and Stromsmoe, 1970). For this study, we chose one representative of the phenomenological group—the Duhem model.

The contribution of hysteresis to the force output of MR dampers has been recognized rather early (Dyke et al., 1996). Following on from Dyke et al., numerous phenomenological or lumped parameter models have been developed and applied for the purpose of predicting the hysteretic output of MR dampers (Wang and Liao, 2011). Typical approach involved studying the relationship between force/torque vs. input current and displacement/velocity and then fitting a particular model to damper data from experiments. With such a methodology, only total hysteresis can be studied. Few authors attempted to analyze the magnetic hysteresis independently of other hysteretic contributors (Szczygłowski, 2001; An and Kwon, 2003; Zheng et al., 2015; Guo et al., 2018; Li et al., 2019). The mechanical/hydraulic hysteresis has its origin in flow mechanics due to the fluid's compressibility and the lumped fluid mass (inertia) traveling back and forth through the annulus (Gołdasz and Alexandridis, 2012). For comparison, the magnetic hysteresis is an inherent property of ferromagnetic materials and does not disappear in the DC limit, which is what the hydraulic hysteresis does. Including the magnetic hysteresis operator, therefore, brings numerous benefits. First, it facilitates control through either sensor-based or sensorless approach as proven with other electrical actuators and drives (Erol et al., 2012). The implementation of the magnetic hysteresis operator will allow for a model-based control, too. Second, it allows taking into account the effects already in the design process. For instance, Kubik and Gołdasz (2019), in the parametric study on the MR damper dynamic behavior with the so-called vector hysteresis approach, showed that the use of such models may yield improvements in understanding the MR damper physics and deliver a better product. Simply analyzing prior art, e.g., the study of hysteresis of an MR brake as in An and Kwon (2003) accomplished with the Hodgdon model highlights significant advantages in predicting the output of the brake on including the magnetic hysteretic operator.

In general, the purpose of the study is to present means for distinguishing the contribution of particular hysteretic operators to the output of MR dampers. To accomplish the goal, we reconstruct the magnetic behavior of a long-stroke flow-mode MR damper with one magnetic hysteretic operator to obtain the induced flux variation against the exciting current. The sensorless flux reconstruction technique we used allows inspection of the damper's magnetic hysteretic behavior without any knowledge of its internals. Finally, a first-order phenomenological damping force model based on a Maxwell model is employed to explore the contribution of the remaining mechanisms.

The paper is organized as follows. Section 2 contains the description of the dual hysteresis model concept of an MR damper. In the section we describe both the magnetic hysteretic operator and the mechanical model. Furthermore, in section 3, we explain the test setup and the hardware used. Next, section 4 presents model identification results and a comparison of the hysteretic models' performance against selected experimental data sets. Finally, conclusions are presented in section 5.

2. DAMPER MODELING

To predict the hysteretic behavior of a typical single-tube flow-mode MR damper as in **Figure 1**, we developed a phenomenological model of the device. The cylinder tube houses a piston assembly that separates the fluid volumes into the upper (rebound) volume and the lower (compression) volume. The floating gas cup separates the compression chamber from pressurized gas for volume compensation. The piston features a solenoid with a fixed-height annular gap for magnetizing the MR fluid flowing through it as in **Figure 1**. There is a thru-rod electrical connection between the current driver (not shown) and the coil. The induced flux travels across the core, the annular gap, the ring and the cylinder tube to return to the core through the annular gap again. As illustrated, there is also a flux leakage path from the tube through the MR fluid and the rod.

Specifically, we model viscous losses, friction, and offset force due to the accumulator. Moreover, we assume the model would capture the effects of fluid compressibility, field-dependent pressure drop, as well as basic dynamics of the MR actuator's electromagnet although in a simplified manner. The model incorporates two fundamental components reflecting the force build-up process in the actuator: the electromagnet model and the MR effect model.

First, the dynamics of the electromagnet is captured with a non-linear hysteretic inductor concept. The model can be analyzed by looking up the relationship between the exciting (magnetizing) current and the resulting induced flux (linkage). Second, the behavior of the fluid is examined further with a first-order phenomenological model of the damping force. The inductor model and the force model are related by a non-linear flux-to-force coupling.

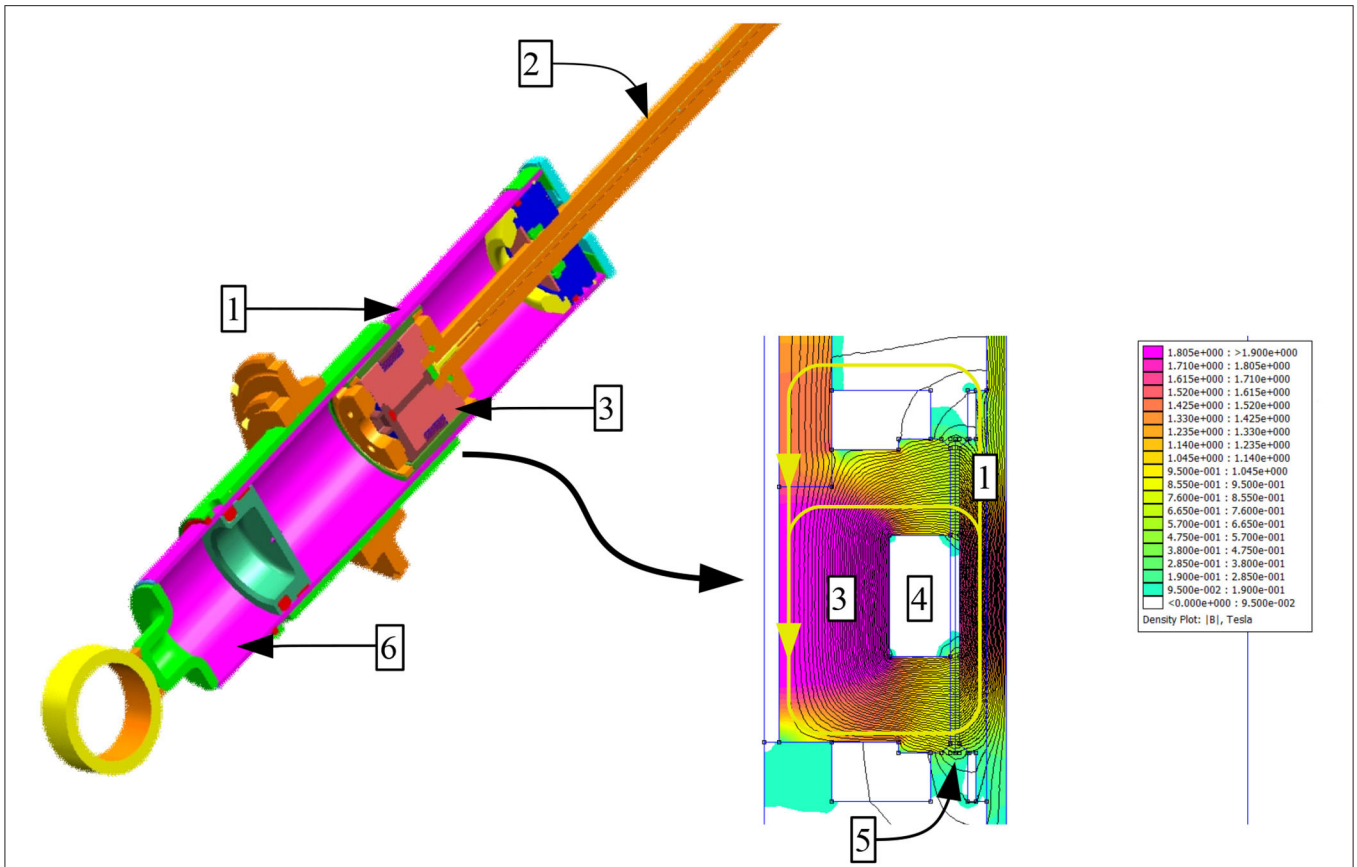

FIGURE 1 | MR vehicle suspension damper and exemplary flux density map (piston assembly); 1-cylinder and ring, 2-rod, 3-core, 4-coil assembly, 5-annulus, and 6-gas chamber.

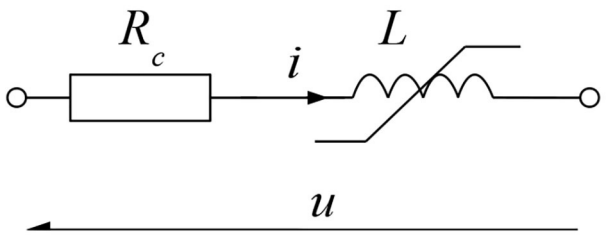

FIGURE 2 | Block diagram of the proposed inductor model—reproduced from Gołdasz et al. (2018a) under the CC BY 4.0 license.

2.1. Non-linear Inductor Modeling With Hysteresis

Let us consider the simplest non-linear lumped parameter model of an MR actuator as shown in **Figure 2**. The model includes the input voltage source $u(t)$, the coil resistance R_c, and the non-linear inductance $L(i)$ in series with the resistor. The model equation is then as follows:

$$u(t) = iR_c + \frac{d\lambda}{dt} \tag{1}$$

where u – supply voltage, i – coil current, and $\lambda = L(i)i$ – magnetic flux linkage, and $L(i)$ – coil inductance. Equation (1) represents the dynamics of a simple non-linear inductor. The relationship $\lambda(i)$ can be further expanded to include other phenomena.

In the presented form the model copies the average flux induced in the electromagnet, and its parameters can be estimated independently of the hysteretic force component. Equation (1) may represent a simple non-linear inductor model with no hysteresis or assume more complex forms. In the present study we chose to proceed with the Duhem hysteresis model.

2.2. Duhem Model

The relationship between the flux linkage λ and the coil current i of the inductor in **Figure 2** can be described using the following Duhem hysteresis operator (Mayergoyz et al., 1989)

$$\frac{d\lambda}{dt} = a\left|\frac{di}{dt}\right|\left[f(i) - \lambda\right] + g(i)\frac{di}{dt} \tag{2}$$

We select the shape functions $f(i)$ and $g(i)$ as follows:

$$\begin{cases} f(i) = b_1 \tanh(b_2 i) \\ g(i) = d \end{cases} \tag{3}$$

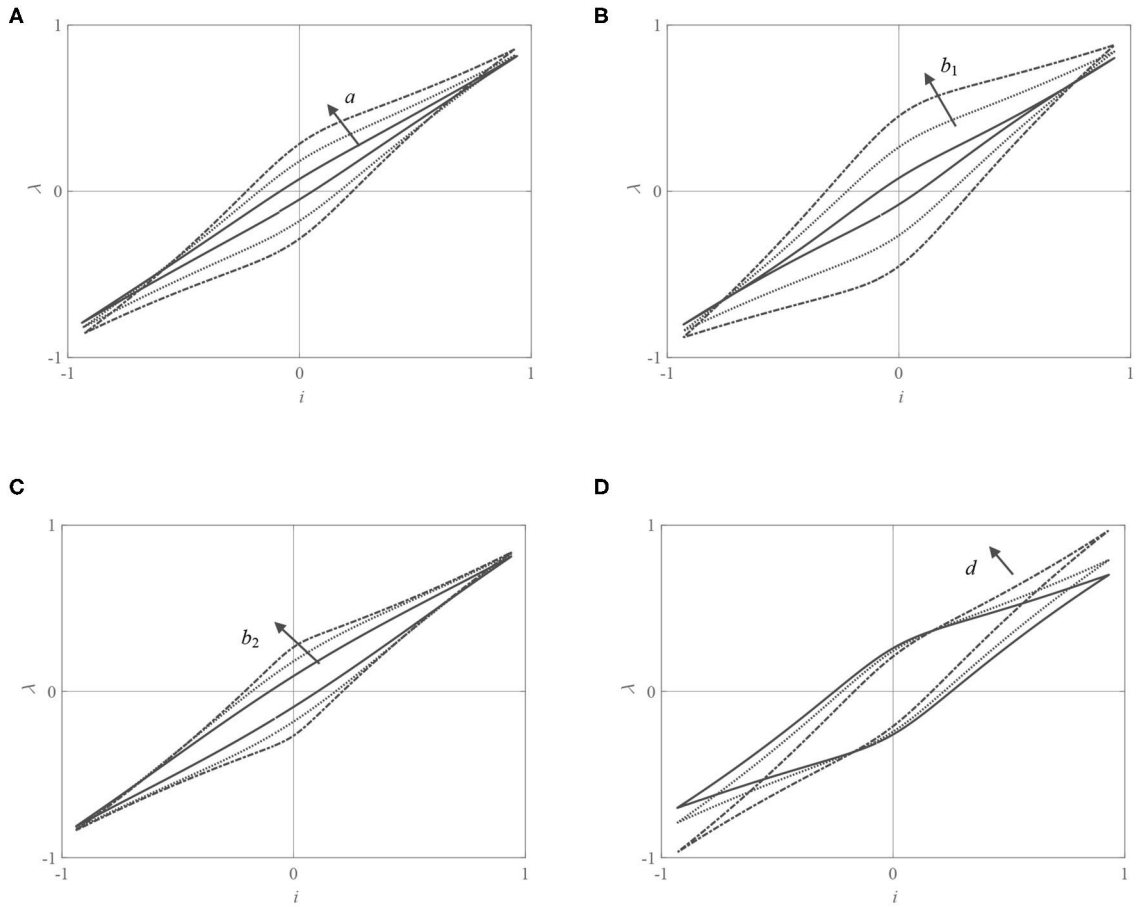

FIGURE 3 | (A–D) Duhem model: impact of model parameters on the normalized $\lambda - i$ loop.

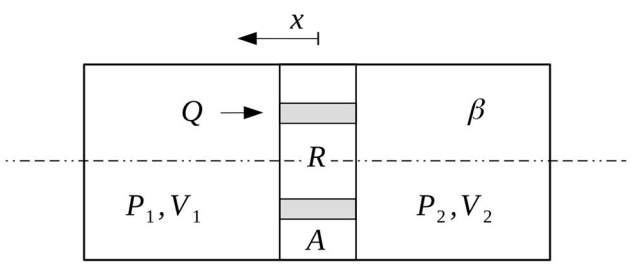

FIGURE 4 | MR damper simplified layout.

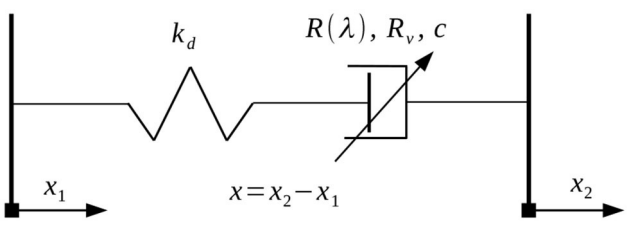

FIGURE 5 | Block diagram of the hysteretic model (gas force not shown); x_1, x_2—displacements.

The model incorporates a set of four tuning parameters (a, b_1, b_2, d), which can be identified from experimental data. In the study, we assume the parameters are current dependent—the examined object is non-linear. Typical identification procedures rely on fitting the model to measurements as demonstrated by Chwastek and Szczygłowski (2008) or Gołdasz et al. (2019), usually by means of least-squares quality metrics. The Duhem model parameters are not directly related to the material's physical properties, e.g., remanence, coercivity, contrary to the famous Jiles-Atherton model, for instance. In the anhysteretic case ($a = 0$) the inductor model reduces to that of a non-linear one without hysteresis, i.e., $\lambda = d(i)i$. Then, an initial estimate of the parameter d at a given current level can be provided from coil inductance calculations using lumped parameter models or more advanced finite-element techniques, for example. Once the parameter d is fixed, the parameters a and b_1 can be played with to arrive at the correct hysteresis width. Finally, the rate tuning

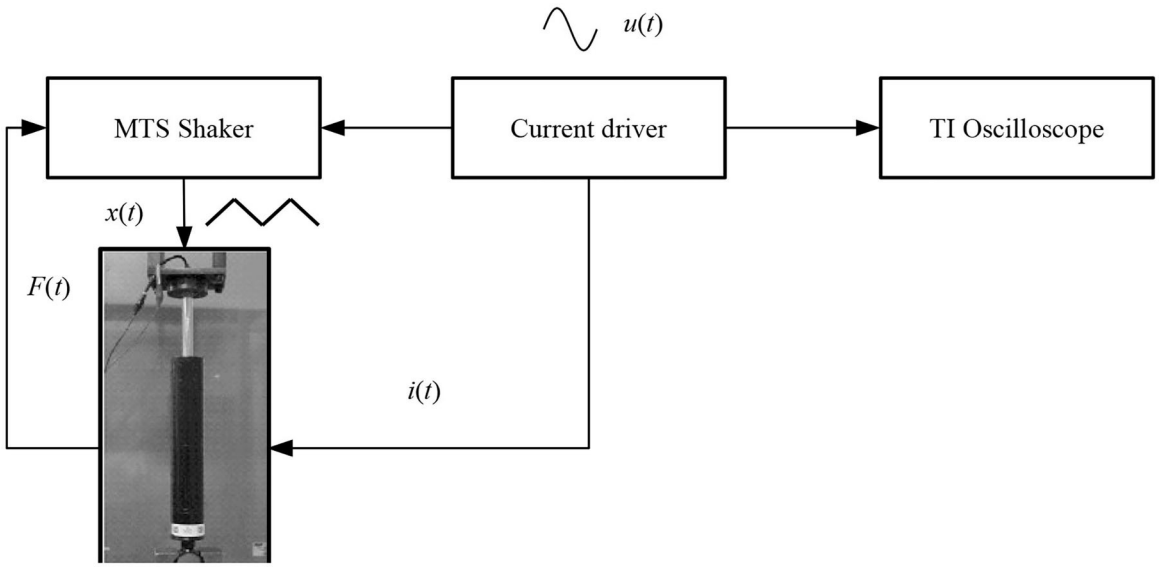

FIGURE 6 | Damper test rig layout.

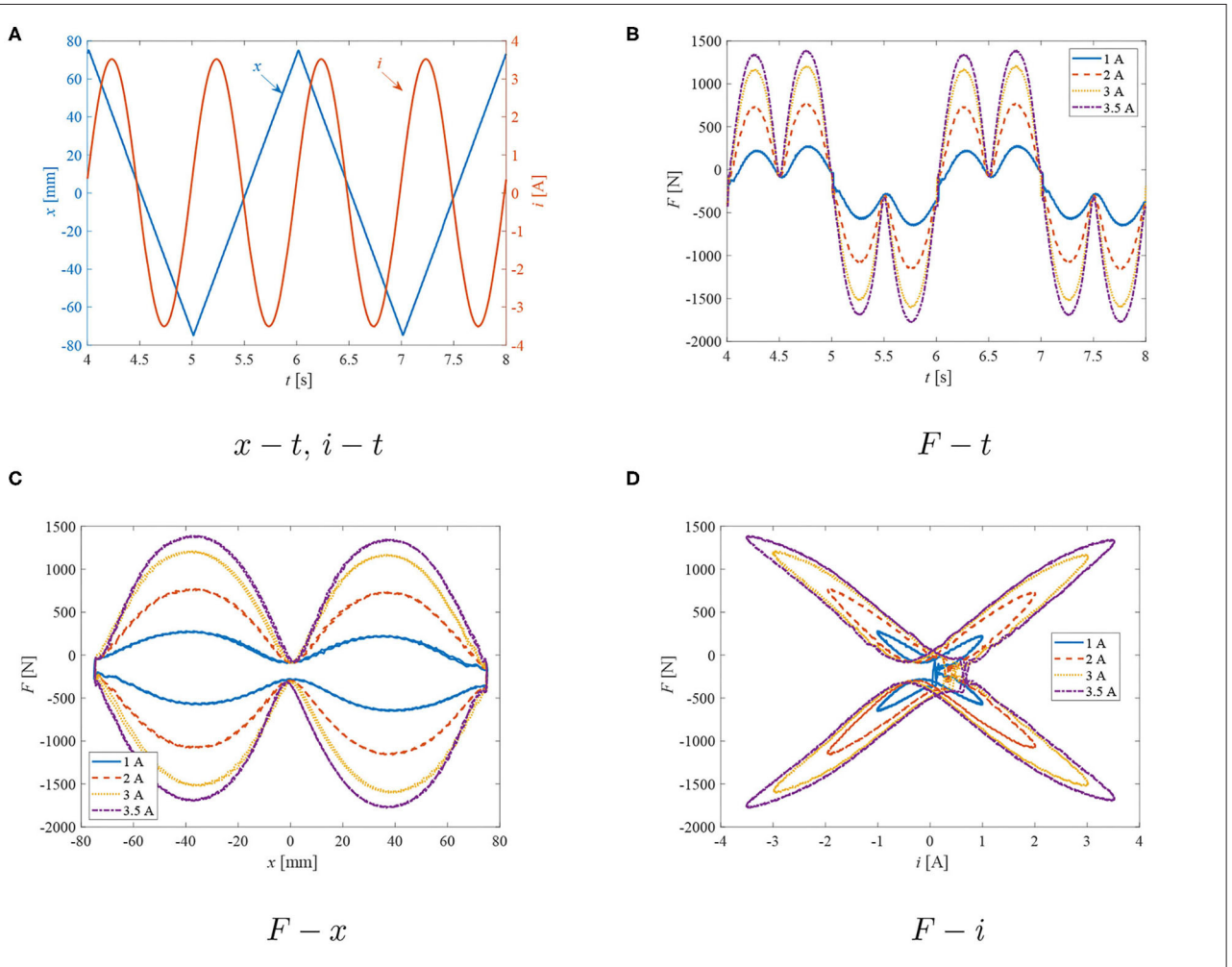

FIGURE 7 | Test results: exemplary excitation inputs, time histories of force, force-displacement, and force-current loops. **(A)** $x-t, i-t$. **(B)** $F-t$. **(C)** $F-x$. **(D)** $F-i$.

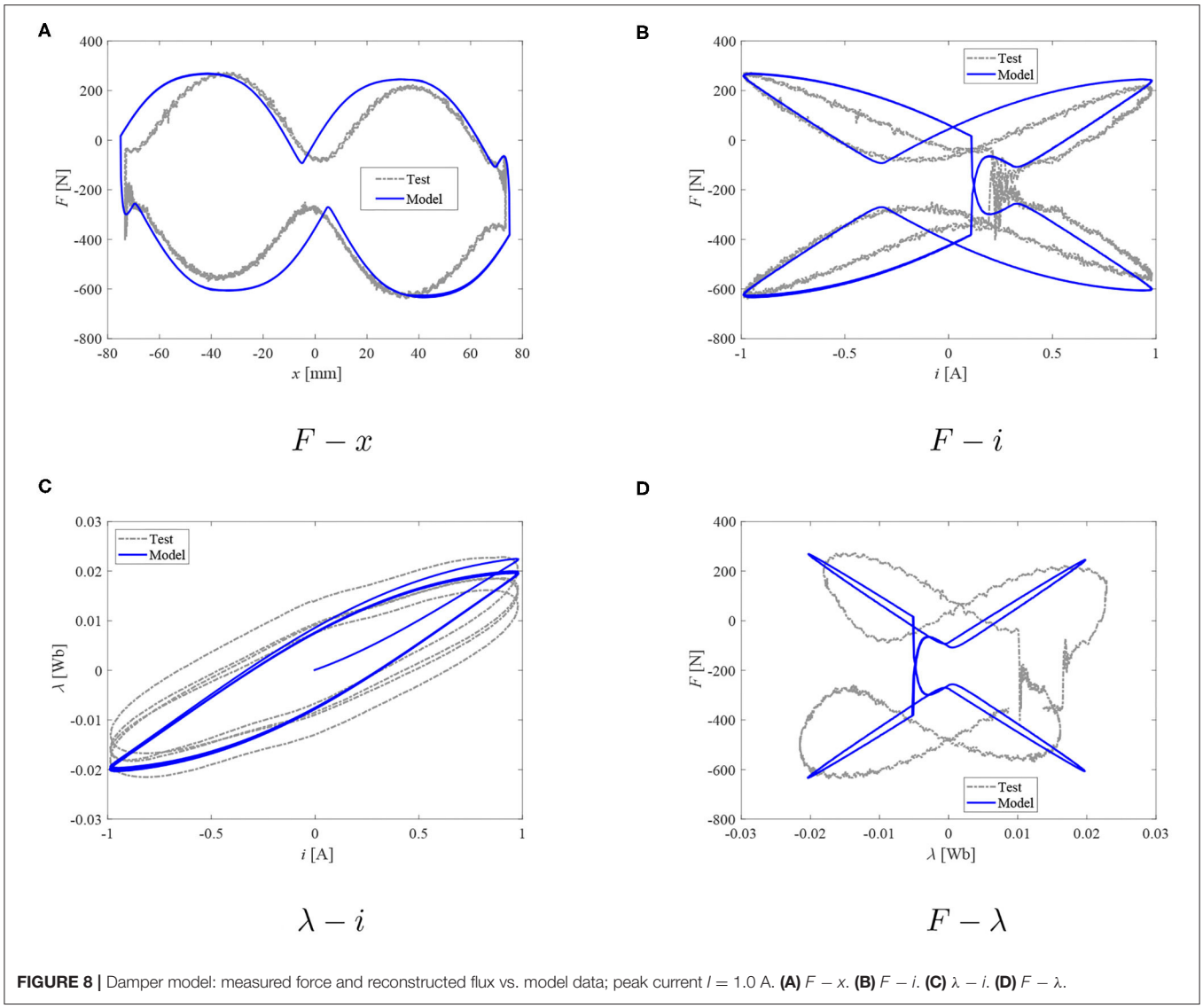

FIGURE 8 | Damper model: measured force and reconstructed flux vs. model data; peak current $I = 1.0$ A. **(A)** $F - x$. **(B)** $F - i$. **(C)** $\lambda - i$. **(D)** $F - \lambda$.

parameter b_2 of the hyperbolic tangent function can be adjusted to match the $\lambda - i$ curve's slope. The particular form of the shape function was preferred for consistency and ease of use.

The model parameter set can then be used for varying the hysteresis width and shape. In **Figure 3**, the authors reveal the impact that each parameter of the model has on the $\lambda - i$ normalized loop shape; the arrow in each figure shows the direction of particular parameter increase. In the normalized plots, the flux and current variation range is from -1 to 1.

In this context, the Duhem operator is a non-linear system model driven by the coil current i. Its output is the flux linkage $\lambda(t)$. In the analyzed form, the Duhem model has the advantage over other hysteretic models, e.g., the Bouc-Wen model, for being less complex, as it accepts half of the parameters (that the standard Bouc-Wen model requires) for successful operation as shown in Gołdasz et al. (2018b).

2.3. Phenomenological Model of an MR Damper

Next, we examine the simplest first-order Maxwell model incorporating a non-linear dashpot in series with a spring. The model is assumed to ignore higher-order dynamics due to mass effects. Only the compressibility of fluid chambers is taken into account as main contributor to the damper hysteresis. The non-linear Maxwell model is functionally identical to the model examined by Gołdasz and Alexandridis (2012) as well as Simms et al. (2004). As a partial proof, let us then consider the cylinder housing with an MR valve located in the piston as in **Figure 4**. The piston is driven by the prescribed displacement $x(t)$, thus forcing the fluid through the valve at the volumetric rate Q. The pressure drop across the piston is $\Delta p = P_1 - P_2$. Considering the variation of pressures in each fluid chamber, we yield

$$\begin{cases} -Q + A\dot{x} = \frac{V_1}{\beta}\dot{P}_1 \\ Q - A\dot{x} = \frac{V_2}{\beta}\dot{P}_2 \end{cases} \tag{4}$$

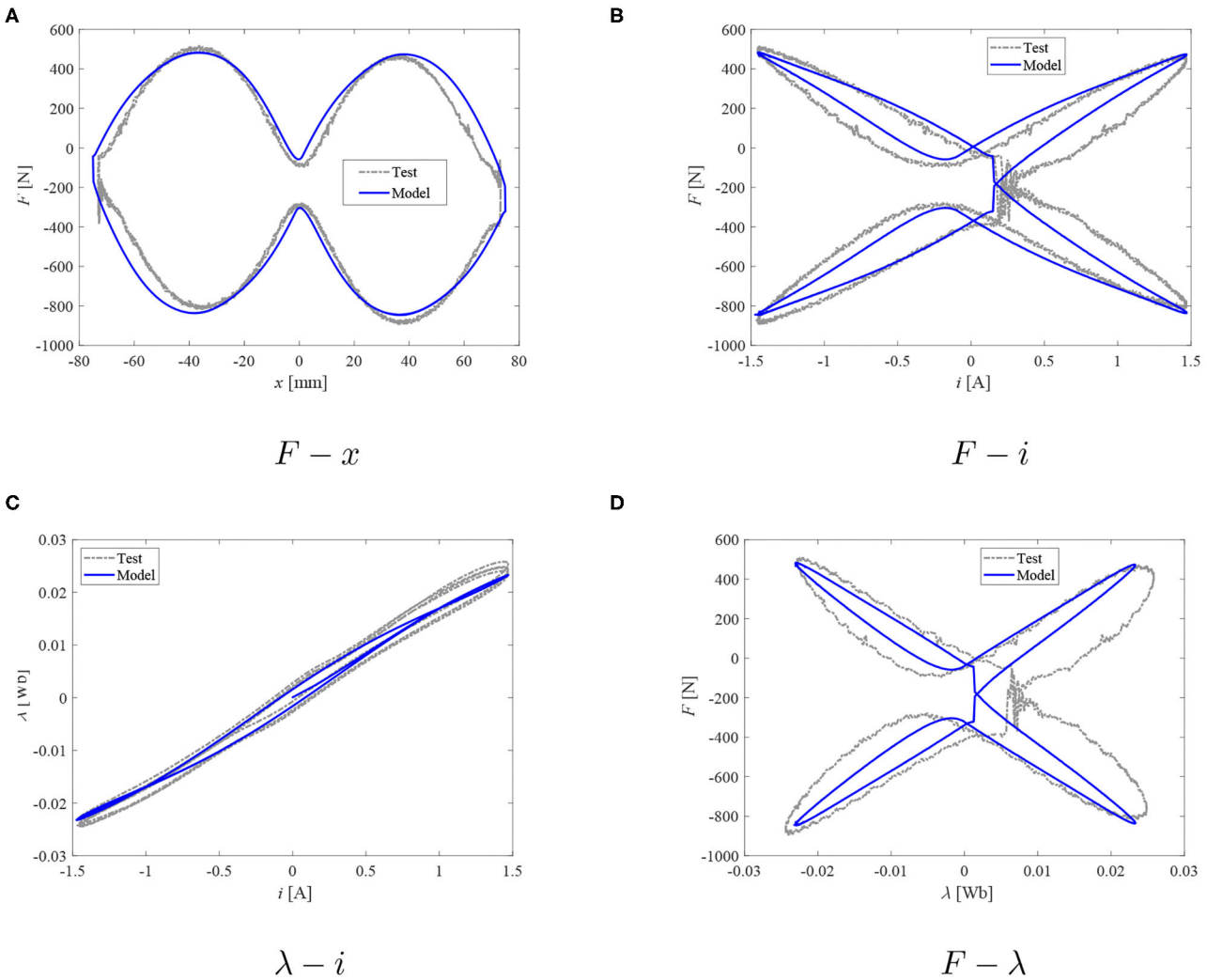

FIGURE 9 | Damper model: measured force and reconstructed flux vs. model data; $I = 1.5$ A. **(A)** $F - x$. **(B)** $F - i$. **(C)** $\lambda - i$. **(D)** $F - \lambda$.

where β-bulk modulus. Assuming the volumes $V_1 = V_2 = V$ and transforming the above system of equations gives

$$\Delta\dot{p}\frac{V}{2\beta} = A\dot{x} - Q \tag{5}$$

where A is the piston cross-section area. In general, the pressure drop across the MR valve and the flow rate are related by a generic non-linear function $Q = f(\Delta p, \lambda)$. By way of simplification, we further assume $Q = \Delta p/R(\lambda)$ and $R = R(\lambda)$ is field-dependent hydraulic resistance (which further reduces to a (non)linear hydraulic resistance in the absence of flux). Substitution then gives

$$\Delta\dot{p}\frac{VR(\lambda)}{2\beta} + \Delta p = R(\lambda)A\dot{x}, \tag{6}$$

or multiplying by the piston cross-section area to get the output force F yields

$$\frac{VR(\lambda)}{2\beta}\dot{F} + F = R(\lambda)A^2\dot{x} \tag{7}$$

This can be rewritten into a more generic form as follows:

$$\zeta(\lambda)\dot{F} + F = F_d(\lambda, v) \tag{8}$$

where ζ is the field-dependent time constant. As an example, we represent the force shape function F_d to be

$$F_d(t) = F_v + F_\lambda = R_v\dot{x} + R_\lambda(\lambda)\tanh(c\dot{x}) \tag{9}$$

where the force component F_v represents viscous losses proportional to the velocity $\dot{x}$, R_v denotes hydraulic resistance due to viscous losses, F_λ copies the field-dependent force due to the MR effect. $R_\lambda = R(\lambda)A^2$ is a link between the

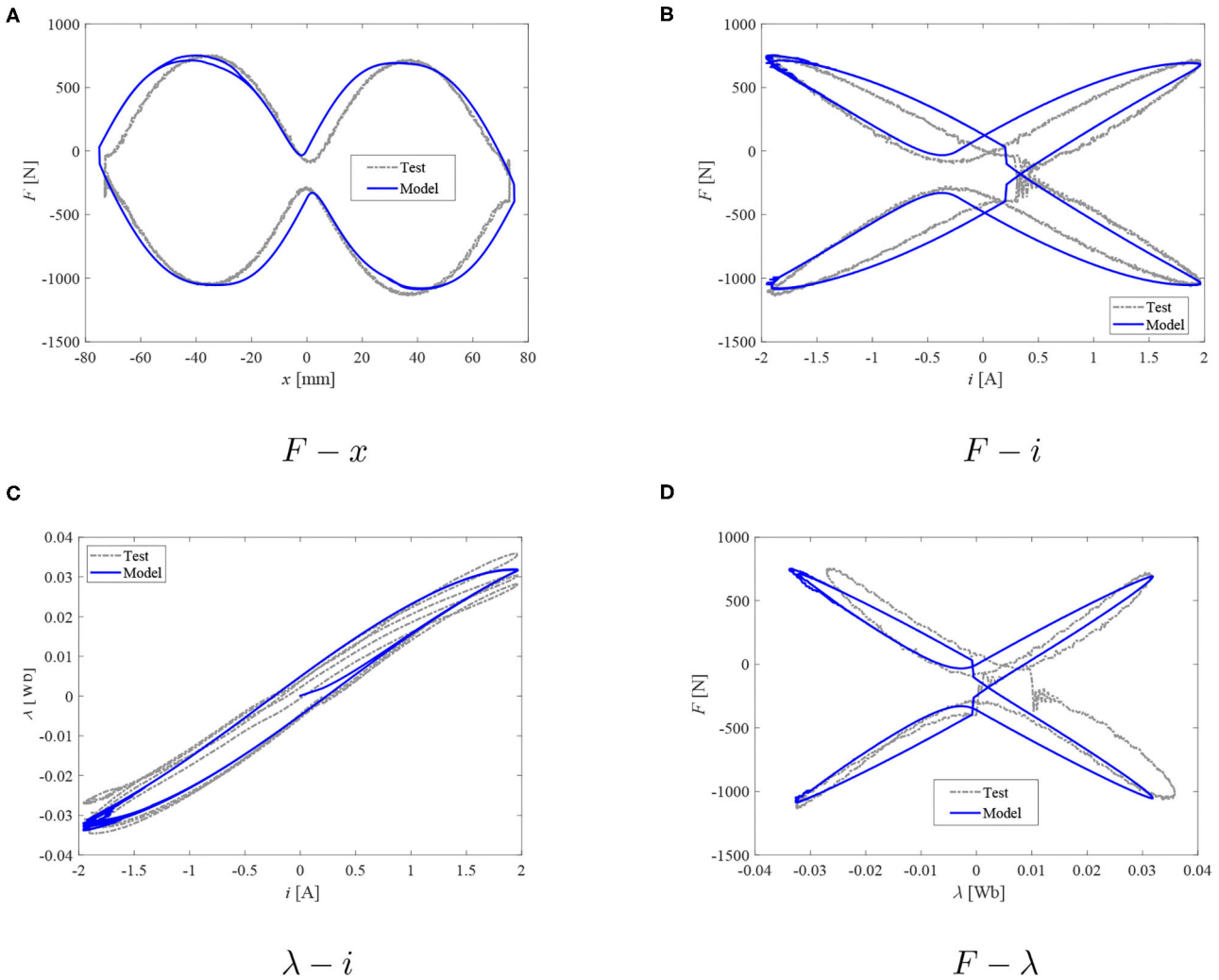

FIGURE 10 | Damper model: measured force and reconstructed flux vs. model data; $I = 2.0$ A. **(A)** $F - x$. **(B)** $F - i$. **(C)** $\lambda - i$. **(D)** $F - \lambda$.

damping force model and the inductor model. The model may incorporate friction force as well as force offset due to the presence of the pressurized accumulator. Moreover, c defines the force increase rate against the velocity $\dot{x}$. The model's simple form, as shown in **Figure 5**, is particularly convenient in model/parameter identification problems; the parameter k_d represents all compliances present in the damper. Note that if fixed flux input is assumed, then the effect of force evolution against the velocity may be easily analyzed independently of the other excitations. Under time-varying current excitations, the flux build-up is copied by the inductor component, including a relevant hysteretic operator (see Equation 1), whereas the force change against the flux (as well as the velocity $\dot{x}$ and the displacement x) is taken care of by Equation (8).

As shown, the model parameters can be deduced from the damper's geometry and material properties. However, due to unknown internals of the tested commercial MR damper, we estimate them from damping force measurements.

3. TEST INPUTS AND HARDWARE

The model requires measurements of quantities from which the investigated models can be identified and their parameters estimated, namely, flux and force. Although both could be estimated simultaneously, and all measurements were carried out at the same time, we decided to rely on the sequential approach. First, to acquire the $\lambda - i$ relationship for the damper, magnetic flux was extracted from voltage and current data via integration (and high-pass filtering for drift removal). The measurements were accomplished over a 20 s time span and by sampling the data at the frequency of 1 kHz. The data acquisition system was under the control of an AD/DA I/O board. The tested unit was a flow-mode linear commercial damper by BWI Group for a passenger car featuring an MR valve with one annular gap and one coil assembly. The long-stroke damper's coil resistance is appr. 1.1 Ω incl. electrical connections, and the device can be operated up to 5 A. More detailed information on

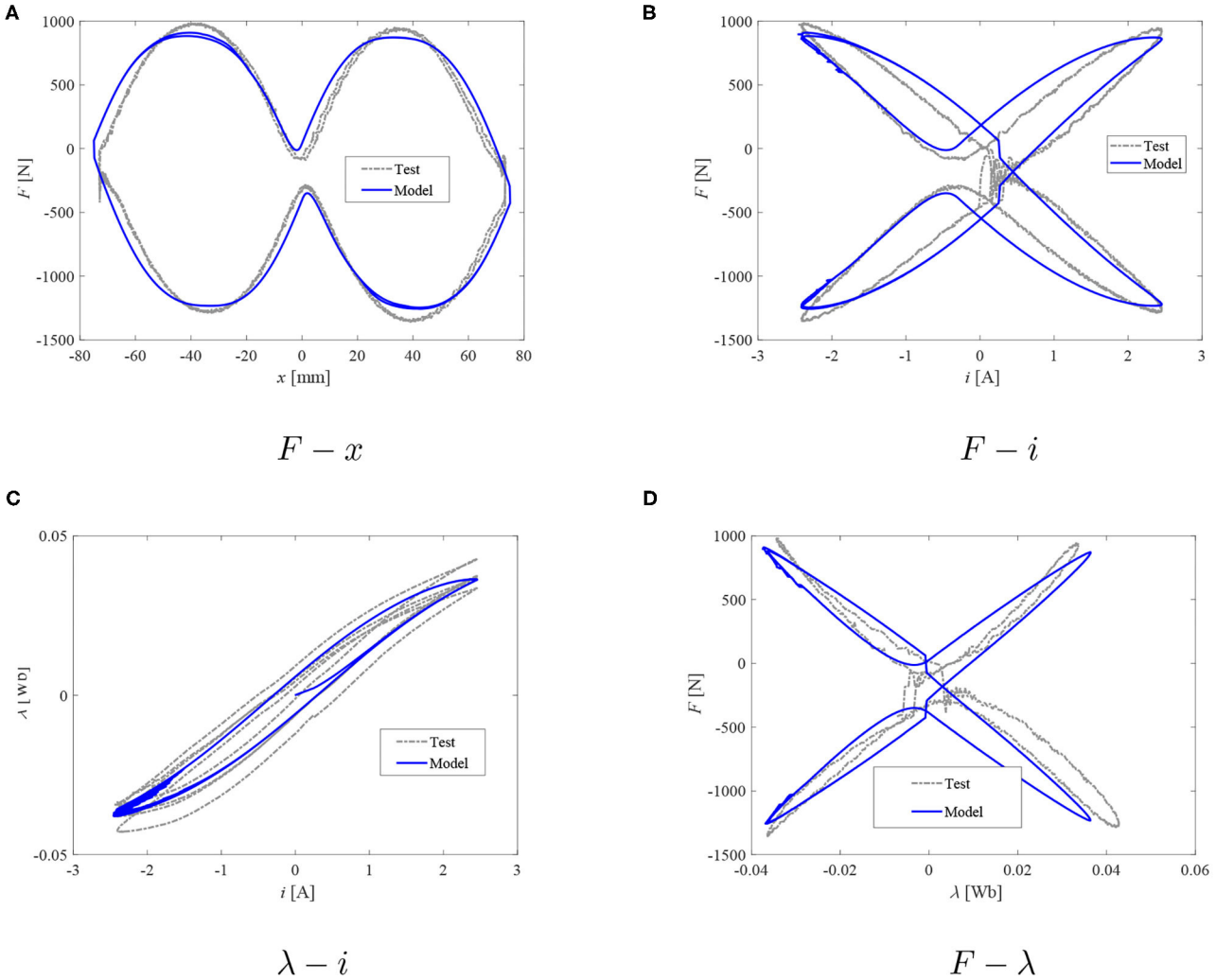

FIGURE 11 | Damper model: measured force and reconstructed flux vs. model data; $I = 2.5$ A. **(A)** $F - x$. **(B)** $F - i$. **(C)** $\lambda - i$. **(D)** $F - \lambda$.

the tested damper incl. transient response, frequency response and other characteristics can be found in Jastrzębski and Sapiński (2017), and the reader should refer to these for further details.

The damper was tested on a mechanical MTS810 shaker, and the displacement was acquired from the stroker's internal sensor, see **Figure 6**. In our experiments, the damper was subjected to constant velocity (triangular displacement) inputs using the above 1 Hz sine wave current input superimposed on the displacement profile $x(t)$ as in **Figure 7A**. The peak-to-peak displacement was 150 mm, and the triangular displacement wave frequency was set to be 0.5 Hz. During the experiments, the input voltage was adjusted to result in peak coil currents $I = \{1, 1.5, 2, 2.5, 3, \text{and } 3.5\}$ A. The magnetic flux time histories were then reconstructed as already mentioned.

4. RESULTS AND DISCUSSION

Below, we show the obtained experimental results and then apply the proposed model for predicting the dampers characteristics.

Damper measurement results are highlighted in **Figures 7–13**. In particular, **Figure 7A** contains an exemplary time history of the excitation inputs (displacement, current) plotted over a selected 4 s time span. In **Figure 7B**, we plot time histories of the damping force corresponding to the abovementioned current peak levels. The results are complemented by the plots of the damping force vs. the input displacement in **Figure 7C** and the damping force vs. the measured coil current in **Figure 7D**. In the plots, the damping force is offset by the gas force due to the pressurized accumulator present in the monotube damper; the commercial damper was gas-charged at $P_0 = 2.6$ MPa. The gas pressure was measured at mid-

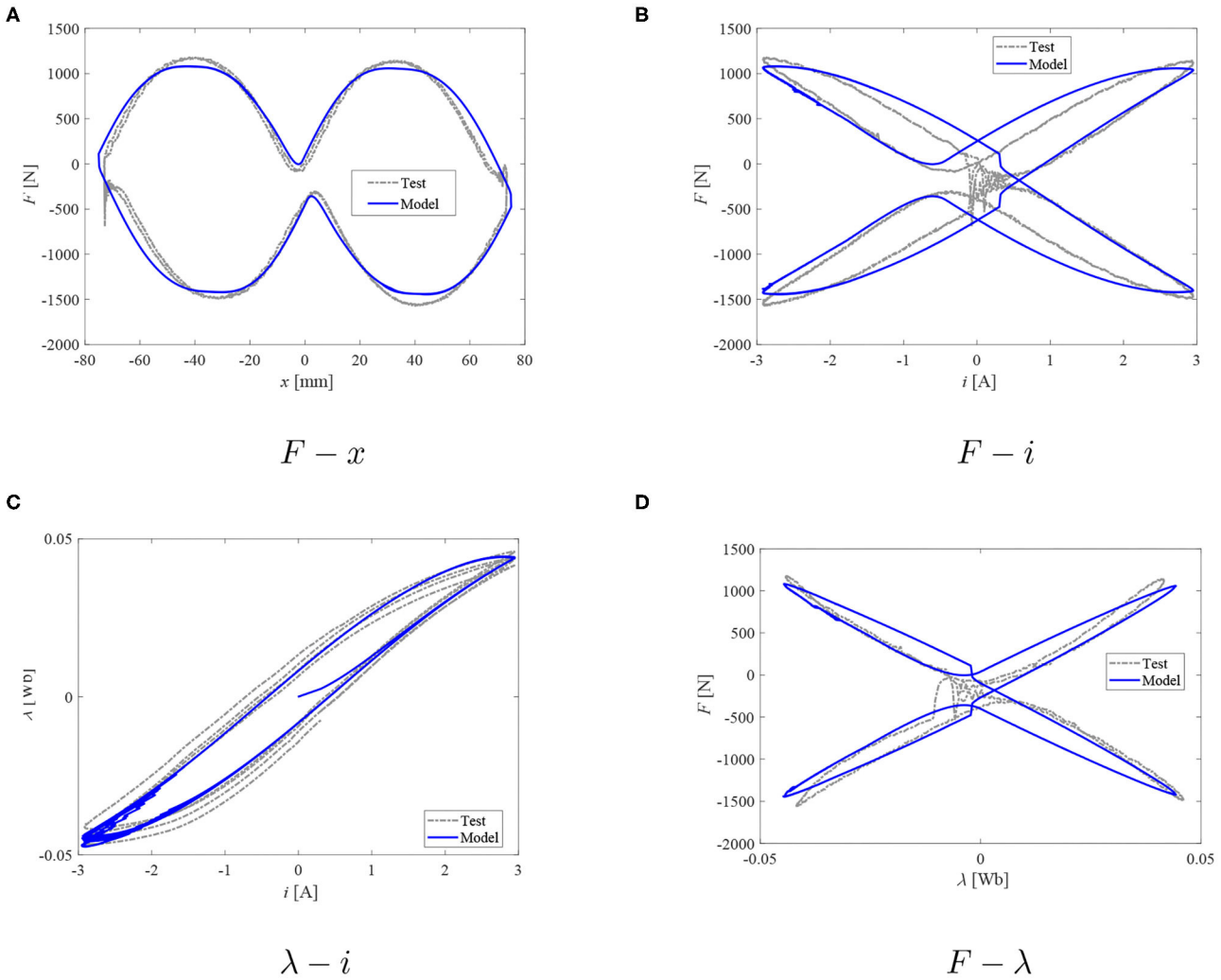

FIGURE 12 | Damper model: measured force and reconstructed flux vs. model data; $I = 3.0$ A. **(A)** $F - x$. **(B)** $F - i$. **(C)** $\lambda - i$. **(D)** $F - \lambda$.

stroke. The gas volume was estimated by pushing the piston rod downwards from a fully extended position (full rebound) to the fully collapsed one (full compression). The other bias force which can be observed in the data is friction (determined directly from the experimental data—$F_r \approx 70$ N). The viscous damping coefficient was estimated by plotting the force vs. velocity at zero current condition. Furthermore, the flux linkage information was acquired by post-processing voltage and current as already mentioned; the flux integration procedure was applied for predicting the magnetic hysteresis of an MR damper and explained in detail in Gołdasz et al. (2019). There are several unavoidable issues with flux integration. First, the flux's initial value was unknown; that issue was solved by demagnetizing the damper after each measurement. Second, as the damper is stroked and/or the current is applied to the coil, the internal temperature increases. As a result, the coil resistance varies with temperature; the issue could be solved by, for example, using a sensory coil wrapped around the core, though this was not possible due to a lack of access to the internals of the damper. Third, measurement noise and integration errors are further accumulated in the process resulting in the flux linkage signal drift. That issue was at least partially solved by filtering to remove the signal bias and trend/drift. These issues may have influenced the outcome of the study.

When the peak current increases from 1 to 3.5 A, on the inductor part, the parameter a was determined to decrease from the maximum value of 3 down to 1.4. On the other hand, the parameter b_1 increased from 0.03 to 0.08 (3.5 A) with the increasing current. At the same time, the rate tuning parameter b_2 varied from 0.7 to 0.25, and the parameter d was found to vary from 0.015 to 0.004. The time constant ζ was determined to be nearly constant – 0.015 to 0.018 s, and the off-state damping coefficient $R_v = 120$ Ns/m, and $c = 15$ s/m. The parameter $R(\lambda)$ was found to be equal to 18 kN/Wb (1 A), increasing with the current up to 28.8 kN/Wb (3.5 A).

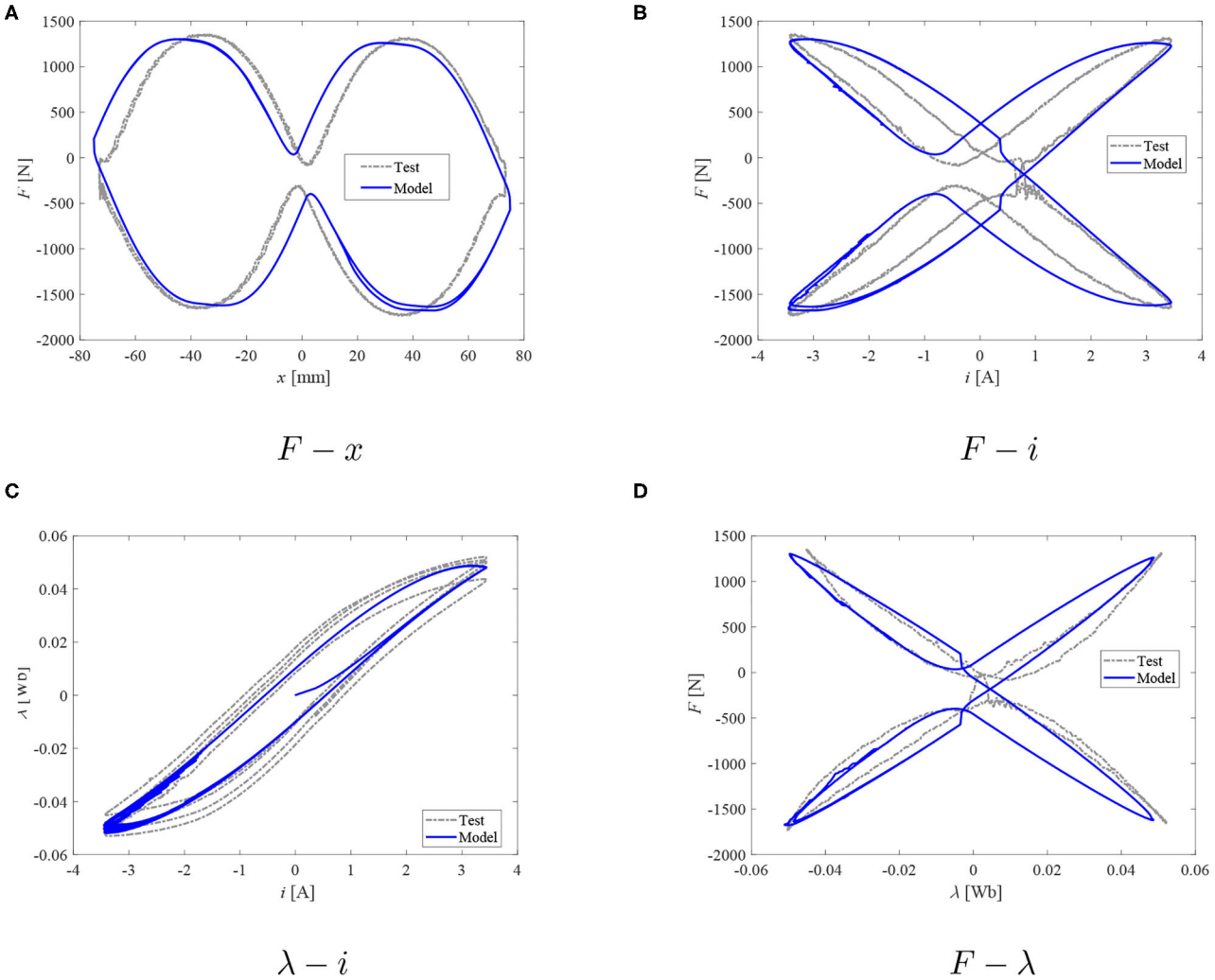

FIGURE 13 | Damper model: measured force and reconstructed flux vs. model data; $I = 3.5$ A. **(A)** $F - x$. **(B)** $F - i$. **(C)** $\lambda - i$. **(D)** $F - \lambda$.

Based on the observations of plots in **Figures 8–13**, it seems that the evolution of damping force against the current and/or magnetic flux can be well-studied with the proposed dual hysteretic approach. At all current levels above 1 A, the model is capable of providing good quality performance in predicting both the $F - x$ loops, the $F - i$ relationship, as well as the $F - \lambda$ plots. The force behavior at transition points as well as the hysteresis width and shape have been well-captured with the proposed approach. At the lowest current case (1 A), only the $F - \lambda$ predictions are not acceptable. The flux as well as force levels are well-predicted; however, the $F - \lambda$ loop's width is poorly captured, and the transition points are in the wrong quadrants of the $F - \lambda$ system of coordinates which can be observed also in the $F - x$ loop of the same figure. The model's poor prediction at the lowest peak current level is likely to be due to the above mentioned flux estimation problems.

5. SUMMARY AND CONCLUSIONS

Hysteresis has been a well-known phenomenon influencing the force/torque output of MR dampers. Prior art on this topic usually included studying the total or combined hysteresis by considering the relationship of the damping force or torque vs. displacement/velocity and current, thus ignoring the distinct nature of magnetic hysteresis and the hydraulic/mechanical hysteresis. The first one is an inherent property of ferromagnetic materials forming the damper's electromagnetic circuit. It is of a different nature to the mechanical (hydraulic) hysteresis of the devices since it does not vanish in the DC limit (as the excitation frequency approaches zero). Understanding the contribution of the two mechanisms is then vital in developing a good quality model. In MR dampers, magnetic hysteresis not only degrades any current-based control scheme performance but also reduces the actuator's dynamic range.

To distinguish between the two mechanisms, the present study extends the concept of a non-linear inductor with magnetic hysteresis (which is then linked to the damping force model). The inductor concept (based on the Duhem hysteretic operator) is employed for copying the $\lambda - i$ characteristics of the solenoid. In the presented form, it simply captures the average flux variation in the structure. It requires estimating the model parameter values from the damper measurements. As such, it may be only used during a control algorithm development stage and is not suitable, for example, for damper sizing studies. The lumped parameter form may, however, be convenient for model-based control studies. Replacing the Duhem operator with the Jiles-Atherton (whose parameters are linked to magnetization characteristics features) model or the vector hysteresis modeling approach would, however, make it suitable for solving such problems at early stages of the development process, though often at the expense of higher computing cost.

The mechanical mechanisms contribution to the force output are then captured with a phenomenological Maxwell-based model of the damper featuring a spring in series with a non-linear dashpot. As demonstrated, the presented procedure allows independent interpretations of the contribution of each analyzed mechanism.

The phenomenological approach undertaken by the authors employs *a posteriori* models whose parameters can be computed from experimental data. Only control studies can thus be supported with it. That is in contrast with the multiphysics technique presented by Kubik and Gołdasz (2019) where the authors showed a hybrid finite-element/lumped parameter approach that can be employed at a design stage.

To further summarize and clarify, in the present study we highlighted an approach targeted toward separation of the hysteretic output of an MR flow-mode damper into two distinct hysteretic operators, namely, mechanical/hydraulic hysteresis and magnetic flux hysteresis. With the proposed approach each mechanism can be studied independently. The presented technique relies on the flux sensorless estimation technique which is particularly convenient if no access to the internal components of a damper can be gained. The damper model is phenomenological and comprises parameters that can be extracted from measurements. Moreover, it allows for the independent analyses of each hysteresis mechanisms with any existing hysteretic model. Both the Duhem model and the derived Maxwell type model were used here for illustration purposes.

Finally, application of the model in more complex transient studies requires adopting a more advanced inductor concept so that the effects of eddy currents and the hysteresis dependence on the excitation input frequency are well-captured. The advanced inductor concept is a subject of on-going study. Moreover, work on a state estimation technique based on the non-linear Kalman filter is in progress. Implementing it is crucial given the flux integration problems mentioned in the previous section.

DATA AVAILABILITY STATEMENT

The raw data supporting the conclusions of this article will be made available by the authors, without undue reservation.

AUTHOR CONTRIBUTIONS

JG conceived the model and carried out simulations. BS and ŁJ planned and carried out experiments. MK processed data, participated in model verification and contributed to the interpretation of the results. All authors provided critical feedback and helped shape the research, modeling results and manuscript.

FUNDING

This research had received funding from the National Agency for Academic Exchange (NAWA Poland) grant no. PPI//APM/2018/1/00027/DEC/1 and the statutory grant no. E3/611/2019/DS (Cracow University of Technology).

REFERENCES

An, J., and Kwon, D. (2003). Modeling of a magnetorheological actuator including magnetic hysteresis. *J. Intell. Mater. Syst. Struct*. 14, 541–550. doi: 10.1177/104538903036506

Chua, L., and Stromsmoe, K. (1970). Lumped-circuit models for nonlinear inductors exhibiting hysteresis loops. *IEEE Trans. Circ. Theory* 17, 564–574. doi: 10.1109/TCT.1970.1083192

Chwastek, K., and Szczygłowski, J. (2008). Estimation methods for the Jiles-Atherton model parameters-a review. *Electric. Rev*. 12, 145–148. Available online at: https://www.researchgate.net/profile/Krzysztof_Chwastek/publication/233991499_Estimation_methods_for_the_Jiles-Atherton_model_of_hysteresis_-_a_review/links/0fcfd50dd9c804d14f000000/Estimation-methods-for-the-Jiles-Atherton-model-of-hysteresis-a-review.pdf

Dyke, S., Spencer, B., Sain, M., and Carlson, J. (1996). Modeling and control of magnetorheological dampers for seismic response reduction. *Smart Mater. Struct*. 5, 565–575. doi: 10.1088/0964-1726/5/5/006

Erol, O., Gonenc, B., Senkal, D., Alkan, S., and Gurocak, H. (2012). Magnetic induction control with embedded sensor for elimination of hysteresis in magnetorheological brakes. *J. Intell. Mater. Syst. Struct*. 23, 427–440. doi: 10.1177/1045389X11435432

Gołdasz, J., Sapiński, B., and Jastrzębski, Ł. (2018a). Assessment of the magnetic hysteretic behaviour of MR dampers through sensorless measurements. *Shock Vibrat*. 2018, 1–21. doi: 10.1155/2018/3740208

Gołdasz, J., Sapiński, B., and Jastrzębski, Ł. (2018b). "On the application of Bouc-Wen hysteresis approach for modeling of MR actuators," in *ACTUATOR 2018; 16th International Conference on New Actuators* (Bremen), 1–5.

Gołdasz, J., Sapiński, B., and Jastrzębski, Ł., and Kubik, M. (2019). "Applicability of magnetic hysteresis model for predicting the behaviour of MR dampers," in *9th ECCOMAS Thematic Conference on Smart Structures and Materials* (Paris), 1671–1681.

Gołdasz, J., and Alexandridis, A. (2012). Medium-and high-frequency analysis of magnetorheological fluid dampers. *J. Vibrat. Control* 14, 2140–2148. doi: 10.1177/1077546311428637

Guo, P., Xie, J., and Guan, X. (2018). Dynamic model of MR dampers based on a hysteretic magnetic circuit. *Shock Vibrat*. 2018, 1–13. doi: 10.1155/2018/2784950

Jastrzębski, Ł., and Sapiński, B. (2017). Experimental investigation of an automotive magnetorheological shock absorber. *Acta Mech. Automat*. 11, 253–259. doi: 10.1515/ama-2017-0039

Jiles, D., and Atherton, D. (1984). Theory of ferromagnetic hysteresis. *J. Appl. Phys*. 55:2115. doi: 10.1063/1.333582

Jolly, M., Bender, J., and Carlson, J. (1999). Properties and applications of commercial magnetorheological fluids. *J. Intell. Mater. Syst. Struct*. 10, 5–13. doi: 10.1177/1045389X9901000102

Kubik, M., and Gołdasz, J. (2019). Multiphysics model of an MR damper including magnetic hysteresis. *Shock Vibrat*. 2019:3246915. doi: 10.1155/2019/3246915

Kubik, M., Machacek, O., Strecker, Z., Roupec, J., and Mazurek, I. (2017). Design and testing of magnetorheological valve with fast force response time and great dynamic force range. *Smart Mater. Struct*. 26:047002. doi: 10.1088/1361-665X/aa6066

Li, Z., Gong, Y., Li, S., and Wang, W. (2019). Magnetic hysteresis compensation control of a magnetorheological damper. *Front. Mater*. 6:299. doi: 10.3389/fmats.2019.00299

Macki, J., Nistri, P., and Zecca, P. (1993). Mathematical models for hysteresis. *SIAM Rev*. 35, 94–123. doi: 10.1137/1035005

Mayergoyz, I., Friedman, G., and Salling, C. (1989). Comparison of the classical and generalized Preisach hysteresis models with experiments. *IEEE Trans. Magnet*. 25, 3925–3927. doi: 10.1109/20.42479

Mayergoyz, I. D., Friedman, G., and Salling, C. (1989). Comparison of the classical and generalized Preisach hysteresis models with experiments. *IEEE Trans. Magnet*. 25, 3925–3927.

Mazgaj, W. (2010). *Determining the Magnetic Field Distribution in Soft Magnetic Materials Incl. Hysteresis and Anisotropy*. Wydawnictwo Politechniki Krakowskiej, Krakow.

Rabinow, J. (1948). The magnetic fluid clutch. *Electric. Eng*. 67:1167. doi: 10.1109/EE.1948.6444497

Simms, N., Holmes, N., and Stanway, R. (2004). A unified modelling and model updating procedure for electrorheological and magnetorheological dampers. *Smart Mater. Struct*. 13, 100–121. doi: 10.1088/0964-1726/13/1/012

Szczygłowski, J. (2001). Influence of eddy currents on magnetic hysteresis loops in soft magnetic materials. *J. Magnet. Magnet. Mater*. 223, 97–102. doi: 10.1016/S0304-8853(00)00584-9

Wang, D., and Liao, W. (2011). Magnetorheological fluid dampers: a review of parametric modelling. *Smart Mater. Struct*. 20:023001. doi: 10.1088/0964-1726/20/2/023001

Zheng, J., Li, Y., Li, Z., and Wang, J. (2015). Transient multi-physics analysis of a magnetorheological shock absorber with the inverse Jiles-Atherton hysteresis model. *Smart Mater. Struct*. 24:105024. doi: 10.1088/0964-1726/24/10/105024

Conflict of Interest: JG is employed by BWI Group.

The remaining authors declare that the research was conducted in the absence of any commercial or financial relationships that could be construed as a potential conflict of interest.

frontiers in Materials

ORIGINAL RESEARCH
published: 23 November 2020
doi: 10.3389/fmats.2020.591283

Semi-Active Scissors-Seat Suspension With Magneto-Rheological Damper

Hongtao Zhu, Xiaoting Rui, Fufeng Yang, Wei Zhu and Junjie Gu*

Institute of Launch Dynamics, Nanjing University of Science and Technology, Nanjing, China

A cab seat suspension with a magneto-rheological (MR) fluid damper is introduced in this paper. A unified-format model for the MR damper is proposed to describe the dynamic characteristics of the MR damper. Also, a simple force-inverse model and a viscous damping tracking model are used for the coil current solution. A digital integrator and an extended Kalman filter are respectively adopted to obtain the vibration velocity of the chair frame and the relative motion velocity of the MR damper piston. A new skyhook control base with viscous damping tracking is applied to the semi-active seat suspension. In the simulation, compared with passive seat suspension under different displacement excitation (2, 4, 6, 8 Hz-sine, and random), the acceleration root mean square of the seat suspension with the MR damper is reduced by 52.2%, 32.2%, 41.3%, 50.8%, and 34.6%, respectively. In the experiment, the acceleration root mean square is reduced by 11.2%, 41.2%, 45.8%, and 31.5%, respectively under different displacement excitation (2, 4, 6, and 8 Hz-sine).

Keywords: magneto-rheological damper, semi-active seat suspension, skyhook control, Bingham model, Bouc-Wen model, viscous damping tracking

OPEN ACCESS

Edited by:
Xian-Xu Bai,
Hefei University of Technology, China

Reviewed by:
Phu Xuan Do,
Vietnamese-German University, Vietnam
Jong-Seok Oh,
Kongju National University, South Korea

****Correspondence:***
Xiaoting Rui
ruixt@163.net

Specialty section:
This article was submitted to Smart Materials, a section of the journal Frontiers in Materials

Received: *05 August 2020*
Accepted: *14 September 2020*
Published: *23 November 2020*

Citation:
Zhu H, Rui X, Yang F, Zhu W and Gu J (2020) Semi-Active Scissors-Seat Suspension With Magneto-Rheological Damper. Front. Mater. 7:591283. doi: 10.3389/fmats.2020.591283

INTRODUCTION

Many drivers suffer from occupational diseases, including stomach disease, heart disease, and anxiety disorder. Part of those diseases are caused by the vibration of a cab. In recent years, the application of cabs has increased, so it has become necessary to reduce the vibration of cab seats by adopting some additional controllable components, of which the magneto-rheological (MR) damper is a superior candidate. An MR damper has been applied to many aspects of engineering (Choi et al., 2016), because of its advantageous features including low-power consumption, force controllability, and rapid response. The MR damper mainly consists of MR fluid which is a designable and controllable smart material whose apparent yield strength can be changed sharply within milliseconds, by the supply of an external magnet, from a free-flowing viscous liquid to a semi-solid one (Rabinow, 1951).

The nonlinear dynamic characteristics of the MR damper limit its application in engineering. In recent years, scholars have completed an extensive amount of research on the dynamic characteristics of MR dampers. Among this research, the Bingham model (Nishiyama et al., 2002; Sun et al., 2010; Fusi et al., 2014) and the Bouc-Wen model (Spencer et al., 1997; Ikhouane and Rodellar, 2005; Bahar et al., 2009; Rodríguez et al., 2009) are commonly used in applications. The Dahl model, which is used to describe solid friction (Dahl, 1976), has also been used by some scholars to describe the hysteretic characteristics of the MR damper (Spencer et al., 1997; Ikhouane and Rodellar, 2005; Bahar et al., 2009; Rodríguez et al., 2009). Neural networks models have also been applied in the modeling of an MR damper. However, the neural network lacks the necessary

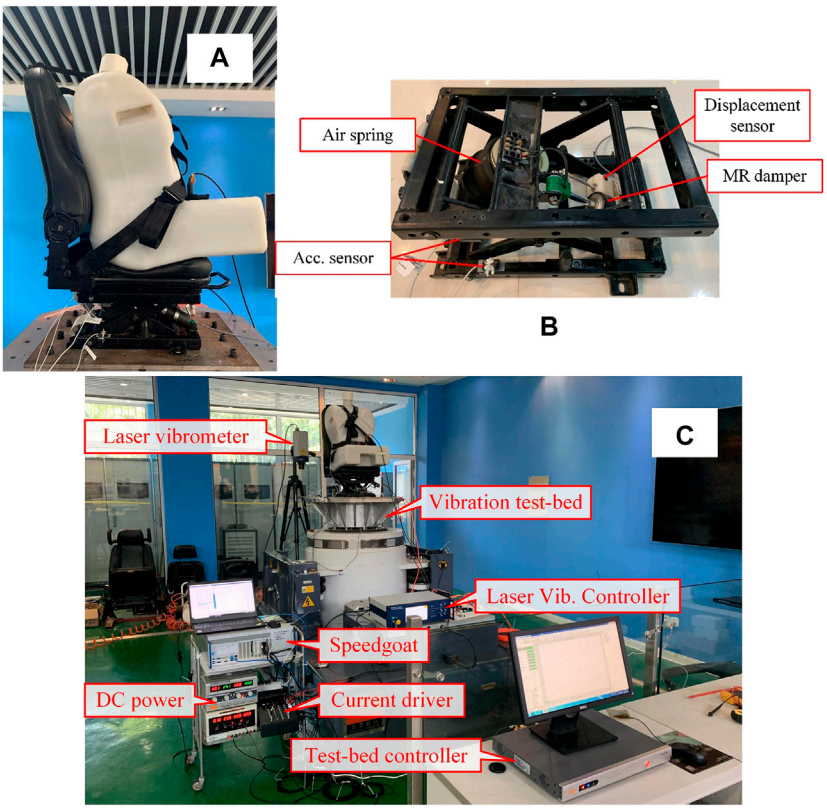

FIGURE 1 | The structure of the scissors-linkage seat suspension and experiment setup: **(A)** seat photo; **(B)** the structure of the scissors-linkage seat suspension; **(C)** the experiment setup.

physical meaning when describing the hysteresis model of the magneto-rheological damper. In most engineering applications of magneto-rheological dampers, the desired damping force needs to be converted into electric current. Therefore, an inverse model of magneto-rheological dampers is essential. Tsang et al. (2006) gives a simplified dynamic inverse model of an MR damper based on the Bingham model and the Bouc-Wen model. Also, neural network models have been widely used in dynamic inverse models (Xia, 2003; Karamodin et al., 2007; Gao and Wang, 2008; Bhowmik et al., 2010).

In semi-active seat suspension vibration isolation control, the skyhook control is still one of the main methods of the engineering application (Hatwalane, 2016). Lee and Jeon (2002) uses a 2-state skyhook control (on-off skyhook control) for seat suspension with an MR damper. Choi et al. put MR dampers into commercial seats applying the skyhook control. In Choi and Han (2007), a no-jerk skyhook control was proposed to reduce acceleration jerk. A sliding-mode control based on a human body model was used in MR damper seats in Choi and Han (2007), but it is difficult to realize in engineering. The H^{∞} control was applied to the vibration isolation control of the seat suspension with an MR damper by Yao et al. (2013). Bai et al. (2016) and Bai et al. (2017) put a rotary MR damper into the seat suspension for both longitudinal and vertical vibration attenuation. A variety of advanced controllers were designed for seat suspension with MR dampers by Phu et al. (2017), Xuan et al. (2017), and Phu et al. (2019).

In this paper, the MR damper is applied into commercial air-spring cab seats. The structure of the seat suspension used in the paper is shown in **Figure 1**. The main contributions in this paper are given as follow: 1) a unified-format model for an MR damper combining the Bingham model and the Bouc-Wen model is proposed; 2) a viscous damping tracking model based on the Bingham model is applied into a skyhook control; 3) an improved on-off control is proposed for comparison; and 4) a low-cost 3-sensor semi-active seat structure is put forward, in which the digital integrator and an extended Kalman filter are adopted for signal processing.

The paper is organized as follows: *System Configuration and Modeling* mainly introduces the system structure and system modeling; a new skyhook control is introduced in *Vibration Isolation Control*; the simulation results of sine displacement excitation and random displacement excitation are discussed in *System Simulation*; the signal processing of the sensor is given in *Signal Processing*; and the experimental results are shown in *Experiment*.

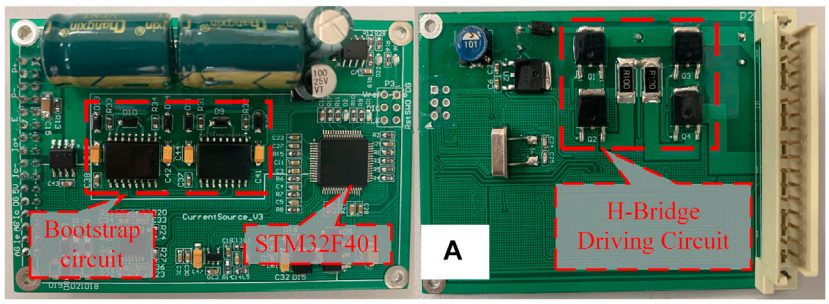

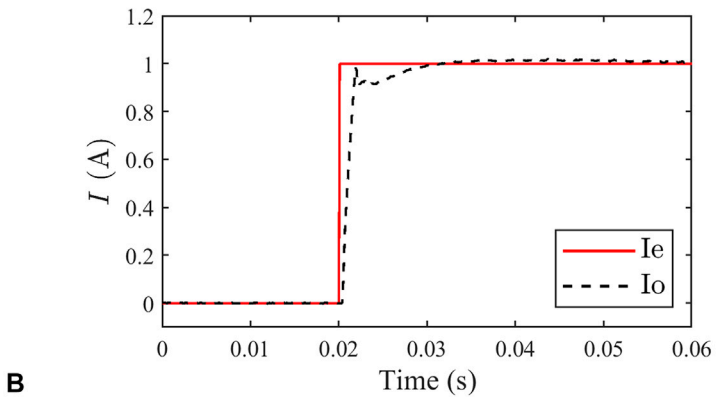

FIGURE 2 | Current driver: **(A)** PCB board; **(B)** step response.

SYSTEM CONFIGURATION AND MODELING

System Configuration

The structure of a scissors seat in this paper is given in **Figure 1B**. From **Figure 1B**, we can see that a scissors seat is mainly composed of a shear bar, an air spring, and an MR damper. The shear bar is mainly used to keep the seat mechanism stable, and the air spring is used to provide seat support rigidity. The MEMS (Micro-Electro-Mechanical System) acceleration sensor is used to measure the acceleration of the chair frame and the base, and MEMS has the advantages of long life, small size, and low price. The resistance ruler, whose accuracy can reach 0.01 mm, is used to measure the stroke of the MR damper. Also, compared to other types of displacement sensors, the resistance ruler is cheap and suitable for the market.

A coil current driver is used to provide a controlled current for the MR damper. The current driver used in this paper is composed of a power circuit, a microcontroller (MCU), a bootstrap circuit, and a H-bridge drive circuit. The microcontroller selects STM32F401 of ST Co., and its main frequency can reach up to 84 MHz. **Figure 2A** shows the PCB board of the current driver designed in this paper.

In simulation, the current driver of the MR damper is regarded as a typical 1-st system, and its transfer function is given as follows:

$$T_{cs}(s) = \frac{1}{\tau_{cs}s + 1} \tag{1}$$

where, τ_{cs} is the time constant of the coil current driver ($\tau_{cs} = 1e - 3$ s). The 1A-step response of the coil current driver is shown in **Figure 2B**.

Modeling for the Magneto-Rheological Damper System

Unified-Format Model for the Magneto-Rheological Damper

In order to facilitate the discussion, an unified-format model is established for an MR damper.

$$F_d = kz_d + c\dot{z}_d + f_c\bar{\omega} \tag{2}$$

In **Eq. 2**, z_d is the relative displacement of damper piston, and zd is the relative velocity; k is the stiffness of the compensator in the damper (straight single-rod damper), c represents the equivalent viscous damping coefficient of the MR damper; and f_c is the coulomb friction.

When the model takes the Bingham model (Zhu et al., 2019), $\bar{\omega} = sign(\dot{z}_d)$.

$$F_d = kz_d + c\dot{z}_d + f_c\text{sign}(\dot{z}_d) \tag{3}$$

where, sign $(\cdot)$represents the sign function.

When the model takes the normalized Bouc-Wen model (Zhu et al., 2019) and there is

$$\begin{cases} F_d = kz_d + c\dot{z}_d + f_c\bar{\omega} \\ \dot{\bar{\omega}} = \rho\left[\dot{z}_d - \sigma|\dot{z}_d||\bar{\omega}|^{n-1}\bar{\omega} + (\sigma - 1)\dot{z}_d|\bar{\omega}|^n\right] \end{cases} \tag{4}$$

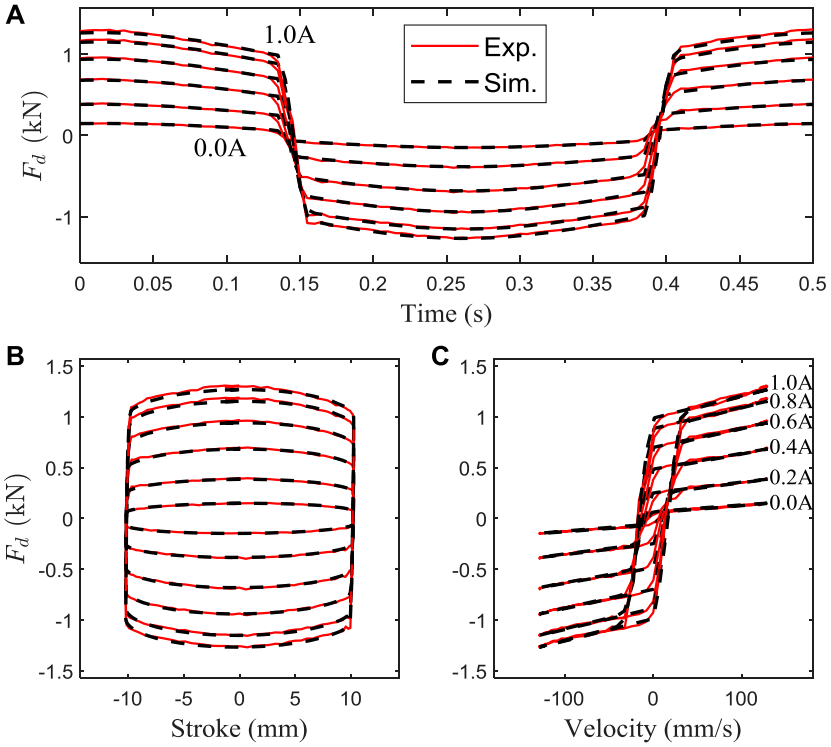

FIGURE 3 | Comparison between the predicted and experimental data (normalized Bouc-Wen model): **(A)** the damping force vs. time; **(B)** the damping force vs. stroke; **(C)** the damping force vs. velocity.

TABLE 1 | Fitting results of MR damper parameters.

Para	Value	Unit
c_1	1984.8	N · s/m
c_0	638.55	N · s/m
λ_c	1.5353	—
f_1	1336.4	N
f_0	60.331	N
λ_f	1.1943	—
ρ_1	7,018	m^{-1}
ρ_0	44,836	m^{-1}
λ_ρ	4.0485	—
k_c	1864.9	N · s/(m · A)
k_f	1041.9	N/A

In **Eq. 4**, ρ, σ, and n are the shape parameters of the normalized Bouc-Wen model. And the normalized Bouc-Wen model is stable and dissipative when $\rho > 0$, $\sigma > 0.5$, $n \geq 1$. It is not difficult to identify the parameters using the method in Zhu et al. (2019) and the comparison between the predicted and experimental data (normalized Bouc-Wen model) is given in **Figure 3**.

The exponential function is used in the parameter fitting and the fitting results are shown **Table 1**.

$$c(I) = c_1\left(1 - e^{-\lambda_c I}\right) + c_0 \tag{5}$$

$$f_c(I) = f_1\left(1 - e^{-\lambda_f I}\right) + f_0 \tag{6}$$

$$\rho(I) = (\rho_1 - \rho_0)\left(1 - e^{-\lambda_\rho I}\right) + \rho_0 \tag{7}$$

where, I represents the coil current of the MR damper.

The fit curves of parameters (ρ, σ, and n) are shown in **Figure 4** and fitting values are in good agreement with the experimental values.

When the current is small, the parameters (c and f_c) have a linear relation with the coil current of the MR damper.

$$c(I) \approx k_c I + c_0 \tag{8}$$

$$f_c(I) \approx k_f I + f_0 \tag{9}$$

Force-Inverse Model of the Magneto-Rheological Damper

The expected force of the MR damper is noted as f_e and the form of the force-inverse model is given in **Eq. 10**.

$$I_e = F_d^{-1}(f_e) \tag{10}$$

where, I_e is the expected current of the MR damper and $F_d^{-1}(\cdot)$ is the inverse model representation of the MR damper.

$$F_d(\dot{z}_d, \bar{\omega}, I) = c(I)\dot{z}_d + f_c(I)\bar{\omega} \tag{11}$$

At the same time, under the condition of a small current, the equivalent viscous damping coefficient c and coulomb friction force f_c still meet the linear relationship in **Eqs 8** and **9**. The expected current of the MR damper can be expressed as

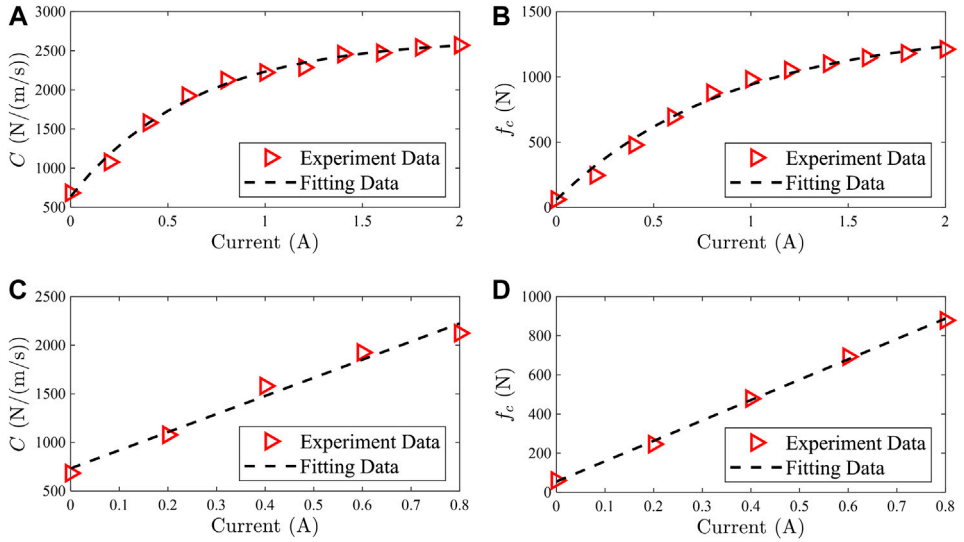

FIGURE 4 | Parameter fit curve: **(A)** nonlinear fitting of parameter *c*; **(B)** nonlinear fitting of parameter f_c; **(C)** linear fitting of parameter *c*; **(D)** linear fitting of parameter f_c.

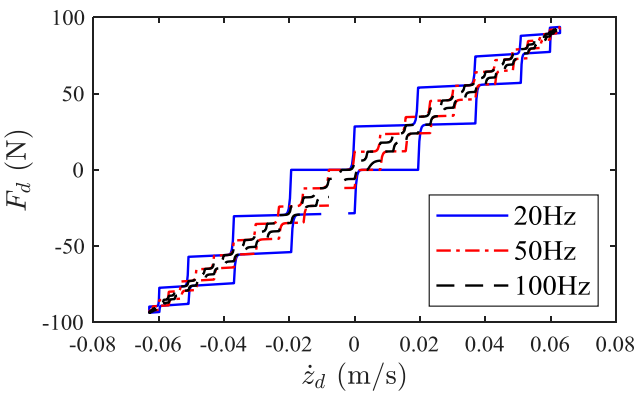

FIGURE 5 | Simulation results of viscous damper tracking.

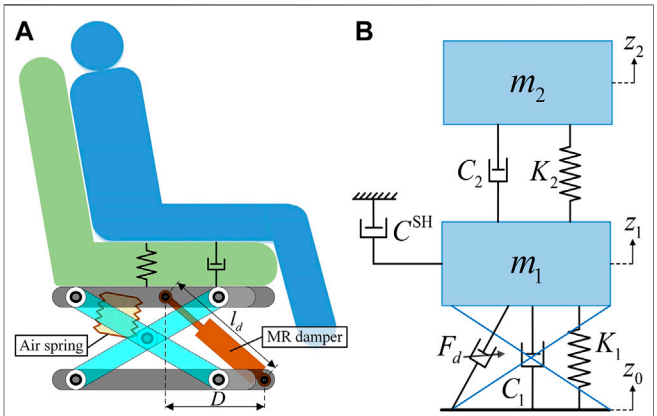

FIGURE 6 | The schematic diagram of the seat system: **(A)** the structure of the scissors-linkage seat; **(B)** the schematic diagram of the skyhook control for the seat suspension.

$$I_e = \frac{f_e - c_0\dot{z}_d - f_0\bar{\omega}}{k_c\dot{z}_d + k_f\bar{\omega}} \tag{12}$$

When the model takes the Bingham model, $\bar{\omega} = sign(\dot{z}_d)$, then

$$I_e = \begin{cases} 0, & |\dot{z}_d| < \varepsilon_v \; or \; (f_e - c_0\dot{z}_d - f_0\bar{\omega})\dot{z}_d < 0 \\ \dfrac{f_e - c_0\dot{z}_d - f_0\bar{\omega}}{k_c\dot{z}_d + k_f sign(\dot{z}_d)}, & others \end{cases} \tag{13}$$

where, $\varepsilon_v > 0$ velocity threshold constant.

Viscous Damping Tracking

Due to the energy consumption characteristics of the MR damper, it is impossible to generate the active force, so the expected force of the MR damper is the viscous damping force, which is:

$$F_e = C_e\dot{z}_d \tag{14}$$

where, F_e is the expected damping force, and C_e is the expected viscous damping coefficient.

Also, according to **Eqs 8** and **9**, the expected current form of the MR damper is:

$$I_e = \frac{(C_e - c_0)\dot{z}_d - f_0\bar{\omega}}{k_c\dot{z}_d + k_f\bar{\omega}} \tag{15}$$

When the model takes the Bingham model, $\bar{\omega} = sign(\dot{z}_d)$, then

$$I_e = \frac{(C_e - c_0)\dot{z}_d - f_0 sign(\dot{z}_d)}{k_c\dot{z}_d + k_f sign(\dot{z}_d)} = \frac{(C_e - c_0)|\dot{z}_d| - f_0}{k_c|\dot{z}_d| + k_f} \tag{16}$$

TABLE 2 | Parameter value of the seat suspension system.

Parameter	Value	Unit
m_1	15	kg
K_1	1.70e4	N/m
C_1	1.00e2	N/(m/s)
m_2	70	kg
K_2	3.02e5	N/m
C_2	2.14e3	N/(m/s)
C_d	4.17e3	N/(m/s)
D	0.165	m

The Bouc-Wen model is used as the accurate model of the MR damper, and the viscous damping tracking simulation is carried out under different control frequencies (20, 50, and 100 Hz). The simulation results are shown in **Figure 5**, and when the current control frequency is small, the F_d-$\dot{z}_d$ curve shows obvious serration. It is evident from **Figure 5** that the higher the control frequency, the better the viscous damping tracking effect.

Modeling for the Seat Suspension System

The schematic diagram of the seat suspension model is shown in **Figure 6**. In the schematic diagram, the seat suspension system is regarded as a 2-DOFs system.

According to the Newton formula, the dynamic equation of the seat suspension model is established as follows:

$$\begin{cases} m_2\ddot{z}_2 = -K_2(z_2 - z_1) - C_1(\dot{z}_2 - \dot{z}_1) \\ m_1\ddot{z}_1 = -K_1(z_1 - z_0) - C_1(\dot{z}_1 - \dot{z}_0) + K_2(z_2 - z_1) \\ \qquad + C_1(\dot{z}_2 - \dot{z}_1) + F_d \end{cases} \tag{17}$$

where m_1 and m_2 are the mass of the seat and the driver, respectively; z_0 is the base displacement input, and z_1 represents the displacements the seat; K_1 and K_2 represent the stiffness of airspring and cushion respectively.

$$\begin{cases} F_d = -\dfrac{\sqrt{l_d^2 - D_d^2}}{l_d}\left(c\dot{l}_d + f_c\bar{\omega}\right) \\ \dot{\bar{\omega}}(t) = \rho\left[\dot{l}_d(t) - 0.5\left|\dot{l}_d(t)\right|\left|\bar{\omega}(t)\right|^{n-1}\bar{\omega}(t) + 0.5\dot{l}_d(t)\left|\bar{\omega}(t)\right|^2\right] \end{cases} \tag{18}$$

In **Eq. 18**, l_d represents the length of the MR damper and $\dot{l}_d$ is the time derivative of l_d; D is the distance constant which is defined in **Figure 6**. The expressions of l_d and $\dot{l}_d$ are given as follows:

$$l_d^2 = D_d^2 + (z_1 - z_0 + H_{10})^2 \tag{19}$$

$$\dot{l}_d = \frac{\sqrt{l_d^2 - D^2}}{l_d}(\dot{z}_1 - \dot{z}_0) \tag{20}$$

The parameter value of the seat suspension system for the simulation is given in **Table 2**.

In the above table, C_d is the viscous damping coefficient of the passive hydraulic damper, which is used for comparison with the effect of the MR damper.

VIBRATION ISOLATION CONTROL

Skyhook Control

Skyhook control (SH) is one of the most widely used control strategies in suspension control. As shown in **Figure 6B**, a hypothetical ceiling damper is placed between the seat frame and the ideal ceiling, and its damping coefficient is C^{SH}. The expected force of continuous skyhook control is noted as F^{SH}.

$$F^{SH} = -C^{\mathrm{SH}}\dot{z}_1 \tag{21}$$

Considering the nonlinear dynamic characteristics of the MR damper, the expected current of the MR under continuous SH control is:

$$I^{\mathrm{SH}} = F_d^{-1}(-F^{SH}) \tag{22}$$

where, $F_d^{-1}(\cdot)$ is the form of the force-inverse model which is given as **Eq. 10**

On-Off Control

When the skyhook damping coefficient C_{SH} tends to infinity, the control strategy is an on-off control strategy, and the control output switches between the maximum and the minimum. This is also called a two-state skyhook control in some literature (Choi and Han, 2007).

$$I_e = \begin{cases} I_{\min}, & \dot{z}_1\dot{z}_{10} \le 0 \\ I_{\max}, & \dot{z}_1\dot{z}_{10} > 0 \end{cases} \tag{23}$$

In order to avoid frequently switching the current output, the above formula is improved as follows:

$$I_e = \begin{cases} I_{\min}, & \dot{z}_1\dot{z}_{10} \le 0 \\ I_{\max}, & \dot{z}_1\dot{z}_{10} > 0 \text{ and } |\dot{z}_1| > \varepsilon_a \text{ and } |\dot{z}_{10}| > \varepsilon_r \\ I_{\min} + \dfrac{|\dot{z}_1|}{\varepsilon_a}I_{\max}, & \dot{z}_1\dot{z}_{10} > 0 \text{ and } |\dot{z}_1| < \varepsilon_a \text{ and } |\dot{z}_{10}| > \varepsilon_r \\ I_{\min} + \dfrac{|\dot{z}_{10}|}{\varepsilon_r}I_{\max}, & \dot{z}_1\dot{z}_{10} > 0 \text{ and } |\dot{z}_1| > \varepsilon_a \text{ and } |\dot{z}_{10}| < \varepsilon_r \\ I_{\min} + \dfrac{|\dot{z}_1\dot{z}_{10}|}{\varepsilon_a\varepsilon_r}I_{\max}, & \textit{others} \end{cases} \tag{24}$$

Where, $\varepsilon_a > 0$ is the absolute velocity threshold constant; $\varepsilon_r > 0$ is the relative velocity threshold constant is the form of force-inverse model is given in **Eq. (10)**. And, the larger the values of ε_a and ε_r, *the smoother the current output.*

Skyhook Control Based on Viscous Damping Tracking

Since $K_2 \gg K_1$, the system in **Eq. 17** can be approximated as a single-degree-of-freedom vibration system, there is:

$$m\ddot{z}_1 = -K_1(z_1 - z_0) - C_1(\dot{z}_1 - \dot{z}_0) - C_{10}(\dot{z}_1 - \dot{z}_0) \tag{25}$$

where, $m = m_1 + m_2$; C_{10} the virtual viscous damping between the seat frame and the base, which is produced by the action of the MR damper.

According to **Eq. 20**, there is:

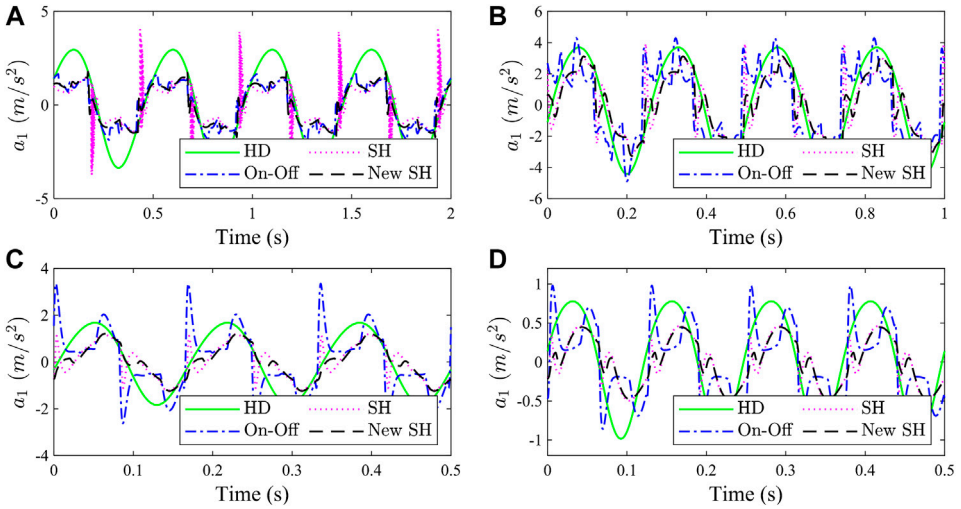

FIGURE 7 | Simulation results of sinusoidal displacement excitation: **(A)** 2 Hz, **(B)** 4 Hz, **(C)** 6 Hz, and **(D)** 8 Hz.

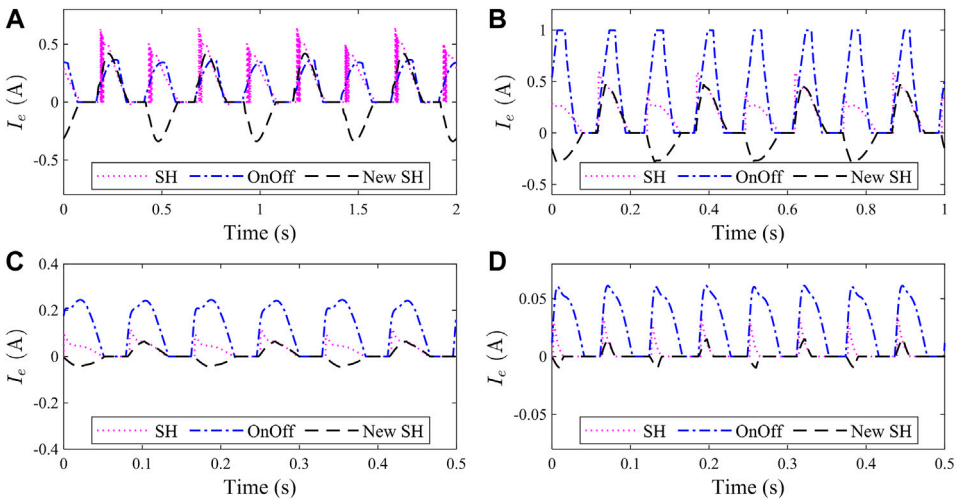

FIGURE 8 | Expected current of MR damper: **(A)** 2 Hz, **(B)** 4 Hz, **(C)** 6 Hz, and **(D)** 8 Hz.

$$C_{10} = C_{SH}\frac{\dot{z}_1}{\dot{z}_{10}} \tag{26}$$

In **Eq. 26**, $\dot{z}_{10}$ is the relative speed of the chair frame to the base, $\dot{z}_{10} = \dot{z}_1 - \dot{z}_0$.

Since the value of C_1 is small, the natural frequency and damping ratio of the single-degree-of-freedom system is given as follows:

$$\begin{cases} \omega_n = \sqrt{\dfrac{K_1}{m}} \\ \zeta = \dfrac{C_{10}}{2m\omega_n} = \dfrac{C_{10}}{c_c} \end{cases} \tag{27}$$

where, $c_c = 2m\omega_n$, is the critical damping coefficient.

The value range of C_{10} is defined as $C_{10} \in [c_{\min}, c_{\max}]$. When $C_{10} = c_c$, the system will not generate resonance, so the values range of C_{10} is given as:

$$\begin{cases} c_{\min} = 0 \\ c_{max} = c_c \end{cases} \tag{28}$$

Considering that the value of C_{10} is close to 0, there is:

$$C_{10} = \begin{cases} C_{\min}, & \dot{z}_1\dot{z}_{10} < 0 \\ C_{SH}\dfrac{\dot{z}_1}{\varepsilon_r}, & |\dot{z}_{10}| < \varepsilon_r \\ C_{SH}\dfrac{\dot{z}_1}{\dot{z}_{10}}, & others \end{cases} \tag{29}$$

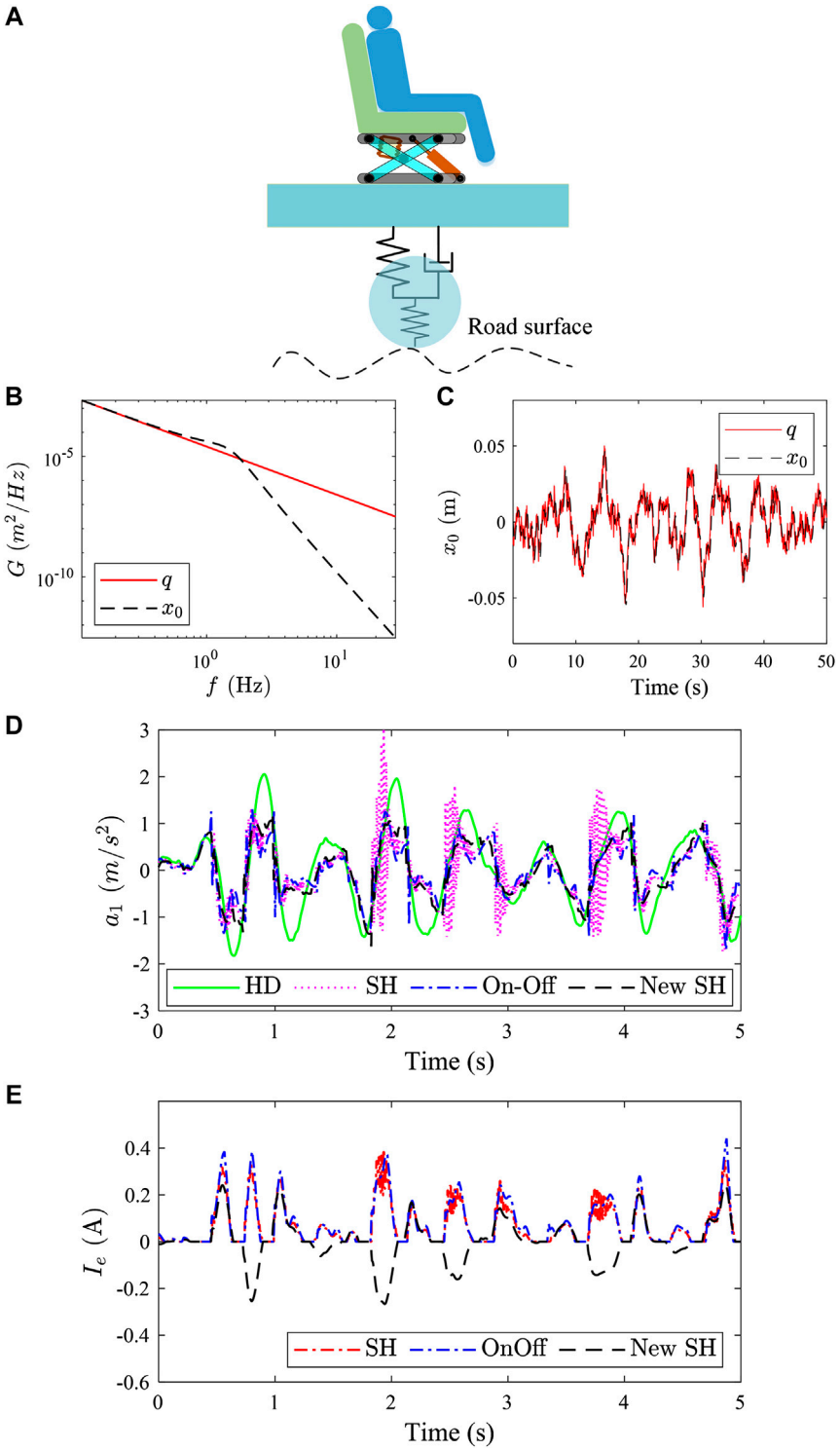

FIGURE 9 | Random input for seat suspension (v = 10m/s, road C): **(A)** schematic diagram of seat excitation; **(B)** displacement excitation PSD curve, **(C)** displacement excitation time-domain curve, **(D)** simulation results of seat suspension under random displacement excitation; and **(E)** expected current of the MR damper under random displacement excitation.

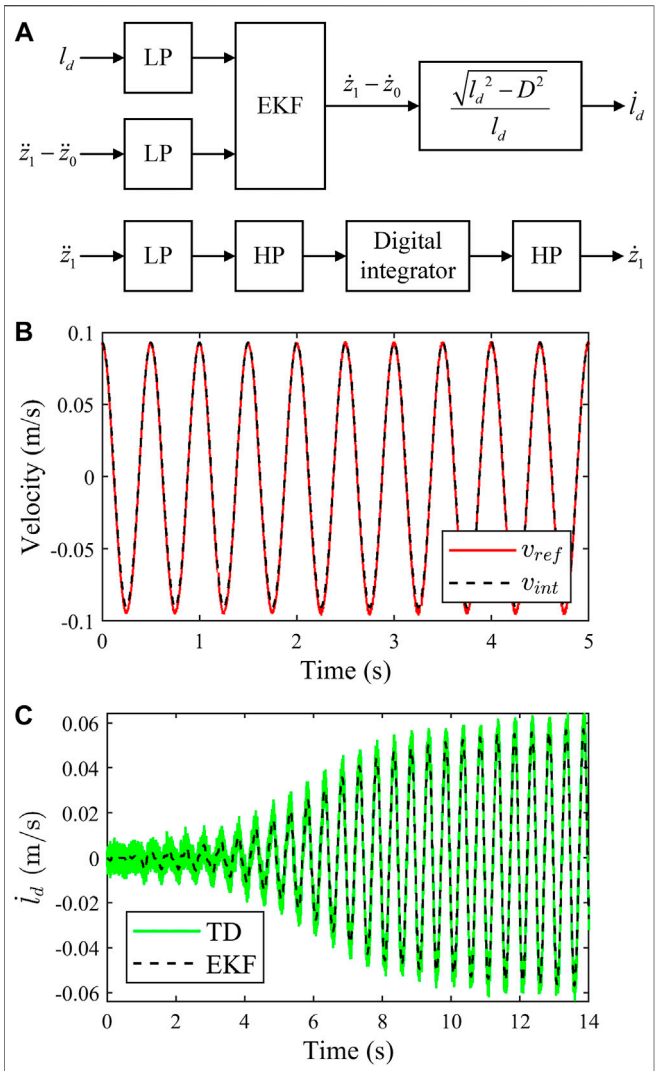

FIGURE 10 | The signal processing diagram and results: **(A)** the signal processing diagram; **(B)** acceleration signal integration results; and **(C)** EKF signal fusion results.

Bringing the value range of **Eq. 28** into **Eq. 29**, there is:

$$C_{10} = \begin{cases} c_{\min}, & C_{10} < c_{\min} \\ c_{\max}, & C_{10} > c_{\max} \\ C_{10}, & others \end{cases} \tag{30}$$

According to the seat geometry, the desired damping coefficient C_e of the MR damper is:

$$C_e = \frac{l_d^2}{l_d^2 - D^2} C_{10} \tag{31}$$

According to **Eq. 16**, the expected current of the MR damper can be obtained as follows:

$$I_e = \frac{l_d^2}{l_d^2 - D^2} \frac{C_{10}|\dot{z}_d|}{k_c|\dot{z}_d| + k_f} \tag{32}$$

If an unidirectional current is applied to the iron core of the MR damper for a long time, the iron core will have residual magnetism. In order to avoid residual magnetism of the iron core, the current direction is continuously changed during current control in **Eq. 33**.

$$I_e = I_e sign(\dot{z}_d) \tag{33}$$

SYSTEM SIMULATION

Sinusoidal Input

According to ISO2631–1, the sensitive frequency range of the human body is about 2–8 Hz. Therefore, sinusoidal base displacement (2, 4, 6, 8 Hz) is adopted to the seat displacement excitation. The simulation results of the sinusoidal displacement excitation at different frequencies is shown in **Figure 7**. In **Figure 7**, "HD" represents the passive hydraulic damper; "SH" represents the skyhook control; "On-Off" represents the on-off control; and "New-SH′ represents the skyhook control based on viscous damping tracking.

Compared with seat suspension with passive hydraulic dampers, the acceleration of the seat suspension with the MR damper, is significantly reduced under different-frequency displacement base excitation. Compared with passive suspension, under 2 Hz-sinusoidal displacement excitation, the acceleration RMS of the MR damper seat suspension with different control methods (SH, On-Off, and New-SH) decreased by 52.0%, 56.9%, and 52.2%, respectively. Under 4 Hz-sinusoidal displacement excitation, it decreased by 30.0%, 14.0%, and 32.2%. Under 6 Hz-sinusoidal displacement excitation, it decreased by 38.6%, 5.2%, and 41.3%. Under 8 Hz-sinusoidal displacement excitation, it decreased by 48.2%, 22.6%, and 50.8%. The following conclusions can be drawn from **Figure 7**: 1) the acceleration RMS reduction effect of "SH" and "New-SH" is similar, but the acceleration peak of "New-SH" is smaller; 2) the improved on-off control in this paper performs better in the low frequency (near natural frequency), but poorly in the high frequency region.

The expected current of the MR damper under sinusoidal displacement excitation is shown in **Figure 8**. Compared with the traditional skyhook control and on-off control, the expected current of the skyhook control based on viscous damper tracking is smoother. This is because the SH control proposed in this paper converts the active force into the desired damping coefficient of the MR damper, and limits the value range of the desired viscosity coefficient within a reasonable range.

Random Input

According to ISO-8608, the displacement PSD (power spectrum value) of road space surface is:

$$G_q(n) = G_q(n_0)\left(\frac{n}{n_0}\right)^{-W} \tag{34}$$

In **Eq. 34**, n represents the spatial frequency (unit: m^{-1}); n_0 represents the reference spatial frequency ($n_0 = 0.1 m^{-1}$); $G_q(n_0)$ is the displacement PSD of reference spatial frequency n_0

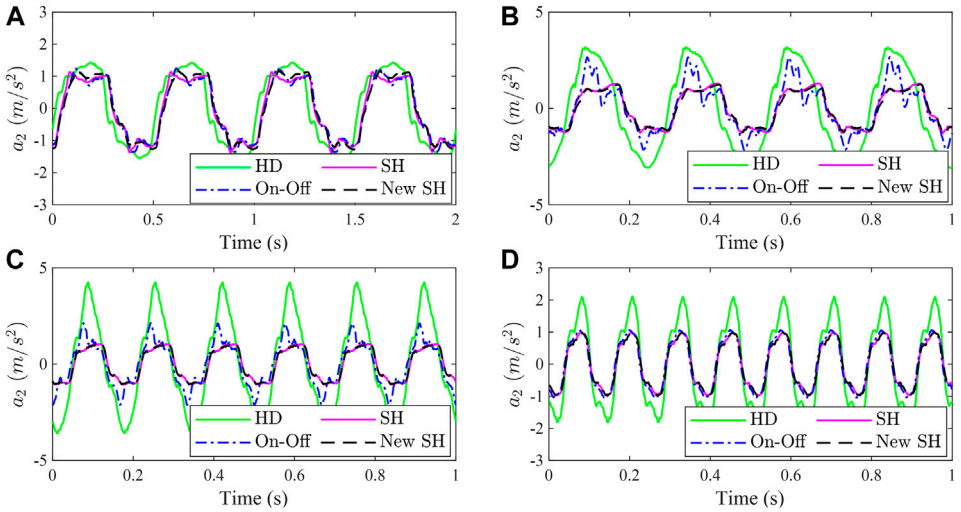

FIGURE 11 | Experimental results of sinusoidal displacement excitation: **(A)** 2 Hz, **(B)** 4 Hz, **(C)** 6 Hz, and **(D)** 8 Hz

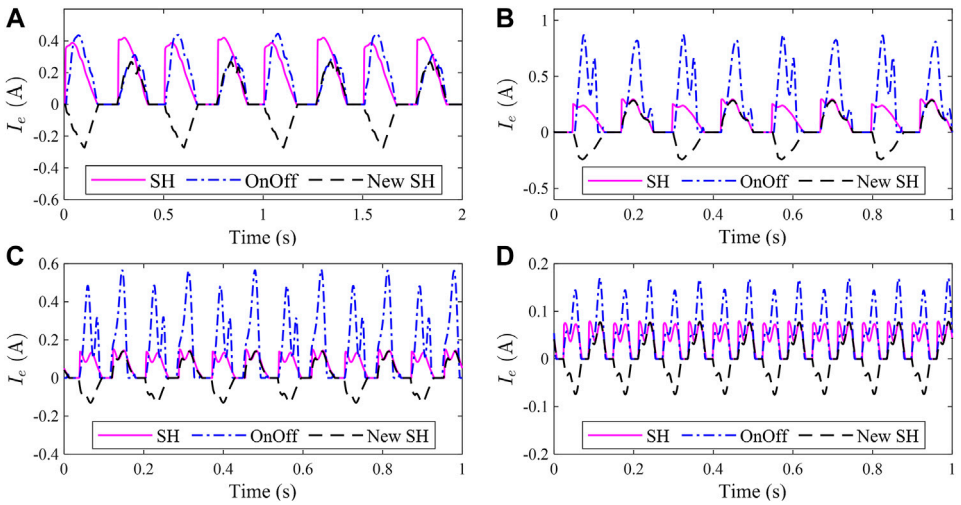

FIGURE 12 | Expected current of the MR damper: **(A)** 2 Hz, **(B)** 4 Hz, **(C)** 6 Hz, and **(D)** 8 Hz

(unevenness coefficient, unit: m^2/m^{-1}); W is the frequency index (empirical value: $W = 2$).

The vehicle speed is recorded as v and the time frequency is noted as f.

$$f = vn \tag{35}$$

Then the displacement PSD of the road time unevenness is:

$$G_q(f) = \frac{1}{v} G_q(n) \tag{36}$$

Using the sine superposition method, it is not difficult to get the time unevenness of the road surface $q(t)$:

$$q(t) = \sum_{i=1}^{N} \sqrt{G_q\left(\frac{f_i^{\text{mid}}}{v}\right)} \frac{\Delta f_i}{v} \sin\left(2\pi f_i^{mid} t + \theta_i\right) \tag{37}$$

where, f_i^{mid} is the interval center frequency; Δf_i is the frequency range size; θ_i is the random phase of the sine wave, which satisfies uniform distribution on $[0, 2\pi]$.

The seat displacement excitation z_0 is actually the vibration of the body, which is the result of the action of the road surface excitation on the vehicle body through the suspension of the vehicle. Its working principle is shown in the **Figure 9**.

The filtering effect of the vehicle body on the road excitation is regarded as a typical second-order filter, and its transfer function is:

$$T_{2nd}(s) = \frac{\omega_n^2}{s^2 + 2\xi\omega_n s + \omega_n^2} \tag{38}$$

In **Eq. 38**, ω_n is the natural frequency of the typical second link, and ξ is the damping ratio. The values of ω_n and ξ can be properly

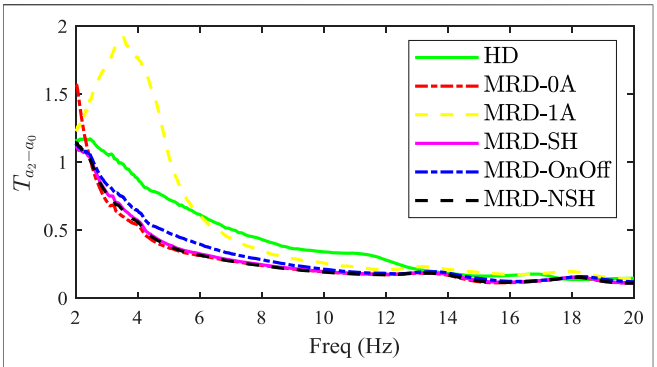

FIGURE 13 | The results of the 2–40 Hz frequency sweep experiment.

selected according to the mass of the vehicle body, and the stiffness and damping coefficient of the suspension system. ω_n = 9.78 rad/s and ξ = 0.4 are taken in this paper.

The displacement PSD of z_0 is noted as $G_{z_0}(f)$ and there is:

$$G_{z_0}(f) = \left|T_{2nd}(j2\pi f)\right|^2 G_q(f) \tag{39}$$

when the vehicle speed is 10 m/s and the road type is C. The displacement PSD curve and time-domain curve is shown in **Figures 9B,C**.

The seat suspension simulation results under the above displacement excitation is give in **Figure 9D**. It is not difficult to conclude from **Figure 9D** that, compared with the traditional passive seat suspension, the vibration isolation effect of the seat suspension using the MR damper is significantly improved. Under the random displacement excitation in **Figure 9C**, the acceleration RMS of the seat frame is reduced by 28.0%, 38.9%, and 34.6%, respectively for those three control strategies (SH, On-Off, and New-SH).

SIGNAL PROCESSING

Figure 10A shows the block diagram of the signal processing in this paper. The seat frame acceleration signal passes through the low-pass filter (LP), high-pass filter (HP), and digital integrator in sequence to obtain the vibration velocity of the seat frame. The relative velocity of the piston of the MR damper is obtained through the extended Kalman filter (EKF).

Acceleration Signal Integration

The transfer function of the first-order high-pass filter is given as follows:

$$T_{hp}(s) = \frac{\tau_{hp}s}{\tau_{hp}s + 1} \tag{40}$$

where, τ_{hp} is the time constant of the first-order high-pass filter.

Through bilinear transformation, it is not difficult to get the discrete transfer function of the high-pass filter:

$$H_{hp}(z) = \frac{1 - z^{-1}}{\frac{T_s}{\tau_{hp}} + 1 + \left(\frac{T_s}{\tau_{hp}} - 1\right)z^{-1}} \tag{41}$$

In **Eq. 41**, T_s is the signal sampling time.

In signal integration, the following form of the digital integrator is used:

$$H_{\text{int}}(z) = \frac{T_s(z+1)}{2(z-1)} \tag{42}$$

The vibration velocity signal measured by the laser vibrometer is used as a reference signal, and the acceleration signal integration experiment results are shown in **Figure 10B**. **Figure 10B**, v_{ref} represents the velocity reference signal measured by the laser vibrometer; v_{int} is the velocity signal obtained by integrating the acceleration signal. v_{int} and v_{ref} are in good agreement in **Figure 10B**.

Extended Kalman FilterSignal Fusion

The state vector of EKF is noted as $x_k = \left[z_1 - z_0 + H_{10} \quad \dot{z}_1 - \dot{z}_0 \quad \ddot{z}_1 - \ddot{z}_0\right]_k^T$ and the output vector is noted as $y_k = \left[l_d \quad \ddot{z}_1 - \ddot{z}_0\right]_k^T$.

The constant acceleration (CA) model is established and T_{KF} is the sampling period of EKF. The discrete form of the CA model is given as follows:

$$\begin{cases} x_k = \Phi_{k,k-1}x_{k-1} + w_k \\ y_k = h(x_k) + v_k \end{cases} \tag{43}$$

In **Eq. 44**, w_k is the state disturbance; v_k is the measurement noise; and $\Phi_{k,k-1}$ is the state transition matrix.

$$\Phi_{k,k-1} = \begin{bmatrix} 1 & T_{KF} & T_{KF}^2/2 \\ 0 & 1 & T_{KF} \\ 0 & 0 & 1 \end{bmatrix} \tag{44}$$

$$h(x_k) = \begin{bmatrix} l_d \\ \ddot{z}_1 - \ddot{z}_0 \end{bmatrix} \tag{45}$$

$$l_d = \sqrt{(z_1 - z_0 + H_{10})^2 + D^2} \tag{46}$$

Q_k is defined as the covariance matrix of state disturbance w_k and there is:

$$Q_k = E\left(w_k w_k^T\right) = \sigma_a \begin{bmatrix} T_{KF}^5/20 & T_{KF}^4/8 & T_{KF}^3/6 \\ T_{KF}^4/8 & T_{KF}^3/6 & T_{KF}^2/2 \\ T_{KF}^3/6 & T_{KF}^2/2 & T_{KF} \end{bmatrix} \tag{47}$$

H_k is defined as the Jacobian matrix of $h(x_k)$

$$H_k = \frac{\partial h}{\partial x_k} \tag{48}$$

The steps of the EKF algorithm are given in the following equation:

$$\begin{aligned} \hat{\mathrm{x}}_{k|k-1} &= \Phi_{k,k-1}\hat{\mathrm{x}}_{k-1|k-1} \\ \mathrm{P}_{k|k-1} &= \lambda\Phi_{k,k-1}\mathrm{P}_{k-1|k-1}\Phi_{k,k-1} + \mathrm{Q}_{k-1} \\ \mathrm{K}_k &= \mathrm{P}_{k|k-1}\mathrm{H}_k\left[\mathrm{H}_k\mathrm{P}_{k|k-1}\mathrm{H}_k + \mathrm{R}_k\right]^{-1} \\ \hat{\mathrm{x}}_{k|k} &= \hat{\mathrm{x}}_{k|k-1} + \mathrm{K}_k\left[\mathrm{y}_k - \mathrm{H}_k\hat{\mathrm{x}}_{k|k-1}\right] \\ \mathrm{P}_{k|k} &= [\mathrm{I} - \mathrm{K}_k\mathrm{H}_k]\mathrm{P}_{k|k-1} \end{aligned} \tag{49}$$

In **Eq. 49**, $\hat{x}_{k|k-1}$ is the one-step state prediction; $P_{k|k-1}$ is the error variance of the one-step prediction; K_k is the Kalman filter gain;

$\hat{x}_{k|k}$ is the k-time state estimation; $P_{k|k}$ is the error variance estimation; λ is the forgetting factor which is used to improve the tracking performance of the algorithm; and R_k is the covariance matrix of measurement noise which is defined in **Eq. 50**.

$$R_k = E\left(v_k v_k^T\right) = \begin{bmatrix} r_l & 0 \\ 0 & r_a \end{bmatrix} \tag{50}$$

where, r_l is the measure error variance for the displacement sensor and r_a is the relative acceleration measurement error variance.

The experimental results of the damper piston relative velocity is given in **Figure 10C**. In **Figure 10C**, "TD" represents the result of the tracking differentiator (Wang et al., 2003) and "EKF" represents the result obtained by EKF. The experimental results show that the noise of the damper piston relative speed is smaller and the signal has a good tracking performance. **Figure 10C** shows that, adopting EKF, the relative velocity of the damper piston has smaller noise and a good tracking performance.

EXPERIMENT

Experimental Setup

As it is shown in **Figure 1C**, the experimental setup is mainly composed of DC power, a real-time control system (Speedgoat IO135 with MATLAB/Simulink, Switzerland), a laser Doppler vibrometer (LDV, type: OFV-505/OFV-5000, Polytec, Germany), a vibration test-bed, a scissors-seat with an MR damper, and a coil current driver. As a rapid control prototype, speedgoat is used to collect and store sensor signals, and output the desired current signal of the MR damper. The LDV is used to measure the vibration velocity of the chair surface as a velocity reference to verify the accuracy of the acceleration signal integration. The vibration test-bed is adopted to provide displacement excitation for the seat suspension. The current driver is used to provide controlled current for the coil of the MR damper.

Sinusoidal Input Experiment

The experimental results of sinusoidal displacement excitation are shown in **Figure 11**. Compared with passive suspension, under 2 Hz-sinusoidal displacement excitation, the acceleration RMS of the MR damper seat suspension with different control methods (SH, On-Off, and New-SH) decreased by 11.4%, 12.0%, and 11.2%, respectively. Under 4 Hz-sinusoidal displacement excitation, it decreased by 38.4%, −4.9%, and 41.2%. Under 6 Hz-sinusoidal displacement excitation, it decreased by 43.6%, 8.6%, and 45.8%. Under 8 Hz-sinusoidal displacement excitation, it decreased by 31.2%, 30.1%, and 31.5%.

The expected current of the different control strategies under sine displacement excitation are shown in **Figure 12**. Experimental results show that, compared to traditional skyhook control and on-off skyhook control, the desired current of new skyhook method based on the viscous damping tracking proposed in this paper is relatively smoother and smaller, which can reduce system power consumption to some extent.

Frequency-Sweep Experiment

The 2–40 Hz sine wave sweep excitation put into the seat suspension, and the acceleration transmission rate in frequency-domain are defined as follows:

$$T_{a_2-a_0}(j\omega) = \frac{|\mathcal{F}(a_2)|}{|\mathcal{F}(a_0)|} \tag{51}$$

where, $\mathcal{F}(\cdot)$ is the Fourier transform; a_0 and a_2 are acceleration the stiffness of base and dummy respectively; $T_{a_2-a_0}$ is the acceleration transmissibility.

Figure 13 shows the results of the 2–40 Hz frequency sweep experiment, in which "MRD-0A′ represents the MR damper with a 0 A current and "MRD-1A′ represents the MR damper with a 1A current. It can be seen from the **Figure 13** that, compared with passive suspension, the seat suspension with the MR damper has good vibration isolation performance at different frequencies.

CONCLUSION

In this work, a low-cost 3-sensor seat suspension structure with an MR damper was established, in which a digital integrator and an extended Kalman filter were adopted to enhance the signal quality in signal processing. A unified-format model for the MR damper and a viscous damping tracking model based on the Bingham model were proposed. Simulation results show that, compared to traditional skyhook control and on-off control, the new SH control with viscous damping tracking had a good performance in reducing acceleration jerk and smoothing the expected current output. However, in the experiment, the vibration isolation effect of "SH" and "New SH" was similar, and the difference between them was that the output current of "New SH" was small and smooth, which reduced the power consumption of the system to a certain extent.

DATA AVAILABILITY STATEMENT

The original contributions presented in the study are included in the article/supplementary material, further inquiries can be directed to the corresponding author/s.

AUTHOR CONTRIBUTIONS

As the first author of this paper, HZ have completed most of the work in this paper. XR, WZ, and JG funded this paper. FY assist to complete the experiment.

ACKNOWLEDGMENTS

The authors wish to acknowledge the financial support of the National Natural Science Foundation of China (Grant No. 51975298), the National Natural Science Foundation of China (Grant No. 11902158), the Natural Science Foundation of Jiangsu Province, China (Grant No. BK20181301), and the Fundamental Research Funds for the Central Universities (No. 30919011240).

REFERENCES

Bahar, A., Pozo, F., Acho, L., Rodellar, J., and Barbat, A. (2009). Parameter identification of large-scale magnetorheological dampers in a benchmark building. *Comput. Struct.* 88, 198–206. doi:10.1016/j.compstruc.2009.10.002

Bai, X. X., Jiang, P., Pan, H., and Qian, L. J. (2016). "Analysis and testing of an integrated semi-active seat suspension for both longitudinal and vertical vibration control," in *Active and passive smart structures and integrated systems 2016*. International Society for Optics and Photonics, Vol. 9799, 979921.

Bai, X.-X., Jiang, P., and Qian, L.-J. (2017). Integrated semi-active seat suspension for both longitudinal and vertical vibration isolation. *J. Intell. Mater. Syst. Struct.* 28(8), 1036-1049. doi:10.1177/1045389X16666179

Bhowmik, S., Høgsberg, J. B., and Weber, F. (2010). "Neural network modeling of forward and inverse behavior of rotary MR damper," in Proceedings of NSCM-23. The 23rd Nordic seminar on computational mechanics, Stockholm, Sweden, October 21–22, 2010. Editor A. Eriksson and G. Tibert (The Royal Institute of Technology), 169–172.

Choi, S.-B., and Han, Y.-M. (2007). Vibration control of electrorheological seat suspension with human-body model using sliding mode control, *J. Sound Vib.* 303, 391–404. doi:10.1016/j.jsv.2007.01.027.

Choi, S. B., Li, W., Yu, M., Du, H., and Do, P. X. (2016). State of the art of control schemes for smart systems featuring magneto-rheological materials. *Smart Mater. Struct.* 25, 043001. doi:10.1088/0964-1726/25/4/043001.

Dahl, P. R. (1976). Solid friction damping of mechanical vibrations. *AIAA J.* 14, 1675–1682. doi:10.2514/3.61511.

Fusi, L., Farina, A., and Rosso, F. (2014). Retrieving the Bingham model from a bi-viscous model: some explanatory remarks, *Appl. Math. Lett.* 27, 11–14. doi:10.1016/j.aml.2013.08.009.

Gao, M., and Wang, C. Z. (2008). Inverse modelling of MR damper based on ANFIS technique and its application. *J. Vib. Shock* 27(3), 140–141. doi:10.3901/CJME.2008.04.040

Hatwalane, S. (2016). "Review of driver seat suspension using MR fluid damper," in AMET-2016 (Pune, India: MIT College of Engineering). doi:10.14741/Ijcet/22774106/Spl.4.2016.66

Ikhouane, F. A., and Rodellar, J. (2005). On the hysteretic bouc-wen model. *Nonlinear Dynam.* 42, 79–95. doi:10.1007/s11071-005-0070-x.

Karamodin, A., Kazemi, H. H., Rowhanimanesh, A., Totonchi, A., and Reza, H. (2007). Semiactive control of structures using neuro-inverse mode of MR dampers. *Scientia Iranica*, 16(3). doi:10.1243/09544097JRRT240

Lee, Y., and Jeon, D. (2002). A study on the vibration attenuation of a driver seat using an MR fluid damper, *J. Intell. Mater. Syst. Struct.* 13, 437–441. doi:10.1106/104538902028606.

Nishiyama, H., Fushimi, S., and Nakano, M. (2002). Numerical simulation of MR fluid damping characteristics using a modified Bingham model. *J. Intell. Mater. Syst. Struct.* 13, 647–653. doi:10.1177/1045389x02013010007.

Phu, D. X., Quoc Hung, N., and Choi, S.-B. (2017). A novel adaptive controller featuring inversely fuzzified values with application to vibration control of magneto-rheological seat suspension system. *J. Vib. Contr.* 24(21), 5000-5018. doi:10.1177/1077546317740479.

Phu, D. X., Hung Nguyen, Q., and Choi, S.-B. (2019). New hybrid optimal controller applied to a vibration control system subjected to severe disturbances, *Mech. Syst. Signal Process.* 124, 408–423. doi:10.1016/j.ymssp.2019.01.036.

Rabinow, J. (1951). The magnetic fluid clutch. *J. Inst. Electr. Eng.* 1952, 33–34. doi:10.1049/jiee-2.1952.0007

Rodríguez, A., Iwata, N., Ikhouane, F., and Rodellar, J. (2009). Model identification of a large-scale magnetorheological fluid damper, *Smart Mater. Struct.* 18, 015010. doi:10.1088/0964-1726/18/1/015010.

Spencer, B. F., Dyke, S. J., Sain, M. K., and Carlson, J. D. (1997). Phenomenological model for magnetorheological dampers, *J. Eng. Mech.* 123, 230–238. doi:10.1061/(asce)0733-9399(1997)123:3(230).

Sun, Y., Thomas, M., and Masounave, J. (2010). A quasi-Bingham model for predicting electrorheological fluid behaviour, *Multidiscip. Model. Mater. Struct.* 6, 141–165. doi:10.1108/15736101011055301.

Tsang, H. H., Su, R. K. L., and Chandler, A. M. (2006). Simplified inverse dynamics models for MR fluid dampers. *Eng. Struct.* 28, 327–341. doi:10.1016/j.engstruct.2005.06.013.

Wang, X., Chen, Z., and Yuan, Z. (2003). Design and analysis for new discrete tracking-differentiators. *Appl. Math. Chin. Univ.* 18, 214–222. doi:10.1007/s11766-003-0027-0.

Xia, P.-Q. (2003). An inverse model of MR damper using optimal neural network and system identification. *J. Sound Vib.* 266, 1009–1023. doi:10.1016/s0022-460x(02)01408-6.

Xuan, P. D., An, J. H., and Seung-Bok, C. (2017). A novel adaptive PID controller with application to vibration control of a semi-active vehicle seat suspension. *Appl. Sci.* 7, 1055. doi:10.3390/app7101055

Yao, H. J., Fu, J., Yu, M., and Peng, Y. X. (2013). Semi-active control of seat suspension with MR damper. *J. Phys. Conf. Ser.* 412, 012054. doi:10.1088/1742-6596/412/1/012054

Zhu, H., Rui, X., Yang, F., Zhu, W., and Wei, M. (2019). An efficient parameters identification method of normalized Bouc-Wen model for MR damper. *J. Sound Vib.* 448, 146–158. doi:10.1016/j.jsv.2019.02.019

Conflict of Interest: The authors declare that the research was conducted in the absence of any commercial or financial relationships that could be construed as a potential conflict of interest.

frontiers in Materials

ORIGINAL RESEARCH
published: 18 December 2020
doi: 10.3389/fmats.2020.595100

Fabrication and Characterisation of Magnetorheological Shear Thickening Fluids

Vladimir Sokolovski[1], *Tongfei Tian*[2]*, *Jie Ding*[3]* and *Weihua Li*[1]

[1]School of Mechanical, Materials, Mechatronic and Biomedical Engineering, University of Wollongong, Wollongong, NSW, Australia, [2]School of Science, Technology and Engineering, University of the Sunshine Coast, Sippy Downs, QLD, Australia, [3]Defence Science and Technology Group, Port Melbourne, VIC, Australia

In this article, a magnetorheological shear thickening fluid (MRSTF) was fabricated based on magnetorheological (MR) material and shear thickening fluid (STF). The STF was firstly fabricated as the liquid phase, and carbonyl iron particles were then mixed with the prefabricated STF to synthesise a series of MRSTFs with various iron concentrations. Then, a rheometer was used to measure their viscosities by varying the shear rate under various magnetic fields. Both static and dynamic tests were conducted to study the rheology of MRSTFs under different magnetic fields. The tested results revealed that the MRSTF showed shear thickening under zero magnetic field and MR effect with increasing applied magnetic field. It was also noted that the viscosity of the MRSTFs can be controlled by both shear rate and the applied magnetic field. The concentration of iron particles played an important role in the MRSTFs' rheological properties. The MRSTFs with higher iron particle concentrations revealed lower shear thickening effects but higher MR effects, which means the MRSTF with higher iron concentration can be treated as an effective MR fluid. Meanwhile, the MRSTF with low iron concentration displays good shear thickening effect under weak magnetic field. To summarise the behavior of MRSTFs with various iron concentrations and under different magnetic fields, three regions were proposed to provide guidelines to design MRSTFs and assist in their applications.

Keywords: magnetorheological, shear thickening, fabrication, viscosity, storage modulus, loss modulus

OPEN ACCESS

Edited by:
Janusz Goldasz,
Cracow University of Technology, Poland

Reviewed by:
JinHyeong Yoo,
Naval Surface Warfare Center, United States
Jiong Wang,
Nanjing University of Science and Technology, China

***Correspondence:**
Tongfei Tian
ttian@usc.edu.an
Jie Ding
jie.ding@dst.defence.gov.au

Specialty section:
This article was submitted to Smart Materials, a section of the journal Frontiers in Materials

Received: *15 August 2020*
Accepted: *28 October 2020*
Published: *18 December 2020*

Citation:
Sokolovski V, Tian T, Ding J and Li W (2020) Fabrication and Characterisation of Magnetorheological Shear Thickening Fluids. Front. Mater. 7:595100. doi: 10.3389/fmats.2020.595100

INTRODUCTION

Smart materials and structures have taken a central role in many recent developments of the intelligent materials around the world because of their highly functional and changeable properties in relative applications. The merits of these new intelligent materials include offering optimized performance of existing engineering products, as well as offering new solutions with improved and more robust capabilities (Tian, 2014; Peters et al., 2016; Majumdar et al., 2017). They can be adopted to various client needs in practical structures like sensors and actuators in many engineering, automotive, aerospace, and military applications. Consequently, the field of intelligent materials research has attracted a large number of researchers and significant financial investments in development of new materials designed to enhance and improve every aspect of today's living (Ding et al., 2013; Chen et al., 2017; Avila et al., 2018).

Magnetorheological fluid (MRF) is a type of smart material which consists of ferro particles, carrier fluid, and additives. When the MRF is subjected to a magnetic field, the fluid greatly increases

its apparent viscosity, to the point of becoming a viscoelastic solid. Typical choices of carrier fluid include minerals like silicone oils, polyesters, polyether, synthetic hydrocarbons, and water. MRFs also contain micro-sized ferro magnetic particles which play a key role in the change of their viscosity under applied magnetic field. With no magnetic field present, particles do not exhibit specific orientation and distribute randomly in the carrier fluid, so the apparent viscosity of the fluid remains at low values. When a magnetic field is applied, the particles start to become magnetized and attract each other along the direction of the magnetic flux density forming a gap spanning anisotropic chain-like structure. Eventually, the field-affected fluid will transform into semi-solid state with a large dynamic yield stress of several orders of magnitudes higher than that at zero magnetic field condition, which signals the minimum requirement to make the suspension flow. Generally speaking, good MRFs should exhibit sound saturation magnetization, small coercivity/remnant magnetization, effective MR effect over a wide range of temperature variation, and stability against flocculation and chemical oxidation. The most referred engineering applications of MRFs are MR dampers, which are used in vehicle suspension, civil buildings, and shock absorbers (Dong et al., 2016; Chen and Chen, 2020; Hou and Liu, 2020; Hua et al., 2020).

Shear thickening fluid (STF) is a type of non-Newtonian fluid whose viscosity dramatically increases when it experiences a sudden strike or impact. A common example of STF is a mixture of corn starch and water. It is widely known that a person does not sink into this kind of solution if they run over on it. But they can sink if they stand still or walk over it. STFs are usually made from nanoparticles and carrier liquid. When the shear stress or shear rate is applied, hydroclusters will be formed from the nanoparticles because of collisions with other neighboring nanoparticles, which produces a rapid rise in viscosity. The nanoparticles will even lock together and harden when rapidly struck if the shear stress or shear rate is high enough, and the STF will behave like in a solid state. When the stress is removed or if the shear rate decreases, the material returns to its original fluid-like state (Cossa, 2019).

Because of the unique properties of STFs, they have gained enormous attention around the world, and significant amount of research has been investigated for their applications. Their behavior change has found lots of industrial and commercial applications like dampers, personal protective equipment, and even more in prosthetic limb replacement materials. In the past decade, STFs made from silica nanoparticles loaded in carrier fluids, such as polyethylene glycol, and impregnated in a fabric, have gained attention by military and law enforcement agencies to have potential for usage in liquid body armour and bulletproof vests. The most common application focuses on impregnating Kevlar fabrics with STFs in order to improve its stab resistance and to reduce the number of layers required for maximum penetration resistance (Li et al., 2008; Petel et al., 2015; Wagner and Wetzel, 2007; Grover et al., 2020). STFs can also be used in smart structures due to their unique shear thickening properties (Zhou et al., 2016).

In combining both MRF and STF, novel magnetorheological shear thickening fluid (MRSTF) can be achieved. Zhang et al. (2008) firstly synthesized MRSTF from iron particles and STF at the weight ratios of 5:100, 10:100, 50:100, and 200:100. Then, they investigated the thixotrope of MRSTFs (Zhang et al., 2010). Yang et al. (2015) developed and tested a linear damper working with two MRSTFs which contained 20 and 80% weight fractions of iron particles, respectively. Their results showed the damper with 20% iron displaying both MR effect and shear thickening effect, while the damper with 80% iron worked more like a conventional MR fluid-filled damper, because its shear thickening effect is restrained and the MR effect becomes more obvious with higher iron volume.

In this study, we investigate rheological properties of STFs and MRSTFs, in an effort to present a guideline of three regions of MRSTFs' behavior to apply this novel smart material, which can provide an improved impact performance and dependencies of the MR effect when an external magnetic field is applied. The MRSTFs were fabricated with mixing already prepared STF and carbonyl iron particles. Their dependencies of viscosity/complex viscosity/storage modulus/loss modulus on shear rate and frequency, exposed to various magnetic fields, were tested. The effects of iron particle concentration, magnetic field, and shear rate on rheological properties of the MRSTF were discussed. In order to achieve this again, both steady state and oscillatory tests were conducted. The main objective and motivation of this study was an attempt to first assess the performance of the already developed materials and to try to find ways on how to improve them, and at the same time, researching new techniques that could be of a great importance in various applications. The results of this work, we believe, will create valuable foundation groundwork in determining selection of input materials and quantities to conform with the application requirements, particularly in future improvements in performance and mechanical protection for the applications of MRSTFs (Ding et al., 2011).

MATERIALS AND EXPERIMENTS

Materials and Fabrications

The STF was the base material for MRSTF, and its nano-particles were fumed silica (S5505; Sigma-Aldrich, Germany) with 14 nm primary particles size, 200–300 nm of aggregation size, and a surface area of approximately 200 m^2/g. The carrier fluid was ethylene glycol (102466; Sigma-Aldrich, Germany) with a density of 1.113 g/ml. Compared with the STF made of corn starch and water, the STF made of ethylene glycol and fumed silica has less sedimentation and is more stable (White et al., 2010).

Before the fabrication of STF, fumed silica was put in a beaker and dried in a vacuum oven at a temperature of 100°C for 10 h to evaporate all the moisture out of the material. Then, the carrier fluid was mixed with fumed silica at the weight ratio 3:1, and a blender was employed to mechanically stir the two components until a liquid compound was achieved. Finally, the resulting suspensions were placed in a vacuum chamber for 30 min to eliminate involved air bubbles, and the STF was achieved.

Carbonyl iron particles (C3518; Sigma Aldrich, Germany) were chosen as the ferro particles for the MRSTFs, which have 5 μm particle size and 7.86 g/cm^3 density. The carrier phase was the pre-fabricated STF with 25 wt% fumed silica. For fabrication of MRSTFs, the carbonyl iron particles were mixed with the STF

TABLE 1 | Concentration of the components in MRSTFs.

MRSTF	Ethylene glycol [g]	Fumed silica [g]	Carbonyl iron [g]	Weight fraction of iron (%)
0% Fe	75	25	0	0
5% Fe	75	25	5.26	5
10% Fe	75	25	11.11	10
15% Fe	75	25	17.65	15

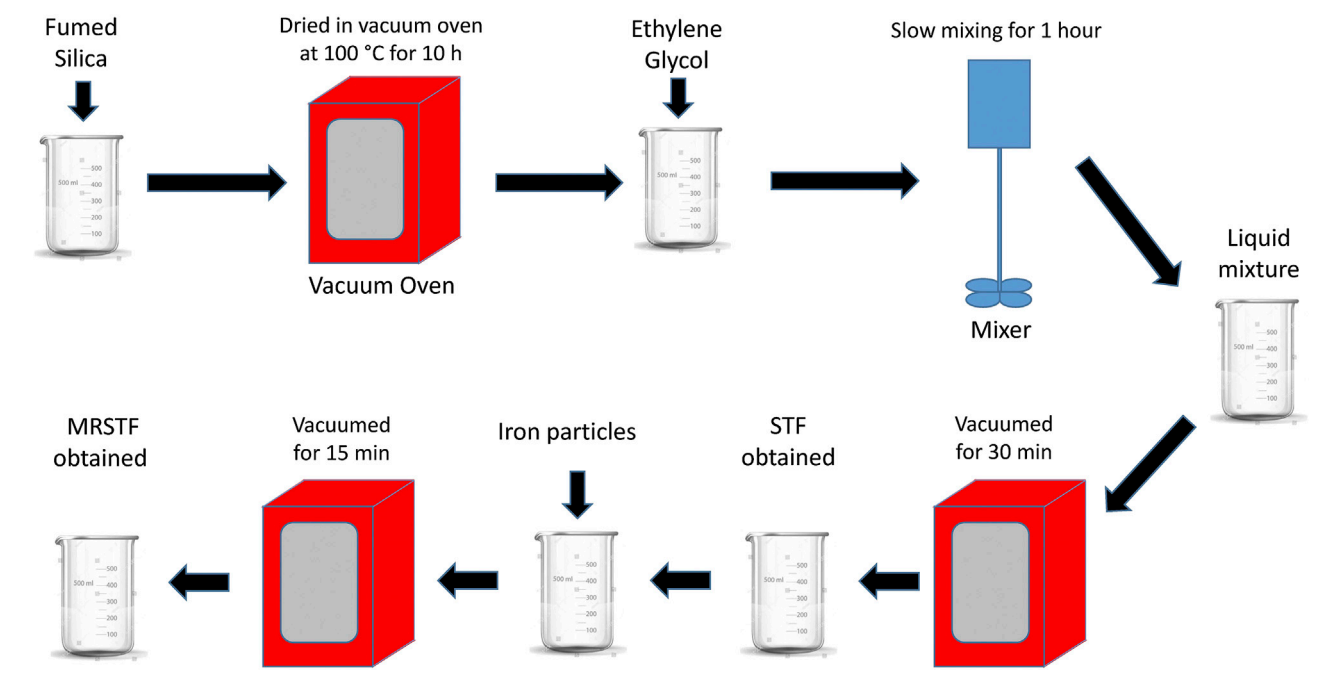

FIGURE 1 | Diagram of fabrication process for STF and MRSTF.

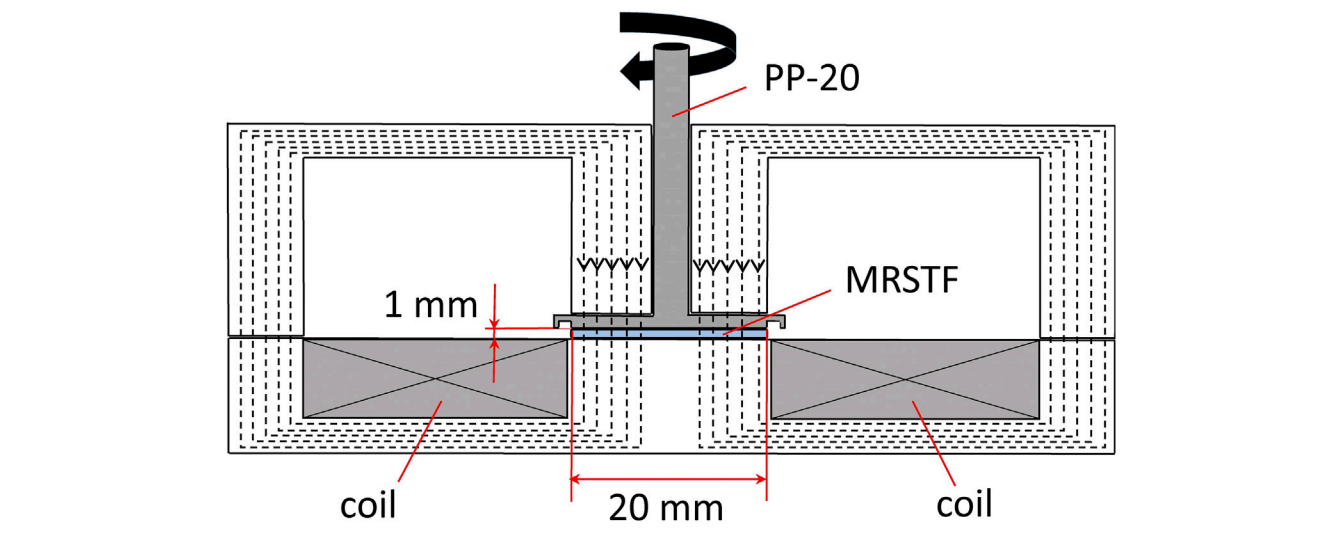

FIGURE 2 | Experimental setup of the magnetic field application device used to apply magnetic field and measure MR effects of the MRSTF samples.

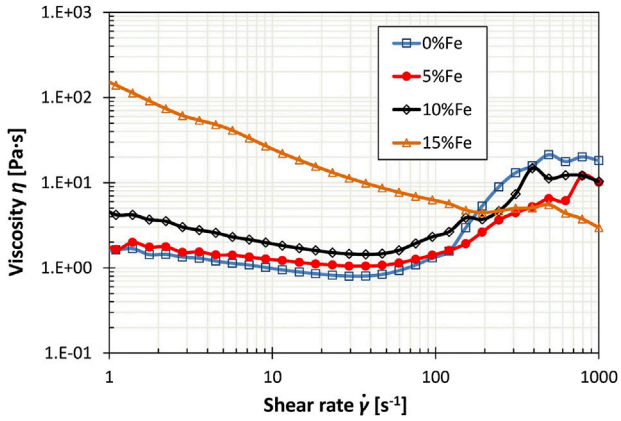

FIGURE 3 | Viscosity versus shear rate for MRSTFs with different iron concentrations.

at a specific weight ratio, which is summarized in **Table 1**. After 15 min in a vacuum chamber to get rid of air bubbles, the MRSTF was obtained. **Figure 1** shows the manufacturing process for both base STF and MRSTFs.

Measurements

A rotating rheometer (MCR 301, Anton Paar, Germany) was used to measure the rheological properties of the MRSTFs, and a temperature control device (Viscotherm VT2, Anton Paar, Germany) was used to ensure the measuring temperature at 25°C. A flat measuring geometry (PP-20, Anton Paar, Germany) with 20 mm diameter was used for the rheological testing. Measuring gap of the test was 1 mm. When testing MRSTFs' MR properties with the rheometer, a magnetic induction accessory (MRD180; Anton Paar, Germany) was used to introduce and control the magnetic fields at 0, 110, 220, 330, and 440 mTesla. **Figure 2** shows how the magnetic field is generated and applied to the MRSTF samples in the measurements. The measured data were collected using a rheometer and simultaneously transferred to the PC. A software Rheoplus was used to view the data in the PC screen.

Three types of tests were performed to assess rheological properties of the STF and MRSTF samples, including 1) steady-state test, 2) dynamic oscillatory amplitude sweep test, and 3) dynamic oscillatory frequency sweep test. In a steady-state test, the specimen was rotated isothermally by varying the shear rate from 0.1 to 1,000 s^{-1}, and the viscosity of the sample was measured using the rheometer. For both dynamic oscillatory tests, the specimen was oscillated with controlling the input shear strain amplitude and frequency; meanwhile, the storage and loss moduli and complex viscosity of the specimen were measured. The storage modulus G' represents the elastic property of the viscoelastic behavior of MRSTFs, in which quasi describes the solid-state behavior of the sample. The loss modulus G" characterizes the viscous portion of the viscoelastic behavior, which can be seen as the liquid-state behavior of the sample. The complex viscosity η^* represents the frequency-dependent viscosity function determined for a viscoelastic fluid by subjecting it to oscillatory shear stress (Han et al., 2016). In the dynamics oscillatory amplitude sweep test, the shear strain amplitude was increased stepwise from 0.01% to 100% while the frequency was maintained at a constant value of 1 Hz. This kind of test was used to describe the behavior of the specimen, by which we can obtain the specimen's limit of the linear viscoelastic region (LVE) as well as its viscoelastic character. In the dynamic oscillatory frequency sweep test, the applied frequency increased stepwise from 0.1 to 100 Hz while keeping the shear strain amplitude constant at 1%. The frequency sweep was generally used to describe the behavior of the samples at slow changes of stress as well as time-dependent behavior of a sample in the nondestructive deformation range.

All experimental data were collected using the sensors embedded in the rheometer and transferred simultaneously to a PC, in which the software Rheoplus was used to display the data in both curves and tables. All data were exported from the tables in Rheoplus into Excel and plotted.

TABLE 2 | Table representing the ratio between maximum viscosity vs critical viscosity for different concentrations of Fe particles.

MRSTF	Viscosity at the critical shear rate η_c	Maximum viscosity η_{max}	Shear thickening effect η_{max/η_c}
0% Fe	0.80	20.1	25.13
5% Fe	1.05	12.1	11.52
10% Fe	1.44	12.2	8.47
15% Fe	13.35	16.5	1.24

RESULTS AND ANALYSIS

Steady-State Test

The steady-state test for all MRSTFs was performed where MRSTF samples were rotated isothermally by varying the shear rate from 0.1 to 1,000 s^{-1}. **Figure 3** represents the rheological property of all four MRSTFs at 25°C. It can be observed that for 0% Fe shear rate increase from 1 s^{-1} to the critical shear rate $\dot{\gamma}_c$ (around 30 s^{-1}), a shear thinning behavior is observed, with a local minimum viscosity of η_c = 0.8 Pa·s. When shear rate increases from critical shear rate to the maximum shear rate $\dot{\gamma}_{max}$ (around 600 s^{-1}), a shear thickening effect is observed with a maximum viscosity of η_{max} = 20.1 Pa·s. The shear thickening effect of the STF is defined as a ratio between of the maximum viscosity over the viscosity at the critical shear rate η_{max}/η_c = 25.13. With the increase of the iron concentration in MRSTF, the viscosity of MRSTF increases. Meanwhile, the local minimum viscosity of the MRSTF increases, which decreases the shear thickening effect. **Table 2** represents the shear thickening effect of all MRSTFs depending on the iron concentration.

Figure 4 shows the viscosity of 15% Fe versus shear rate under different magnetic fields. It is obvious to see that with the increase of applied magnetic flux density, the viscosity of the sample increases, which is the evidence of the magnetorheological (MR) effect. It is also noted that this MRSTF sample shows a clear shear

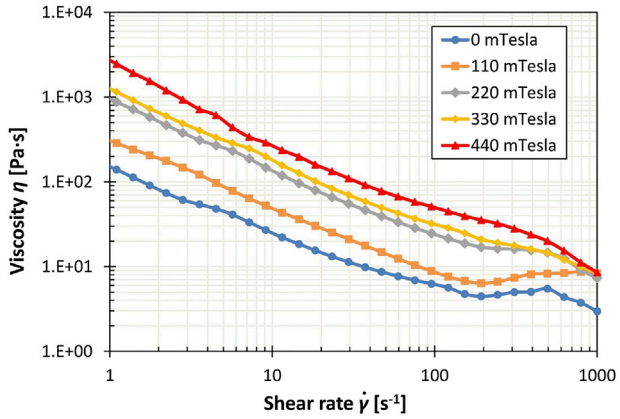

FIGURE 4 | Viscosity of 15% Fe MRSTF as a function of shear rate under different magnetic fields.

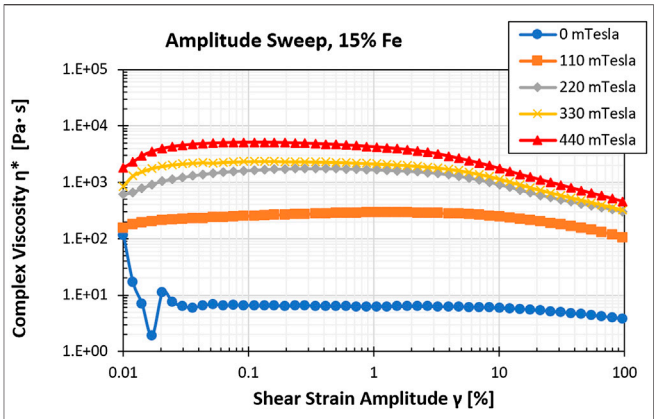

FIGURE 6 | Complex viscosity η^* of 15% Fe as a function of shear strain amplitude γ under different magnetic fields.

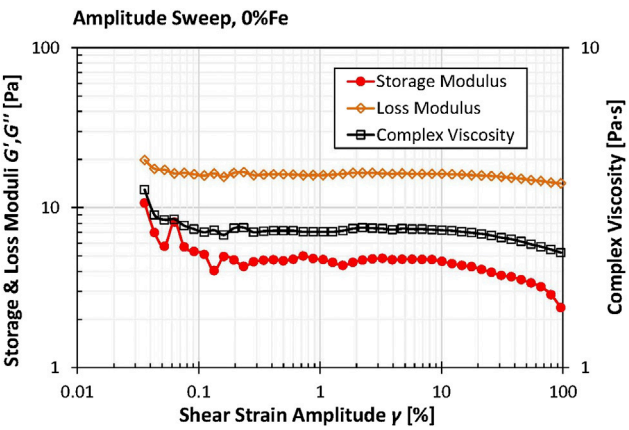

FIGURE 5 | Storage and loss moduli and complex viscosity versus shear strain amplitude for 0% Fe.

thickening effect without magnetic field, and the shear thickening performance gets weaker when the applied magnetic field is stronger. At 330 and 440 mTesla, the shear thickening effect was not able to be observed as the viscosity of the sample is dominated by the magnetic field. Similar trends have been observed in the MRSTF with 5% Fe and 10% Fe.

Dynamic Oscillatory Amplitude Sweep Test

Dynamic oscillatory amplitude sweep tests were performed where sinusoidal strain amplitude was applied from the range of 0.01 to 100%, while keeping the frequency constant at 1 Hz, at the constant room temperature of 25°C. **Figure 5** shows the storage and loss moduli and complex viscosity versus shear strain amplitude for 0% Fe without magnetic field, which is the base STF without iron particles.

Figure 5 shows that the storage modulus of 0% Fe does not change too much within 10% shear strain amplitude, which indicates that the limit of linear viscoelastic range for the 0% Fe is 10% shear strain amplitude. The loss modulus and complex viscosity of 0% Fe both stay steady within 20% shear strain amplitude and then slightly decrease with the amplitude increases. The loss modulus of 0% Fe is greater than its storage modulus in the amplitude sweep test, which means the 0% Fe shows a liquid state in this test.

The magnitudes of the magnetic field used in the tests were 0, 110, 220, 330, and 440 mTesla. **Figure 6** shows how the complex viscosity of 15% Fe changes with increasing shear strain amplitude under different magnetic fields.

We can clearly see how complex viscosity increases when stronger magnetic field is applied, which proves the strong MR effect of 15% Fe. This trend has been observed for all three MRSTFs. It is also noted that the under each magnetic field, complex viscosity increases when strain amplitude starts from 0.01% and reaches a plateau value, after which it started to decrease and reached its minimum value when the strain amplitude range approaches 100%.

Figures 7 shows storage and loss moduli of 15% Fe as a function of shear strain amplitude for the range from 0.01 to 100%, respectively. It is evident that each time a stronger magnetic field is applied, both storage and loss moduli increase. This proves the MR effect of MRSTF again. When the applied magnetic field increases from 330 to 440 mTesla, the increase of moduli is relatively smaller than the increase at lower magnetic field, which is due to the saturation of the MRSTFs. For each curve of the storage modulus versus shear strain amplitude, the storage modulus shows a linear range at lower strain amplitudes and decreases after a critical value of the shear strain amplitudes is reached. It is observed that the linear range of storage modulus decreases at a stronger magnetic field. The samples 5% Fe and 10% Fe also had trends similar to the 15% Fe sample.

Dynamic Frequency Oscillation Sweep Testing

Dynamic oscillatory frequency sweep tests were performed where shear strain amplitude was kept constant at 1%, while varying the frequency from 0.1 to 100 Hz, at a constant room temperature of 25°C. In this frequency sweep test, storage and loss moduli and

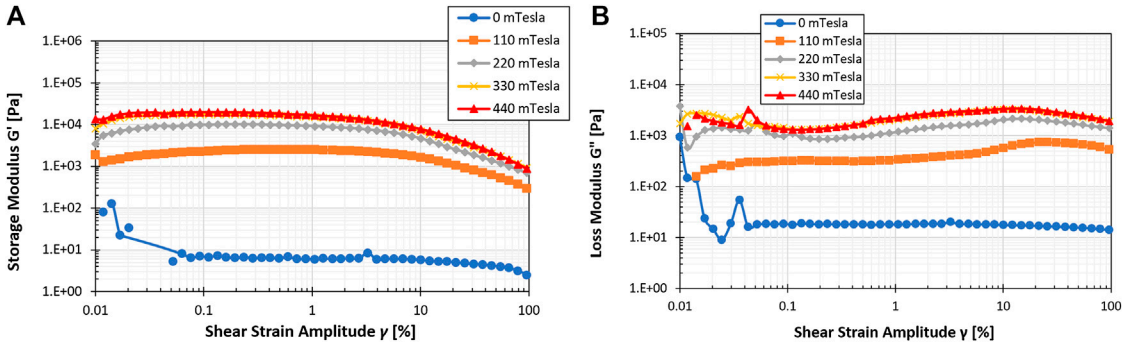

FIGURE 7 | Storage and loss moduli of 15% Fe as functions of shear strain amplitude under different magnetic fields.

the complex viscosity were measured under different magnetic fields of 0, 110, 220, 330, and 440 mTesla. The complex viscosity of 15% Fe versus frequency under different magnetic fields is shown in **Figure 8**.

With the increase of applied magnetic field, the complex viscosity of 15% Fe has higher values, which is the MR effect due to the iron particles. It is also noted that without magnetic field (0 mTesla), the complex viscosity has an increase region which is between two decrease regions. The increase of complex viscosity is from the base STF which is the evidence of the shear thickening effect. However, when the applied magnetic field gets stronger, the shear thickening effect is weaker and the complex viscosity mainly shows a decrease trend with increase in the frequency. The reason of this phenomenon is the iron particles in MRSTF, which influence the formation of hydro-clusters causing the shear thickening. Consequently, the MRSTF behave more like an MRF when the applied magnetic field is high enough.

Storage and loss modulus were also analysed in the frequency sweep tests, and they are summarized in **Figure 9**.

Figure 9 shows the storage and loss moduli as functions of frequency for the 15% Fe under different magnetic fields. Again, it is evident from the MR effect that each time a stronger magnetic field is applied, the storage and loss moduli both increase. When the applied magnetic field increases from 220 to 440 mTesla, the increment is smaller than that with lower magnetic field.

In **Figure 9a**, it is noted that for each curve, the storage modulus increases with the applied frequency, and the increase trend is stronger at lower magnetic field than the higher magnetic field. In **Figure 9b**, the loss modulus of 15% Fe shows an increase without magnetic field, and it mostly remains constant under an applied magnetic field, which means that the iron particles in MRSTF are greatly affected by the magnetic field. For 5% Fe and 10% Fe, trends were observed to be similar to the 15% Fe.

Comparison Among the Magnetorheological Shear Thickening Fluids

For the steady-state tests performed on the MRSTF with 15% iron content displayed in **Figure 4**, where viscosity is observed as a function of shear rate and different magnetic fields, it can be

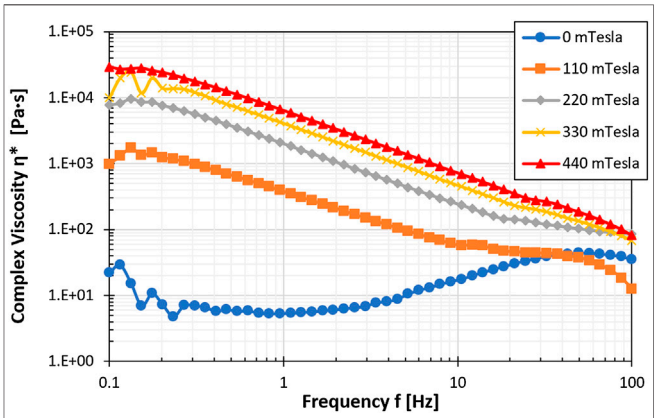

FIGURE 8 | Complex viscosity η^* as a function of frequency under different magnetic fields.

concluded that the increase of iron particle concentration and magnetic field obviously restrain the shear thickening phenomenon. The shear thickening can only be observed at a higher shear rate and zero magnetic field (0 mTesla) or very low magnetic field (110 mTesla). Obviously, with the increase in the magnetic field, the MR effect improved but shear thickening cannot be observed in experiments because of the high concentration of iron particle. When the magnetic field is greater than 220 mTesla, the 15% Fe shows an obvious shear thinning behavior and the viscosity increased with magnetic field strength as expected, i.e., it shows the MR effect like conventional MR fluids.

The shear thickening performance η_{max/η_c} was only recorded for 0 and 110 mTesla in the amounts of: 8/0.928 = 8.62 and 9/6 = 1.5. This proves that the high micron-particle-based MRSTFs have similar behavior to conventional MR fluids.

To assess the magnetorheological and shear thickening behavior of MRSTF, the following graphs are collated to compare the storage and loss moduli as functions of strain amplitude and frequency for all MRSTFs with different iron concentrations.

Figures 10 and **11** compare the storage and loss moduli of all four MRSTFs in shear strain sweep tests and frequency sweep at the magnetic field of 440 mTesla, respectively.

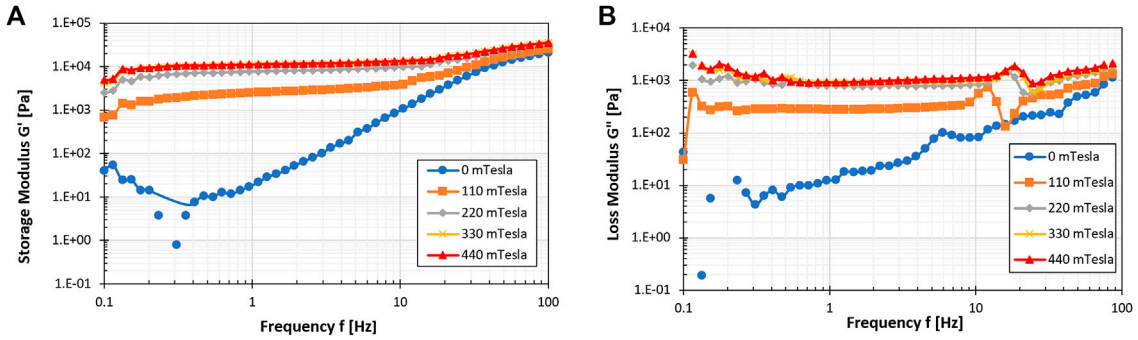

FIGURE 9 | Storage and loss moduli of 15% Fe as functions of frequency for different magnetic fields.

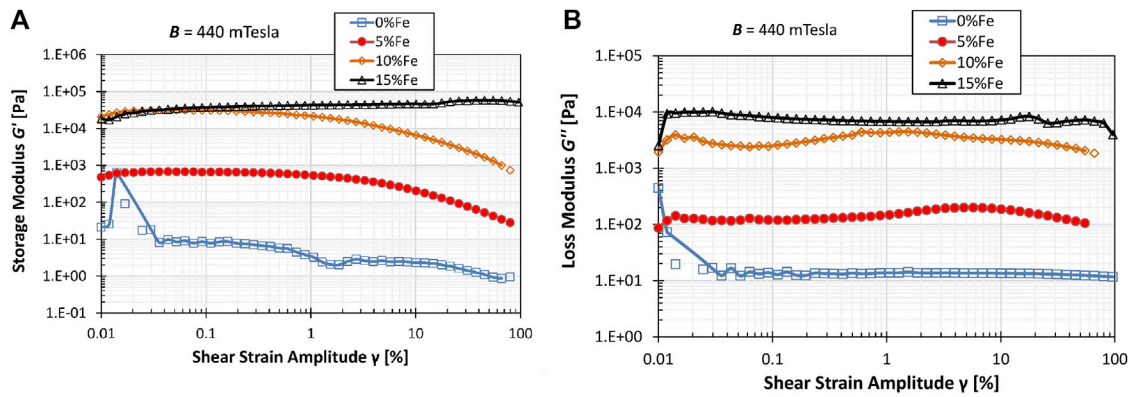

FIGURE 10 | Comparison among all MRSTFs in shear strain sweep tests. **(A)** Storage modulus ***G′*** versus shear strain amplitude; **(B)** loss modulus ***G″*** versus shear strain amplitude.

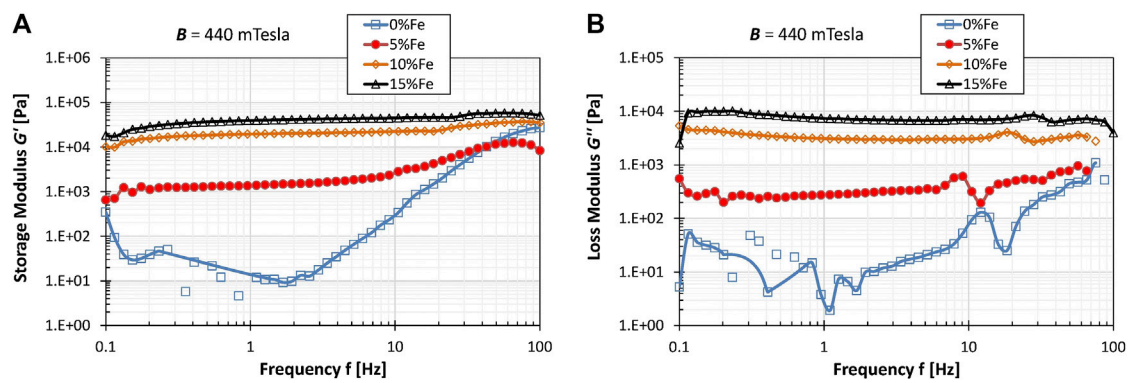

FIGURE 11 | Comparison among all MRSTFs in frequency sweep tests. **(A)** Storage modulus ***G′*** versus frequency; **(B)** loss modulus ***G″*** versus frequency.

In **Figures 10** and **11**, at 440 mTesla magnetic field, the MRSTF with higher iron concentration show higher storage and loss moduli, which is due to the contribution of iron in MRSTFs. As shown in **Figure 11**, it is noted that in frequency sweep at 440 mTesla, the storage modulus of all MRSTFs has an increase trend and the sample with lower iron concentration has a larger increase. For loss modulus, the graphs for 0% Fe and 5% Fe show an increase after the 1 Hz frequency, and the increase is weaker in the sample with 5% Fe. With the higher iron centration, the 10% Fe and 15% Fe do not show any increase in loss modulus. At other magnetic fields, the comparisons among all samples also have similar trends.

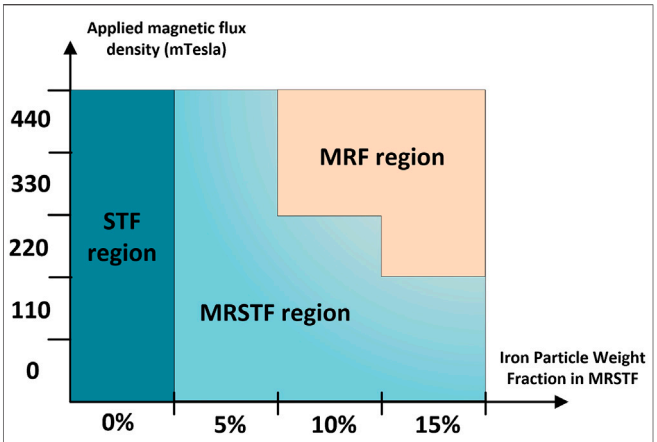

FIGURE 12 | Correlation between iron particle weight fraction and applied magnetic flux density.

Figure 12 summarizes and presents the behavior of MRSTF with various iron particles at different weight concentrations (0, 5, 10, and 15%) and under different magnetic flex densities (0, 110, 220, 330, and 440 mTesla).

For the MRSTFs, they can behave in three different regions, namely, STF region, MRSTF region and MRF region. In STF region, it only shows shear thickening effect and the MR effect does not exist. It can be clearly observed that the MRSTF with zero iron content is in the STF region. With the increase of iron concentration in MRSTFs, they experience both shear thickening phenomenon and MR effect when neither of the iron concentration nor applied magnetic field has high values. It is worthy to state that with the increase of either iron centration or applied magnetic field, the MRSTFs behave closer to the MRF and show lower shear thickening effect. In the MRSTF region, the MRSTFs can be controlled by both magnetic field and applied shear rate. When both the iron concentration and the magnetic field reach high values, the MRSTF behave in the MRF region, where the shear thickening effect diminishes with only presence of MR effect, so the viscosity of the fluids depends purely on the strength of the applied magnetic field.

It can be predicted that for the MRSTF with the iron concentration higher than 15wt%, the boundary of MRF region and MRSTF region will be at lower magnetic field than the 15% Fe MRSTF. Similarly, if the 5% Fe MRSTF is under the magnetic field much stronger than 440 mTesla, the transition from the MRSTF region to the MRF region will occur. The three regions can be used as a guideline on the design of MRSTF, which will benefit the applications of MRSTF as well.

CONCLUSION

In this study, the MRSTFs with different iron concentrations were fabricated from the base STF, and their rheological properties were measured with a rheometer in different types of tests. The results show that both storage and loss moduli of MRSTFs correlate and increase each time when stronger magnetic field is applied. This proves the MR effect of MRSTF. The experimental results also show that when the applied magnetic field was not strong enough, the shear thickening effect can be observed in the MRSTFs. With the flux density of the applied magnetic field raised, the MRSTF behaved with a clear MR effect. It means the viscosity of the MRSTFs can be controlled by both magnetic field and shear rate. The concentration of iron particles also played an important role in the rheological properties of MRSTFs. The sample with higher iron particle concentration showed a lower shear thickening effect but higher MR effect, which means the MRSTF with higher iron concentration can be treated as an effective MR fluid. Meanwhile, the MRSTF with low iron concentration can show good shear thickening effect under weak magnetic field. In strain amplitude sweep tests, when strain amplitude further increases past the critical rate, a slight decrease in both storage and loss moduli was observed. For the oscillatory frequency tests, similar increases in storage and loss moduli were observed, with the increase in magnetic fields. For the frequency increase beyond the critical frequency, slight increases of both moduli were recorded. Three regions of the MRSTF's behavior were proposed to provide the guideline to design the MRSTFs and contribute to their applications.

DATA AVAILABILITY STATEMENT

The raw data supporting the conclusions of this article will be made available by the authors, without undue reservation.

AUTHOR CONTRIBUTIONS

TT, JD, and WL designed the experiments. VS fabricated the MRSTF, conducted the measurements, and analysed the experimental data. All authors contributed to the article and approved the submitted version.

ACKNOWLEDGMENTS

The authors appreciate the DSTG-UOW matching PhD scholarships.

REFERENCES

Avila, A. F., de Oliveira, A. M., Leão, S. G., and Martin, M. G. (2018). Aramid fabric/nano-size dual phase shear thickening fluid composites response to ballistic impact. *Compos. Part A-Appl. S.* 112, 468–474. doi:10.1016/j.compositesa.2018.07.006

Chen, D. C., and Chen, L. R. (2020). Application of the Taguchi method for finite element analysis of a shear-type magnetorheological fluid damper. *Adv. Mech. Eng.* 12, 1–11. doi:10.1177/1687814019900397

Chen, Q., Liu, M., Xuan, S., Jiang, W., Cao, S., and Gong, X. (2017). Shear dependent electrical property of conductive shear thickening fluid. *Mater. Des.* 121, 92–100. doi:10.1016/j.matdes.2017.02.056

Cossa, K. N. (2019). Basic concepts on rheology and application of shear thickening fluids in protective gear. *SN Appl. Sci.* 1, 1284. doi:10.1007/s42452-019-1315-5

Ding, J., Li, W. H., and Shen, S. Z. (2011). Research and applications of shear thickening fluids. *Recent Pat. Mater. Sci.* 4, 43–49. doi:10.2174/1874464811104010043

Ding, J., Tian, T., Meng, Q., Guo, Z., Li, W., Zhang, P., et al. (2013) Smart multifunctional fluids for lithium ion batteries: enhanced rate performance and intrinsic mechanical protection. *Sci. Rep.* 3, 2485. doi:10.1038/srep02485

Dong, C., Miao, Y., Mi, Z., Song, Q., and Jie, F. (2016). Carbonyl iron powder surface modification of magnetorheological elastomers for vibration absorbing application. *Smart Mater. Struct.* 25, 115005. doi:10.1088/0964-1726/25/11/115005

Grover, G., Verma, S. K., Thakur, A., Biswas, I., and Bhatacharjee, D. (2020). The effect of particle size and concentration on the ballistic resistance of different shear thickening fluids. *Mater. Today* 28, 1472–1476. doi:10.1016/j.matpr.2020.04.823

Han, W., Zhao, T., and Wang, X. (2016). Steady shear viscosity and oscillatory complex viscosity of poly(p-phenylene terephthalamide) solutions in sulfuric acid. *Rheol Acta* 55, 257–266. doi:10.1007/s00397-016-0918-7

Hou, S., and Liu, G. (2020). Research on theoretical modelling and parameter sensitivity of a single-rod double-cylinder and double-coil magnetorheological damper. *Math. Probl. Eng.* 2020, 5489896. doi:10.1155/2020/5489896

Hua, D., Liu, X., Sun, S., Sotelo, M. A., Li, Z., and Li, W. H. (2020). A magnetorheological fluid filled soft crawling robot with magnetic actuation, *IEEE-ASME T. Mech.* 10. doi:10.1109/TMECH.2020.2988049

Li, X., Cao, H. L., Gao, S., Pan, F. Y., Weng, L. Q., Song, S. H., et al. (2008). Preparation of body armour material of Kevlar fabric treated with colloidal silica nanocomposite. *Plast. Rubber Compos.* 37, 223–226. doi:10.1179/174328908X309439

Majumdar, A., Laha, A., Bhattacharjee, D., and Biswas, I. (2017). Tuning the structure of 3D woven aramid fabrics reinforced with shear thickening fluid for developing soft body armour. *Compos. Struct.* 178, 415–425. doi:10.1016/j.compstruct.2017.07.018

Petel, O. E., Ouellet, S., Loiseau, J., Frost, D. L., and Higgins, A. J. (2015). A comparison of the ballistic performance of shear thickening fluids based on particle strength and volume fraction. *Int. J. Impact Eng.* 85, 83–96. doi:10.1016/j.ijimpeng.2015.06.004

Peters, I. R., Majumdar, S., and Jaeger, H. M. (2016). Direct observation of dynamic shear jamming in dense suspensions. *Nature* 532, 214. doi:10.1038/nature17167

Tian, T. (2014). *Study of shear thickening/stiffened materials and their applications, PhD thesis*, University of Wollongong

Wagner, J. W., and Wetzel, E. D. (2007). *Advanced body armor utilizing shear thickening fluids*. U.S. Patent No 7498276B2. Washington, DC: U.S. Patent and Trademark Office.

White, E., Chellamuntu, M, and Rhotstein, J. (2010). Extensional rheology of a shear-thickening cornstarch and water suspension. *Reol. Acta* 49, 119–129. doi:10.1007/s00397-009-0415-3

Yang, J., Sun, S., Li, W., Du, H., Alici, G., and Nakano, M. (2015). Development of a linear damper working with magnetorheological shear thickening fluids. *J. Intel. Mat. Syst. Str.* 26, 1811–1817. doi:10.1177/1045389X15577653

Zhang, X. Z., Li, W. H., and Gong, X. L. (2008). Study on magnetorheological shear thickening fluid. *Smart Mater. Struct.* 17, 015051. doi:10.1088/0964-1726/17/1/015051

Zhang, X. Z., Li, W. H., and Gong, X. L. (2010). Thixotropy of MR shear-thickening fluids. *Smart Mater. Struct.* 19, 125012. doi:10.1088/0964-1726/19/12/125012

Zhou, H., Yan, L., Jiang, W., Xuan, S., and Gong, X. (2016). Shear thickening fluid–based energy-free damper: design and dynamic characteristics. *J. Intel. Mat. Syst. Str.* 27, 208–220. doi:10.1177/1045389x14563869

Conflict of Interest: The authors declare that the research was conducted in the absence of any commercial or financial relationships that could be construed as a potential conflict of interest.

frontiers in Materials

ORIGINAL RESEARCH
published: 08 February 2021
doi: 10.3389/fmats.2020.590328

A General Modeling Approach for Shock Absorbers: 2 DoF MR Damper Case Study

Jorge de-J. Lozoya-Santos[1], Juan C. Tudon-Martinez[2], Ruben Morales-Menendez[1], Olivier Sename[4], Andrea Spaggiari[3] and Ricardo Ramírez-Mendoza[1]*

[1]Tecnológico de Monterrey, Monterrey, México, [2]School of Engineering and Technologies, Physics and Math Department, Universidad de Monterrey, San Pedro Garza García, México, [3]Department of Sciences and Methods for Engineering (DISMI), University of Modena and Reggio Emilia, Reggio Emilia, Italy, [4]GIPSA-Lab, Grenoble Institute of Technology, Grenoble, France

A methodology is proposed for designing a mathematical model for shock absorbers; the proposal is guided by characteristic diagrams of the shock absorbers. These characteristic diagrams (Force-Displacement, Velocity-Acceleration) are easily constructed from experimental data generated by standard tests. By analyzing the diagrams at different frequencies of interest, they can be classified into one of seven patterns, to guide the design of a model. Finally, the identification of the mathematical model can be obtained using conventional algorithms. This methodology has generated highly non-linear models for 2 degrees of freedom magneto-rheological dampers with high precision (2–10% errors).

Keywords: semi-active, modeling, magnetorheological, shock absorber, simulation

OPEN ACCESS

Edited by:
Ramin Sedaghati, Concordia University, Canada

Reviewed by:
Jong-Seok Oh, Kongju National University, South Korea
Kittipong Ekkachai, National Electronics and Computer Technology Center, Thailand

****Correspondence:***
Jorge de-J. Lozoya-Santos
jorge.lozoya@tec.mx

Specialty section:
This article was submitted to Smart Materials, a section of the journal Frontiers in Materials

Received: *01 August 2020*
Accepted: *21 December 2020*
Published: *08 February 2021*

Citation:
Lozoya-Santos Jde-J, Tudon-Martinez JC, Morales-Menendez R, Sename O, Spaggiari A and Ramírez-Mendoza R (2021) A General Modeling Approach for Shock Absorbers: 2 DoF MR Damper Case Study. Front. Mater. 7:590328. doi: 10.3389/fmats.2020.590328

1 INTRODUCTION

A dynamic mathematical model for an automotive shock absorber must accurately simulate its behavior and accommodate nonlinearities (e.g., friction, hysteresis, and inertia) over a frequency range with a maximum value lower than 30 Hz in the automotive field. The characteristics of the *Force-Velocity* (*FV*) and *Force-Displacement* (*FD*) diagrams of an automotive shock absorber are crucial. **Table 1** summarize the acronym definitions. Many modeling methods currently exist. The ideal method needs to be generic and allows the adjustment of a model based on a visual analysis of the characteristic diagrams because these provide the information for the design of the suspension. A *Passive* (*p*) Shock Absorber has a damping capacity defined by its mechanical design that varies with the displacement and oscillation frequency. Its *FV* and *FD* characteristic diagrams are constant, and it may be designed for comfort or surface grip (or a balance of both). *Semi-Active* (*SA*) shock absorbers have a capacity defined by their mechanical design and by an external signal that causes one of its mechanical properties to vary. When there is no external signal, their state is *P*. Their *FV* and *FD* diagrams can vary. The three most commonly used commercial technologies are *p*, *Magneto-Rheological* (*MR*), and *Electro-Hydraulic* (*EH*); these are compared in **Table 2**.

Some models have been developed with parameters that have no physical meaning, such as 1) *p*, Duym (1997), 2) *MR*, Choi et al. (2001) and Savaresi et al. (2005b), and 3) *EH*, Codeca et al. (2008). The models that have parameters with physical meaning, such as the phenomenological models, are also classified as 1) *p*, Duym (2000) and Carrera-Akutain et al. (2006), 2) *MR*, Wang and Kamath (2006) and Choi et al. (2001), and 3) *EH*, Heo et al. (2003). Examples of models whose parameters are linked to the characteristic diagrams are 1) *p*, Basso (1998) and Calvo et al. (2009) and 2) *MR*, Guo et al. (2006) and Ma et al. (2007). The latter are of primary interest because the parameters can predict the efficiency of the shock absorber during a vehicle maneuver. **Table 3** summarizes the variables definition.

TABLE 1 | Acronym definitions.

DoF	Degree of freedom
EH	Electro-hydraulic
FD	Force displacement
FV	Force velocity
MR	Magneto-rheological
p	Passive
SA	Semi-active

Because the *FV* diagram resembles a sigmoid function, three models have successfully used trigonometric functions (hyperbolic tangent and arc tangent) to model hysteresis. Kwok et al. (2006) proposed using a function that includes hysteresis based on the sign of the displacement:

$$F_{\text{Kwok}} = \tanh\left[\underbrace{r_{\text{pre}}\dot{z}}_{\text{dampening}} + \underbrace{h_{\text{pre}} sign(z)}_{\text{hysteresis}}\right] \tag{1}$$

Guo et al. (2006) introduced a function that depends on both the sign and the displacement magnitude:

$$F_{Guo} = \tanh\left(\underbrace{r_{pre}\dot{z}}_{\text{dampening}} + \underbrace{h_{pre} z}_{\text{hystresis}}\right) \tag{2}$$

Çesmeci and Engin (2010) combined the force and hysteresis using a sigmoid function and the acceleration sign:

$$F_{\text{Çes}} = \tan^{-1}\left[\underbrace{r_{pre}\dot{z}}_{\text{dampening}} + \underbrace{h_{pre} sign(\ddot{z})}_{\text{hysteresis}}\right] \tag{3}$$

The results are satisfactory in terms of the *FV* diagrams for constant frequencies, amplitudes, and excitations, but are nevertheless limited in precision in terms of dynamics. Sims et al. (2004) proposed a method of high precision results, but the model was not generalized and required specific tests. Ma et al. (2007) proposed the modification of *p* shock absorber models by multiplying the force by a current-dependent force. Boggs (2009) developed a nonlinear model that included hysteresis using a delay of force with a first-order filter; it did not include the friction associated with the stiffness of the mechanical design. All the proposals presented above are computationally costly. **Table 4** compares these models.

A generic model design method based on characteristic diagrams to obtain a model that can be identified and simulated with a generic tools is proposed, Lozoya-Santos et al. (2015). The methodology proposes the decomposition of the measured force in two components: *p* and *SA* force components, **Figure 1**.

This paper deals particularly with the suitability of this method to understand and model a damper using its characteristic diagrams when it has one damping control input. The specimen to be used in this work has two control inputs, Golinelli and Spaggiari (2017): electric current and the pressure in the accumulator. In this context, the work focuses on the application of the method to analyze the effect of more than one control input on the damping force and in the characteristic diagrams, and a further method extension to include such effects. Other phenomenal aspects such as cavitation due to a fault of the damper and leaks of oil or pressure from the damper are out of scope. **Section 2** presents the fundamentals of the method, and **Section 3** describes the method. The proposal is demonstrated using a case study in **Section 4** where all steps are implemented in detail. Finally, the research project is concluded in **Section 5**.

2 FUNDAMENTALS

The total force of a semi-passive shock absorber can be expressed with two terms, Dixon (2008):

$$F_{D|M} = F_P + F_{SA|M} \tag{4}$$

where $F_{D|M}$ is the total force given a certain excitation M, F_p is the term related to mechanical phenomena, and $F_{SA|M}$ is the term related to the excitation M.

When $F_D = F_P$, the shock absorber is *p*.

2.1 Characteristic Diagrams

The characteristic diagrams show the kinematic performance when the excitation is zero $F_{D|M} = 0$. When force $F_{SA|M\neq 0} = F_{D|M\neq 0} - F_P$ is evaluated, the characteristic diagrams are

TABLE 2 | Comparison of the different shock absorber technologies.

Characteristic	*p*	*MR*	*EH*
Hysteresis	Low	Low	Low
Principle	Constant flow	Change of viscosity	Area of variable flow
Excitation	—	Electric current	Electric current
Excitation range	—	0–2.5 A @ 12 V	0–5 A
Power	—	30 W	>60 W
Speed of response	—	15–40 m s	10–60 m s
Other applications	Safety	Clutches, brakes, prosthesis	Flow control
Advantages	Maintenance cost	Actuation system	Proportional response
Disadvantage	Performance	Cost	Maintenance
Technological maturity	High	High	High
Service life	80,000 km	32,000 km	40,000 km
Relative cost [%]	100	~5,000	~7,000

TABLE 3 | Variables definition.

Variable	Description	Units
Ω	Frequency	rads/s
A	Amplitude	mm
M	Excitation (exogenous variable)	—
k_a, k_b	High and low stiffness	N/m
k_{SA}	Semi-active stiffness In the pre-yield zone for $F_{SA\|M}$	N/m
Z	Displacement	m
$\dot{z}$	Speed	m/s
$\ddot{z}$	Acceleration	m^2/s
c_a, c_b	High and low damping slope	Ns/m
c_{SA}	Semi-active damping in the pre-yield zone for $F_{SA\|M}$	Ns/m
m_d	Body mass of the shock absorber	kg
m_{SA}	Virtual mass of the shock absorber when $M > 0$	kg
F_{Kwok}	Nonlinear force of kwok model Kwok et al. (2006)	N
r_{pre}	Coefficient in the pre-yield zone related to damping	s/m
h_{pre}	Coefficient in the pre-yield zone related to hysteresis	1/m
F_{Guo}	Nonlinear force of the guo model Guo et al. (2006)	N
$F_{Çes}$	Nonlinear force of the Çesmeci model Çesmeci and Engin (2010)	N
$F_{D\|M}$, F_D	Damping force	N
F_P, $F_{SA\|M}$	Damping force, p and SA component of $F_{D\|M}$	N
$\{a, b, c, d, e, f, g, h\}$	Straight lines in the characteristic diagrams	—
$\{A, B, C, D, E, F, G, H\}$	Points in the characteristic diagrams	—
k_p	Stiffness in p shock absorber model	N/m
c_p	Damping in p shock absorber model	Ns/m
c_{pre}	Damping coefficient in pre-yield zone	Ns/m
c_{pos}	Damping coefficient in post-yield zone	Ns/m
f_0	Constant damping force	N
τ	Response time constant of $F_{D\|M}$ due to excitation changes	S
ωB, ωM, ωA	Bandwidth for low, medium and high frequencies	Hz
v_1	Speed threshold for changing from pre-yield to post-yield zone for F_P	m/s
v_2	Speed threshold for changing from pre-yield to post-yield zone for $F_{SA\|M}$	m/s
g_{SA}	Slope of the semi-active force due to the excitation applied, M	N/(Excitation units)
θ	Auxiliary variable	
$\text{coefficient}_{\text{subscript+}}$	Coefficient with respect to $\dot{z} > 0$	—
$\text{coeffcient}_{\text{subscript−}}$	Coefficient with respect to $\dot{z} < 0$	—
F_s, f_s	Sigmoidal damping force on F_P	N
$f_{h,z}$	Sigmoidal damping force with hysteresis due to z for F_P	N
$f_{h,\ddot{z}}$	Sigmoidal damping force with hysteresis due to $\ddot{z}$ for F_P	N
$f_{pre-c,z,M}$	Damping force in the pre-yield zone dependent on z for F_{SA}	N
$f_{pre-c,\dot{z},M}$	Damping force in the pre-yield zone dependent on $\dot{z}$ for F_{SA}	N
$f_{c,s}$	Sigmoidal damping force magnitude	N
f_{h1}	Damping force magnitude for $f_{h,z}$	N
f_{h2}	Sigmoidal damping force magnitude for $f_{h,\ddot{z}}$	N
r_s	Damping coefficient sigmoidal for F_P	s/m
h_s	Damping coefficient sigmoidal with hysteresis for F_P	1/m
r_z	Damping coefficient in the pre-yield zone due to z for F_P	s/m
h_z	Damping coefficient in the pre-yield zone with hysteresis due to z for F_P	1/m
$r_{\ddot{z}}$	Damping coefficient in the pre-yield zone due to $\ddot{z}$ for F_P	s/m
$h_{\ddot{z}}$	Damping coefficient in the pre-yield zone with hysteresis due to $\ddot{z}$ for F_P	1/m
$r_{\dot{z},M}$	Damping coefficient sigmoidal due to $\dot{z}$ for F_{SA}	s/m
$r_{z,M}$	Damping coefficient in the pre-yield zone due to z for F_{SA}	s/m

denoted as *SA* and show the controllable dampening variation due to an exogenous variable, ideally independent of the kinematics.

The exogenous variable affects the *SA* characteristic diagrams depending on the technology. For *MR* and *ER*, the variable modifies the fluid and therefore the dynamic of the stiffness and dampening coefficients in the *FD* and *FV* diagrams. For *EH*, the *FV* diagram will vary proportionally to the exogenous variable, and the dynamics of the *FD* diagram are independent. The *FD*, *FV* and force-acceleration (*FA*) characteristic diagrams shown in **Figure 2** can be represented by eight lines $\{a, \ldots, h\}$ and eight points $\{A, \ldots, H\}$; each x line is followed by a point X. These points represent events caused by kinematics and/or the exogenous variable and are common in the

TABLE 4 | Models comparison.

Author/Year	Sims et al. (2004)	Ma et al. (2007)	Boggs (2009)
Goal	Prototyping and simulation	Simulation	Simulation
Experiments	Standard/Variable	Standard	Standard
Parameters	k_p, c_p, m_d, c_{pre}, c_{pos}	Depend on the model	k_p, c_p, F_s, τ
Bandwidth	0–15 Hz	0–5 Hz	0–15 Hz
Nonlinearity	Friction, hysteresis	Semi-active yield	Hysteresis
Technology	*ER*, *MR*	*MR*	*p*
Model	Algebraic with tanh	Dependent of excitation	Nonlinear dynamics
Advantages	Parametric	—	Computation
Disadvantages	Multiple experiments, complex	No meaning on characteristic diagrams	

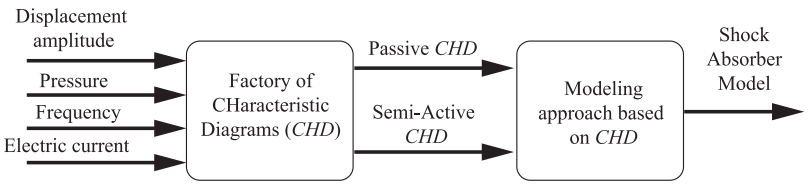

FIGURE 1 | General block diagram of the *CHD*-based approach for shock absorbers modeling.

three diagrams; we refer to them as characteristic points. The direction of the curves is clockwise in the *FD* and *FV* diagrams and counterclockwise in the *FA* diagram.

There are three types of points in the characteristic diagrams. Yield point is the point at which the slope of the line decreases. In the *FV* and *p* diagrams, this point is related to the actuation of valves with a larger orifice at a limit speed. In the *FV* and *SA* diagrams, it is related to the change in behavior of the fluid (viscous to viscoplastic). Point of return is the point at which the speed changes direction and the slope of the line changes sign. It is present in all *FV* diagrams. Restoring point is the point at which the slope of the line increases with the same sign. In the *FV* and *p* diagrams, it occurs when the valve system deactivates the larger orifice valves and increases the damping. In the *FV* and *SA* diagrams, the chains formed by the magnetic phenomenon in the *MR*/*ER* fluid are restored, causing a sudden increase in the viscosity of the fluid. The yield and restoring points are related to the two main damping coefficients: high and low coefficient,

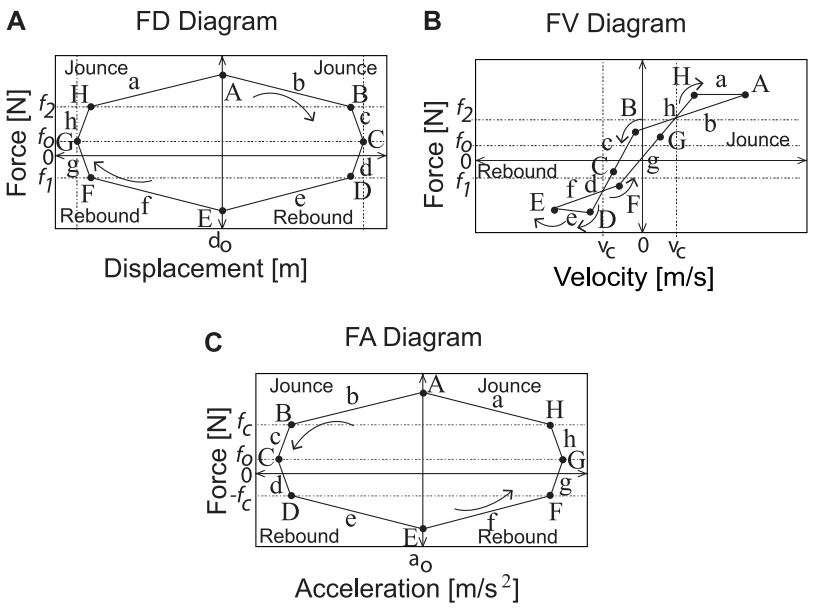

FIGURE 2 | Characteristic diagrams.

TABLE 5 | Characteristic points in the *FV* diagram.

Operation	Compression	Extension	*p*	*SA*
Lines	a, b, c, h	d, e, f, g	ω	ω, M
Yield	H	D	ω, α	M, ω, α
Restoring	F	B	ω, α	M, ω, α
Return	A	E	ω, α	M

TABLE 6 | *FD* line diagram for the *p* and *SA* cases.

Lines	*p*			*SA*		
	ωB	ωM	ωA	ωB	ωM	ωA
A	k_b	$\rightarrow 0$	$\rightarrow 0$	k_{SA}	$\rightarrow 0$	~ 0
B	k_b	$\rightarrow 0$	$\rightarrow 0$	k_{SA}	$\rightarrow 0$	~ 0
C	k_b	k_a	k_a	k_{SA}	k_{SA}	k_{SA}
D	k_b	k_a	k_a	k_{SA}	k_{SA}	k_{SA}
E	k_b	$\rightarrow 0$	$\rightarrow 0$	k_{SA}	$\rightarrow 0$	~ 0
F	k_b	$\rightarrow 0$	$\rightarrow 0$	k_{SA}	$\rightarrow 0$	~ 0
G	k_b	k_a	k_a	k_{SA}	k_{SA}	k_{SA}
H	k_b	k_a	k_a	k_{SA}	k_{SA}	k_{SA}
Variable with more influence In the Characteristic diagrams		Ω		ω, M	M	

TABLE 7 | *FV* line diagram for the *p* and *SA* cases.

Lines	*p*			*SA*		
	ωB	ωM	ωA	ωB	ωM	ωA
A	c_a	c_b	$\rightarrow 0$	c_{SA}	$\rightarrow 0$	~ 0
B	c_a	c_b	$\rightarrow 0$	c_{SA}	$\rightarrow 0$	~ 0
C	c_a	c_a	c_a	c_{SA}	c_{SA}	c_{SA}
D	c_a	c_a	c_a	c_{SA}	c_{SA}	c_{SA}
E	c_a	c_b	$\rightarrow 0$	c_{SA}	$\rightarrow 0$	~ 0
F	c_a	c_b	$\rightarrow 0$	c_{SA}	$\rightarrow 0$	~ 0
G	c_a	c_a	c_a	c_{SA}	c_{SA}	c_{SA}
H	c_a	c_a	c_a	c_{SA}	c_{SA}	c_{SA}
Variable with more influence In the Characteristic diagrams		ω		ω, M	M	

TABLE 8 | *FA* line diagram for the *p* and *SA* cases.

Lines	*p*			*SA*		
	ωB	ωM	ωA	ωB	ωM	ωA
A	$\rightarrow 0$	m_D	m_D	$\rightarrow 0$	$\rightarrow 0$	m_{SA}
B	$\rightarrow 0$	m_D	m_D	$\rightarrow 0$	$\rightarrow 0$	m_{SA}
c	$\rightarrow \infty$	m_D	m_D	$\rightarrow \infty$	$\rightarrow \infty$	$\rightarrow \infty$
d	$\rightarrow \infty$	m_D	m_D	$\rightarrow \infty$	$\rightarrow \infty$	$\rightarrow \infty$
e	$\rightarrow 0$	m_D	m_D	$\rightarrow 0$	$\rightarrow 0$	m_{SA}
f	$\rightarrow 0$	m_D	m_D	$\rightarrow 0$	$\rightarrow 0$	m_{SA}
g	$\rightarrow \infty$	m_D	m_D	$\rightarrow \infty$	$\rightarrow \infty$	$\rightarrow \infty$
h	$\rightarrow \infty$	m_D	m_D	$\rightarrow \infty$	$\rightarrow \infty$	$\rightarrow \infty$
Variable with more influence In the Characteristic diagrams			Ω			

Rakheja and Sankar (1985), Warner (1996), Hong et al. (2002), and Savaresi and Spelta (2007). A ratio higher than 5:1 for the high/low coefficient in extension and compression can be used for a symmetric shock absorber, and a ratio higher than 2:1 in compression can be used for an asymmetric shock absorber. Any changes in these specifications in the *FV* diagram will be reflected in the *FD* and *FA* diagrams. **Table 5** shows the quadrants where the characteristic points are found based on the *FV* diagram.

The analysis of the characteristic diagrams will be performed in three frequency ranges relevant to the automotive field: low frequency (ωB) [0.5–3] Hz, medium frequency (ωM) [3–7] Hz and high frequency (ωA) [7–15] Hz, Warner (1996). The slopes of the lines and coordinates of the characteristic points change according to: 1) oscillation frequency, ω; 2) oscillation amplitude (α) of the displacement of the piston in the *p* diagrams (p), and 3) the exogenous variable M.

In *p* diagrams, *FD* diagrams (**Figure 2A**) show a low stiffness, represented by slope k_b in all lines for ωB. The slope of the stiffness increases, k_a in lines c, d, g, h, and in lines a, b, e, f it tends to be zero for frequencies in the $[\omega M - \omega A]$ range. The slopes always have the same sign as the speed $sign(\dot{z})$, **Table 6** (the variables that most affect the slopes are shown). In the *SA* diagrams and *FD* diagrams, the lines have a k_{SA} slope that is similar across the speed range in ωB. This slope is the same for lines c, d, g, h and tends to be zero in lines a, b, e, f for ωM and ωA. The slopes are always positive, **Table 6**.

The *p* diagrams and *FV* diagrams (**Figure 2B**) reveal high damping, represented by slope c_a in all lines for ωB. With damping, the slope c_a, does not change in lines c, d, g, h, and in lines a, b, e, f tending to be a low damping, the slope c_b tends to be less for frequencies in the $[\omega M - \omega A]$ range. In the ωA $c_b \rightarrow 0$ range, **Table 7**, the slopes are always positive and affected by ω. In the *SA* diagrams, with regard to the *FV* diagrams, a large damping c_{SA} of the lines is similar across the speed range in ωB. This slope is the same for lines c, d, g, h, and tends to be zero in lines a, b, e, f for ωM and ωA. The slopes are always positive and are mainly affected by ω and M at low frequencies and by M only in ωM and ωA, **Table 7**.

In the *p* diagrams, *FA* diagrams (**Figure 2C**), the slope is almost zero in lines a, b, e, f and infinite for c, d, g, h in ωB. Acceleration does not affect the force. The slope md appears in all the lines $[\omega M - \omega A]$. The frequency greatly affects the force due to its quadratic effect on acceleration. The slopes are always positive, **Table 8**. In the *SA* diagram, the slopes in ωB and ωM are the same as in ωB in the *p* diagrams. The acceleration has no effect on the *SA* force. At high frequencies, ωA, it is possible to observe a positive slope, m_{SA} for yield lines a, b, e, f. The acceleration does not affect the *SA* force significantly, **Table 8**.

A model is presented for each frequency range; for ωB is:

$$F_{D|M} = \underbrace{k_b sign(\dot{z}) z + c_a \dot{z} + m_d s \ddot{z}}_{F_P} + \underbrace{M[k_{SA} z + c_{SA} \dot{z}]}_{F_{SA|M}} \quad (5)$$

For frequencies ωM and ωA, the force components F_P and $F_{SA|M}$ of the proposed model in **Eq. 4** are as follows:

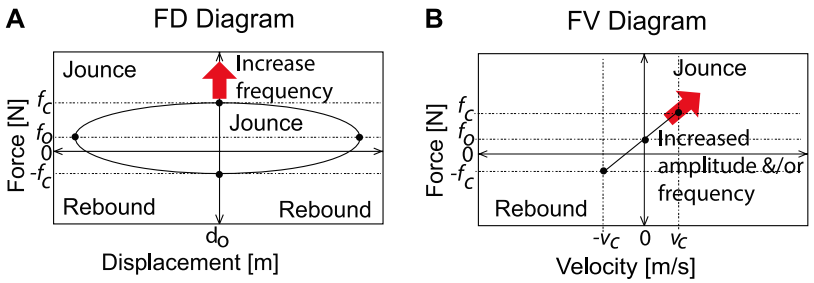

FIGURE 3 | Characteristic diagrams at *ωB*, *Type-0*.

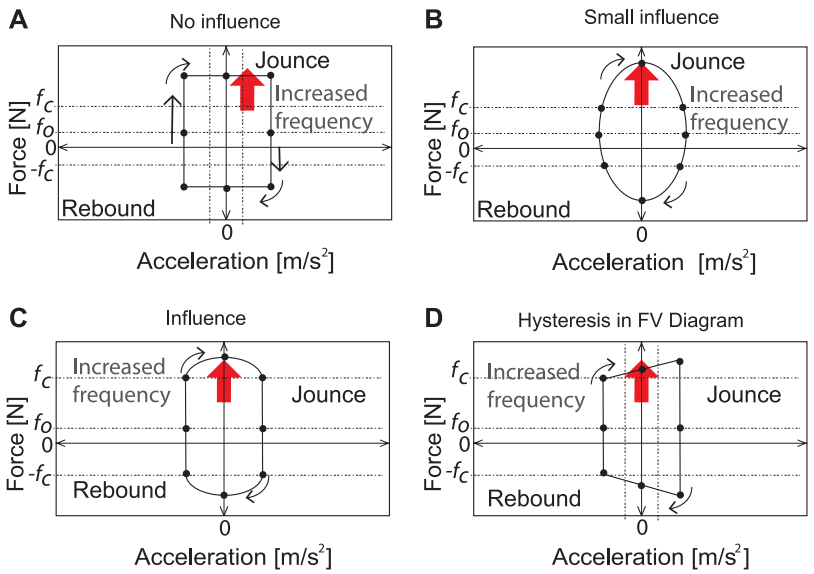

FIGURE 4 | Types of *FA* characteristic diagrams.

$$F_P = \begin{cases} k_a sign(\dot{z})z + c_a\dot{z} + m_d\ddot{z} & \dot{z} < v_1 \\ F_p(v_1) + c_b\dot{z} + m_d\ddot{z} & \dot{z} > v_1 \end{cases} \quad (6)$$

$$F_{SA|M} = \begin{cases} M(k_{SA}z + c_{SA}\dot{z}) & \dot{z} < v_2 \\ M[g_{SA}sign(\dot{z})] + m_{SA}\ddot{z} & \dot{z} > v_2 \end{cases} \quad (7)$$

The three equations are similar to that presented by Joarder (2003); however, the characteristic points are dynamic and have a function of frequency ω, amplitude α, and excitation *M*, **Table 5**. To propose a generic dynamic model, we classified the characteristic diagrams *FD*, *FV*, and *FA* according to the frequency range and the combination of characteristic points. The proposed classification has seven patterns: 1) *Type 0* for *ωB*, 2) Types (1, 2, 3, 4) for *ωM*, and 3) Types (5, 6) for *ωA*.

Type-0. In diagrams *p*, points *A*, *B*, and *H* are equal in compression and points *D*, *E*, and *F* are the same between them. If the shock absorber is asymmetric, the slopes of lines *d* and *g* are the same and different from those of lines *c* and *h*, which have the same slope, **Figure 3**. If the shock absorber is symmetric, then *E* = -*A*, *D* = -H and *F* = -*B*.

The *FD* diagram shows a constant compressibility, k_b, with perfect ovals, **Figure 3A**. The *FV* diagram is a line with high damping c_a, **Figure 3B**. Slopes *D*, *C*, *G*, and *H* are equal. Lines *A*, *B*, *E*, and *F* have zero length. It is highly unusual for these to show hysteresis in the *FV* diagram. The effect of acceleration is negligible, **Figure 4A**. The frequency and amplitude of the displacement increases the magnitude of the characteristic points. In the *SA* diagrams, the frequency and amplitude of the displacement as well as the exogenous variable increase the characteristic points. The latter is the most significant in the ordinates of the points.

Type-1. In the *p* case, this is the ideal type for an automotive shock absorber, **Figure 5**. The yield, restoring, and return points are all present. The high slopes of lines *c* and *h*, and of *d* and *g* are equal, just as the slopes of lines *a* and *b* in compression, and *f* and *e* in extension are the same. The yield points *H* and *D*, and restoring points *B* and *F* are the same between them in the compression quadrants, as well as the two that correspond to the extension quadrant. There is no hysteresis. The effect of

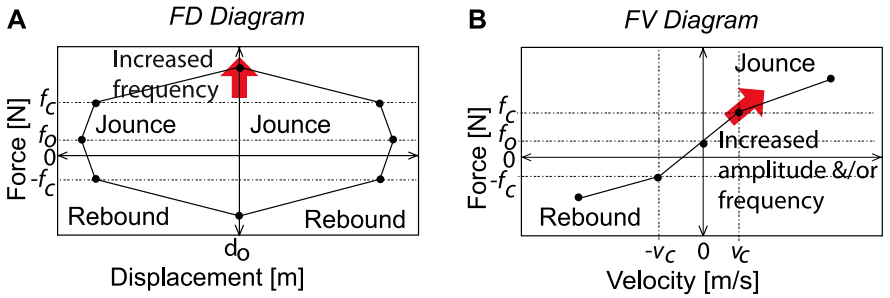

FIGURE 5 | Characteristic diagrams at *ωM*, *Type-1*.

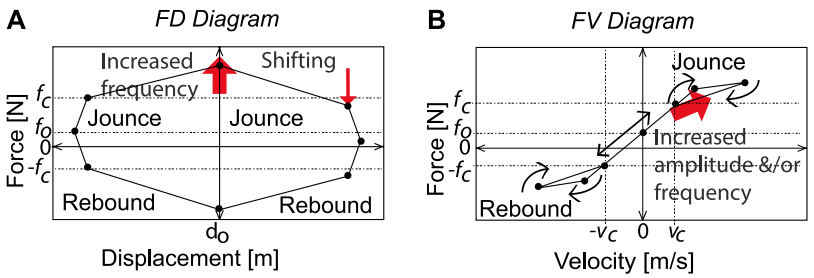

FIGURE 6 | Characteristic diagrams at *ωM*, *Type-2*.

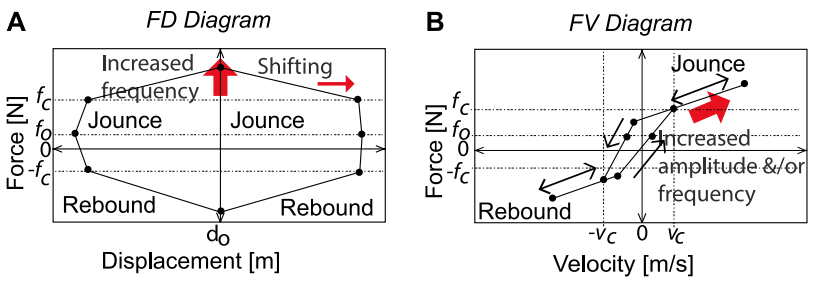

FIGURE 7 | Characteristic diagrams at *ωM*, *Type-3*.

acceleration is negligible, **Figures 4A** and **4B**. This type does not exist in *SA* systems.

Type-2. These are the typical diagrams of an automotive shock absorber, **Figure 6**. The difference with respect to *Type-1* is that the abscissa and ordinate of the yield point *H* are greater compared to the restore point *B*. This causes hysteresis at high speed due to the viscosity of the fluid. The effect of acceleration may not be significant, **Figure 4B**. This diagram type is typical of *SA* diagrams, although it is regularly idealized at high speeds and represented as *Type-1*. The characteristics of the *MR*/*ER* fluid define the dynamic of the yield and restoring points.

Type-3. This type is also observed in automotive applications, **Figure 7**. The abscissa and ordinate of point *B* are smaller than those of point *H*, resulting in line *b* being longer than line *a*. The abscissa of *B* is much smaller than that of *H*; in particular, point *B* is closer to zero in the horizontal speed axis and further from zero in the horizontal displacement axis. This behavior causes hysteresis at low speed due to the compressibility of the fluid. When there is symmetry, point $F = -H$, and point $F = -B$. The effect of acceleration is negligible **Figure 4A**. These phenomena are typical in *SA* diagrams, but at high frequencies the viscosity of the *MR*/*ER* fluid does not have as fast a response as the oscillation frequency, causing a difference in the yield and restore points and generating hysteresis.

Type-4. This type is atypical of *p* diagrams. It is the expected response of force $F_{SA|M=cte}$ in a shock absorber, **Figure 8**. The force is independent over almost the entire speed range, except in the vicinity of $\dot{z} = 0$. If the force in this vicinity tended to be zero, then force *SA* would be ideal. The slopes of *a*, *b*, *f*, and *e* are zero due to the independence of speed at medium and high magnitudes. The yield points are *H* and $D = -H$, and the restore points are *B* and $F = -B$ for symmetric cases. The

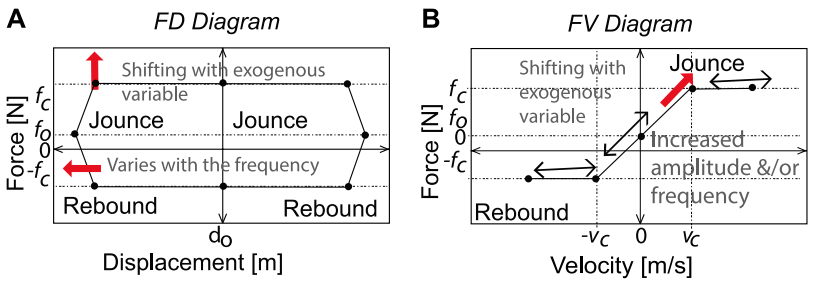

FIGURE 8 | Characteristic diagrams at *ωM*, *Type-4*.

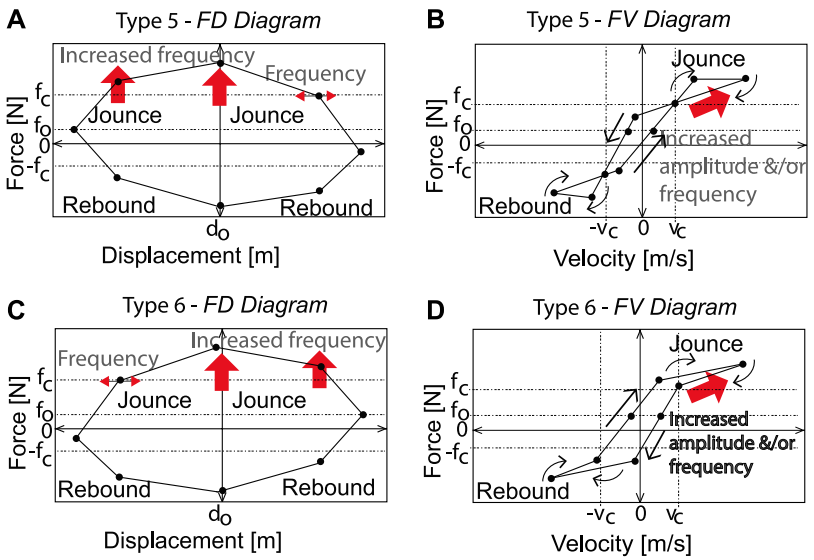

FIGURE 9 | Characteristic diagrams at *ωA*, *Type-5* and *Type-6*.

points of return *A* and *E* = -*A* are equal, and their ordinate is equal in magnitude to yield points *H* and *F* = -*H*. The ordinate of the yield points is proportional to the magnitude of the exogenous variable. The slopes of lines *c*, *d*, *g*, and h may be sensitive to speed and to the exogenous variable and can increase as either variable increases. The change of the abscissa is very small, from five to 1. There is no hysteresis in the *FV* diagram, and the effect of acceleration is not significant, **Figures 4A** or **Figure 4B**.

Type-5. In *p* diagrams, this type may appear in extreme operating conditions, **Figure 9**. It is a mix of *Type-2* and *Type-3*, and there is hysteresis due to the compressibility and viscosity phenomena of the fluid. The effect of acceleration may be significant, **Figure 4C**. This type is atypical of *SA* diagrams unless the shock absorber is *ER*/*MR* or if there is hysteresis in the response of the proportional valves.

Type-6. This type is very unusual for an automotive shock absorber, **Figures 9C** and **9D**. The ordinates (force) of restore points *B* and *F* increase, and the ordinates of yield points *D* and *H* decrease. Due to the high frequency (speed), the yield and restore points occur faster, namely, *Types-2* and *Types-3* are inverted because the mechanical components are forced and do not recover their designed operating condition. The effect of acceleration is highly significant, **Figure 4D**. This type is atypical of *SA* diagrams.

2.2 Generic Model Definition

The proposed generic model of the shock absorber includes two terms.

$$F_D = F_{P+,-} + F_{SA+,-} \tag{8}$$

where $F_{P+,-}$ is the component of the damper force F_D associated with the passive part, that is, when the input (exogenous input, for example current) is zero, $F_{SA+,-}$ is the component of the damper force F_D when the input (exogenous input, for example current) is different from zero, that is to say, it is the semi-active component (SA) of the shock absorber. The subscripts +, − can represent the mechanical exerted force of the shock absorber when the velocity is positive, +, or negative, −. In model identification, the parameter identification method gets the values of the model parameters using two sets of the data. Each set corresponds to

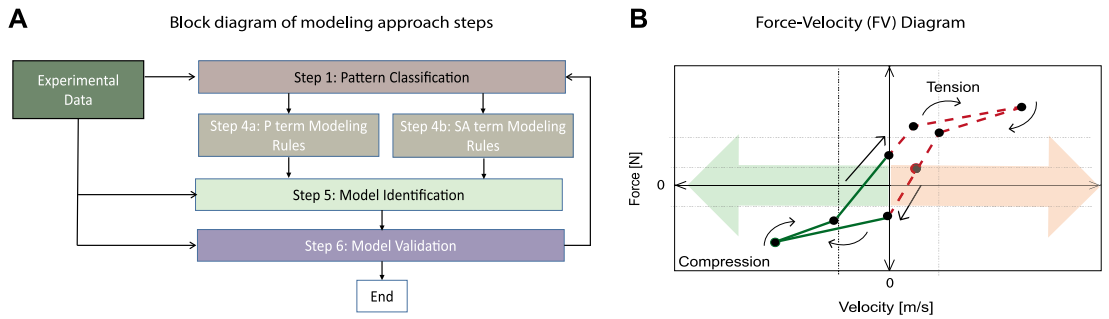

FIGURE 10 | Basic methodology **(A)** The description of the methodology step by step, **(B)** A characteristic diagram Force-Velocity pointing the tension and compression shapes of the force, the arrows divide the diagram in positive and negative velocities. Sometimes it will be necessary to have identified model parameter values depending on the sign of the velocity of the piston.

positive and negative velocity, respectively. This model definition applies if the FV characteristic diagram presents non-linear and non-isotropic behavior (e.g., the behavior is not similar when the shock absorber is in a state of tension rather than in compression), **Figure 10B**.

F_P term definition. The first term is F_P, which models the behavior when an exogenous variable is not applied;

$$F_P = f_0 + c_p\dot{z} + k_p z + m_D\ddot{z} + f_s + f_{h,z} + f_{h,\dot{z}} \tag{9}$$

where:

$$f_s = f_{c,s}\left(\frac{r_s\dot{z} + h_s z}{1 + |r_s\dot{z} + h_s z|}\right)$$

$$f_{h,z} = f_{h_1}\left(\frac{r_z\dot{z} + h_z sign(z)}{1 + |r_z\dot{z} + h_z sign(z)|}\right)$$

$$f_{h,\ddot{z}} = f_{h_2}\left(\frac{r_{\ddot{z}}\dot{z} + h_{\ddot{z}} sign(\ddot{z})}{1 + |r_{\ddot{z}}\dot{z} + h_{\ddot{z}} sign(\ddot{z})|}\right)$$

Equation 9 is the F_P term of the force of the *SA* shock absorber. Coefficient f_0 is an initial compensation force; c_p is the viscous damping coefficient that describes the speed dependent force and is related to as c_b. The internal stiffness coefficient, k_p, represents the displacement dependent force and is related to k_b. The virtual mass m_D describes the acceleration dependent force, $f_s = F_{\text{Guo}}$, which is the damping force that represents the sigmoidal behavior. Finally, terms $f_{h,z} = F_{Kwok}$ and $f_{h,\ddot{z}} = F_{\text{Çes}}$ model the hysteresis effect at ωB and ωA. To ensure a computationally efficient system, it uses a squash function, Yonaba et al. (2010), $f(\theta) = \theta/(1 + |\theta|)$ where θ is the function argument that defines the sigmoidal form, instead of the frequently used hyperbolic tangent.

F_{SA} term definition. The second term is the F_{SA}, which models the force when the exogenous variable acts on the damping, **Eq. 8**. Because the shock absorber *SA* may have asymmetric behavior in the *FV* diagram, the coefficients of the model are different for positive and negative speeds.

$$F_{SA} = Mg_{SA}\left[f_{pre-c,\dot{z},M} + f_{pre-c,z}\right] \tag{10}$$

where:

TABLE 9 | Rules for modeling the *p* diagrams. *ωA*

Model	Type of diagram			Function
	ωB	ωM	ωA	
Simple	0 or 1	1	1	f_s
	0 or 1	1	[a]	
Inertial simple	0 or 1	1	2	$f_s + f_{h,\ddot{z}}$
	0 or 1	2	2	
	0 or 1	2	6	
	0 or 1	1	6	
Stiff simple	0 or 1	1	3	$f_s + f_{h,z}$
	0 or 1	3	3	
Complete	0 or 1	2	5	$f_s + f_{h,z} + f_{h,\ddot{z}}$
	0 or 1	3	5	

[a]*Indicates a simple model fits for low and medium frequencies domains, i. e., the precision at ωA is not significant.*

$$f_{pre-c,\dot{z},M} = \left(\frac{r_{\dot{z},M}\dot{z}M}{1 + |r_{\dot{z},M}\dot{z}M|}\right)$$

$$f_{pre-c,z} = \left(\frac{r_{z,M}z}{1 + |r_{z,M}z|}\right)$$

Equation 10 is the F_{SA} term, where g_{SA} is the gain in force per each *M* unit, the $f_{pre-c,\dot{z},M}$ term simulates force *SA* at low speeds at which damping depends on the speed and excitation, and $f_{pre-c,M}$ simulates the stiffness effect on force *SA*.

3 MODELING APPROACH

This methodology is divided in four steps, **Figure 10A**.

Step 1: Pattern classification.

The first step of the methodology is to classify the pattern of the characteristic diagram that was generated experimentally from the shock absorber. This classification allows the definition of the specific model equation from a set of options. The classification uses the type patterns defined and built for the *p* and SA forces: {*Type-0*, . . . , *Type-6* } according to **Section 2.1**.

TABLE 10 | Rules for modeling the *SA* characteristic diagrams.

Model	Type of diagram			Function	
	ωB	ωM	ωA	Option 1	Option 2
Simple	0 or 4	4	4	$f_{pre-c,\dot{z},M}$	—
Complete	0 or 4	4, 6 or 5	6 or 5	$f_{pre-c,\dot{z},M}$	$f_{pre-c,\dot{z},M} + f_{pre-c,z}$

Step 2a: Modeling Rules for the F_P term.

A set of rules defines the model for the F_P term, **Table 9**. If the shock absorber is passive, the method considers only these rules. The base **Eq. 9** suits the shock absorber performance in terms. To perform this step, it must have computed all the characteristic diagrams in the bandwidths of interest and for the displacement, velocity and acceleration. The logic to follow is: if the type of diagram in the ωB, ωM and ωA bandwidths corresponds to a set of column values, then the F_P term of the F_D model adds the term indicated in the column *Function* to the term $F_P = f_0 + c_p\dot{z} + k_p z + m_D\ddot{z}$. Then, the F_P term takes the name indicated in the *Model* column of **Table 9**.

Step 2b: Modeling Rules for the F_{SA} term.

Similarly, a set of rules defines the model for the F_{SA} term, **Table 10**. The base **Eq. 10** models the semi-active force in a characteristic diagram of a shock absorber when it acts the exogenous input with a signal M. The logic to follow is: if the type of diagram in the ωB, ωM and ωA bandwidths corresponds to a set of column values, then the F_{SA} term of the F_D model becomes the term indicated in the column *Function* to the model $F_D = F_P$. Then, the F_{SA} term takes the name indicated in the *Model* column of **Table 10**.

Symmetry of the damping force in the characteristic diagrams. If the shock absorber is symmetric, damping force equals in shape and magnitude in tension and compression zones (positive and negative forces), the method proposes the following formulation:

$$F_D = \underbrace{f_0 + c_p\dot{z} + k_p z + m_D\ddot{z} + \text{function}_{\text{PAS}}}_{\text{passive force}} + \underbrace{Mg_{SA}\left(\text{function}_{SA}\right)}_{\text{Semi-active force}} \tag{11}$$

If the shock absorber is asymmetric, the method proposes to consider a generic model as in **Eq. 12**.

$$F_D = f_0 + \begin{cases} \underbrace{c_{p+}\dot{z} + k_{p+}z + m_{D+}\ddot{z} + \text{function}_{PAS+}}_{\text{passive force}} + \underbrace{Mg_{SA+}\left[\text{function}_{SA+}\right]}_{\text{semi-active force}}\dot{z} > 0 \\ \underbrace{c_{p-}\dot{z} + k_{p-}z + m_{D-}\ddot{z} + \text{function}_{PAS-}}_{\text{passive force}} + \underbrace{Mg_{SA-}\left[\text{function}_{SA-}\right]}_{\text{semi-active force}}\dot{z} \le 0 \end{cases} \tag{12}$$

where the subscript signs indicate if the speed is positive (+) or negative (-).

Step 3: Model identification

The identification process of the model uses the trust-region reflective optimization algorithm, Coleman and Li (1996). The nonlinear least-squares optimization method with the sum of squared errors objective function and the bounded solution space of parameters to be identified applies this algorithm. The main non-linearities that relate the input data to the output data are saturation and hysteresis. When the calculations from the identification data result in indefinite derivatives (very noisy data or with unpredictable discontinuities), use direct search methods, Wright (1996). These methods can be useful when experimental data from different tests are used as a single sequence of serial data to carry out the identification because there will be discontinuities developed at the end of each test data set joined sequentially.

Step 4: Model validation

To validate the results, the Error-to-Signal Ratio (*ESR*) index is proposed, which is the quotient of the variance of the estimation error and the variance of the experimental force, Savaresi et al. (2005a). Testing and identification data are different. An $ESR \sim 0$ indicates that the model is perfect; while an $ESR \sim 1$ indicates a trivial model that estimates an average value. If the result is not satisfactory, we suggest using patterns {*Type-0*, . . . , *Type-6* } for the classification. If the identified model does not fill the precision needs, the methodology suggests reviewing the characteristic diagrams to reclassify the pattern types and repeat the model definition process and validation. .

Figure 11 specifies the proposed methodology. The identification of the mathematical modeling of four commercial shock absorbers (*p*, continuous *MR*, On/Off *MR*, and a continuous *EH* technology) validates this method, Lozoya-Santos et al. (2015). The models produced less than 5% of modeling error, evidenced in a set of qualitative plots and quantitative indexes.

4 CASE STUDY

4.1 2-Degree-of-Freedom (*2DoF*) *MR* Damper

A *MR* damper prototype has a novel architecture that differs from the existing ones by the presence of an internal counter-rod placed at the bottom of the damper, Golinelli and Spaggiari (2015), **Figure 12**. It uses a bottom-rod fixed to the end plug and coupled with the piston head. The bottom-rod has the same diameter of the upper-rod so that there is no volume variation. During piston movement, the bottom-rod is moving the chamber obtained into the piston head. The chamber is also directly connected to the canal through the upper-rod to bring out the wire of the coil. In such a manner, this configuration avoids the over-pressure or depression phenomenon within the chamber. Two coils were adopted. The longer axial length of the piston head allows maximizing the concatenated magnetic flux. The pressure system is composed of a stepper motor that converts the motion from rotary to translatory by a screw and nut mechanism. This system controls a slider that insists on the volume of *MR* fluid. Lowering the volume of fluid causes an increase of the internal pressure. The magnetic flux array (incoherent multiple

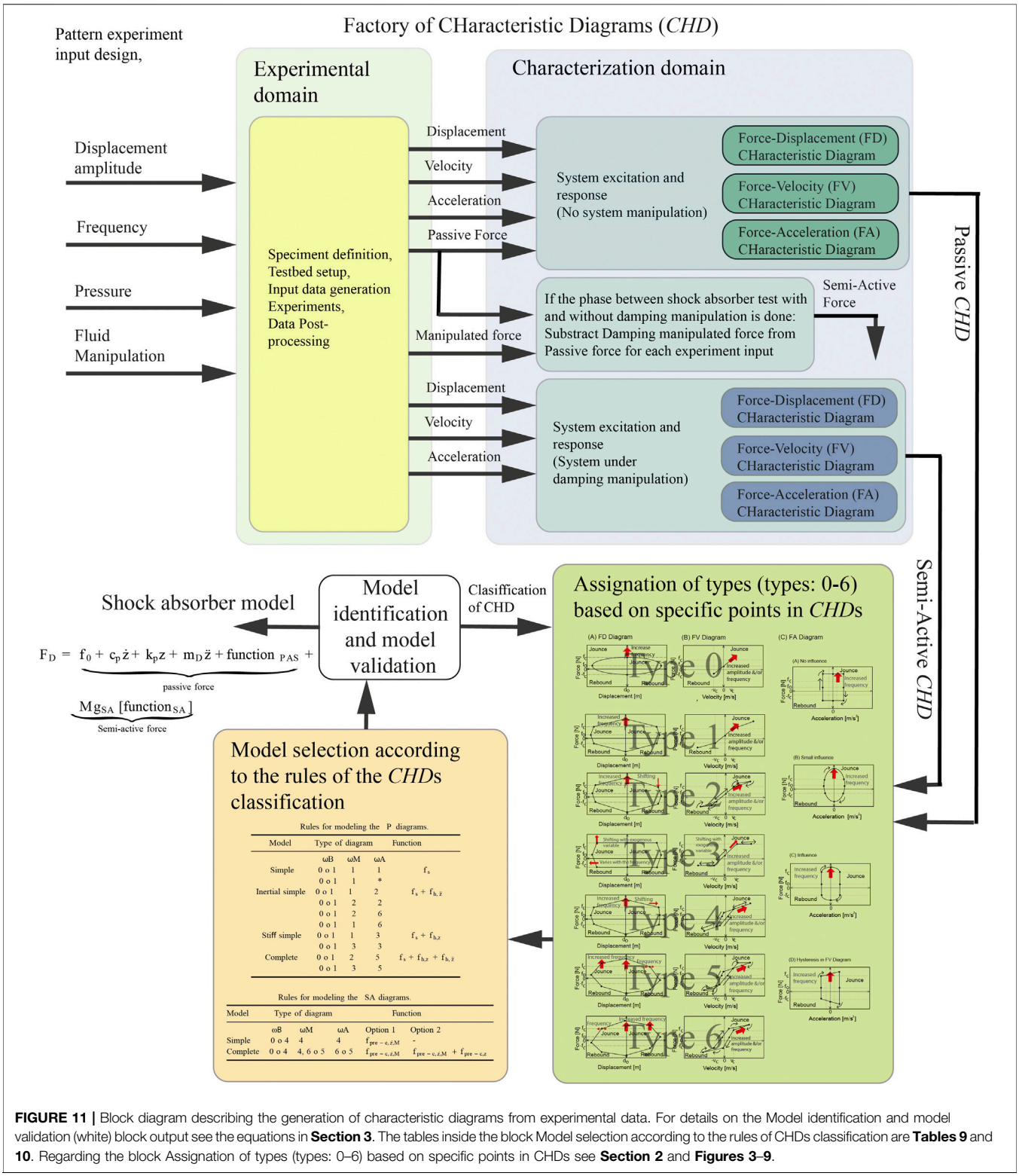

FIGURE 11 | Block diagram describing the generation of characteristic diagrams from experimental data. For details on the Model identification and model validation (white) block output see the equations in **Section 3**. The tables inside the block Model selection according to the rules of CHDs classification are **Tables 9** and **10**. Regarding the block Assignation of types (types: 0–6) based on specific points in CHDs see **Section 2** and **Figures 3–9**.

coils) decreases of the overall inductance of the circuit that allows, compared to others, less response time of the same device.

The system works without the volume compensator and presents a precise internal pressure control. The architecture includes no protruding elements, a thermal compensation system, and cavitation prevention. For full details on the design and explanation of the functioning of this specimen, see Golinelli and Spaggiari (2017). The *MR* damper assembly

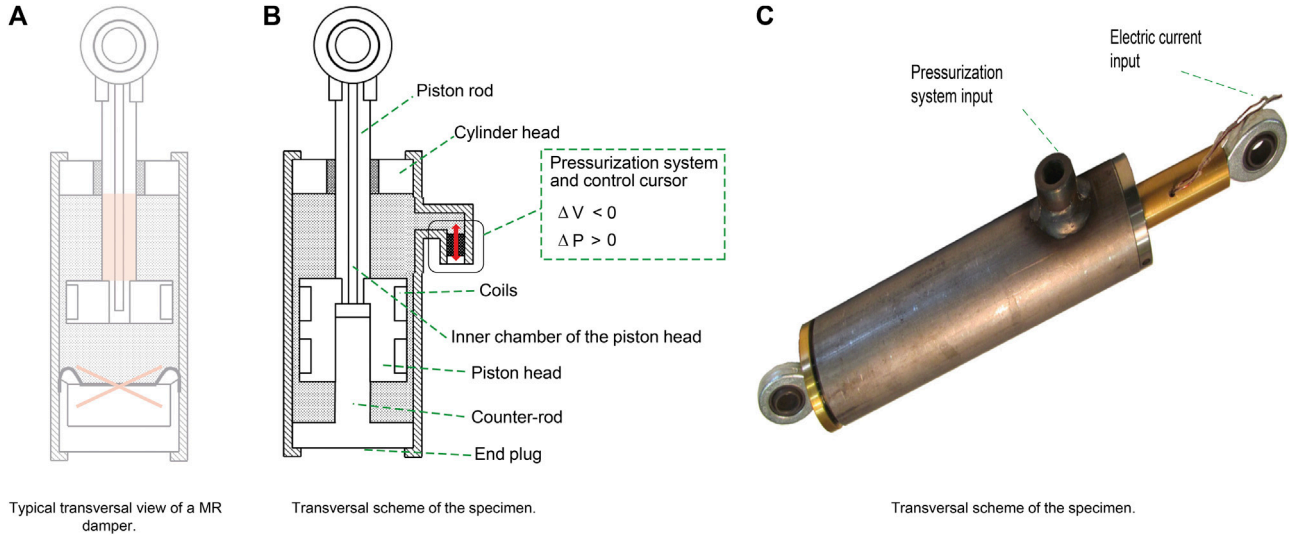

FIGURE 12 | Architecture of the *2DOFMR* Damper specimen and assembly.

TABLE 11 | *2DoF MR* Damper technical specifications.

Specification	Value
Maximum force [N]	2000
Maximum velocity [mm/s]	150
Stroke [mm]	50
Maximum input current [A]	2
Maximum body diameter [mm]	50
Maximum pressure [bar]	40

TABLE 12 | *DoE* specification of the used experimental data in this modeling approach. The maximum velocity value ($V_{max} = 2Af$) is 31.41 mm/s.

			Experiment								
Characteristic	**Variable**	**Units**	**1**	**2**	**3**	**4**	**5**	**6**	**7**	**8**	**9**
Amplitude	*A*	[mm]	5								
Frequency	*f*	[Hz]	1				2				
Current	*I*	[A]	0			1			2		
Pressure	*p*	[Bar]	0	20	40	0	20	40	0	20	40
Replicates			3	3	3	3	3	3	3	3	3
Experimental points			54								

uses commercial components: a hydraulic cylinder, its cylinder head, and two ball joint ends. The piston rod, the piston head, and the bottom rod are manufactured custom parts. The prototype, **Figure 12C**, shows the electric current as well as the pressure inputs. Golinelli and Spaggiari (2015). The technical specifications of the *2DoF-MR* damper is listed in **Table 11**.

This device shows cavitation phenomena when no pressure is applied. On the other hand, when pressure is applied, it shows a similar behavior expected from a *MR* damper, no matter the applied level of electric current, Golinelli and Spaggiari (2017). The inclusion of cavitation in mathematical models of (*p* or *SA*) shock absorbers it is not a trivial task.

The Design of Experiments (*DoE*) methodology for this specimen and the experimental data was presented in Golinelli and Spaggiari (2017). The damper was tested under sinusoidal displacements. The variables involved are amplitude *A* and frequency *f* of the sinusoidal input, current *I* and a pressure level *p*. The chosen amplitude level was *5* mm. Each test lasted for 20 cycles with a sampling rate of 512 Hz. *DoE* was selected, a summary of the used variables and their values are reported in **Table 12**. For the testbed and details of the sensor and instrumentation system, please see Golinelli and Spaggiari (2017).

We would like to add that the sinusoidal test pattern and constant current permits the identification of precise models for the motion dynamics. These data patterns allow describing the non-linearities of the damper force with a persistent frequency at different manipulations, Tudon-Martinez et al. (2019) addressing the hysteresis phenomenon due to the friction and inertia. It is of interest to use this signal since it allows evaluating the vehicle vertical dynamics of the suspension at different frequencies, including the resonance frequencies of the chassis (around 1–2 Hz) and unsprung mass (around 8–9 Hz) in typical cars of class 1 Lozoya-Santos et al. (2012b) and Poussot-Vassal (2008). Moreover, it has been evidenced that this pattern performs good model parameter identification since a cross validation process with other richer displacement dynamics experiments has shown high precision in damping force estimation, Lozoya-Santos et al. (2012a). Regarding the dynamic response of the damping force due to a change in the electric current, typically the *MR*/*ER* fluid transient responses are between 20 and 30 m s before the reach of the steady state, Lozoya-Santos et al. (2012a). So, a first order model with these dynamics is typically added in the semi-active damper model electric current input/voltage to include the transient responses Lozoya-Santos et al. (2012b) and Savaresi et al. (2005b). The use of the sinusoidal test has been validated in a previous work where we compare the input motion patterns, and this signal was well suited to model damper nonlinearities,

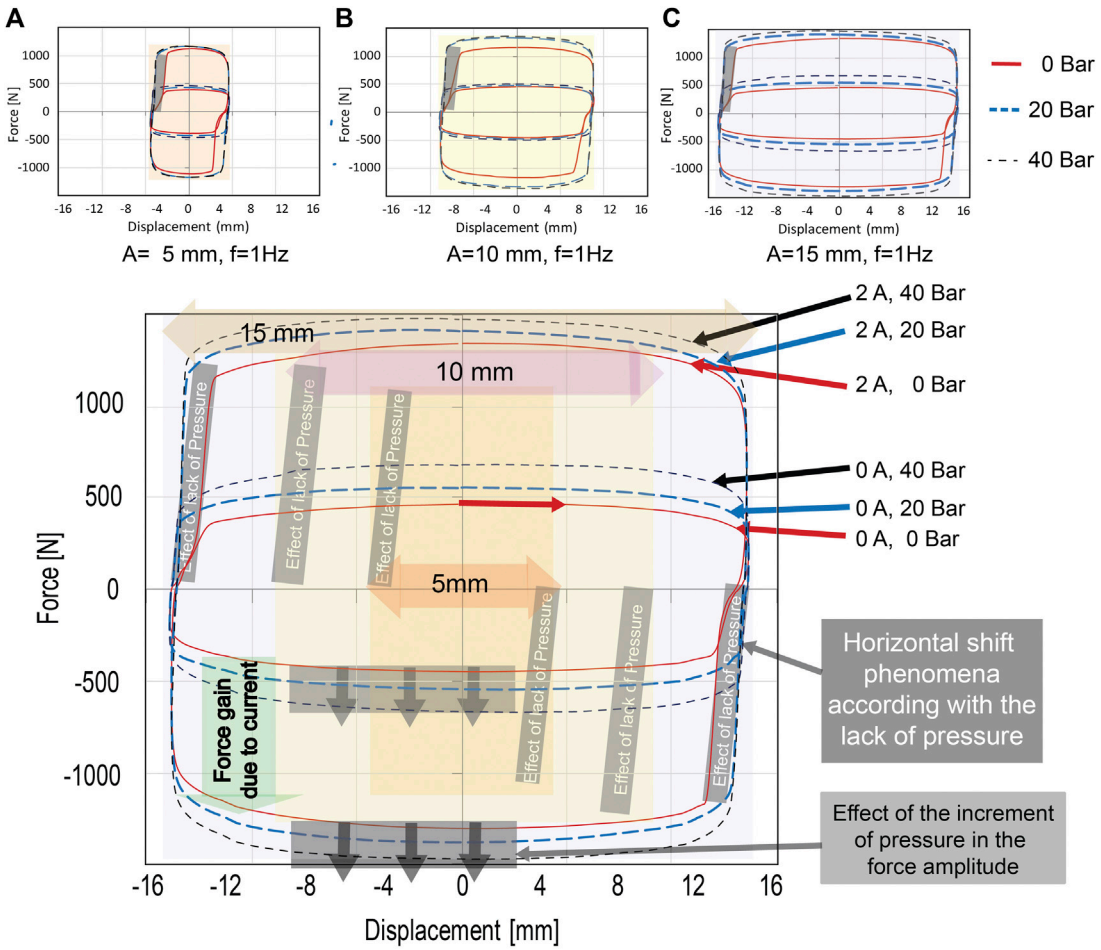

FIGURE 13 | *FD* Characteristic diagrams for a *2 Degrees of Freedom MR* shock absorber for the three cases of electric current (0, 1 and 2 A) and pressure (0, 20 and 40 bar). The first upper row shows the three *FD* diagrams for the different amplitudes. The second row shows the *FD* diagram, where it is emphasized the effects of pressure and electric current on the damping force, and how it changes according to the displacement amplitude.

compared with white noise content signals. This paper's scope regarding stroke displacement frequency is focused on a body comfort evaluation bandwidth.

4.2 Results

This subsection shows, step by step, the method application for the modeling of the described specimen in **Section 4**.

Step 1. Generation of the characteristic diagrams and its pattern classification.

The first step consists of the plotting of the characteristic diagrams *FD* and *FV* for all the experiments in **Table 12**. **Figures 13** and **14** show the plots and a similar behavior due to the effect of the pressure and the electric current increments. The cavitation is present when the displacement changes its direction and crosses the zero of the vertical axis, i.e., negative displacement, positive force, and positive displacement and negative force. In such a moment, the cavitation appears as a change of slope of the damping force vs. the displacement. This phenomenon is present repetitively in each cycle for each test, amplitude, and electric current when internal pressure is 0 bar, **Figures 13A–C**.

When the internal pressure changes to 20 and 40 bar respectively, the cavitation and the dynamics in the vicinity of zero phenomena decrease considerably. Regarding to the presence of pressure, it supplies a damping force increment in a quasi-linear ratio, **Figure 13** second row, approximately a 5*N*/bar. The effect of the increment of electric current, it is similar to well-known *MR* dampers in literature. The increment of electric current generates an approximated change with a ratio 500*N*/*A*.

In the *FV* characteristic diagram, the effect of the lack of pressure (0 bar) increases the complexity of the hysteresis phenomena. When the force tends to be zero from the yield zone, a monotonic decrement on the slope force-velocity before the zero force, and a monotonic increment of the slope after the zero appears, until the force yielding point. These dynamics modifies the typical hysteretical behavior of these devices. A final remark, the *FV* diagram qualitatively shows a left shift between positive and negative force over the horizontal axis, **Figures 14A–C**. Regarding to the internal pressure increment, a

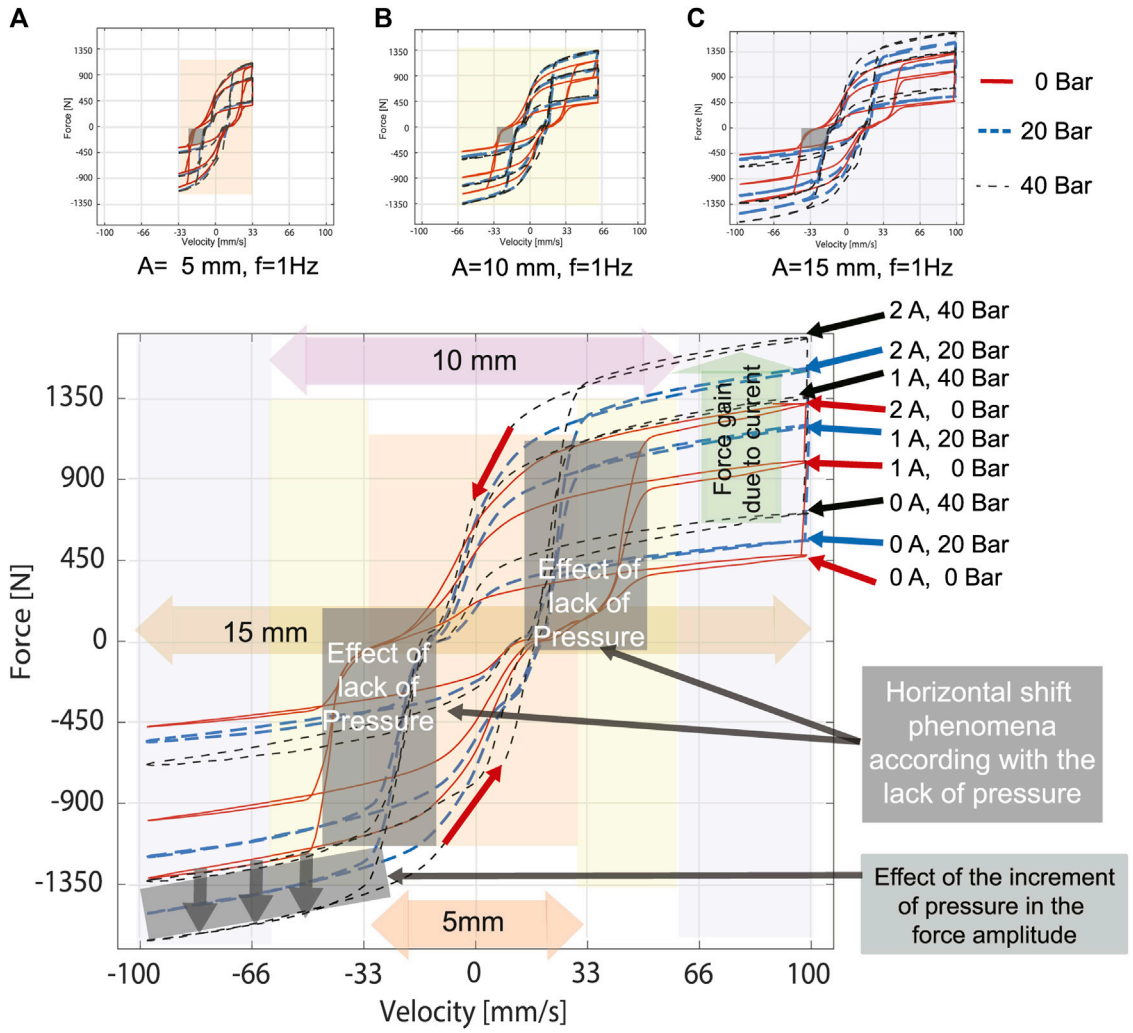

FIGURE 14 | *FV* Characteristic diagrams for a *2 Degrees of Freedom MR* shock absorber for the three cases of electric current (0, 1 and 2 A) and pressure (0, 20 and 40 bar). The first upper row shows the three *FV* diagrams for the different amplitudes. The second row shows a *FV* diagram, where it is emphasized the effects of pressure and electric current on the damping force, and how it changes according to the velocity amplitude.

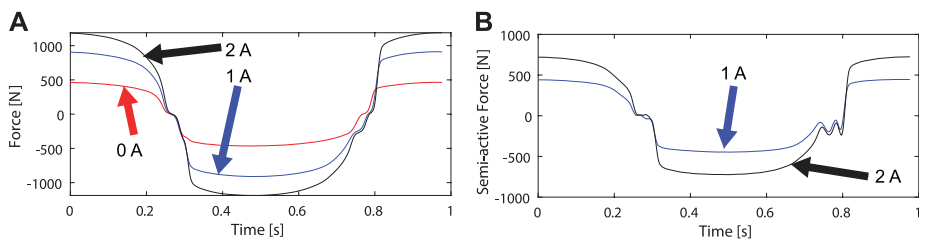

FIGURE 15 | The transient behavior of the damping forces in the specimen for a 5 mm experiment, 20 bar input pressure and the three values of electric current: **(A)** damping force f_D for 0A, 1A and 2A, **(B)** semi-active force due only to the electric current for 1A and 2A (computed by subtraction) $f_{D|1A,20Bar} - f_{D|0A,20Bar}$, and $f_{D|2A,20Bar} - f_{D|0A,20Bar}$.

quasi linear force gain for each unit of pressure can be seen, **Figure 14**, since from 0 to 20 bar, the force gain is different than from 20 to 40 bar.

The total damping force, f_D, shows the above-mentioned dynamics in the vicinity of zero in the transient response, **Figure 15A**. It can be seen how the force increases for a

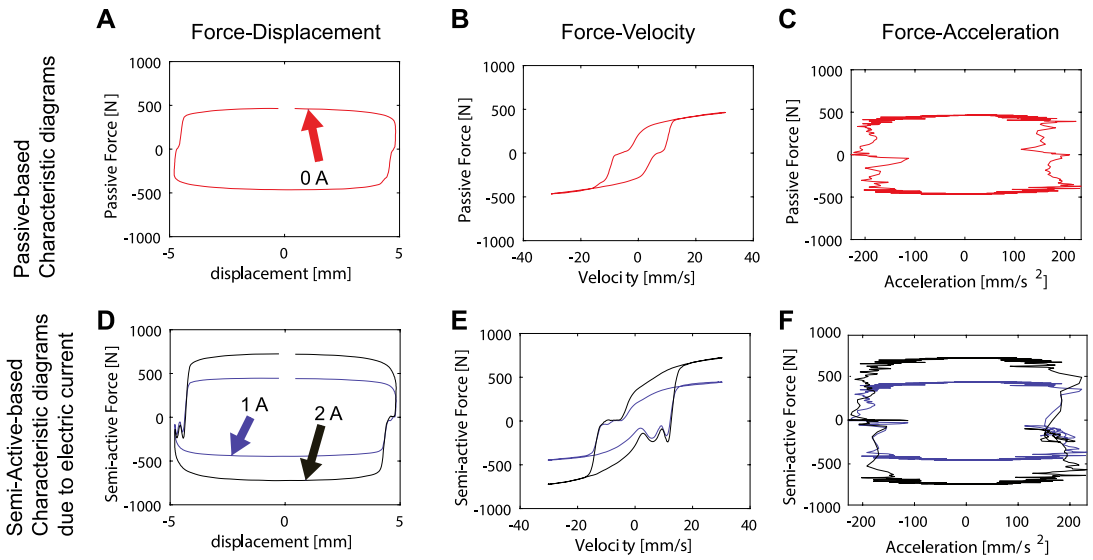

FIGURE 16 | Characteristic diagrams according to the proposed method. The *FD*, *FV* and *FA* characteristics diagrams for *p* (first row) and *SA* (second row) forces agree with specified types in classification schemes.

change in the electric current magnitude. The semi-active forces due to the electric currents, $f_{SA|1A} = f_{D|1A} - f_{D|0A}$, and $f_{SA|2A} = f_{D|2A} - f_{D|0A}$ also reflects the effect of the pressure around zero force crossings, **Figure 15B**.

The *p* and *SA* characteristic diagrams *FD*, *FV*, and *FA* display some of the specific patterns to do the classification. The *p* diagrams present similar characteristics to the type 3 with the influence of the acceleration in the damping force because of the shape of the *FA* plot, **Figures 16A–C**. Regarding the semi-active damping force characteristic diagrams, the shapes classifies as a type five, regardless of the added dynamics for the pressure input in the vicinity of zero force.

The characteristic diagrams of the pressure vs. the force when the electric current is constant, **Figure 17**, compares the force dynamics when pressure is not present and when it increments in a constant ratio. It shows the *FD* and *FV* characteristics diagrams for the semi-active force generated from 0 to 20 Bars ($f_{D|20bars} - f_{D|0bars}$), **Figure 17**(first row) and the semi-active force generated from 20 to 40 Bars ($f_{D|40bars} - f_{D|20bars}$), **Figure 17**(second row). The analyzed experimental data set is the 5 mm amplitude data set for all the electric currents and pressures. For the subtraction $f_{D|20bars} - f_{D|0bars}$, a peak of semi-active damping force (which shows a linear effect on the magnitude of the electric current) appears on both characteristic diagrams, **Figure 17** (first row). However, when the analyzed semi-active force corresponds to the damping force generated due to the change from 20 to 40 bars, it seems that the peak is not present in the diagram. There is no cavitation, **Figure 17** (second row). So, this method of analysis can be used to detect such a condition of the shock-absorber.

Steps 2a and 2b: Modeling Rules for the F_P and F_{SA} terms.

According to **Table 9** for the *p* diagrams and **Table 10** for the *SA* diagrams, the proposed classification, **Table 13**, sets the modeling approach focused on two model types: a) a model one based on the stiffness simple model for the *p* force and the complete model for the *SA* force, b) a complete-complete model in both forces.

Step 3: Model identification

The model identification process used the experimental set with 20 bar, since when the pressure is present, the complexity of the dynamics diminishes to that of a typical MR damper. All the amplitudes and electric current values were included. All the possible models were identified, **Table 14**. The lowest *ESR*s correspond to the model *Stiffness Simple - Simple* and for the model *Complete-Complete*. This result agrees with the model selection according to the presented methodology.

The identified parameters for the Complete-Complete *MR* damper model is shown in **Table 15**.

Step 4: Model validation

The characteristic diagrams, **Figures 18A–C**, the forces comparison, **Figure 18D**, the relation electric current vs. force, **Figure 18E** and the transient response, **Figure 18F**, qualitatively show the proposed model matches with the *MR* damper dynamics.

The proposed method of modeling using the generation and classification of *p* and *SA* characteristic diagrams fits this specimen, when the pressure is present inside the chambers. The quantitative, **Table 14** and qualitative results, **Figure 18**, provide evidence and validate this proposal.

The characterization of the dynamics and the effect of the control inputs based on the subtraction of the damping forces when the input under study remains constant, allows for better

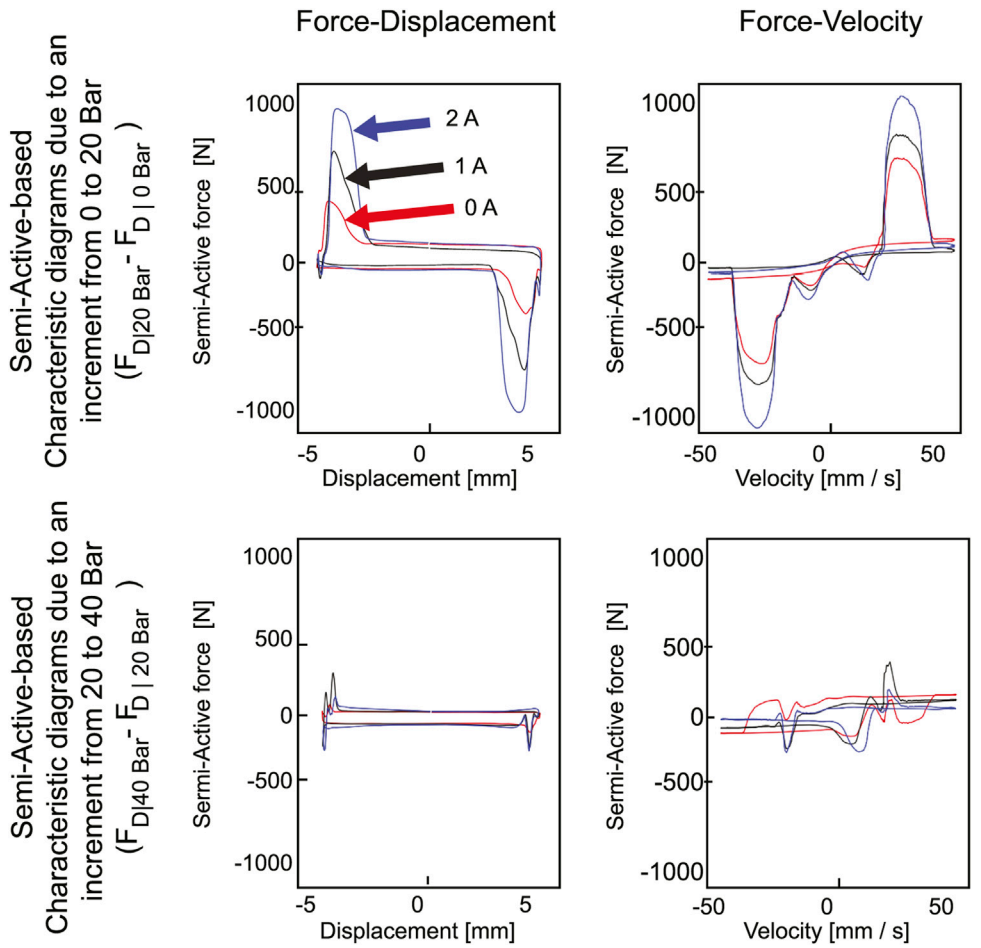

FIGURE 17 | Characteristic diagrams of the semi-active force generated by the constant increments of the pressure according to the proposed method.

TABLE 13 | Classification of characteristic diagrams and proposed models. It only takes into account one frequency, since the analyzed test is a 1 Hz signal.

	p Model		*SA* model	
Component	**Rule**	**Model**	**Rule**	**Model**
1-*MR 2DoF* (continuous)	3	Stiff simple	5	Complete
2- *MR 2DoF* (continuous)	5	Complete	5	Complete

TABLE 14 | Model estimation performances using *ESR* index.

Model		***ESR***
Passive	Semi-active	
Simple	Simple	0.0213
Simple	Complete	0.0188
Stiffness simple	Simple	0.0244
Stiffness simple	Complete	0.0160
Inertial simple	Simple	0.0212
Inertial simple	Complete	0.0186
Complete	Simple	0.0184
Complete	Complete	0.0160

understanding the diagrams, in this case, it has also been used for the pressure, **Figure 17**. Each input has its own impact on the damping force. An interesting aspect is the appropriateness of the approach to understanding the effect of the pressure variation using the subtracted damping force. It was evidenced that such a pressure effect can be analyzed as an additive component in a further improvement of this method, using some recent results in fault detection of shock absorbers, Hernández-Alcántara et al. (2016).

5 CONCLUSION

A methodology for the modeling of *p* and *SA* shock absorbers based on standard experimental tests has been presented and used with a two degrees of freedom shock absorber. The characteristic diagrams were constructed using experimental data to guide the designer in the development of the structure of the model, starting with a generic equation that introduced a simplified mathematical structure. We experimentally validated the proposal with the specimen. The obtained results had errors below 5%.

TABLE 15 | Identified model parameters for the Complete-Complete approach.

Parameter number	Parameter name	Function on the model	Velocity > 0	Velocity < 0	Unit
C1	f_0	Offset	−0.1941	−45.1065	N
C2	c_p	Damping	−3.7911	−0.2774	Ns/mm
C3	k_p	Stiffness	89.2199	−1.5460	N/mm
C4	m_D	Mass	0.7599	0.0957	kg
C5	$f_{c,s}$	Stiffness gain	2,303.0421	−672.6543	N
C6	r_s	Stiffness	0.0023	−0.1279	s/mm
C7	h_s	Stiffness	−0.0368	−0.2162	1/mm
C8	f_{h_1}	Inertia gain	−622.9134	−48.9551	N
C9	r_z	Inertia	−0.2141	730.8866	s/mm
C10	h_z	Inertia	−2.8172	−495.4853	Unitless
C11	g_{SA}	Semi-active gain	448.6180	435.0991	N/A
C12	$r_{\dot{z},M}$	Sigmoidal shape	0.0496	0.0645	s/(mm-A)

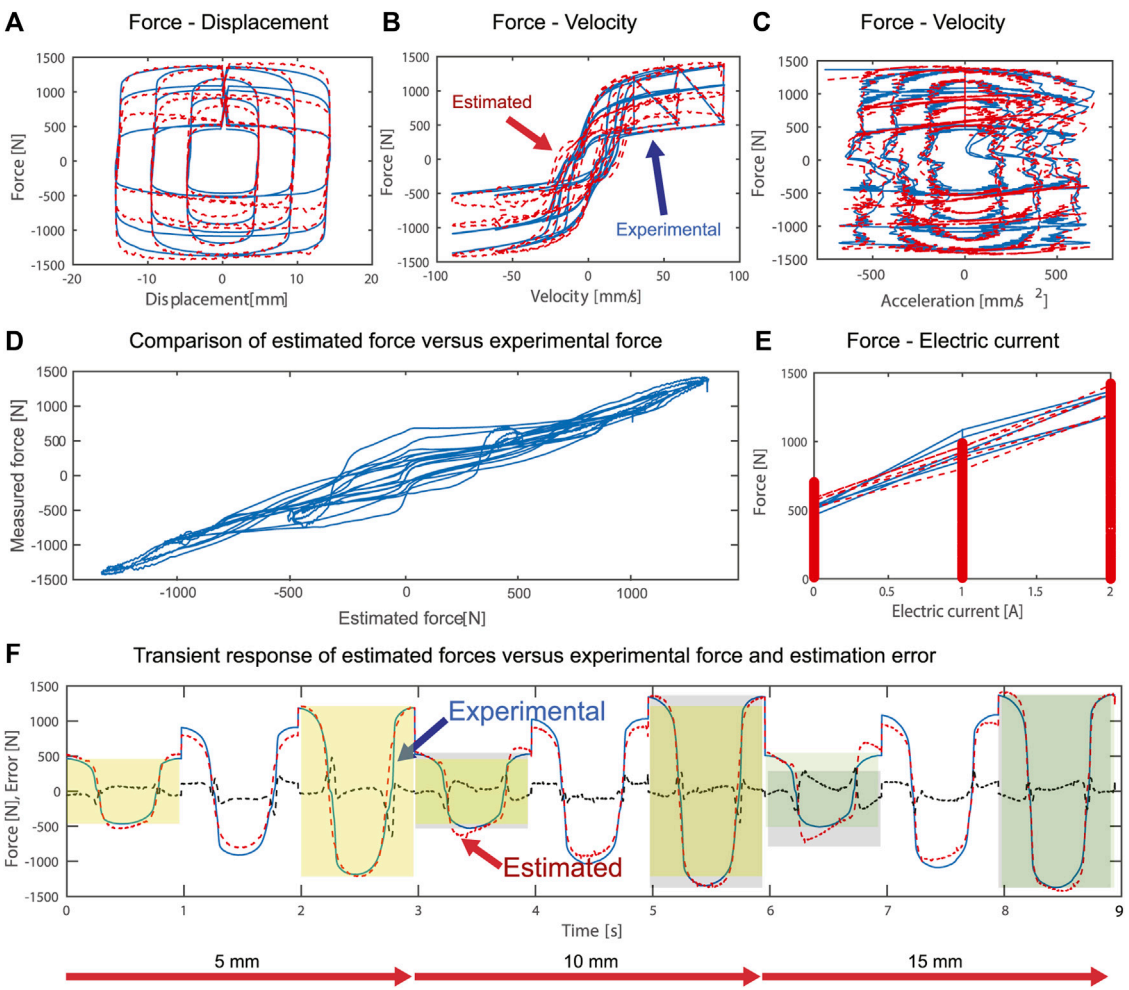

FIGURE 18 | Characteristic diagrams, transient response and estimated vs. experimental forces plots for the Complete-Complete *MR* damper model.

The present method needs to be extended to include the modeling of the damping force generated for the variation of internal pressure as control input, so a set of new models will be added for such classification.

DATA AVAILABILITY STATEMENT

The raw data supporting the conclusions of this article will be made available by the authors, without undue reservation.

AUTHOR CONTRIBUTIONS

JL-S, OS, RM-M and RR-M conceived and designed the analysis. JL-S and JT-M collected the non 2DoF shock absorber data. AS collected the data for the 2DOF MR damper. JL-S and JT-M performed the analysis. JL-S, AS and JT-M contributed data and analysis tools. JL-S wrote the paper.

FUNDING

This work was supported by a CONACYT Grant 2012-2014, "Programa de Estimulo a la Innovacion" in category "BILATERAL" with grant number 142183, and the 2011 "Programa de Estimulo a la Innovacion" in category "PROINNOVA" with grant number 132758.

ACKNOWLEDGMENTS

The authors want to acknowledge the support from Luc Dugard from Gipsa-Lab, Grenoble Institute of Technology, and Ricardo Prado, Professor in Tecnologico de Monterrey. Also, JL-S wants to thanks to the support from GIPSA-Lab in Grenoble, France.

REFERENCES

Akutain, X. C., Vinolas, J., Savall, J., and Biera, J. (2006). A parametric damper model validated on a track. *Ijhvs* 13, 145–163. doi:10.1504/ijhvs.2006.010015

Basso, R. (1998). Experimental characterization of damping force in shock absorbers with constant velocity excitation. *Veh. Syst. Dyn.* 30, 431–442. doi:10.1080/00423119808969459

Boggs, C. M. (2009). The use of simulation to expedite experimental investigations of the effect of high-performance shock absorbers. Ph.D. thesis. Blacksburg (VA): Virginia Polytechnic Institute and State University.

Calvo, J. A., López-Boada, B., Román, J. L. S., and Gauchía, A. (2009). Influence of a shock absorber model on vehicle dynamic simulation. *Proc. Inst. Mech. Eng. - Part D J. Automob. Eng.* 223, 189–203. doi:10.1243/09544070jauto990

Çesmeci, S., and Engin, T. (2010). Modeling and testing of a field-controllable magneto-rheological fluid damper. *Int. J. Mech. Sci.* 52, 1036–1046. doi:10.1016/j.ijmecsci.2010.04.007

Choi, S.-B., Lee, S.-K., and Park, Y.-P. (2001). A hysteresis model for the field-dependent damping force of a magnetorheological damper. *J. Sound Vib.* 245, 375–383. doi:10.1006/jsvi.2000.3539

Codeca, F., Savaresi, S. M., Spelta, C., Montiglio, M., and Leluzzi, M. (2008). "Identification of an electro-hydraulic controllable shock absorber using black-block non-linear models," in *17 IEEE international conference on control applications*, San Antonio, TX, September 3–5, 2008 (New York, NY: IEEE), 462–467.

Coleman, T. F., and Li, Y. (1996). An interior trust region approach for nonlinear minimization subject to bounds. *SIAM J. Optim.* 6, 418–445. doi:10.1137/0806023

Dixon, J. C. (2008). *The shock absorber handbook*. West Sussex, United Kingdom: Wiley.

Duym, S. (1997). An alternative force state map for shock absorbers. *Proc. Inst. Mech. Eng. - Part D J. Automob. Eng.* 211, 175–179. doi:10.1243/0954407971526344

Duym, S. W. R. (2000). Simulation tools, modelling and identification, for an automotive shock absorber in the context of vehicle dynamics. *Veh. Syst. Dyn.* 33, 261–285. doi:10.1076/0042-3114(200004)33:4;1-u;ft261

Golinelli, N., and Spaggiari, A. (2015). Design of a novel magnetorheological damper with internal pressure control. *Frattura ed Integritaá Strutturale.* 9, 13–23. doi:10.3221/igf-esis.32.02

Golinelli, N., and Spaggiari, A. (2017). Experimental validation of a novel magnetorheological damper with an internal pressure control. *J. Intell. Mater. Syst. Struct.* 28, 2489–2499. doi:10.1177/1045389x17689932

Guo, S., Yang, S., and Pan, C. (2006). Dynamic modeling of magnetorheological damper behaviors. *J. Intell. Mater. Syst. Struct.* 17, 3–14. doi:10.1177/1045389x06055860

Heo, S.-J., Park, K., and Son, S.-H. (2003). Modelling of continuously variable damper for design of semi-active suspension systems. *Ijvd.* 31, 41–57. doi:10.1504/ijvd.2003.002046

Hernández-Alcántara, D., Tudón-Martínez, J. C., Amézquita-Brooks, L., Vivas-López, C. A., and Morales-Menéndez, R. (2016). Modeling, diagnosis and estimation of actuator faults in vehicle suspensions. *Contr. Eng. Pract* 49, 173–186. doi:10.1016/j.conengprac.2015.12.002

Hong, K.-S., Sohn, H.-C., and Hedrick, J. K. (2002). Modified skyhook control of semi-active suspensions: a new model, gain scheduling, and hardware-in-the-loop tuning. *J. Dyn. Syst. Meas. Contr.* 124, 158–167. doi:10.1115/1.1434265

Joarder, M. N. (2003). Influence of nonlinear asymmetric suspension properties on the ride characteristics of road vehicle. Master's thesis. Montreal, Canada: Concordia University.

Kwok, N. M., Ha, Q. P., Nguyen, T. H., Li, J., and Samali, B. (2006). A novel hysteretic model for magnetorheological fluid dampers and parameter identification using particle swarm optimization. *Sensor Actuator Phys.* 132, 441–451. doi:10.1016/j.sna.2006.03.015

Lozoya-Santos, J. d.-J., Hernández-Alcantara, D., Morales-Menendez, R., and Ramírez-Mendoza, R. A. (2015). Modelado de Amortiguadores guiado por sus Diagramas Característicos. *Revista Iberoamericana de Automática e Inform. Industrial RIAI.* 12, 282–291. doi:10.1016/j.riai.2015.05.001

Lozoya-Santos, J., Morales-Menendez, R., Ramirez-Mendoza, R. A., Tudón-Martínez, J. C., Sename, O., and Dugard, L. (2012a). Magneto-rheological damper, an experimental study. *J. Intell. Mater. Syst. Struct.* 23, 1213–1232. doi:10.1177/1045389X12445035

Lozoya-Santos, J. d. J., Morales-Menendez, R., and Ramírez Mendoza, R. A. (2012b). Control of an automotive semi-active suspension. *Math. Probl Eng.* 2012, 1–21. doi:10.1155/2012/218106

Ma, X. Q., Rakheja, S., and Su, C. Y. (2007). Development and relative assessments of models for characterizing the current dependent hysteresis properties of magnetorheological fluid dampers. *J. Intell. Mater. Syst. Struct.* 24, 487–502. doi:10.1177/1045389X06067118

Poussot-Vassal, C. (2008). Commande robuste LPV multivariable de Chassis. Ph.D. thesis. Grenoble, France: INP Grenoble.

Rakheja, S., and Sankar, S. (1985). Vibration and shock isolation performance of a semi-active on-off damper. *J. Vib. Acoust. Stress Reliab. Des.* 107, 384–403. doi:10.1115/1.3269279

Savaresi, S. M., Bittanti, S., and Montiglio, M. (2005a). Identification of semi-physical and black-box non-linear models: the case of MR-dampers for vehicles control. *Automatica.* 41, 113–127. doi:10.1016/j.automatica.2004.08.012

Savaresi, S. M., Silani, E., and Bittanti, S. (2005b). Acceleration-driven-damper (ADD): an optimal control algorithm for comfort-oriented semiactive suspensions. *ASME Trans: J. Dyn. Syst. Meas. Contr.* 127, 218–229. doi:10.1115/1.1898241

Savaresi, S. M., and Spelta, C. (2007). Mixed sky-hook and ADD: approaching the filtering limits of a semi-active suspension. *J. Dyn. Syst. Meas. Contr.* 129, 382–392. doi:10.1115/1.2745846

Sims, N. D., Holmes, N. J., and Stanway, R. (2004). A unified modelling and model updating procedure for electrorheological and magnetorheological vibration dampers. *Smart Mater. Struct.* 13, 100–121. doi:10.1088/0964-1726/13/1/012

Tudon-Martinez, J. C., Hernandez-Alcantara, D., Amezquita-Brooks, L., Morales-Menendez, R., Lozoya-Santos, J. d. J., and Aquines, O. (2019). Magneto-rheological dampers-model influence on the semi-active suspension performance. *Smart Mater. Struct.* 28, 105030. doi:10.1088/1361-665x/ab39f2

Wang, L. X., and Kamath, H. (2006). Modelling hysteretic behaviour in magnetorheological fluids and dampers using phase-transition theory. *Smart Mater. Struct.* 15, 1725–1733. doi:10.1088/0964-1726/15/6/027

Warner, B. (1996). An analytical and experimental investigation of high performance suspension dampers. Ph.D. thesis. Montreal, Canada: Concordia University.

Wright, M. H. (1996). Direct search methods: once scorned, now respectable. *Pitman Res. Notes Math. Ser.* 191–208.

Yonaba, H., Anctil, F., and Fortin, V. (2010). Comparing sigmoid transfer functions for neural network multistep ahead streamflow forecasting. *J. Hydrol. Eng.* 15, 275–283. doi:10.1061/(asce)he.1943-5584.0000188

Conflict of Interest: The authors declare that the research was conducted in the absence of any commercial or financial relationships that could be construed as a potential conflict of interest.

frontiers in Materials

ORIGINAL RESEARCH
published: 22 April 2021
doi: 10.3389/fmats.2021.590390

Damping Variation Effects in Vehicle Semi-active MR Suspensions: A Stress Concentration Analysis

Carlos A. Vivas-Lopez[1], *Juan C. Tudon-Martinez*[1]*, *Alfonso Estrada-Vela*[2], *Jorge de Jesus Lozoya-Santos*[2] *and Ruben Morales-Menendez*[2]

[1]School of Engineering and Technologies, Universidad de Monterrey, San Pedro Garza García, Mexico, [2]School of Engineering and Sciences, Tecnológico de Monterrey, Monterrey, Mexico

Semi-active vehicle suspensions are used to improve the limited comfort performance of passive vehicle suspensions by varying the damping coefficient according to a control strategy. These benefits have been usually studied in a transient and frequency domain, but rarely in a multi-body dynamic analysis considering the mechanical components and their joints. In this study, the controllability effects of a magnetorheological (MR) damper on the mechanical components of a McPherson automotive suspension are investigated using a stress concentration analysis. Finite element analysis was used with a Quarter of Vehicle (QoV) suspension model configured with an MR damper, and then compared with the passive damper. The simulation results show that an SA damper in the suspension not only improves the dynamic behavior of a road vehicle, but it also has the positive effect of reducing the stress concentrations in a critical suspension element, the knuckle, that are generated by high amplitude road profiles such as rough roads or dangerous street bumps.

Keywords: magneto-rheological damper, finite element analyses, semi-active suspension, quarter of vehicle, vehicle dynamics

OPEN ACCESS

Edited by:
Ramin Sedaghati, Concordia University, Canada

Reviewed by:
Xiaomin Dong, Chongqing University, China
Jiong Wang, Nanjing University of Science and Technology, China
Masoud Hemmatian, Concordia University, Canada

***Correspondence:**
Juan C. Tudon-Martinez
juan.tudon@udem.edu

Specialty section:
This article was submitted to Smart Materials, a section of the journal Frontiers in Materials

Received: *01 August 2020*
Accepted: *15 February 2021*
Published: *22 April 2021*

Citation:
Vivas-Lopez CA, Tudon-Martinez JC, Estrada-Vela A, de Jesus Lozoya-Santos J and Morales-Menendez R (2021) Damping Variation Effects in Vehicle Semi-active MR Suspensions: A Stress Concentration Analysis. Front. Mater. 8:590390. doi: 10.3389/fmats.2021.590390

1 INTRODUCTION

Semi-active (SA) suspension systems have become one of the best options for improving the performance of conventional passive dampers (Lord-Corporation, 2018). They have a wide range of applications, from home appliances to transportation vehicles, to structural applications (Kumar et al., 2019). Magnetorheological (MR) dampers are the most used type of SA suspension system in the industry (Jiang et al., 2012). These types of dampers have the advantages of a continuously adjustable damping coefficient with a fast transition response, a relatively low energy input to operate, and require minimal packaging (Alghamdi et al., 2014).

SA and active suspension systems are appearing more frequently in passenger vehicles and with current market demands, the automotive industry requires original equipment manufacturers (OEMs) to achieve shorter product development process times (Vinodh et al., 2013), especially with the incursion of startups disrupting this field (Ferràs-Hernández et al., 2017). In order to cope with rapidly changing market demands and bigger competition, one of the main ways to achieve shorter product development times is to use concurrent techniques instead of a linear process (Kušar et al., 2004). In this process, rapid prototyping, computer-aided design, and engineering are essential tools. One of the most critical steps in this process is the virtual validation of the design, which is achieved by finite element methods (FEM).

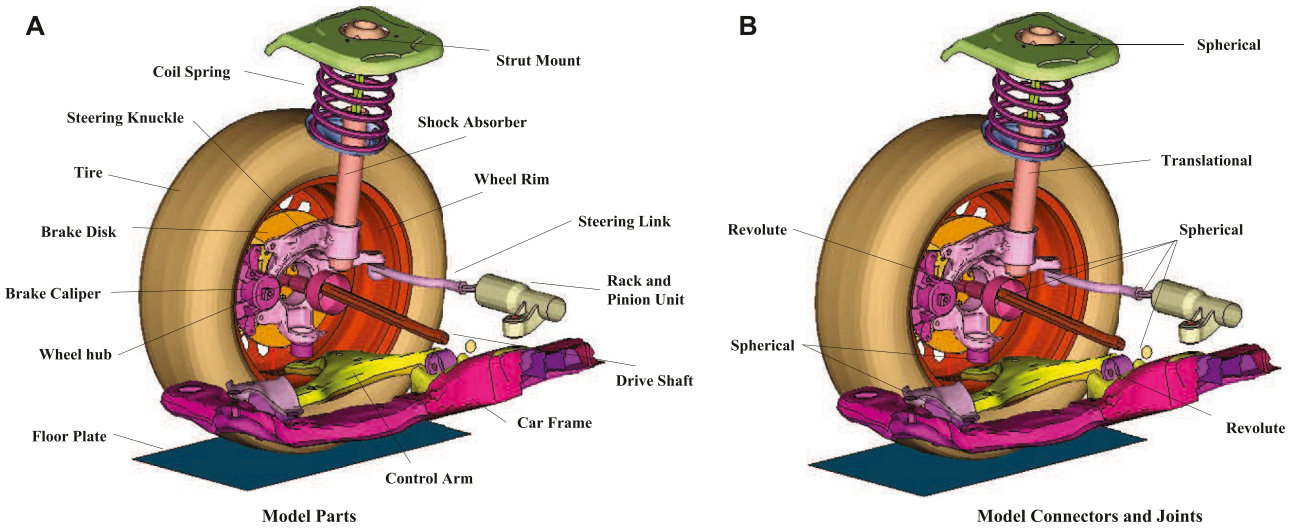

FIGURE 1 | McPherson suspension in a QoV model of a sedan vehicle showing its components.

FEM tools are used for different areas of the suspension system. One focus is to represent the nonlinear behavior of the viscous fluid inside the damper, as in (Guo et al., 2019), where the authors proposed a 2D flow model to predict the transition of the MR fluid to the post-yield region. The other main topic is to analyze the mechanical behavior of suspension components. In (Ossa et al., 2011), the authors used a FEM analysis to predict failure in ball joints. In (Kulkarni et al., 2016), the authors analyzed the effects of increased vehicle mass on the suspension system element life of in-wheel motor vehicles; and in (Lee and Yang, 2013), the authors developed a method to evaluate the torsional stiffness of a torsional beam under different load applications.

The effects of the controllable damping coefficient, on how the vehicle behaves regarding handling and ride comfort, is also being studied (Jugulkar et al., 2016). evaluated a damper design capable of changing its coefficient by actively opening or closing flow holes (Alexandru, 2020), studied different control strategies to improve driving performance, and (Tudon-Martinez et al., 2019) analyzed how the damper model affects the control strategy performance. In addition (Tudón-Martínez and Morales-Menendez, 2015), proposed a method to use the controllability characteristics to compensate when a failure occurs in the damper.

From the presented review, it is clear that the focus in literature has been on the effects on vehicle dynamics generated by an adaptable suspension system, rather than on the mechanical implications on its components. Thus, an analysis of the mechanical effects of controllability in suspension elements equipped with an MR damper was conducted in this study. This case study included a quarter of the vehicle multi-body model evaluated by LS-DYNA®, which is a general-purpose finite element program capable of simulating highly non-linear and transient dynamic problems.

Recently, some studies have researched the force, strength and/or stress analysis in automotive suspensions with passive dampers for particular vehicle designs, such as solar vehicles or racing cars, and especially for fatigue analysis purposes (Ijagbemi et al., 2016; Odabaşi et al., 2019; Rui et al., 2019). All of these analyses have been carried out in simulation scenarios using different multi-Physics software. In this study, a multi-physics software is also used to perform the FEM analysis. The main contribution of this paper is a stress concentration analysis of an automotive SA suspension control system in tandem with a dynamic behavior analysis (in both time and frequency), showing how these results may complement the performance evaluation task in the design process of new SA suspension products (e.g., dampers, sensors, controllers, etc.).

The article is structured as follows: In **Section 2**, the model description, FEM considerations, controllers to be used as the study case, and the proposed tests are presented. Then, in **Section 3**, the results are presented, first detailing the characteristics of the experimental MR damper, then its frequency and time performance compared to a passive damper, and finally a stress concentration analysis using FEM for a multi-body model of a McPherson automotive suspension. Finally, **Section 4** concludes that the semi-activity property of an MR damper can reduce the stress concentrations in the suspension components in contrast to a passive damper and introduces further work from this research group.

2 MATERIALS AND METHODS

A multi-body dynamic model of a Quarter of Vehicle (QoV) was used with FEM simulations of the suspension system at different damping configurations. **Figure 1** illustrates the general elements of a typical McPherson suspension assembly, also it is the multi-body model representation programmed in the LS-DYNA® software.

2.1 QoV Model

The FEM simulations used to analyze the stress concentration of an SA suspension system are based on a decentralized QoV topology. A typical QoV model is represented by a sprung mass (m_s) and an unsprung mass (m_{us}), as shown in

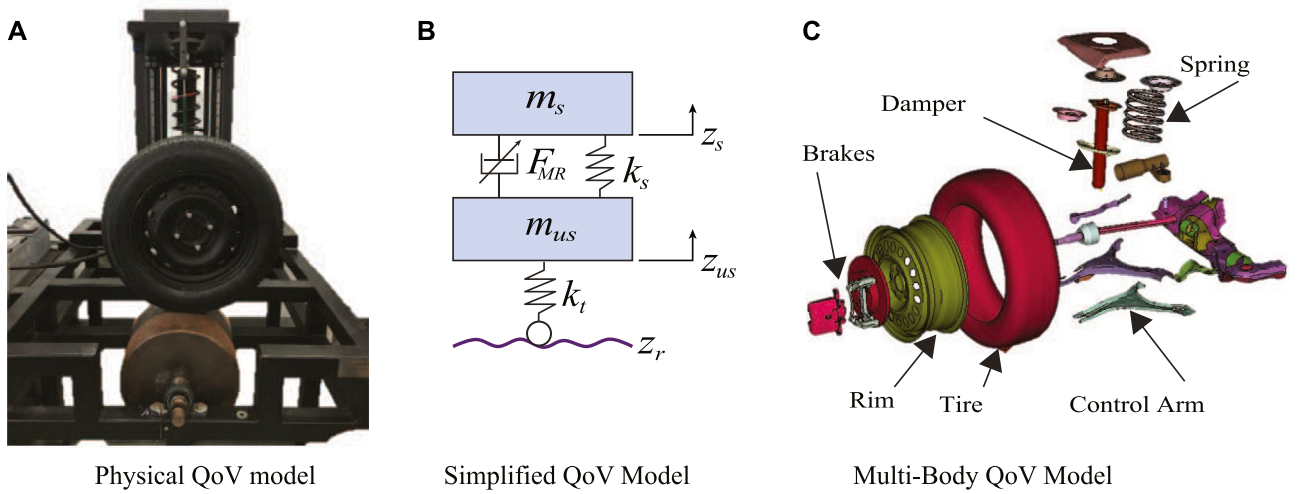

FIGURE 2 | Different QoV model conceptualizations: **(A)** physical platform, **(B)** 2-dimension simplified representation and **(C)** the multi-body model used in the study.

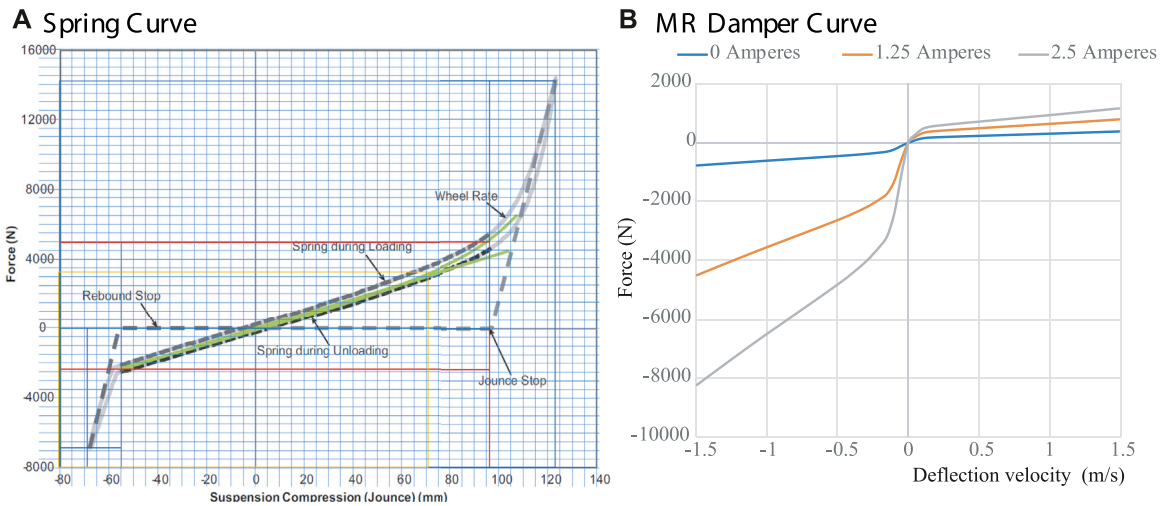

FIGURE 3 | (A) Stiffness force of the coil spring [Solid-Gray—Real curve, Dashed-Gray—Linearized curves and Solid-Green proposed value] and **(B)** variable damping force of an MR damper [Blue—0A, Orange—1.25 A and Gray—2.5 A].

Figure 2B. The linear spring stiffness coefficient k_s and an MR damper force (F_{MR}) represent the suspension components between both masses that absorb/eliminate road disturbances. The stiffness coefficient k_t models the wheel tire. The vertical position of the mass m_s (m_{us}) is defined by z_s (z_{us}), while z_r corresponds to the road disturbance. The system dynamics are given by

$$\begin{aligned} m_s\ddot{z}_s &= -k_s(z_s - z_{us}) - F_{MR}, \\ m_{us}\ddot{z}_{us} &= k_s(z_s - z_{us}) - k_t(z_{us} - z_r) + F_{MR}. \end{aligned} \tag{1}$$

The QoV model parameters of **Eq. 1** are identified on the experimental platform in **Figure 2A**. **Figure 3A** presents the real characteristic curve of the coil spring, the linear zone of the spring stiffness is marked with a green line and its corresponding jounce/rebound stop regions marked with dashed-gray lines. From this figure two data points where obtained, a constant parameter (43.2 N/mm) for the simplified QoV simulations and a look-up table for the finite element analysis (FEA) model. **Figure 3B** shows the variable damping force of an experimental MR damper whose actuation varies from 0 to 2.5 A. The damper stroke is 40 mm, and it has asymmetric performance in its compression/extension effects. The characterization of these components was performed independently of the QoV topology using a universal material testing machine. **Figure 2C** shows an exploded view of the QoV model with all suspension components to illustrate the mechanical joints considered in this study for the FEA tests.

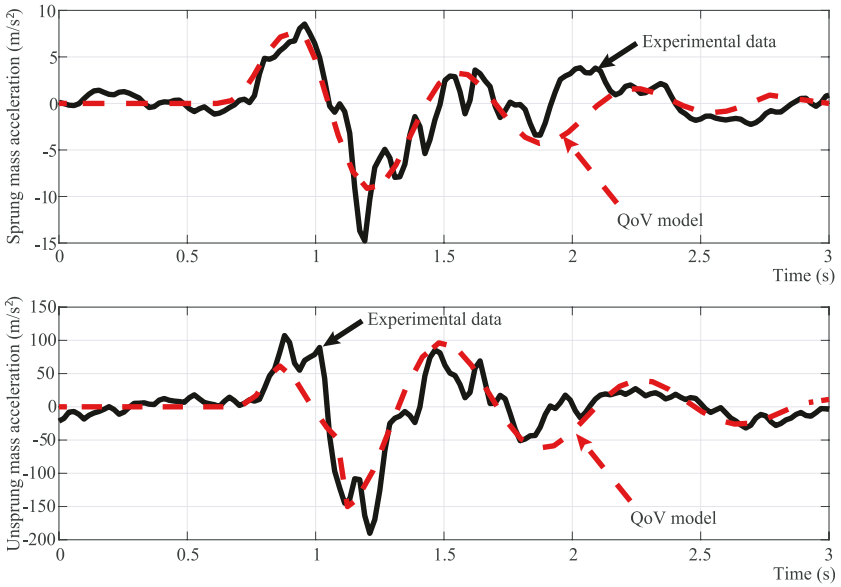

FIGURE 4 | Performance of the identified QoV model (dashed-red) parameters compared to experimental data (solid-black). **(A)** Sprung. **(B)** Unsprung mass curve.

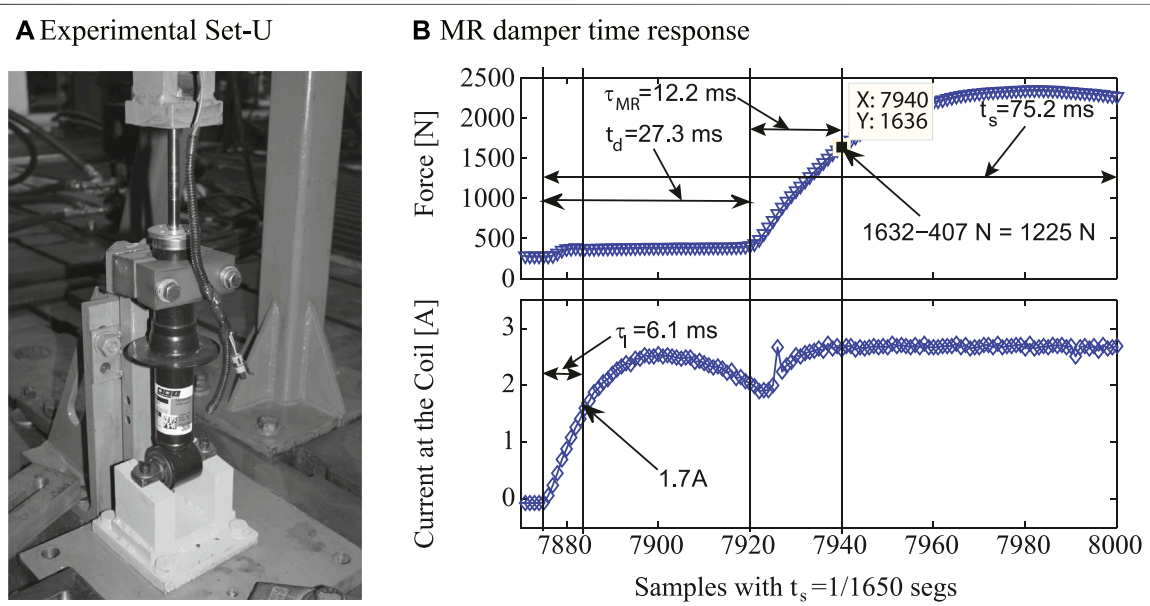

FIGURE 5 | Experimental MR damper tested in a universal material testing machine and its time-response dynamics.

In order to estimate the values of the m_s, m_{us}, and k_t parameters a linear least-squares method was used, the performance of which is shown in **Figure 4**. The experimental data was obtained measuring the accelerations of the m_s and m_{us} under a road profile test. The data was then compared with the resultant model under the same road input. The estimation of the sprung mass of the QoV model is 415 kg, and for the unsprung mass is 80 kg, both associated with a sedan-type commercial car. The estimated linear tire stiffness is 225 N/mm. In the simulation tests, the wheel-road contact is ensured.

2.2 MR Damper Characterization and Modeling

The MR damper considered in this study is manufactured by BWI, **Figure 5A**, and it uses electric current levels (u) from 0 to

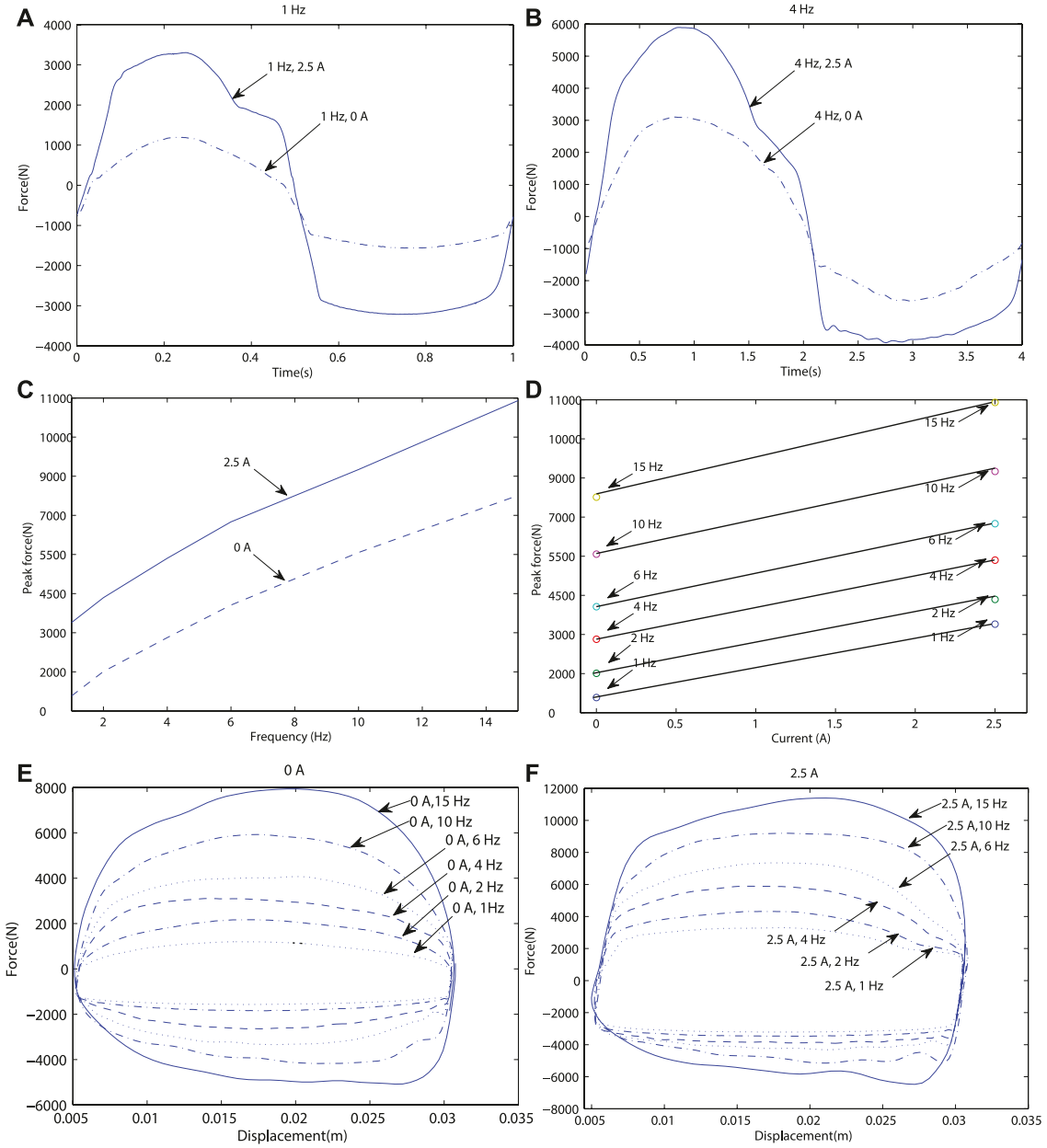

FIGURE 6 | Operational characteristics of the MR damper.

2.5 A, with 0 A being associated with the lowest damping coefficient and 2.5 A with the maximum level. The MR damper has an approximate rod stroke of ±40 mm and a calculated transient response of 39 m **Figure 5B**. The time response presented in **Figure 5B** was obtained using a triangular displacement input to the damper to ensure a constant speed neglecting other dynamical effects, then at the middle of the displacement a change in current was introduced to the damper coil to modify the generated damping force. The resultant time reported is from the moment the current signal is commanded to the time force, reaching 90% of its final value.

Figure 6 shows the general controllability characteristics of the MR device and its variable energy absorption capacity. A key characteristic the damping force of an MR shock-absorber is that it can be increased by means of the current signal, but also by increasing the excitation frequency. For instance, **Figures 6A,B** show that the force increments when the electric current is changed, and this effect is consistent when the frequency of motion increases. **Figure 6C** clearly shows the direct proportionality between the electric current and MR force as well as the direct proportionality between the excitation frequency and MR force. Similarly, **Figure 6D** shows how the maximum force value changes depending

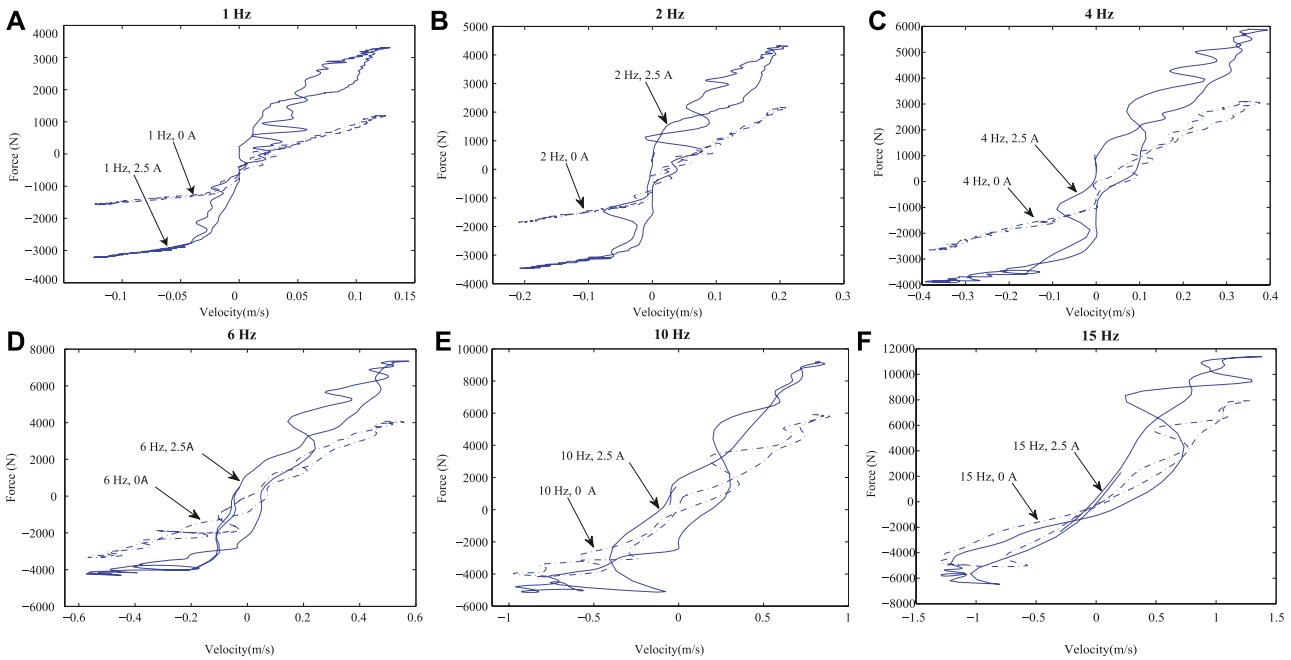

FIGURE 7 | FV characteristic curves of the MR damper at different frequencies [1, 2, 4, 6, 10, and 15 Hz] and electric current inputs [0 A (dashed-blue) and 2.5 A (solid-blue)].

TABLE 1 | Estimated parameters for the asymmetric algebraic model of (Guo et al., 2006).

Parameter	Extension	Compression	Units
f_c	1355.30	605.63	N/A
c_0	6366.46	3838.21	Ns/m
c_1	5.92	53.46	Ns/m
k_0	0.01	−5171.11	N/m
k_1	10.56	24.45	N/m

on the electric current input and the excitation frequency, in a directly proportional manner. **Figures 6E,F** show the Force-Displacement (FD) characteristic maps. It should be noted that the MR damper has asymmetrical behavior, that is, the maximum achievable force level is lower when the damper is subjected to a compression force than when it is in extension, this effect is especially noted when increasing the frequency. Extension behavior, the positive force part of the graph, has a

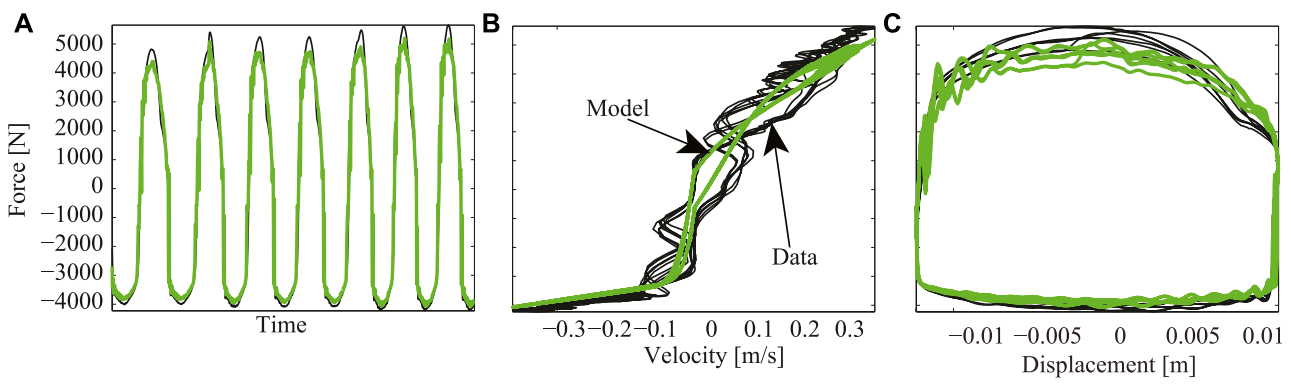

FIGURE 8 | MR damper model (green) performance evaluation vs measured data (black): **(A)** Transient response of the model, **(B)** FV characteristic curve, and **(C)** FD characteristic curve. In this case, the experiment was performed with electric current of 2.5 A as damper control input and 4 Hz as frequency of excitation of the shock absorber deflection.

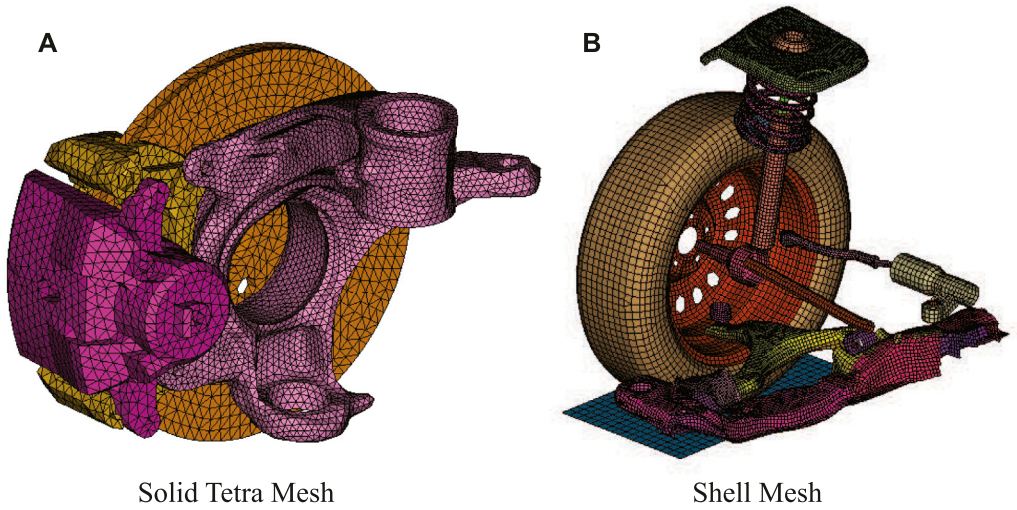

FIGURE 9 | Mesh used on the different elements for the FEA analysis of the QoV model.

more linear increment than compression behavior, which increments tend to flatten faster, as it can be seen in **Figure 4B**.

Figure 7 presents in further detail the force dependency on the excitation frequency by analyzing the Force-Velocity (FV) characteristic curves. For this characterization, a fixed amplitude sinusoidal signal, which only changes its frequency, was applied to the damper deflection. It is also worth mentioning that the velocity scale in each figure is different, so the full effect of the frequency could be observed. **Figure 7** presents the FV diagrams for two electric current levels, 0 and 2.5 A, at frequency set of {1, 2, 4, 6, 10, 15} Hz. It can be observed that as the frequency increases, the hysteresis of the force also increases; this effect is caused by the turbulent flow generated inside the tube (Zhang et al., 2016). It can also be observed that the asymmetry between the jounce/rebound effects increases at a higher frequency of motion (de J Lozoya-Santos et al., 2012), and (Vivas-Lopez et al., 2015).

This experimental characterization was used to propose approximated FV curves, as shown in **Figure 3B**, for the MR damper, which was then programmed into the LS-DYNA® software for the FEM simulations.

The MR damper model used for the FEM analysis was proposed by Guo et al. (Guo et al., 2006). This model focuses on reproducing the nonlinear bi-viscous and hysteretic behaviors of the MR fluid. The nonlinear MR damping force (F_{MR}) modeled is defined by

$$F_{MR} = \underbrace{c_0\dot{z}_{def} + k_0 z_{def}}_{\text{passive damping force}} + uf_c\, tanh\left(c_1\dot{z}_{def} + k_1 z_{def}\right), \qquad (2)$$

where the five coefficients have physical meaning, $z_{def} = z_s - z_{us}$ is the suspension deflection and $\dot{z}_{def} = \dot{z}_s - \dot{z}_{us}$ is the deflection velocity. The characteristics of a linear elastomer is included in the stiffness factor k_0, where c_0 is a passive damping coefficient. u is the control input applied to the damper (in this case, varying from 0 to 2.5 A), f_c is related to the dynamic yield force of the MR fluid, while c_1 and k_1 are coefficients related to the pre-yield and post-yield regions of the SA damper.

To represent the asymmetry of the MR damper in **Eq. 2**, two sets of parameters were estimated, one for when the damper is under compression and the other set for when the damper is under extension. The parameters are listed in **Table 1**.

Figure 8 shows a qualitative evaluation of the fit performance of the estimated model in comparison to the experimental data. In these plots, it can be observed that the considered model captures most of the behavior of the real data, with slight saturation near the maximum forces achieved by the real damper. For a more extensive modeling and qualitative evaluation study of the performance of the algebraic model of (Guo et al. 2006) for the MR damper, readers can refer to the work by (Tudón-Martínez et al., 2012).

2.3 FEM Considerations

The developed model includes most of the parts of the front suspension. It was simplified by using a shell mesh with an average size of 8 mm for most of the parts, as shown in **Figure 9B**, while the knuckle and brake caliper are modeled using a solid tetra mesh with an average size of 5 mm, as shown in **Figure 9A**.

The QoV model was constrained by allowing only vertical displacement on the car frame and strut mount. All other parts were constrained only by their mechanical connections, which were simplified with revolute, spherical, and translational joints to properly model the load transfer and kinematics of the suspension mechanism. Contact mechanics were defined for all parts and gravity was implemented. Motion along the z-axis was prescribed to the rigid floor plate to simulate road input.

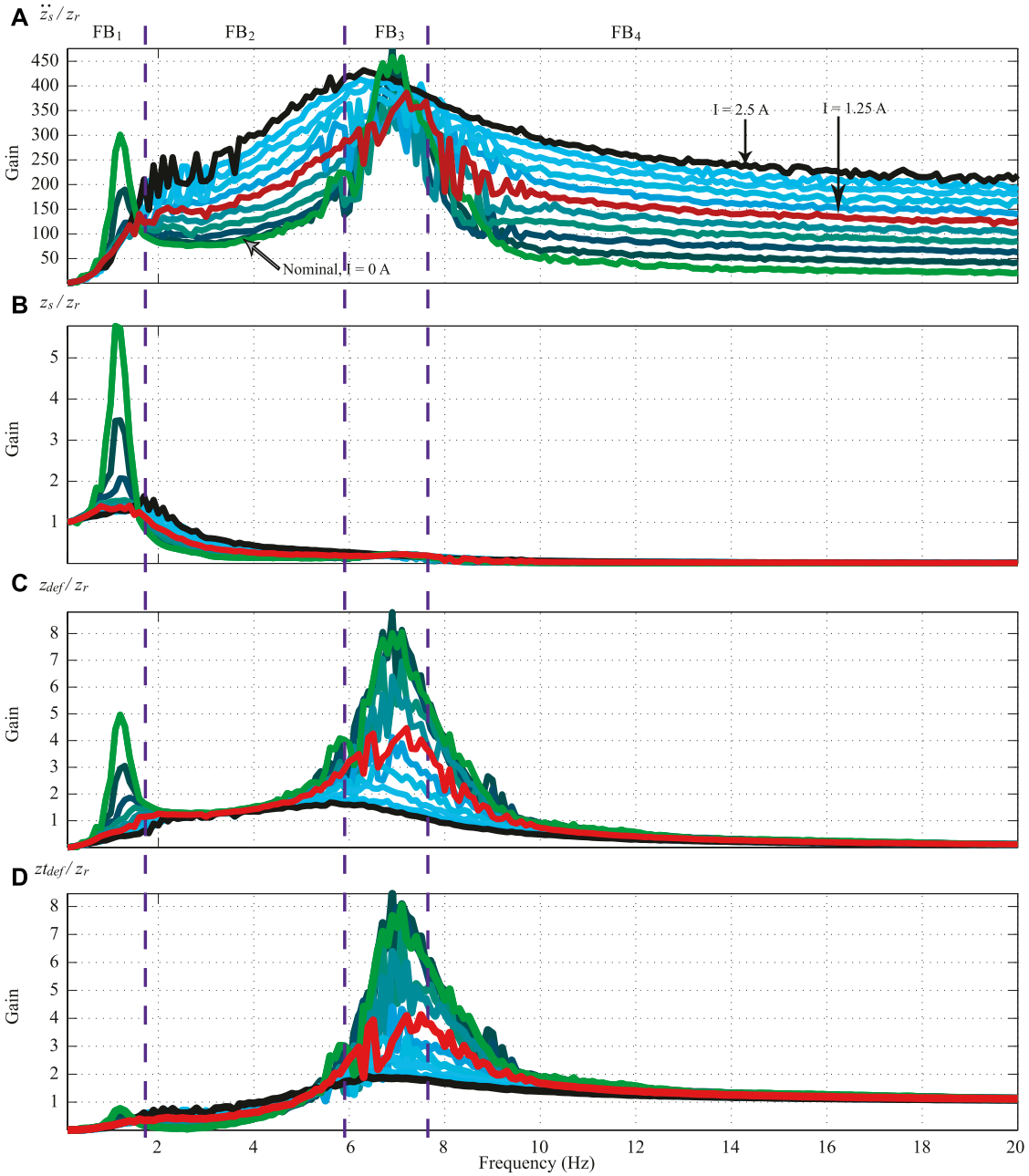

FIGURE 10 | Frequency response analysis for the simplified QoV model dynamics at different electric current inputs [open-loop] (0 A light green, 1.25 A red, 2.5 A black, intermediated levels different tones of blue).

Because the steering knuckle takes most of the load by supporting the wheel, tire, brakes, and sprung mass of the vehicle during vertical dynamics, the analysis focused on this part, which was modeled as cast iron with material properties: density = 7.850e-09 kg/m^3, Young's modulus = 170 GPa, yield stress = 304 MPa, ultimate stress = 502 MPa, and Poisson ratio = 0.29.

The suspension spring and damper were simplified using 1D elements that allow a direct input of the force vs. displacement and force vs. velocity curves, respectively. The tire was simplified as well using a 1D spring element to maintain consistency within the model.

2.4 SA Controller Assessment

In this study, two semi-active QoV-based control strategies were considered to regulate the MR damper actuation in the FEM simulations. The frequency estimation based (FEB) controller proposed in (de Jesus Lozoya-Santos et al., 2011) and the Mix-1 sensor (Mix 1) control algorithm proposed by Savaresi and Spelta (2009) were selected to regulate the MR damper actuation in this

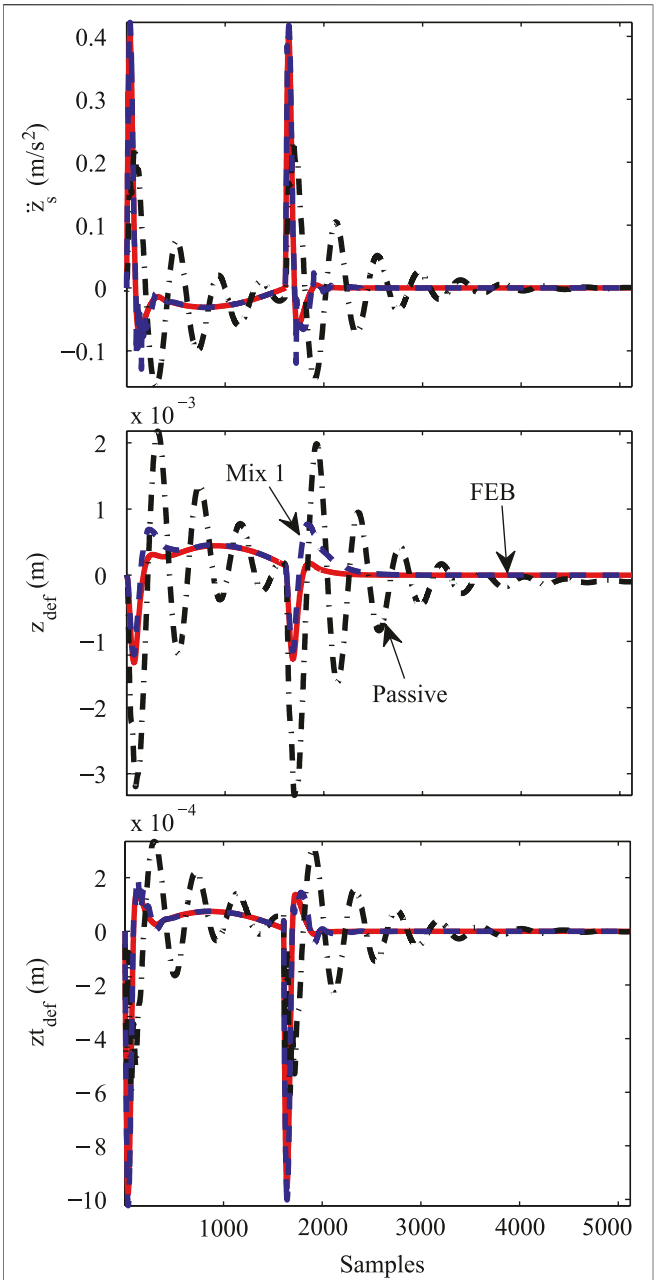

FIGURE 11 | Time domain response of the simplified QoV model for a bump test, comparing the performance of Mix-1 (dashed-blue) and FEB (dashed-red) controllers vs. a passive damper (dashed-black).

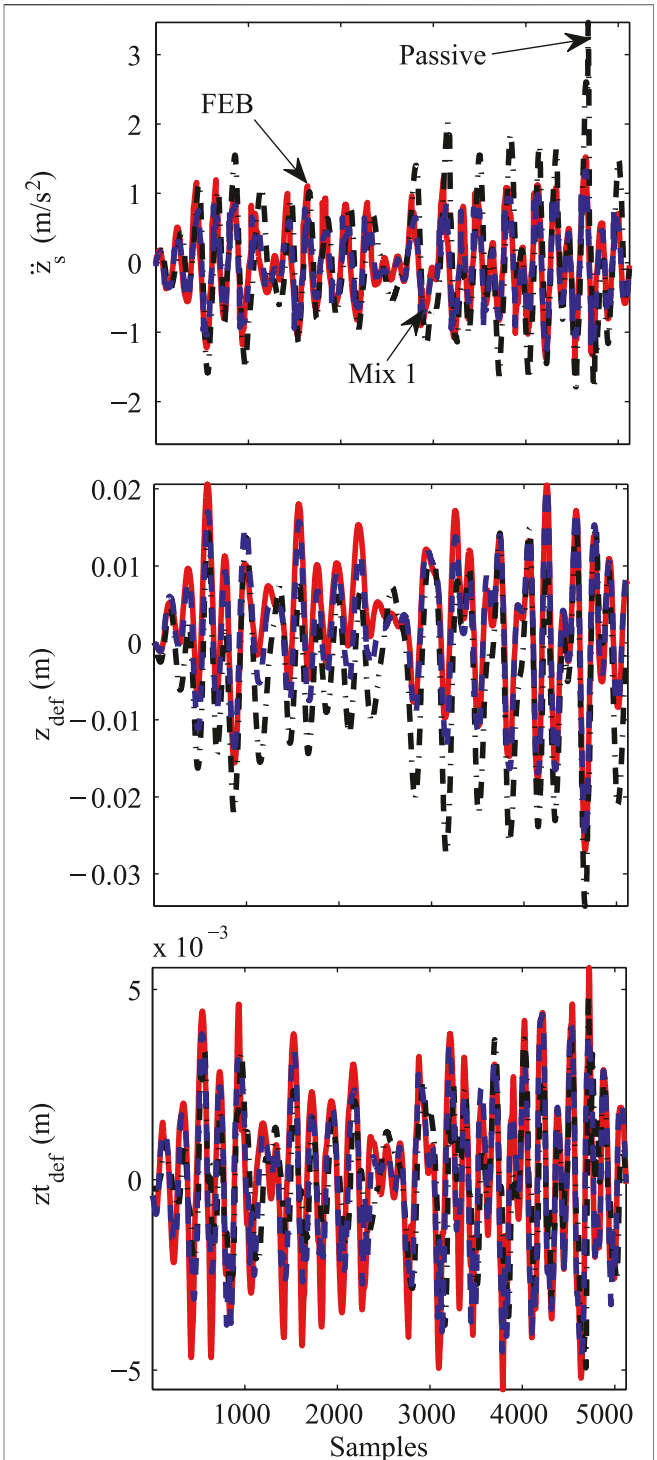

FIGURE 12 | Time domain response of the simplified QoV model for Test 2, comparing the performance of Mix-1 (dashed-blue) and FEB (dashed-red) controllers with respect to a passive damper (dashed-black).

study. Both controllers have better comfort performance than the classical Sky-Hook controller, and their actuation is softer.

The FEB control algorithm is given by

$$F_{MR} = \begin{cases} F_{\text{soft}}\,(I_{\min}) \\ F_{\text{hard}}\,(I_{rm\max}) \end{cases} \quad \begin{array}{l} \widehat{f} \in \{FB_1, FB_2, \ldots, FB_i\}, \\ \text{otherwise}, \end{array} \tag{3}$$

where the MR damping force is soft/hard at the minimum/maximum actuation (electric current), and $\widehat{f}$ is the frequency of the suspension motion that must be estimated. The objective

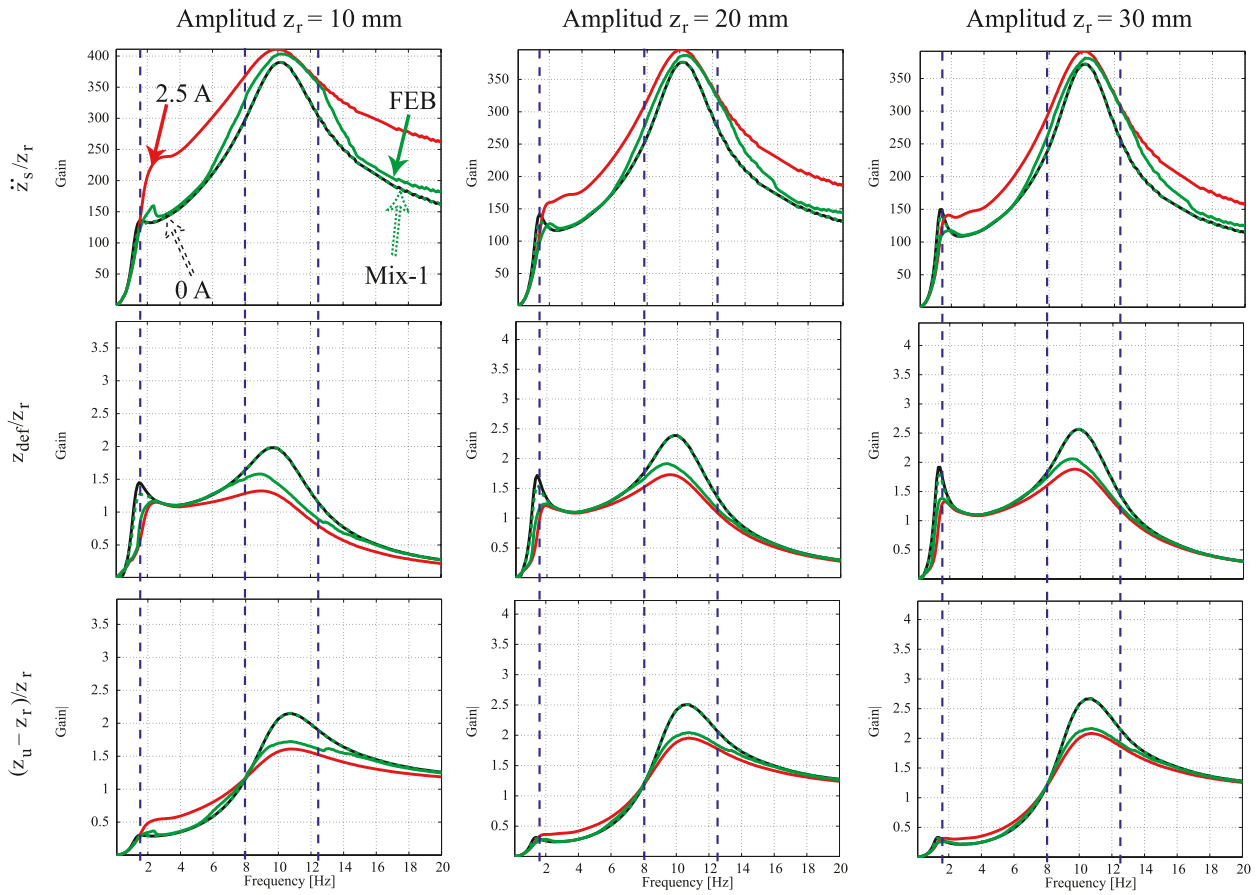

FIGURE 13 | Frequency response analysis of the QoV model at different excitation signals comparing the performance of the Mix-1 (dashed-green) and FEB (solid-green) controllers with respect to the softest [0 A] (dashed-black) and hardest [2.5 A] (solid-red) suspension system.

is to determine the desired frequency bands (FB_i) for the controller by analyzing the frequency response of the suspension at different control input levels (de Jesus Lozoya-Santos et al., 2011).

The Mix 1 controller requires two states of the damper, and the control law is given by

$$F_{MR} = \begin{cases} c_{\max}\dot{z}_{def} & \text{if } (\ddot{z}_s^2 - \alpha^2\dot{z}^2) \le 0, \\ c_{\min}\dot{z}_{def} & \text{if } (\ddot{z}_s^2 - \alpha^2\dot{z}^2) > 0, \end{cases} \tag{4}$$

where α is a frequency parameter of design.

Note that both controllers are extremely simple to design and operate. At each sampling interval, the controllers select a soft or hard damping force according to the dominant frequency content in the vertical motion of the chassis (sprung mass).

The assessment of the SA controller in this study is divided into three sections:

- Comfort and road-holding performance in the time response of the SA suspension controllers in comparison to a passive damper. Passenger comfort can be measured by the vertical motion of the sprung mass (position or acceleration) and the road-holding performance by the tire deflection ($zt_{def} = z_{us} - z_r$).
- Comfort and road-holding performance in the frequency response of the SA suspension controllers in comparison to a passive damper.
- Stress concentrations in the mechanical elements of a SA suspension system due to the MR damper controllability compared to those caused by a passive damper, analyzed by FEM simulations.

2.5 Simulation Tests

Two different simulation tests were used in the aforementioned SA controller assessment:

- Test 1: A 50 mm amplitude bump at 20 km/h vehicle velocity. This test allows the evaluation of the transient performance of the suspension under a typical bump disturbance.
- Test 2: An ISO 8608 road profile test (type D) at a vehicle velocity of 60 km/h. This test was used to assess the MR damping force in a typical suspension environment by considering the normal frequency content of the vehicle vertical movement (from 0 to 20 Hz).

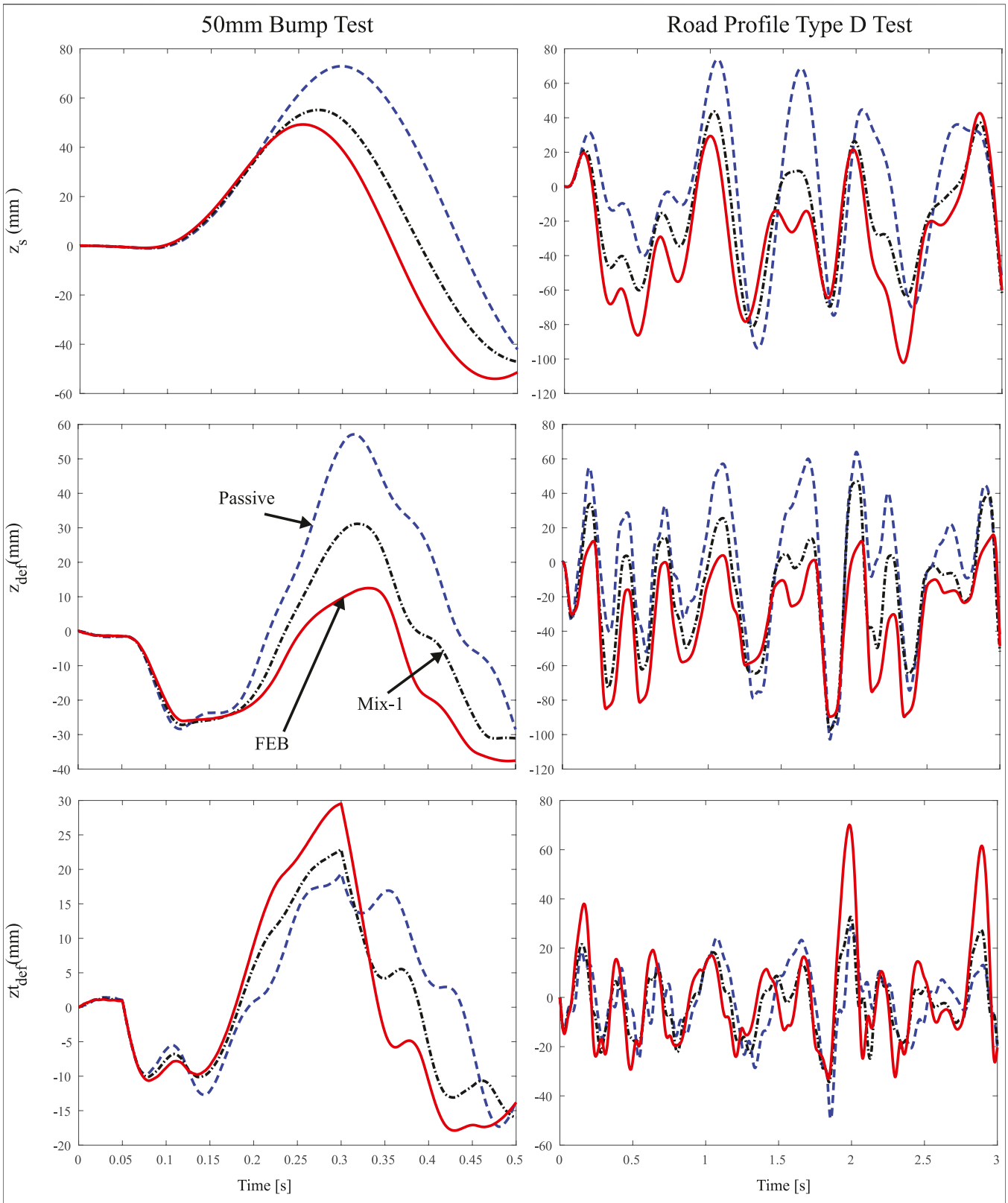

FIGURE 14 | Time domain response for Test 1 and Test 2 performed with the FEM simulation. Performance comparison of Mix-1 (dashed-black) and FEB (solid-red) controllers with respect to a passive damper (dashed-blue).

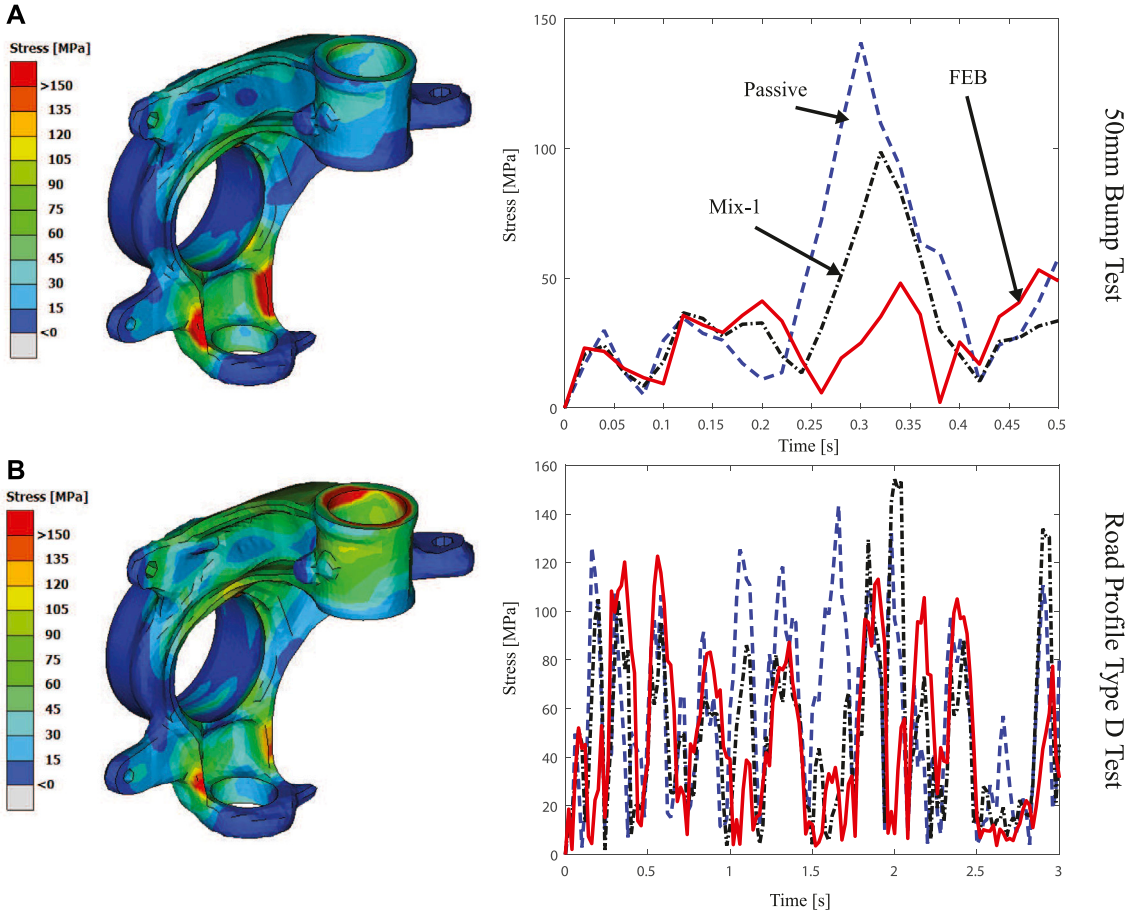

FIGURE 15 | Average Von Mizes stress generated in the knuckle due to different road profiles [**(A)** 50 mm bump road test **(top)** and **(B)** Type D road profile **(bottom)**] under different control strategies [Passive (dashed-blue), FEB (solid-red) and Mix-1 (dashed-black)].

As a benchmark for the controller assessment, both tests were also performed on a passive suspension. Time and frequency response analyses were carried out in a Matlab/Simulink® environment and the FEM simulations with the LS-DYNA® software.

3 RESULTS AND DISCUSSION

In this section, the simulation results in the time and frequency domains for the SA controller are discussed along with the FEM simulation results.

3.1 QoV Controllers Evaluation

The considered MR damper model, defined in **Eq. 2**, was embedded in the QoV model dynamics of **Eq. 1** to assess the time and frequency performance of the SA suspension controllers. This evaluation was carried out using the Matlab-Simulink® software.

Because the FEB and Mix-1 control algorithms use the frequency response analysis of the SA suspension for design, **Figure 10** illustrates the frequency response of the open-loop QoV model dynamics at several electric current inputs; z_r is a sinusoidal signal with an amplitude of 30 mm from 0 to 20 Hz. In **Figure 10**, each color line corresponds to the frequency response of the quarter car suspension system at different electric current value, from 0 to 2.5 A. In this case, **Figure 10A** is the frequency response of the sprung mass acceleration, **Figure 10B** is the position of the sprung mass, **Figure 10C** is the suspension deflection and **Figure 10D** the tire deflection. Due to the electric current modifies the viscous damping coefficient in the semiactive shock-absorber, making it softer or harder, the responses of the quarter car suspension system vary according to the damper force, i.e., according to the electric current value as damper control input. These variations occur mainly close to the frequencies of resonance of the sprung and unsprung mass of the quarter car suspension system.

In these plots of **Figure 10**, it can be observed that there are four frequency bands of interest. For example, in FB_1 (that encloses the resonance frequency of m_s), the acceleration and position of the sprung mass has a higher gain at 0 A and is reduced when the electric current is at maximum (2.5 A). On the other hand, in FB_3 (which encloses the resonance frequency of

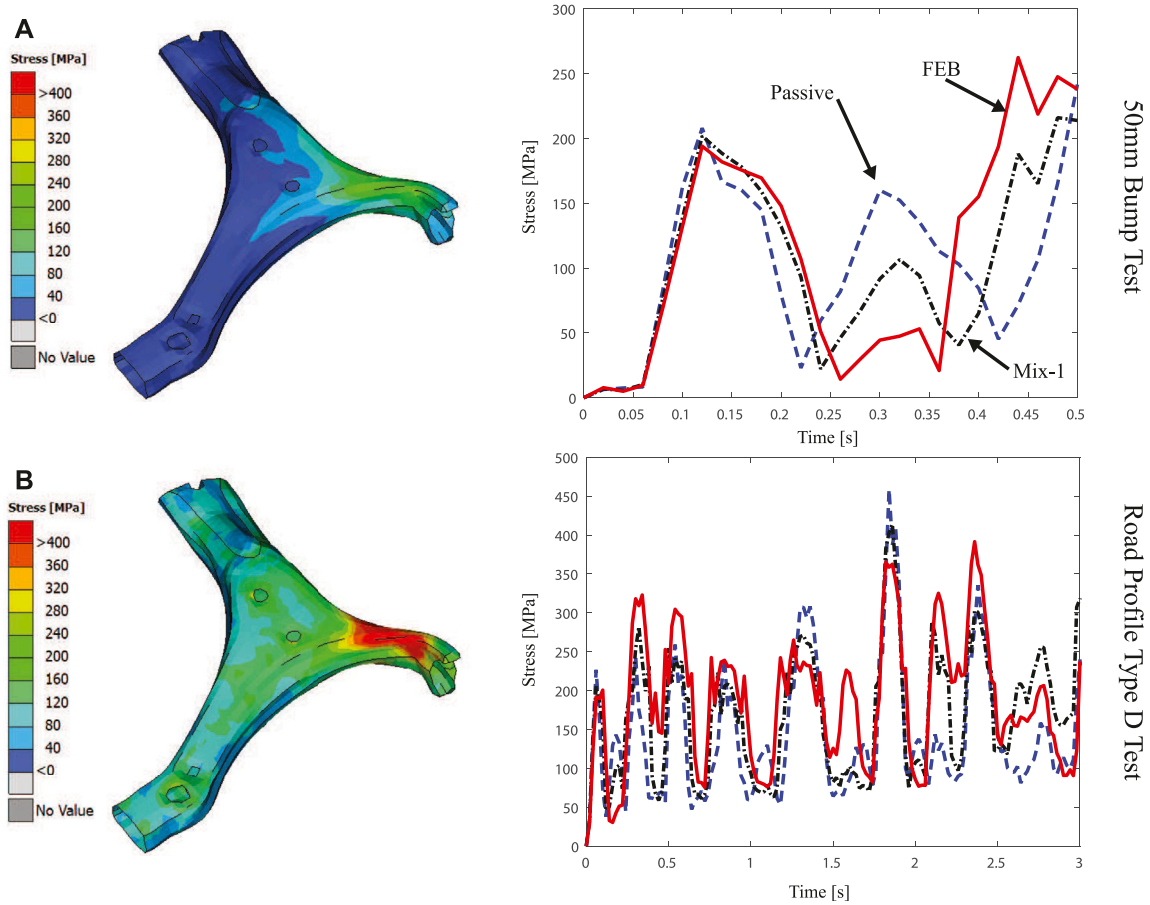

FIGURE 16 | Average Von Mizes stress generated in the Control Arm due to different road profiles [**(A)** 50 mm bump road test **(top)** and **(B)** Type D road profile **(bottom)**] under different control strategies [Passive (dashed-blue), FEB (solid-red) and Mix-1 (dashed-black)].

m_{us}), the sprung mass acceleration has a lower gain when the electric current is below 1.25 A, and in this same FB_3, the tire deflection is lower when the electric current is greater than 1.25 A, meaning that the damping configuration in this frequency band can be oriented to passenger's comfort or road-holding performance in opposite ways. These findings were used to design the FEB and Mix-1 controllers for comfort or road-holding control orientations.

Figure 11 illustrates the assessment of the transient response of the SA controllers for Test 1, considering two bumps. Clearly both SA controllers have better comfort and road-holding performance than the passive suspension, because the motion is lower and softer in the $\ddot{z}_s$ and zt_{def} signals, respectively. Also, the suspension deflection z_{def} is lower for the SA dampers than for the passive damper, i.e., the MR damper has less vertical movement than the passive one.

For Test 2, the time response of the different damping configurations is shown in **Figure 12**. In this case, the SA suspension controllers offer better passenger comfort and less suspension deflection movements than the passive damper. However, because the road profile is sufficiently rough, the tire deflection is similar for all damping configurations.

To assess the frequency performance of the SA suspension controllers, sinusoidal signals in z_r from 0 to 20 Hz at three different amplitudes (10, 20, and 30 mm) were used. Note that both controllers have lower gain in the sprung mass acceleration than the hardest suspension (at 2.5 A). The best comfort performance for the whole frequency range was obtained with the Mix-1 control algorithm. However, by analyzing the frequency response of the tire deflection in **Figure 13**, the FEB controller had lower gain z_{tdef}/z_r than the softest suspension (at 0 A) around the frequency band FB_3, i.e., close to the resonance frequency of m_{us}. Since the FEB controller is oriented to make the suspension harder at high vehicle velocities (i.e., at frequencies around the resonance frequency of m_{us}), the tire has less deflection such that the gain z_{tdef}/z_r of this controlled system is lower than that one obtained at 0 A, because at 0 A the damper is softer and consequently the tire will have more vertical motion. This means that the Mix-1 controller is better for comfort, while the FEB controller maintains the best balance between comfort and road-holding.

3.2 FEM Evaluation

The QoV model parameters, including the MR damper model coefficients, were introduced into the LS-DYNA® software for the

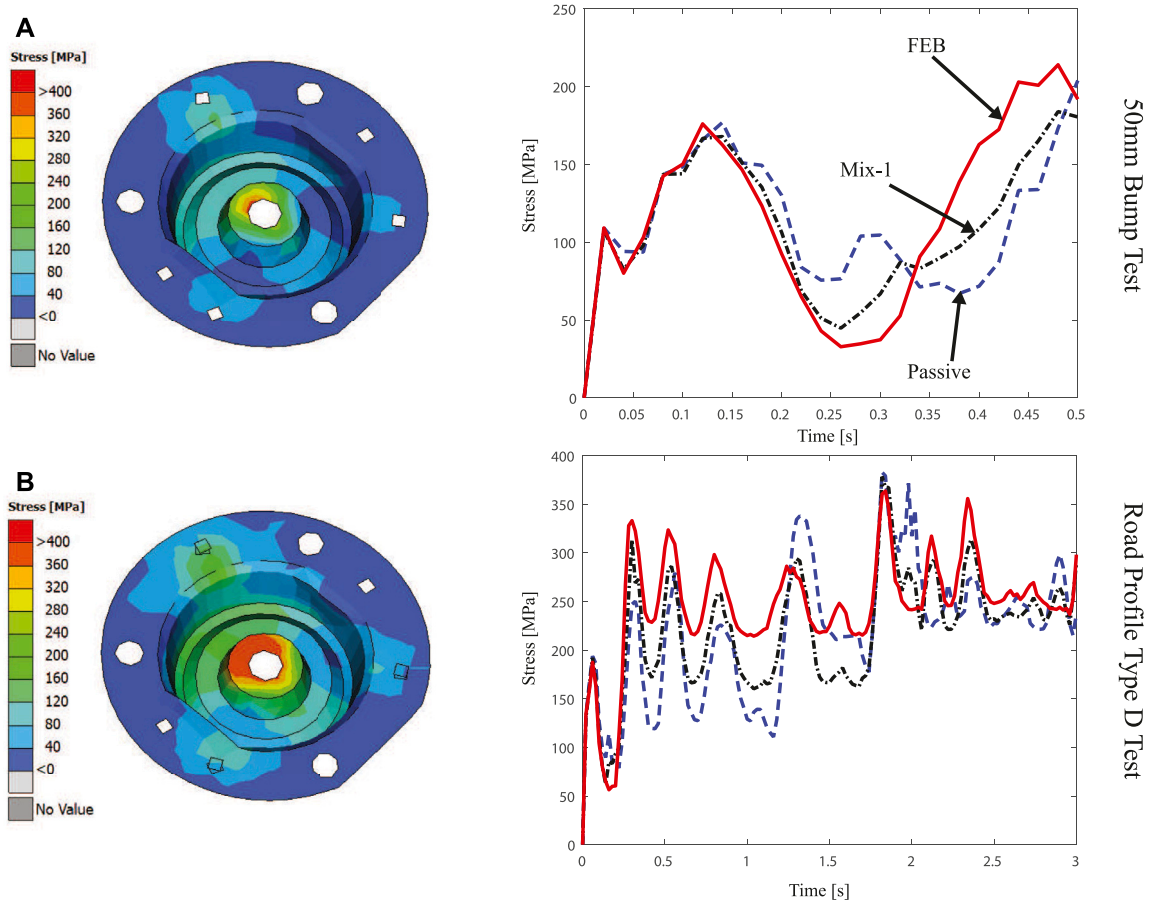

FIGURE 17 | Average Von Mizes stress generated in the Wheel Mount due to different road profiles [**(A)** 50 mm bump road test **(top)** and **(B)** Type D road profile **(bottom)**] under different control strategies [Passive (dashed-blue), FEB (solid-red) and Mix-1 (dashed-black)].

FEM simulations. As in Matlab/Simulink, in the multi-physics program LS-DYNA®, the same tests were performed considering the two SA suspension controllers in comparison with the passive damper.

Figure 14 shows the time domain response of the SA suspension controllers for both tests compared to the passive suspension. The results are congruent with the simulations in Matlab/Simulink, i.e., the SA controllers improve the suspension performance compared to a passive damper. The passive damper shows a higher suspension deflection z_{def} than the SA controllers for both tests, i.e., it has less dissipation capability for the suspension movement. Similarly, the SA controllers have minor magnitudes in the oscillations of the sprung mass position z_s for both tests, i.e., the SA controllers improve the passenger's comfort in comparison to the passive suspension. The tire deflection in the FEM simulations has similar behavior for all damping configurations as it occurs in the simulations with Matlab/Simulink.

To evaluate the effect of the MR damper in the mechanical suspension elements, the three McPherson suspension components with the most stressed concentrations were selected in this analysis: steering knuckle, control arm, and wheel mount. **Figure 15** presents the stress concentrations at the steering knuckle of the suspension caused by different road profiles. **Figure 15A** represents the stress concentration for the bump test and **Figure 15B** for the ISO road profile test. It can be seen from these figures that having an SA suspension control strategy helps to decrease the stress concentration at the knuckle, possibly contributing to extended life of the component.

Figure 16 presents the stress concentrations at the control arm of the suspension. **Figure 16A** represents the stress concentration for the bump test, here, having any control strategy contributes to reducing the rebound effect after the abrupt movement caused by the bumper at 0.3 s. **Figure 16B** shows the effects of the ISO road profile test, in this case having a control strategy reduces the maximum generated stress in comparison with respect to the passive damper, e.g. the 450 MPa generated by the passive damper around the 2 s are reduce up to 350 MPa using the FEB controller. For this element, the biggest concentration is located at the base of the arm, where it assembles with the chassis.

The third element is the wheel mount, in **Figure 17** the stress concentrations at this element are presented. **Figure 17A** represents the stress concentration for the bump test, for this one the Mix-1-sensor strategy achieves a better overall performance, maintaining low stress during the rebound after

the bump, as well as during the setting movement at the end of the test. **Figure 17B** shows that by having a passive damper the mean stress value remains lower, but reaches bigger values at peak moments, while the control strategies have a slightly higher average stress during the test but with lower maximums.

The material used for these elements was HSLA steel with a yield stress of 550 MPa and an ultimate stress of 650 MPa, considering those numbers, in none of the elements the stress exceeds the linear deformation limit. Also, it can be appreciated that a rougher road profile generates more stress in the component than a single bump, even when the bump is much more aggressive than the profile. The location of the stress concentrations in these suspension components also depend on the road disturbance conditions. The steering knuckle has the largest stress concentration in the section used to assemble it with the lower control arm, when the road has abrupt irregularities such as a bump the vehicle goes at low velocity. Whereas the front strut that assembles the steering knuckle with the damper, is the section with the most stress concentrations when the road irregularities are high and persistent, such as an ISO road profile type D, and the vehicle goes at 60 km/h. For the control arm element, the largest stress concentration, for both road tests, is located at the base of the arm used to assemble the suspension McPherson with the chassis. However, the ISO type D road profile test generates more stress (up to 450 MPa) than the bump test (up to 260 MPa). Similar to the control arm, the wheel mount element has the biggest stress concentration in the same location for both road tests, in this case the section used to assemble it with the damper rod. The ISO type D road profile test generates more stress (up to 380 MPa) than the bump test (up to 215 MPa).

A well-balanced SA suspension control strategy, such as the FEB controller, demonstrates not only the reduction of undesirable movement in the cabin, but also reduces the stresses generated in the suspension elements caused by high amplitude road profiles. The Mix-1-Sensor control law also behaves better than a passive suspension; however, being oriented to comfort, it causes much higher stresses on the suspension elements than the FEB controller.

4 CONCLUSIONS AND FUTURE WORK

During the course of this study, the benefits of a semi-active (SA) suspension system equipped with a magneto-rheological (MR) damper were confirmed using a simplified Quarter of Vehicle (QoV) model and with a complex multibody model evaluated using sophisticated multi-physics software. Using different SA control strategies, a semi-active damper can truly improve the dynamic performance of a passenger vehicle. In addition, an effect that is not well-known is the possibility of reducing stress concentrations in the suspension elements. Although the stress concentration analysis in automotive suspensions is not widely described in the literature, this paper demonstrates, with simulations based on a Finite Element Method (FEM), that a SA suspension control strategy helps to decrease the stress concentration at the knuckle, contributing to extending the life of the suspension components. FEM simulations in a quarter of cars illustrate that a rough road profile concentrates more stress in the McPherson suspension components than a single bump, i.e., the constant vibration caused by the rough road will wear the suspension components more than sudden bumps in the road.

On the other hand, the selection of the SA suspension control strategy is also an important key to decreasing the stress concentrations at the suspension components. When the SA suspension controller is road-holding oriented, the stress concentrations will be reduced but the comfort performance can be deteriorated. It is therefore recommended to use a balanced or hybrid control strategy between comfort and road holding objectives.

In future work, the authors will extend this study to evaluate not only stress concentrations at a single point in time but will also carry out a fatigue analysis to describe the controllability effects on the suspension elements in the long term for a full vehicle. In addition, in light of the new generation of electric vehicles, this study may also be extended to include in-wheel motor electric vehicles because the extra mass attached to the unsprung mass represents an additional challenge.

DATA AVAILABILITY STATEMENT

The raw data supporting the conclusion of this article will be made available by the authors, without undue reservation.

AUTHOR CONTRIBUTIONS

All authors of this paper contributed equally to this work. All authors have read and agreed to the published version of the manuscript.

REFERENCES

Alexandru, C. (2020). A study on the semi-active suspension systems used for motor vehicles. *Jriss* 2, 16–25. doi:10.33727/JRISS.2020.1.3:16-25

Alghamdi, A. A., Lostado, R., and Olabi, A.-G. (2014). *Magneto-rheological fluid Technology. chapter 3.* Berlin, Germany: Springer. 43–62. doi:10.1007/978-3-642-45176-83

de Jesus Lozoya-Santos, J., Morales-Menendez, R., Tudón-Martínez, J. C., Sename, O., Dugard, L., and Ramirez-Mendoza, R. (2011). Control strategies for an automotive suspension with a mr damper. *IFAC Proc. Volumes* 44, 1820–1825. doi:10.3182/20110828-6-it-1002.03641

de-J Lozoya-Santos, J., Morales-Menendez, R., Ramirez-Mendoza, R., Tudón-Martinez, J. C., Sename, O., and Dugard, L. (2012). Magnetorheological damper-an experimental study. *J. Intell. Mater. Syst. Structures* 23, 1213–1232. doi:10.1177/1045389X12445035

Ferràs-Hernández, X., Tarrats-Pons, E., and Arimany-Serrat, N. (2017). Disruption in the automotive industry: a cambrian moment. *Business Horizons* 60, 855–863. doi:10.1016/j.bushor.2017.07.011

Guo, P., Xie, J., Dong, X., and Huang, Y. (2019). A two-dimensional axisymmetric finite element analysis of coupled inertial-viscous-frictional-elastic transients in magnetorheological dampers using the compressible herschel-bulkley fluid model. *Front. Mater.* 6, 293. doi:10.3389/fmats.2019.00293

Guo, S., Yang, S., and Pan, C. (2006). Dynamic modeling of magnetorheological damper behaviors. *J. Intell. Mater. Syst. Structures* 17, 3–14. doi:10.1177/1045389X06055860

Ijagbemi, C. O., Oladapo, B. I., Campbell, H. M., and Ijagbemi, C. O. (2016). Design and simulation of fatigue analysis for a vehicle suspension system (vss) and its effect on global warming. *Proced. Eng.* 159, 124–132. doi:10.1016/j.proeng.2016.08.135

Jiang, X.-z., Wang, J., and Hu, H.-s. (2012). Semi-active control of a vehicle suspension using magneto-rheological damper. *J. Cent. South. Univ.* 19, 1839–1845. doi:10.1007/s11771-012-1217-9

Jugulkar, L. M., Singh, S., and Sawant, S. M. (2016). Analysis of suspension with variable stiffness and variable damping force for automotive applications. *Adv. Mech. Eng.* 8, 168781401664863. doi:10.1177/1687814016648638

Kulkarni, A., Ranjha, S. A., and Kapoor, A. (2016). Fatigue analysis of a suspension for an in-wheel electric vehicle. *Eng. Fail. Anal.* 68, 150–158. doi:10.1016/j.engfailanal.2016.05.020

Kumar, J. S., Paul, P. S., Raghunathan, G., and Alex, D. G. (2019). A review of challenges and solutions in the preparation and use of magnetorheological fluids. *Int. J. Mech. Mater. Eng.* 14, 13. doi:10.1186/s40712-019-0109-2

Kušar, J., Duhovnik, J., Grum, J., and Starbek, M. (2004). How to reduce new product development time. *Robot Comput. Integr. Manuf.* 20, 1–15. doi:10.1016/S0736-5845(03)00049-8

Lee, D., and Yang, C. (2013). An analytical approach for design and performance evaluation of torsion beam rear suspension. *Finite Elem. Anal. Des.* 63, 98–106. doi:10.1016/j.finel.2012.09.002

Lord-Corporation (2018). *Magneto-rheological (mr) suspension systems—for industrial applications*. Cary, NA: Lord-Corporation.

Odabaşi, V., Maglio, S., and Sorrentino, S. (2019). Static stress analysis of suspension systems for a solar-powered car. *FME Trans.* 47, 70–75. doi:10.5937/fmet1901070O

Ossa, E. A., Palacio, C. C., and Paniagua, M. A. (2011). Failure analysis of a car suspension system ball joint. *Eng. Fail. Anal.* 18, 1388–1394. doi:10.1016/j.engfailanal.2011.03.013

Rui, R., Gong, B., and Fang, Z. (2019). Force and strength analysis of fsae racing suspension based on spatial analytic geometry. *IOP Conf. Ser. Mater. Sci. Eng.* 612, 032022. doi:10.1088/1757-899x/612/3/032022

Savaresi, S. M., and Spelta, C. (2009). A single-sensor control strategy for semi-active suspensions. *IEEE Trans. Contr. Syst. Technol.* 17, 143–152. doi:10.1109/tcst.2008.906313

Tudon-Martinez, J. C., Hernandez-Alcantara, D., Amezquita-Brooks, L., Morales-Menendez, R., Lozoya-SantosLozoya-Santos, J. d. J. J., and Aquines, O. (2019). Magneto-rheological dampers-model influence on the semi-active suspension performance. *Smart Mater. Struct.* 28, 105030. doi:10.1088/1361-665X/ab39f2

Tudón-Martínez, J. C., Lozoya-Santos, J. J., Morales-Menendez, R., and Ramirez-Mendoza, R. A. (2012). An experimental artificial-neural-network-based modeling of magneto-rheological fluid dampers. *Smart Mater. Struct.* 21, 085007. doi:10.1088/0964-1726/21/8/085007

Tudón-Martínez, J. C., and Morales-Menendez, R. (2015). Adaptive vibration control system for mr damper faults. *Shock and Vibration* 2015, 1. doi:10.1155/2015/163694

Vinodh, S., Devadasan, S. R., Vimal, K. E. K., and Kumar, D. (2013). Design of agile supply chain assessment model and its case study in an indian automotive components manufacturing organization. *J. Manufacturing Syst.* 32, 620–631. doi:10.1016/j.jmsy.2013.04.001

Vivas-Lopez, C. A., Hernández-Alcantara, D., Morales-Menendez, R., Ramírez-Mendoza, R. A., and Ahuett-Garza, H. (2015). Method for modeling electrorheological dampers using its dynamic characteristics. *Math. Probl. Eng.* 2015, 1. doi:10.1155/2015/905731

Zhang, H., Zhang, N., Min, F., Rakheja, S., Su, C., and Wang, E. (2016). Coupling mechanism and decoupled suspension control model of a half car. *Math. Probl. Eng.* 2016, 1. doi:10.1155/2016/1932107

Conflict of Interest: The authors declare that the research was conducted in the absence of any commercial or financial relationships that could be construed as a potential conflict of interest.

frontiers in Materials

ORIGINAL RESEARCH
published: 10 May 2021
doi: 10.3389/fmats.2021.640316

Design and Performance Test of a Magnetic Rate Controlled Stage Damper

Guo-Jun Yu[1], Shao-Jie Zhu[1], Cheng-Bin Du[2], Ling-Yun Wang[1] and Jun-Chi Huang[1]*

[1] Faculty of Civil Engineering and Mechanics, Jiangsu University, Zhenjiang, China, [2] Department of Engineering Mechanics, Hohai University, Nanjing, China

In order to control the vibration of civil building structures, a magnetic rate-controlled stage damper (MRCSD) is designed based on a magnetorheological shear thickening fluid (MR-STF). The key technology and performance test of the damper and the parameter identification of the mechanical model are studied. The experimental results show that the main cylinder filled with MR-STF combines the magnetorheological (MR) effect and the shear thickening effect, which has a strong impact on energy dissipation and vibration reduction. Therefore, the designed damper is superior to the traditional viscous damper. With the increase of magnetic field strength, the shear thickening effect of the MR fluid is inhibited and the MR effect is more obvious. The MRCSD can improve the performance of vibration isolation and vibration reduction by controlling damping. Under a different intensity of earthquake, the maximum output can reach 250.2 kN; the mechanical model of the MRCSD is established; and the design parameters of the damper are determined. The theoretical results obtained from the mechanical model of the MRCSD are consistent with the experimental results, which show that the parameter identification method is feasible and effective.

Keywords: magnetorheological shear thickening fluid, magnetic rate controlled stage damper, magnetic field finite element method, parameter identification, performance analysis

OPEN ACCESS

Edited by:
Janusz Goldasz,
Cracow University of Technology, Poland

Reviewed by:
Zhao-Dong Xu,
Southeast University, China
Xuan Shouhu,
University of Science and Technology of China, China
Xianzhou Zhang,
Independent Researcher, Tomago, Australia

****Correspondence:***
Guo-Jun Yu
gjyu9@ujs.edu.cn

Specialty section:
This article was submitted to Smart Materials, a section of the journal Frontiers in Materials

Received: *11 December 2020*
Accepted: *06 April 2021*
Published: *10 May 2021*

Citation:
Yu G-J, Zhu S-J, Du C-B, Wang L-Y and Huang J-C (2021) Design and Performance Test of a Magnetic Rate Controlled Stage Damper. Front. Mater. 8:640316. doi: 10.3389/fmats.2021.640316

INTRODUCTION

In the past 10 has made a lot of achievements [Xu et al., 2003;years, domestic research on magnetorheological fluids (MRFs) Guo et al., 2020; Yang et al., 2020]. Chen et al. (2010) studied the effects of surfactants and thixotropic agents on the sedimentation stability of MRF. Zhu et al. (2019) prepared a MR fluid with iron nanoparticles using a direct current (DC) arc plasma as a dispersion phase, and the experimental results of the MR performance and settlement stability show that the MR fluid with iron nanoparticles has a significant MR effect, and the settlement stability is better than that of carbonyl iron powder. Yi (2011) studied the effect of different surface activities on the stability of MR fluids. Liang and Ou (2006) and Ou and Li (2009)'s self-developed MR dampers have been successfully applied to the wind–rain induced vibration control of the cable-stayed cables of the Binzhou Yellow River Bridge in Shandong Province and achieved good control results. The

multiwinding MR damper designed by Feng et al. (2019) has a higher dynamic range and efficiency than the traditional multiwinding MR damper. Liu et al. (2018) proposed a new type of permanent magnet MR damper for stay cables, which can adjust the damping force by changing the magnetic pole direction of the permanent magnet. It has good working performance and a good control effect on the vibration in each stage of the stay cables. Based on the MR characteristics of the MR fluid, Zhou et al. (2017) designed a dual exit MR damper that can be applied to a vibration reduction system.

As a new type of intelligent fluid, the shear thickening liquid (STF) can respond to external stimulations, such as vibration and shock, without the effect of an external electromagnetic field (Zhao et al., 2018). In recent years, the study of the mechanical properties and mechanism of the STF has attracted extensive attention of researchers (Dullens and Bechinger, 2011; Trulsson et al., 2012; Picano et al., 2013; Seto et al., 2013; Brown and Jaeger, 2014; Wyart and Cates, 2014; Peters et al., 2016; Qin et al., 2017; Wei et al., 2017; Wu, 2018; Liu, 2019). Because of its rapid, significant, and reversible changes in mechanical behavior under the action of external forces, the STF has shown tremendous application prospects in the fields of vibration absorption, individual protection, and shock resistance (Zhou et al., 2016). With the in-depth study of the STF, the impact resistance of the STF has been paid more attention and gradually used in the manufacture of protective devices. Yu et al. (2019) studied a STF isolator with variable damping characteristics, which effectively solved the inherent shortcomings of the linear damping of the traditional isolator. Zhang et al. (2008) designed a single-rod viscous damper with STF as a viscous medium and studied its dynamic characteristics. Liang (2013) developed a new shock transmission unit (STU) with a maximum output of 300 kN based on Silly Putty and tested its slow, fast, and dynamic mechanical properties on a static and dynamic universal testing machine. The results show that the STU has strong rate sensitivity. The greater the test speed, the greater the stiffness of the STU (Liang, 2013; Liang and Zhang, 2015). At present, the STU has been widely used in large civil engineering structures such as the Nanjing Yangtze River Bridge, the Jinmeng Yellow River Bridge, the Dalian Puwan Sea-Crossing Bridge, and the Shuohuang Heavy-Duty Railway Bridge. The MR damper developed based on MR technology has excellent performance and belongs to a kind of intelligent control device with a high proportion of application. At present, its application scope is expanding constantly (Xu and Shen, 2003; Kruti et al., 2014a,b; Choi et al., 2016; Xu et al., 2016; Ying et al., 2019).

It can be seen from the above literature review that the effectiveness of MR dampers for vibration isolation has been confirmed. MR dampers are the most mature energy dissipators in the field of vibration reduction. From the energy viewpoint, its working principle is to change the energy spectrum structure of the vibration source excited by the system to suppress the vibration by dissipating and reducing energy at an appropriate frequency. However, the single working mechanism of vibration reduction leads to the traditional MR damper depending on the damping and vibration reduction, which will not alleviate the rigidity of the civil engineering structure due to its own rigidity. That causes deformation or even failure due to insufficient degree under huge impact load. Therefore, the damper designed in this paper overcomes the said shortcomings and achieves the effect of anti-impact energy dissipation and damping energy dissipation to reduce vibrations.

This paper is presented in the following order. In section "Material Preparation and Testing," MR-STF materials for damper design are prepared. Section "Structural Design and Theoretical Analysis of Mechanical Model of MRCSD" shows the detailed structure and working principle of a magnetic rate-controlled stage damper (MRCSD). Section "Magnetic Circuit Design" introduces the magnetic circuit design of the damper. Section "Performance Test of MRCSD" tests the performance of the damper. Section "Mechanical Model and Parameters Identification" establishes the mechanical model of the damper and determines its parameters. Section "Conclusion" contains some conclusions.

MATERIAL PREPARATION AND TESTING

The MR-STF has both the MR effect and the shear thickening effect. It can be used as a normal "speed control" material and a "fault prevention" material when there is no magnetic field. It has the characteristics of self-adaptation and self-enhancement. The damper can adapt to the environment of different vibration excitation frequencies.

In this experiment, ferric carbonyl (Cl) particles with an average particle size of 3.5 μm were used as magnetic particles; nano-sized silica (SiO_2) particles were used as dispersion phase particles of the STF; ethylene glycol ($HOCH_2CH_2OH$) was used as a dispersion medium of the STF; and anhydrous ethanol was used as a diluent of the STF. In addition, the MR and shear thickening effects of the MR shear thickening fluid (MR-STF) consist of prepared STF and carbonyl iron particles. All the reagents are of analytical purity and purchased from Sinopharm Chemical Reagent Co., Ltd. in China.

The soft magnetic particles used in this paper are carbonyl iron powder produced by Jiangsu Tianyi Ultrafine Metal Powder Co., Ltd., China under the brand name MPS-MRF-15. Its specifications and properties are shown in **Table 1**. The average particle size of carbonyl iron powder is 3.5 μm.

The MR-STF is a new intelligent material with magnetic sensitivity/rate sensitivity. The MR-STF has better stability than the traditional MRF and has a MR effect and shear thickening effect.

Preparation of the MR-STF: The carrier liquid is added to the powder, and the two components are mechanically mixed for 1 h with a stirrer. The resulting suspension is then placed in a vacuum chamber for several hours to eliminate air bubbles. The primary particle size of silica is 1–5 μm, and the density is 2.6 g/ml (s5631, from Sigma Aldrich). The STF is composed of nanosilica particles, glycol, and high-concentration suspension.

TABLE 1 | The performance index of carbonyl iron powder.

Fe content	C content	N content	O content	Average granularity	Loose packing density	Vibration compaction density
98.1%	0.74%	0.9%	0.26%	3.5 μm	2.8 g·cm^{-3}	4.25 g·cm^{-3}

The series of MR shear thickening fluids were prepared by using carbonyl iron particles and STF with different weight fraction ratios.

The rheological properties of the MR-STF were measured by the MCR302 rheometer produced by Anton Paar of Austria. **Figure 1A** shows the curve between viscosity and shear rate of the MR-STF without magnetic field, while **Figure 1B** shows the relationship between viscosity and shear rate of the MR-STF with magnetic field. **Figure 1B** shows that the MR-STF samples have the MR effect.

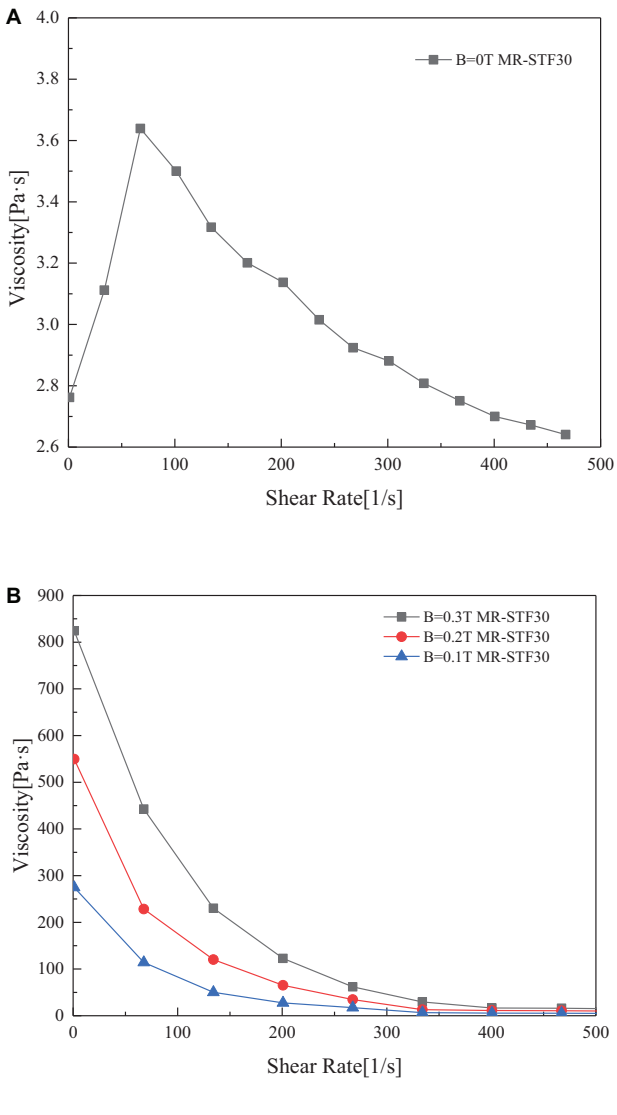

FIGURE 1 | Measured curves between viscosity and shear rate of the MR-STF **(A)** without and **(B)** with magnetic field.

STRUCTURAL DESIGN AND THEORETICAL ANALYSIS OF THE MECHANICAL MODEL OF THE MRCSD

The displacement limit of the damper is designed based on the requirement of story displacement of a structure in an earthquake zone. According to the relevant provisions of the Code for Seismic Design of Buildings (GB 50011-2010) on the maximum floor displacement and floor height ratio (the limit value of the displacement angle between floors), if the height of a single floor is 3 m, there is 3 m × 1/50 = 60 mm, so the maximum design displacement of the damper is ± 60 mm. Considering the displacement of the structure at high frequency and small amplitude, the maximum compression of the decoupling spring is 4 mm.

Structural Design

In this paper, a MR shear thickening fluid with shear thickening effect and MR effect is manufactured. Based on the rate sensitivity and magnetic sensitivity of the MR shear thickening fluid, a MRCSD is designed, which is suitable for various vibration excitation environments and has the function of anti-impact energy dissipation. The basic structure of the damper is shown in **Figure 2**. It mainly consists of a piston rod, a cylinder, a piston, front and rear end caps, coils, and permanent magnets.

Working Principle

The MRCSD has two working units: the main piston part and the auxiliary piston part. The main piston part bears the function of shock resistance and energy dissipation. Through the design of a permanent magnet and an excitation coil, the auxiliary piston part can realize the energy dissipation with continuous variable damping.

The basic working principle of the MRCSD is as follows: The MRCSD is designed with a parallel connection of the main piston part of the anti-impact energy dissipation and the sub-piston part with dual characteristics of MR effect and shear thickening effect. The damper designed in this paper drives the piston to move under the excitation of the external environment. When the seismic displacement is small, the energy dissipation performance is low. The main piston starts to work. With the increase of the displacement, the permanent magnet arranged in the secondary piston produces the MR effect in the working gap between the secondary piston and the main cylinder body, and the energy dissipation performance of the damper increases. When the seismic displacement is large, the energy dissipation performance of the damper increases. After the main piston and the auxiliary piston work together, the output of the damping force can be adjusted by controlling the current. The dual characteristics of the MR effect and the shear thickening effect at the working clearance

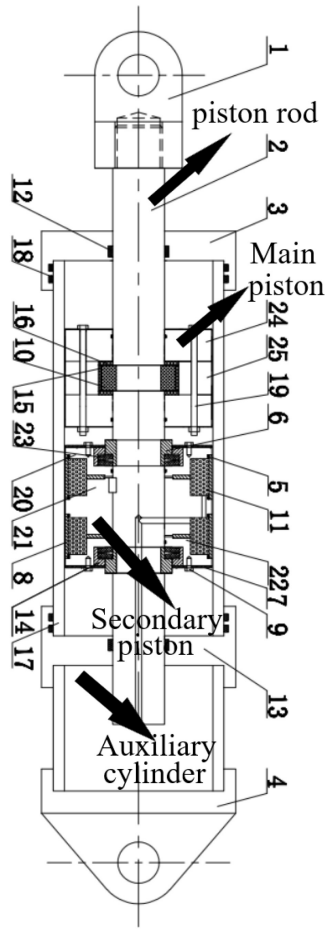

Serial number	Name	Number
25	Main piston 2	1
24	Main piston 1	2
23	Butterfly spring	4
22	Vice piston 3	1
21	Vice piston 2	1
20	Vice piston 1	1
19	Bolt	4
18	O-ring 2	4
17	Main cylinder block	1
16	Sleeve baffle	2
15	Half ring sleeve 2	1
14	Half ring sleeve 1	1
13	Connecting cylinder head	1
12	YX type sealing ring	1
11	Coil	2
10	Semicircular 2	1
9	Screw	8
8	Coil sleeve	1
7	Magnetically insulated copper sheet	2
6	Semicircular 1	2
5	O-ring 1	4
4	Rear cover	1
3	Front cover	1
2	Piston rod	1
1	Single ear ring for shaft	1

Damper assembly drawing

FIGURE 2 | Structural form of the MRCSD.

of the auxiliary piston can be realized, and the vibration reduction effect of the impact energy dissipation and the damping energy dissipation can be achieved. Finally, the effect of continuous variable damp and energy dissipation can be achieved.

Theoretical Analysis of the Mechanical Model

Aiming at a new type of MR stage damper designed in this paper, the mechanical model theory of a MR stage damper is put forward. The basic design parameters of damper structure can be derived from the damping force formula of shear valve viscous damper (Chen, 2012) and can be given by

$$F_1 = \frac{2\pi K L_1 \cdot (R_2^2 - r^2) \cdot \left[(R_1^2 - r^2)(m+1)\right]^m}{\left\{2m\left[\frac{2m+2}{2m+1}R_1 \cdot \left(\frac{h_1}{2}\right)^{\frac{1}{m}+2} + \left(\frac{h_1}{2}\right)^{\frac{1}{m}+3} \cdot \frac{11m^2+12m+3}{(2m+1)(3m+1)}\right]\right\}^m} \cdot V^m \quad (1)$$

In the model, $_{R_1}$ is the inner diameter of the damper cylinder block, r is the radius of the piston rod, $_{R_2}$ is the radius of the main piston, $_{L_1}$ is the width of the main piston, K is the dynamic viscosity of the fluid medium, m is the flow index, $_{h_1}$ is the working clearance of the main piston, and V is the velocity of the piston.

According to the different simplified forms, there are different theoretical calculation formulas for the damping force of shear valve type MR dampers, but the most widely used formula which can directly reflect the relationship between damping force and physical parameters is (Yu et al., 2012)

$$F = \frac{3\eta L[\pi(D^2 - d^2)]^2}{4\pi D h^3} v + \frac{3L\pi(D^2 - d^2)}{4h}\tau_y sgn(v) \quad (2)$$

where F is the damping force, L is the effective length of the piston, D is the inner diameter of the cylinder block, d is the diameter of the piston rod, h is the working clearance, V is the moving speed of the piston, τ_y is the shear yield strength of the MR fluid, and η is the zero-field apparent viscosity of the MR fluid.

The dynamic viscosity of the fluid medium can be derived by introducing the correction term Eq. (2) and can be expressed as

$$K(x) = \begin{cases} kx \cdot sgn(x) sgn(v), S \le C \\ -kx, xsgn(v) < C - S, S > C \\ kx, C - S < xsgn(v) < 2C - S, S > C \\ 0, xsgn(v) > 2C - S, S > C \end{cases} \quad (3)$$

where S is the amplitude of the damper, C is the maximum compression of the disk spring, and k is the elastic constant of the disk spring.

$$F = \begin{cases} F_1 + K(x), \quad -4mm \sim 4mm \\ -\left\{F_1 + \frac{3\eta L_2\left[\pi(D^2 - d^2)\right]^2}{4\pi D h_2} \cdot v \right. \\ \left. + \frac{3L_2\pi(D^2 - d^2)}{4h_2} \cdot \tau_y sgn(v)\right\}, \quad -60mm \sim -4mm \\ F_1 + \frac{3\eta L_2\left[\pi(D^2 - d^2)\right]^2}{4\pi D h_2^3} \cdot v \\ + \frac{3L_2\pi(D^2 - d^2)}{4h_2} \cdot \tau_y sgn(v), \quad 4mm \sim 60mm \end{cases} \quad (4)$$

where F is the damping force of the damper, $_{K(x)}$ is the damping force of the dish spring, $_{F_1}$ is the damping force of the main piston of the damper, $_{L_2}$ is the effective length of the auxiliary piston, and $_{h_2}$ is the working clearance of the auxiliary piston.

Equation 4 provides the guidelines for the design of the size of the MRCSD. After repeated adjustment of the design process, the basic structural parameters of the MRCSD are shown in **Table 2**.

MAGNETIC CIRCUIT DESIGN

Finite Element Simulation of the Magnetic Circuit

The magnetic circuit of the MRCSD mainly includes the magnetic circuit of the auxiliary piston. The magnetic circuit of the auxiliary piston is simulated by the finite element method to determine the parameters of the magnetic circuit. Next, the finite element model of the auxiliary piston is established by using the ANSYS software developed by ANSYS Corporation in the United States. The size of the permanent magnet in the magnetic circuit and the number of turns of the excitation coil are determined by the finite element simulation analysis of the auxiliary piston.

Figure 3A shows the finite element model of the auxiliary piston. A1 is 45 steel; A2 is MR fluid; A3 is air; A4 and A5

TABLE 2 | Basic structural parameters of the MRCSD.

MR-STF complex viscosity	kPas	AMRe/RMRe	MPa/%
MR-STF dosage	5,993 ml	Damper cylinder wall thickness	15 mm
Working clearance of main piston	1 mm	Working clearance of auxiliary piston	1.2 mm
Outer diameter of main piston	198 mm	External diameter of auxiliary piston	197.6 mm
Limit stroke of main piston	60 mm	Limit stroke of auxiliary piston	60 mm
Working clearance length of main piston	132 mm	Working clearance length of auxiliary piston	160 mm
Effective stroke of decoupling spring	4 mm	Number of turns of auxiliary piston coil	800
Piston rod diameter	70 mm	Maximum power	<120 W
Current range of auxiliary piston	0–3 A		

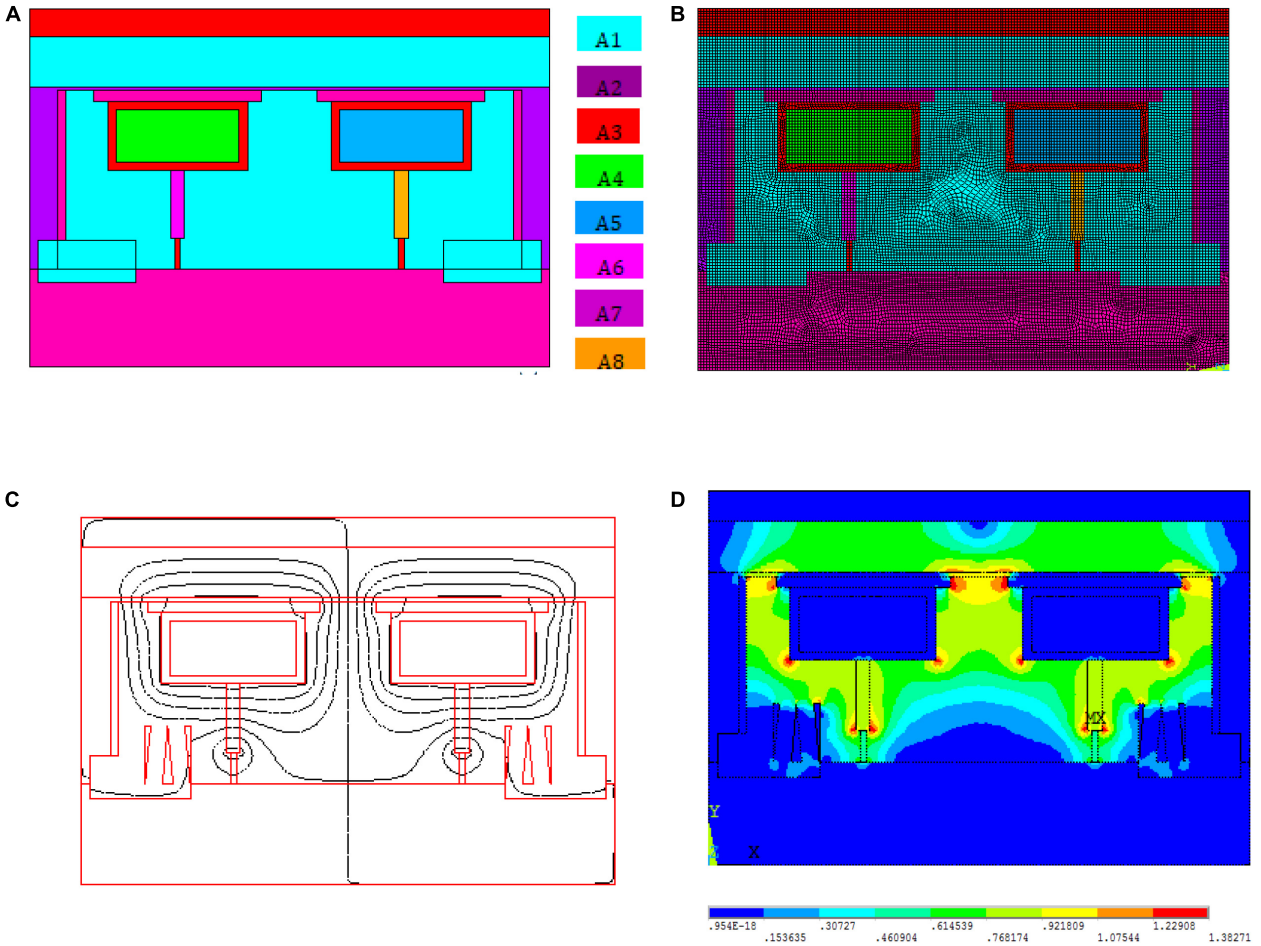

FIGURE 3 | Finite element model of magnetic circuit structure and results: **(A)** material partition, **(B)** finite element mesh, **(C)** distribution of magnetic lines, and **(D)** total flux density distribution.

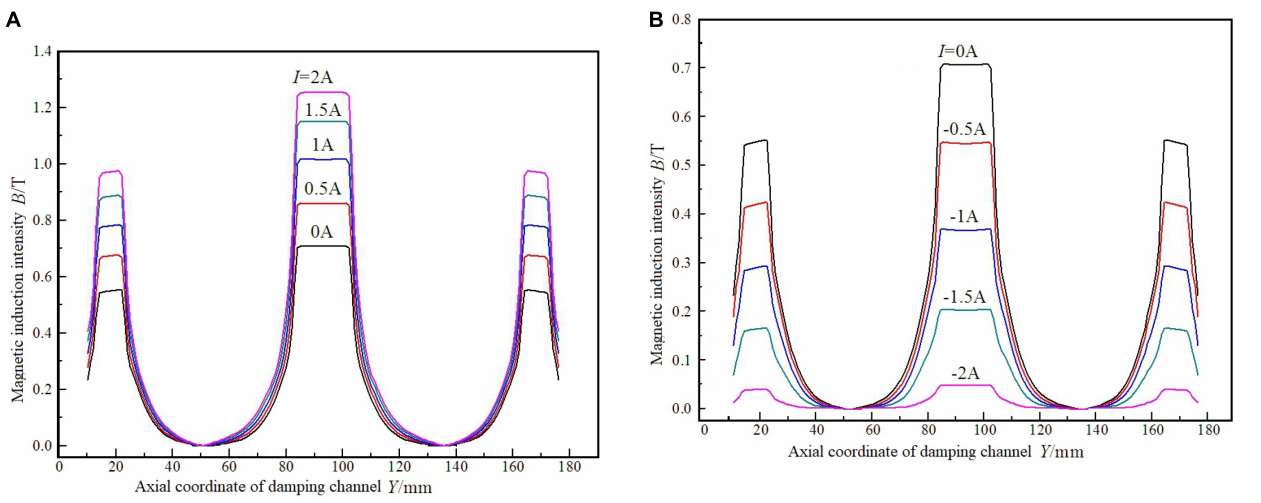

FIGURE 4 | Magnetic induction intensity at working clearance of subpiston. **(A)** Current I is positive. **(B)** Current I is negative.

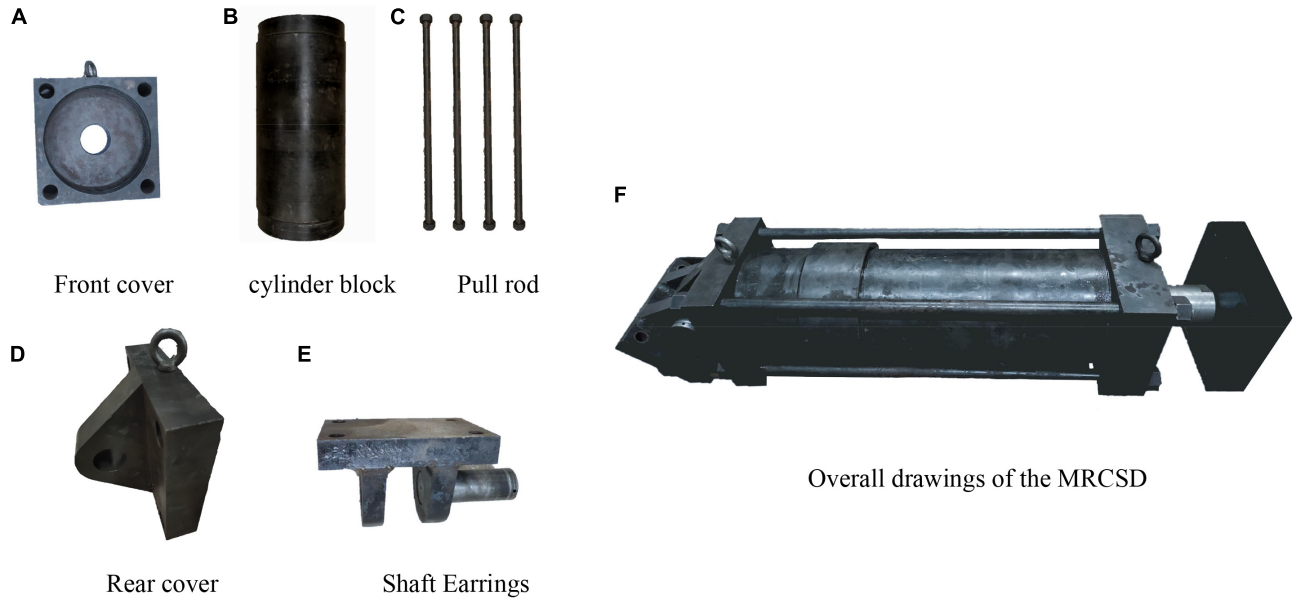

FIGURE 5 | Main components and overall drawings of the MRCSD: **(A)** front cover, **(B)** cylinder block, **(C)** pull rod, **(D)** rear cover, **(E)** shaft earrings, and **(F)** overall drawings of the MRCSD.

are excitation coils; A6 is 0Cr18Ni9 stainless steel; and A7 and A8 are N30 NdFeB permanent magnets. Considering the opposite direction of coercivity of A7 and A8, they are defined as two kinds of materials, respectively, when defining material properties. **Figure 3B** shows its finite element meshing diagram, in which the number of elements is 24,085 and the number of nodes is 24,397.

The distribution nephogram of the magnetic line and the magnetic induction intensity of the magnetic circuit of the auxiliary piston is shown in **Figures 3C,D**.

Magnetic Induction Curve

When the input current I of the excitation coil varies between −2 and 2 A, different magnetic induction intensities can be obtained at the working gap, as shown in **Figure 4**. When the current is in the positive direction, the magnetic induction intensity at the working gap increases with the increase of the current, and with the increase of the current, the increase of the magnetic induction intensity at the working gap decreases, which is caused by the nonlinearity of the material permeability and the saturation magnetic induction intensity close to the material. When the current is negative, the magnetic induction intensity at the working gap decreases with the increase of the current. It can be seen that the interaction between permanent magnet and excitation coil not only realizes the bidirectional adjustment of the damping force of the auxiliary piston but also ensures the output of the damper in case of power failure. It can also be seen from the figure that the magnetic induction intensity in the damping channel mainly concentrates on the magnetic poles, and the magnetic induction intensity between the poles is very small. Therefore, the magnetic induction intensity at each pole can be approximately considered when calculating the damping force of MR dampers.

After the preparation of the MR-STF material, the design of magnetic circuit structure, and simulation analysis, a MRCSD is manufactured. The main components and the overall diagram of the damper are shown in **Figure 5**.

PERFORMANCE TEST OF THE MRCSD

The shear performance test machine of the MRCSD adopts the SDS-300 servo dynamic and static test machine provided by the National Mechanical Experiment Center of Hohai University. The experimental setup is shown in **Figure 6**. The DC power supply is used to connect the excitation coil of the damper secondary piston. During the experiment, the displacement amplitude of the damper is controlled, and the mechanical properties of the damper are tested under the conditions of small displacement, large displacement, and impact. The maximum displacement is 4 mm in the case of small displacement and 60 mm in the case of large displacement, and the input current range was −2 to 2 A.

Under different working conditions, the test results of the MRCSD are shown in **Figure 7**.

Figure 8 shows the load displacement curve of the MRCSD when a different current is applied under different working conditions. It can be seen from the figure that the damping force of the damper increases with the increase of the current and decreases with the decrease of the current, while the damping force changes linearly with the current.

(1) Under the condition of small displacement of a different current, that is, when the amplitude of the damper does not exceed the maximum compression of the Belleville spring by 4 mm, only the main piston works alone, and the dynamic characteristic curve of the damper is shown in **Figure 7A**. The curves of damping force in the figure are inclined to some extent, which is caused by the influence of the Belleville spring. When the piston rod deviates from the balance position, it compresses the spring, and the damping force of the damper increases with the increase of displacement; when the piston rod returns to the balance position, the spring loosens and the damping force decreases with the decrease of the displacement.

(2) Under the condition of large displacement of different current, that is, when the amplitude of the damper exceeds the maximum compression of the Belleville spring by 4 mm, the main piston and the auxiliary piston work together. The load displacement curve of the damper is shown in **Figure 7B**. It can be seen from the figure that both sides of the damping force curve incline to a certain extent, which is caused by the disk spring when the piston rod returns to the balance position from the maximum displacement. Similarly, this characteristic is also beneficial to the vibration control of the structure.

Compared with the damper output under small displacement and large displacement, it can be seen that under small displacement, the adjustable range of the damper output is 37.5–170.6 kN, and the adjustable multiple of the damping force is about 4.5; under large displacement, the adjustable range of the damper output is 192.8–250.2 kN, and the adjustable range of the damping force is about 1.3. It can be seen that for the MRCSD, in the case of small displacement, the output of the damper is smaller, but the adjustable multiple is higher. In the case of large displacement, the adjustable multiple of the damping force is smaller, but the maximum output of the damper is larger. Compared with the traditional oil damper, the MRCSD is more suitable for the vibration control of civil engineering structures.

The hysteretic curves of load displacement under different loads, strokes, and frequencies can reflect the damping dissipation capacity of the device. The test data and theoretical calculation data of the damper's damping characteristics can be seen in **Table 3**.

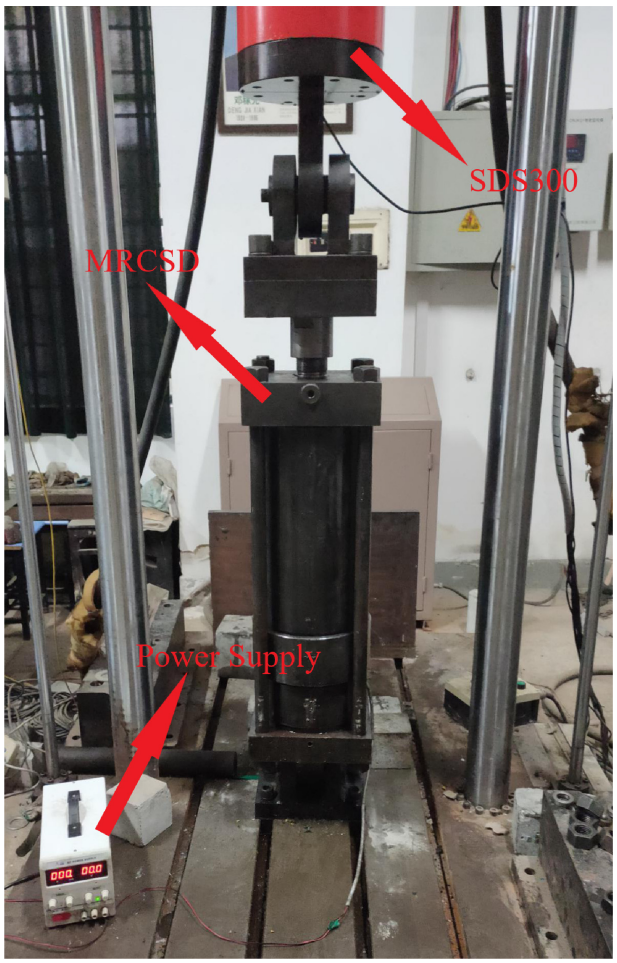

FIGURE 6 | Experimental device of the MRCSD.

MECHANICAL MODEL AND PARAMETERS IDENTIFICATION

Mechanical Model of the MRCSD

It can be seen from the analysis of the mechanical characteristics of the damper that the damping force of the MRCSD is delayed relative to the input displacement. This phenomenon of energy loss is generally called "hysteresis." In order to better describe the mechanical characteristics of the MRCSD, due to the effect of the disk spring, and considering the hysteresis characteristics of the MR damping force and the space phenomenon. Therefore, in combination with Formula (1), the correction formula of the damping force model of the anti-impact energy dissipation damper is shown in Eq. (4):

$$F_2 = \left\{ \frac{3\eta L_2 \left[\pi(D^2 - d^2)\right]^2}{4\pi D h_2^3} v + \frac{3L_2\pi(D^2 - d^2)}{4h_2} \tau_y sgn(v) \right. \\ \left. \left[1 + \mathrm{f}(\mathrm{x})\right] \right\} \cdot \mathrm{L}(x) + F_1 \left[1 + \mathrm{f}(\mathrm{x})\right] + K(x) \quad (5)$$

Among them,

$$\mathrm{L}(x) = \begin{cases} 0, & |S| \le 4 \\ 1, & 4 < |S| \le 60 \end{cases}$$

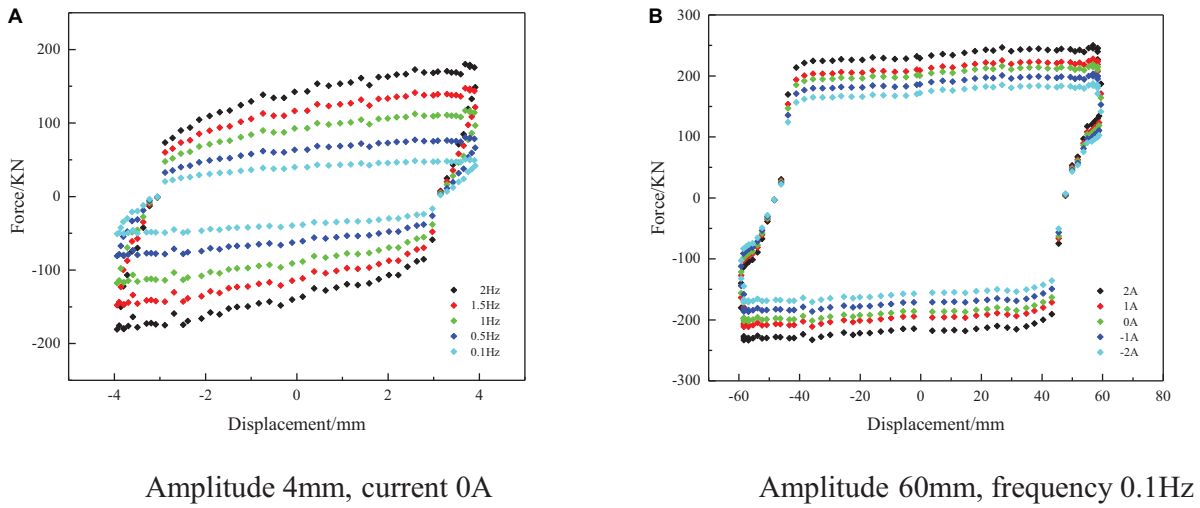

FIGURE 7 | Model and experimental results for force-displacement relationship curves: **(A)** small displacement and **(B)** large displacement.

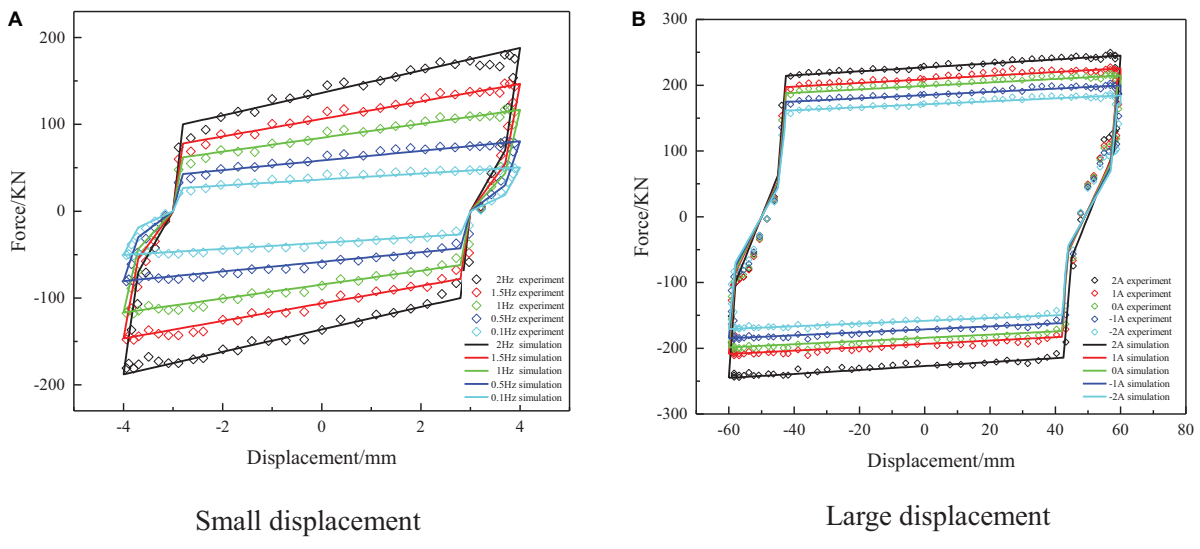

FIGURE 8 | Load displacement curve of MRCSD under different working conditions. **(A)** Amplitude of 4 mm, current of 0 A. **(B)** Amplitude of 60 mm, frequency of 0.1 Hz.

$$f(x) = \begin{cases} \dfrac{xsgn(v) + S - 2x_0}{x_0}, \\ \qquad -S \le xsgn(v) \le x_0 - S \\ -1, \quad x_0 - S \le xsgn(v) \le x_0 + x_1 - S \\ \dfrac{xsgn(v) + S - 2x_0 - x_1}{x_0}, \\ \qquad x_0 + x_1 - S \le xsgn(v) \le 2x_0 + x_1 - S \\ 0, \quad 2x_0 + x_1 - S \le xsgn(v) \le S \end{cases}$$

where S is the amplitude of the damper, x_0 is the absolute value of the lag critical displacement, x_1 is the space of the damper, C is the maximum compression of the Belleville spring, and k is the elastic constant of the Belleville spring.

Parameters Identification

In this paper, the test data of small displacement and large displacement at 0.1 Hz excitation frequency are selected to identify the parameters of the mechanical model. **Figure 7** shows the comparison of the experimental results and fitting curves

TABLE 3 | Comparison of theoretical value and experimental value.

Electric current/A		**2**
Small displacement/kN	Theory	187.9
	Experiment	170.6
Large displacement/kN	Theory	252.6
	Experiment	250.2

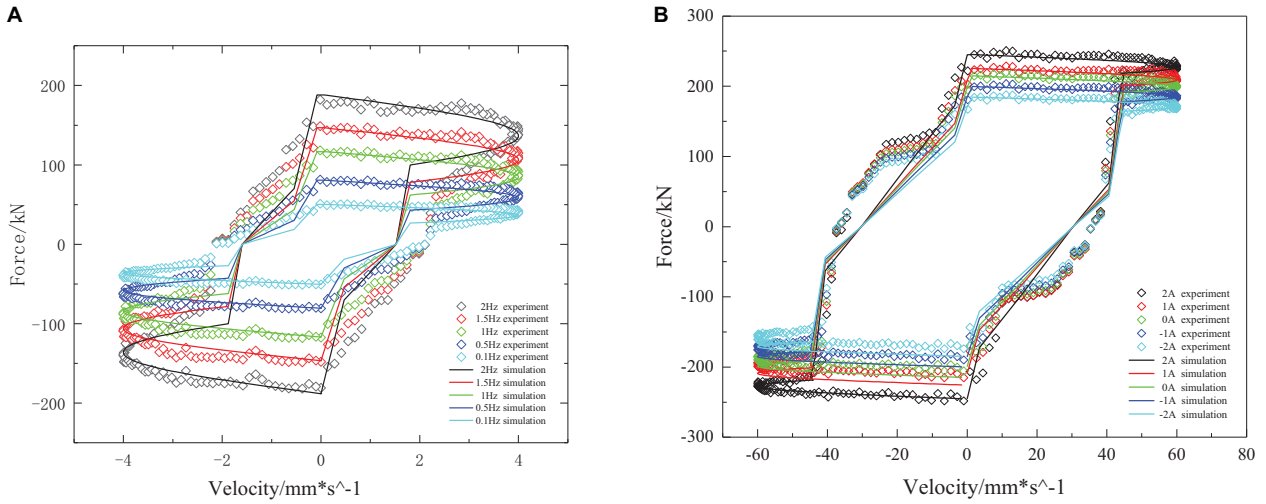

FIGURE 9 | Force–velocity relationship curves: **(A)** small displacement and **(B)** large displacement.

of small displacement and large displacement under different currents. It can be seen from the figure that the dynamic model can well describe the force displacement hysteretic curve of the MRCSD.

It can also be seen from the corresponding force–velocity relationship curve shown in **Figure 9** that the damper force has strong speed sensitivity when the small displacement is shifted, and the damping force increases rapidly when the speed increases. At the same time, the force–speed curve of the damper is fuller when the size displacement is lowered. When the speed increases, the damping force decreases, and the damping force increases when the velocity decreases. There is an obvious damping force lag phenomenon, and the damping force lag phenomenon should be fully considered when establishing the mathematical model of the damper.

CONCLUSION

In this paper, a MRCSD is designed and developed, which can be adapted to the environment of different vibration excitation frequencies. The dynamic mechanical properties of the damper are tested. Based on the comparison between the test results and the theoretical calculation results, the rationality and correctness of the intelligent damper design are verified. Some conclusions can be drawn as follows:

(1) The MR shear thickening fluid used in the damper was prepared and its dynamic mechanical properties were tested. The experimental results show that when the mass fraction of iron particles is lower than a certain value, the MR effect and shear thickening behavior can be observed. At the same time, the new intelligent fluid can be controlled by magnetic field and shear rate. With the concentration of iron particles, the shear thickening effect of the MR-STF is inhibited, while the MR effect is more obvious.

(2) We analyze the development process of MRCSD from the magnetic circuit finite element analysis and structural finite element analysis. The finite element results show that: (1) the structure size and the number of turns of the coil meet the design index, and the magnetic field utilization rate of the magnetic circuit design is higher; (2) with the increase of the positive current, the magnetic induction intensity in the working area gap increases gradually; (3) with the increase of the negative current, the magnetic induction intensity in the working area gap decreases gradually.

(3) The experimental results of the proposed damper show that the MRCSD has the characteristics of control damping, and can achieve the effect of isolation and vibration reduction under different earthquake intensities. The maximum output of the damper can reach 250.2 kN. These indicate that the damper achieves the expected design goal.

DATA AVAILABILITY STATEMENT

The original contributions presented in the study are included in the article/supplementary material, further inquiries can be directed to the corresponding author/s.

AUTHOR CONTRIBUTIONS

All authors listed have made a substantial, direct and intellectual contribution to the work, and approved it for publication.

FUNDING

This work was supported by the National Natural Science Foundation of China (Grant No. 51508237) and the Primary Research and Development Plan of Jiangsu Province (Grant No. BE2017167).

REFERENCES

Brown, E., and Jaeger, H. M. (2014). Shear thickening in concentrated suspensions: phenomenology, mechanisms and relations to jamming. *Rep. Prog. Phys.* 77:046602. doi: 10.1088/0034-4885/77/4/046602

Chen, W. (2012). Theoretical and experimental study on viscous dampers. *Huazhong Univ. Sci. Technol.* 2020:3025863.

Chen, W., Du, C., and Wan, F. (2010). Effects of surfactants and thixotropic agents on the sedimentation stability of magnetorheological fluids. *Funct. Mater. Dev.* 141, 55–58.

Choi, S., Li, W., Yu, M., Li, W., Yu, M., Du, H., et al. (2016). State of the art of control schemes for smart systems featuring magneto-rheological materials. *Smart Mater. Struct.* 25:043001. doi: 10.1088/0964-1726/25/4/043001

Dullens, R. P. A., and Bechinger, C. (2011). Shear thinning and local melting of colloidal crystals. *Phys. Rev. Lett.* 107:138301.

Feng, L., Liu, S., Zhao, J., Wang, X., and Zhao, D. (2019). The design of an innovative multi-winding magnetorheology damper featuring embedded flow passage. *Smart Mater. Struct.* 562:012141. doi: 10.1088/1757-899x/562/1/012141

Guo, Y. Q., Zhang, J., He, D.-Q., and Li, J.-B. (2020). Magnetorheological elastomer precision platform control using OFFO-PID algorithm. *Adv. Mater. Sci. Eng.* 2020:3025863.

Kruti, S., Phu, D. X., and Choi, S. -B. (2014a). Rheological properties of bi-dispersed magnetorheological fluids based on plate-like iron particles with application to a small-sized damper. *J. Appl. Phys.* 115:203907. doi: 10.1063/1.4879681

Kruti, S., Phu, D. X., Seong, M., and Upadhyay, R. V. (2014b). A low sedimentation magnetorheological fluid based on plate-like iron particles, and verification using a damper test. *Smart Mater. Struct.* 23:027001. doi: 10.1088/0964-1726/23/2/027001

Liang, J. (2013). Design and testing of shock transmission device for bridge protection. *Appl. Mech. Rev.* 405–408, 1517–1520. doi: 10.4028/www.scientific.net/amm.405-408.1517

Liang, J., and Ou, J. (2006). Viscous damping control analysis of wind-induced buffeting of long-span cable-stayed bridge deck. *Seism. Eng. Eng. Vibr.* 26, 139–144.

Liang, J., and Zhang, X. H. (2015). Rheological properties of SP in shock transmission application. *J. Mater. Civil Eng.* 27:04014250. doi: 10.1061/(asce)mt.1943-5533.0001227

Liu, M. (2019). Study on performance optimization and application of shear thickener. *China Univ. Sci. Technol.*, China.

Liu, P., Ma, L., Wang, B., and Wang, Z. (2018). Study on the new type of permanent magnet MR damper for stay cable and its parameter optimization. *Bridge Construct.* 48, 51–55.

Ou, J. P., and Li, H. (2009). Design approaches for active, semi-active and passive control systems based on analysis of characteristics of active control force. *Earthq. Eng. Eng. Vibr.* 8, 493–506. doi: 10.1007/s11803-009-9119-z

Peters, I. R., Majumdar, S., and Jaeger, H. M. (2016). Direct observation of dynamic shear jamming in dense suspensions. *Nature* 532, 214–217. doi: 10.1038/nature17167

Picano, F., Breugem, W. P., Mitra, D., and Brandt, L. (2013). Shear thickening in non-Brownian suspensions: an excluded volume effect. *Phys. Rev. Lett.* 111:098302.

Qin, J., Zhang, G., and Shi, X. (2017). Shear thickener and its composite materials. *Eng. Design Guides* 31, 59–64.

Seto, R., Mari, R., Morris, J. F., and Denn, M. B. (2013). Discontinuous shear thickening of frictional hard-sphere suspensions. *Phys. Rev. Lett.* 111:218301.

Trulsson, M., Andreotti, B., and Claudin, P. (2012). Transition from the viscous to inertial regime in dense suspensions. *Phys. Rev. Lett.* 109:118305.

Wei, X., Sun, R., and Wang, Q. (2017). Properties of shear thickening liquid and its application in flexible stab resistant materials. *Synthet. Fiber* 46, 40–43.

Wu, Z. (2018). *Study on Energy Consumption Characteristics of Shear Thickening Liquid and Its Application in Vehicle Impact Resistance*. Nanjing: Nanjing University of Aeronautics and Astronautics.

Wyart, M., and Cates, M. E. (2014). Discontinuous shear thickening without inertia in dense non-Brownian suspensions. *Phys. Rev. Lett.* 112:098302.

Xu, Z., Shen, Y., and Guo, Y. (2003). Semi-active control of structures incorporated with magnetorheological dampers using neural networks. *Smart Mater. Struct.* 12, 80–87. doi: 10.1088/0964-1726/12/1/309

Xu, Z. D., Liao, Y. X., Ge, T., and Xu, C. (2016). Experimental and theoretical study of viscoelastic dampers with different matrix, rubbers. *J. Eng. Mech.* 2016:04016051. doi: 10.1061/(asce)em.1943-7889.0001101

Xu, Z. D., and Shen, Y. P. (2003). Intelligent Bi-state control for the structure with magnetorheological dampers. *J. Intellig. Mater. Syst. Struct.* 14, 35–42. doi: 10.1177/1045389x03014001004

Yang, Y., Xu, Z.-D., Xu, Y.-W., and Guo, Y.-Q. (2020). Analysis on influence of the magnetorheological fluid microstructure on the mechanical properties of magnetorheological dampers. *Smart Mater. Struct.* 29:115025. doi: 10.1088/1361-665x/abadd2

Yi, C. (2011). *Preparation, Performance Test and Constitutive Model of MR Fluid*. Chongqing: Chongqing University.

Ying, Q., Wen, H. X., and Jing, X. (2019). Study on structures incorporated with MR damping material based on PSO algorithm. *Front. Mater.* 6:37. doi: 10.3389/fmats.2019.00037

Yu, G., Du, C., and Wan, F. (2012). Design and performance test of high energy consumption self decoupling MR damper. *Vibr. Test Diagn.* 32, 426–431.

Yu, M., Li, B., Niu, Z., Xue, W., and Zhao, P. (2019). Study on dynamic characteristics of variable damping vibration isolator based on shear thickening liquid. *Equip. Environ. Eng.* 16, 33–38.

Zhang, X. Z., Li, W. H., and Gong, X. L. (2008). The rheology of shear thickening fluid (STF) and the dynamic performance of an STF-filled damper. *Smart Mater. Struct.* 17, 035027.1–035027.7.

Zhao, P., Yu, M., Chen, Q., and Wu, Z. (2018). Buffer mechanism and mechanical properties of shear thickening liquid. *J. Vibr. Eng.* 31, 966–973.

Zhou, H., Yan, L. X., Jiang, W. Q., Xuan, S. H., and Gong, X. (2016). Shear thickening fluid-based energy-free amper: design and dynamic characteristics. *J. Intellig. Mater. Syst. Struct.* 27, 208–220. doi: 10.1177/1045389x14563869

Zhou, Y., Zhu, W., and Rui, X. (2017). Design and performance analysis of dual exit MR damper. *Noise Vibr. Control.* 37, 178–181.

Zhu, W., Tong, Y., Yu, X., Fan, S., and Ju, B. (2019). Preparation and properties of nano iron particle magnetorheological fluid. *Astronaut. Gen. Technol.* 3, 56–61.

Conflict of Interest: The authors declare that the research was conducted in the absence of any commercial or financial relationships that could be construed as a potential conflict of interest.

Advantages of publishing in Frontiers

OPEN ACCESS
Articles are free to read for greatest visibility and readership

FAST PUBLICATION
Around 90 days from submission to decision

HIGH QUALITY PEER-REVIEW
Rigorous, collaborative, and constructive peer-review

TRANSPARENT PEER-REVIEW
Editors and reviewers acknowledged by name on published articles

Frontiers
Avenue du Tribunal-Fédéral 34
1005 Lausanne | Switzerland

Visit us: www.frontiersin.org
Contact us: frontiersin.org/about/contact

REPRODUCIBILITY OF RESEARCH
Support open data and methods to enhance research reproducibility

DIGITAL PUBLISHING
Articles designed for optimal readership across devices

FOLLOW US
@frontiersin

IMPACT METRICS
Advanced article metrics track visibility across digital media

EXTENSIVE PROMOTION
Marketing and promotion of impactful research

LOOP RESEARCH NETWORK
Our network increases your article's readership